

REPORT 12

# METALLURGICAL RESEARCH AND DEVELOPMENT FOR CERAMIC ELECTRON DEVICES

## FINAL REPORT

1 JULY 1962 — 30 JUNE 1965

TR-66-1

R/E-66-115

Prepared For

**U.S. ARMY ELECTRONICS COMMAND**

Fort Monmouth, New Jersey 07703

D. A. TASK NUMBER OST - 7776 - 11 - 017 - 38

CONTRACT NUMBER DA 36 - 039 SC- 90903

CLEARINGHOUSE FOR FEDERAL SCIENTIFIC AND TECHNICAL INFORMATION			
Hardcopy	Microfiche		
\$ 8.00	\$ 2.25	494	PP 12
ARCHIVE COPY			



DIVISION OF VARIAN

301 Industrial Way  
San Carlos, California

DISTRIBUTION OF THIS DOCUMENT IS UNLIMITED

AD 636950

AUG 18 1965

# NOTICES

## DISCLAIMERS

The findings in this report are not to be construed as an official Department of the Army position, unless so designated by other authorized documents.

The citation of trade names and names of manufacturers in this report is not to be construed as official Government indorsement or approval of commercial products or services referenced herein.

## DISPOSITION

Destroy this report when it is no longer needed. Do not return it to the originator.

Report No. 12

METALLURGICAL RESEARCH & DEVELOPMENT

FOR

CERAMIC ELECTRON DEVICES

Final Report

Prepared for

U. S. ARMY ELECTRONICS COMMAND

FT. MONMOUTH, NEW JERSEY 07703

D. A TASK NO. OST-7900-21-223-15

CONTRACT NO. DA 36-039 SC-90903

EIMAC, DIVISION OF VARIAN ASSOCIATES  
301 Industrial Way  
San Carlos, California

TR-66-1  
R/E 66-115

DISTRIBUTION OF THIS DOCUMENT IS UNLIMITED

REPORT NO. 12

FINAL REPORT

METALLURGICAL RESEARCH & DEVELOPMENT  
FOR CERAMIC ELECTRON DEVICES

1 July 1962 - 30 June 1965

OBJECT OF STUDY:

To examine the basic mechanisms of adherence in ceramic-to-metal seals and the problems connected with the use of such seals in electron tubes. The rf properties of the seal shall receive particular attention.

By: L. Reed  
W. Wade  
S. Vogel  
R. McRae  
C. Barnes

This research is a part of project DEFENDER sponsored by the Advanced Research Projects Agency, Department of Defense, under ARPA Order No. 318-62 Project Code No. 7300, and was conducted under the technical guidance of the U. S. Army Electronics Command, Fort Monmouth, New Jersey, 07703.

CONTRACT NO. DA 36-039 SC-90903  
DA TASK NO. OST-7900-21-223-15

  
L. Reed, Manager  
Research & Sp. Engineering

EIMAC, DIVISION OF VARIAN ASSOCIATES  
Final Report  
January 1966

DISTRIBUTION OF THIS DOCUMENT IS UNLIMITED



## TABLE OF CONTENTS

<u>SECTION</u>		<u>PAGE NO.</u>
1.0	PURPOSE	1
	1.1 Purpose of Contract	1
	1.2 Objective of Program	1
	1.3 Tasks	1
2.0	ABSTRACT	3
3.0	PUBLICATIONS, LECTURES, REPORTS AND CONFERENCES	5
4.0	TASK 1 SEAL PARAMETER STUDY	8
	4.1 General Ceramic Considerations	10
	4.2 Special Ceramics	15
	4.2.1 Introduction	15
	4.2.2 Microstructure Consider- ations	19
	4.2.3 The Glassy Phase	34
	4.3 Commercial Bodies- Microstructure Considerations	101
	4.4 Exploratory Metallizing Studies	107
	4.4.1 Introduction	107
	4.4.2 The Paint	114
	4.4.3 Firing Conditions	114
	4.4.4 Sintering of the Metalli- zing	114
	4.4.5 Solution of Molybdenum	120
	4.4.6 Adherence	122
	4.4.7 Chemical Reduction	123
	4.4.8 Glassy Phase Inter- diffusion	129
	4.4.9 Composition of the Glassy Phase	138
	4.4.10 Seal Strength versus Metallizing Temperature	145
	4.4.11 Seal Strength as a Function of Brazing	147
	4.4.12 Initial Metallizing Tests	150
	4.4.13 Comments on Sealing Mechanisms	158

<u>SECTION</u>		<u>PAGE NO.</u>
4.5	Studies Using the Special Bodies	159
4.5.1	Introduction of Seal Parameter Study	159
4.5.2	Seal Parameter Studies	162
4.5.3	Supplementary Studies	200
4.6	Shear Test Study	220
4.6.1	Sample Geometry	220
4.6.2	Testing Methods	220
4.6.3	Test Results and Discussion	222
4.7	References - Task I	227
5.0	TASK II, BERYLLIA AND QUARTZ STUDY	231
5.1	Beryllia Ceramics	231
5.2	Fused Quartz-to-Metal Seals	241
5.3	References - Task II	243
6.0	TASK III - ELECTRICAL STUDIES	244
6.1	General Introduction	244
6.1.1	Sources of Electrical Loss	244
6.1.2	Electrical Properties as a Function of Micro- structure and Chemistry	245
6.1.3	Program of Experimental Studies	248
6.2	d.c. Electrical Measurements	249
6.2.1	Temperature Coefficient of d.c. Resistivity of Metallizing	249
6.2.2	Effect of Wetting Layer (Overplate) on the Resistivity of the Metallizing	277

<u>SECTION</u>		<u>PAGE NO.</u>
6.3	rf CONDUCTION LOSS MEASUREMENTS	285
6.3.1	Introduction	285
6.3.2	Selected Measurement Technique	287
6.3.3	Sample Preparation	287
6.3.4	Equipment and Experimental Procedures	291
6.3.5	Equipment Checkout	300
6.3.6	Results	306
6.3.7	Discussion of Results	316
6.4	Dielectric Losses	350
6.4.1	Introduction	350
6.4.2	Sample Preparation and Experimental Set-up	353
6.4.3	Experimental Procedure and Results	359
6.4.4	Discussion	366
6.4.5	Comparison of Various Metallizings on +99% Alumina Bodies	380
6.5	High Power Measurements	390
6.5.1	Introduction	390
6.5.2	Calorimetric Test Cell	391
6.5.3	Cold Testing	397
6.5.4	Calorimetric Instrumentation	398
6.5.5	Calorimetric Measurements	404
6.6	References - Task III	429
7.0	SUMMARY	430
7.1	Introduction	430
7.2	Basic Seal Considerations	430
7.3	Supporting Studies	433
7.4	Electrical Studies	439
8.0	CONCLUSIONS	442
9.0	RECOMMENDATIONS	444

<u>SECTION</u>	<u>PAGE NO.</u>
10.0 ACKNOWLEDGEMENTS	445
11.0 SUBCONTRACTS	446
12.0 IDENTIFICATION OF KEY TECHNICAL PERSONNEL	447
13.0 APPENDIX I - Factors Influential in Bonding Ceramics to Metals	449
14.0 APPENDIX II - Detailed Table of Contents	454

## LIST OF FIGURES

<u>FIGURE NO.</u>		<u>PAGE NO.</u>
4.01	Tensile test piece B	13
4.02	Tensile test piece A (CLM-15)	14
4.03	Revised pseudo-binary phase equilibrium diagram of the $\text{CaO/SiO}_2\text{-Al}_2\text{O}_3$ system derived from the ternary $\text{CaO-SiO}_2\text{-Al}_2\text{O}_3$ diagram	17
4.04	Revised pseudo-binary phase equilibrium diagram of the $2 \text{ SiO}_2/\text{CaO-Al}_2\text{O}_3$ system derived from the ternary $\text{CaO-SiO}_2\text{-Al}_2\text{O}_3$ diagram	18
4.05	Model of two spherical particles, radius R, showing sintering by volume diffusion, indicating the flux of vacancies (and counter-flow of material) from a lens of radius of curvature $R_1$ to an internal grain boundary.	20
4.06	Surface tension forces, F, due to a pressure $\Delta P = \frac{-2 \gamma}{r}$ acting as a solid-melt-solid interface causing increased solubility of the solid. r is the radius of curvature indicated.	23
4.07	Particle size distribution of Alcoa A-14 alumina before processing.	25
4.08	Average grain size of 941, 942, 992 and Body G as a function of firing temperature. Time at temperature was three hours.	26
4.09	Microstructure of 941 ceramic (400X)	29
4.10	Microstructure of 942 ceramic (400X)	30
4.11	Microstructure of 992 ceramic (400X)	31
4.12	Modulus of rupture of the 941, 942 and 992 bodies	35

<u>FIGURE NO.</u>		<u>PAGE NO.</u>
4.13	Atomic model of glass structure (after Zachariassen).	36
4.14	Electron photomicrographs (3500X) of polished surfaces of special alumina bodies (a) 941 (1700), (b) 941 (1650), (c) 941 (1600), and (d) 941 (1550). The numbers in parentheses are the body firing temperatures in °C.	45
4.15	Electron photomicrographs (3500X) of polished surfaces of special alumina bodies (a) 942 (1750), (b) 942 (1700), (c) 942 (1650), and (d) 942 (1600). The numbers in parentheses are the body firing temperatures in °C.	46
4.16	Electron photomicrographs (3500X) of polished surfaces of special alumina bodies (a) 992 (1800), (b) 992 (1750), and (c) 992 (1700). The numbers in parentheses are the body firing temperatures in °C.	47
4.17	Schematic presentation of a typical glassy phase region of a high alumina ceramic showing the effects of polishing the surface.	50
4.18	Electron photomicrograph of 941 alumina ceramic at 21,500X magnification showing the glassy phase between the grain boundaries of alumina particles.	56
4.19	Electron photomicrograph of 942 ceramic at 21,500X magnification showing the glassy phase spreading over the alumina crystal and in the grain boundaries between the alumina ceramic.	57
4.20	Electron photomicrograph of 992 body at 21,500X magnification showing the glassy phase.	58
4.21	Glass-sapphire corrosion samples with 1:1 SiO <sub>2</sub> /CaO glass containing no Al <sub>2</sub> O <sub>3</sub> initially. Samples were reacted at (a) 1500°C (b) 1675°C (c) 1750°C. The glass is the wide band across the center of each photograph.	64

FIGURE NO.PAGE NO.

- |      |  |    |
|------|--|----|
| 4.22 | Glass-sapphire corrosion samples with 1:1 SiO <sub>2</sub> /CaO glass containing 20% Al <sub>2</sub> O <sub>3</sub> initially. Samples were reacted at (a) 1500°C and (b) 1675°C. The glass is in the band across the center of each photograph (400X).  | 65 |
| 4.23 | Glass-sapphire corrosion samples with 1:1 SiO <sub>2</sub> /CaO glass containing 40% Al <sub>2</sub> O <sub>3</sub> initially. Samples were reacted at (a) 1500°C and (b) 1675°C. The glass is in the wide band across the center of the top photograph and in the lower two-thirds of the bottom photograph. (400X)   | 66 |
| 4.24 | Viscosity versus Al <sub>2</sub> O <sub>3</sub> content for melts with 1:1 SiO <sub>2</sub> /CaO ratio. Dash lines indicate probable viscosity of supercooled melt at indicated temperature.   | 74 |
| 4.25 | Viscosity versus Al <sub>2</sub> O <sub>3</sub> content for melts with 2:1 SiO <sub>2</sub> /CaO ratio. Dash lines indicate probable viscosity of supercooled melt at indicated temperature.   | 75 |
| 4.26 | Self-diffusion values for oxygen <sup>12</sup> (1), silicon <sup>11</sup> (2), aluminum <sup>13</sup> (3), and calcium <sup>11</sup> (4) for melt C and aluminum <sup>13</sup> (5) for melt B, together with values of "convective diffusion" for melts C (6) and D (7) derived from alumina solution in these melts <sup>15</sup> . Also included are estimated Ca <sup>2+</sup> values for melt B (8) obtained by extrapolating data contained in reference 30. (See text for key to melts.) | 79 |
| 4.27 | Coefficient of thermal expansion versus Al <sub>2</sub> O <sub>3</sub> content of three glass compositions.  | 84 |
| 4.28 | Schematic diagram of contact angle experiment and cross-section of sessile drop.   | 86 |
| 4.29 | Schematic cross-section of furnace used in wetting angle study.  | 90 |
| 4.30 | Contact angle versus dewpoint of 1:1 SiO <sub>2</sub> /CaO melts on sapphire.  | 93 |

<u>FIGURE NO.</u>		<u>PAGE NO.</u>
4.31	Contact angle versus dewpoint of 2:1 SiO <sub>2</sub> /CaO melts on sapphire.	94
4.32	Contact angle versus dewpoint of 3:1 SiO <sub>2</sub> /CaO melts on sapphire.	95
4.33	Contact angle versus dewpoint of 1:1 SiO <sub>2</sub> /CaO melts on molybdenum.	96
4.34	Contact angle versus dewpoint of 2:1 SiO <sub>2</sub> /CaO melts on molybdenum.	97
4.35	Contact angle versus dewpoint of 3:1 SiO <sub>2</sub> /CaO melts on sapphire.	98
4.36	Ceramographic cross-section of Body A showing tabular alumina crystal form and the glassy phase situated between the grains. (400X).	102
4.37	Electron photomicrograph of Body A showing the glassy phase in the boundaries between the alumina grains. (24,200X)	103
4.38	Electron photomicrograph of Body A after a thermal etch at 1100°C in dry hydrogen. (18,400X)	104
4.39	Electron photomicrograph of Body A after a thermal etch at 1100°C in wet hydrogen. (28,000X)	105
4.40	Electron photomicrograph of Body A after a thermal etch at 1100°C in air. (28,000 X)	106
4.41	The microstructures of three +99% alumina bodies investigated in the seal parameter and electrical studies.	108
4.42	Particle size distribution for P-1 metallizing paint obtained by using a Coulter counter.	112
4.43	Particle size distribution for P-4M metallizing paint obtained by using a Coulter counter.	113



<u>FIGURE NO.</u>		<u>PAGE NO.</u>
4.44	Density versus composition of molybdenum-glass composites sintered at 1425°C.	118
4.45	Density versus composition of molybdenum-glass composites sintered at 1600°C.	119
4.46	Analysis of gases evolved from a metallizing paint in the form of a layer 1" x 1" by 10 mils thick on alumina ceramic, under non-equilibrium conditions.	125
4.47	Percent weight loss of P-1 metallizing on Body A as a function of unfired sprayed weight of coating.	126
4.48	Unfired sprayed weight of metallizing paints P-1 and P-2 on Body A versus microscopically measured fired thickness. Supersedes curve of third quarterly report. Firing time was 1/2 hour at 1425°C.	127
4.49	P-2 metallizing on Body A sintered at 1425°C for 1/2 hour in a H <sub>2</sub> /3N <sub>2</sub> , + 100°C dewpoint atmosphere. The copper plate, copper braze to cupro-nickel can be seen to infiltrate the porous molybdenum sponge.	128
4.50	P-1 metallizing on Body A. Sinter fired at 1425°C for 1/2 hour in a H <sub>2</sub> /3N <sub>2</sub> , + 100°F dewpoint atmosphere. Close inspection of the glassy interfacial layer between the metallizing and ceramic reveals its crystalline nature. Copper plate, Au-Cu-Ni braze to 70/30 cupro-nickel at 1040°C/10 minutes.	130
4.51	Photomicrographs of P-1 on Body A showing relationship between glassy interaction zone thickness and metallizing thickness (400X).	131
4.52	Electron probe microanalysis trace scan across Body A, P-1 metallizing processed at 1425°C, 1/2 hour, H <sub>2</sub> /3N <sub>2</sub> atmosphere, +80°F dew point.	132
4.53	Electron probe micro-analysis trace for silicon across entire seal region giving evidence of glassy phase migration.	133

<u>FIGURE NO.</u>		<u>PAGE NO.</u>
4.54	Interpreted electron probe microanalysis trace averaged over four scans of P-1 metallizing on Body A.	134
4.55	Interpreted electron probe microanalysis trace averaged over four scans of P-1 metallizing on Body A. Continuation of Fig. 4.54.	137
4.56	Electron photomicrograph of metallizing P-1 on Body A (nicoro braze) metallized at 1425°C for 1/2 hour. (8000X)	144
4.57	Seal tensile strength with P-1 metallizing on Body A versus metallizing sintering temperature.	146
4.58	P-2 metallizing on Body E, 99% alumina. Metallized at 1425°C for 1/2 hour.	152
4.59	Top: Body H, 3 $\mu$ evaporated molybdenum metallizing, copper braze, P-1 metallizing - Body A.  Bottom: Body H, 1 $\mu$ , evaporated molybdenum metallizing copper braze 70/30 cupro-nickel metal member.	160
4.60	Lucalox* cylinder (top) and sapphire disc (bottom) assembled for leak check and tensile testing.	168
4.61	Plots of tensile strength of ceramic-to-metal seals on 941 alumina bodies originally fired at 1550°C, 1600°C, 1650°C, and 1700°C versus metallizing temperature.	177
4.62	Plots of tensile strength of ceramic-to-metal seals on 942 alumina bodies originally fired at 1600°C, 1650°C, 1700°C, and 1750°C versus metallizing temperature.	178

---

\*General Electric Co. Trade Name.

<u>FIGURE NO.</u>		<u>PAGE NO.</u>
4.63	Plots of tensile strength of ceramic-to-metal seals on 992 alumina bodies originally fired at 1700°C, 1750°C, and 1800°C versus metallizing temperature.	179
4.64	Plots of peel strength of ceramic-to-metal seals brazed with copper on 941 alumina bodies originally fired at 1550°C, 1600°C, 1650°C, and 1700°C versus metallizing temperature.	180
4.65	Plots of peel strength of ceramic-to-metal seals brazed with copper on 942 alumina bodies originally fired at 1600°C, 1650°C, 1700°C and 1750°C versus metallizing temperature.	181
4.66	Plots of peel strength of ceramic-to-metal seals brazed with copper on 992 alumina bodies originally fired at 1700°C, 1750°C, and 1800°C versus metallizing temperature.	182
4.67	Plots of peel strength of ceramic-to-metal seals brazed with CuAg on 941 alumina bodies originally fired at 1550°C, 1600°C, 1650°C, and 1700°C versus metallizing temperature.	183
4.68	Plots of peel strength of ceramic-to-metal seals brazed with CuAg on 942 alumina bodies originally fired at 1600°C, 1650°C, 1700°C, and 1750°C versus metallizing temperature.	184
4.69	Plots of peel strengths of ceramic-to-metal seals brazed with CuAg on 992 alumina bodies originally fired at 1700°C, 1750°C, 1800°C versus metallizing temperature.	185
4.70	Photomicrographs of ceramic-to-metal seals on alumina body 941 (1550) metallized with P-4M at 1300°C (top) and 1800°C (bottom) showing the structural changes which occur when the ceramic is metallized at very high temperatures. (400X)	189

**FIGURE NO.****PAGE NO.**

- |      |   |     |
|------|---|-----|
| 4.71 | Photomicrographs of ceramic-to-metal seals on alumina body 942 (1650) (top) and 992 (1800) (bottom) both metallized with P-4M at 1800°C. Interlocking grain structure may be seen at the interface between the molybdenum metallizing and the alumina surface. (400X) | 191 |
| 4.72 | Photomicrographs of ceramic-to-metal seals on alumina body 942 (1700) made with P-4M metallizing sintered at 1425°C (top) and 1600°C (bottom). The glassy phase migrated into the metallizing when sintered at 1600°C, but not at 1425°C. (400X)                      | 194 |
| 4.73 | Photomicrographs of ceramic-to-metal seals on Lucalox* (top) and alumina ceramic 941 (1600) (bottom) both metallized with P-4M at 1800°C. The molybdenum metallizing was etched for 4 sec. with a solution of potassium ferricyanide and sodium hydroxide. (800X)     | 196 |
| 4.74 | Peel strength versus secondary crystallite level in 941 ceramic after simulated braze cycles in dry hydrogen at 1100°C for various times. Kovar (K) or cupro-nickel (CN) peel tabs subsequently brazed at 800°C with Cu-Ag.   | 209 |
| 4.75 | Secondary crystallite level and peel strength of 941 ceramic after simulated braze cycles in dry hydrogen at 1100°C for various times. Kovar peel tabs subsequently brazed at 800°C with Cu-Ag.   | 210 |
| 4.76 | Peel strength versus secondary crystallite level in 941 ceramic after simulated braze cycles in wet hydrogen at 1100°C. Kovar peel tabs subsequently brazed at 800°C using Cu-Ag. Numbers indicate time of simulated braze cycle.                                     | 211 |

---

\*General Electric Co. Trade Name.

FIGURE NO.PAGE NO.

- |      |   |     |
|------|---|-----|
| 4.77 | Secondary crystallite level and peel strength of 941 ceramic as a function of the length of time of simulated braze cycles at 1100°C in wet hydrogen. Kovar peel tabs subsequently brazed at 800°C with Cu-Ag.                    | 212 |
| 4.78 | Peel strength versus secondary crystallite level in 942 ceramic after simulated braze cycles in dry hydrogen at 1100°C for various times. Kovar (K) on cupro-nickel (CN) peel tabs subsequently brazed at 800°C with Cu-Ag.       | 213 |
| 4.79 | Secondary crystallite level and peel strength of 942 ceramic after simulated braze cycles in dry hydrogen at 1100°C for various times. Kovar peel tabs subsequently brazed at 800°C with Cu-Ag.                                   | 214 |
| 4.80 | Peel strength versus secondary crystallite level in 942 ceramic after simulated braze cycles in wet hydrogen at 1100°C. Kovar peel tabs subsequently brazed at 800°C using Cu-Ag. Numbers indicate time of simulated braze cycle. | 215 |
| 4.81 | Secondary crystallite level and peel strength of 942 ceramic as a function of the length of time of simulated braze cycles at 1100°C in wet hydrogen. Kovar peel tabs subsequently brazed at 800°C with Cu-Ag.                    | 216 |
| 4.82 | Shear test assembly consisting of two cylinders joined with an O.D.-I.D. braze.   | 221 |
| 4.83 | Concentric cylinder shear test specimen in loading position in Instron testing machine.   | 223 |
| 5.01 | Microstructure of a 96% beryllia ceramic (400X) which shows similar characteristics to a 96% alumina ceramic.   | 232 |
| 5.02 | Microstructure cross-section of a ceramic metal seal of P-1 metallizing paint on a 96% beryllia ceramic (400X).   | 233 |

<u>FIGURE NO.</u>		<u>PAGE NO.</u>
5.03	Photomicrographs of P-3 metallizing sintered at 1325°C (top) and 1425°C (bottom) on beryllia body BB. Cu-Au 60/40 braze, copper braze washer (400X).	234
5.04	Electron microprobe trace of seal made with metallizing paint P-3 on beryllia body BA.	236
5.05	Electron microprobe trace of seal made with metallizing paint P-3 on beryllia body BB.	237
5.06	Photomicrograph of fused quartz-to-metal seal. The thickness of the deposited molybdenum layer is near the limit of resolution of the microscope. (400X)	242
6.01	Schematic representation of Fig. 4.50 illustrating the electrical path length and width through the metallizing.	247
6.02	Measurement of thermal coefficient of resistivity in metallizing on ceramic. Test sample strapped to ceramic heater.	251
6.03	Circuitry for measurement of thermal coefficient of resistivity.	253
6.04	Resistance versus temperature of test sample No. 10 (metallizing P-3 on Body A).	254
6.05	Measured resistance ratio $R_T/R_0$ of three samples as a function of temperature.	255
6.06	Measured resistance ratio vs temperature of test samples. 1) molybdenum strip, 0.002" thick, unannealed. 2) molybdenum strip, 0.001" thick, unannealed. 3) molybdenum strip, 0.001" thick, annealed. 13) P4-M on Body A. 14) P4-M on Body E ceramic. 26) molybdenum, evaporated on Body E ceramic. 27) molybdenum evaporated on Body E ceramic, fired at 1425°C for 1/2 hour in wet hydrogen-nitrogen atmosphere.	261

FIGURE NO.PAGE NO.

- 6.07 Measured resistance ratios vs temperature of test samples. 1) molybdenum strip, 0.002", unannealed. 4) P-1 on Body A ceramic. 5) P-1 on Body A ceramic, thickness reduced by machining. 6) P-1 on Body A ceramic, partly leached with nitric acid. 18) P-1 on Body A ceramic, fired at 1600°C. 262
- 6.08 Measured resistance ratios vs temperature of test samples. 1) molybdenum strip, 0.002", unannealed. 7) paint P-1 on Body E ceramic. 8) paint P-1 on Body E, thickness slightly reduced by machining. 9) paint P-1 on Body E thickness further reduced. 22) P-1 (modified with 1/6 molybdenum content of regular P-1 paint) on Body E ceramic. 263
- 6.09 Measured resistance ratios vs temperature of test samples. 1) molybdenum strip, 0.002" thick, unannealed. 10) paint P-3 on Body A ceramic. 11) paint P-3 on Body A ceramic, thickness reduced by machining. 12) paint P-3 on Body E ceramic. 264
- 6.10 Measured resistance ratio vs temperature of test samples. 7) paint P-1 on ceramic Body E. 24) paint P-1 on ceramic, slightly electropolished. 25) paint P-1 on ceramic Body E, heavily electropolished. 265
- 6.11 Measured resistance ratios vs temperature of test samples. 4) paint P-1 on ceramic Body A. 15) paint Ti-11 on ceramic. 16) paint Ti-11 on ceramic Body A, slightly machined. 17) paint Ti-11 on ceramic Body A, leached with nitric acid. 19) paint Ti-11 on ceramic Body A, heavily leached with nitric acid. 28) paint Ti-11 on ceramic Body E, oxidized in air. 29) paint Ti-11 on ceramic Body E, heavily oxidized in air. 266
- 6.12 Photomicrographs (400X) of test samples. Metallizings in a), b), c) have been overlaid after the measurements. 267

<u>FIGURE NO.</u>		<u>PAGE NO.</u>
6.13	Photomicrographs (400X) of test samples. Metallizings have been overplated after the measurements.	268
6.14	Photomicrographs (400X) of test samples. Metallizings in a), b), c) have been overplated after the measurements.	269
6.15	Interaction of Ni wetting layer with P-1 metallizing on Body A ceramic. Relative resistance as a function of processing steps. Data obtained from four samples of Group I, Table 6-4.	280
6.16	Interaction of Ni wetting layer with P-1 metallizing on Body A. Relative resistance as a function of processing steps. Data obtained from four samples of Group 2, Table 6-4.	281
6.17	Interaction of Ni wetting layer with P-1 metallizing on Body A. Relative resistance as a function of processing steps. Data obtained from four samples of Group 3, Table 6-4.	282
6.18	Interaction of Cu wetting layer with P-1 metallizing on Body A ceramic. Relative resistance as a function of processing steps.	283
6.19	Relative resistance of metallized and overplated Body A substrates as a function of sinterfiring. (1) 0.3 mil metallizing, 0.07 mil Ni-plate; (2) 0.3 mil metallizing, 0.02 mil Ni-plate; (3) 0.6 mil metallizing, 0.07 mil Ni-plate; (4) 0.5 mil metallizing, 0.3 mil Cu-plate.	284
6.20	RF conductivity test assembly. Showing layered structure of an iron barrier layer seal and showing back up ceramic used to reduce seal stresses.	289
6.21	Block diagram of admittance bridge equipment for measuring $I^2R$ conduction losses in metallizing.	292



<u>FIGURE NO.</u>		<u>PAGE NO.</u>
6.22	Close-up of admittance bridge showing Magic-T and matched resonators. Ceramic samples in foreground.	293
6.23	Admittance bridge equipment.	294
6.24	Admittance bridge test resonator.	295
6.25	Plot of micrometer reading versus published resistivity of the six calibration assemblies (see text). Selected data from actual seals included for reference.	302
6.26	Plot of relationship between concentricity of ceramic-metal seal in test cavity, $\Delta TIR$ , and change in measured cavity loss (in mils of insertion of lossy material into standard cavity) as sample holder is rotated.	304
6.27	$Q_0$ of standard cavity used in conduction loss measurement plotted as a function of micrometer reading. Selected data giving the various $Q$ 's of the test cavity with various assemblies including the standard are included for reference.	305
6.28	Skin depth at 9.15 Gc versus electrical resistivity.	318
6.29	Photomicrographs (400X) of sample #226, a seal with active metals evaporated on a polished ceramic (top), and sample #228 with copper evaporated on a polished ceramic (bottom).	327
6.30	Photomicrographs of P-2 metallizing fired at 1425°C (top) and 1550°C (bottom). Subsequently copper plated, Fe barrier layer, Cu-Ag braze (400X).	329
6.31	Conductive loss data for P-2 metallizing on Body A. Metallizing sintered at 1425°C unless otherwise noted.	330

<u>FIGURE NO.</u>		<u>PAGE NO.</u>
6.32	Conductive loss data for P-1 on Body A. Metallizing sintered at 1425°C.	333
6.33	Photomicrographs of Cu-Ag braze penetration through Fe barrier layer into Cu (top) and Ni (bottom) metallizing overplate (400X).	334
6.34	Microprobe analysis of iron barrier layer seal. Data was averaged.	335
6.35	Microprobe analysis of iron barrier layer seal described in text showing silver scan across seal in the region of a grain boundary discontinuity in the iron barrier layer.	336
6.36	Photomicrograph of conduction loss sample #93 (P-1, Body A, Cu plate, Fe barrier layer, Cu-Ag braze). (850X).	337
6.37	Microprobe analysis of Mo and Cu in conduction loss sample #93 (P-1 Body A, Cu plate Fe barrier layer, Cu-Ag braze). Ag and Ni were below limit of detectability. Scans were parallel to metallizing -- ceramic interface 0.0005 in. into metallizing.	338
6.38	Schematic cross-section of ceramic-to-metal seal with iron-nickel barrier layer (top); photomicrograph (400X) of sample #207 (bottom).	340
6.39	Plot of $I^2R$ losses at 9.15 Gc versus metallizing thickness for P-1 on Body A with overplate of copper or nickel. All specimens were prepared with a barrier layer and a CuAg eutectic braze and 70/30 Cu-Ni metal member (see text).	341
6.40	Photomicrograph (400X) of sectioned sample #205, showing failure of barrier layer and detachment of portion of metallizing. See Table 6-8 for data.	342
6.41	Photomicrographs (400X) of sectioned sample #205 showing disruption of iron barrier layer (dark) and partial dissolution of copper overplate. See Table 6-8 for data.	343

FIGURE NO.PAGE NO.

6.42	Photomicrographs (400X) of samples #200 (top) with 53 units of relative loss, #201 (center) with 66 units of relative loss, #202 (bottom) with 88 units of relative loss. See Table 6-8 for data.	345
6.43	Photomicrographs (400X) of sample #224 (top) and sample #225 (bottom).	346
6.44	$I^2R$ (conduction) losses versus metallizing thickness for P-1 on Lucalox* with overplate of copper or nickel. The specimens were prepared with a barrier layer and a CuAg eutectic braze (see text).	349
6.45	Resonator for dielectric loss measurements.	352
6.46	Redesigned dielectric loss cavity.	354
6.47	Block diagram of "Q" measurement for dielectric loss data at ceramic-metal seal interface.	356
6.48	Block diagram of "Q" measurement for dielectric loss data at ceramic-to-metal seal interface.	357
6.49	Typical data plot and Q calculation for dielectric loss measurement.	360
6.50	Dielectric loss factor for selected ceramic bodies versus frequency. Values are from manufacturers' data sheets.	368
6.51	Dielectric loss for alumina bodies versus frequency.	369
6.52	The dielectric test cavity Q as a function of ceramic disc thickness.	370
6.53	Loss factor at 2 Gc versus dielectric loss test cavity $Q_0$ plotted from manufacturers loss figures and test data on Body A, Body H and Linde Sapphire. The line is drawn through the values obtained during the second test series. The $Q_0$ intercepts of three selected data points are indicated for reference only (see text).	371

---

\*General Electric Co. Trade Name.

FIGURE NO.PAGE NO.

- |      |   |     |
|------|---|-----|
| 6.54 | Photomicrograph of Body H test sample (400X) #95 (500 Å Ti, 5,000 Å Mo evaporated, Cu plated to 0.17 mil)   | 375 |
| 6.55 | Reduction in cavity Q resulting from noted metallizing paint only on 0.060" thick Body A ceramic discs. Test frequency 2 Gc. Sintering time 1/2 hour at 1425°C unless noted. Single surface metallized unless noted.                                  | 376 |
| 6.56 | Reduction in cavity Q resulting from noted metallizing paint only on 0.060" thick Body H ceramics 99.5% Al <sub>2</sub> O <sub>3</sub> . Test frequency 2 Gc. Sintering time 1/2 hour at 1425°C unless noted. Single surface metallized unless noted. | 377 |
| 6.57 | Photomicrographs of Body H test samples (400X). Top: #81A (1.6 mil of P-1 metallizing). Bottom: #82A (1.7 mil of P-1 metallizing, leached).   | 381 |
| 6.58 | Photomicrograph of Body H test sample (400X) #78 S2 (0.5 mil of P-1 metallizing, leached and sanded off).   | 382 |
| 6.59 | Photomicrographs of P-1 (top) and P-7 (bottom) on Linde sapphire. Dielectric loss samples sintered one-half hour at 1425°C (400X).  | 383 |
| 6.60 | Photographs of sectioned dielectric loss specimens (0.200 in. wide by 0.060 in. thick) showing P-1 metallizing diffusion into Body 992 (1750) at 1425°C with increasing time (10X).   | 385 |
| 6.61 | Photomicrographs of P-7 metallizing reaction with Body 992 (1750) at 1425°C for increasing times (400X).  | 386 |
| 6.62 | Dielectric loss test cavity Q <sub>0</sub> with various ceramic samples in gap. The unmetallized and metallized samples were fired at 1425°C for 1/2 hour.  | 387 |

<u>FIGURE NO.</u>		<u>PAGE NO.</u>
6.63	Dielectric loss test cavity $Q_0$ versus 1425°C firing time. Ceramic was Body 992 (1750) in all cases.	388
6.64	Five-channel waveguide test cell used in second series of high power calorimetric loss measurement.	392
6.65	Cross-section of waveguide test cell shown in Fig. 6.64 with three test seals.	393
6.66	Schematic diagram of test set-up for second series of high power calorimetric loss measurements shown also in Figs. 6.70, 6.71 and 6.72.	401
6.67	Schematic diagram of set-up used to calibrate thermopiles for the second series of high power calorimetric loss measurements.	402
6.68	Photograph of thermopile calibration equipment diagrammed in Fig. 6.67.	403
6.69	Block diagram of microwave circuitry used in second series of high power calorimetric loss measurements.	405
6.70	Test set-up for second series of high power calorimeter loss measurements at 8 kmc.	407
6.71	Close-up of test cells and thermopiles in test set-up for second series of high power calorimetric loss measurements.	408
6.72	Close-up of test set-up for second series of high power calorimetric loss measurements showing signal generator (8 kmc), amplifier, and klystron at 1.4 r.	409
6.73	Power loss in dielectric-to-metal seal section of waveguide test cell vs metallizing thickness as a fraction of transmitted power.	418
6.74	Sectioned seals in test cells No. 3 and No. 6.	419

<u>FIGURE NO.</u>		<u>PAGE NO.</u>
6.75	Electron microprobe analyses of seals in test cell No. 3 (top) and No. 6 (bottom).	421
6.76	Top: Body I ceramic with P-1 metallizing, thin nickel plating and Cu-Ag braze. Bottom: Body I ceramic with P-1 metallizing, copper plating, and Cu-Ag braze showing part of a braze gap.	425
7.01	Schematic representation of a metallized layer on a) single crystal sapphire b) a 99.5% alumina body c) a 94% alumina body.	432
7.02	Diagrammatic representation of drum peel and tab peel test fixturing.	434
7.03	a) Schematic diagram of seal showing laminar construction (idealized). b) Application of tensile stress to laminate results in effective opposing of compressive stresses in the lower-modulus, nonmetallic phases, which partially offsets the tensile stress. The lower the modulus for a given material strength (of the reaction zone material) the greater the seal strength. c) Application of shear stress is equally felt by all layers of laminate and weakest layer determines the seal strength.	435
7.04	Ceramic-to-metal seal, using Body E, showing parting in the weakest layer of the seal. Silver-copper braze alloy has penetrated the unplated Kovar giving the weakest zone.	436

# LIST OF TABLES

<u>TABLE NO.</u>		<u>PAGE NO.</u>
4- 1	Nominal Composition in Weight Percent of Ceramic Bodies Referred to in Text	11
4- 2	Manufacture of Special Ceramic Bodies	12
4- 3	Fired Densities versus Firing Temperature (3 hours) for Special Bodies	28
4- 4	Glass Structure as a Function of Network Modifier Ion	37
4- 5	Co-ordination Number and Bond Strength of Oxides	39
4- 6	Anion Complexes in a CaO-SiO <sub>2</sub> -Al <sub>2</sub> O <sub>3</sub> Melt of the 1:1 CaO/SiO <sub>2</sub> Composition and the Correlation with Melt Viscosity (at 1500°C)	41
4- 7	Anion Complexes in a CaO-SiO <sub>2</sub> -Al <sub>2</sub> O <sub>3</sub> Melt of the 1:2 CaO/SiO <sub>2</sub> Composition and the Correlation with Melt Viscosity (at 1500°C)	42
4- 8	Weight Percent Glass Phase from Photomicrograph Measurements	43
4- 9	Crystal Species Present in Ceramic Bodies under Equilibrium Conditions	44
4-10	Summary of X-ray Diffraction Data on Special Alumina Bodies (Interior-Powder Samples)	53
4-11	Some Properties of the Glassy Phase of Special Alumina Bodies	55
4-12	Summary of X-ray Diffraction Data on Special Alumina Bodies (Surface Condition)	59
4-13	Electron Probe Microanalyses of Glass Layer of Sapphire-Glass Sandwiches	67

<u>TABLE NO.</u>		<u>PAGE NO.</u>
4-14	Average Results for Analyses of Glass Zone of Glass-Sapphire Reaction Couples	69
4-15	Contaminants in Phase 2 of Sample #343	72
4-16	Correlation of Sag-Bar Results on the Special Ceramics with Viscosity and Chemical Composition	76
4-17	Percent Thermal Expansion of Crystal Species from 25°C. after Floyd <sup>36</sup> .	81
4-18	Thermal Expansion Coefficients of Glasses	83
4-19	Wettability of Seal Components at 1550-1600°C	88
4-20	Solubility of Metal in Melt	89
4-21	Wetting Angles of Glasses on Molybdenum and Sapphire	92
4-22	Nominal Composition in Weight Percent of Metallizing Paints Referred to in Text	109
4-23	Composition of Metallizing Paints Discussed in Text	110
4-24	Sintering of Molybdenum Powders in an H <sub>2</sub> /3N <sub>2</sub> atmosphere, 30° Dewpoint	115
4-25	Sintered Densities of Glass-Molybdenum Composites	117
4-26	Molybdenum Concentrations in Glasses Melted at Temperature for 1/2 Hour in Molybdenum Boats as Determined by Spectrographic Analysis	121
4-27	Surface Appearance of Metallized Surfaces After Acid Leaching Treatments	139
4-28	Summary of X-Ray Diffraction Analysis	140



<u>TABLE NO.</u>		<u>PAGE NO.</u>
4-29	Relative Amounts of Anorthite Present in Metallizing Layer (Peak Height) and Occurrence of Anorthite Main Peak	141
4-30	Spectrographic Analysis of Leached Metallized Surface Indicating the Strongest $\text{FeO} \cdot \text{Al}_2\text{O}_3$ Concentration 2 - 2B	142
4-31	Spectrographic Analysis Data on Leachates and Swabs from Acid Leached Metallizings P-1 and P-2 on Body A	143
4-32	Tensile Test Results psi on Body A Metal-Ceramic Seals Brazed with Copper, under Various Furnace Conditions	148
4-33	Peel Test Results (Pounds) on Body A Metal-Ceramic Seals	149
4-34	Tensile Strength Results for Pure Refractory Metal and Metal-Oxide Paints on 94%, 97% and 99% Alumina Ceramics. Copper Braze - No Washer	151
4-35	Tensile Test Data of the Special Paints on Body A (94% Alumina) and Body H (99.5% Alumina) Using a Copper Braze and 20 Mil, 70-30 Cupro-Nickel Metal Washer	155
4-36	Spectrographic Analysis of P-4M Metallizing Paint	163
4-37	Metallizing Scratch Hardness	165
4-38	Metallizing Resistance, Ohms	167
4-39	Seal Leak Check	170
4-40	Seal Tensile Strength, psi	171
4-41	Seal Peel Strength, lbs	173
4-42	Tensile Strength of Seals to Polished and Unpolished Lucalox of Three Grain Sizes	192

<u>TABLE NO.</u>		<u>PAGE NO.</u>
4-43	Tab Peel Results	201
4-44	Secondary Phases Found in Ceramic-Metallizing Interface by X-Ray Diffraction Analysis	205
4-45	Peel Strength of Seals to Heat Treated Ceramics, Kovar Unless Otherwise Indicated as Cupro-Nickel (cn)	207
4-46	Secondary Phases Present in Ceramic-Metallizing Interface	208
4-47	Mechanical Properties of Two Frequently Used Metal Members	219
4-48	Shear Test Results Obtained from Concentric Cylinder Specimen Geometry	224
5- 1	Chemical Composition of Beryllia Ceramics	235
5- 2	Beryllia Tensile Test Results I	239
5- 3	Beryllia Tensile Test Results II	240
6- 1	Measured Thermal Coefficients of dc Resistivity	257
6- 2	Metallizing Dimensions and Resistances of Samples in Table 6-1	260
6- 3	Computed Thermal Coefficients of Electrical Resistivity	276
6- 4	Thicknesses of Metallizing and Plating on Representative Test Samples. Measured Resistances, Surface Resistances and Deducted Resistances	278
6- 5	Conduction Loss Data at 9.15 Gc on Body A Test Pieces Glued to Noted Sample Holder	301
6- 6	Series 1, Conduction Loss Data at 9.15 Gc on Body A Test Pieces Sealed to Cupro-Nickel (70-30) with Copper Braze	307

TABLE NO.PAGE NO.

6- 7	Series 2, Conduction Loss Data at 9.15 Gc on Body A Test Pieces with Ag-Cu Braze Sealed to Cupro-Nickel (70-30)	308
6- 8	Series 3, Barrier Layer Seals	311
6- 9	Series 3, Loss in Standard Ceramic-to-Metal Seals	312
6-10	Series 3, Evaporation Metallized Seals	313
6-11	Non-Metallic "Seals"	315
6-12	Room Temperature Resistivity of Selected Copper, Nickel and Molybdenum Alloys	325
6-13	Room Temperature Resistivity of Selected Braze Materials	347
6-14	Series 1, Dielectric Loss Data on Body A (94% $Al_2O_3$ ) as Received and When Painted with Noted Metallizing	361
6-15	Series 1, Dielectric Loss Data on Body H (99.5% $Al_2O_3$ ) as Received and When Coated with Noted Metallizing	362
6-16	Series 2, Dielectric Loss Data at 2Gc on Body H (99.5% $Al_2O_3$ ) and Sapphire with Noted Metallizing, Sintered 1/2 Hour at 1425°C, No Plating. Ceramic Discs Nominally 0.060 inches Thick	364
6-17	Dielectric Loss Data at 2 Gc on Body 992 (1750) with Noted Metallizing. Sintering Time at 1425°C Noted. No Plating. Ceramic Discs Nominally 0.060" Thick	365
6-18	Series 3, Dielectric Loss Data at 2Gc on Body H Test Samples with Noted Metallizing and Subsequent Treatment	367

TABLE NO.PAGE NO.

6-19	Dielectric Loss Increase in Body H (99.5% $\text{Al}_2\text{O}_3$ ) Resulting from Application of P-3 (g), $\text{SiO}_2$ , $\text{TiO}_2$ , $\text{MnO}_2$ Glass, to One Surface	373
6-20	Physical Characteristics of Test Cells	394
6-21	Test Cell VSWR Measurement Results	399
6-22	High Power rf Loss Measurement Results	414

## 1.0 PURPOSE

### 1.1 Purpose of Contract

The purpose of the contract was to investigate the factors contributing to radio frequency power losses in ceramic-to-metal seals and to examine the basic mechanisms of adherence in these seals and the problems connected with their use in electron tubes. Data obtained by other workers gave evidence that heating of the seal region, as distinct from the main portion of the window occurs. This heating is due to rf interactions with the materials in the seal region. Therefore, the specific objectives of this contract were to investigate the factors contributing to rf losses in the seal region and to gain a more fundamental understanding of the various phenomena which combine to effect a mechanically strong, vacuum tight seal with desirable electrical properties.

This contract is part of the window investigations being conducted under Project DEFENDER, a program involving the development of superpower microwave tubes. Other window work under Project DEFENDER included Contract DA 36-039 SC-90818 with Eitel-McCullough on multipactor suppression.

### 1.2 Objectives of Program

The objectives of the program were the following:

- a) To gain a fundamental understanding of the pertinent parameters involved in effecting a ceramic-to-metal seal,
- b) Measurement of the rf losses of ceramic-to-metal seals in order to learn more about their source and nature and their relationship to the metallurgical properties of such seals,
- c) Evaluation of research data accumulated during the program to provide a basis for the fabrication of seals, with improved mechanical and electrical characteristics, and model seals especially suitable for further fundamental studies.

### 1.3 Tasks

To achieve the objectives of the program, the following tasks were pursued:

Task 1 - Investigation of the Pertinent  
Parameters of the Formation of  
Ceramic-to-Metal Seals

Seal parameter studies included work on the following factors which affect seal properties:

- a) Diffusion rates and viscosity of the components of the seal.
- b) Sintering mechanisms of metallizing particles.
- c) Corrosion of alumina by seal components.
- d) Surface tension relationships among the different phases of the seal.
- e) Thermal expansion of the various phases present in the seal.

**Task 2 - Preparation of Seals for Beryllia and Fused Quartz**

Beryllia-to-metal and fused quartz-to-metal seals were prepared utilizing the information and experience gained in these studies for the improvement of seals and sealing techniques.

**Task 3 - Radio Frequency Studies Designed to Obtain a Quantitative Understanding of Seal Losses**

Radio frequency work included studies of the effect of temperature on the seal losses and determination of how and to what extent the metal, braze, metallizing, and ceramic contribute to these losses.

Fifteen special 94% and 99% alumina ceramics in the system  $\text{SiO}_2\text{-CaO-Al}_2\text{O}_3$  with a  $\text{SiO}_2/\text{CaO}$  ratio of 1:1 and 2:1 were fabricated and their behavior characterized. A combination of phase diagram interpolations, density and strength determinations, optical and electron microscope planimetric and crystal growth studies, X-ray diffraction and electron microprobe studies, and chemical analysis of their glassy phases, established that equilibrium was very nearly reached at their maturing temperature. Cooling tended to freeze in the high temperature state although crystal phases such as anorthite, gehlenite and calcium hexaluminate were partially precipitated in some cases.

It was tentatively established that the rate determining mechanism of alumina solution both during the initial processing of the ceramic and during its subsequent reaction during metallizing with refractory metal paints containing oxide additions, was the chemical reaction rate.

The composition of the bulk and surface grain boundary phases of the ceramic was used to determine the viscosity of its melt phase. This, in turn, was used to predict the occurrence of highly electrical conductive, high strength, vacuum tight, ceramic-to-metal seals when metallized with a pure metal paint. Devitrification, thermal expansion, sintering, surface energy, dissolution, diffusion, crystal size, microscope, X-ray diffraction, electron microprobe and spectrographic studies were also used to predict the occurrence of high and low strength vacuum tight ceramic-to-metal seals on the twelve complex metallizing paint systems investigated.

Lucalox\*, sapphire, beryllia and fused quartz vacuum tight seals were made and their sealing mechanisms were examined as were those of several commercial alumina ceramics.

It was established that chemical and/or semi-conducting bond mechanisms were responsible for the actual sealing process of refractory metal to the oxide substrate.

---

\*General Electric Company trade name for a 99.75% alumina body.

For this bonding to occur either the metal phase had to be deposited on the oxide substrate by vapor phase processes or the oxide phases had to move by viscous flow processes (e.g., glassy phase migration) in order that the initial atom to atom contact could be made.

The electrical studies included dc resistance measurements, low power rf conduction and dielectric loss studies, and high power loss studies. It was shown that the metallizing layer is made up of metallic, semi-conductive and insulating layers. Conduction losses are minimized by using thin metallizing and a copper braze. Dielectric losses are only important for +99% aluminas and they account for a quarter of the total metallizing losses. The total metallizing losses are about 25% of the total window losses which, in turn, are about 0.3% of the transmitted power at 10 Gc.

In addition to usage on high power klystrons. the low loss metallizing development in this study can profitably be used on planar triodes and reflex klystrons.



The following conferences were held and reports presented during the final quarter to discuss progress and to disseminate information gained during the course of the contract. All previous publications, lectures, reports, and conferences were listed in the eleven preceding quarterly reports.

On May 6th, L. Reed, Eitel-McCullough, Inc., presented a review of the complete program on ceramic-to-metal seals at the USAECOM, Fort Monmouth, New Jersey.

On May 18th a meeting was held at EIMAC, San Carlos, California, to discuss the factors influential in bonding ceramics to metals. Present at the meeting were other contractors who were contributing to the ARPA sponsored project DEFENDER, as well as a representative from USAECOM. They were Stanley Leefe, USAECOM; O. Heil, Heil Scientific Laboratories; J. White, Sperry Electronic Tube Division; S. Colgate, Florida University; L. Reed, EIMAC; W. Wade, EIMAC. The conclusions of that meeting are presented in Appendix I of this report.

On June 15th L. Reed of Eitel-McCullough, Inc., presented a summary of the program to Col. Hill of ARPA at the Pentagon, Washington, D. C. Also present were P. M. Lally and A. Saharian of Sperry-Gainsville (Sperry Electronic Tube Division), L. Feinstein of Stanford Research Institute, L. Kaplan, G. Wurthmann, I. Reingold and Miss B. Malley of USAECOM, and W. Wade of Eitel-McCullough, Inc.

On October 20th L. Reed of Eitel-McCullough presented the paper, "The Electrical Behavior of Ceramic-to-Metal Seals", by S. Vogel, W. Wade, R. McRae and L. Reed, at the International Electron Devices Meeting in Washington, D. C.

PAPERS AND PUBLICATIONS FOR CONTRACT NO. DA 36-039 SC-90903

1. L. Reed, "Microstructure of Output Windows", Paper presented at meeting on window problems at Varian Associates, Palo Alto, California, February 6-7, 1963.
2. L. Reed, "General Discussion of the Role of the Electron Probe Microanalyzer in the Investigation of Ceramic-to-Metal Sealing", Paper presented to Signal Corps personnel at Fort Monmouth, N. J., sponsored by L. L. Kaplan of USAF/AFRL, February 7, 1964.
3. L. Reed and W. Wade, "Discussion of Metallurgical Research and Development for Ceramic Electron Devices", Paper presented to students in the School of Mineral Technology, University of California, Berkeley, California, February 11, 1964.
4. L. Reed, "Survey of the Factors Affecting Ceramic-to-Metal Sealing", Paper presented at the Fall Meeting of the Electronics Division of the American Ceramic Society, Philadelphia, Pennsylvania, September 16-18, 1964.
5. L. Reed, "Progress in Ceramics and Ceramic Seals", Paper presented at the Seventh National Conference on Tube Techniques, New York, N. Y., September 28-30, 1964.
6. R. McRae, C. Barnes and L. Reed, "rf Losses in Ceramic-to-Metal Seals", Paper presented at the Seventh National Conference on Tube Techniques, New York, N. Y., September 28-30, 1964.
7. S. Vogel, "Calorimetric Measurements of Radio Frequency Losses in Dielectric-to-Metal Seals", Paper presented in a Technical Seminar arranged by L. Kaplan at Fort Monmouth, N. J., October 2, 1964.
8. L. Reed, "Report on the Metallizing Workshop in Philadelphia", Paper presented at the Pacific Coast Regional Meeting of the American Ceramic Society, San Francisco, California, October 29, 1964.
9. L. Reed and R. McRae, "Evaporated Metallizing on Ceramics", American Ceramic Society Bulletin, vol. 44 (1), 12-13, (1965).

10. L. Reed, S. Vogel, W. Wade and R. McRae, "The Electrical Behavior of Ceramic-to-Metal Seals", Paper presented at the International Electron Devices Meeting, Washington, D C., October 20, 1965.

A metallized ceramic made by a conventional refractory metal metallizing process\* is composed of a sintered molybdenum porous sponge which has been infiltrated by a solidified oxide melt during a high temperature sintering process. On cooling the solidified melt phase, sometimes referred to as the "glassy phase", bonds both to the ceramic and the porous sponge to form a strong vacuum tight metallizing layer. The seal melt phase is formed from the grain boundary phase(s) of the ceramic and/or non-metallic addition(s) to the metallizing paint.

A complete ceramic-to-metal seal is made by brazing this metallized ceramic to a metal member. A wetting layer which can be plated on is sometimes employed to facilitate a good wetting action by the braze. Many attempts have been made to further characterize the ceramic-to-metal sealing process, but the interrelation of the many phenomena involved, which include chemical reaction, viscosity, diffusion, sintering, surface energy (wetting), have made the task very difficult.

As a first step toward understanding these phenomena, a comprehensive interpretative analysis of ceramic-to-metal sealing technology was presented in the 1st, 2nd, 3rd and 4th Quarterly Reports. This review is not repeated in this final summary report.

Concurrent with and following the above analysis, experimental work was carried out on both "simple" and complex metallizing systems.

The simple system consisted of a single phase molybdenum metal paint metallized onto well-characterized one or three component "special ceramic bodies". It was hoped to be able to treat the subject from a quantitative scientific viewpoint. In practice, the interrelation of the many phenomena involved highlighted the difficulties of attaining such a goal within the modest effort allowed for this task.

On the other hand, it is also important to obtain a qualitative understanding of commercial complex metallizing systems. The success achieved in analyzing a complex

---

\*Unless specifically mentioned discussion of metallizing in this report refers to this process.

system by carrying out selected "exploratory studies" was gratifying.

The following sections present the pertinent observations and experiments conducted concerning the various components constituting a ceramic-to-metal seal; the ceramic, the metallizing, the wetting and brazing layer, and the metal member. The investigations are brought into focus by considerations of the total seal.

Both commercially obtainable and specially made ceramic bodies were studied extensively throughout this program. A major effort was made to characterize the grain boundary phase of the ceramic. Experiments were conducted to determine if the grain boundary phase has attained equilibrium at temperature. The properties of the grain boundary phase such as its chemical composition, viscosity, diffusion, surface tension, thermal expansion were determined. This information is of value in interpreting the data obtained in the subsequent studies.

Key "exploratory studies" on all aspects of the metallizing process are next reported. The most significant key experiments outlined here concern the use of the electron microprobe to follow the movement of the various ionic species in the seal volume.

Finally, the "special bodies" are used to systematically examine the complex seal process. The statistical nature of the strength property of a seal is very evident in an examination of this data as also are opposing trends of various properties. Thus for example, the increased stress induced in a Kovar-to-ceramic seal brazed at  $1110^{\circ}\text{C}$  rather than  $800^{\circ}\text{C}$  can be offset by the partial devitrification of the glassy layer, but its complete devitrification augments the critical stress situation.

Some attempt is made in the final section to develop a shear test for testing ceramic-to-metal seals. Much work on the measurement and analysis of stresses in ceramic-to-metal seals needs to be done and the present work should only be considered a first step in this direction.

#### 4.1 General Ceramic Considerations

Both commercially obtainable and specially made ceramics were investigated on this program.

Commercially obtainable ceramics are complex in formulation due to the varied raw materials used. Furthermore, their processing is proprietary so that a rigorous discussion of the end product cannot be attempted. While much of the present study was conducted with commercial ceramics, special bodies were also fabricated to overcome the above objections.

The chemical composition of the ceramics considered on the program is given in Table 4-1. The shapes of the special bodies are given in Table 4-2.

The special bodies were manufactured after a careful review was made of typical commercial bodies, including those listed in Table 4-1, which seemed to give rise to the widest variation in metallizing behavior. The microstructure and physical properties of the special ceramics were investigated with particular attention being paid to the so-called "glassy phase" of the ceramics as distinct from the alumina crystal phase and the pore volume.

The special 99% body and one 94% body have  $\text{SiO}_2/\text{CaO}$  in the ratio 2:1. A second special 94% body has the  $\text{CaO}/\text{SiO}_2$  ratio 1:1. A total of four hundred tensile test pieces were made of each body together with suitable specimens for thermal stress analysis and rf loss measurements. The tensile test pieces were used for peel test measurements also; they conform to the Sperry design Fig. 4.01.<sup>1</sup> The thermal stress cylinders are 1" x 1-7/8" x 0.125" wall. The ends are flat to 0.2 mil.\* The thermal sag bars are 6"  $\pm$  0.1" long by 1"  $\pm$  wide by 0.18"  $\pm$  0.005" thick. The low power rf loss specimens are in the form of flat rings 1.203" OD x 0.703" ID x 0.100" high and disc shapes 0.200" diameter x 0.60" thick.

The commercial bodies had tensile and peel test pieces made from them which conformed to the ASTM CLM-15 design Fig. 4.02.<sup>2</sup> The rf loss specimens are of the

---

\*The cylinders were fabricated for use in the event that a future study on ceramic microstructure would be programmed.

**TABLE 4-1**

**Nominal Composition in Weight Percent\* of Ceramic Bodies  
Referred to in Text**

Body	Network (+) Intermediate	Network Former (+)		Network Modifier (+) MO	
	Al <sub>2</sub> O <sub>3</sub>	SiO <sub>2</sub>	ZrO <sub>2</sub>	CaO	MgO
<b><u>Special Bodies</u></b>					
941**	94	3	-	3	-
942**	94	4	-	2	-
992**	99	0.6	-	0.3	-
Lucalox <sup>++</sup>	99.75	-	-	-	0.25
Sapphire	100	-	-	-	-
<b><u>Commercial Bodies</u></b>					
A	94	4	0.5	1	0.8
C	97	1.5	-	1.2	-
E	99	0.6	-	0.15	0.15
G	94	4	-	1	1
H	99.5	0.25	-	0.05	0.25
I	95.5	2.0	-	0.5	2.0

\*Best estimate from spectrographic analysis.

\*\*Firing temperature in °C usually included in parentheses after composition code, i.e., 992 (1750).

<sup>†</sup>See section 4.2.3.1.

<sup>++</sup>General Electric Co. Trade Name.

---

**TABLE 4-2****Manufacture of Special Ceramic Bodies**

		Firing Temperature °C				
	X	1550	1600	1650	1700	1750
<u>99% Body</u>						
Tensile Test Pcs.	200	-	50	50	50	50
Thermal Stress Cylinders	10	-	4	4	4	4
rf Discs	20	-	10	10	10	10
rf Rods	10	-	5	5	5	5
<u>94% Bodies</u>						
Tensile Test Pcs.	150	50	50	50	50	50*
Thermal Stress Cylinders	10	4	4	4	4	4*
rf Rings	20	10	10	10	10	10
rf Discs	10	5	5	5	5	5
Thermal Sag Bars	4	1	1	1	1	1*

Notes: Time at temperature is three hours.

X was 1750°C for 992, 1700°C for 942 and 1650°C for 941.

\*Substitute 1500°C firing for the 1750°C firing for the 941 body.

---



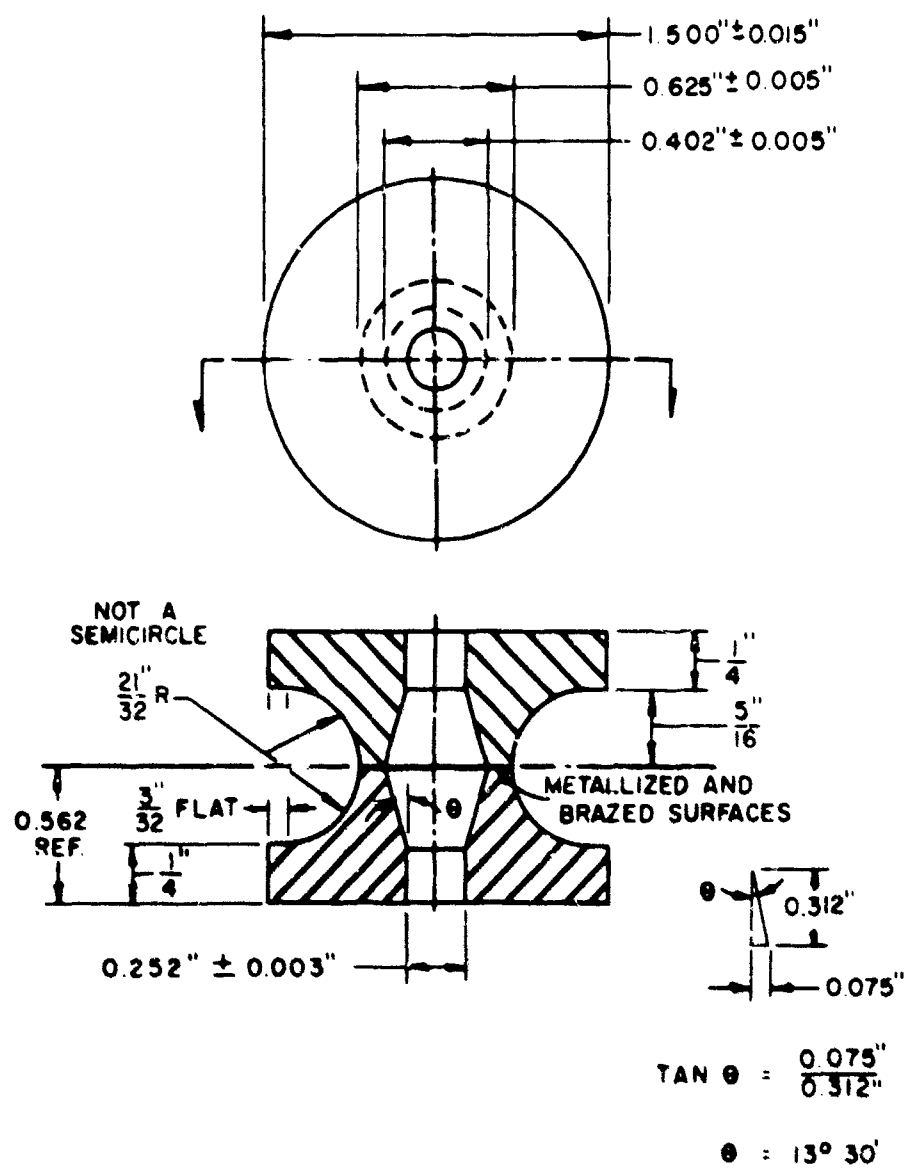


Figure 4.01: Tensile test piece B

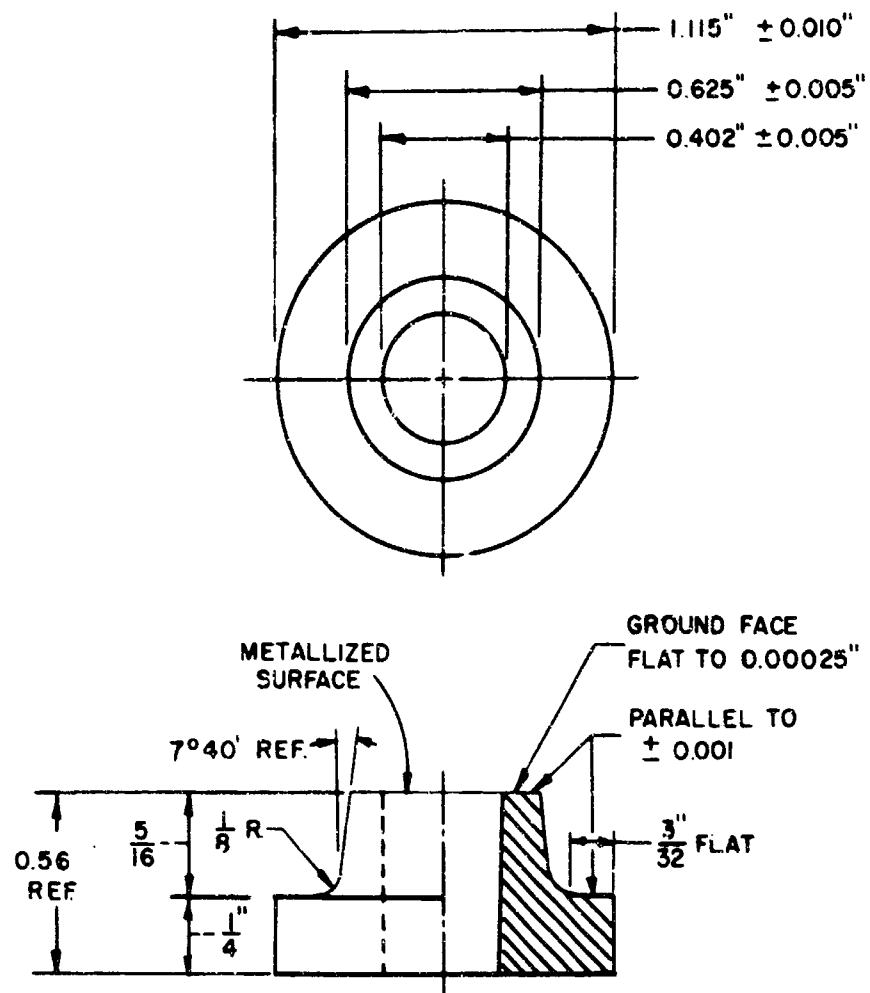


Figure 4.02: Tensile test piece A (CLM-15)

geometry given above and also in the form of sheets 25 and 50 mil thick x 0.680" x 1.360" for high power window tests and bars 0.300" x 0.500" x 6.0" for dc electrical measurement tests.

Further details on the above and other special shapes will be found under the appropriate section later in the text.

## 4.2 Special Ceramics

### 4.2.1 Introduction

The basic study portion of the program dictated that the characteristics of the ceramic be well known. With this in mind, the three component  $\text{CaO-SiO}_2\text{-Al}_2\text{O}_3$  system was selected and ceramics manufactured within this system according to the schedule laid down in Table 4-2.

Summarizing, the following compositions were selected for study:

1. 94% alumina  $\text{CaO/SiO}_2$  ratio 1:1, designated 941.
2. 94% alumina  $\text{CaO/SiO}_2$  ratio 1:2, designated 942.
3. 99% alumina  $\text{CaO/SiO}_2$  ratio 1:2, designated 992.
4. 99.75% alumina, Lucalox\*, 0.25%  $\text{MgO}$ .
5. 100% alumina single crystal sapphire.

The rationale behind the selection of the above bodies is as follows: The 94% compositions were selected on two counts.

1. more easily detectable concentration gradients could be detected using the electron microprobe and dielectric loss measuring equipment than would be the case for the 992 alumina.
2. the study is oriented to basic sealing mechanisms of all high grade aluminas.

---

\*General Electric Co. Trade Name.

The trend in high power rf windows is to use the high aluminas, +97%; hence a reason for the inclusions of the latter three bodies.

Sapphire, however, was not primarily included for study on the basis of being a material of use in electron tubes, but rather to provide useful information on sealing and rf loss mechanisms.

Lucalox\* was chosen for similar reasons as it was considered to be the simplest ceramic available being glass free and pore free. Lucalox\* does have useful output window characteristics. The 0.25% of magnesia is combined with alumina as  $MgO \cdot Al_2O_3$  spinel in the grain boundaries of the alumina grain. Three average grain sizes were obtained 5, 20 and 40  $\mu$ , so that the effect of grain size could be studied independently of other complicating factors.

Most commercial ceramics contain four or more oxides; the selection of a three-oxide system allows quantitative predictions to be made with regard to the amount of glassy phase and crystalline phases present if the phase diagram is known. Representation of selected compositions on a two-dimensional phase diagram may be easily made. Figures 4.03 and 4.04 show such cuts through the ternary  $CaO-SiO_2-Al_2O_3$  phase diagram as compiled by Osborn and Muan<sup>5</sup> with later revisions by Gentile and Foster<sup>6</sup>. Supporting viscosity<sup>5-7</sup>, surface tension<sup>8</sup>, density<sup>8</sup>, diffusion<sup>9-13</sup> and chemical reactivity data<sup>14-16</sup> are available for the  $CaO-SiO_2-Al_2O_3$  system.

In addition to the considerations discussed above the selection of  $CaO$  over  $MgO$  and  $Al_2O_3$  over  $BeO$  was based on the fact that the light elements  $Mg$  and  $Be$  are below the quantitative detection level for electron probe microanalysis with the equipment available to the project. (Beryllia ceramics are considered in Task II of this report.)

The above range of ceramics enables us to interpolate results for ceramics in the range 94% - 100% alumina and also enables extrapolations to be made within the system. General concepts should also be applicable to more complex diverse situations. This latter statement assumes that the characteristics of the ceramic being used are known. This is not always the case.

---

\*General Electric Co. Trade Name.

Pseudo Binary Phase Diagram  
of  $\text{CaO} \cdot \text{SiO}_2 - \text{Al}_2\text{O}_3$

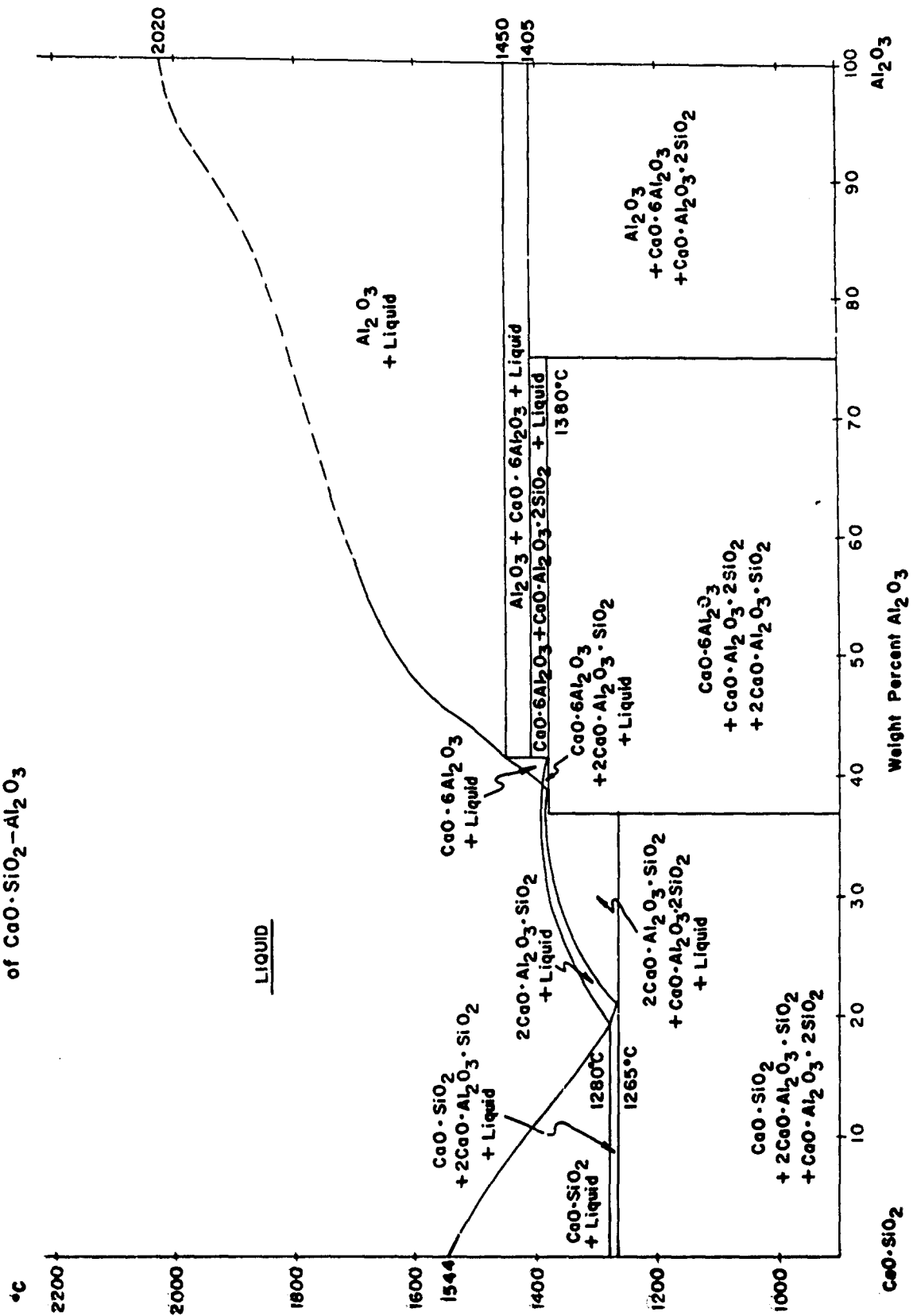


Figure 4.03: Revised pseudo-binary phase equilibrium diagram of the  $\text{CaO}/\text{SiO}_2\text{-Al}_2\text{O}_3$  system derived from the ternary  $\text{CaO-SiO}_2\text{-Al}_2\text{O}_3$  diagram.

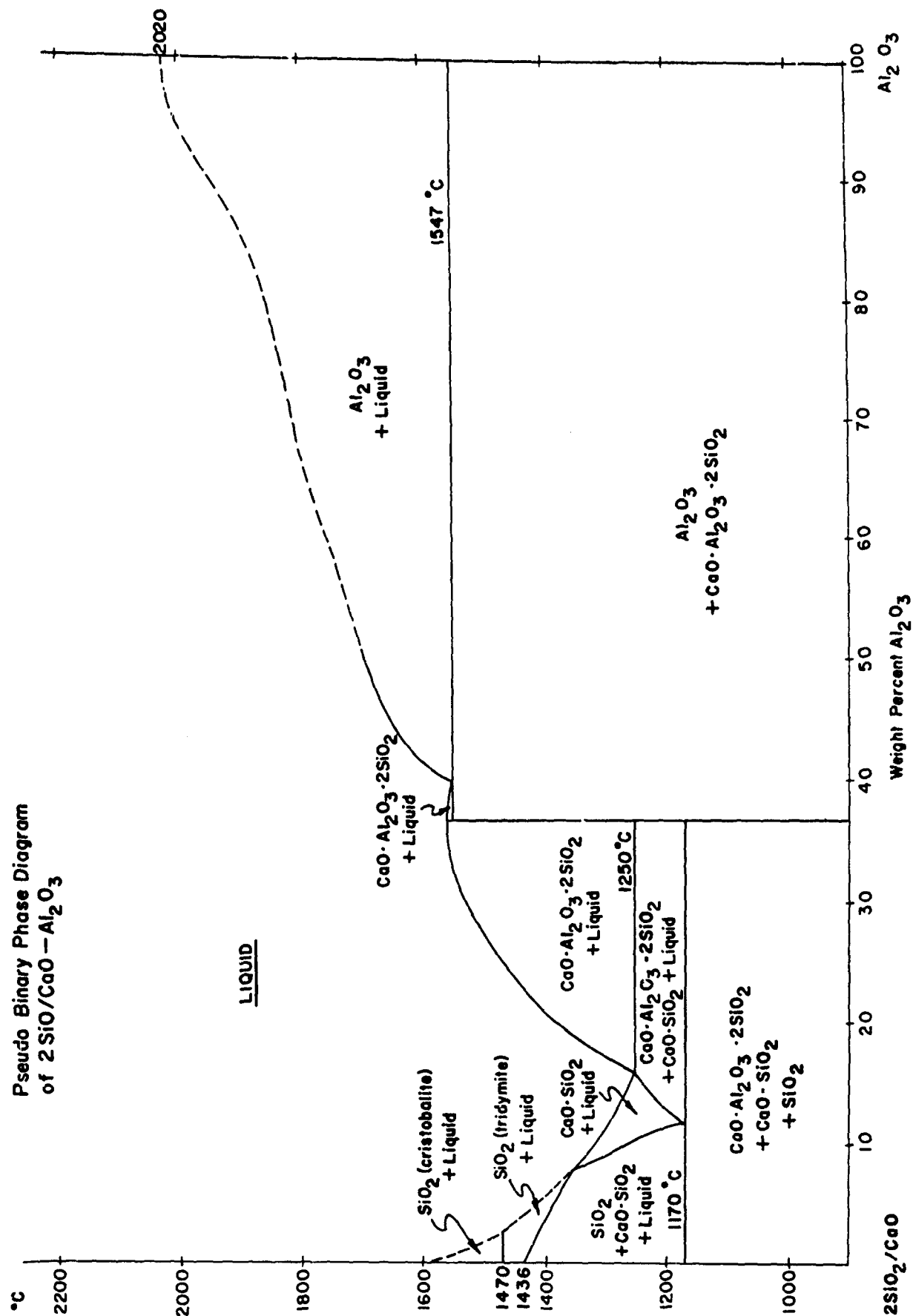


Figure 4.04: Revised pseudo-binary phase equilibrium diagram of the  $2\text{SiO}_2/\text{CaO}-\text{Al}_2\text{O}_3$  system derived from the ternary  $\text{CaO}-\text{SiO}_2-\text{Al}_2\text{O}_3$  diagram.

#### 4.2.2 Microstructure Considerations

Alumina ceramics consist of

- i. A grain boundary phase(s)
- ii. Predominantly an alumina crystalline phase
- iii. A pore volume.

The grain boundary phase(s) will, in the case of the 941 and 942 ceramics, consist of  $\text{CaO}$ ,  $\text{SiO}_2$  and  $\text{Al}_2\text{O}_3$  components. At the temperature at which the ceramics are made, these components will react to form a molten phase. This "melt" phase will eventually reach chemical equilibrium and be saturated with alumina<sup>15</sup>. If chemical equilibrium is attained, the amount of alumina in the melt will correspond to the amount shown on the liquidus line at the temperature indicated, this temperature being the temperature at which the special bodies are fired (made or matured) for 3 hours, see Table 4-2.

On cooling under equilibrium conditions, i.e., very slowly, the melt phase will deposit alumina on existing grains and then completely crystallize to give the equilibrium species noted in the appropriate phase diagram, Fig. 4.03 or 4.04. The phases which crystallize will depend on the initial composition of the body.

In actual ceramic practice, ceramic bodies are seldom cooled so slowly as to allow the system to maintain equilibrium and to permit the melt phase to completely crystallize. If the cooling rate is very rapid or the melt is very viscous (high in silica), the melt will supercool to a glass, if the cooling rate is somewhat slower, or the melt is a less viscous fluid, the melt will cool to a mixture of crystals and glass. In both cases, some alumina will deposit on the existing alumina grains, thereby altering the melt composition. When cooling under non-equilibrium conditions, the phase distribution of the system departs from that described in Fig. 4.04 because liquid phase (glass) is retained to room temperature. The extent of this departure from equilibrium is determined by the cooling rate.

When the ceramic is reheated to a temperature approaching the melting point, but not to the liquidus point, of the glass phase in the grain boundaries, further crystallization termed devitrification will occur. The species which devitrify may or may not be the equilibrium phases, shown in Fig. 4.03 and 4.04.

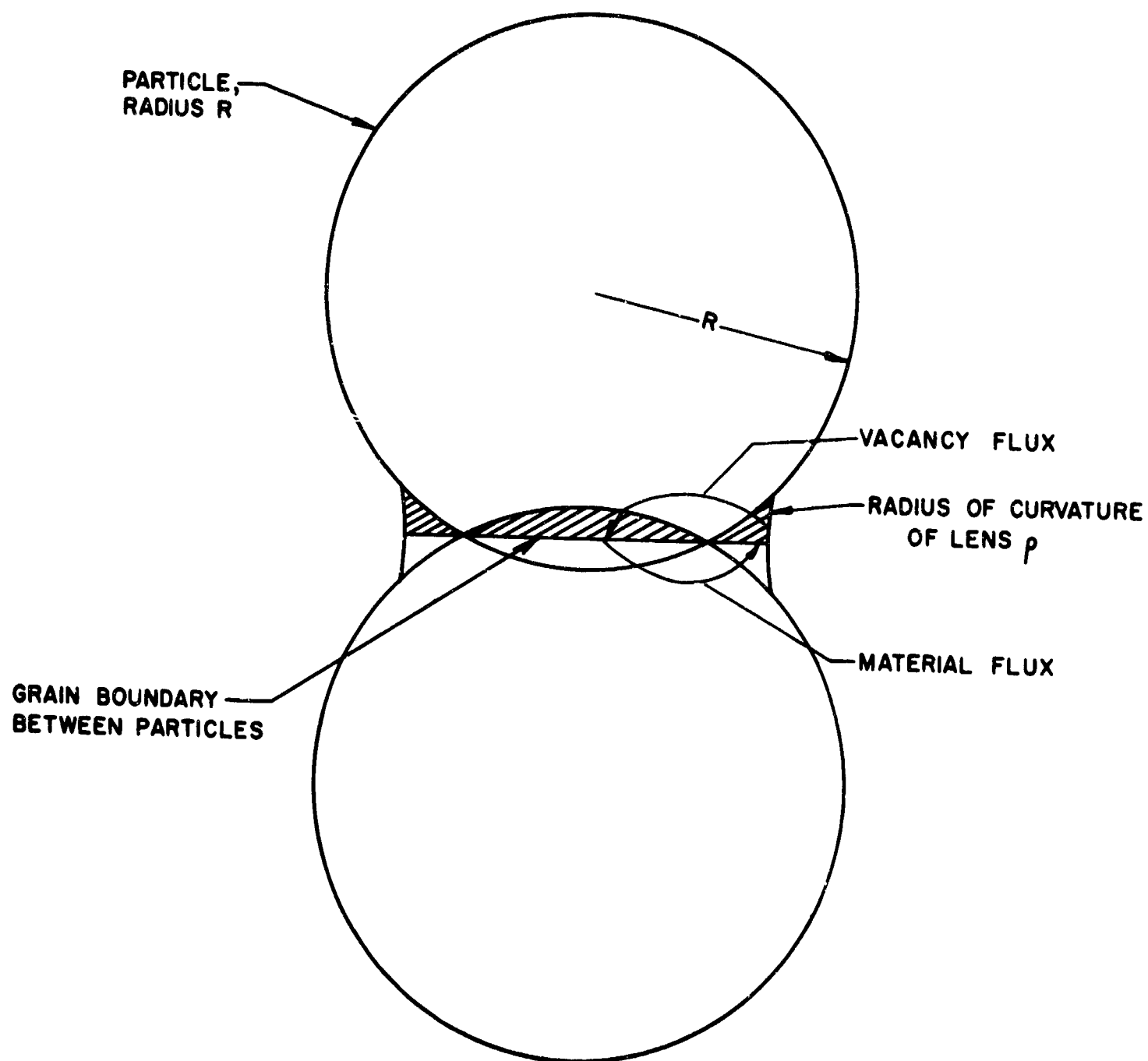


Figure 4.05: Model of two spherical particles, radius  $R$ , showing sintering by volume diffusion, indicating the flux of vacancies (and counter-flow of material) from a lens of radius of curvature  $R_1$  to an internal grain boundary.



If the ceramic is reheated to a temperature above the solidus, the grain boundary phase(s) will start to melt, taking some alumina into solution. When the liquidus temperature is exceeded (above the original firing temperature), the grain boundary phase is completely molten and will take further alumina into solution. This situation was actually an experimental fact in the case of ceramics which were metallized at 1800°C.

The grain boundary phases in alumina ceramics is somewhat loosely referred to as the "glassy phase". We will use this time-honored term in this report with the understanding that it is only a convenient term used to describe the grain boundary phases discussed above.

The extent of the pore volume is determined by many factors and their elimination is considered below, together with the factors causing crystal growth.

The size of the alumina crystals depends on

1. the firing temperature
2. the firing time
3. the particle size and size distribution of the alumina calcine
4. the type and quantity of flux used
5. the cooling rate.

Alumina ceramics that contain 100% alumina or form no liquid phases rely on solid state sintering processes to cause densification and crystal growth.

Coble<sup>1</sup> has summarized the work done on the initial sintering of alumina based on volume diffusion mechanisms. The model considered is two spheres touching each other, Fig. 4.05. Basically, the Kelvin equation applies.

$$\Delta C = \frac{\gamma_{sg} \cdot \delta^3}{kT} \cdot \frac{1}{\rho}$$

where  $\Delta C$  = Change in vacancy concentration between the curved lenses formed at point of contact of the spheres and the bulk of the material

- $C_0$  = Vacancy concentration of flat surface  
 $\gamma_{sg}$  = Surface energy  
 $\delta^3$  = Vacancy volume  
 $k$  = Boltzmann's constant  
 $T$  = Absolute temperature  
 $\rho$  = Radius of curvature of lens.

This vacancy concentration gives rise to a material diffusion flux and can be described by Ficks law of diffusion. Applying Ficks equations, we can obtain the quantity of matter transferred from one point in the system to another, and hence obtain a sintering or densification rate for the process.

A description of the kinetics of the complete sintering process using a more complicated geometric model for the final states of sintering has also been attempted<sup>8,19</sup>. The concepts discussed above are again employed.

Grain growth proceeds simultaneously with the densification process. The driving force for the process is the difference in surface energy between the fine grained material and larger grain sized product resulting from the decrease in grain boundary area and total boundary energy<sup>20</sup>.

Three overlapping stages of densification can be observed in bodies containing a liquid phase -

- Phase 1. Initial re-arrangement of the structure caused by viscous flow of the melt phase, due to surface energy forces.
- Phase 2. Solution and transport of alumina through the liquid phase as discussed immediately below.
- Phase 3. Finally, solid state sintering as discussed above.

The densification of a ceramic and the growth of a primary crystal phase in the presence of a secondary liquid phase as a function of increase time, temperature

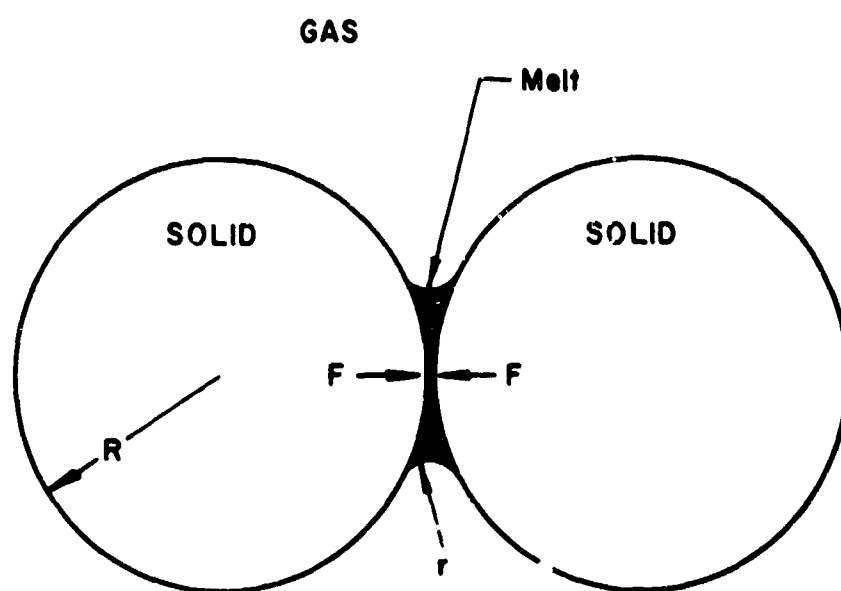


Figure 4.06: Surface tension forces,  $F$ , due to a pressure  $\frac{\Delta P = -2\gamma \cos \theta}{r}$  acting as a solid-melt-solid interface causing increased solubility of the solid.  $r$  is the radius of curvature indicated.

and decreasing particle size has been outlined<sup>21</sup>. Liquid-solid surface tension forces tend to draw the particles of alumina together, Fig. 4.06. A particle-particle pressure is generated. This pressure increases the chemical potential of the alumina in the immediate vicinity. The alumina goes into solution and if the system is in chemical equilibrium will redeposit on other alumina grains that are at a lower chemical potential. Densification results. In general a change in particle shape is involved in this process. This process slows as a solid skeleton of the primary crystal phase forms. Further densification will then largely take place by a solid state sintering process.

Crystal growth will accompany Phase 2 especially if the amount of liquid phase involved is large; this process is termed<sup>†</sup>a Type I activated solid-liquid-solid diffusion grain growth process.\* Later grain growth processes will take place by a second type<sup>†</sup> (Type II) of normal solid-liquid-solid diffusion process together with a solid-solid transport of material across grain boundaries. The driving force for both of these latter processes is the difference in energy between the fine grained material and the larger grain sized product. Grain growth via a liquid grain boundary will be expected to be slower than across a solid-solid grain boundary.

The rate of deposition in both Type I and Type II processes is determined by the rate of formation of lattice steps on the alumina crystal surface and by the rate of migration of these steps across the surface. The steps are due to dislocations, surface nucleation and crystal imperfections due to impurities on the alumina crystal surface.

The special alumina bodies, 941, 942, and 992, are made from Alcoa A-14 alumina with a grain size distribution prior to processing as shown in Fig. 4.07. Pure  $\text{SiO}_2$  powder and pure  $\text{CaCO}_3$  were used as fluxes.

The bodies were fired for three hours at selected temperatures. The grain sizes of the bodies are plotted in Fig. 4.08, and the fired densities are given

---

\*The driving force for growth will be the same as for Phase 2 densification, i.e., interfacial particle-particle pressure generated by surface tension forces.

<sup>†</sup>By the authors

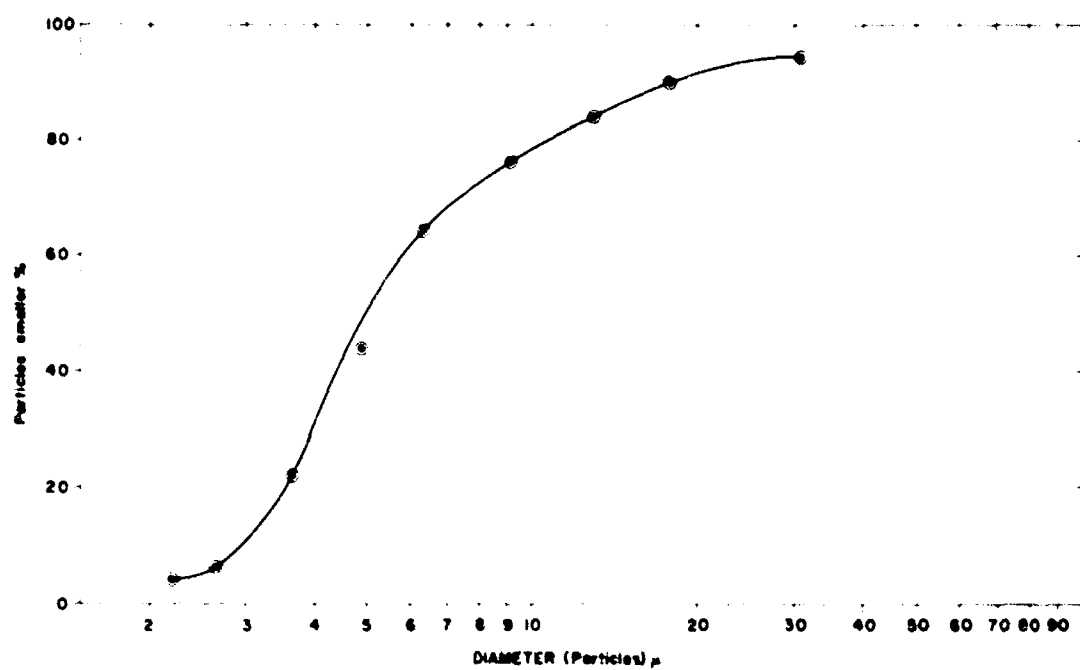


Figure 4.07: Particle size distribution of Alcoa A-14 alumina before processing.

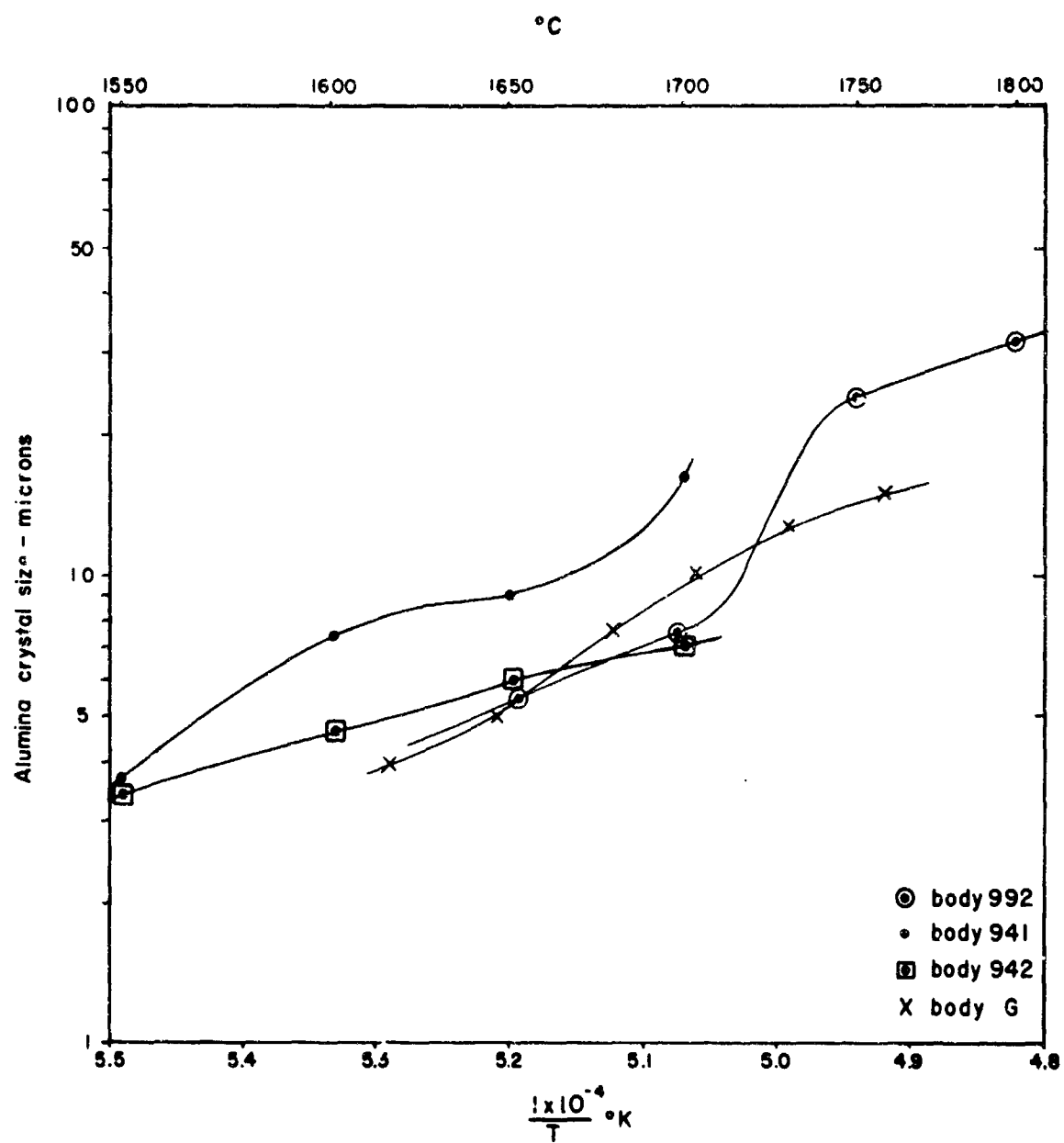


Figure 4.08: Average grain size of 941, 942, 992, and Body G as a function of firing temperature. Time at temperature was three hours.

in Table 4-3. The grain size of Body G (94% alumina, 4% SiO<sub>2</sub>, 1% CaO, 0.8% MgO) is also plotted on the same graph. The photomicrographs of the bodies are shown in Figs. 4.09, 4.10 and 4.11. The primary alumina crystal phase and the "glassy phase" existing in the grain boundaries can be clearly seen.

The 992 ceramic contains approximately 2% of liquid phase at the firing temperature. This is insufficient for a rearrangement process to occur so that initial densification will occur by a Phase 2 solution-diffusion-precipitation process, and by a solid-solid transport of material, Phase 3. Densification is largely complete by 1700°C. However, grain growth in this system is at a minimum below 1700°C because -

- i. The presence of sub-micron pores in the solid-solid grain boundaries "peg" their movement.
- ii. The presence of a small amount of grain boundary liquid phase means that a solution-diffusion-precipitation bridging process must occur. This process is slower than transport of material across a solid interface.

Above 1700°C, grain boundary porosity is largely eliminated within the 3-hour time-temperature limit and many solid-solid bridging contacts have formed so that grain growth proceeds rapidly.

Densification in the 941 and 942 systems proceeds via overlapping Phase 1, 2 and 3 mechanisms. Examination of their microstructures and the density data shows that Phase 1 is complete and Phase 2 is essentially complete by 1550°C in the case of the 941 ceramic, and 1600°C in the case of the more viscous flux phase of the 942 ceramic. The subsequent small increase in density above this temperature is due to solid state diffusion processes.

Grain growth in the ceramic proceeds in three predominant but overlapping stages.

- i. A large relative increase in grain growth is observed during the Phase II densification process due to the Type I activated solid-liquid-solid diffusion process

TABLE 4-3

Fired Densities versus Firing Temperature (3 hours) for Special Bodies

Composition	Firing Schedule					
	1500°C	1550°C	1600°C	1650°C	1700°C	1750°C 1800°C
992 (see below)	---	---	---	3.49	3.72gm/cc	3.77gm/cc 3.77gm/cc
942 "	---	---	---	---	3.72	3.77 3.77
941 "	---	3.190	3.59gm/cc	3.62gm/cc	3.61gm/cc	3.56gm/cc ---
	---	---	3.60	3.62	3.61	3.54 ---
	---	3.57gm/cc	3.60gm/cc	3.59gm/cc	3.56gm/cc	---
	3.47	3.58	3.60	3.58	3.55	---

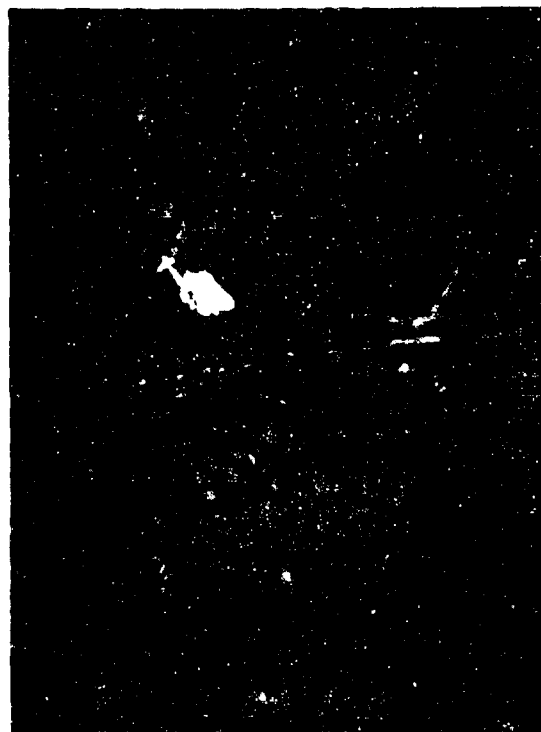
## Composition:

Composition	Raw Material		Fired Composition	
992	98.95% $\text{Al}_2\text{O}_3$		99.01% $\text{Al}_2\text{O}_3$	
	0.50 $\text{SiO}_2$		0.62 $\text{SiO}_2$	
	0.5 $\text{CaCO}_3$		0.31 $\text{CaO}$	
			Balances $\text{Fe}_2\text{O}_3$ , $\text{Na}_2\text{O}$	
942	92.75% $\text{Al}_2\text{O}_3$		94.00% $\text{Al}_2\text{O}_3$	
	3.78 $\text{SiO}_2$		3.96 $\text{SiO}_2$	
	3.47 $\text{CaCO}_3$		1.98 $\text{CaO}$	
941	92.05% $\text{Al}_2\text{O}_3$		94.00% $\text{Al}_2\text{O}_3$	
	2.78 $\text{SiO}_2$		2.97 $\text{SiO}_2$	
	5.17 $\text{CaCO}_3$		2.97 $\text{CaO}$	





1550°C



1600°C



1650°C



1700°C

Figure 4.09: Microstructure of 941 ceramic (400X).



1550°C



1600°C



1650°C



1700°C

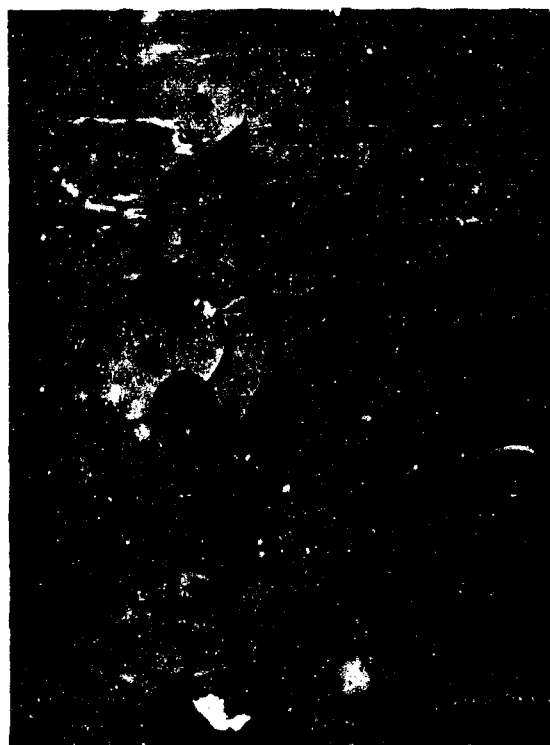
Figure 4.10: Microstructure of 942 ceramic (400X).



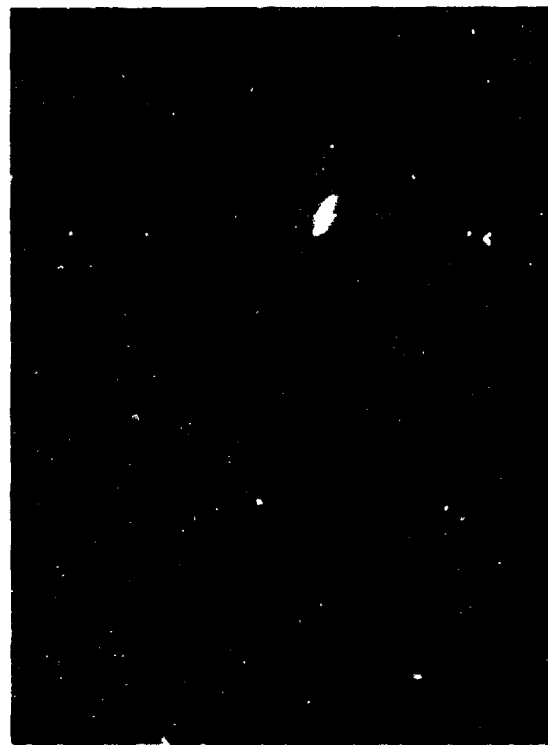
1650°C



1700°C



1750°C



1800°C

Figure 4.11: Microstructure of 992 ceramic (400X).

- ii. Then slow grain growth proceeds by a Type II solid-liquid-solid diffusion process as in the 941 and 942 bodies fired at 1600°C-1700°C
- iii. Fast grain growth then proceeds as the role of the solid-solid diffusion process increases in importance, as is uniquely noted for the 942 body, fired at 1750°C.

The sag bar results, 4.2.3.3.1, confirm the presence of a substantial solid crystal skeleton for this ceramic. If the above theories of densification and grain growth are correct, it implies that a very close approach to the equilibrium amount of alumina in the melt phase will occur above 1500°C for the 941 body and above 1600°C for the 942 body.

The average grain growth in the latter two stages is experimentally determined to be identical for both the 941 and 942 bodies but the range of crystal size for the 941 ceramic is greater than for the 942 ceramic. This may be because two different grain growth mechanisms are predominant. The diffusion transport of material by either Type I or Type II solid-liquid-solid diffusion process will be faster in the lower silica content melt phase. This would indicate that the solid-solid diffusion process has proceeded further in the 942 ceramic due to exclusion of the glass phase from the grain boundaries due to a high or solid-melt interfacial energy.\*

An alternative explanation is possible if crystal growth in these bodies via the solution-diffusion-precipitation processes is predominant in both cases. Crystal growth must be controlled by a composition insensitive crystal solution or precipitation rate rather than by the rate of diffusion transport, as the rate of diffusion is known to be composition sensitive.

Studies carried out on melt-sapphire couples (Section 4.2.3.2.6) show that the dissolution rate of alumina grains by the flux in ceramic bodies could be controlled by the interfacial chemical reaction until equilibrium conditions are reached, this will also be composition sensitive. However, subsequent solutions will

---

\*This is borne out by the 1800°C results taken from metallizing data.

occur by:

- i. surface tension forces generating pressure at alumina-melt-alumina interfaces as previously explained, Type I
- ii. preferential solution of grains having a small particle size and hence a larger solubility than the larger grains, Type II.

Since the interfacial energies in both the 941 and 942 systems are approximately equal, at least in wet  $H_2/3N_2$  (Section 4.2.3.4), the rate of solution in both systems will be equal, i.e., it will be composition insensitive.

Precipitation will occur on the alumina lattice steps which are energetically most stable. This will be the same for both systems since the impurity level in the alumina is constant, the process is also composition insensitive to a first approximation.

Crystal growth in the last stage, the solid state grain growth process, can be expected to be equivalent for both systems since only alumina-to-alumina contact is involved. In this region, crystal growth is in fact similar to that for the 992 body.

Much more experimentation is needed to provide a clearer picture of these processes.

The larger grain size of the 94% aluminas fluxed with  $CaO$  and  $SiO_2$  as compared to the body fluxed with  $CaO$ ,  $MgO$  and  $SiO_2$ , Body C is interesting (Fig. 4.08). It is known that the rearrangement and solution-precipitation densification processes are complete by  $1550^\circ C^{22}$ . A sub-micron spinel layer  $MgO \cdot Al_2O_3$  may form on the alumina grains. This would hinder any solid state or solid-liquid-solid mode of grain growth. In addition  $MgO$  in solution in the  $Al_2O_3$  is known to hinder grain growth. For example, the process variations underlying the manufacture of Lucalox\* have been investigated.<sup>23</sup> The addition of traces of magnesia to form a solid solution of  $MgO$  in the  $Al_2O_3$  results in elimination of exaggerated grain growth. Larger

---

\*General Electric Co. Trade Name.

amounts, up to 0.25% are beneficial in reducing the normal grain growth by alumina grain boundary "pegging" with the finely dispersed  $\text{MgO} \cdot \text{Al}_2\text{O}_3$  spinel phase formed in the grain boundaries.  $\text{MgO}$  is also found to have a beneficial effect on limiting grain growth in the initial sintering stage of the alumina which results in a higher end point density. Although solid state grain growth only becomes predominant at the higher temperatures (within the times normally encountered in the maturing of most ceramic bodies) it is important throughout the process in bodies containing as much as 94% of alumina.

The plot of the Modulus of Rupture of three special bodies is given in Fig. 4.12. As the fired density increases, the strength of the body will increase because porosity is eliminated. However, the strength of ceramics decreases as its crystal size increases and the amount of "glassy phase" increases. Thus the Modulus of Rupture displays a maximum at a certain temperature for each body corresponding to the lowest temperature at which a maximum density is achieved.

#### 4.2.3 The Glassy Phase

##### 4.2.3.1 Molecular Structure

A brief interpretive review of the structure of the glassy state is desirable in order to appreciate the material considered in the remainder of Section 4.2.

Glass is a supercooled liquid possessing no long range atomic order in the liquid or "solid" state. This property is due to "network forming" ions which coordinate with oxygen anions to form a three dimensional network. Fused silica,  $\text{SiO}_2$ , itself is a glass.

The silicon ion is considered to be tetrahedrally coordinated with four oxygen ions in a three dimensional array, Fig. 4.13, to form an anionic network structure. The Si-O distance, 1.62 Å (at room temperature) is smaller than the sum of the normal radii of the  $\text{Si}^{4+}$  and  $\text{O}^{2-}$  ions. The oxygen ion linking two silicon neighbors does not lie on the line joining these ions but is displaced to  $140^\circ$  indicating a compromise between purely ionic bonding with an angle of  $180^\circ$  and a purely homopolar angle of  $109^\circ$ . From this the Si-O bond is assumed to be 50% ionized at room temperature.

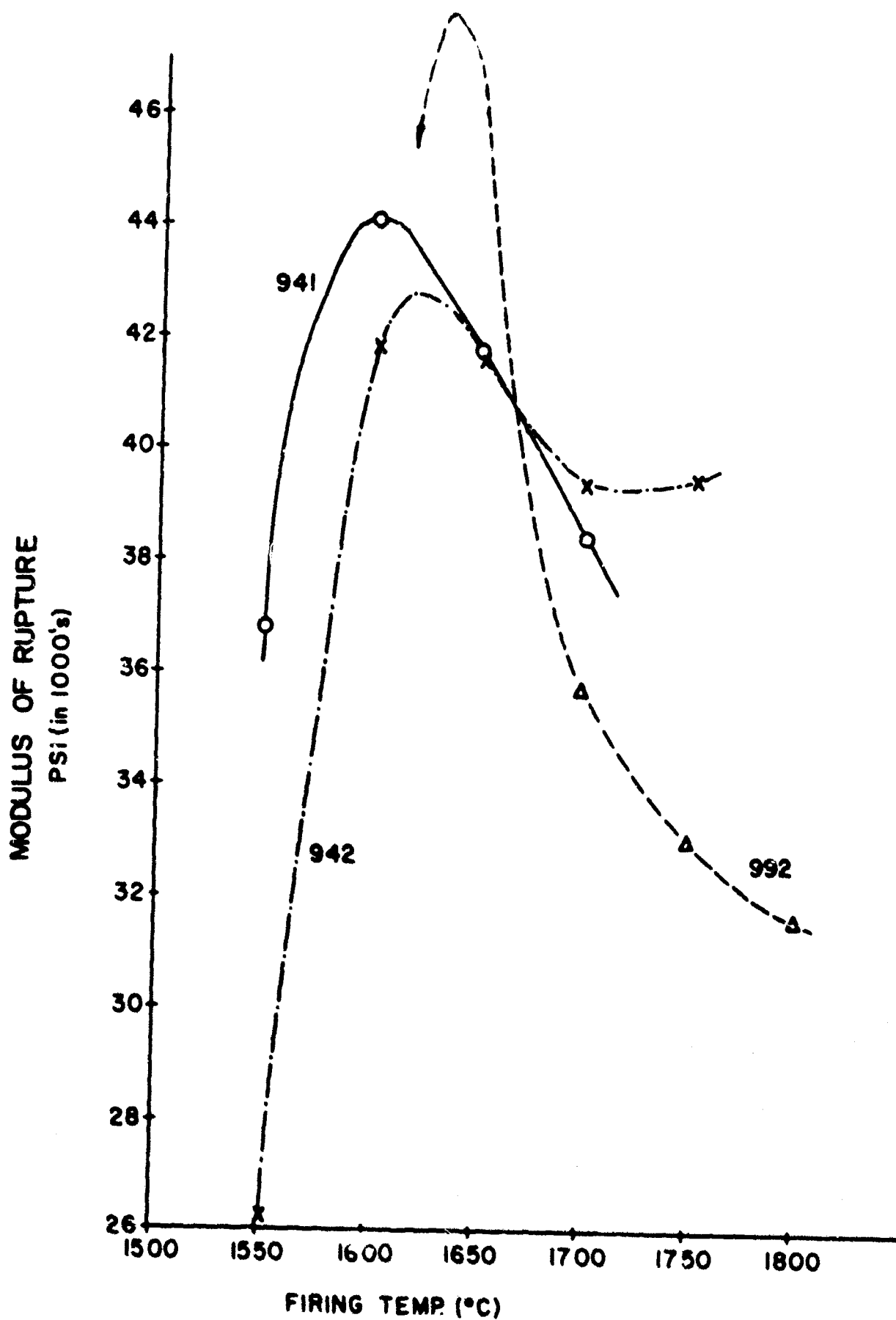
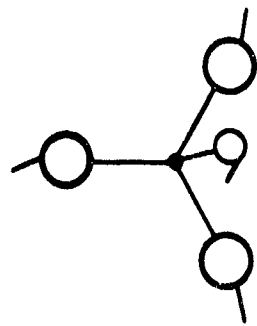
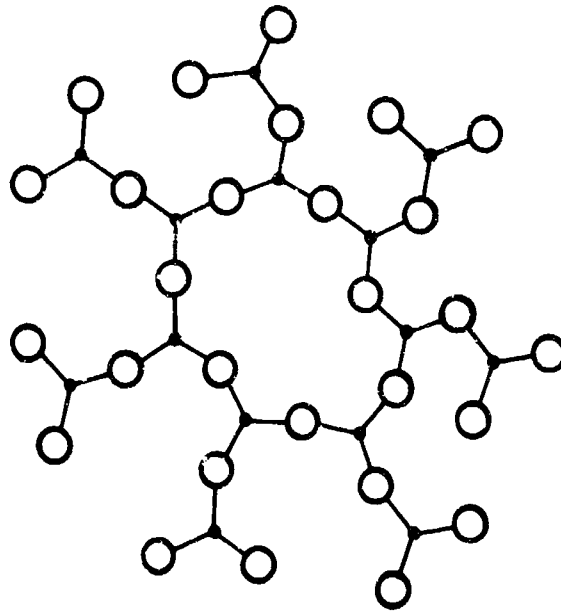


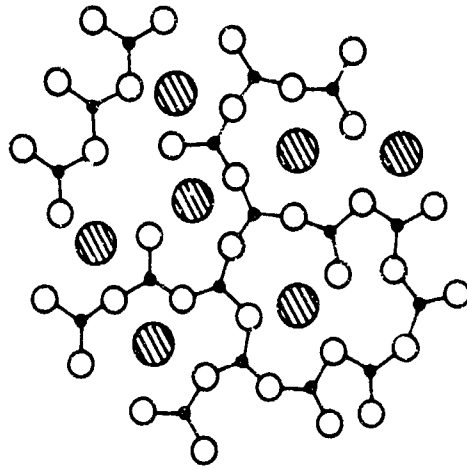
Figure 4.12: Modulus of rupture of the 941, 942 and 992 bodies.



(a)  
Silicate tetrahedron  
3 - Dimensions



(b)  
Glassy silica network  
2 - Dimensions



(c)  
Calcium silicate glass network  
2 - Dimensions

Figure 4.13: Atomic model of glass structure (after Zachariasen).



As metal ions are added as oxides to silica to form, for example,  $\text{Na}_2\text{O} \cdot \text{SiO}_2$ ,  $\text{MgO} \cdot \text{SiO}_2$ ,  $\text{CaO} \cdot \text{SiO}_2$ , the network is broken up. The  $\text{Mn}^{2+}$  ion coordinates with oxygen ions which are only bound to one silicon ion as in Fig. 4.13. The  $\text{Mn}^{2+}$  ion will coordinate with more than four oxygens; in addition, its M-O single (chemical) bond energy is less than the Si-O bond energy. This type of ion is called a network modifier.

The following table indicates typical silicate anions which will form as MO is added to the melt.

TABLE 4-4

Glass Structure As a Function of Network Modifier Ion

<u>Composition</u>			<u>O/Si</u>	<u>Anion Structure</u>
$\text{SiO}_2$		$\text{SiO}_2$	2	Network of silicate anions
$\text{MO} \cdot 2\text{SiO}_2$	or	$\text{M}^{2+}, \text{Si}_2\text{O}_5$	2-2.5	Sheet of silicate anions
$\text{MO} \cdot \text{SiO}_2$	or	$\text{M}^{2+}, \text{SiO}_3$	2.5-3	Chain and ring silicate anions
$2\text{MO} \cdot \text{SiO}_2$	or	$\text{M}^{2+}, \text{SiO}_4$	3-4	Island silicate anions

The table is expressed in O/Si ratios.

In addition to network forming and network modifying cations, a third type of cation exists that contributes to glass structure called an intermediate ion. For example,  $\text{Al}^{3+}$  when coordinated with four oxygens is a network former. When six-fold coordinated with oxygen ions it is a network modifier. This occurs because the Al/O radius ratio of 0.43 is so close to the critical value of 0.414 for the transition from octahedral six fold ( $6\text{Al}^{3+}$ ) to tetrahedral four fold coordination ( $4\text{Al}^{3+}$ ) that the ion can occur in either or both states. When  $4\text{Al}^{3+}$  coordinated it can replace  $\text{Si}^{4+}$  in the silicate network; when  $6\text{Al}^{3+}$  it modifies the network. The readily polarized oxygen ion suffers considerable distortion in the former

case. A measure of this polarization is provided by comparing the Al-O distance in 6-fold and 4-fold coordination which is 1.9 Å and 1.7 Å respectively.

An intermediate ion is incapable of forming a network of its own ions, for instance alumina,  $\text{Al}_2\text{O}_3$  is fully crystallized, whereas silica,  $\text{SiO}_2$ , may exist as a glass. (However, glasses composed largely of  $\text{CaO}$ ,  $\text{Al}_2\text{O}_3$  and also  $\text{BeO}$ ,  $\text{Al}_2\text{O}_3$  have been observed to form).

Table 4-5 gives a list of ion network formers and modifiers as discussed above.

The simple picture of glass structure presented thus far is not completely so. Some evidence has accumulated which shows that glass does have a structure. The properties of glass are also dependent on the previous history of the material.

The glass phases that we are concerned with in alumina ceramics are composed of an alumina-silicate anionic network with modifying cations such as  $\text{Ca}^{2+}$ ,  $\text{Mg}^{2+}$ ,  $\text{Cu}^{2+}$ ,  $\text{Mn}^{2+}$  in the interstices. The role of ions such as  $\text{Al}^{3+}$ ,  $\text{Fe}^{3+}$ ,  $\text{Ti}^{4+}$ ,  $\text{Zr}^{4+}$ , are as network intermediates, i.e., they can exist in the silicate network to form an alumina-silicate network, and in the network interstices, depending on the coordination number assumed by the cation.

When a three dimensional silicate (or alumina-silicate) network is not formed, e.g., O/Si 2.5, Table 4.4, the glass is unstable and will devitrify (crystallize) under prolonged heating in a temperature range suitable for nuclei formation and crystal growth. Conversely, under conditions of severe quenching, devitrification may not occur at the point  $2\text{MO} \cdot \text{SiO}_2$ . This is attributed to divalent cations, especially Be and Mg, bridging isolated silica tetrahedra. In general, however, when  $\text{O/Si} > 4$  the melt will crystallize on cooling.

The  $\text{CaO-SiO}_2\text{-Al}_2\text{O}_3$  glass melts considered in this report will have some properties of the room temperature glassy state, but may also be expected to display other characteristics because of the high temperatures involved, ( $1200^\circ\text{C}$ - $2000^\circ\text{C}$ ). The glass melt will also have an equilibrium structure depending on the time at temperature and rate of cooling from this temperature.

TABLE 4-5

Co-ordination Number and Bond Strength of Oxides  
(Taken from K. H. Sun J. Am. Ceram. Soc., 30, 277 (1947))

	M in MO <sub>x</sub>	Valence	Dissocia- tion Energy per MO <sub>x</sub> (kcal/mole)	Co- ordina- tion Number	Single- Bond Strength (kcal/mole)
Glass formers	B	3	356	3	119
	Si	4	424	4	106
	Ge	4	431	4	108
	Al	3	402-317	4	101-79
	B	3	356	4	89
	P	5	442	4	111-88
	V	5	449	4	112-90
	As	5	349	4	87-70
	Sb	5	339	4	85-68
	Zr	4	485	6	81
Intermediates	Ti	4	435	6	73
	Zn	2	144	2	72
	Pb	2	145	2	73
	Al	3	317-402	6	53-67
	Th	4	516	8	64
	Be	2	250	4	63
	Zr	4	485	8	61
	Cd	2	119	2	60
Modifiers	Sc	3	362	6	60
	La	3	406	7	58
	Y	3	399	8	50
	Sn	4	278	6	46
	Ga	3	267	6	45
	In	3	259	6	43
	Th	4	516	12	43
	Pb	4	232	6	39
	Mg	2	222	6	37
	Li	1	144	4	36
	Pb	2	145	4	36
	Zn	2	144	4	36
	Ba	2	260	8	33
	Ca	2	257	8	32
	Sr	2	256	8	32
	Cd	2	119	4	30
	Na	1	120	6	20
	Cd	2	119	6	20
	K	1	115	9	13
	Rb	1	115	10	12
	Hg	2	68	6	11
	Cs	1	114	12	10

Tables 4-6 and 4-7 give the molecular structures that can exist in silicate melts based on the network theory. We have anticipated the viscosity, section 4.2.3.3.1, by inserting viscosity data in these tables. As expected, as the alumina silicate anions become more complex, the viscosity increases. However, since the entry of the  $4\text{Al}^{3+}$  into the network is dependent on the  $\text{Al}_2\text{O}_3/\text{CaO}$  ratio being less than one, with  $\text{Al}_2\text{O}_3/\text{CaO}$  compositions greater than one, the viscosity will decrease because the network structure is loosening with the introduction of  $6\text{Al}^{3+}$  into network modifier positions. This ratio is exceeded at the 47% level for the 1:1  $\text{SiO}_2/\text{CaO}$  ratio and 37% for the 2:1  $\text{SiO}_2/\text{CaO}$  ratio. Many of the physical and electrical properties in the  $\text{CaO-SiO}_2\text{-Al}_2\text{O}_3$  system behave similarly, i.e. the direction of the property under consideration changes as the  $\text{Al}_2\text{O}_3/\text{CaO}$  ratio passes through one. The subject of glass structure is considered in some detail in the 3rd Quarterly Report and elsewhere<sup>15</sup>.

#### 4.2.3.2 Composition and Amount

Glass flow out from the ceramic into the porous molybdenum metallizing sinter sponge is one phenomena responsible for seal strength. It is important to know the mineralogical and chemical composition and the amount of the "glassy phase" of the special ceramics in order to predict their metallizing behavior.

The alumina microstructure considerations discussed earlier, Section 4.2.2, indicate that if one accepts the theories of sintering and grain growth which are forwarded, equilibrium is reached when the grain growth process becomes complete due to a Type 2 solid-liquid-solid and a solid-solid material transport process. This is above  $1550^\circ\text{C}$  for the 941 ceramic and  $1600^\circ\text{C}$  for the 942 ceramic.

Various techniques were used in order to further characterize the glass phase. They included a study of existing phase diagrams, planimetric measurements of optical and electron photomicrographs of selected areas of the ceramics, x-ray diffraction analysis of the ceramics, electron microprobe scans across the ceramic, chemical analysis of the glassy phase and chemical reaction rate studies on glass-sapphire couples were also investigated.

$\text{Al}_2\text{O}_3$   
wt.

0

5

20

25

30

35

40

50

60

100

—

TABLE 4-6

Anion Complexes in a CaO-SiO<sub>2</sub>-Al<sub>2</sub>O<sub>3</sub> Melt  
of the 1:1 CaO/SiO<sub>2</sub> Composition  
and the Correlation with Melt Viscosity (at 1500°C)

Al <sub>2</sub> O <sub>3</sub> wt. %	Mole %	O/Al, Si	O/Si	Al/Si	Ions	Viscosity Poise
0	0	3	3	0	(Si <sub>3</sub> O <sub>9</sub> ) <sup>-6</sup> , Ca <sup>2+</sup> ; rings and chains	2.0
5	-	-	-	-		4.5
20	22	2.46	3.9	.55	n(Si <sub>1.33</sub> Al <sub>.66</sub> O <sub>5</sub> ) <sup>-2.7n</sup> , Ca <sup>2+</sup> ; (sheet)	9.5
25						12
30	33	2.25	4.5	1.0	n(Si <sub>0.5</sub> Al <sub>0.5</sub> O <sub>2.25</sub> ) <sup>-ln</sup> , Ca <sup>2+</sup> ; network	14
35						15
40	43	2.1	5.7	1.5	(Si-Al O <sub>7</sub> ) <sup>-7</sup> +Al <sup>3+</sup> , Ca <sup>2+</sup>	15
50	54	2.0	6.5	2.3	Forms unstable glasses on cooling composed of alumino-silicate anions and six fold Al <sup>3+</sup> ions and Ca <sup>2+</sup> ions in modifier positions	-
60	63	1.85	8.0	3.4		-
100	100	1.5	∞	∞	Al <sup>3+</sup> + O <sub>2</sub> <sup>-</sup> melt	-

TABLE 4-7

Anion Complexes in a  $\text{CaO-SiO}_2\text{-Al}_2\text{O}_3$  Melt  
of the 1:2  $\text{CaO/SiO}_2$  Composition and the Correlation  
with Melt Viscosity (at  $1500^\circ\text{C}$ )

$\text{Al}_2\text{O}_3$ wt. %	O/Al, Si	O/Si	Al/Si	Ions	Viscosity Poise
0	2.5	2.5	0	$n(\text{Si}_2\text{O}_5)^{-2}, \text{Ca}^{2+}$ ; sheet structure	--
5					37
20	2.15	3.25	.5	$n(\text{Si}_{0.66}, \text{Al}_{.33}^{0.2.15})^{-.66n},$ $\text{Ca}^{2+}$ ; network structure	65
25					80
30	2.05	3.7	.8	$n(\text{Si}_{.54}, \text{Al}_{.44}^{0.2.05})^{-.6n},$ $\text{Ca}^{2+}$ ; network structure	100
40	1.93	4.4	1.3	$(\text{Si}, \text{Al O}_7)^{-7}, \text{Al}^{3+}, \text{Ca}^{2+}$ ; forms unstable glasses on cooling	--
100	1.5	$\infty$	$\infty$	$\text{Al}^{3+} + \text{O}^{-2}$ , alumina melt	--

#### 4.2.3.2.1 Equilibrium Phase Diagram Studies

If the system is in equilibrium, then it is possible to predict the amount and composition of the various phases from the  $\text{CaO-SiO}_2\text{-Al}_2\text{O}_3$  phase equilibrium diagram. The binary cuts given in Figs. 4.03 and 4.04 can give the amount of melt phase existing at the solidus and liquidus. This has been calculated for the 941, 942 and 992 bodies and is given in Table 4-8, columns 5 and 6. The equilibrium crystal species present are given in Table 4-9.

TABLE 4-8

Weight Percent Glass Phase from Photomicrograph  
Measurements  
(Values obtained from electron and light  
photomicrographs)

Body Type	Ceramic Firing Temp. °C	Weight Percent Glass from Photos		Equilibrium Amounts of Melt	
		Electron	Light	At Firing Temp.	At Invariant Point, 1405°C
<u>1</u>	<u>2</u>	<u>3</u>	<u>4</u>	<u>5</u>	<u>6</u>
941	1700	7.5	17.7	14.2	10.3
941	1650	7.3	n.d.	12.4	10.3
941	1600	6.7	1.2	11.6	10.3
941	1550	6.6	n.d.	11.1	10.3
942	1750	8.4	n.d.	14.7	10.0
942	1700	8.4	13.3	12.1	10.0
942	1650	7.0	n.d.	10.9	10.0
942	1600	7.4	n.d.	10.3	10.0
992	1800	1.3	5.4	3.0	1.66
992	1750	1.2	5.35	2.5	1.66
992	1700	1.25	n.d.	2.0	1.66

While it is probable that chemical equilibrium is attained at the firing temperature of these bodies, experimental proof was sought to confirm this possibility. Also it is important to know whether this high temperature state is "frozen in" on cooling or whether it tends to adjust to a lower temperature equilibrium situation. The remaining sections of 4.2.3.2 attempt to answer these questions. It is shown that equilibrium at temperature is approached and that the system does tend to adjust to a lower temperature equilibrium on cooling. The latter fact is supported by the sag bar studies reported in section 4.2.3.3.1.

TABLE 4-9

Crystal Species Present in Ceramic Bodies  
under Equilibrium Condition

Ceramic	Primary	Secondary
941	$\text{Al}_2\text{O}_3$	$\text{CaO} \cdot 6\text{Al}_2\text{O}_3^*$ , $\text{CaO} \cdot \text{Al}_2\text{O}_3 \cdot 2\text{SiO}_2^{**}$
942	$\text{Al}_2\text{O}_3$	$\text{CaO} \cdot \text{Al}_2\text{O}_3 \cdot 2\text{SiO}_2^{**}$
992	$\text{Al}_2\text{O}_3$	$\text{CaO} \cdot \text{Al}_2\text{O}_3 \cdot 2\text{SiO}_2^{**}$

\*Calcium hexa-aluminate

\*\*Anorthite

#### 4.2.3.2.2 Optical and Electron Microscope Studies

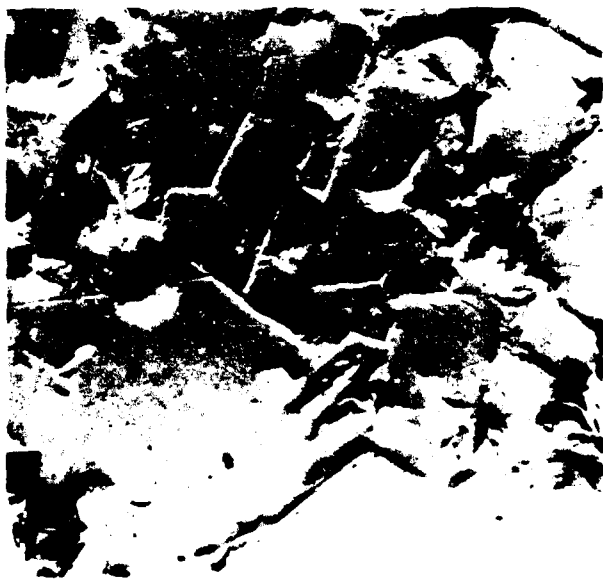
Measurements of the amounts of secondary or glassy phase in the special alumina ceramic bodies using the line-intercept fraction method were made using a series of electron photomicrographs of the special bodies listed in Table 4-8. Pictures of six different areas of a polished sample of each body were made in order to provide a representative sampling of the materials. A magnification of 3500X was used because it was a good compromise between the high magnification required for good resolution of phase boundaries and the amount of area required for a representative sampling of the surface.

Examples of areas of each sample are presented in Figs. 4.14, 4.15 and 4.16. The areas occupied by corundum crystals ( $\alpha\text{-Al}_2\text{O}_3$ ) and the glassy phase are easily distinguishable in each photograph.

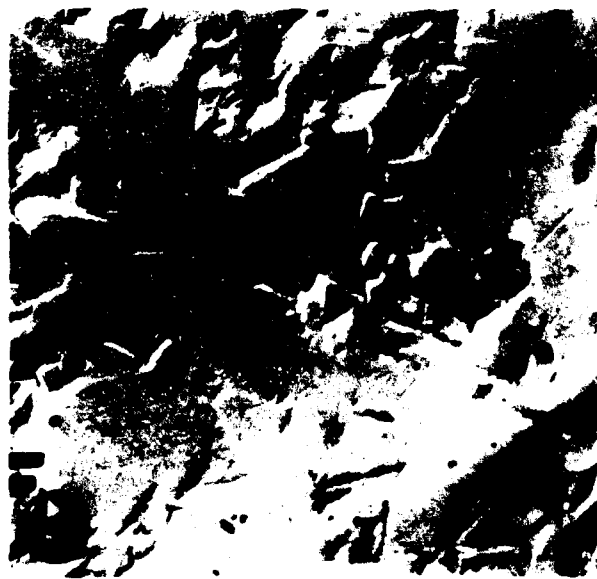
The sample preparation technique is described in detail in the Sixth (pp. 59-60) and Seventh (p. 28) Quarterly Reports.

The line intercept fraction measurements were made by placing a sheet of tracing graph paper over each photomicrograph which was taped to a lighted tracing board. The photomicrographs were 24 cm. by 21 cm. and the graph paper was aligned so that 23 vertical lines (one every centimeter) crossed each photograph. Each line was marked to the nearest 1/2 millimeter to indicate the portions

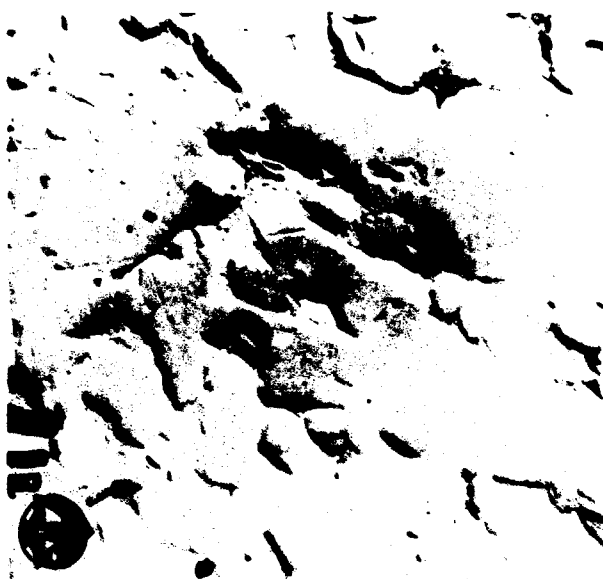




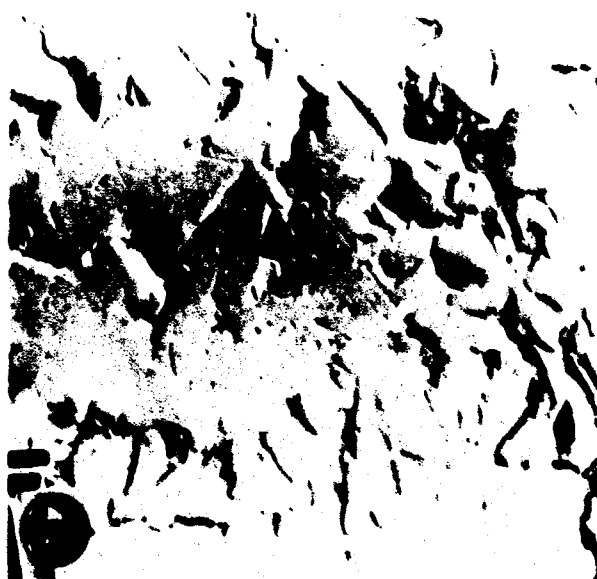
a



b



c



d

Figure 4.14: Electron photomicrographs (3500X) of polished surfaces of special alumina bodies (a) 941 (1700), (b) 941 (1650), (c) 941 (1600), and (d) 941 (1550). The numbers in parentheses are the body firing temperatures in °C.

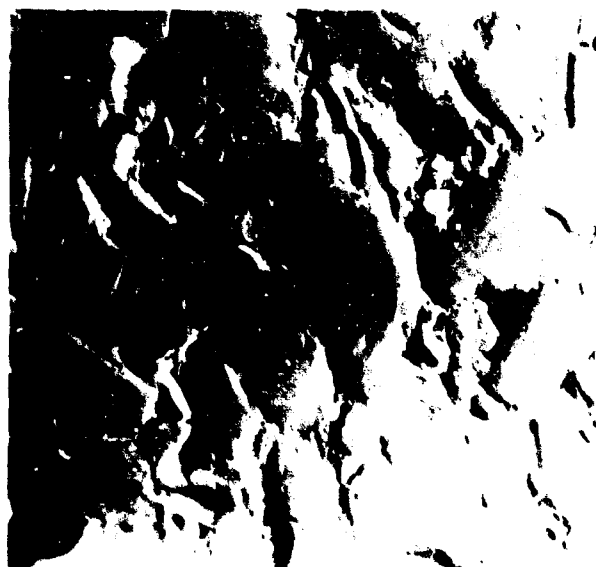
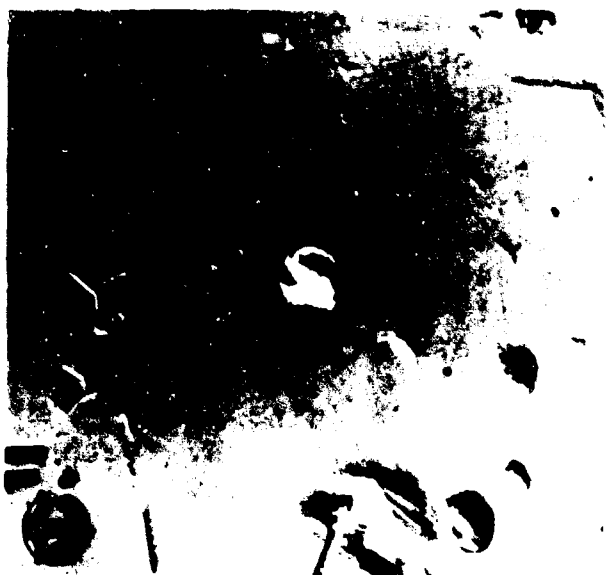


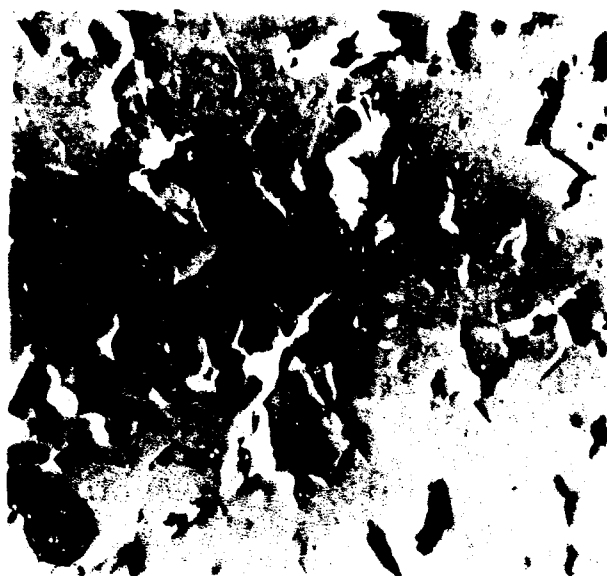
Figure 4.15: Electron photomicrographs (3500X) of polished surfaces of special alumina bodies (a) 942 (1750), (b) 942 (1700), (c) 942 (1550), and (d) 942 (1600). The numbers in parentheses are the body firing temperatures in °C.



a



b



c

Figure 4.16: Electron photomicrographs (3500X) of polished surfaces of special alumina bodies (a) 992 (1800), (b) 992 (1750), and (c) 992 (1700). The numbers in parentheses are the body firing temperatures in °C.

traversing corundum crystals, glassy phase regions and voids. The fraction glass in each photomicrograph was calculated by dividing the total length of the line traversing glassy regions by the total length of lines traversing corundum crystals and glass regions. The numbers thus obtained were line-intercept fraction glass and were equal to the volume fraction of glass in the bodies with zero percent porosity. The weight percent of glass was calculated assuming a specific gravity of 4.0 gm/cc for corundum and 2.6-2.8 gm/cc for the glass.<sup>8,24</sup>

Similar measurements were made using light photomicrographs (1000X) taken with a metallograph. Data were not obtained for all bodies, but representative samples of each composition were measured.

The results obtained from both electron and light photomicrographs are presented in Table 4-8 for comparison. The difference in the two sets of values is most noticeable and is discussed in detail below. Values obtained from light photomicrographs were roughly twice as large as electron photomicrograph values for the same bodies.

The fifth and sixth columns in Table 4-8 list the quantities of secondary or melt phase which would be present if equilibrium were reached in each special ceramic body at each of two temperatures. The fifth is the temperature at which the ceramic was fired, and the sixth is the temperature of the invariant point, i.e. the temperature at which all remaining melt crystallizes on cooling under equilibrium conditions. The amounts of melt phase present in a body at each temperature represent the maximum and minimum amounts, respectively, that one would expect to find in each body. For example, body 941 (1700) should contain 14.2 weight percent melt at its firing temperature of 1700°C if equilibrium is reached. If equilibrium is maintained during cooling, the body would contain 10.3 percent melt at the invariant point, 1405°C, just before the secondary crystalline phase (3) began to precipitate. These values were calculated for each body using the "lever rule"\* and the pseudo-binary phase equilibrium diagrams in Figs. 4.03 and 4.04.

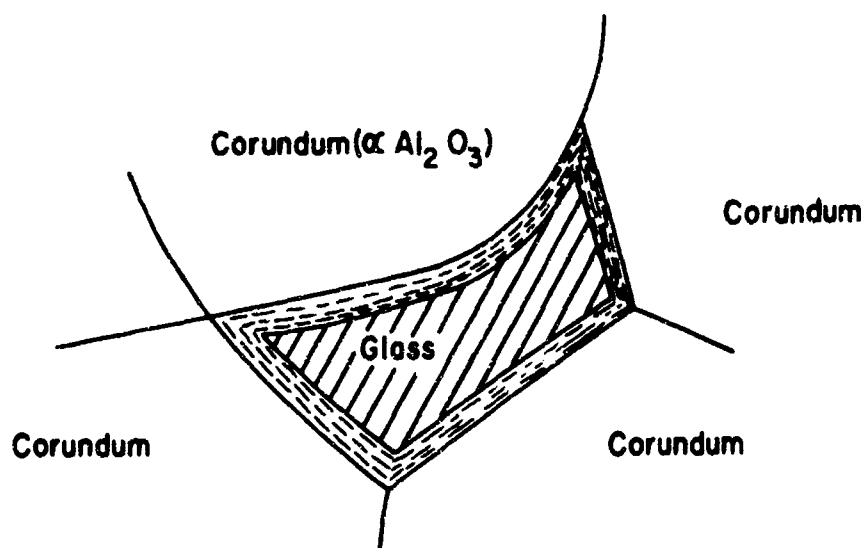
---

\*The lever rule is a means of determining the amount of each phase present at any point within a two phase region of a binary phase equilibrium diagram. The point is located by the composition and temperature of the system.

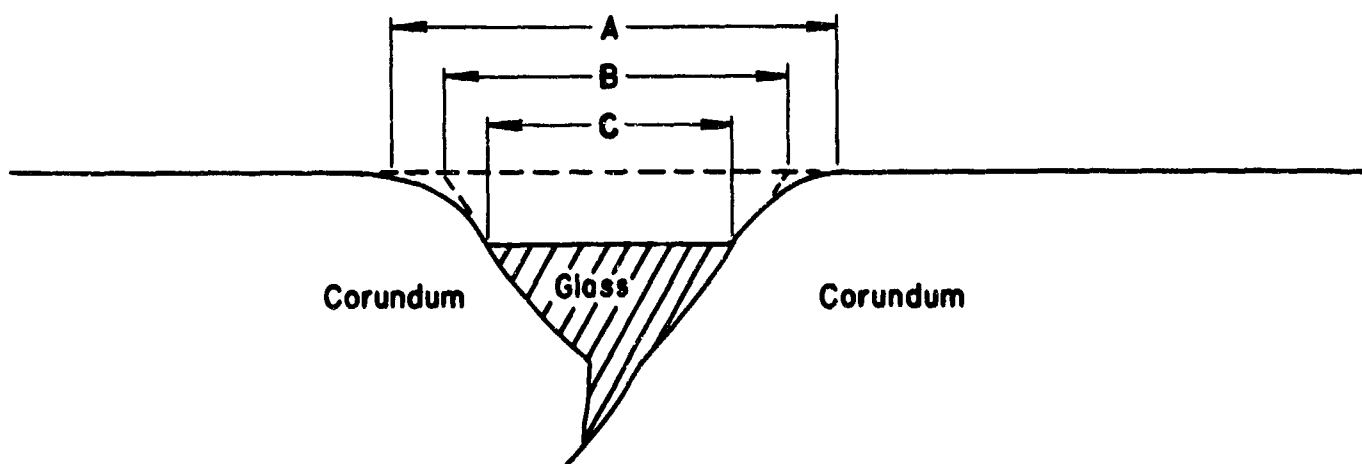
In order for these alumina bodies to maintain equilibrium during cooling, alumina must precipitate from the melt to continue the growth of the corundum crystal phase. However, as is subsequently discussed in section 4.2.3.3.1, the viscosity of the melt phase increases rapidly as the temperature drops below 1450°C so the diffusion of  $Al^{+3}$  and Al complexed ions necessary for continued precipitation and growth of the primary corundum crystal phase is so reduced that the system only sluggishly approaches equilibrium. Rapid cooling thus traps some alumina in the melt and holds it while the melt is super-cooled to the glassy state. Because of the additional alumina in the melt, the quantity of melt is greater than it would be if equilibrium conditions were maintained. Therefore, the amount of melt measured in Body 941 (1700) should be somewhere between 14.2 percent, the maximum amount that could be present at 1700°C and 10.3 percent, the minimum amount that would be present at 1405°C, the invariant point. (Even if some calcium hexaluminate and anorthite secondary crystalline phases were able to nucleate and grow below the invariant point temperature, they would do so within the "glassy areas" and would be counted as glass when line-intercept techniques are used to interpret the photomicrographs).

The fact that all values obtained by line-intercept-fraction measurements were outside the possible range of values as discussed above was disappointing, but can be explained. The most likely source of error was the surface relief of the samples and the difference this causes in the two types of photomicrographs used in the study. Measurements made on electron photomicrographs consistently gave values below the theoretical minimum amounts, but the values generally fell in descending order indicating a strong relationship to the firing temperatures. Measurements made on light photomicrographs gave values above the theoretical maximum, but again showed good correlation to the firing temperatures.

Relief in the sample surface is practically impossible to eliminate because it results from the fact that the corundum crystal phase is much harder than the glassy phase. Consequently, any polishing operation depresses the softer glassy areas with respect to the rest of the surface. Reference to Fig. 4.17 will help to explain how surface relief could have produced the errors in the glass phase measurements. The upper sketch in Fig. 4.17 shows a typical glassy region surrounded by corundum crystals in the surface of a ceramic sample. The surfaces of the



**Top view of glassy region in alumina surface.**



**Cross section through glassy region in alumina surface.  
Dash lines indicate contours before polishing.**

**Figure 4.17: Schematic presentation of a typical glassy phase region of a high alumina ceramic showing the effects of polishing the surface.**

corundum crystals all lie generally in the same plane, while the glassy region is slightly depressed and its surface lies in a plane below that of the corundum. The edges of the corundum crystals are rounded during polishing and slope down to meet the glass surface.

When a shadowed carbon replica is made of this surface feature, contours are faithfully reproduced so that the subsequent electron photomicrograph of the replica displays all aspects of the feature in perfect focus. The exact location of the interface between the glass surface and the sloping corundum crystal can be seen. On a line intercept measurement the extent of the glassy region would then be marked as the distance "C" in the lower sketch of Fig. 4.17.

A photomicrograph of the same area taken with a conventional Metallograph at 800X does not bring the entire feature into focus because the depth of focus is usually less than the depth of the feature. This type of photomicrograph is normally taken with the upper surface (corundum crystals) in focus and the voids or glassy regions slightly out of focus. A line intercept measurement of the feature would then include the distance "A" as the glassy region, because the actual region would be fuzzy and the true boundary difficult to locate.

The correct or original extent of the glassy region as indicated in Table 4-8 and the previous discussion, is somewhere between the extreme values obtained from the two types of photomicrograph. This should be the distance "B" shown in Fig. 4.17 which indicates the extent of the glassy region before it was worn down preferentially and before the sharp edges of the corundum crystals were rounded by polishing. The dotted lines indicate the original glass-crystal interface. The possibility of estimating the original interface location has been considered, but this could be misleading and no more accurate than averaging the values obtained from measurements on the two types of photomicrograph. In most cases such averages are within the limits set by equilibrium calculations. However, for our purposes, it is desirable to locate accurately the correct value for the amount of glass within the range of possible values, not just to determine that it is within the range.

The location of this value within the range is very important because it must be used in an application of the "lever rule" and phase equilibrium diagrams to determine

the amount of  $\text{Al}_2\text{O}_3$  dissolved in the melt. The melt composition (and temperature) determines its viscosity, which in turn is a major factor in determining metallizing behavior characteristics of the melt such as mass flow and ionic diffusion rates. When several steps are required to arrive at the desired result as in this case, the accuracy of each step must be optimized to avoid compounding errors.

Because of the nature of the  $\text{CaO-Al}_2\text{O}_3\text{-SiO}_2$  system, an error in determining the amount of glass or melt phase results in a magnified error in determining the  $\text{Al}_2\text{O}_3$  content of that phase. While the amount of melt varies over an allowable span of approximately 4% (Table 4-8), the amount of dissolved  $\text{Al}_2\text{O}_3$  which causes the change in the amount of melt, varies over a span of about 20 percent. Consequently, an error of 10 percent in determining the amount of melt would produce an error of 40 percent in computing the percentage of  $\text{Al}_2\text{O}_3$  in the melt. This error would not have a great effect on viscosities determined for 1:1  $\text{SiO}_2/\text{CaO-Al}_2\text{O}_3$  melts, but would have importance in determining the viscosities of 2:1  $\text{SiO}_2/\text{CaO-Al}_2\text{O}_3$  melts, especially at lower temperatures. Therefore the  $\text{Al}_2\text{O}_3$  contents of melts must be accurately determined if subsequent determinations of melt viscosity and diffusion coefficients are to be accurate.

In conclusion, it should be noted the quality of the results (accurate to within a few percent) is comparable to those obtained by other workers<sup>25</sup>. As the results are not good enough for the present purpose (which requires values to within a few tenths of a percent for use in subsequent calculations of the glassy phase composition), similar calculations by other workers should be treated with reserve.

#### 4.2.3.2.3 Mineralogical Analysis

The equilibrium phases present in the ceramics as given by the equilibrium phase diagrams were shown in Table 4-9. In order for these phases to crystallize and no other, the alumina content of the melt phase must be a minimum of 42% for the 941 body and 37% for the 942 and 992 bodies.

The three series of bodies were crushed to a powder form for X-ray diffraction analysis. The results are presented in Table 4-10 and are discussed below in conjunction with the phase equilibrium diagrams, Figs. 4.03 and 4.04. In the terminology used in regard to the X-ray data, a trace is 2% or more, a minor phase is 4% or more.



TABLE 4-10

Summary of X-Ray Diffraction Data on Special Alumina Bodies  
(Interior -- Powder Samples)

Ceramic	Original Firing Temp. °C	As Received	Refire 1425°C, 1/2 hour
		Minor + Phase	Minor + Phase + Trace + Phase <sup>+</sup>
941	1550	Gehlenite	Calcium Hexaluminate -
		Calcium Hexaluminate	
941	1600	Calcium Hexaluminate	Calcium Hexaluminate
941	1650	-	-
941	1700	-	-
		Calcium Hexaluminate	Calcium Hexaluminate
942	1550	No Data	Anorthite
942	1600	Aluminum Calcium Ortho Silicate	No Data
942	1650	-	-
942	1700	-	-
942	1750	Anorthite	No Data
992	1650	No Data	No Data
992	1700	-	-
992	1750	-	-
992	1800	-	-
		Calcium Hexaluminate	Anorthite
			Anorthite
<sup>+</sup> Crystalline			

The 941 body is examined first. The 941-1550 underfired body, Table 4-11, Fig. 4.09, Fig. 4.14, shows the presence of a non-equilibrium phase - Gehlenite ( $2\text{CaO} \cdot \text{SiO}_2 \cdot \text{Al}_2\text{O}_3$ ) co-existing with the two equilibrium phases, indicating that the alumina content of the glass phase of this ceramic is in the range 37-43% giving complete melt formation at a maximum temperature of  $1450^\circ\text{C}$  and a minimum of  $1400^\circ\text{C}$ .

The  $1600^\circ\text{C}$  firing gives the equilibrium phases expected, indicating an alumina content in the range 42-48% having a melt range from  $1450$ - $1600^\circ\text{C}$ . The anorthite phase is the last phase to crystallize in this system, and its presence in only a trace amount indicates that the melt tends to supercool to give some glass phase.

Based on the foregoing, it is logical to assume that the melt from both the  $1650^\circ\text{C}$  and  $1700^\circ\text{C}$  firing supercools from the firing temperatures with the precipitation of some alumina, giving an alumina content in the glass phase of 42-52% and 42-57% ranges respectively.

An examination of the  $1425^\circ\text{C}$  refire is instructive. Two crystal phases are resorbed in body 941-1550 $^\circ\text{C}$  which further tie down the concentration of alumina in the melt phase to 39-41%, the melt supercools to a glass and primary  $\text{CaO} \cdot 6\text{Al}_2\text{O}_3$  crystals. The anorthite is reabsorbed in the 941-1600 body as  $1425^\circ\text{C}$  is above the crystallization temperature of  $1405^\circ\text{C}$  (Fig. 4.03) and some of the  $\text{CaO} \cdot 6\text{Al}_2\text{O}_3$  is resorbed giving a melt which supercools to a mixture of glass and  $\text{CaO} \cdot 6\text{Al}_2\text{O}_3$ .

The 941-1650 $^\circ\text{C}$  continues to present a supercooled glass phase, while the 941-1700 $^\circ\text{C}$  shows some tendency towards devitrification as may be expected of a higher alumina content in the glass phase. Table 4-11 presents the derived data discussed above.

The X-ray data on the 942 and 992 ceramics may be analyzed similarly and the range of alumina content in the glass phase obtained similarly; this data is presented in Table 4-11.

The electron microscope photographs, Figs. 4.15, 4.16 and 4.17 do not reveal the presence of crystalline phases because of polishing difficulties.

An examination of the surface condition of the bodies is also of interest. This is shown in Table 4-12.

TABLE 4-11

Some Properties of the Glassy Phase  
of Special Alumina Bodies

Ceramic	Firing Temp.	Alumina Content of Melt Phase	Equilibrium Melt Range	Presence of Glass as Major Grain Boundary "as Received"	Presence of Glass After 1425°C Firing
941	1550	39-41 <sup>+</sup>	1400-1450	doubtful, C*	yes C
	1600	42-48	1450-1600	yes, C	yes-more, C
	1650	42-52	1450-1650	yes -	yes -
	1700	42-57	1450-1700	yes -	yes C
942	1550	<37- <sup>+</sup>	1547	no C	no C
	1600	<37- <sup>+</sup>	1547-1600	no C	no C
	1650	37-44	1547-1650	yes -	doubtful C
	1700	37-50	1547-1700	yes -	doubtful C
	1750	37-58	1547-1750	doubtful C	no C
992	1650	37-44	1547-1650	yes -	yes -
	1700	37-50	1547-1700	yes -	yes -
	1750	37-58	1547-1750	yes -	yes C
	1800	37-66	1547-1800	yes C	yes C

---

\*C denotes presence of crystalline phase

<sup>+</sup>definitely non-equilibrium

---

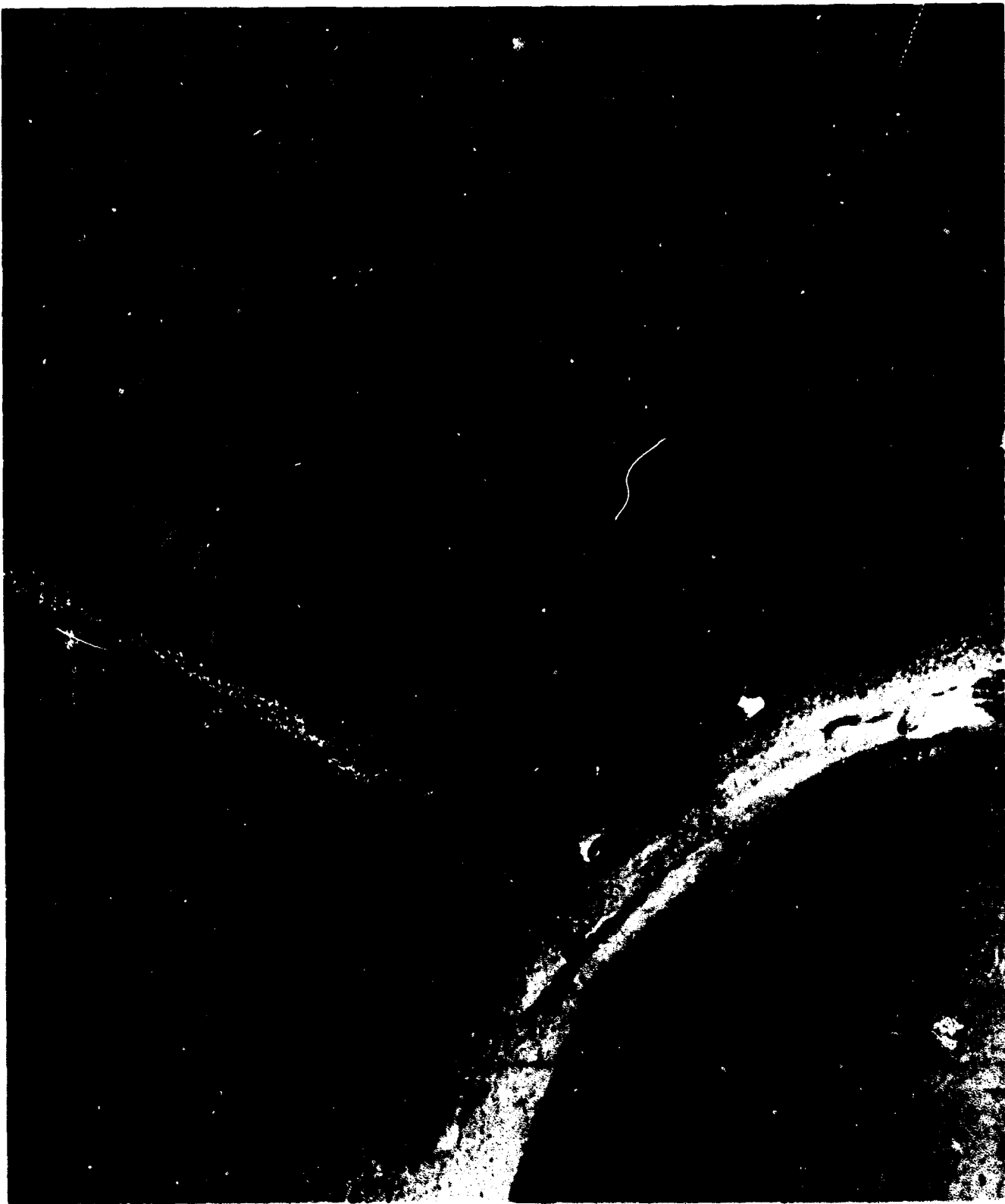


Figure 4.18: Electron photomicrograph of 941 alumina ceramic at 21,500X magnification showing the glassy phase between the grain boundaries of alumina particles.

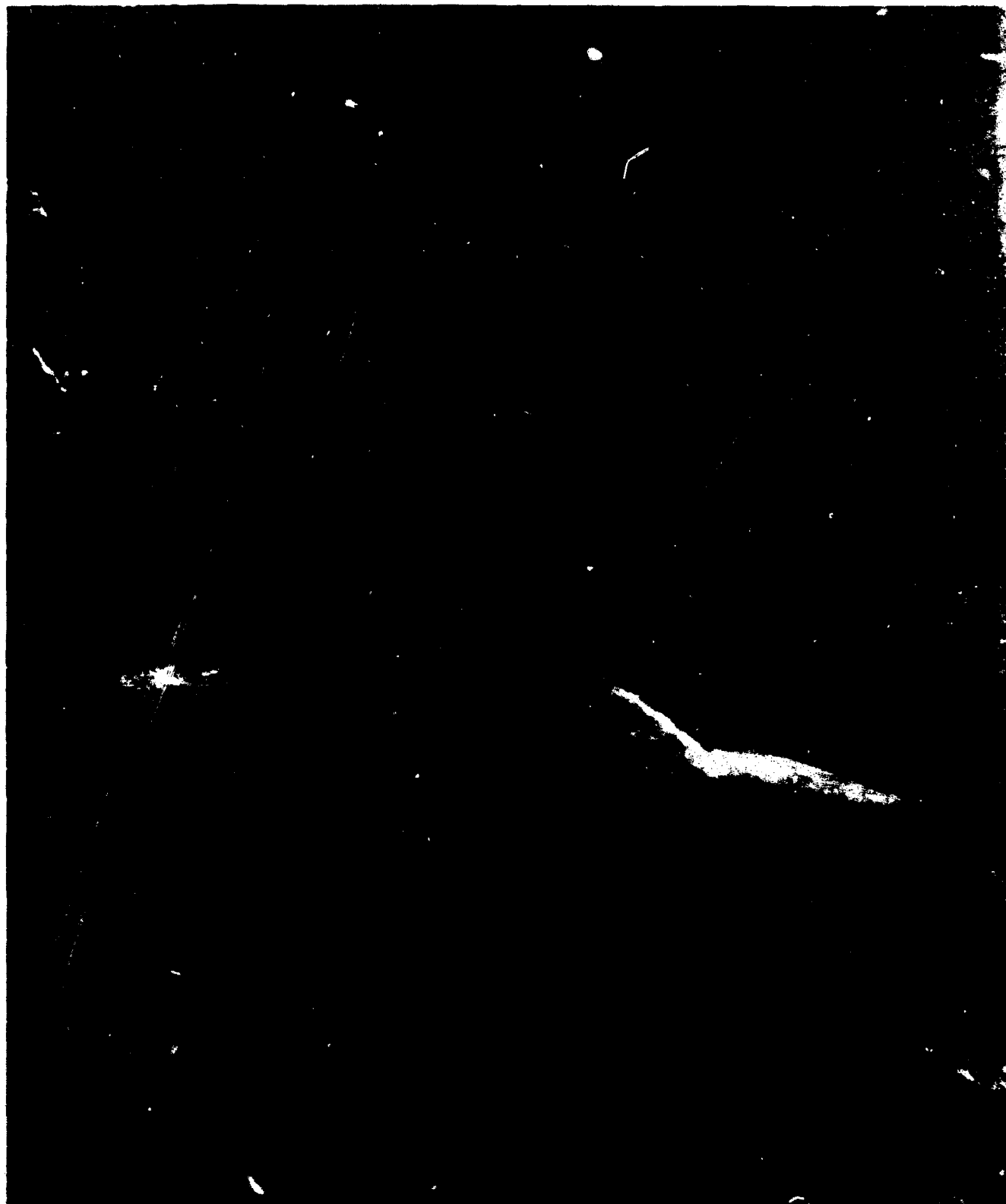


Figure 4.19: Electron photomicrograph of 942 ceramic at 21,500X magnification showing the glassy phase spreading over the alumina crystal and in the grain boundaries between the alumina ceramic.



Figure 4.20: Electron photomicrograph of 992 body, at 21,500X magnification showing the glassy phase.

TABLE 4-12

Summary of X-Ray Diffraction Data on Special Alumina Bodies  
(Surface Condition)

Ceramic	Original Firing Temp. °C	As Received			Refire 1425°C	
		Minor Phase <sup>+</sup>	Trace Phase <sup>+</sup>	Trace Phase <sup>+</sup>	Minor Phase <sup>+</sup>	Trace Phase <sup>+</sup>
941	1500					
	1550	Gehlenite	Anorthite		-	-
	1600	Gehlenite	Anorthite		-	-
	1650	-	-		-	-
	1700	-	-		-	-
942	1550	-	Anorthite		Anorthite	-
	1600	-	-		Anorthite	-
	1650	-	-		Anorthite	-
	1700	-	-		Anorthite	-
	1750	-	-		Anorthite	-
992	1600	-	Anorthite		-	Anorthite
	1650	-	-		-	Anorthite
	1700	-	-		-	Anorthite
	1750	-	-		-	Anorthite
	1800	-	-		-	Anorthite
<sup>+</sup> Crystalline						

The 941 body shows the absence of  $\text{CaO} \cdot 6\text{Al}_2\text{O}_3$ , noted in the center of the body showing that the faster rate of surface cooling induces more glass to be formed than in the interior of the body. The formation of gehlenite as the most predominate phase on the surface in the "as fired" material at the lower temperature indicates that the crystallization occurred as a devitrification product during cooling.

The lack of crystallinity of the "as received" surface of the 942 and 992 bodies indicates a glass phase. This glass phase may be completely devitrified to anorthite on reheating to  $1425^\circ\text{C}$ . The presence or absence of the crystal phases in the boundaries was confirmed by the electron microscope as is typically shown in Figs. 4.18, 4.19 and 4.20.\*

The differences in the composition and amounts of glass present in the three ceramics and also the ground (originally the body interior) versus un-ground (as received surface) differences in composition will be of significance when discussing the behavior of the metallized ceramics.

The data obtained using the X-ray/phase diagram technique is considered to be of significant value.

#### 4.2.3.2.4 Electron-Microprobe Analysis

Historically the first technique employed on the program to determine alumina content was the electron microprobe. The basic problem encountered with the microprobe was one of resolution, see the Sixth Quarterly Report, pp. 50-59. The grain boundary widths of the ceramic are of the order of one micron which is comparable in size with the diameter of the beam. However, selected areas of the higher temperature fired ceramics contained glassy areas 2 to 3 microns in diameter. Even so, due to secondary X-ray fluorescence effects and selective differential absorption of Ca K-alpha and Si K-alpha radiation by overhanging alumina crystals and the evaporated aluminum film covering the surface, erroneous readings were obtained; the  $\text{SiO}_2/\text{CaO}$  ratios being variable and averaging much too low.

It was regretfully decided to discontinue this investigation and to use the microprobe for tasks more suited to its capabilities.

---

\*Space precludes the presentation of the more than 100 photographs obtained on the ceramics showing the "as received" or "heat treated" surfaces.



#### 4.2.3.2.5 Chemical Analysis

The chemical analysis technique, using in the preliminary series of experiments a HCl solvent and later a HF solvent, (9th Quarterly Report, pp. 21-22) showed promise.

The experimental procedure required that the ceramic sample first be crushed to minus 60 mesh. A dried and weighed sample of the pulverized sample was then leached in warm 1:1 HCl for at least 24 hours. The remaining corundum crystallites were filtered and weighed. Steps were taken to remove iron introduced in the crushing step. This consisted of washing the sample in a solution which dissolved the iron without attacking the glass or crystalline phases of the ceramic. (The resistance of corundum crystals to attack by HCl was determined by exposing a sample with one micron average particle size to the acid under the same conditions of time, temperature and concentration that were used for the leaching step. Six weight percent of the corundum was dissolved.)

The alumina body 941 (1700) was used in all solution work up to this time. Two gram samples crushed below 60 mesh were soaked in 100 ml of 1:1 HCl for lengths of time ranging from one to 32 hours. At the end of the soaking period the solvent and insoluble material were separated by filtering, then the insoluble material was dried and weighed. The filtrate was analyzed for Si, Ca, Al, and Fe.

Invariably the relationship between the time and the amount of the sample dissolved was the reverse of what it should have been. That is, the samples which were exposed to the acid solution for longer times had more rather than less insoluble material retained on the filter paper. Subsequent chemical analysis of the filtrate showed much less silicon in relation to the amounts of aluminum and calcium that there should have been. The silica was precipitating as silica gel and being retained with the insoluble fraction. The amount of soluble material observed in the several experiments varied from 7 to 10.5 weight percent. This was less than it would have been if the silica had not precipitated, but was close enough to the calculated range of 10.3 to 14.2 percent glassy phase to expect reasonable accuracy from the technique if the proper solvent is used.

In order to overcome the difficulty of silicate precipitation which was encountered using only HCl, a solvent containing HF and H<sub>2</sub>SO<sub>4</sub> in 4:1 ratio was prepared. The HF

dissolves silica and reacts to form  $\text{SiF}_4$  (a gas) and water. This type of reaction removes silicon from the glass structure and leaves an amorphous mass that is easily dissolved. Here again, the solubility of the crystalline  $\text{Al}_2\text{O}_3$  in the solvent must be accurately determined because it is large enough to affect the accuracy of the results, and therefore some correction of the data for this factor is necessary.

The procedure is similar to that used with  $\text{HCl}$ . The insoluble material is separated and weighed and the solute is analyzed for Ca, Al and any metal ion which may be introduced by crushing the sample.  $\text{SiF}_4$  is driven off by repeatedly evaporating the sample to dryness and repeating the solution step with fresh acids.

The results again indicated that no greater accuracy could be obtained than with other techniques. It was seen that further improvements in the accuracy of this method would require an inordinate amount of effort in relation to the overall scope of the program. It was therefore decided to divert this effort to more productive areas of the program.

#### 4.2.3.2.6 Reaction Rate Studies

It had formerly been assumed that ceramic systems were very sluggish in their approach to equilibrium, but at the high temperatures employed to manufacture alumina ceramics, the fluid glassy phases present in alumina ceramics may enable a close approach to equilibrium as can be seen from the X-ray data presented in 4.2.3.2.3. Also, work by Barrett and Reed<sup>15</sup> showed that corrosion of alumina (sapphire) by large volumes of  $\text{CaO} \cdot \text{SiO}_2$ - $\text{Al}_2\text{O}_3$  glass was initially controlled by the interfacial chemical reaction which changed to a diffusion controlled mechanism with a build up of product in a Nernst layer of the order of 100 microns thick. Thus it is reasonable to expect an equilibrium condition to occur over the 1 micron glassy phase thickness of the grain boundary of alumina ceramics.

In order to confirm this, a series of glass-sapphire sandwiches was made by placing minus 325 mesh, 1:1  $\text{SiO}_2/\text{CaO}$  glass containing 0%, 20% or 40%  $\text{Al}_2\text{O}_3$  between sapphire discs. The discs were about 0.035 inches thick and had an optical polish on the side in contact with the glass. Each unit was fired to one of three temperatures, 1500°C, 1675°C, or 1750°C in air for three hours and then cooled rapidly.

In each case, a portion of the sapphire was dissolved by the glass, depending on the reaction temperatures and the amount of  $\text{Al}_2\text{O}_3$  placed in the glass initially. The amount and distribution of the  $\text{Al}_2\text{O}_3$  in the glass layer will depend upon the rates of solution and/or diffusion of  $\text{Al}_2\text{O}_3$  through the glass as well as the initial  $\text{Al}_2\text{O}_3$  content of the glass.

The samples were prepared for microprobe examination by mounting and polishing them metallurgically. Photomicrographs of the polished samples appear in Figs. 4.21, 4.22 and 4.23. The preferential attack of the glass phase on the sapphire revealed the hexagonal crystal habit of the sapphire. This observation proved that under the conditions of the present experiment the rate of attack was chemically controlled, at least during the initial stages of the reaction. The sample containing 40%  $\text{Al}_2\text{O}_3$  fired at  $1750^\circ\text{C}$  could not be recovered because it stuck to the setter and shattered when it was removed. The glass containing 40%  $\text{Al}_2\text{O}_3$  heated at both  $1500^\circ\text{C}$  and  $1675^\circ\text{C}$  appears to have partially crystallized. Possibly these are the only samples in which the glass became saturated with  $\text{Al}_2\text{O}_3$ .

It was initially planned to determine the amount of alumina present by using the technique of weighing the sapphire discs before and after corrosion by a given amount of glass.<sup>15</sup> This approach failed in this case because only the 1 mil edge of the glass was exposed. Thus the reacted glass melt could not be dissolved by either HCl or HF without dissolving considerable quantities of the alumina substrates.\*

The sectioned and polished couples were submitted for electron microprobe examination. The results of the initial analysis are reported in Table 4-13. The results indicated that equilibrium was not attained. Moreover, anomalies in the data such as less alumina dissolved at a higher temperature were surprising. Detailed consideration of these results is presented in the Eighth Quarterly Report, pp. 29-32.

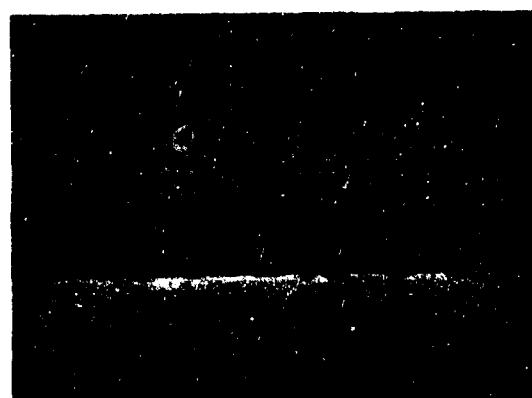
Further microprobe studies were made of glass-sapphire reaction couples #341, 342 and 343 toward the end of the program. The glass layer between the sapphire discs was about 15 microns thick. The concentration of alumina was the same across the layer (within experimental accuracy: 4 micron resolution) and had increased to more than 30 weight

---

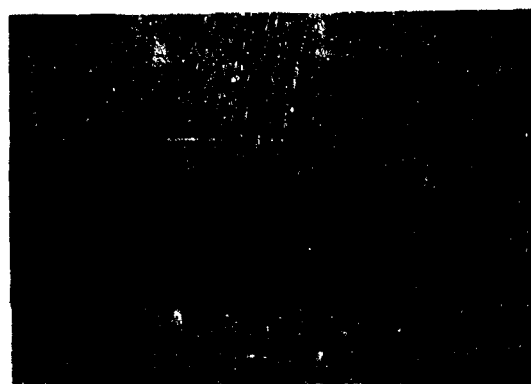
\*A hot furnace removal technique for one of the discs might solve this problem.



a



b



c

Figure 4.21: Glass-sapphire corrosion samples with 1:1  $\text{SiO}_2/\text{CaO}$  glass containing no  $\text{Al}_2\text{O}_3$  initially. Samples were reacted at (a)  $1500^\circ\text{C}$  (b)  $1675^\circ\text{C}$  (c)  $1750^\circ\text{C}$ . The glass is the wide band across the center of each photograph.



a



b

Figure 4.22: Glass-sapphire corrosion samples with 1:1  $\text{SiO}_2/\text{CaO}$  glass containing 20%  $\text{Al}_2\text{O}_3$  initially. Samples were reacted at (a)  $1500^\circ\text{C}$  and (b)  $1675^\circ\text{C}$ . The glass is in the band across the center of each photograph (400X).



a



b

Figure 4.23: Glass-sapphire corrosion samples with 1:1  $\text{SiO}_2/\text{CaO}$  glass containing 40%  $\text{Al}_2\text{O}_3$  initially. Samples were reacted at (a)  $1500^\circ\text{C}$  and (b)  $1675^\circ\text{C}$ . The glass is in the band across the center of the top photograph and in the lower two-thirds of the bottom photograph. (400X)

TABLE 4-13

Electron Probe Microanalyses of Glass Layer  
of Sapphire-Glass Sandwiches

Sample Number	Initial Glass Composition	Reaction Temperature	Percent Alumina in Glass after Reaction
336	1:1SiO <sub>2</sub> /CaO, <u>0%Al<sub>2</sub>O<sub>3</sub></u>	Not reacted*	0
337	"	1500°C	27.6
338	"	1675°C	21.5
339	"	1750°C	24.1
340	1:1SiO <sub>2</sub> /CaO, <u>20%Al<sub>2</sub>O<sub>3</sub></u>	Not reacted	18.7
341	"	1500°C	28.7
342	"	1675°C	31.3
343	"	1750°C	21.1
344	1:1SiO <sub>2</sub> /CaO, <u>40%Al<sub>2</sub>O<sub>3</sub></u>	Not reacted	n.d.
345	"	1500°C	44.4
346	"	1675°C	43.1
347	"	1750°C	n.d.

---

\*Fused 10 secs @ 1550°C

---

percent in all cases.

The accuracy of the original microprobe analyses can be considered to be only  $\pm 10$  percent because they were made relative to analyses of pure samples of the elements being analyzed. The second analyses had an accuracy better than  $\pm 5$  percent because the probe data were corrected for characteristic fluorescence absorption, mass absorption, and by the atomic number factor in a computerized program of successive approximations.

The results obtained in the second microprobe analysis appear in Table 4-14.

The alumina values are in all cases higher than those obtained in the first probe work. In addition, it was discovered that the glass in sample #343 was actually a two-phase system, thus accounting for the discrepancy reported in Table 4-13. This was first discovered with the microprobe, then verified visually by very careful microscopic examination. Sample #343 was not an intact sandwich as were #342 and #341, because it fractured when it was quenched. However, several glass pockets up to  $32\mu$  in thickness adhered to one sapphire disc, and these were satisfactory for analysis.

Microscopic examination revealed that samples #341 and 342 appeared much alike, both exhibiting a one-phase glass between the alumina sandwich. The absence of an alumina concentration gradient across the glass layer is interesting. It indicated that the alumina level of the glass was reaction rate controlled (dissolution of  $Al_2O_3$ ) rather than diffusion rate controlled. Resolution of the probe was such that it was safe to say that the alumina concentrations in the glass layers of the samples were level at the values in Table 4-14 to within two microns of either interface with the sapphire sandwich.

This conclusion supports the work of Reed and Barrett<sup>15</sup>. They showed that the initial vigorous chemical reaction occurring at the melt-sapphire interface would disrupt any concentration gradient that might tend to form. Dissolution would be rate controlled by the chemical reaction as long as insufficient product was dissolved to form a Nernst diffusion layer of sufficient thickness such that it could not be totally disrupted by the vigorous surface reaction. When an amount of product sufficient to give a layer greater than 50 microns thick had accumulated,



TABLE 4-14

Average Results for Analyses of Glass Zone of Glass-Sapphire Reaction Couples

Compound	Initial Comp.	Sample 341 (1500°C)			Sample 342 (1675°C)		
		Traverse			Traverse		
		1 (15 $\mu$ )	2 (15 $\mu$ )	3 (15 $\mu$ )	1 (15 $\mu$ )	2 (15 $\mu$ )	
Al <sub>2</sub> O <sub>3</sub>	20.0	33.8	35.0	33.1	33.6	33.4	
SiO <sub>2</sub>	41.4	31.7	32.5	31.9	31.0	30.9	
CaO	38.6	31.4	33.0	32.4	30.2	30.0	
Total	100.0	96.9	100.5	97.4	94.8	94.2	

Compound	Sample 343 (1750°C)					
	Traverse 1 (32 $\mu$ )		Traverse 2 (12 $\mu$ )		Traverse 3 (24 $\mu$ )	
	Phase 1	Phase 2	Phase 1	Phase 2	Phase 1	Phase 2
Al <sub>2</sub> O <sub>3</sub>	73.9	27.2	71.9	phase	73.5	27.4
SiO <sub>2</sub>	23.4	54.8	22.5	present	22.3	51.0
CaO	<0.1	6.9	<0.1	↓	0.4	7.6
Total	97.4	88.9	94.5	γ	96.2	86.0

chemical-diffusion and finally diffusion control would take over with a build up of a product layer extending up to 400 microns into the melt. Whereas in Reed and Barrett's work, the amount and dimensions of the melt phase were to all intents and purposes a semi-infinite system, the present work is a finite system with a 15 micron thickness dimension on the glassy phase. It is obvious, therefore, that the continuing vigorous chemical reaction will at all times destroy the tendency for a concentration gradient to form. A deduction of paramount importance may be made as a result of these observations, i.e., the above condition will also most certainly hold true for the case of alumina dissolution by the fluxes during the firing of the special alumina bodies and the great majority of commercial ceramic bodies as the critical dimension of the grain boundary is of the order of one micron.

It was interesting to note that no relationship existed between the end alumina concentration and the reaction temperature. The alumina concentration having increased by the same amount in both samples #341 and 342 to 13 - 15%. The finding confirmed the earlier work in this and the other  $\text{CaO} \cdot \text{SiO}_2 - \text{Al}_2\text{O}_3$  systems investigated, as shown in Table 4-13, and indicates that chemical equilibrium is not attained (see prior sections).

It would be expected that the reaction rate of the forward reaction

$$\frac{dq}{dt} = K \left( 1 - \frac{\gamma_m c_m}{\gamma_s c_s} \right)$$

would increase as a function of temperature according to the equation

$$K = K_0 e^{-\Delta H/RT}$$

where K is the forward rate reaction constant,  $K_0$  is a constant, R is the gas constant and T is the absolute temperature;  $dq/dt$  is the rate of the forward reaction,  $c_s$  is the saturated alumina concentration, which also increases with temperature,  $c_m$  is the concentration of alumina in the melt and  $\gamma_s$  and  $\gamma_m$  are their respective activities in the melt.

Based on the present data one must assume that either K or  $1 - \frac{\gamma_m c_m}{\gamma_s c_s}$  decreases with temperature increase

or that both are constant. The net result is that  $\Delta H$ , the temperature coefficient of the reaction, is zero.

It has been shown that  $\gamma = 1$  for six fold coordinated alumina over the range of saturation concentration of interest to us (3rd Quarterly Report) and that  $\gamma$  increases with rise of temperature over the region 0% to 50% alumina. It is just possible that this factor could explain the present results.

Other published data however, indicates that the reaction rate does increase with temperature with an activation energy in excess of 50 K cal.

It would be expected that a closer approach to an equilibrium condition would be attained in the grain boundaries of the special alumina ceramics.

A complete sandwich was not available for sample #343, so that we cannot be sure that the CaO has been removed from the system by volatilization in the  $H_2/3N_2$  atmosphere. If this is the case however, then we are left with a very viscous melt high in silica and alumina. Alternatively, Roy<sup>26</sup> has shown that this region of the phase diagram can produce a glass in glass separation. It is therefore possible that this had occurred in sample #343.

Phase I corresponds to the mullite composition,  $2 Al_2O_3 \cdot SiO_2$ . The possible removal of the CaO by volatilization has placed the composition in a region of the CaO-SiO<sub>2</sub>-Al<sub>2</sub>O<sub>3</sub> ternary phase diagram where mullite will be the first phase to crystallize. It will nucleate and grow from the alumina interface. The microprobe data shows that Phase I does indeed extend from the alumina interface into the glassy Phase II. X-ray analysis of the couple is required to establish whether the glass-in-glass hypotheses or the mullite crystallization theory is correct.

If the CaO has not been volatilized, then a region rich in  $CaO \cdot 6Al_2O_3$  must exist. It is possible that this spalled from the sample during its preparation. A spectrographic scan of the sample #343 revealed contamination by several other elements which amounted to 5 to 10% of the sample. These are listed with their approximate concentrations in Table 4-15.

It is possible that this contamination affected the X-ray absorption factors as well as upsetting the total analysis. The source of this contamination was most likely

TABLE 4-15

## Contaminants in Phase II of Sample #343

<u>Element</u>		<u>As Oxides</u>	
Fe	.6 to .9%	$\text{Fe}_2\text{O}_3$	.9 to 1.3
Ti	1 to 2	$\text{TiO}_2$	1.7 to 3.3
K	1 to 2	$\text{K}_2\text{O}$	1.2 to 2.4
Cb	.2	$\text{Cb}_2\text{O}_5$	.7
Zr	.2	$\text{ZrO}_2$	.9
P	.2	$\text{P}_2\text{O}_5$	.5

the polishing operation in which the glass-sapphire picked up the above elements which were left from a previously polished sample.

It should be noted that X-ray analysis of the 941 bodies only confirmed the presence of calcium-containing compounds such as  $\text{CaO} \cdot 6 \text{Al}_2\text{O}_3$  or anorthite, thus indicating that the behavior of the couple is not duplicated in the ceramic body itself in this respect.

Further evaluation of the above microprobe results is not justified until further microprobe studies backed up by electron microscope work and X-ray diffraction work can be programmed.

#### 4.2.3.3 Properties of the Glassy Phase

##### 4.2.3.3.1 Viscosity

Alumina flows plastically above  $1000^\circ\text{C}$ . At  $1000^\circ\text{C}$  the flow is imperceptible, but at  $1800^\circ\text{C}$  long single crystal rods can be bent into U-shaped geometries. The "glassy phase" of polycrystalline alumina ceramics is, however, several orders of magnitude more fluid than the alumina crystal at the same temperature. The amount and type of the glassy phase, therefore, controls the temperature at which the ceramic will sag and the temperature at which the glassy phase is fluid enough to flow out of the grain boundaries of the ceramic onto its surface and into a metallizing sintered porous sponge.

Figures 4.24 and 4.25 show the viscosity of the grain boundary phases in the special ceramics 941, (Fig. 4.24) 942 and 992 (both Fig. 4.25), based on the best values available in the literature. The maximum viscosity in the curves lies approximately at 47% and 37% alumina respectively.

The sag bars listed in Table 4-16 were used to indirectly determine the relative viscosity of the glassy phase of the 941 and 942 series of ceramics at 1425°C.

The bars were placed in a furnace under simulated metallizing conditions such that they had unsupported span of 5 inches over the center section of the 6-inch bar. When the furnace temperature approached the softening point of the glass phase, the bars sagged under their own weight. The extent of the "sag" under these conditions is determined by:

- a. Temperature
- b. The time at temperature
- c. The composition of the glass phase
- d. The amount of the glass phase
- e. Presence of a continuous crystal network structure.

The composition and amount of the glass phase are the only variables in the test results discussed in this report.

The composition of the glass phase is different in the 941 and 942 bodies because of the deliberately introduced differences in the silica-to-calcia ratio. Since silica is a network former, it tends to make a glass more viscous at a given temperature. Conversely, calcia is a network modifier and it will tend to make glass more fluid under similar conditions. Alumina occupies an intermediate position, i.e., it can either be a network former or a network modifier depending on the calcia-alumina ratio in the glass phase. Thus at low alumina percentages the viscosity will increase with alumina content, i.e., it is acting as a network former, whereas at higher alumina percentages, the viscosity will decrease, i.e., it is behaving as a network modifier. This subject is discussed in more detail in the section on structure, 4.2.3.1.

From the above discussion, we can see that the behavior of the 941 and 942 bodies will be different under the sag-bar test conditions described above. The actual results of the test after a sag time of one hour at 1425°C are shown in Table 4-16, column 3. Referring to Figs. 4.03

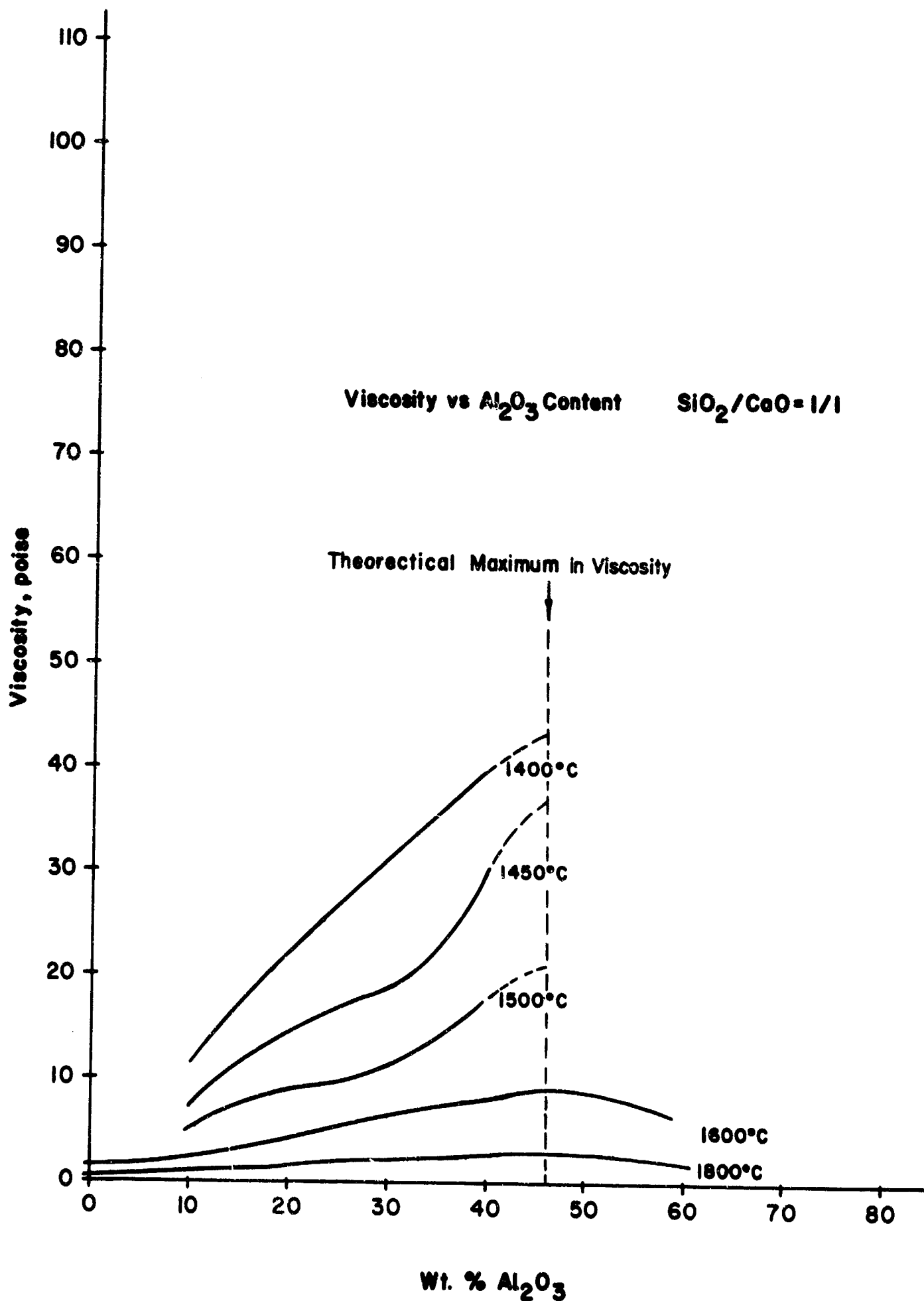


Figure 4.24: Viscosity versus  $\text{Al}_2\text{O}_3$  content for melts with 1:1  $\text{SiO}_2/\text{CaO}$  ratio. Dash lines indicate probable viscosity of melt supercooled to a glass at indicated temperature.

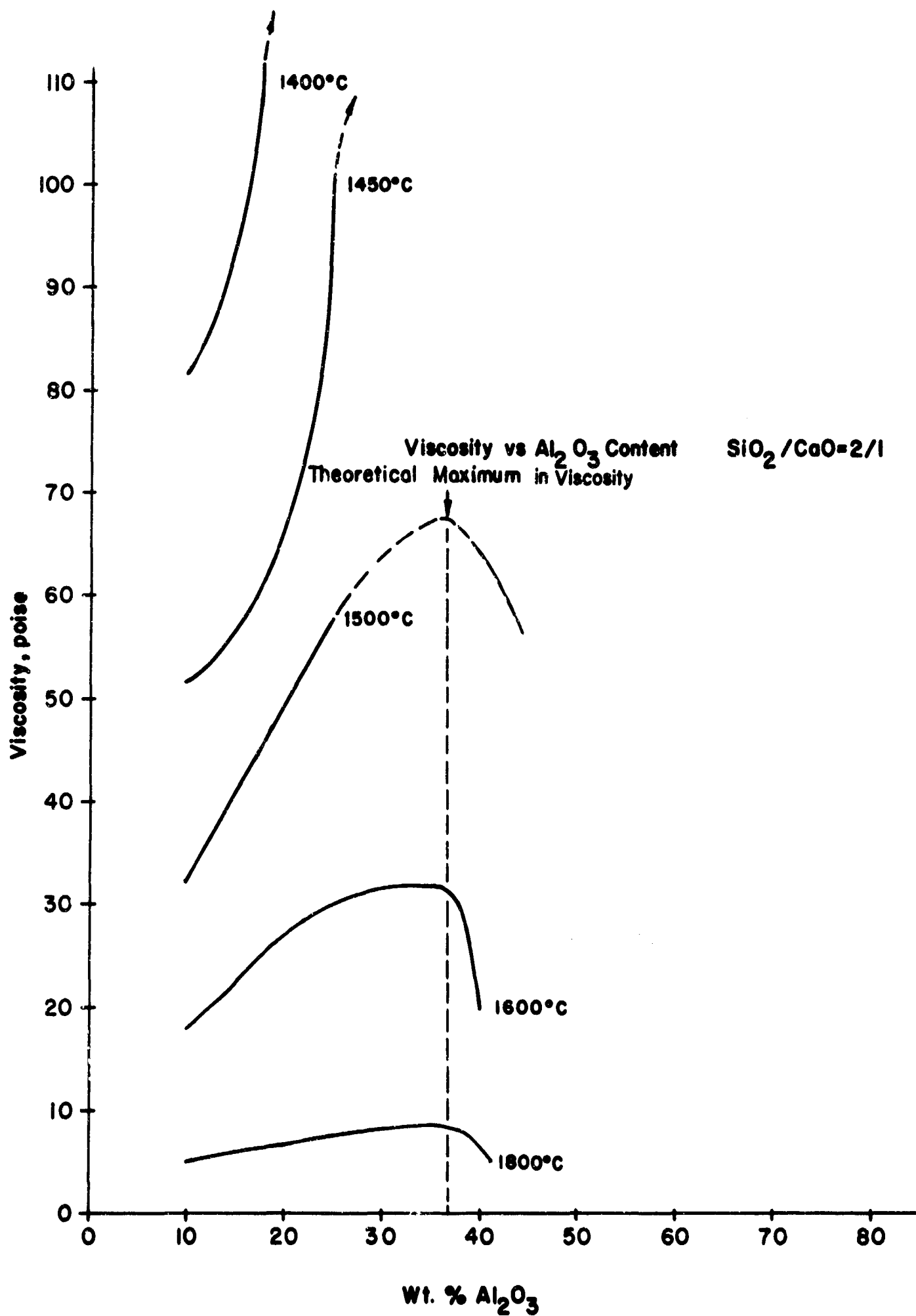


Figure 4.25: Viscosity versus  $\text{Al}_2\text{O}_3$  content for melts with 2:1  $\text{SiO}_2/\text{CaO}$  ratio. Dash lines indicate probable viscosity of supercooled melt at indicated temperature.

TABLE 4-16

Correlation of 1425°C Sag-Bar Results  
on the Special Ceramics with Viscosity and Chemical  
Composition (as determined from  
phase equilibria calculations)

(1) Body Type and Firing Temp. °C	(2) Weight Per Cent Chemical Composition			(3) 1425°C Sag Inches	(4) Viscosity Poise @ 1800°C	(5) Equilibrium Alumina % in Glass Phase		
	SiO <sub>2</sub>	CaO	Al <sub>2</sub> O <sub>3</sub>			(a)	(b)	
941-1500	3	3	94	-	-	-		
941-1550	3	3	94	0.092	2.3	45.6	-	42
941-1600	3	3	94	0.059	2.0	48.1	-	42
941-1650	3	3	94	0.033	1.9	52.0	-	42
941-1700	3	3	94	0.014	1.7	57.8	-	42
942-1500	4	2	94	-	-	-		
942-1600	4	2	94	0.022	4.0	46.3	-	37
942-1650	4	2	94	0.016	3.3	51.0	-	37
942-1700	4	2	94	0.012	2.7	56.3	-	37
942-1750	4	2	94	0.012	1.9	62.6	-	37

(a) at temperature

(b) between entectic point (1400°C for 941, 1512°C for 942) and  
room temperature



and 4.04 and to Table 4-10 and 4-11, it can be seen that the 942 "glassy phase" will be very largely, if not completely, composed of anorthite crystals at 1425°C.

As expected, the less viscous glass/melt phase in the 941 ceramic, as opposed to the more viscous and smaller quantity of glass phase which exists in the 942 ceramic, caused more slump in the 941 ceramic.

The decrease in sag of both series of bodies with increase of their initial firing temperature shows that the viscosity of the melt phase in these bodies is greater for the bodies made at the higher temperatures.

The viscosity data, Figs. 4.24 and 4.25, considered together with that data given in Table 4-11 shows that the alumina content of the 941 glassy phase must progressively increase to a maximum in the region of 40-47% for the 941 series of bodies. Thus, assuming equilibrium at the manufacture temperature (as was done to obtain column 5 in Table 4-11), some but not all of the alumina must precipitate from the melt on cooling; the bodies fired at the higher temperatures retaining more alumina in the glass phase. Little precipitated alumina will redissolve on heating to the 1425°C sag bar test temperature as this nears the solidus line on the phase diagram, Fig. 4.03.

A similar situation occurs in the 942 series of bodies. Again it can be assumed that if alumina equilibrium is attained during the manufacture of the body, alumina will precipitate on cooling prior to the grain boundary phase supercooling to a glassy phase. This glassy phase then almost completely devitrifies to anorthite (and alumina) on reheating to the sag bar temperature of 1425°C. Table 4-10. Thus although the viscosity trend in the 942 body is similar to that of the 941 body, the variation of the sag amount over the series is less because the amount of glassy phase present will be very small.

It is noted that the sag of 942-1700 and 942-1750 is the same. Three explanations or combinations thereof are possible to account for this fact -

- (i) The amount of glass phase is relatively less, see Table 4-8
- (ii) The amount of alumina in the glass phase straddles the viscosity maximum at 37%, Fig. 4.24, and could, for example, be 35%

and 39%. This would result from a departure from equilibrium as discussed in the text of Section 4.2.2. This departure from equilibrium is likely to be more pronounced in the 942 than in the 941 body because of the greater viscosity of the melt phase.

- (iii) Figures 4.08 and 4.10 show that the mechanism of final grain growth in the 942-1750 ceramic is due to solid-solid alumina diffusion. The formation of a substantial rigid skeleton structure in the 942 ceramic can provide an alternative explanation for the levelling out of the sag bar 'sag'.

#### 4.2.3.3.2 Ionic Diffusion

While viscous flow provides the mechanism for mass flow of the melt, ionic diffusion of its various ionic species provides a mechanism for selective migration of cations such as  $\text{Ca}^{2+}$  and anions such as  $\text{Si}_2\text{O}_7^{-6}$ . Fig. 4.26 shows the relative rates of diffusion of the  $\text{Al}^{3+}$ ,  $\text{Si}^{4+}$ ,  $\text{O}^{2-}$  and  $\text{Ca}^{2+}$  in the  $\text{CaO}.\text{SiO}_2\text{-Al}_2\text{O}_3$  system. From this data, it appears that diffusion of  $\text{Si}^{4+}$ ,  $\text{Al}^{3+}$  and  $\text{O}^{2-}$  as silicate and alumina silicate anions does not occur exclusively as the migration rate of the  $\text{O}^{2-}$  ion is much higher than that of the Al and Si ions.

The melts cited in Fig. 4.26 all have a  $\text{SiO}_2/\text{CaO}$  ratio of 1:1. Melt B contains 11% alumina. C contains 20% and D contains 40% alumina. It is to be expected from this data that the higher the  $\text{SiO}_2/\text{CaO}$  ratio for a given alumina content, the lower will be the diffusion rate.

During the formation of the alumina special bodies, the alumina grains are reacting with the calcium-alumino-silicate melt phase that has formed. Reed and Barrett<sup>15</sup> have shown that the bulk reaction between a single or polycrystalline alumina surface and an alumino-silicate glass is initially chemically reaction controlled. A graduated product layer of thickness, called the Nernst layer, is gradually built up. The reaction then becomes diffusion controlled, for the alumina corroded product must diffuse through this layer. It was shown that diffusion coefficients for alumina may be calculated from the experimental data. This is presented in Fig. 4.26.

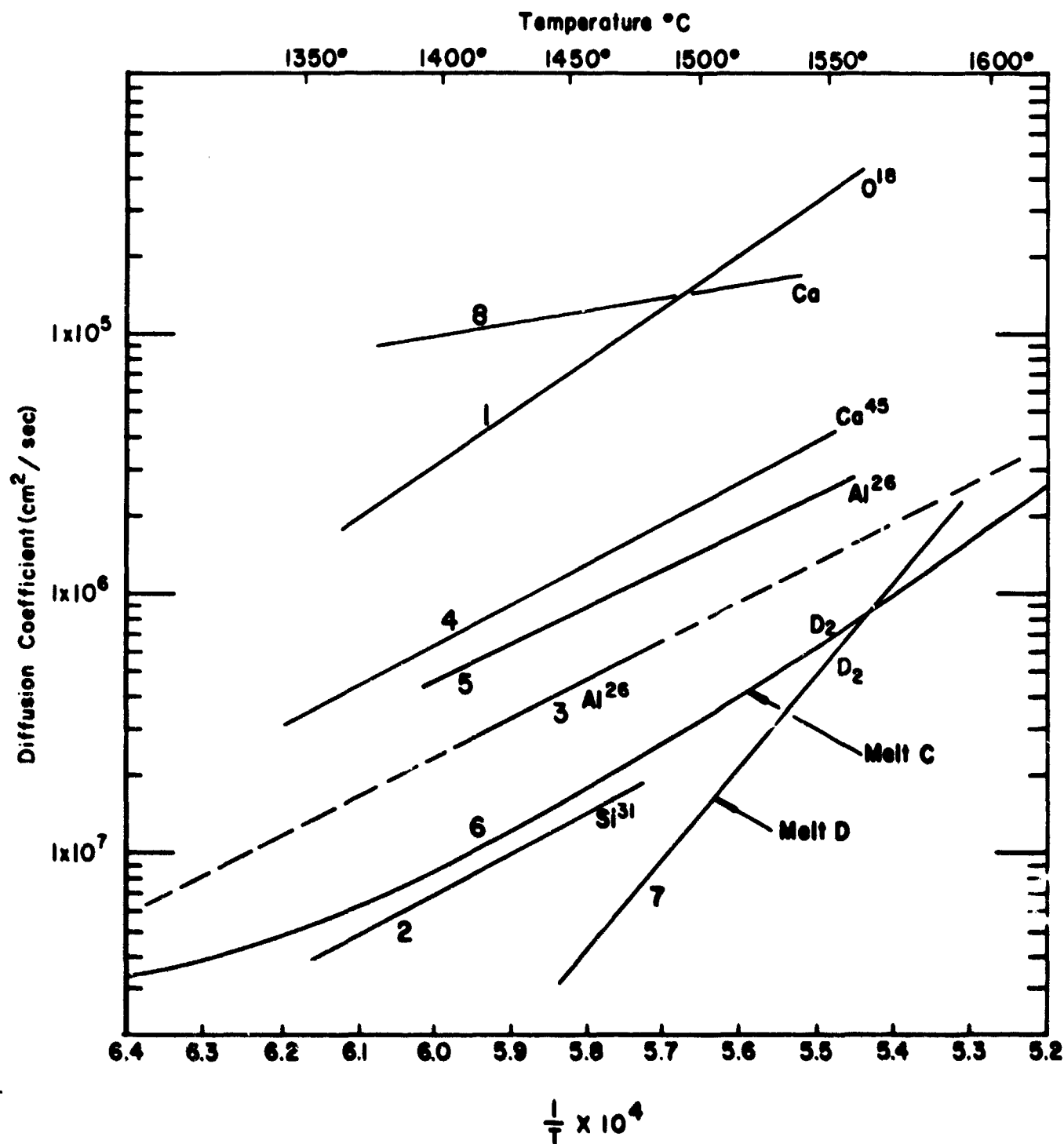


Figure 4.26: Self-diffusion values for oxygen<sup>14</sup> (1), silicon<sup>13</sup> (2), aluminum<sup>15</sup> (3), and calcium<sup>13</sup> (4) for melt C and aluminum<sup>15</sup> (5) for melt B, together with values of "convective diffusion" for melts C (6) and D (7) derived from alumina solution in these melts<sup>17</sup>. Also included are estimated Ca<sup>2+</sup> values for melt B (8) obtained by extrapolating data contained in reference 30. (See text for key to melts.)

The data presented in Section 4.2.3.2.6 shows that it is probable that diffusion control does not take over in the case of alumina body sinter firing, at least prior to equilibrium conditions being established. Data subsequently to be presented also indicates that diffusion control is not the factor determining alumina solution between the non-metallic component of the metallizing and the alumina phase of the ceramic.

Diffusion phenomena does become important in complex metallizing processes where the ions in the non-metallic portion of the metallizing counter diffuse with the ions of the glassy grain boundary phases.

#### 4.2.3.3.3 Thermal Expansion

The thermal expansion of the glassy phase formed in the 941 and 942 system below the annealing temperature\* of their glass component can give a picture of the forms of stress existing in alumina ceramics. The data may also be used to determine the stress existing on a pure metal metallizing layer sintered onto the ceramic surface.

In this study, preliminary thermal expansion measurements of eleven glasses were made. The thermal expansion of several crystalline phases which have been found in high-alumina bodies are shown in Table 4-17<sup>36</sup>.

Thermal expansion coefficients of eleven glass compositions, fused silica, cast molybdenum, and sintered molybdenum were determined with a Brinkman Dilatometer. Samples were in the form of 0.375" diameter rods, approximately one inch long. Sample preparation was discussed on page 23 of the Tenth Quarterly Report.

The Brinkman apparatus is designed to hold the expansion sample horizontally in a controlled atmosphere heating chamber. The sample is held in a high alumina tube, and its dimensional changes are sensed by a lightly spring-loaded alumina rod. The rod is held in very low-friction bearings and is coupled to a transducer which converts mechanical displacement into an electrical signal. The displacement thus read is the difference between the expansion of the sample and the system (the alumina tube and rods). It is, therefore, necessary to standardize the

---

\*The expansion of the melt phase can be calculated from the density data of Barrett and Thomas<sup>8</sup>.

TABLE 4-17

Percent Thermal Expansion of Crystal Species\* from 25°C, after Floyd<sup>36</sup>

Percent Expansion from 25°C to X°C

X°C	200°C	300°C	400°C	500°C	600°C	700°C	800°C	900°C	1000°C
Alumina Al <sub>2</sub> O <sub>3</sub>	.10	.18	.26	.34	.43	.52	.62	.73	.84
Anorthite CaO·Al <sub>2</sub> O <sub>3</sub> ·2SiO <sub>2</sub>	.08	.13	.18	.23	.28	.34	.40	.47	.54
Calcium Hexaluminate CaO·6Al <sub>2</sub> O <sub>3</sub>	.10	.18	.28	.36	.45	.54	.64	.75	.87
Gehlenite 2CaO·Al <sub>2</sub> O <sub>3</sub> ·SiO <sub>2</sub>	.10	.18	.27	.35	.44	.53	.63	.74	.86
Mullite 3Al <sub>2</sub> O <sub>3</sub> ·2SiO <sub>2</sub>	.06	.09	.13	.17	.21	.26	.31	.37	.45
Spinel MgO·Al <sub>2</sub> O <sub>3</sub>	.10	.18	.25	.33	.42	.50	.60	.69	.80

\*All measurements made on "dense polycrystalline bodies."  
 "Secondary phases were not detected in any of these bodies."<sup>36</sup>

system with a known sample such as fused silica. The sample chamber was provided with a flow of argon gas to prevent any chemical reaction such as oxidization of the molybdenum samples.

The procedures employed to obtain the thermal expansion data are described as follows:

Two samples of each glass composition were run. Each of the two was run twice to give a total of four runs per composition. The reported results are therefore averages of four values. The runs were extended to 800°C or 900°C depending on the softening point of the glass.

The furnace heating cycle was programmed for a heating rate of 6°C/min. and controlled automatically. The electrical signal from the transducer was fed to a chart recorder which traced the expansion difference between the system and the sample. By comparison of this trace to similar traces made on fused silica, the true expansion of the samples was determined.

The results appear in Table 4-18 and Fig. 4-27. These are average coefficients of thermal expansion calculated from chart-recorded data. The glass compositions were determined by wet chemical analysis. The difference between the compositions as determined by direct analysis and the nominal batch compositions resulted from the solution of additional alumina into the glasses with high liquidus temperatures, which were melted in alumina crucibles.

The results plotted in Fig. 4-27 show some definite trends. The relative magnitude of the expansion coefficient of each glass was primarily determined by its silica content as was expected. The glass with a 1:1 SiO<sub>2</sub> to CaO ratio (3A) had a high coefficient compared to the glass with a 3:1 ratio (9A) when both contained similar amounts of Al<sub>2</sub>O<sub>3</sub>. The addition of Al<sub>2</sub>O<sub>3</sub> initially caused a reduction of expansion coefficients as the Al<sup>+3</sup> ions entered the glass structure in tetrahedral or network-former positions. When the Al<sub>2</sub>O<sub>3</sub>/CaO mole ratio reached 1:1, additional Al<sup>+3</sup> ions began to occupy octahedral or network modifier positions which caused an increase in expansion coefficients. The similarity of the form of the data with that of the viscosity data is obvious.

TABLE 4-18

## Thermal Expansion Coefficients of Glasses

Glass No.	Thermal Ex- pansion Coefficient in/in/°Cx10 <sup>6</sup>	Mole Ratio SiO <sub>2</sub> /CaO		% Al <sub>2</sub> O <sub>3</sub>	
		Nominal	Actual	Nominal	Actual
100-800°C					
3A	6.78	1:1	1.04:1	15	16.1
10	5.41	1:1	0.85:1	25	22.1
1	6.28	1:1	1.05:1	30	30.1
11	4.82	1:1	0.90:1	40	37.4
2	4.60	1:1	1.08:1	50	52.3
6A	5.47	2:1	1.93:1	15	14.3
4	4.26	2:1	2.2:1	30	37.4
5	4.30	2:1	1.69:1	45	42.4
9A	4.54	3:1	2.66:1	15	29.3
7	3.56	3:1	2.64:1	30	31.2
8	4.59	3:1	2.62:1	40	39.7
Sintered Mo	5.95				
Cast Mo	7.38				
Fused SiO <sub>2</sub>	0.624				

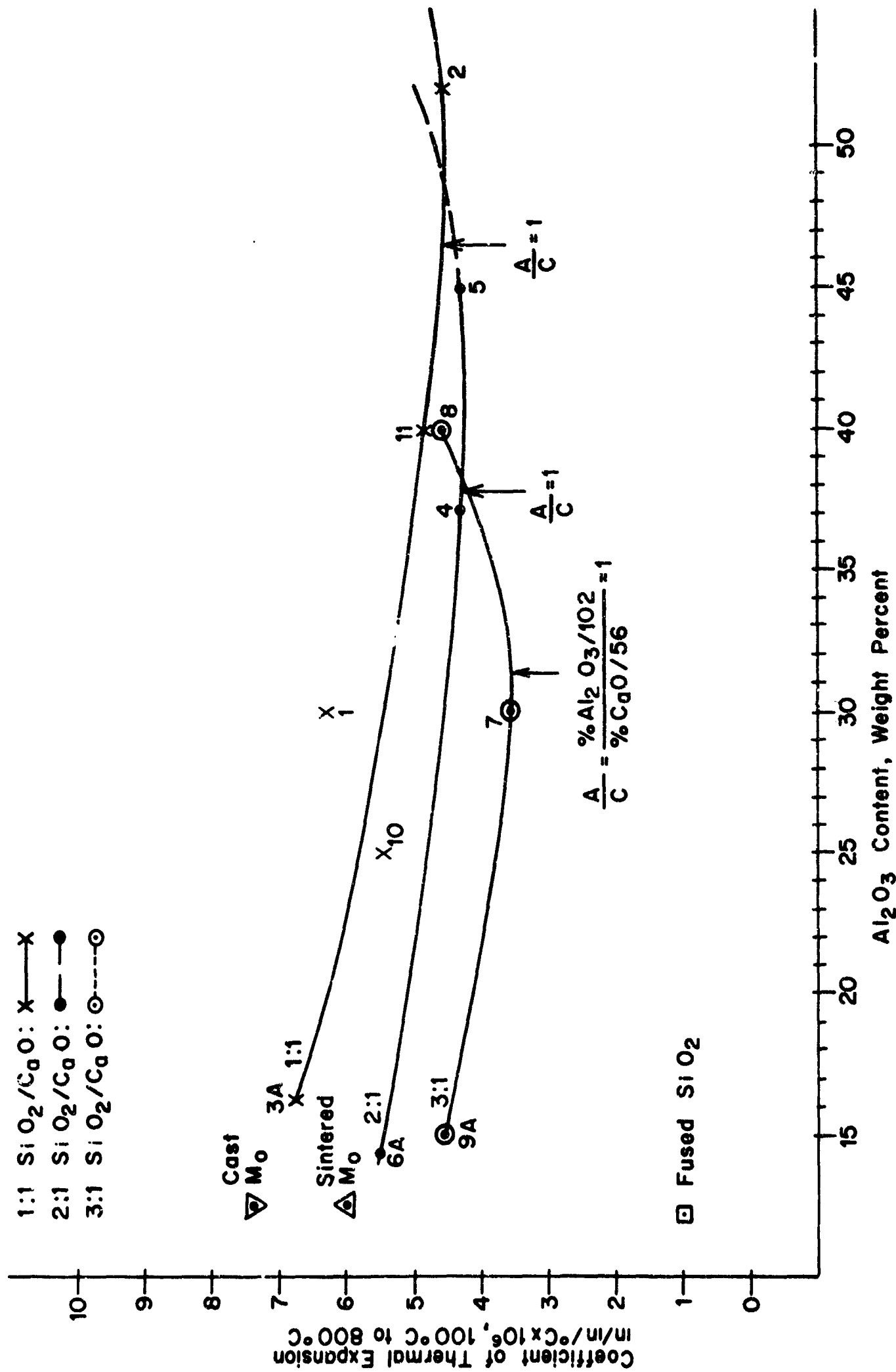


Figure 4.27: Coefficient of thermal expansion versus Al<sub>2</sub>O<sub>3</sub> content of three glass compositions.



Some systematic error may have been introduced by the use of alumina tubes in the system, since the accuracy of the results depended upon the calibration of the system.

Preliminary empirical calculations had indicated a higher expansion for the 1:1 glass.<sup>28</sup> It was hoped that the three glasses would span the range, greater than alumina, between alumina and molybdenum and less than molybdenum. This difference in turn would lead to differences in metallizing strength due to different stress situations. As can be seen from Fig. 4.27, based on the probable alumina contents of the systems being between 37-47%, the thermal expansions are similar and lie below that of molybdenum. This is the most favored situation, i.e., the glass phase will be in compression both in the grain boundaries of the ceramic itself and in the metallizing layer.

In order to obtain a range of high expansion glasses one must evidently synthesize glasses containing the glassy phase of the 941 ceramic plus selected elements that could be incorporated into the non-metallic portion of metallizing points.

#### 4.2.3.3.4 Contact Angle Studies

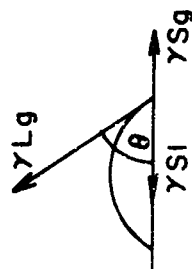
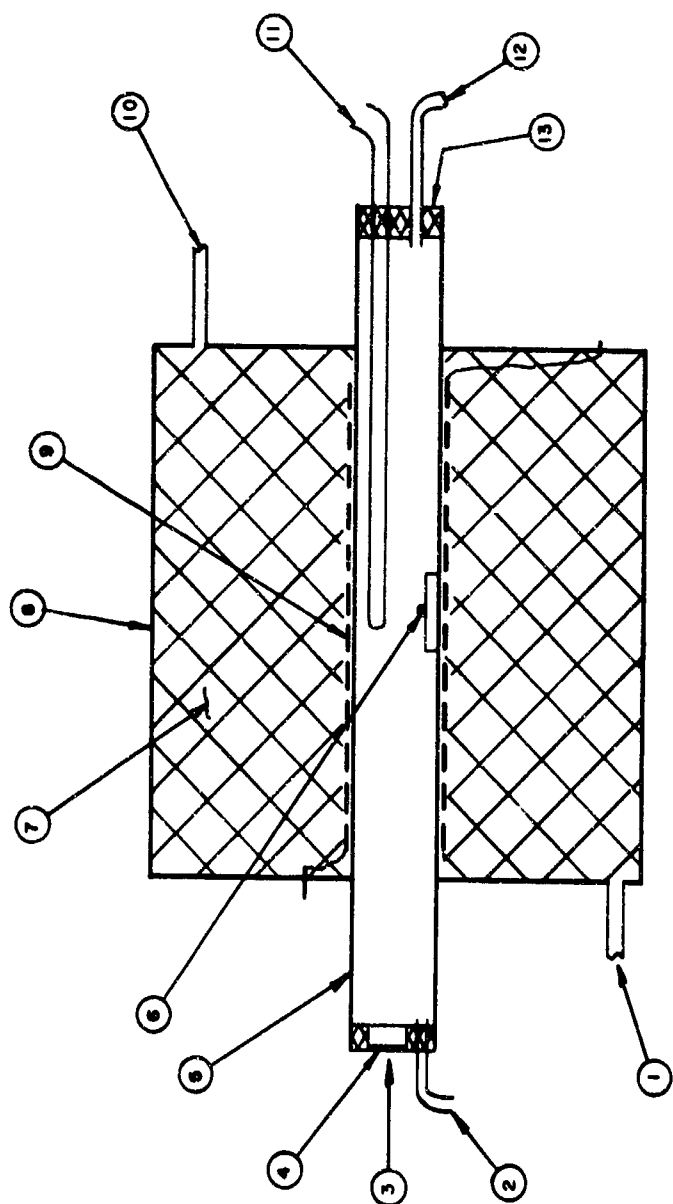
The surface energies of the glass phase in relation to the alumina ceramic and the sintered molybdenum metallizing layer are of primary concern to a basic metallizing study. If adequate wetting and adhesion does not occur a vacuum tight seal cannot be made.

This section presents the results of a preliminary series of experiments and later experiments which used the same glasses deployed in the thermal expansion studies. The section concludes with a brief interpretation of and discussion of the results, further discussion being reserved for a later section on adherence mechanisms.

In both series of experiments the wetting is described in terms of the contact angle that the melt makes with a solid plaque at the metallizing temperature. The lower the contact angle the better the wetting.

The arrangement used in the first series is shown in Fig. 4.28 together with a diagrammatic cross-section of a sessile drop on the plaque. An adequate description of the method used -- the sessile drop method -- may be found in the literature.<sup>29</sup>

1. Exit  $H_2/3N_2$
2. To Dew Point measurement equipment
3. Camera & optical pyrometer
4. Glass window
5. Gas tight alumina tube
6. Contact angle specimen (see below)
7. Alumina powder insulation
8. Furnace case
9. Molybdenum tape furnace elements
10. Dry  $H_2/3N_2$  enter
11. Thermocouple to controller
12. Entrance controlled atmosphere
13. Rubber stopper



$\theta$  = Contact angle

$\gamma_{Lg}$  = Liquid-gas surface tension

$\gamma_{Sg}$  = Solid-gas surface tension

$\gamma_{Ls}$  = Solid-liquid surface tension

$\gamma_{Sg} = \gamma_{Sl} + \gamma_{Lg} \cos \theta$

(Youngs equation)

Figure 4.28: Schematic diagram of contact angle experiment and cross-section of sessile drop.

Substrates examined were molybdenum, tungsten and sapphire. The main melts examined were of the anorthite ( $\text{CaO} \cdot 2\text{SiO}_2 \cdot \text{Al}_2\text{O}_3$ ) and gehlenite ( $2\text{CaO} \cdot \text{SiO}_2 \cdot \text{Al}_2\text{O}_3$ ) composition. The melts were made by compounding the raw oxides and melting them in an alumina crucible (A RR, 99.9% alumina) to establish homogeneity. Impurities such as Fe and Ti were added to similar melts to discover the effects of trace elements in the glassy phase of the ceramic on the wetting of the substrate plaque. A silica-free eutectic melt  $\text{CaO}$  41.5%,  $\text{MgO}$  6.7%,  $\text{Al}_2\text{O}_3$  51.8% (M.P.  $1345^\circ\text{C}$ ) was also investigated. The experiments were carried out at  $1550^\circ\text{C}$ - $1600^\circ\text{C}$  in a hydrogen and hydrogen plus nitrogen atmosphere. The results are given in Table 4-19.

The surface tension studies under wet  $\text{H}_2$  and  $\text{H}_2/3\text{N}_2$  conditions at  $+100^\circ\text{F}$  dewpoint were repeated in an effort to obtain consistent results for the contact angle on molybdenum and tungsten. The contact angle varied from  $30^\circ$  to  $0^\circ$ , i.e. complete spreading. In one case bubbles of gas appeared on top of the liquid sessile drop at temperature. It is thought that the crystal orientation, chemi-absorbed surface layers and outgassing of the metal substrate affects the metal surface condition in a wet atmosphere. This alters  $\gamma_{\text{sg}}$  and  $\gamma_{\text{sl}}$ . This variability in wetting will affect the metallizing behavior of the metallizing system.

A spectrographic analysis of the melts after being melted on plaques shows a variable amount of metal in the melt phase as given in Table 4-20.

In the second series of experiments, the contact angles of nine different glasses on molybdenum and on sapphire were measured. Sessile drops were photographed at temperature, and the contact angles were measured on the photographs. All data were taken in an atmosphere of 3:1 nitrogen to hydrogen by volume, at  $1600^\circ\text{C}$  except (as noted in Table 4-21) where the liquidus temperatures of the glasses were higher, and at dew points of  $0^\circ\text{F}$ ,  $20^\circ\text{F}$ ,  $40^\circ\text{F}$  and  $80^\circ\text{F}$ .

To overcome the difficulties experienced with the first contact angle measurements, a new test furnace was employed.

The test furnace, a sketch of which appears in Fig. 4-29, was a vertical electric resistance type with a tungsten tube heating element. Holes in the heating element, the two molybdenum heat shields, and a viewing port in the water-cooled outer shell permitted observation of the sample

TABLE 4-19

Wettability of Seal Components at 1550-1600°C

System Substrate	Melt	Contact Angle at Various Dew Points *									
		+100°F		+80°F		+40°F		+20°F		-90°F	
		H <sub>2</sub>	H <sub>2</sub> /3N <sub>2</sub>	H <sub>2</sub>	H <sub>2</sub> /3N <sub>2</sub>	H <sub>2</sub>	H <sub>2</sub> /3N <sub>2</sub>	H <sub>2</sub>	H <sub>2</sub> /3N <sub>2</sub>	H <sub>2</sub>	H <sub>2</sub> /3N <sub>2</sub>
Mo	Anorthite	30**	25	35	35	--	35	--	42	62	45
W	Anorthite	20**	13	21	15	25	31	--	26	47	28
Mo	Gehlenite				25						51
W	Gehlenite				10						43
Mo	Anorthite +0.05% Ti				33						35
Mo	Anorthite +0.8% Fe				36						52
Sapphire	Anorthite				24		25				0
Sapphire	Anorthite plus Ti				--						0
Mo	MgO, CaO, Al <sub>2</sub> O <sub>3</sub> Eutectic				10						--

\*Contact angle measured after cooling, subject to  $\pm 5^\circ$  error.

\*\*31° and 24° using camera.

TABLE 4-20

## Solubility of Metal in Melt

Melt	Metal	Solubility	Atmosphere
Anorthite, top of drop	Mo	Mo: 0.002%	Wet, H <sub>2</sub> + N <sub>2</sub>
Anorthite, bottom of drop	Mo	Mo: 0.000%	"
Anorthite, before test	--	Mo: 0.000%	"
MgO, CaO, Al <sub>2</sub> O <sub>3</sub> Eutectic sessile drop	Mo	Mo: 2.0%	"
Anorthite	W	W: 0.1%	

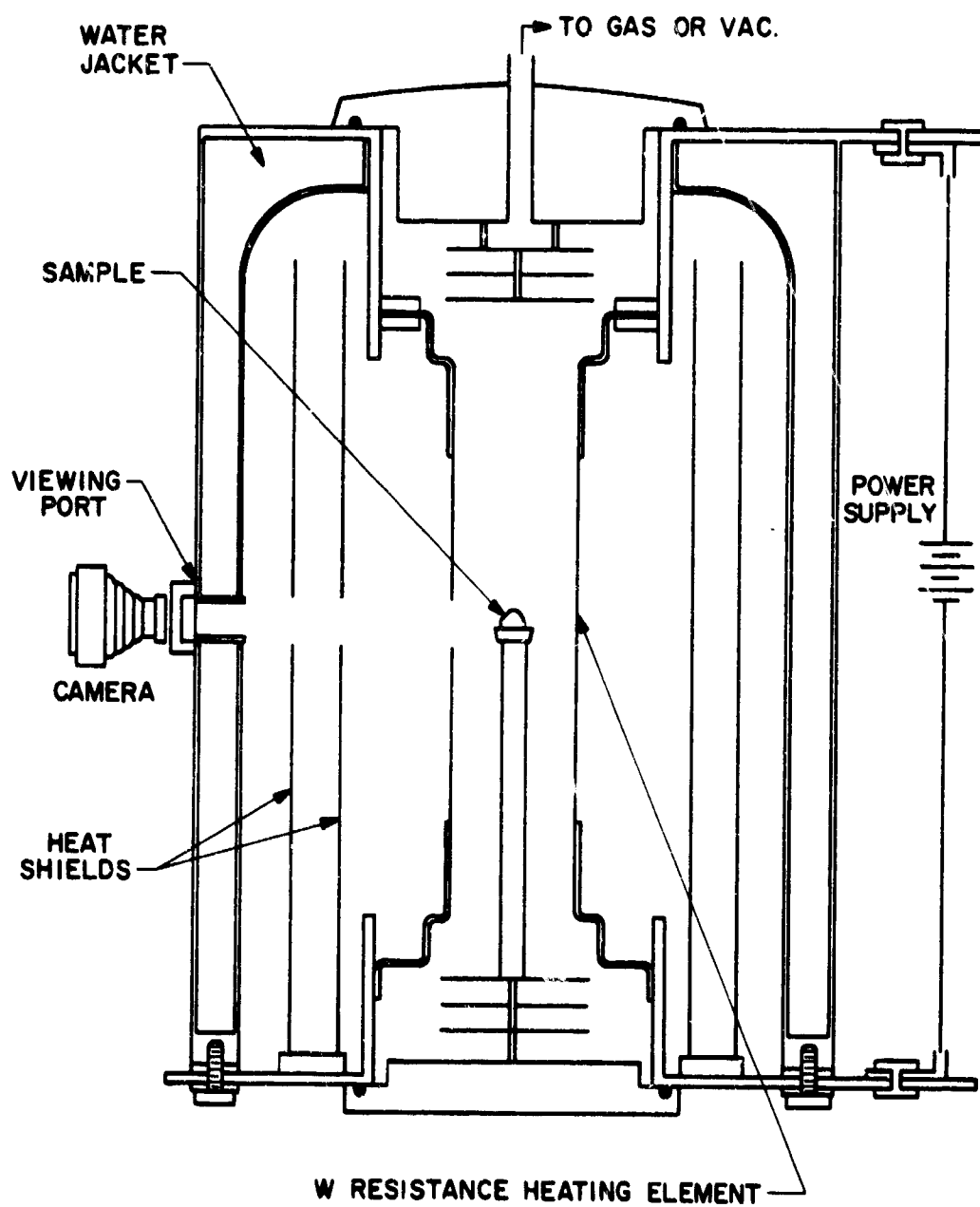


Figure 4.29: Schematic cross-section of furnace used in wetting angle study.

at temperature. Photographs were made through the viewing port and the sample temperature was read with an optical pyrometer to an accuracy of  $\pm 10^{\circ}\text{C}$ . A 10 KW power supply was designed to supply over 700 amps at low voltage to reach operating temperature.

A constant weight of the glass sample (100 mgm on molybdenum and 50 mgm on sapphire) was lightly compacted into a pellet and placed on the substrate which was in turn placed on a pedestal located in the center of the hot zone of the furnace. The furnace was closed and sealed, and the atmosphere changed by repeatedly evacuating the chamber and backfilling with  $3\text{N}_2/\text{H}_2$  gas. The sample was heated to  $1600^{\circ}\text{C}$  (or higher when necessary) in approximately 20 minutes, taking care to expel all gas entrapped in the glass just above the fusion temperature. All furnace conditions except dew point were held constant for the duration of the run.

Because the furnace contained no porous ceramic insulation, the dew point could be varied between  $-100^{\circ}\text{F}$  and  $+100^{\circ}\text{F}$  fairly rapidly. This was not possible in the first series of experiments. The contact angle was allowed to stabilize at  $0^{\circ}\text{F}$  dew point, then the sample was photographed. The dew point was then increased to  $20^{\circ}\text{F}$ , the sample allowed to stabilize and again was photographed. This was repeated at D.P.'s of  $40^{\circ}\text{F}$  and  $80^{\circ}\text{F}$ , then the D.P. was lowered to less than  $25^{\circ}\text{F}$  to observe the reversing effect on the contact angle.

The contact angles were measured on enlarged photographs with good resolution and have an accuracy of about  $\pm 5^{\circ}$ , but reproducibility was no better than  $\pm 15^{\circ}$ . These results are presented in Table 4-21 and Figs. 4.30 through 4.35.

Spectrographic analyses of glass beads 1, 6A and 9A whose contact angles had been measured on molybdenum disclosed trace amounts of molybdenum (0.008%, 0.005% and 0.002% respectively). This evidence confirmed suspicions that the glass did dissolve small amounts of molybdenum.

Adherence of the sessile drops to the sapphire substrates was excellent and it was fair to good on molybdenum. Drops could not be chipped from the sapphire plates, and when removed by leaching in HF, the sapphire surface beneath the drop was noticeably eroded. In most cases, the molybdenum substrates had to be bent through more than  $5^{\circ}$  to pop the glass drop off the surface. They could not be removed by finger pressure alone.

TABLE 4-21

## Wetting Angles of Glasses on Molybdenum and Sapphire

Glass Number** on	Liquidus Temp.	Wetting Angle at Indicated Dewpoint				
		0°F	20°F	40°F	80°F	Less than 25°F
<u>Molybdenum</u>						
1	1350°C	-	46°	14°	11°	24°
1	1350	78°	56	45	24	60
2	1465	25	16	-	6	-
3A	1250	-	45	10	4	-
3A	1250	63	50	42	12	46
4	1605	48	24	20	20	-
4	1605	68	56	44	32	64
5	1625	16	6	4	-	-
5	1625	45	12	5	-	28
6A	1325	48	45	20	6	-
7	1550	62	52	48	45	38
8	1550	30	(15)	21	20	57
9A	1400	66	52	46	-	64
<u>Sapphire</u>	<u>Sub- strate Plane*</u>					
1	19°	1350	21°	-	-	-
2	28	1465	18	-	11	9
3A	17	1250	15	12	10	9
4	27	1605	24	21	18	11
5	19	1625	18	16	15	10
6A	28	1325	26	24	14	-
7	17	1550	30	28	26	23
8	27	1550	27	24	24	24
9A	28	1400	22	17	17	10

\*Angle between C-axis and plane of surface. See pp. 26 & 27, 11th Quarterly Report.

\*\*Glass Compositions, Weight Percent

No.	CaO	SiO <sub>2</sub>	Al <sub>2</sub> O <sub>3</sub>
1	33.8	36.2	30
2	24.2	25.8	50
3A	41.0	44.0	15
4	22.3	47.7	30
5	17.5	37.5	45
6A	27.0	58.0	15
7	16.6	53.4	30
8	14.2	45.8	40
9A	20.2	64.8	15



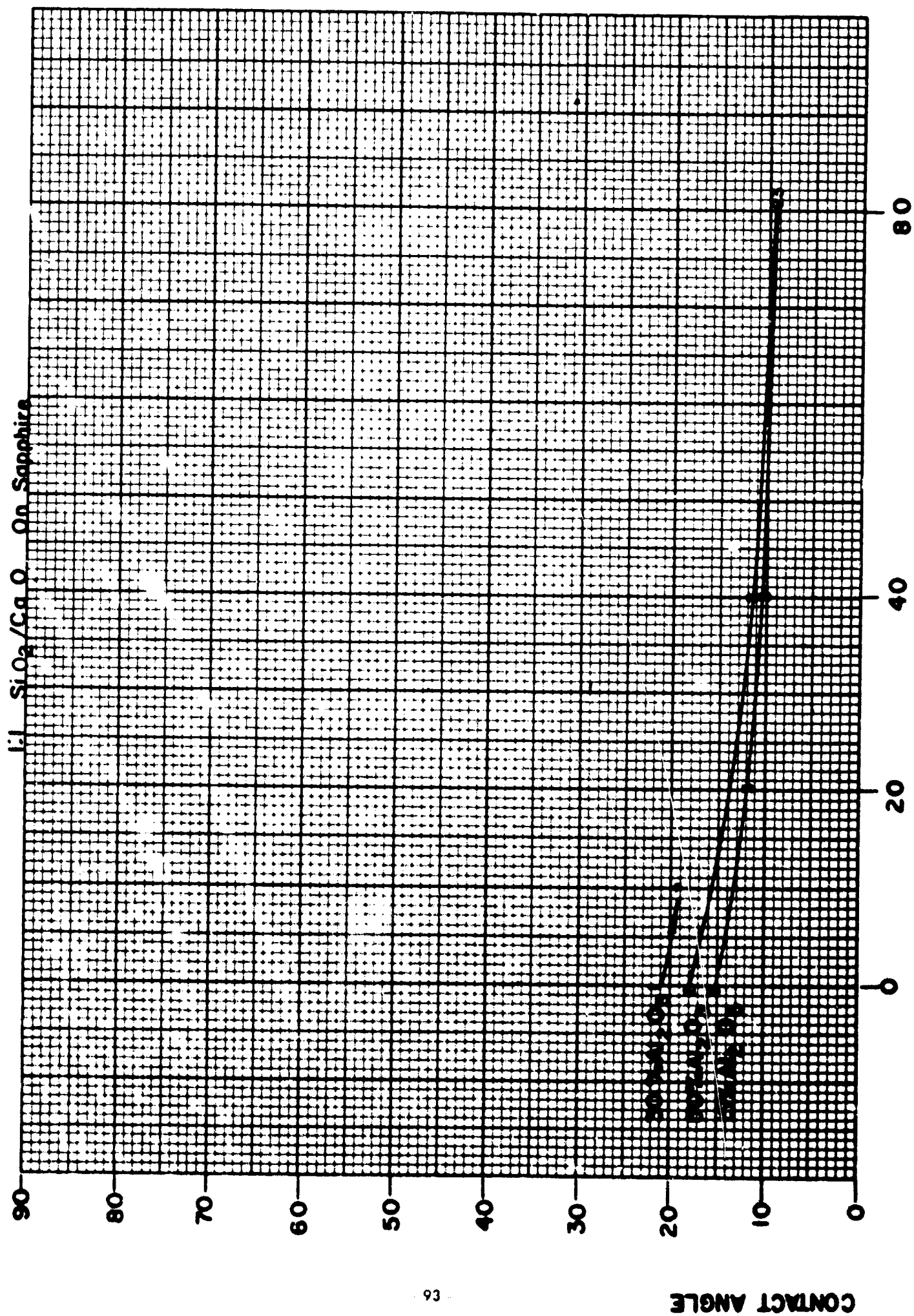


Figure 4.30: Contact angle versus dewpoint of 1:1  $\text{SiO}_2/\text{CaO}$  melts on sapphire.

# 2:1 Si<sub>2</sub>/CaO on Sapphire

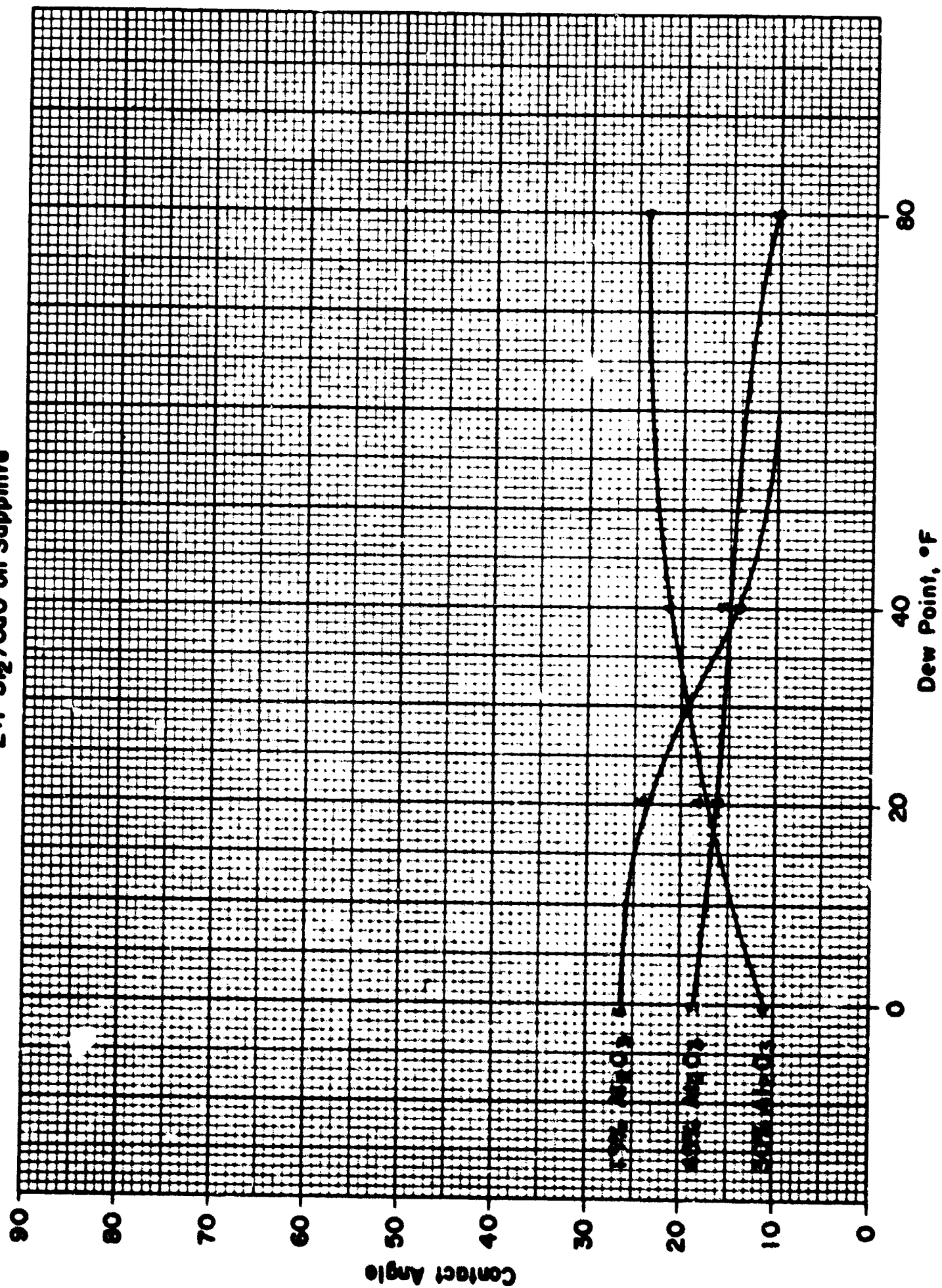


Figure 4.31: Contact angle versus dewpoint of 2:1 SiO<sub>2</sub>/CaO melts on sapphire.

# 3:1 SiO<sub>2</sub>/CaO on Sapphire

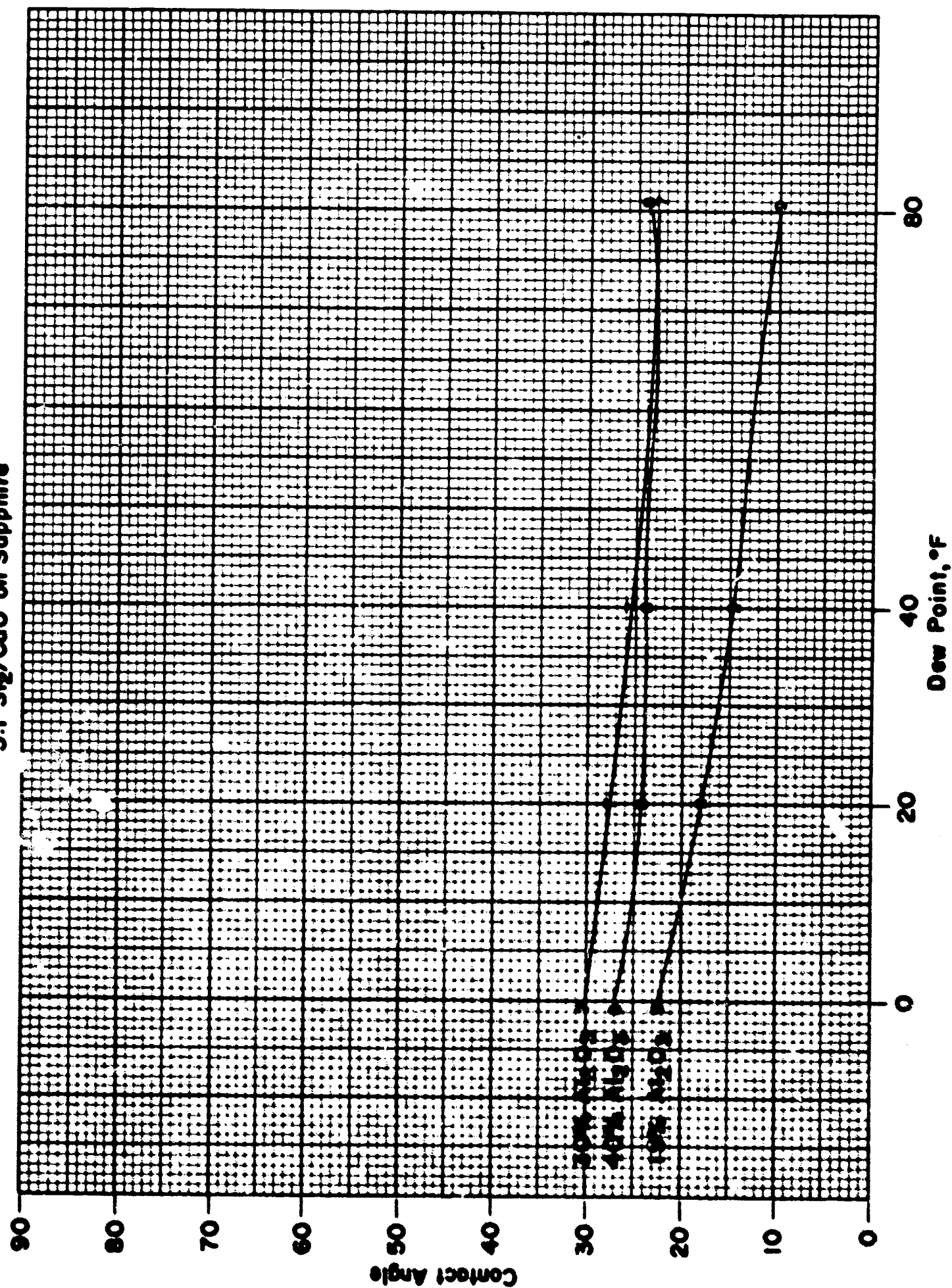


Figure 4.32: Contact angle versus dewpoint of 3:1 SiO<sub>2</sub>/CaO melts on sapphire.

# 1:1 SiO<sub>2</sub>/CaO on Molybdenum

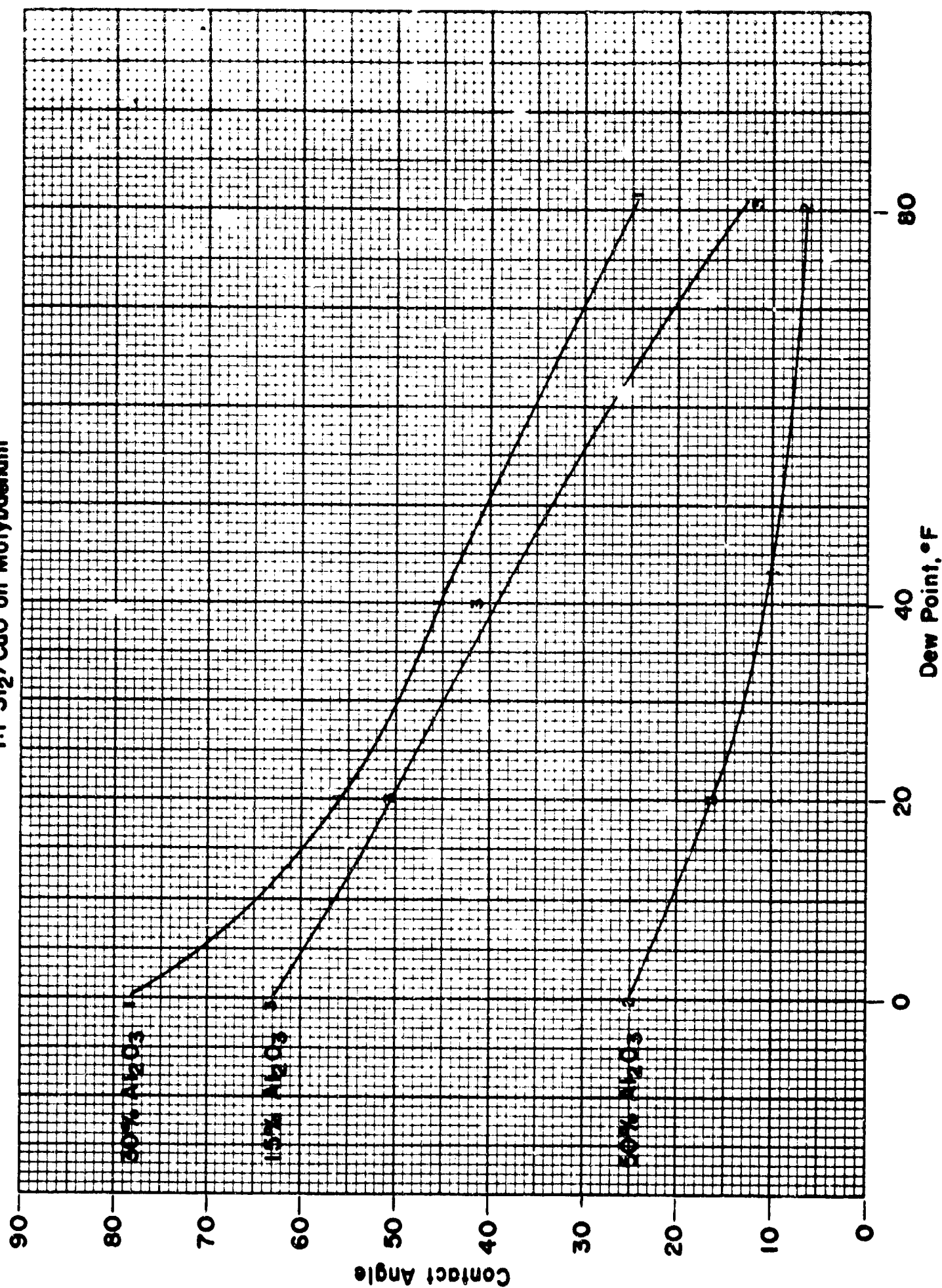


Figure 4.33: Contact angle versus dewpoint of 1:1 SiO<sub>2</sub>/CaO melts on molybdenum.

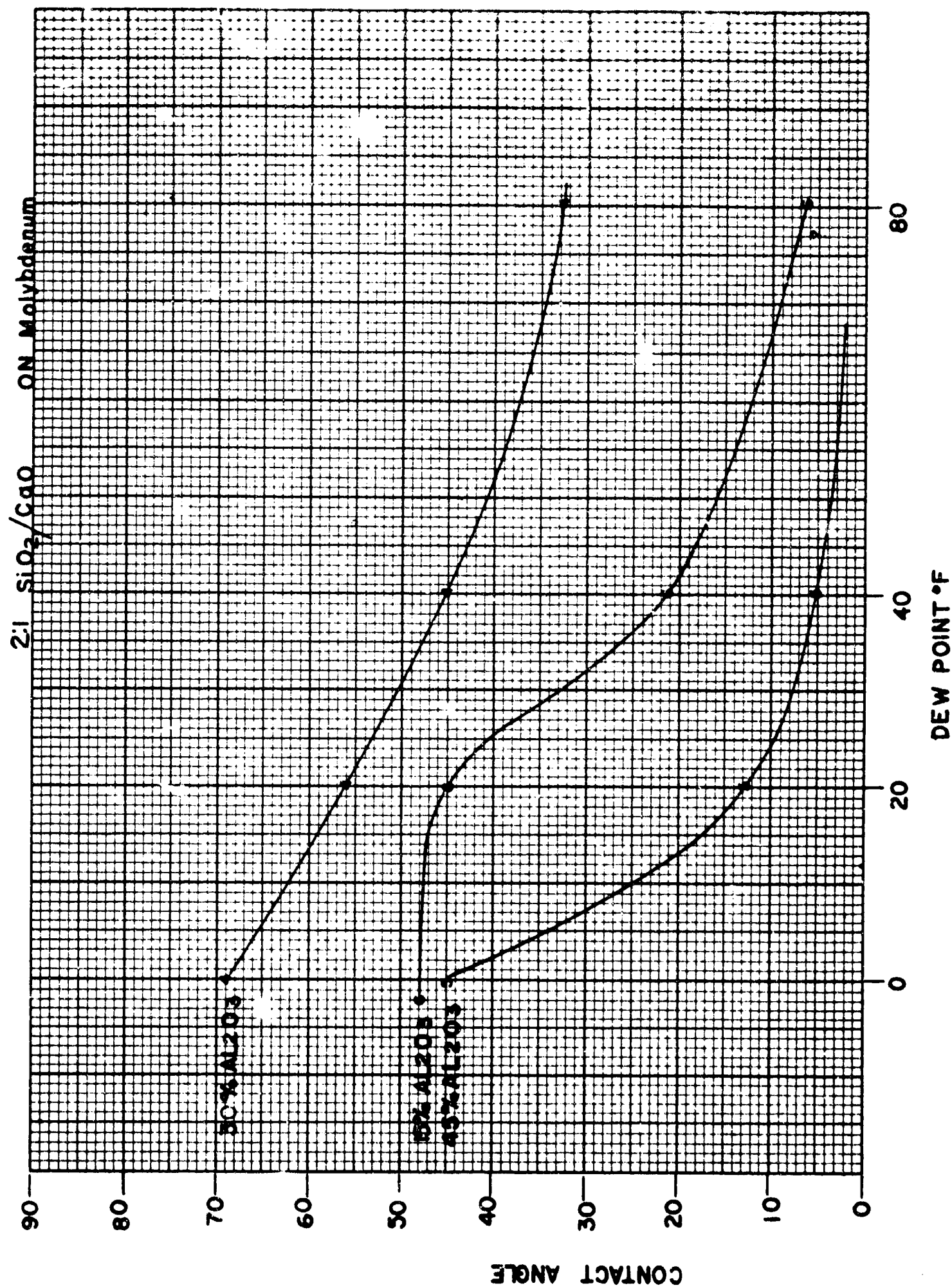


Figure 4.34: Contact angle versus dewpoint of 2:1 SiO<sub>2</sub>/CaO melts on molybdenum.



# 3:1 Si<sub>2</sub>/CaO on Molybdenum

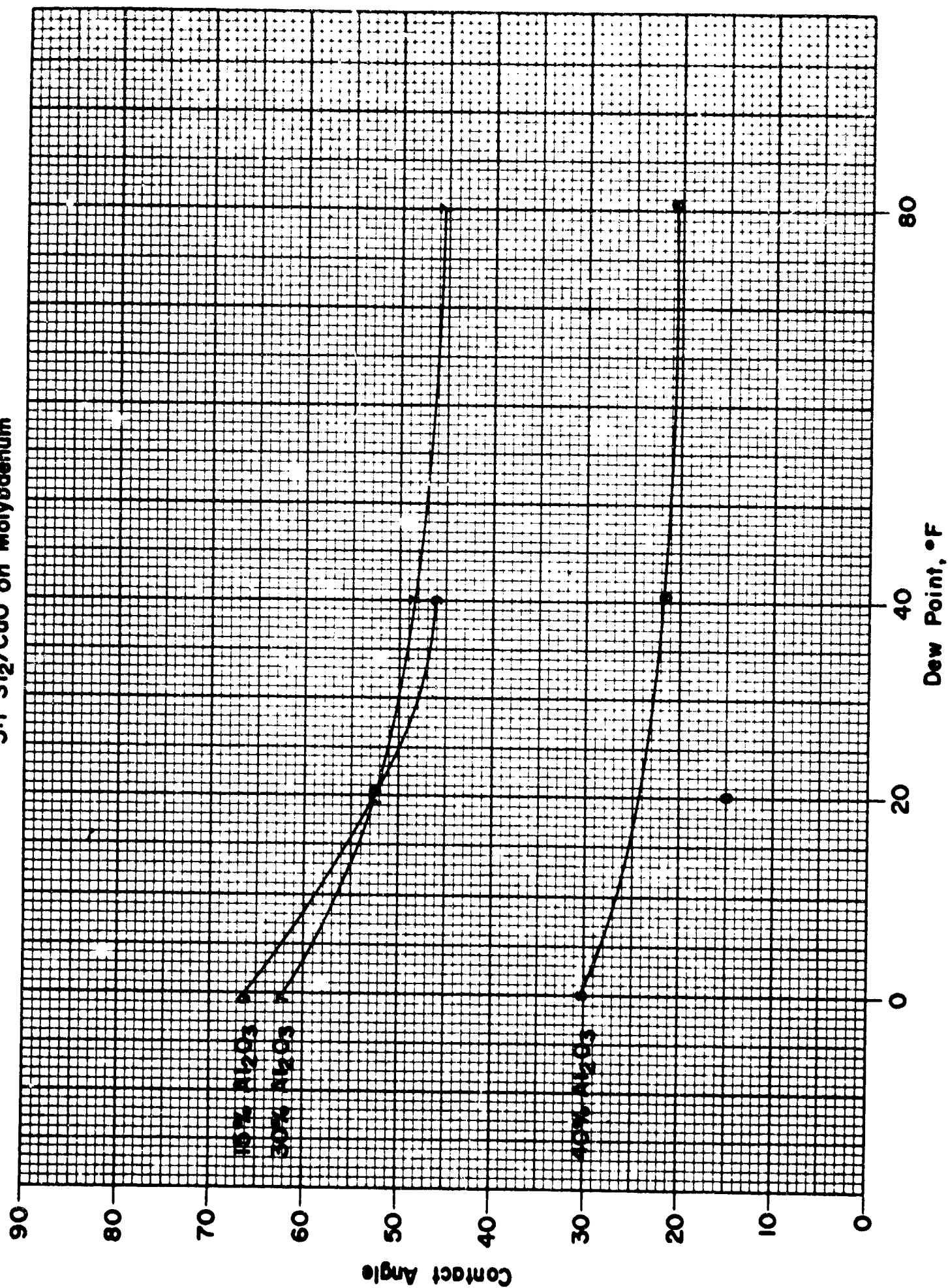


Figure 4.35: Contact angle versus dewpoint of 3:1 SiO<sub>2</sub>/CaO melts on molybdenum.

The general trends of the contact angle variation for the preliminary and final series of results agreed very well except in the one case where the same melt was repeated, the anorthite composition 2:1  $\text{SiO}_2\text{CaO}$ , 37%  $\text{Al}_2\text{O}_3$ . The second series of results showed a greater variation with dew point on the molybdenum substrates.

With all three  $\text{SiO}_2/\text{CaO}$  ratios, the contact angle on molybdenum plaques initially increases with alumina content and then decreases, the intermediate alumina content showing the highest contact angle. (There is also a slight overall trend for the contact angle to increase for all four dew points as the  $\text{SiO}_2/\text{CaO}$  ratio increases.)

From Young's equation -

$$\cos \theta = \frac{\gamma_{sg} - \gamma_{sl}}{\gamma_{lg}}$$

Since  $\gamma_{sg}$  is constant an increase in contact angle must be due to an increase in  $\gamma_{lg}$  and/or  $\gamma_{sl}$  and vice versa.

Barrett and Thomas<sup>8</sup> found that the surface tension ( $\gamma_{lg}$ ) of  $\text{CaO.SiO}_2.\text{Al}_2\text{O}_3$  melts increased with increasing alumina and calcia content. Probably the increase in alumina (and calcia) reduces the screening of the melt cations. This explains the initial increase in contact angle on initially increasing the alumina content of the three systems. The decrease of contact angle at the higher alumina percentage in each melt series must be due to a continuous decrease in  $\gamma_{sl}$ . Thus  $\gamma_{lg}$  and  $\gamma_{sl}$  are acting in opposition to each other.

Water vapor lowers the surface tension of soda-lime glasses as -OH groups can be absorbed to increase the screening of the silicon ions. It follows that the contact angle on molybdenum plaques will also be lowered, as is the case for the four dew points studied. This implies that  $\gamma_{sg} - \gamma_{sl}$  does not change; however, if this quantity increases, the contact angle will also be lowered. Both  $\gamma_{sg}$  and  $\gamma_{sl}$  can be expected to decrease as a layer of -OH ions will cover the molybdenum. However,  $\gamma_{sl}$  will be more affected than  $\gamma_{sg}$  as the -OH surface presented to the melt phase will be energetically similar to the surface ions in the melt while  $\gamma_{sg}$  is initially so high that the surface energy changes are relatively small percentages.

The low apparent\* contact angle on alumina plaques can be explained on the basis that  $\gamma_{1s}$  is essentially zero as a vigorous chemical reaction occurs between the melt and the alumina phase which produces a saturated layer of alumina in the melt phase in thermodynamic equilibrium with the solid alumina phase. The slight change of contact angle with dew point must in this case be due solely to the change in  $\gamma_{sg}/\gamma_{lg}$ . An interpretation of the effect of  $Al_2O_3$  content at a given  $SiO_2/CaO$  ratio is not possible because in all cases it is probable that a saturated layer of alumina exists next to the alumina interface (see diffusion section).

The addition of minor amounts of variable valance ions, in oxides such as  $TiO_x$ , which can change their valance states,  $Ti^{4+} \rightarrow Ti^{3+} \rightarrow Ti^{2+}$ , as the dew point is lowered, produces a constant contact angle regardless of dew point, whereas the addition of variable valance ions that are in their lowest valance state both in wet and dry atmospheres ( $Fe^{2+}$ ) does not influence the general trend with dew point. It is thought that

- (i) the melt reacts with the glass phase,



thus reducing  $\gamma_{1s}$  to a low value, similar to the sapphire-glass situation. Proportioning of oxygen between such systems has been noted elsewhere.

- (ii) the reduction of  $Ti^{4+}$  ion  $\rightarrow Ti^{3+} \rightarrow Ti^{2+}$  ion produces an equivalent oxygen-hydroxal screening action over the entire dew point range so the  $\gamma_{lg}$  is constant.
- (iii)  $\gamma_{sg}$  is so high that small changes such as induced by dew point are not significant.

The type of bonding produced on solidification which may be chemical or semi-conducting in nature is discussed later. (See Appendix I.)

---

\*The true angle will be different due to solution of the alumina, leaving a circular segment in the alumina.



#### 4.3 Commercial Bodies - Microstructure Considerations

The commercial ceramics investigated are shown in Table 4-1.

A detailed discussion of Body A is presented elsewhere;<sup>28,30</sup> a summary of its pertinent properties is presented below.

Figure 4.36 shows a 400X ceramographic cross-section of this body which illustrates the tabular alumina crystal form and the glassy phase located between the grains. The ceramic has an 8 micron average grain size with no grains above 40 microns.

Based on equilibrium phase diagram considerations and planometric measurements, its glassy phase composition was determined to be 50% alumina by weight. The glassy phase was synthesized and the powdered glass placed on alumina and molybdenum plaques. The glass was sufficiently mobile to form sessile drops at 1425°C in a wet H<sub>2</sub>/3N<sub>2</sub> atmosphere; at 1600°C sessile drops on molybdenum varied from 20° in a wet atmosphere to 60° in a dry atmosphere. An electron photomicrograph of this ceramic, which has been thermally etched at 1425°C, Fig. 4.37, clearly shows the surface meniscus of the once fluid glassy phase residing in the grain boundaries between the alumina grains. A further thermal etch at 1100°C in dry hydrogen, in wet hydrogen, or in air produces a devitrification product with a greater crystal size, 1 to 5 microns in the latter cases, Figs. 4.38, 4.39, 4.40. No glassy phase devitrification is noted on specimens etched at 950°C or below. Body G is similar in composition and behavior to Body A. It has already been discussed in this report. These two bodies are typified by the 942 special ceramic.

Body C possesses a larger grain size and much more fluid glassy phase.<sup>28,30</sup> The more fluid glassy phase is due to the lower SiO<sub>2</sub>/MO ratio of the glass. In this case, primary anorthite crystallizes from the glass phase during a 1425°C thermal etch. After a 1100°C etch the associated glassy phase devitrifies to give secondary anorthite and gehlenite crystals. This body has been discussed in detail in the 2nd Quarterly Report, Appendix I. This body is typified by the 941 ceramic body.

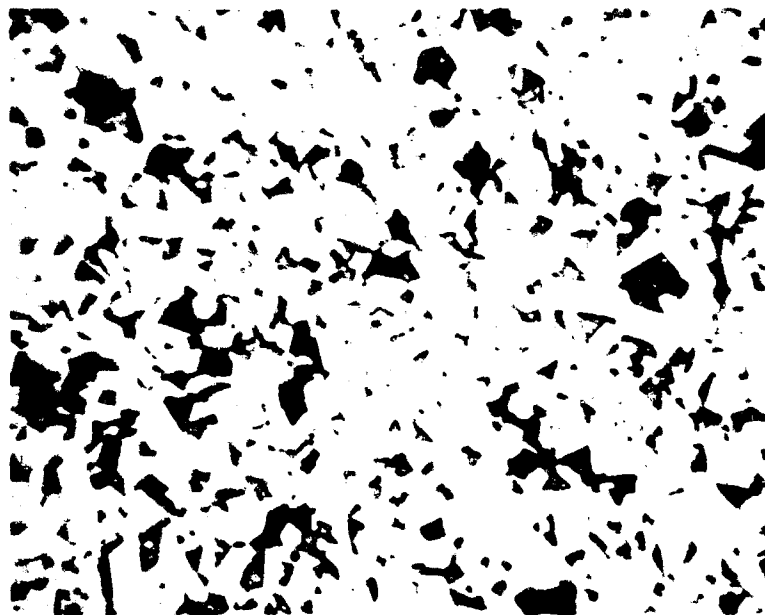


Figure 4.36: Ceramographic cross section of Body A showing tabular alumina crystal form and the glassy phase situated between the grains. (400X)



Figure 4.37: Electron photomicrograph of Body A showing the glassy phase in the boundaries between the alumina grains. (24,200X)



Figure 4.38 Electron photomicrograph of Body A after a thermal etch at 1100 C in dry hydrogen.  
(18,400X)



Figure 4 39. Electron photomicrograph of Body A after a thermal etch at 1100 C in wet hydrogen (28,000X)



Figure 4.40: Electron photomicrograph of Body A after a thermal etch at 1100°C in air. (28,000X)

The microstructure of the three +99% alumina bodies investigated in the seal parameter and electrical studies shows an equiaxed crystal habit, Fig. 4.41, because of the mode of sintering. No distinct glassy phase can be seen in their grain boundaries under the optical microscope. (Sintering occurs largely by solid state processes as opposed to liquid-solid sintering mechanisms for the lower alumina content bodies.

#### 4.4 Exploratory Metallizing Studies

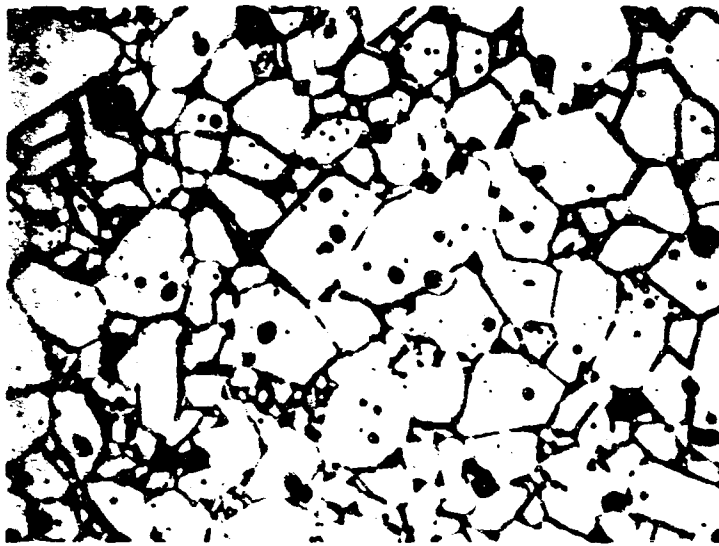
##### 4.4.1 Introduction

In the first four Quarterly Reports on this program, a summation of the physics and chemistry of the metallizing process was given based on an interpretation of the scientific literature directly or indirectly relating to the sealing field.

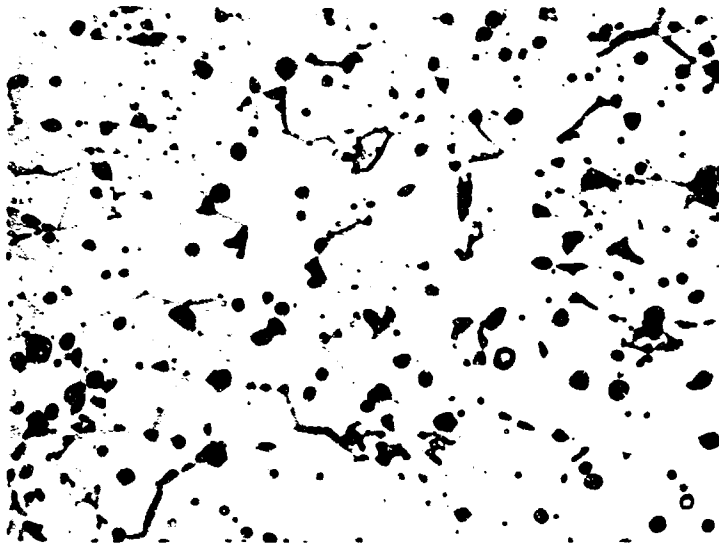
Exploratory studies were carried out in order to lend substance to this interpretation and to form a basis for later studies with the special bodies. This section presents these studies in a logical sequence. They stand on their own, but, of course, for further details the reader is referred to the above reports. The interesting general result that has been obtained from these studies is that despite its complexity, considerable understanding can be obtained of an actual commercial ceramic-metallizing system.

The metallizing paints listed in Tables 4-22 and 4-23 were formulated with several purposes in mind. The main purposes may be listed as follows:

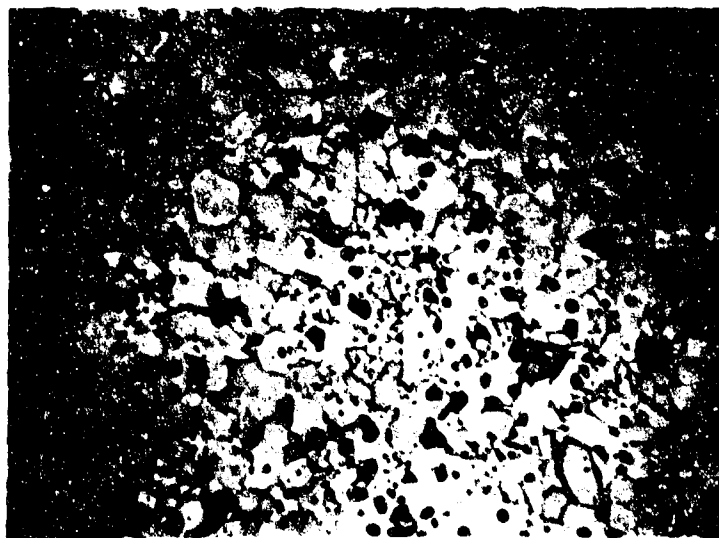
1. P-1 and P-3 are paints which empirically have proven of value for many metallizing applications, so that it was decided to examine them in some detail. Also  $\text{SiO}_2$  and  $\text{Al}_2\text{O}_3$  could not be determined by the microprobe technique early in this program, whereas  $\text{TiO}_2$  (a network intermediate) which would diffuse in a comparable fashion, could be detected.
2. P-2, P-4, P-5, P-6, P-11, P-12 are single phase paints which provide simple metallizing systems capable of analyses by the techniques used on this program.



99% Alumina Body Thermally Etched at 1425°C for 1/2 Hour Showing Primary Corundum – Alumina plus 2% Glass Phase at Grain Boundaries. Ave Porosity 5%, Ave Grain Size 13.5 $\mu$ , Max 60 $\mu$  Min 2.5 $\mu$  Body E



99.5% Thermally Etched 1425°C for 1/2 Hour Showing Primary Corundum – Alumina Phase and 8% Porosity. Ave Grain Size 11.9 $\mu$ , Max 55 $\mu$ , Min 2.8 $\mu$ , Body H



99.5% As for Fig. 5, 7% Porosity, Ave Grain Size 8.5 $\mu$ , Max 45 $\mu$ , Min 2.5 $\mu$ . Body F

Figure 4.41: The microstructures of three +99% alumina bodies investigated in the seal parameter and electrical studies.



TABLE 4-22

Nominal Composition in Weight Percent of Metallizing Paints Referred to in Text\*

Paint	Metal	% Metal	% Melt	Melt Composition, Wt. %	Remarks
P- 1	Mo**	75	25	(84% MnO + 16% TiO <sub>2</sub> )	Proven production paint
P- 2	Mo**	100	0		
P- 2M (1550)	Mo**	100	0		Ground in Mo-lined ball mill with Mo balls; 5" Avg. G.E.
P- 3	Mo**	72	28	(66-2/3% MnO + 16-2/3% SiO <sub>2</sub> + 16-2/3% TiO <sub>2</sub> )	Proven production paint
P- 3(g)	-		100	"	All glass
P- 4	Mo	100	0		-325 mesh Fansteel
P- 4M	Mo	100	0		Ground in Mo-lined mill with Mo balls
P- 5	Mo	100	0		5" Avg. G.E.
P- 6	Mo	100	0		1.65" Avg. Sylvania
P- 7	Mo	80	20	(47% BaO + 53% SiO <sub>2</sub> )	"Low loss"
P- 8	Mo	80	20	(64% MnO + 36% SiO <sub>2</sub> )	"Medium loss"
P- 9	Mo	80	20	(80% CaO.SiO <sub>2</sub> + 20% Al <sub>2</sub> O <sub>3</sub> )	Special ++
P-10	Mo	80	20	(88% CaO.2SiO <sub>2</sub> + 12% Al <sub>2</sub> O <sub>3</sub> )	Special ++
P-11	W+	100			
P-12	Re	100			
P-13	Mo**	80	20	(45% MnO + 55% SiO <sub>2</sub> )	-325 mesh

\*Standard sintering is at 1425°C for 1/2 hour

\*\*As MoO<sub>3</sub>+As WO<sub>3</sub>

++Melt phase has same constituents as special ceramics

Ti-11	Mo	95	5	(TiO <sub>2</sub> )	Used on electrical studies Task 6 only
-------	----	----	---	---------------------	---

TABLE 4-23

## Composition of Metallizing Paints Discussed in Text

Paint	Nominal Composition %	Spectrographic Determination of Minor Constituents*			
		1.0-5.0	0.1-1.0%	0.01-0.1%	0.001-0.01%
P- 1	MoO <sub>3</sub> -75%, MnO <sub>2</sub> , TiO <sub>2</sub> -25%	Al, Si	--	Ca, Ni	Mg, Cu, Fe
P- 2	MoO <sub>3</sub> -100%	Al, Si	--	Mg, Ca	Mn, Fe, Ti
P- 2M	MoO <sub>3</sub> -100%	--	--	--	Si, Al, Mg, Cu, Fe
P- 3	MoO <sub>3</sub> -72%, MnO <sub>2</sub> , TiO <sub>2</sub> , SiO <sub>2</sub> -28%	--	Al	Ca	Cu, Ag, Zn, Mg, Fe, Ni, B
P- 4	Mo - 100%	Si	Al	Ni	Cu, Mn, Fe, Ti, Co
P- 4M	Mo - 100%	--	Si	Al, Fe	Cu, Mn, Ni, Mg, Co, Ca
P- 5	Mo - 100%	Si	Al	Fe	Mg, Cu, Mn, Ni, Ti
P- 6	Mo - 100%	Al, Si	Ni	Mg, Ca, Fe, Cr	Cu, Mn, Ti, Co
P- 7	Mo-80%; BaO, SiO <sub>2</sub> -20%	--	Al, Ni, Cr	Cu, Ag, Ca, Fe	Mg, Mn, Ti, Co
P- 8	Mo-80%; MnO, SiO <sub>2</sub> -20%	--	Al	Ni, Mg, Ca, Fe, Cr	Cu, Ag, Ti, Co
P- 9	Mo-80%; Al <sub>2</sub> O <sub>3</sub> , CaO, SiO <sub>2</sub> -20%	--	Mg, Fe, Cr	Ni	Cu, Mn, Ti, Co
P-10	Mo-80%; Al <sub>2</sub> O <sub>3</sub> , CaO-2SiO <sub>2</sub> -20%	--	Cr	Mg, Fe, Ni	Cu, Mn, Ti, Co, Zr
P-11	WO <sub>3</sub> - 100%	Si	Al	Mg, Fe	Ni, Ca, Mg, Ti
P-12	Re - 100%	Si	Al	Mg, Fe, Ti	Ca, Mn, Ni

\*All amounts should be considered accurate to within a factor of  $\pm 2$ .

3. P-7 was formulated as an electrically low loss paint. It was thought that the  $Ba^{2+}$  ions in the melt phase would provide a nearly lossless condition in the silica network at radio frequencies. This hypothesis appears to be justified.
4. P-8 was formulated as a medium loss paint. It also provides a simple system containing MnO, a common additive to metallizing mixes. It seals well to sapphire and the phase relationships of the MnO-SiO<sub>2</sub>-Al<sub>2</sub>O<sub>3</sub> system are well known so that it can be used to obtain a further understanding of metallizing mechanisms.
5. P-8 and P-9 were formulated because of the extensive knowledge available concerning the melt phase obtained above. Also, the metallizing paint and the special ceramics still form a three component CaO-SiO<sub>2</sub>-Al<sub>2</sub>O<sub>3</sub> system amenable to detailed analysis.

The paints were ground in a ceramic ball mill, unless otherwise noted, with binders and solvents for 48 hours. Particle size distributions for P-1 and P-4M paints are given in Figs. 4.42 and 4.43. These distributions were obtained by using a Coulter counter.\* This instrument works on the principle that a change in electrical properties of an orifice submerging in a suitable solvent occurs when a particle passes through the orifice; the size of the particle passing is related to the magnitude of the electrical change recorded. The run shown in Fig. 4.42 was run on an 18 micron aperture in 4% sodium pyrophosphate in water using Darvan #7\*\* as a dispersing agent prior to introduction in the electrolyte. When dealing with materials of different densities in the same sample, the Coulter counter does not produce a true weight percent curve but rather a volume percent curve. This is due to the fact that the Coulter sensing zone completely ignores

---

\*Coulter Electronics Inc., Chicago, Ill.

\*\*R. T. Vanderbilt Co., New York, N. Y.

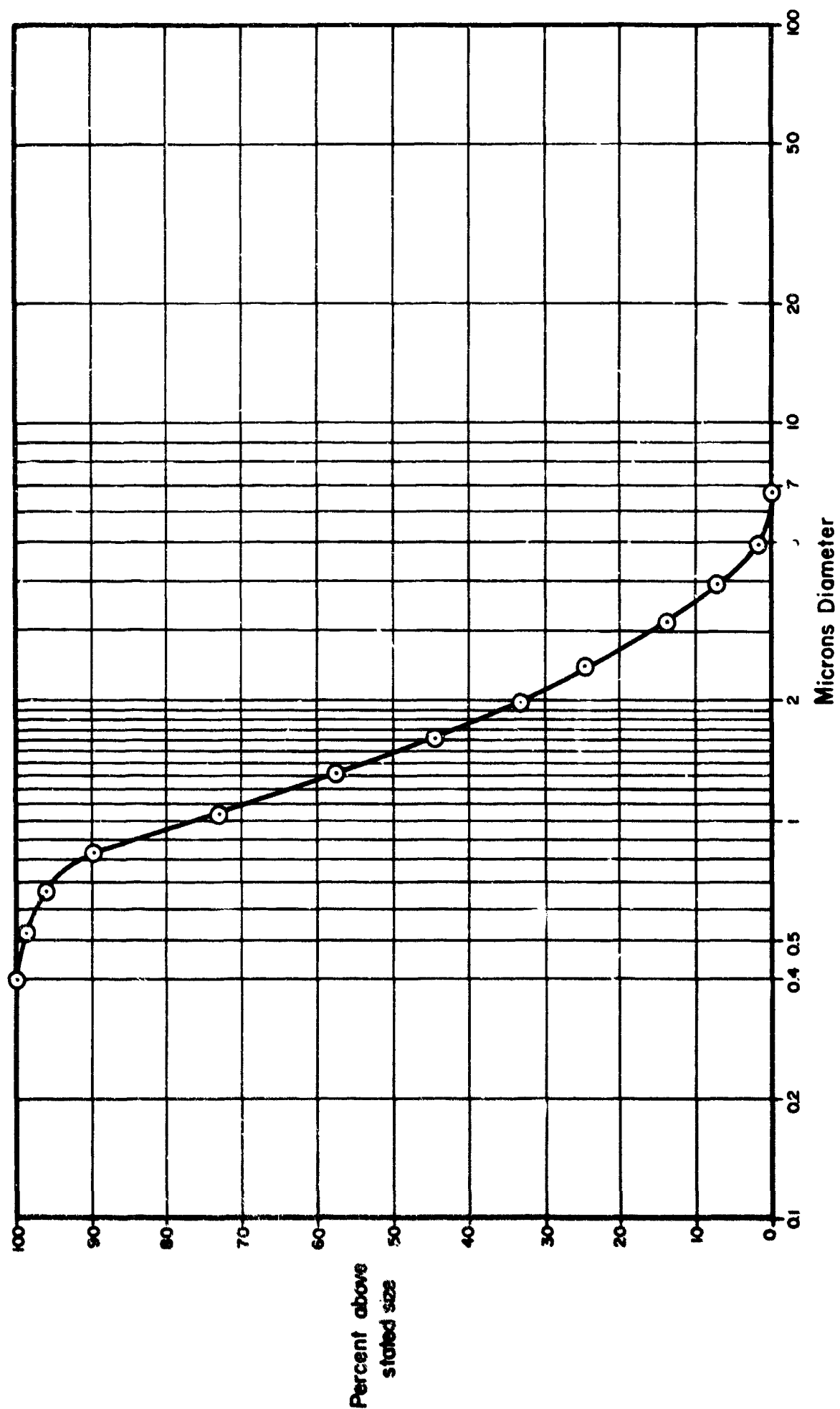


Figure 4.42: Particle size distribution for P-1 metallizing paint obtained by using a Coulter counter.

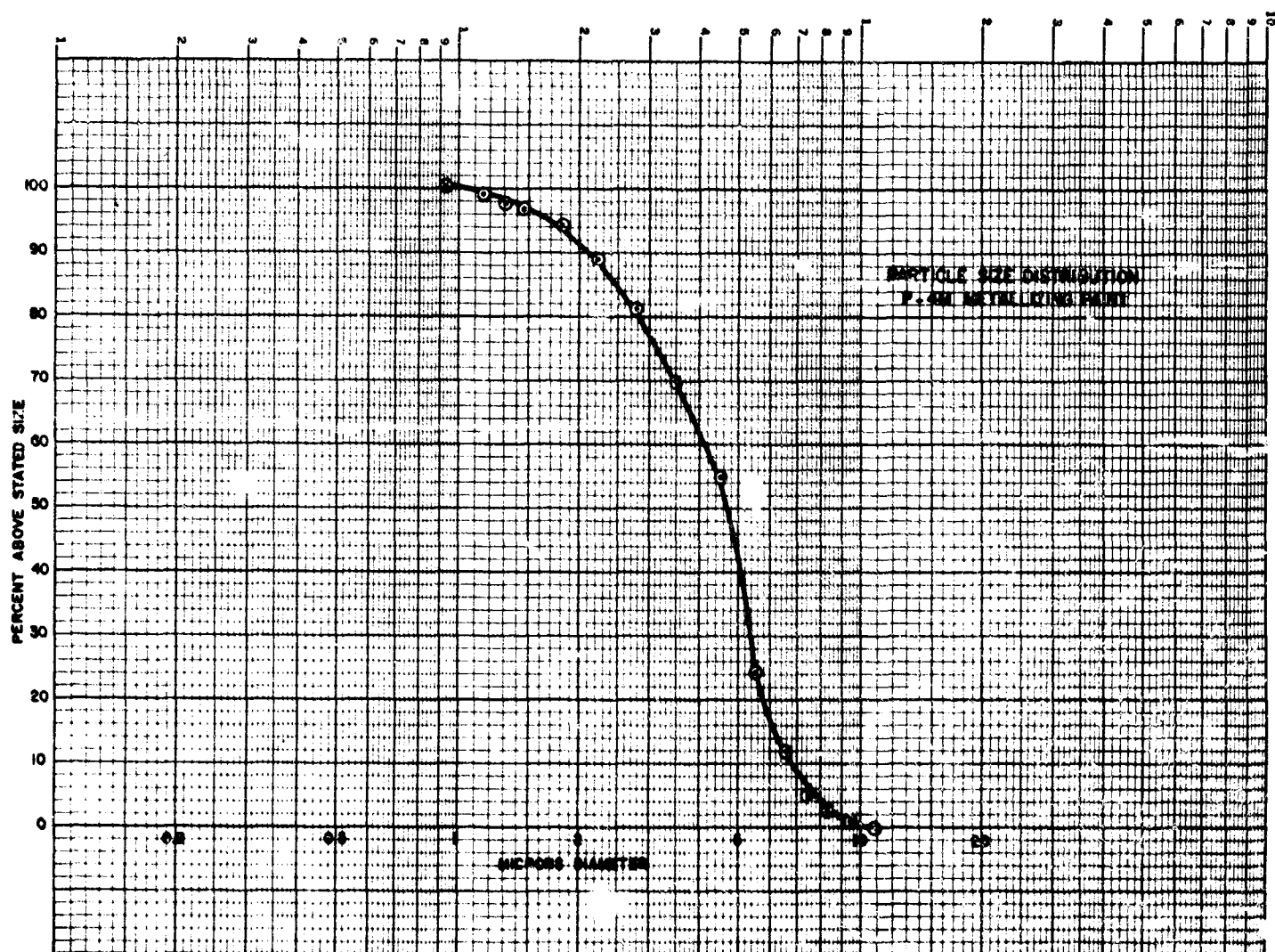


Figure 4.43: Particle size distribution for P-4M metallizing paint obtained by using a Coulter counter.

density and is sensitive only to particle volume.<sup>31</sup>

This technique was used because it was felt that in the complex metallizing paints under study, normal sedimentation techniques would give erroneous readings. The data shown for P-1 paint and P-4M paint is typical of the particle sizes to be expected for the oxide and metal based paints under study.

#### 4.4.2 The Paint

A metallizing paint consists of a refractory metal or metal oxide component, which reduces to a metal in the metallizing operation, to which is sometimes added a nonmetallic component. This "pigment" is suspended in an organic lacquer. A typical mixture contains a methyl ethyl ketone base lacquer, a grinding resin, and a thickening agent. The considerations involved in the manufacture of a metallizing paint are outlined in the Third Quarterly Report, pages 5-13. The paints manufactured on this program are listed in Table 4-22.

The spectrograph and/or typical analysis of some of the paint components are given in Table 4-23.

#### 4.4.3 Firing Conditions

The furnace used for metallizing consisted of a two-inch diameter, three-foot long alumina tube which was wound with molybdenum tape and which was surrounded by pure alumina insulating powder. Water cooled preheat and cooling chambers mated with the ends of the alumina tube. The furnace was capable of 1825°C operation and could be run in a wet or dry reducing atmosphere - or air as required.

An atmosphere of three parts of nitrogen to one part of hydrogen with a dewpoint of 30°C was used to sinter the metallizing paint onto the ceramic at temperatures within the range 1100°C - 1800°C.

#### 4.4.4 Sintering of the Metallizing

The extent to which P-4M paint sinters if placed on an inert substrate is given in Table 4-24. The molybdenum -325 Fansteel\* powder was not ball milled for this study. Ball milling the material would have two effects, firstly

---

\*Fansteel Metallurgical Corporation, North Chicago, Ill.

TABLE 4-24

Sintering of Molybdenum Powders  
in a  $\text{H}_2/\text{N}_2$  Atmosphere, 30°C Dewpoint

Temperature °C	Time Min.	Compacting Pressure Tons/in <sup>2</sup>	Fired Density g/cc
1425	30	1	3.76* $\pm$ 0.03
	30	2	4.40* $\pm$ 0.03
	30	6	5.24* $\pm$ 0.03
1520	20	6	5.3 $\pm$ 0.1
	33	6	5.55 $\pm$ 0.1
	67	6	5.65 $\pm$ 0.1

---

\*Also unfired density

Density of Molybdenum is 10.2 gm/cc

---

it would reduce the particle size of the aggregates and enhance sintering. Secondly, it would introduce impurities and affect sintering.

The compacts at both temperatures were mechanically strong. The data indicates that a volume diffusion densification process is initiated between 1425°C - 1500°C; below this temperature a surface diffusion mechanism predominates with no net densification increase<sup>32</sup>. We can see that even at moderately high pressing pressures the porosity is 50%. Thus a metallizing mix using this molybdenum powder would be expected to be infiltrated extensively by the melt phase, even under these compacting pressures (a necessary condition for a good bond) and which was experimentally confirmed when non-reactive, well-characterized, glass mixtures were used.

Composites of hypothetical molybdenum and glass metallizing paints were ball milled, compacted, and sintered at 1425°C and 1600°C for 1/2 hour in the usual wet metallizing atmosphere. The density of each composite was then measured to determine the effect of the glass addition on the additional consolidation of the metallizing composite.

P-4M paint was used as the zero glass standard. Two glass compositions were added, a 1:1 SiO<sub>2</sub>/CaO (mole ratio) glass with 20% alumina, and a 2:1 SiO<sub>2</sub>/CaO glass with 16% alumina. These compositions represented the eutectics on their respective pseudo-binary phase diagrams, Figs. 4.03 and 4.04.

The glasses were added in one of three amounts, 10%, 20% and 40% by weight to make the glass-molybdenum mixtures. Additional compacts were made only of glass in order to locate the other end of the density versus composition curve.

The results are tabulated in Table 4-25 and plotted in Figs. 4.44 and 4.45. The two figures show the results of sintering at 1425°C and 1600°C respectively. The solid curve in each figure is for compacts containing 1:1 SiO<sub>2</sub>/CaO glass, and the dash curve is for compacts containing 2:1 SiO<sub>2</sub>/CaO glass.

The curves marked "A" indicate the hypothetical densities of composites if the two phases, theoretically dense metal and glass, were mechanically mixed and formed no voids. The curves marked "B" indicate the hypothetical



TABLE 4-25

## Sintered Densities of Glass-Molybdenum Composites

Paint Comp.	Sintered Density gm/cc	
	1425°C	1600°C
P-4M	5.86	6.88
90Mo+10%1:1	7.58	7.19
80Mo+20%1:1	6.19	6.13
60Mo+40%1:1	4.37	4.36
100%1:1	2.2	-
90Mo+10%2:1	5.57	4.21
80Mo+20%2:1	5.35	5.19
60Mo+40%2:1	3.91	n.d.
100% 2:1	2.4	-

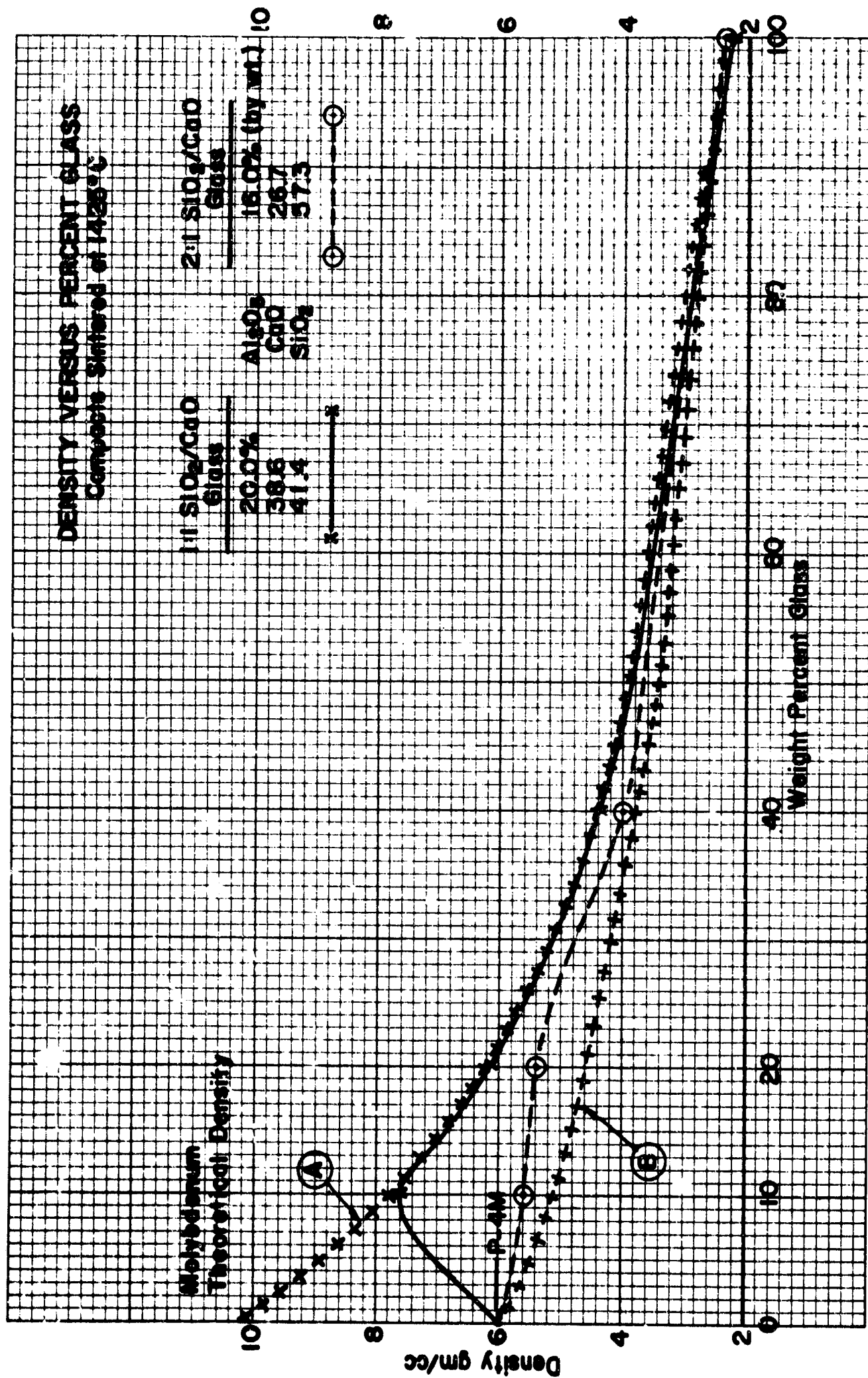


Figure 4.44: Density versus composition of molybdenum-glass composites sintered at 1425°C.

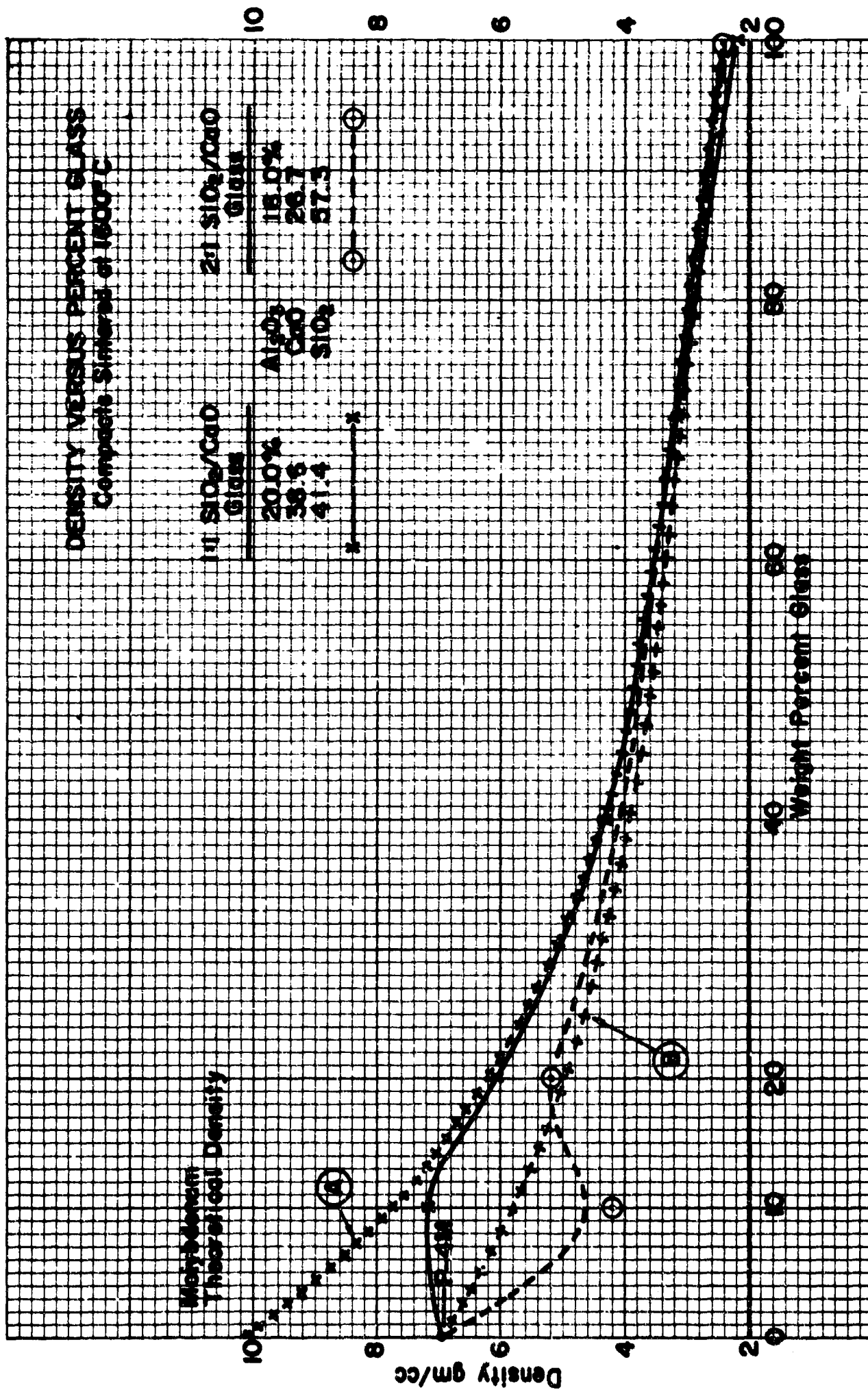


Figure 4.45: Density versus composition of molybdenum-glass composites sintered at 1600°C.

densities of composites if the glass phase and the porous metal phase (considered as closed-pore particles which cannot be infiltrated by the glass phase) are mechanically mixed and form no further voids.

The sintered density of P-4M compacts (5.86 gm/cc sintered at 1425°C, 6.88 gm/cc sintered at 1600°C) was naturally less than theoretical (10.2 gm/cc) because sintering was incomplete at these relatively low temperatures and considerable porosity remained. However, ball milling of the molybdenum powder before compacting and sintering did result in greater densities than those given in Table 4-25 for unground metal powder.

The solid curves in Figs. 4.44 and 4.45 indicate that compacts (or metallizing paint) containing more than ten weight percent 1:1 SiO<sub>2</sub>/CaO glass very closely approach hypothetical, voidless density (Curve A). The dash curves indicate that lower densities were obtained in compacts made with 2:1 SiO<sub>2</sub>/CaO glass because this more viscous melt was not able to penetrate the pores of the molybdenum particles as thoroughly as the relatively fluid 1:1 SiO<sub>2</sub>/CaO melt. However, all but one density value for the sintered composites fell between the minimum and maximum hypothetical densities, Curves A and B, thereby proving that the glass melt did penetrate the molybdenum particles to a considerable extent.

Based on the experimental data, it appears that a non-metallic volume of 30-40% (10% by weight corresponds to 33% by volume) is suitable to produce a dense metallizing layer. More data, especially in the 0-20% glass addition range, is needed before the data can be analyzed further, and the results applied quantitatively to the sintering kinetics taking place in the metallizing layer.

#### 4.4.5 Solution of Molybdenum

One complication occurring in an actual metallizing paint when the non-metallic phase is added as raw CaO, Al<sub>2</sub>O<sub>3</sub> and SiO<sub>2</sub> is the possibility of initial solution of the molybdenum in the melt. Typical amounts are given in Table 4-26. The contact angle experiments reported in Section 4.2.3.3.4 indicated that if the glass were formed prior to being placed in contact with molybdenum, then solution was limited to less than 100 ppm, the one exception being the case of the CaO-MgO-Al<sub>2</sub>O<sub>3</sub> eutectic glass. The evidence strongly points therefore to an initial reaction occurring between the metal oxides and/or carbonates and the molybdenum before the oxide reacts and is neutralized by the silica.

TABLE 4-26

Molybdenum Concentrations in Glasses  
 Melted at Temperature for 1/2 Hour in Molybdenum Boats  
 as Determined  
 by Spectrographic Analysis

Comp. No.	Initial Weight Percent			Soak Temp.	Percent Molybdenum
	CaO	Al <sub>2</sub> O <sub>3</sub>	SiO <sub>2</sub>		
1	33.8	30	36.2	1600	0.007
2	24.1	50	25.9	1700	1.0
3	14.5	70	15.5	1800	0.3
3A	41.0	15	44.0	1500	0.01
4	22.3	30	47.7	1600	0.2
5	17.5	45	37.5	1700	1.0
6A	27.1	15	58.4	1500	1.0
9A	20.2	15	64.8	1500	1.0

A further investigation was made to determine whether the molybdenum was actually dissolved or was present as a finely dispersed separate phase at elevated temperatures. At 400X on a polished section of a glass sample, numerous metallic particles approximately 1 to 15 microns in diameter were observed suspended in the glass. These particles indicated that molybdenum was dissolved in the glass but that a much faster quench rate would be necessary to keep the molybdenum in solution.

The mix -- 47% BaO-53% SiO<sub>2</sub> -- showed darkening of the melt due to solution of the molybdenum during the melt formation process at temperature and its precipitation on cooling. Remelting the glass six times resulted in clarification of the melt due to the Mo in solution at temperature precipitating out onto the wall of the molybdenum crucible because of the insolubility of Mo in a silicate glass.

The influence of the "solution of molybdenum" on the metallizing sintering by a comparison of a paint consisting of raw oxides plus molybdenum versus a glass plus molybdenum was not directly investigated. A CaO-Al<sub>2</sub>O<sub>3</sub> - Mo paint was made and sintered, however. A soft metallizing resulted at 1425°C and 1600°C indicating that sintering was hindered. No explanation is advanced for this phenomena; one observation is that the melt is very fluid. At 1800°C excess melt is absorbed into the alumina ceramic leaving a dense metallizing. Such a metallizing is useful for situations where the presence of silica is undesirable, e.g., in the presence of alkali metals in thermionic convertors, and reactor liquid metal loops.

#### 4.4.6 Adherence

The melt phase must bond to both the alumina ceramic and to the molybdenum metal phase if it is to form a strong seal. Data for the strength of the bond of sessile drops on alumina and molybdenum substrates has been given above\* and was indicated to be good.

During the melting of the various oxide components in molybdenum boats prior to incorporating them into the paints listed in Table 4.26, their relative adherence to the molybdenum boat walls were noted. The BaO.SiO<sub>2</sub> glass did not adhere at all, whereas the 62% MnO-38% SiO<sub>2</sub> melt crept up the walls and adhered so strongly that the boat had to be shattered and the small pieces of molybdenum had to be ground away from the

\* Section 4.2.3.3.4

solidified melt. Obviously a strong chemical bond had formed. Contact angle results on molybdenum and alumina substrates employing this melt,  $\text{MnO-TiO}_2$  or  $\text{MnO-SiO}_2\text{-TiO}_2$ , have been reported elsewhere; they are almost zero.

Two CLM-15 tensile test pieces of Body A were painted with the non-metallic phase  $\text{CaO/SiO}_2\text{-20\% Al}_2\text{O}_3$  and were used to sandwich a sapphire disc. The assembly was heated to  $1425^\circ\text{C}$ . On cooling, a vacuum tight seal with a strength of 7,000 psi was formed.

Next, two CLM-15 tensile test pieces of Body A were butted together and heated to  $1750^\circ\text{C}$ . Again a tensile bond strength of 5,000-10,000 psi developed due to migration of the glassy phase of the ceramic across the joint. A similar test with Body H (99.5%  $\text{Al}_2\text{O}_3$ ) does not give a joint due to the absence of a glass phase in the ceramic.

It was noted that in the surface tension experiments reported earlier that the melts showed good adherence to the refractory metal. Test assemblies were therefore made up as follows: ceramic-melt-molybdenum-metal-melt-ceramic, which were fired in a metallizing cycle. The assemblies pulled with a strength of 2,000-5,000 psi. This latter assembly is equivalent to a metallizing system where the metal and melt phases have separated into discrete layers. In all the cases cited above, the joints were vacuum tight.

Detailed investigation of adherence mechanisms, van der Waals bonding, semi-conduction bonding, chemical bonding, mechanical interlocking would take us beyond the scope of this study. It should be noted, however, that such a study is required to provide the corner stone to our store of knowledge with regard to metallizing.

#### 4.4.7 Chemical Reduction

During the metallizing process, the furnace gases react with the metallizing layer if it contains reactive reducible oxides. An indication of these types of reaction products for P-1 metallizing was provided by carrying out a gas analysis experiment in a combustion furnace. The gas mix was fed into the furnace tube at the rate of 25 cc a minute and the products were fed into a

Burrell Chromatograph\*. These results are shown in Fig. 4.46. A dewpoint of 70°F for the hydrogen was maintained during the run. Nitrogen was not used as it was desired to follow the nitrogen evolution from the nitrocellulose lacquer. The oxygen and nitrogen peaks are not differentiated. The main gas evolution is due to breakdown and reaction of the nitro-cellulose with the metallizing oxides and the wet hydrogen atmosphere.

The components of P-1 metallizing paint were heated separately at 1425°C for one-half hour and then weighed. It was found that  $\text{MoO}_3$  was reduced to the metal while the  $\text{MnO}_2$  and  $\text{TiO}_2$  were reduced to  $\text{TiO}_{1.8}$  and  $\text{MnO}_{0.96}$ . These weight losses will be very sensitive to the dewpoint of the furnace atmosphere.

In connection with the electrical studies, section 7.3.2., weight loss measurements were made of various weights of metallizing paints P-1 and P-2 on 1" diameter discs of Body A, Fig. 4.47. These discs were also cross-sectioned after firing at 1425°C for 1/2 hour to give a relationship between the weight of metallizing paint applied and the thickness of the sintered layer, Fig. 4.48.

The weight loss in P-2 metallizing was 36% which corresponded to 33-1/3% loss of  $\text{O}_2$ , as  $\text{MoO}_3$  is reduced to Mo and 2-3% binder loss. No glass flow out is noted in this system at 1425°C and the layer is only lightly sintered, as is indicated in the cross-section, Fig. 4.49.

(Increasing the metallizing temperature for firing P-2 on Body A from 1425°C to 1550°C resulted in extensive migration of the glassy phase of the ceramic into the seal area.)

The weight loss in P-1 metallizing decreased progressively from 35.1% to 31.5%+indicating a decreasing reduction in a component in the metallizing and/or glassy phase.

Assuming reduction of  $\text{MoO}_3$  to Mo,  $\text{MnO}_2$  to MnO, for the reduction of  $\text{TiO}_2$  to  $\text{TiO}$ , we find total weight loss of 29.7%. If  $\text{TiO}_2$  remains unreduced, it gives a weight loss of 28.9%. Further reduction to Ti gives a loss of 30.5%.

---

\*Burrell & Kromo-tog Model K-2. See "Instruments for Gas & Vapor Chromatography", Catalog 84, Burrell Corporation, 2223 Fifth Avenue, Pittsburg 19, Pa.

+As the metallizing thickness increased



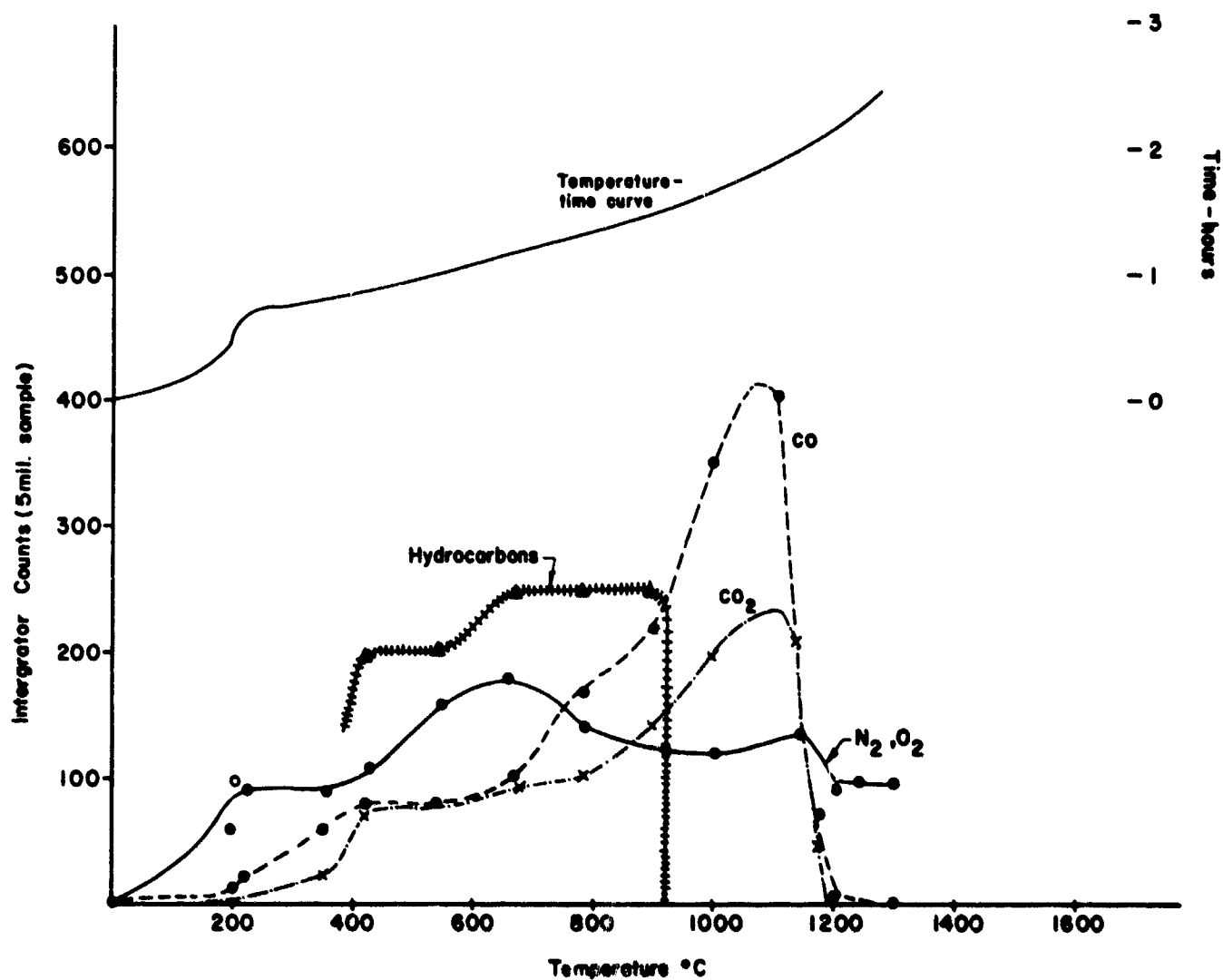


Figure 4.46: Analysis of gases evolved from a metallizing paint in the form of a layer 1" x 1" by 10 mils thick on alumina ceramic, under non-equilibrium conditions.

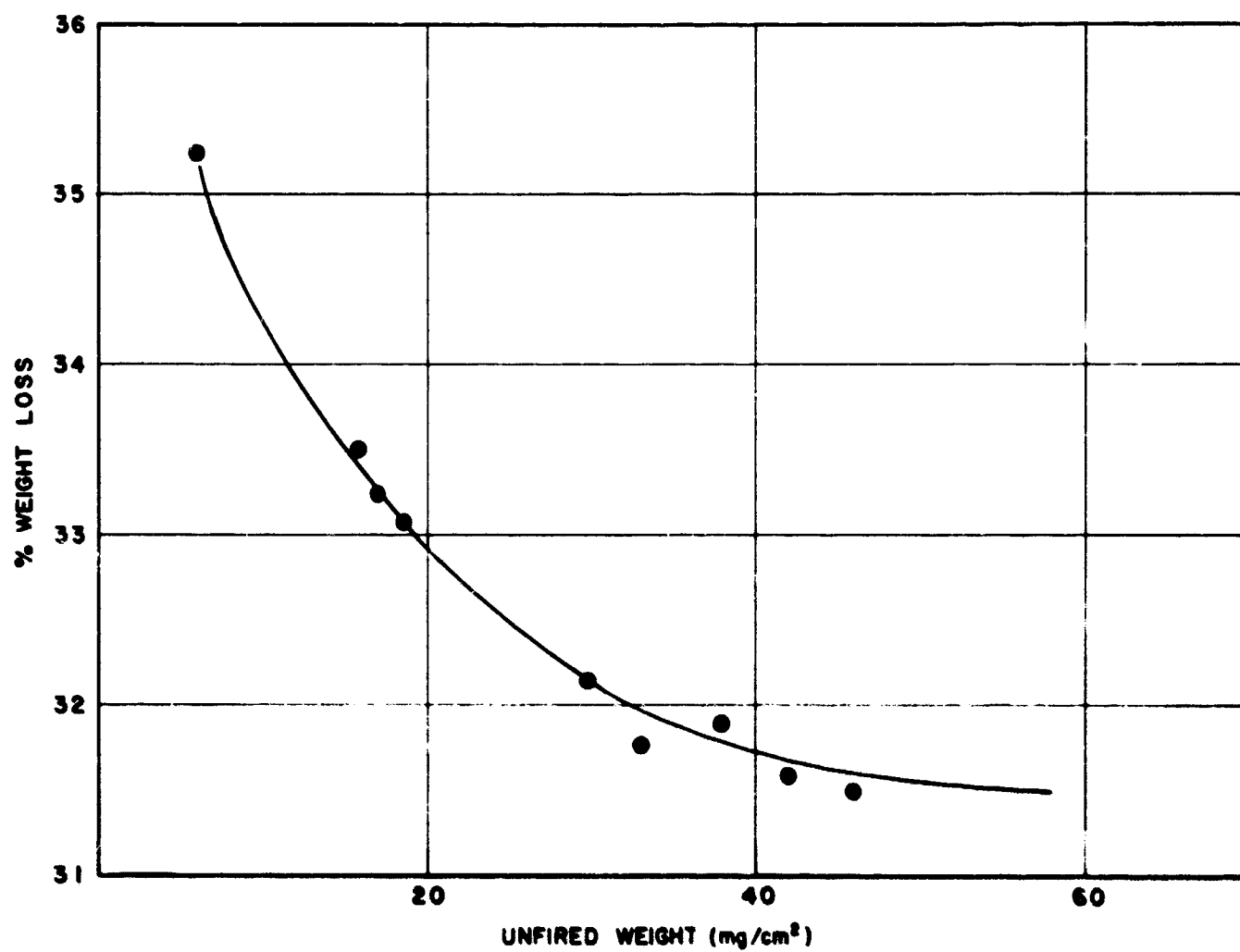


Figure 4.47: Percent weight loss of P-1 metallizing on Body A as a function of unfired sprayed weight of coating.

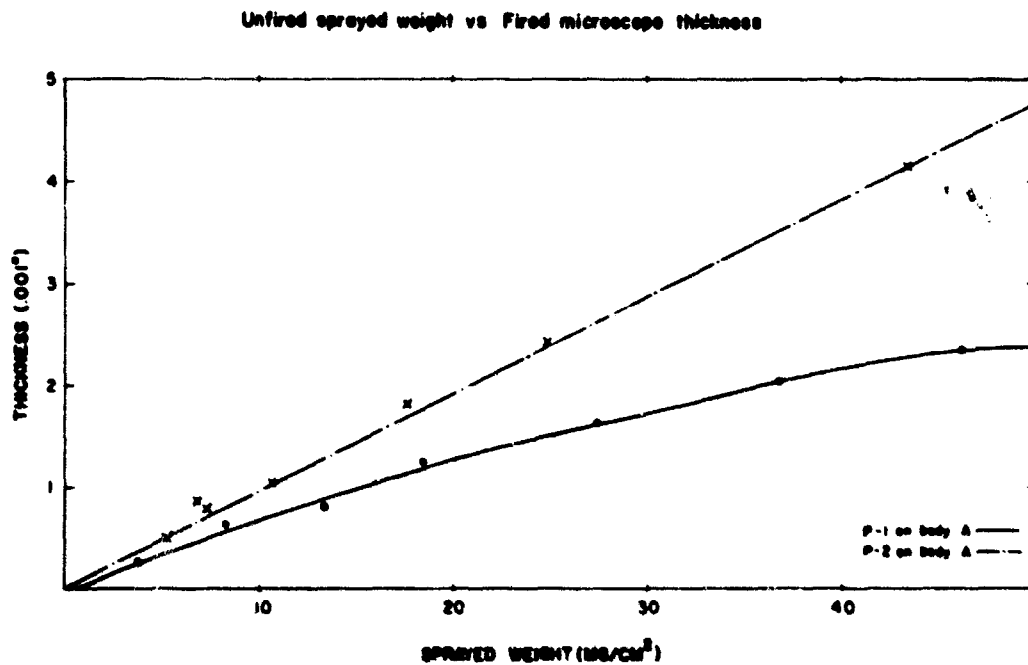


Figure 4.48: Unfired sprayed weight of metallizing paints P-1 and P-2 on Body A versus fired microscopically measured thickness. Supersedes curve of third quarterly report. Firing time was ½ hour at 1425°C.

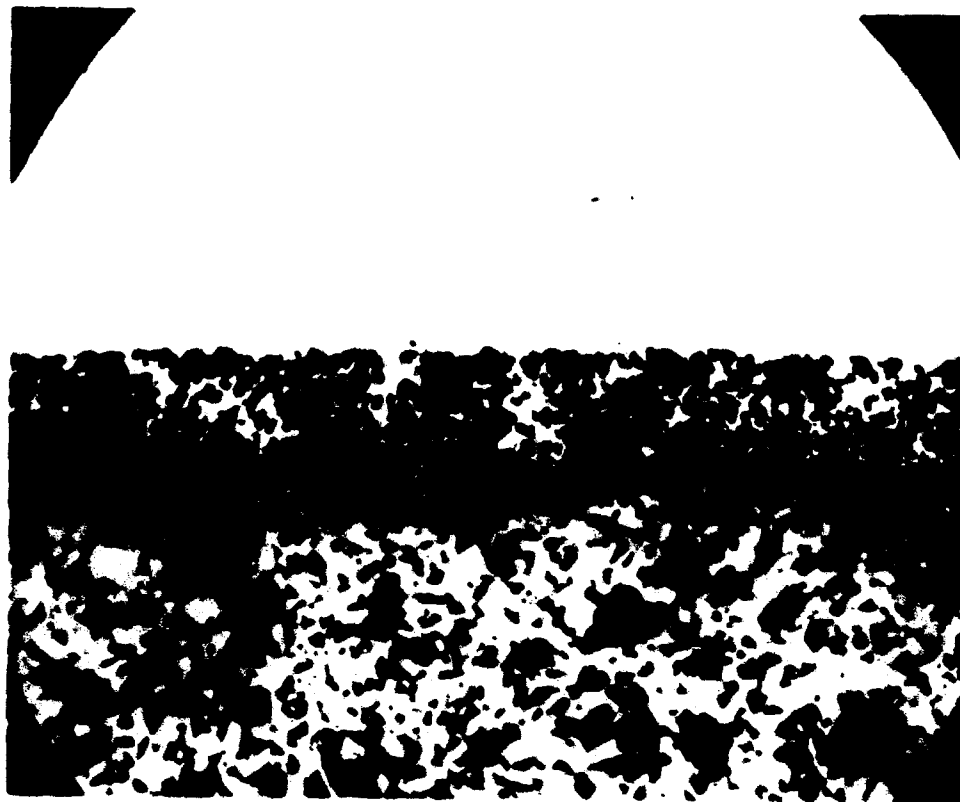


Figure 4.49: P-2 metallizing on Body A sintered at 1425°C for ½ hour in a  $H_2/3N_2$ , +100°C dewpoint atmosphere. The copper plate, copper braze to cupro-nickel can be seen to infiltrate the porous molybdenum sponge.

The difference between these calculated values and the experimental values would give a binder loss of 1% to 2.3% based on the lowest loss in weight values of 31.5%, Fig. 4.47. Actual amount of binder added is 2%. A simple conclusion to draw is that the  $\text{MnO}_2$  is reduced below the  $\text{MnO}$  level to contribute at least a further 2% total weight loss. This would correspond to a formula  $\text{MnO}_{0.5}$ . However, the loss decreases with metallizing thickness, indicating that the reaction is controlled by reaction and interdiffusion with the grain boundary phases of the alumina ceramic. The electron microprobe data presented in Figs. 4.52, 4.53 and 4.54 shows considerable migration of the glassy phase into the metallizing layer. It is probable, therefore, that some of these constituents will be reduced. For instance, the presence of an intermetallic compound  $\text{Mn}_x\text{Ti}_y$  was suspected in the case of Body C with P-1 based on X-ray diffraction data obtained by examination of a fractured metallized surface; thermodynamically the least stable oxide is  $\text{SiO}_2$ , which, while stable in reducing atmospheres in the pure state, may not be so in the situation under study.

Fig. 4.50 also shows that migration of the glass phase into the metallizing occurs. As the thickness of the metallizing increases, however, a perfectly linear increase in the amount of glass flow out does not occur (as the amount of glass flow-out is proportional to the depth to which  $\text{MnO}$  and  $\text{TiO}_2$  can penetrate into the ceramic and lower the viscosity of the glassy phase) thus the thickness increase will show the trend away from linearity indicated in Fig. 4.48. Fig. 4.50 shows a typical seal in this system, while Fig. 4.51 shows cross-sections of various thicknesses of metallizing. This latter figure illustrates very clearly the increase in the amount of glass flow out, and the resulting glassy interaction zone, as the amount of metallizing with its associated fluxes is increased.

#### 4.4.8 Glassy Phase Interdiffusion

A seal similar to that shown in Fig. 4.50 utilizing a copper rather than a Nicoro (Au-Cu-Ni) braze was subjected to the electron microprobe analysis. The results are given in Fig. 4.52.

The distribution curves of titanium and manganese are very similar. Manganese is detected further into the ceramic than titanium. (There is a larger amount of manganese present in the original P-1 paint.) From the seal interface the manganese diffusion into the ceramic, through the glass

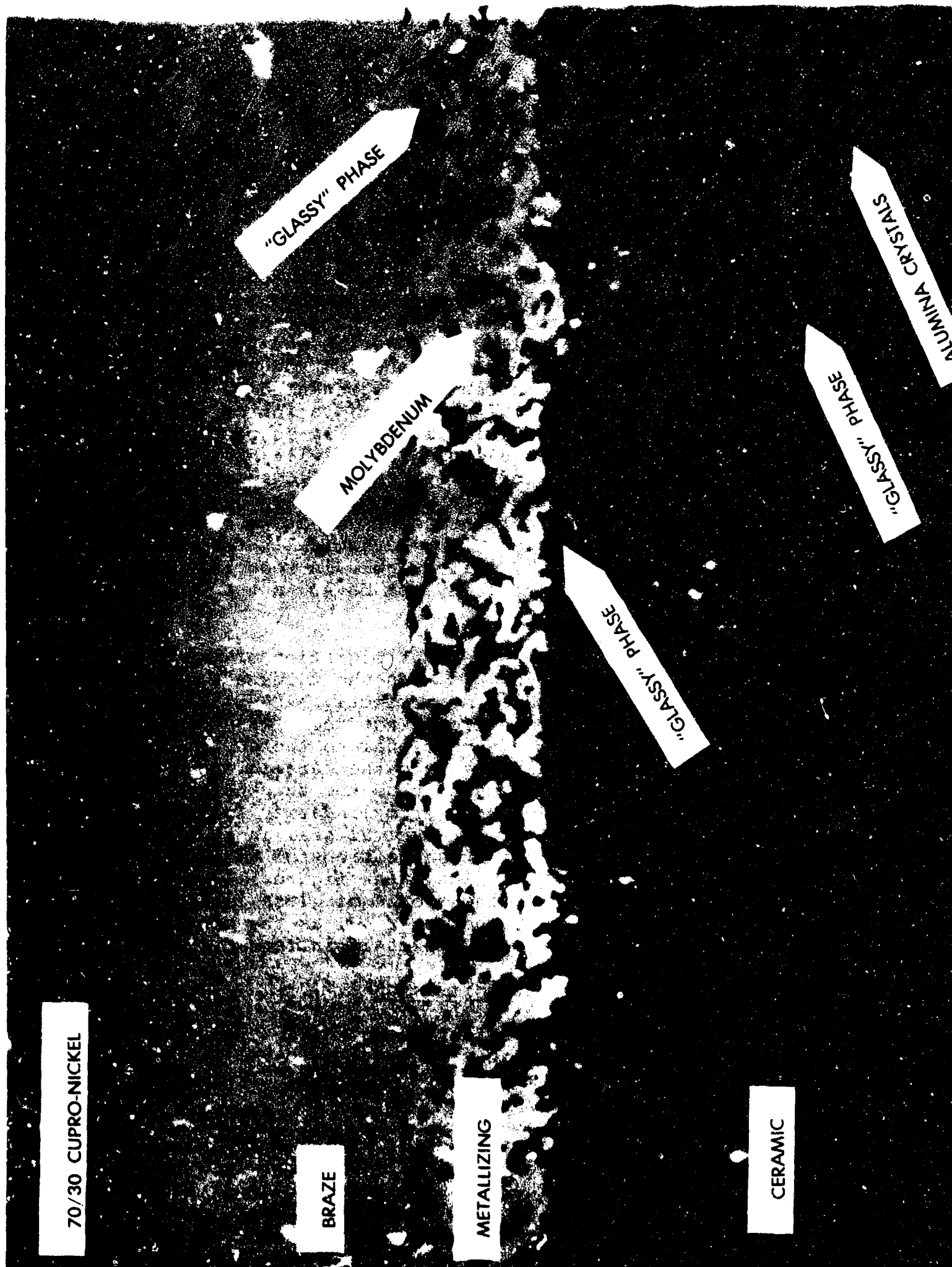


Figure 4.50: P-1 metallizing on Body A. Sinter fired at 1425°C for ½ hour in a  $H_2/3N_2$ , +100°F dewpoint atmosphere. Close inspection of the glassy interfacial layer between the metallizing and ceramic reveals its crystalline nature. Copper plate, Au-Cu-Ni braze to 70/30 cupro-nickel at 1040°C/10 minutes.

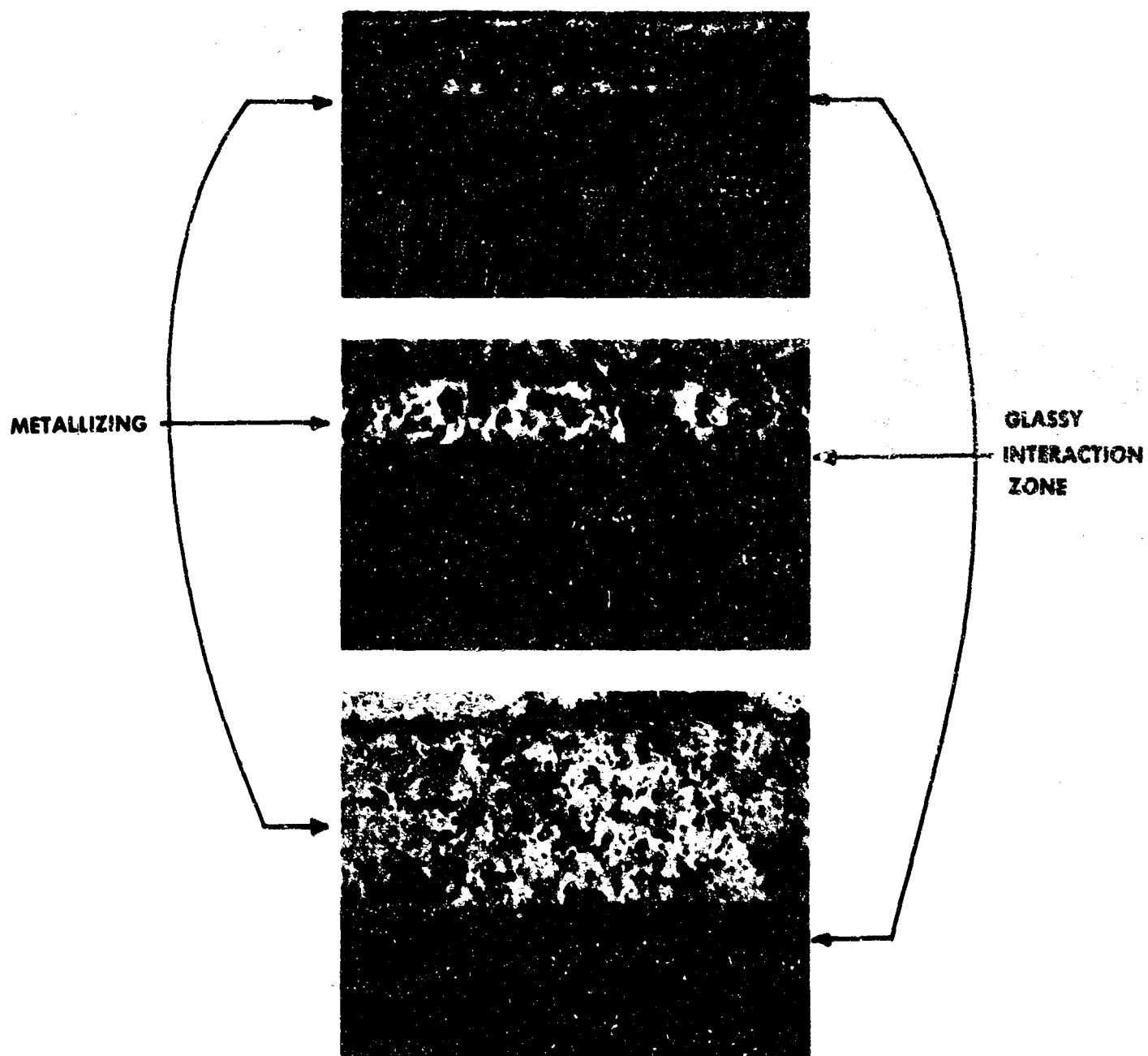


Figure 4.51: Photomicrographs of P-1 on Body A showing relationship between glassy interaction zone thickness and metallizing thickness (400X).

# Electron Probe Microanalysis of Metal-Ceramic Seal Scan#4C

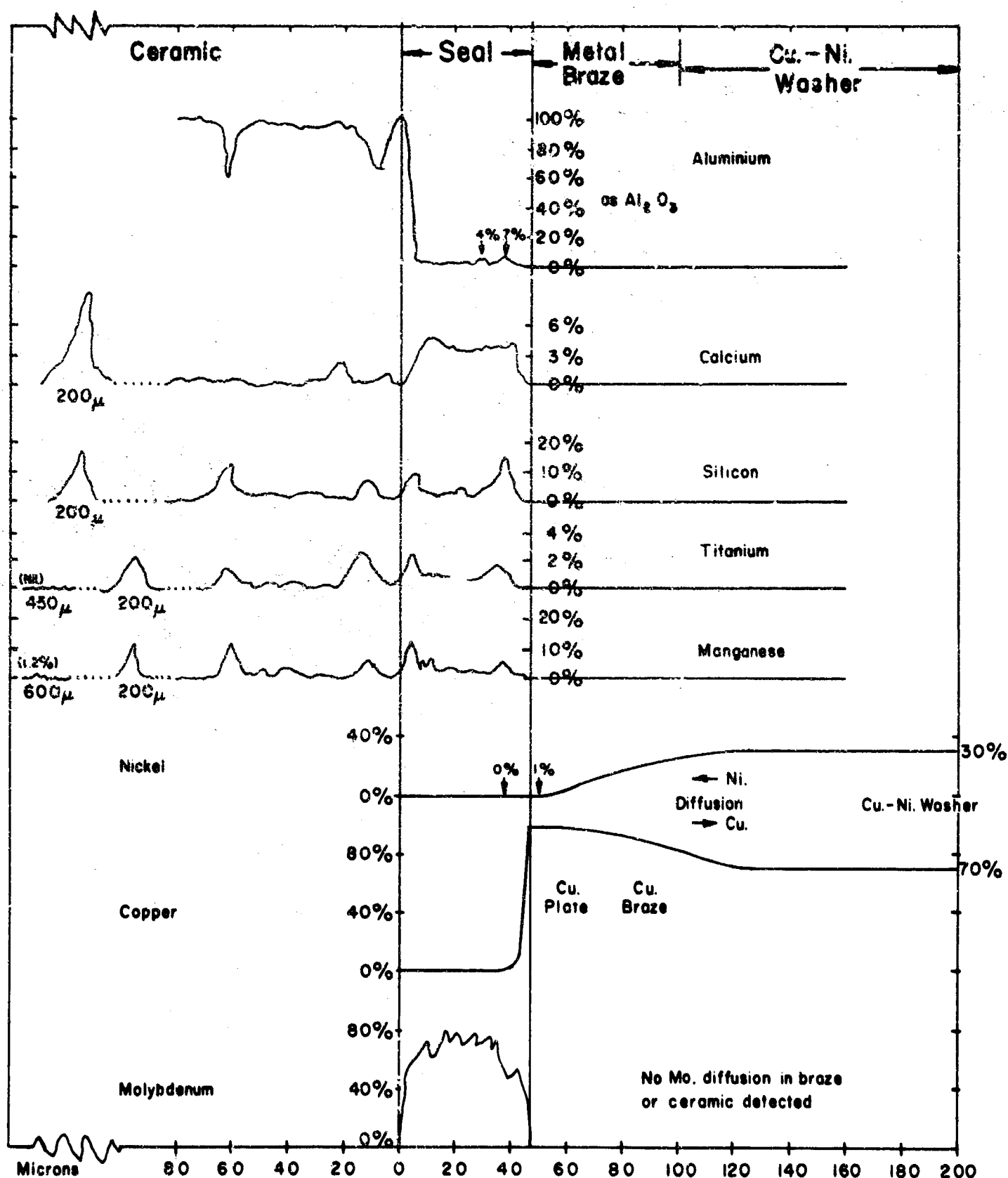
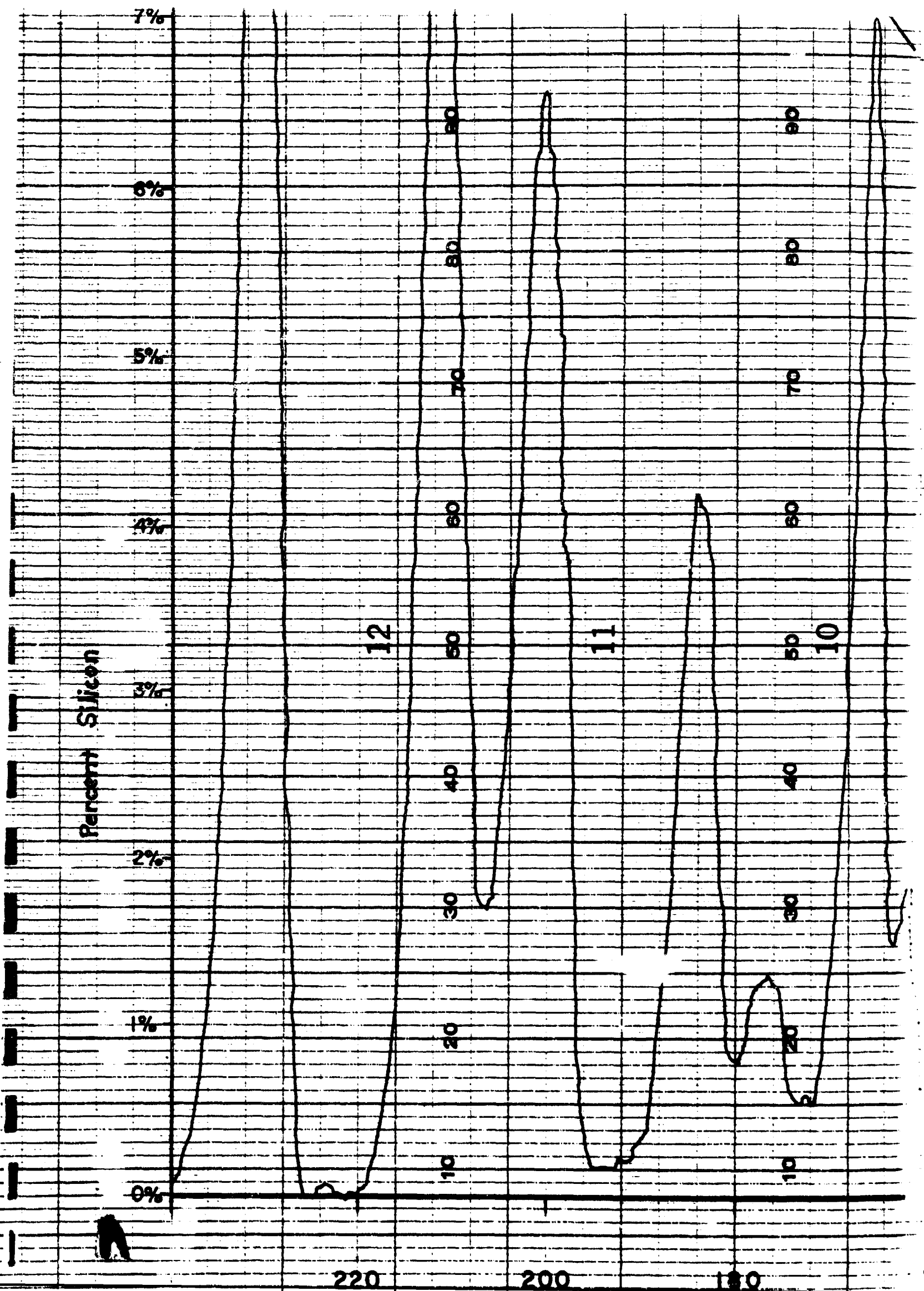


Figure 4.52: Electron probe microanalysis trace scan across Body A, P-1 metallizing processed at 1425°C, 1/2 hour, H<sub>2</sub>/3N<sub>2</sub> atmosphere, +80°F dew point.





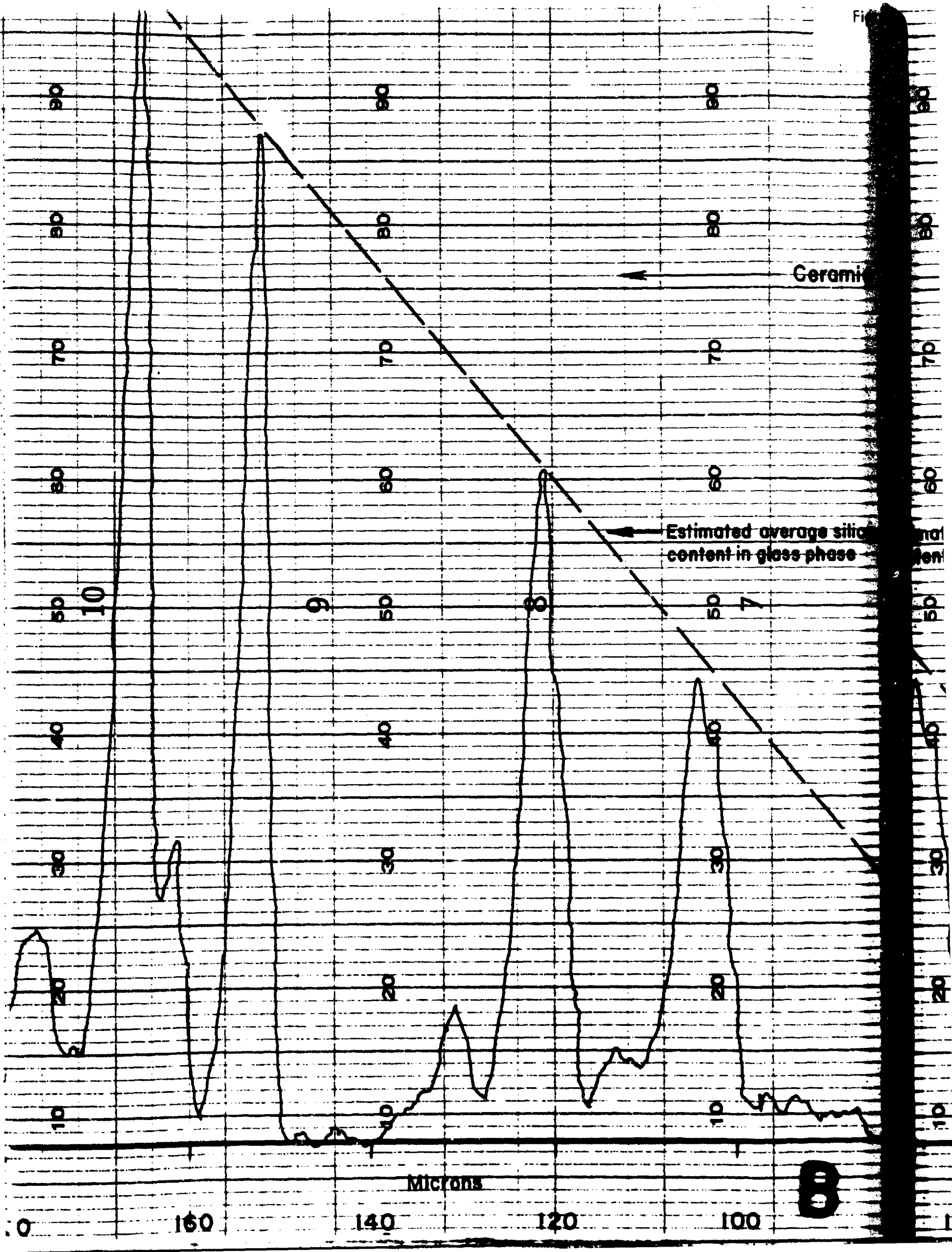
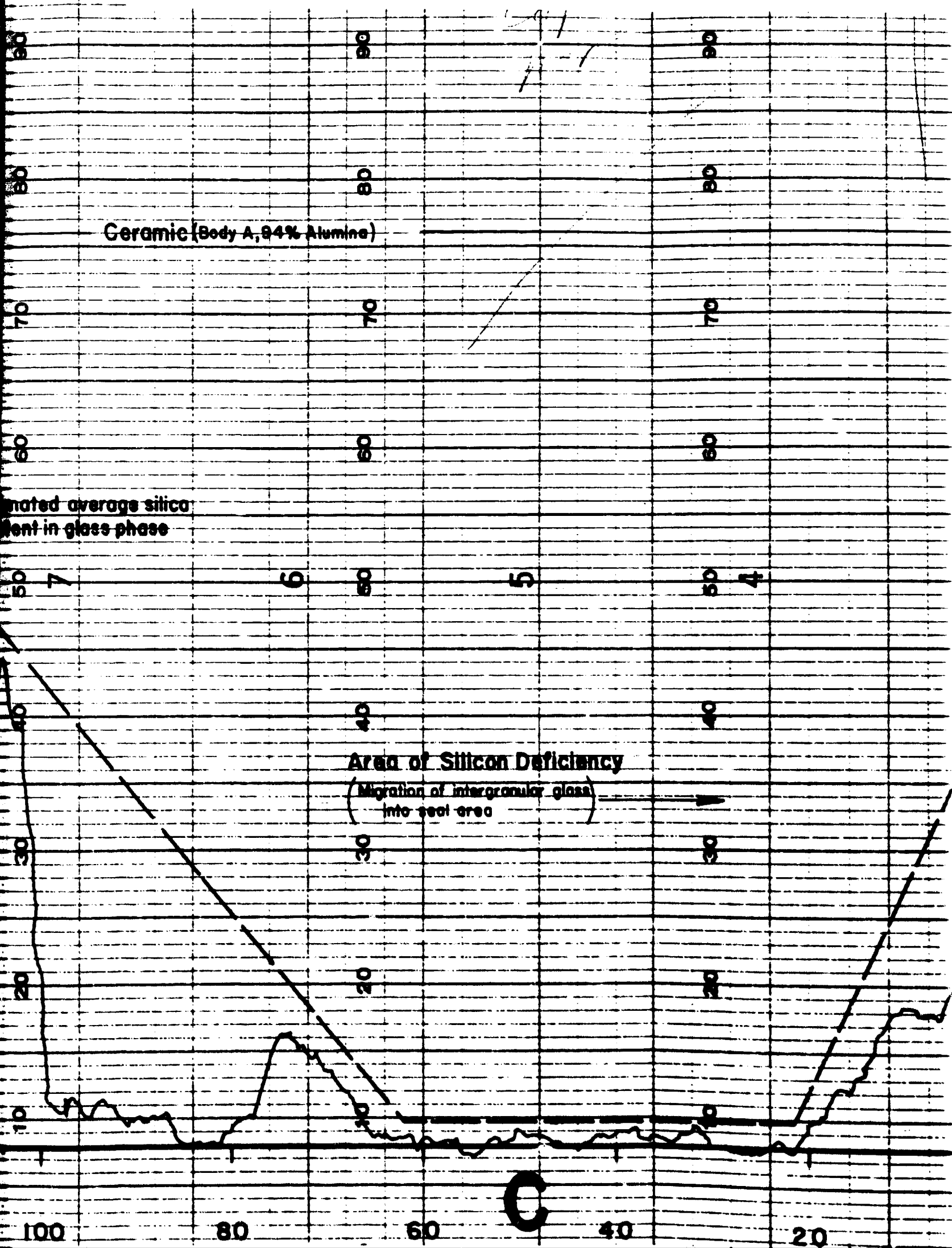
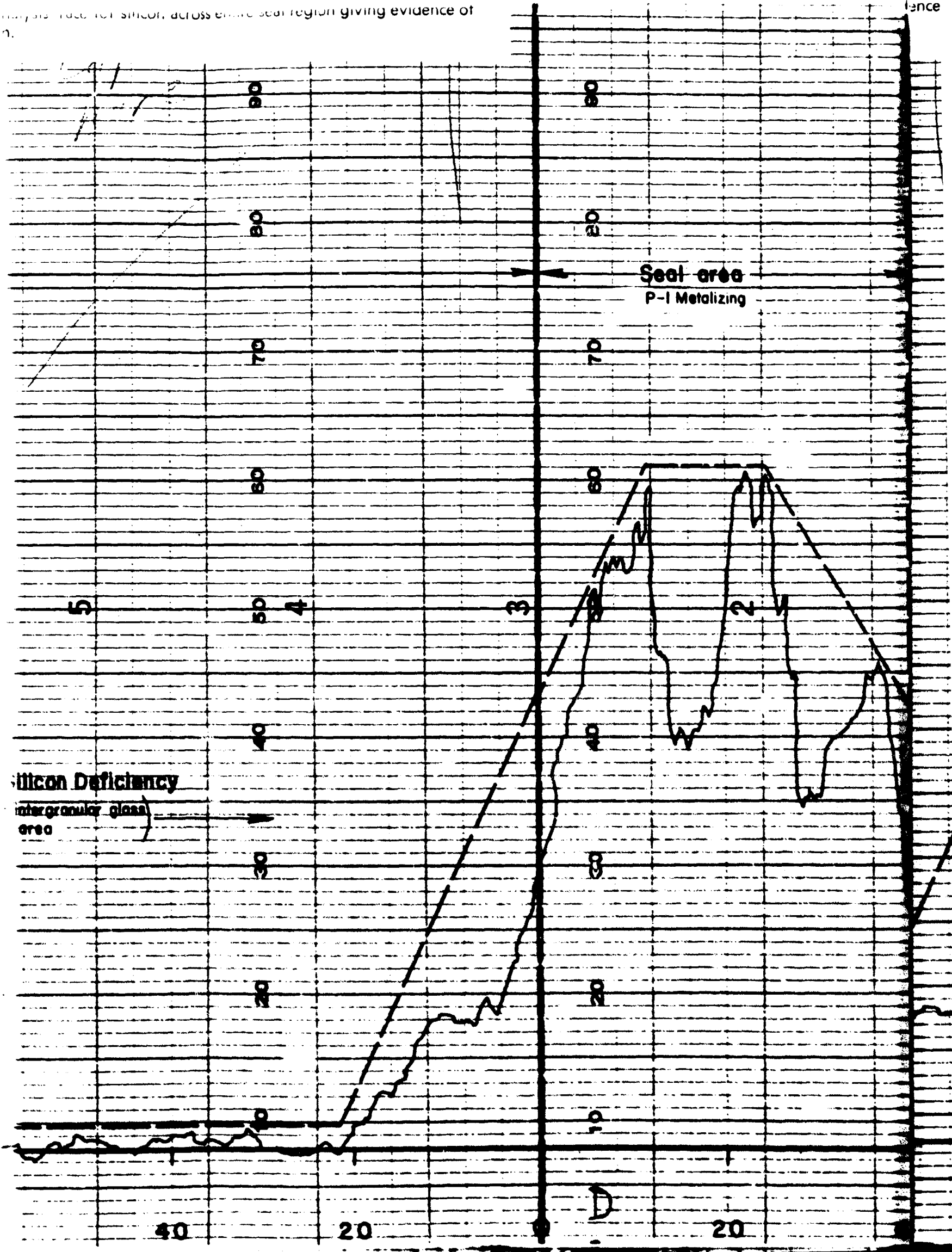


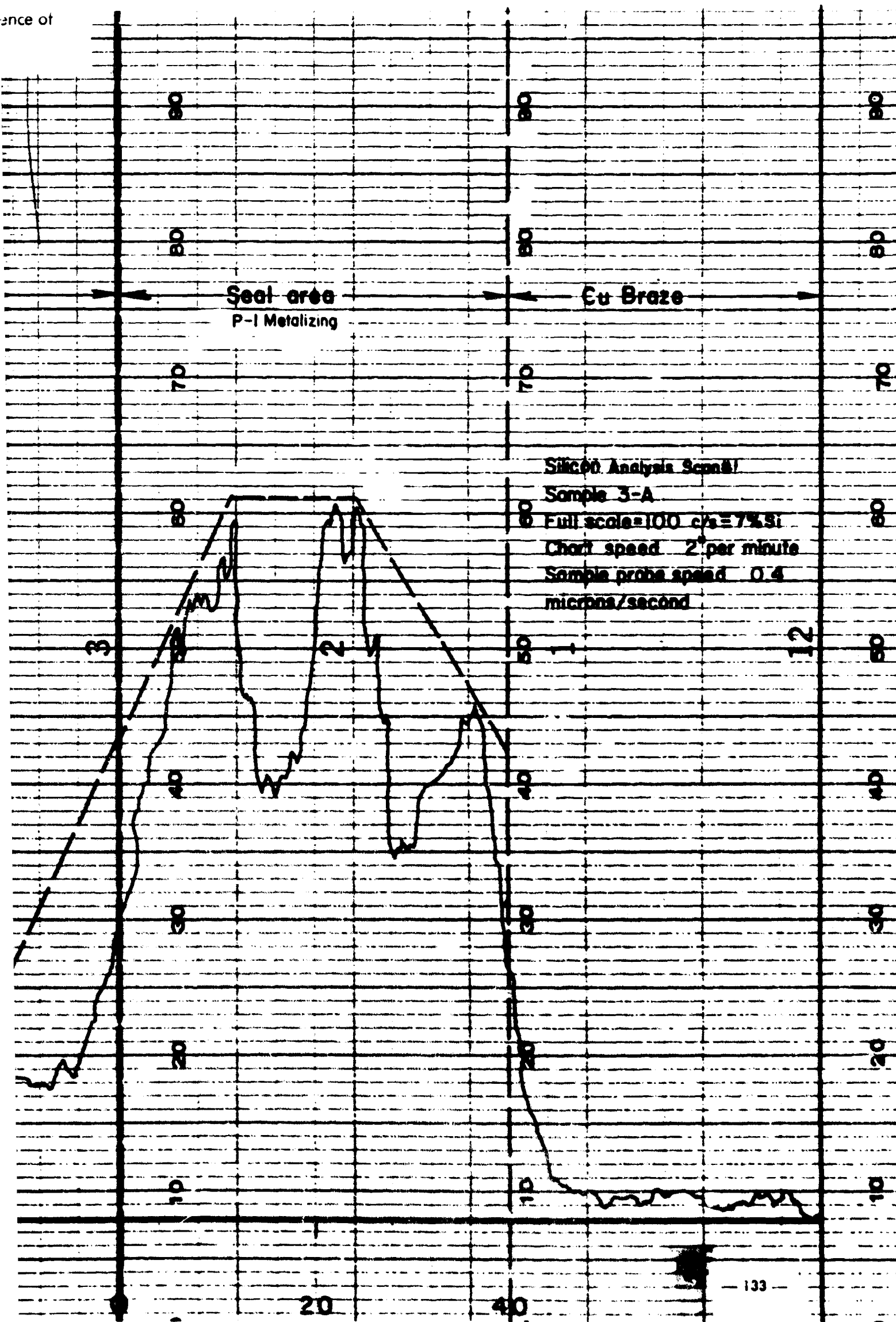
Figure 4.53: Electron probe micro-analysis trace for silicon across entire seal region giving evidence of glassy phase migration.

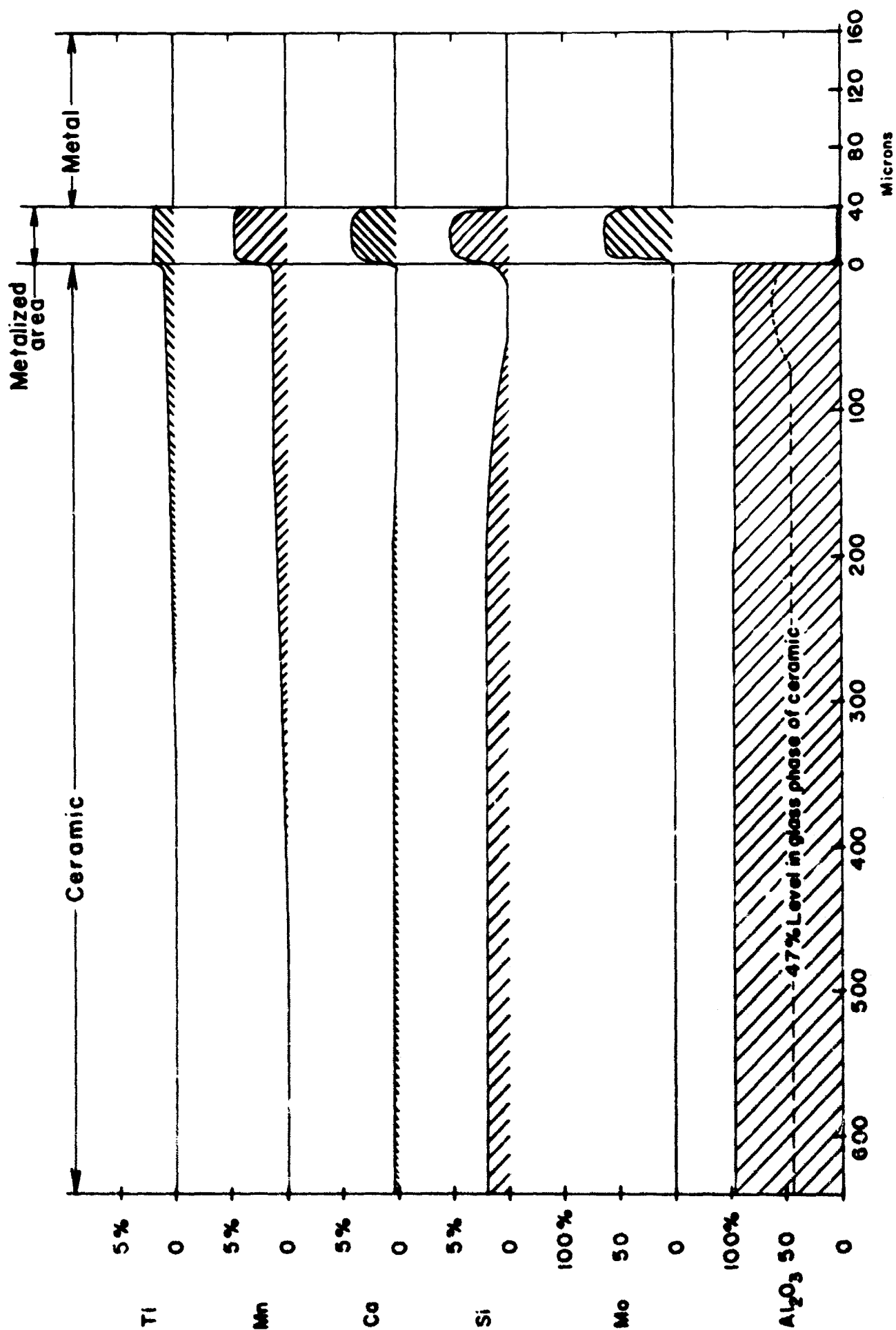


analysis trace for silicon, across entire seal region giving evidence of

ence







Interpreted Probe Analysis, Part A,  
of Sample A-3 (Body A, P-1 metalizing)

Figure 4.54: Interpreted electron probe microanalysis trace averaged over four scans of P-1 metalizing on Body A.

phase, diminishes at about 600 microns, and the titanium, at about 450 microns.

The molybdenum remains within the 45 micron seal, and shows a rather uniform distribution. None of the metallizing elements show a detectable diffusion into the metal braze.

The copper analyses indicate that copper penetrates the molybdenum for about six microns. However, this distance is exaggerated by the irregular interface and the limited resolution of the probe. Nickel from the cupro-nickel sealing washer has diffused into the copper braze, giving a residual concentration gradient.

Silicon has a distribution curve similar to titanium. However, since silicon originates from the intergranular glassy phase of the ceramic, a deficiency of silicon in the 150 micron area of the ceramic adjacent to the seal is apparent.

A more detailed study was made of the glassy phase migration and the resulting silicon deficiency. Fig. 4.53 shows such a trace for silicon across the entire seal region. It is obvious that a considerable amount of silica (as the major component of the glassy phase) has flowed from near the ceramic surface into the metallizing sponge. Silicon peaks further out in the body of the ceramic indicate glassy phase regions.

The calcium distribution curve (Fig. 4.52) also suggests this same deficiency. The calcium curve indicates a possible association with molybdenum in the seal area. In a second trace, the calcium curve showed an inverse relationship to silicon, aluminum, and titanium in some parts of the seal. The existence of a calcium molybdate complex is tentatively suggested by this data and gains some support from the molybdenum solution studies discussed earlier. Other possibilities exist.

Aluminum exists within the seal and appears to be associated with silicon. Quantitative analyses of several points along the seal gave an average value of 3-3/4 %  $\text{Al}_2\text{O}_3$  within the central part of the seal.

The apparent irregularity in concentration gradient is explainable in terms of the phase that the probe is traversing, whether alumina or "glass". A quantitative estimate of the concentration gradients existing is presented

Interpreted Probe Analysis, Part B,  
of Sample A-3 (Body A, P-1 metalizing)

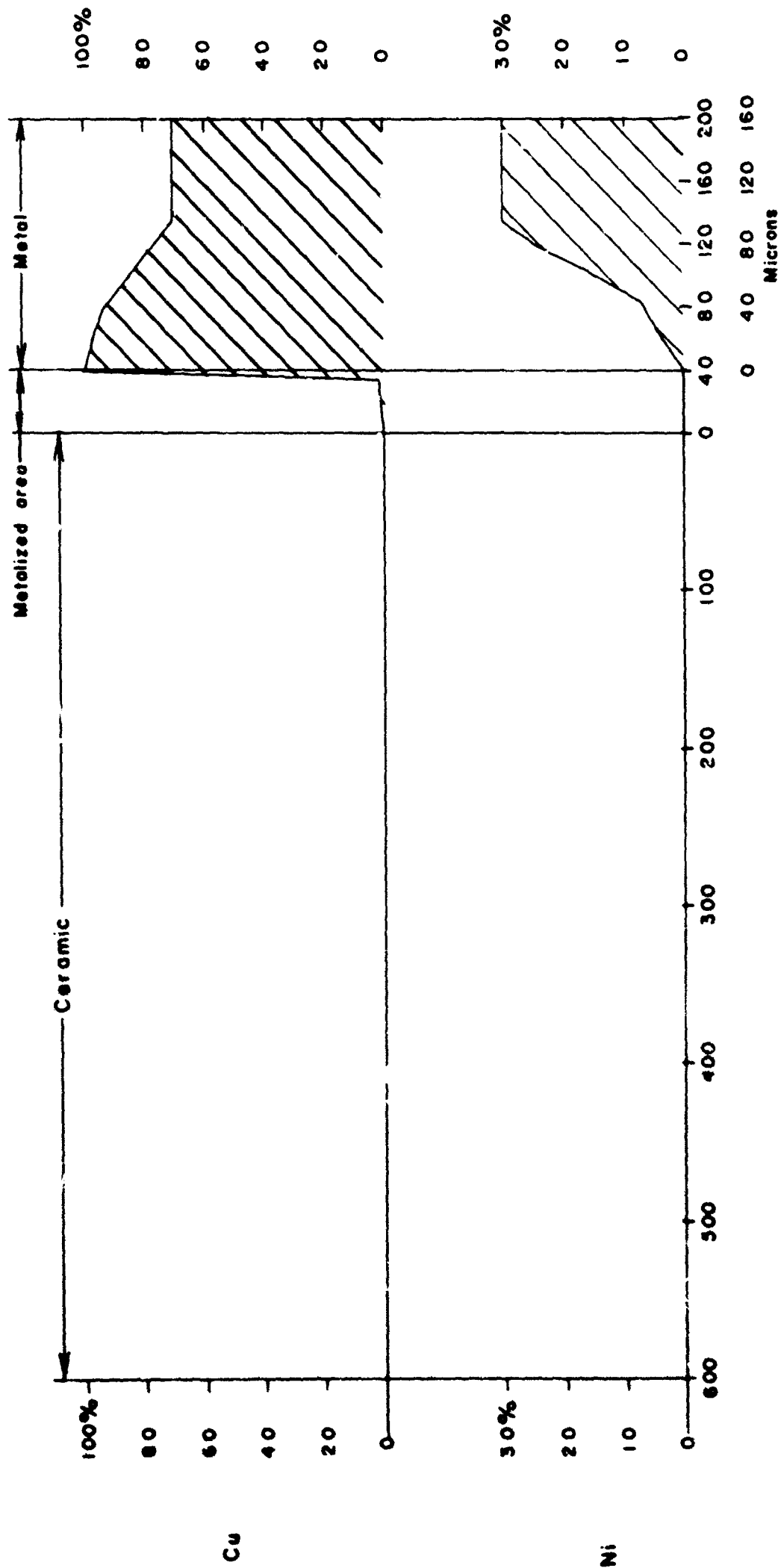


Figure 4.55: Interpreted electron probe microanalysis trace averaged over four scans of P-1 metalizing on Body A. Continuation of Figure 4.54.



to 1% at the molybdenum ceramic interface. The copper varies from 70% in the cupro-nickel, to 85% at the molybdenum-braze interface, to 65% at the molybdenum-ceramic interface.

#### 4.4.9 Composition of the Glassy Phase

The crystal structure of the "glassy" phase of P-1 and P-2 metallizings was investigated by X-ray diffraction (X-R-D) and spectrographic techniques. Metallized 1" diameter ceramic discs of Body A were acid leached according to the following schedule.

<u>Sample No.</u>	<u>Metallizing Heat Treatment</u>
1	P-2 metallizing on Body A ceramic
2	P-1 metallizing on Body A ceramic
3	P-2 metallizing on Body A, reheated to 1100°C in dry furnace (-80°F)
4	P-1 metallizing on Body A, reheated to 1100°C in dry furnace (-80°F)
5	pure molybdenum strip (control).

These samples were treated in the following manner:

- A) as processed - X-R-D on surface
- B) leached with 100 ml of nitric acid for 1 hour
  - 1. liquor decanted - 5 ml. spectrographed
  - 2. sample dried; X-R-D on fragile surface
- C) as for b, base material removed with wet swab
  - 1. swab material - spectrographed
  - 2. sample dried; X-R-D on surface
- D) leached with 60 ml of 50/50 HF and HNO<sub>3</sub> for 15 minutes
  - 1. liquor decanted and 5 ml spectrographed
  - 2. base material swabbed from surface and swab material spectrographed
- E) sample leached with 20% HCl for 15 minutes
  - 1. liquor decanted and 5 ml spectrographed
  - 2. sample dried - X-R-D on surface.

The appearance of the surface after each treatment is given in Table 4-27. The X-R-D results are presented in Table 4-28, and the relative amounts of CaO.2SiO<sub>2</sub>.Al<sub>2</sub>O<sub>3</sub> (anorthite) as determined from peak heights is presented in Table 4-29.

TABLE 4-27

Surface Appearance of Metallized Surfaces  
after Acid Leaching Treatments

Treatment	1 (P-2).	2 (P-1)	3 P-2	4 P-1	5 Mo
Nitric acid	dark brown*	brown	light brown	black	black
Swabbed loose material removed	grey with brown flecks	brown	grey with brown flecks	black	--
HF/HNO <sub>3</sub>	off white	green-grey	white-grey	charcoal-grey	--

\*Took longest to react.

TABLE 4-28

## Summary of X-Ray Diffraction Analysis

Sample	Treatment			
	A	B-2	C-2	E-3
1	Mo	$\gamma$ -Al <sub>2</sub> O <sub>3</sub> Mo CaO.2SiO <sub>2</sub> .Al <sub>2</sub> O <sub>3</sub>	$\gamma$ -Al <sub>2</sub> O <sub>3</sub> Mo --	$\gamma$ -Al <sub>2</sub> O <sub>3</sub> -- --
2	Mo	$\gamma$ -Al <sub>2</sub> O <sub>3</sub> Mo FeO.Al <sub>2</sub> O <sub>3</sub> *	$\gamma$ -Al <sub>2</sub> O <sub>3</sub> Mo FeO.Al <sub>2</sub> O <sub>3</sub> *	$\gamma$ -Al <sub>2</sub> O <sub>3</sub> Mo FeO.Al <sub>2</sub> O <sub>3</sub> *
3	Mo <sub>2</sub> C Mo	$\gamma$ -Al <sub>2</sub> O <sub>3</sub> Mo CaO.2SiO <sub>2</sub> .Al <sub>2</sub> O <sub>3</sub>	$\gamma$ -Al <sub>2</sub> O <sub>3</sub> Mo CaO.2SiO <sub>2</sub> Al <sub>2</sub> O <sub>3</sub>	-Al <sub>2</sub> O <sub>3</sub> Anorthite
4	Mo <sub>2</sub> C Mo	$\gamma$ -Al <sub>2</sub> O <sub>3</sub> Mo FeO.Al <sub>2</sub> O <sub>3</sub> * CaO.2SiO <sub>2</sub> .Al <sub>2</sub> O <sub>3</sub>	$\gamma$ -Al <sub>2</sub> O <sub>3</sub> Mo FeO.Al <sub>2</sub> O <sub>3</sub> * CaO.2SiO <sub>2</sub> .Al <sub>2</sub> O <sub>3</sub>	$\gamma$ -Al <sub>2</sub> O <sub>3</sub> FeO.Al <sub>2</sub> O <sub>3</sub> CaO.2SiO <sub>2</sub> Al <sub>2</sub> O <sub>3</sub> Mo (trace)
5		Mo, orientated		

\*Identified later as spinel phase with only a trace of iron.

TABLE 4-29

Relative Amounts of Anorthite Present in Metallizing  
Layer (Peak Height) and  
Occurrence of Anorthite Main Peak

Sample	Treatment			
	A	B-2	C-2	E-3
1	--	3.215 (8)	--	--
2	--	--	--	--
3	--	3.205 (22)	3.20 (10)	3.20 (3)
4	--	3.205 (20)	3.20 (10)	3.20 (2)

The appearance of  $\text{FeO} \cdot \text{Al}_2\text{O}_3$  (hercynite) phase in a system, where the only iron present was a trace (0.15%) in the ceramic was doubted. The migration rate of iron from the glass phase of the ceramic would have had to be very great. Spectrographic analysis, Table 4-3, of sample 2-2B and a blank ceramic confirmed the doubt. Also X-ray fluorescence showed no iron on the surface of the sample. The possibility therefore arose that the phase was a modified  $\text{MnO} \cdot \text{Al}_2\text{O}_3$  spinel with traces of iron in the lattice. To test this thesis a paint consisting of  $\text{MnO} \cdot \text{SiO}_2$  was made up in eutectic portions (P-8g) and a blob placed on a sapphire disc. The eutectic melts at  $1250^\circ\text{C}$ .

The experiment was performed at  $1425^\circ\text{C}$  in  $\text{H}_2/3\text{N}_2$  +  $100^\circ\text{F}$  dewpoint. The time at temperature was 1/2 hour. The melt on cooling consisted of light brown crystals and a manganese alumino-silicate glass on the sapphire substrate. The crystals and glass were subjected to X-R-D analysis. A pattern identical with the hercynite pattern was again found. The iron content of the sample was less than 0.1%. The indications are that, under the metallizing furnace conditions the usual pattern of  $\text{MnO} \cdot \text{Al}_2\text{O}_3$  spinel (galaxite) is modified to give a pattern very close to hercynite. The crystal structure analysis was not pursued further. The formation of a molybdenum carbide during the dry atmosphere furnace run is also of interest.

TABLE 4-30

Spectrographic Analysis of Leached Metallized Surface  
 Indicating the Strongest  $\text{FeO} \cdot \text{Al}_2\text{O}_3$  Concentration 2-2B

	2-2B Dark Surface		Blank White Surface
Aluminum	46. %	Aluminum	50. %
Silicon	2.4	Silicon	1.3
Calcium	0.18	Calcium	0.12
Magnesium	1.1	Magnesium	0.95
Titanium	1.1	Titanium	0.0086
Zirconium	0.44	Zirconium	0.17
Manganese	0.81	Manganese	0.0078
Molybdenum	1.4	Molybdenum	Not detected*
Boron	0.021	Boron	0.035
Iron	0.028	Iron	0.046
Copper	0.0041	Copper	Not detected**
Other elements	nil	Gallium	0.013
		Zinc	0.024
		Nickel	0.0012
		Chromium	0.00032
		Other elements	nil

\*less than 0.002

\*\*less than 0.00003

TABLE 4-31

Spectrographic Analysis Data on Leachates and Swabs  
from Acid Leached Metallizings P-1 and P-2  
on Body A

Sample	Treatment	Al	Si	Mg	Ca	Fe	Zr	Mo	Mn	Ti
1	B-1	.005	.02	.002	T	.006	--	.4	.001	--
2	(see section 4.4.9)	.01	.02	.003	.005	.006	--	.4	.02	--
3		.008	.02	.002	.006	.01	--	.6	.001	--
4		T	.02	T	--	.007	--	.5	.002	--
5		.002	.01	.001	--	T	--	4.0	.001	--
1	C-1	.004	.01	T	T	--	.01	.04	--	--
2		.05	.02	.02	.25	.008	.02	.5	.04	.02
3		.05	.02	.02	.02	.001	.01	.05	--	--
4		.02	.1	.001	.005	--	.006	.006	.006	.004
5		.005	.01	.02	.005	.004	--	2.0	T	--
1	D-1	P.C.	T	.15	.3	.4	.8	.2	.008	.2
2		P.C.	T	.3	.5	.5	1.5	1.0	.05	.5
3		P.C.	T	.05	.15	.5	2.0	.04	.008	.4
4		P.C.	.08	.6	1.0	1.0	1.5	2.0	.3	1.0
1	D-2	.002	.001	.007	.002	.005		.004	--	
2		.003	.002	.008	.003	.005	--	--	.004	--
3		.005	.002	.02	.04	.004	--	.004	--	--
4		.005	.003	.008	.003	.01	--	.004	.003	--
Blank on swab		.002	T	.02	.007	.006	--	--	--	--
1	E-1	.2	.02	.2	.3	.05	.01	.4	.002	.002
2		.2	.02	.2	.3	.03	.01	.003	.2	.01
3		.2	.1	.2	.4	.06		.008	.001	--
4		.2	.02	.2	.5	.02	.008	.04	.02	.002

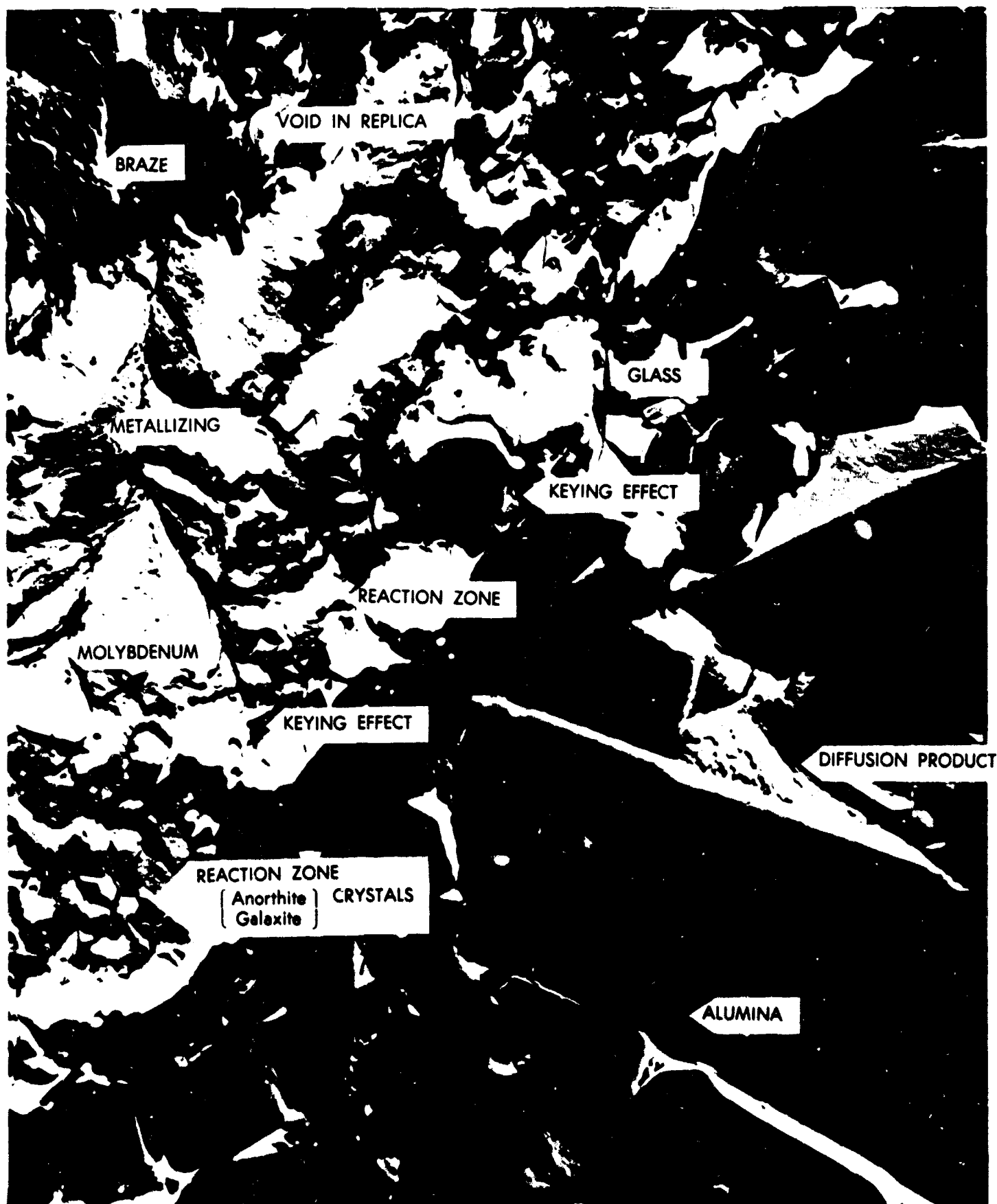


Figure 4.56: Electron photomicrograph of metallizing P-1 on Body A (nicoro braze) metallized at 1425°C for 1/2 hour. (8000X)

The main spectrographic analysis data is present in Table 4-31. Use can be made of this data in assisting in the determination of the placement of ions in the crystal species.

The P-1 data is in error somewhat as a transfer to a glass beaker took place during the processing. The HF solution originally in a polyethylene beaker was evaporated to dryness in a platinum dish. It was reconstituted in a glass beaker to 100 cc with water. A boron, barium, sodium and vanadium (trace) content was noted in the spectrograph analysis.

In an attempt to visually isolate the crystal phases in the ceramic to metal seal, low power electron microscope scans (X8,000) were made of P-1 metallizing on Body A. A typical cross-section is shown in Fig. 4.56. Significantly new details over those revealed by the metallurgical microscope are shown. A definite keying of the corroded alumina crystals into the metallized layer is again noted with a "glassy phase" tightly adhering to the alumina interface. Sub-micron sized anorthite and galaxite can also be seen in the interfacial layer. A crystalline diffusion product can be seen in the alumina grain boundaries.

Note: We can now see how all the tools and experiments performed in this section 4.4 thus far can combine to give the reader a good picture of the "make-up" of the metallizing layer. With this picture in mind one can now turn to experiments designed to correlate the properties thus far discussed with the vacuum tightness, strength and reliability of ceramic-to-metal seals.

#### 4.4.10 Seal Strength Versus Metallizing Temperature

The P-1 paint was painted onto Body A CLM-15 tensile test pieces and sinter fired at various temperatures. The tensile test results are shown in Fig. 4.57. A bell shaped curve was obtained, all samples being vacuum tight with the exception of some of the 1100°C fired series. The 1100°C firing temperature was repeated with -

- 1) P-1 paint ball milled in an alumina mill using steel balls, for 50 and 100 hours.
- 2) P-1 paint ball milled in a steel mill using steel balls for similar times.



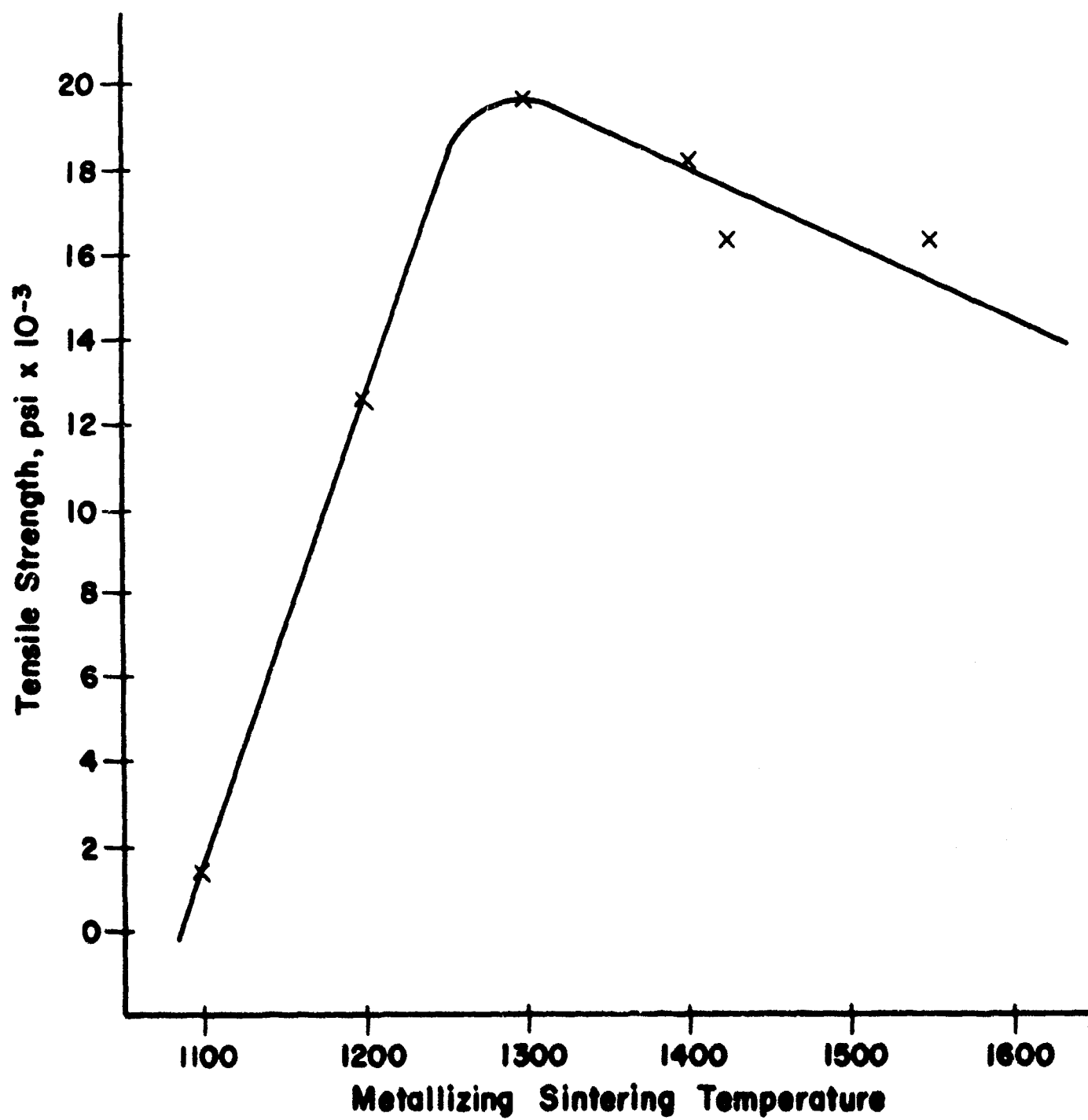


Figure 4.57: Seal tensile strength with P-1 metallizing on Body A versus metallizing sintering temperature.

In all cases, the metallizing was soft and vacuum tight brazes were not obtained. The addition of 1% copper oxide did not consistently produce hard metallizings or vacuum tight brazes even when iron was introduced into the paint via the steel balls; results contrary to expectations occurred. Further work in this area is indicated in order to resolve the inconsistency.

The effect of Cu-Fe on aiding sintering has been previously discussed. (Third Quarterly Report, pp. 62-66.)

Evidently in the simple P-1 system, 1200°C is required to give sufficient mobility to the glass phase to allow adequate adhesion to the molybdenum phase via either a chemical or semi-conducting bonding mechanism.

#### 4.4.11 Seal Strength as a Function of Brazing Conditions

The effects of different brazing cycles, brazing temperatures and furnace atmospheres on the strength of the P-1 and P-2 metallizing was also investigated. The tensile results are shown in Table 4-32.

In addition peel test samples were run on Body A with P-1 and P-2 metallizings following a modified procedure outlined by Cole<sup>33</sup>. The circular band of the CLM-15 test pieces were metallized with a roller gun technique to give a fired thickness of one mil, and bonded to nickel plated 15 mil Kovar. Runs were made in the retort under wet and dry conditions with copper braze (1100°C) and also under wet conditions with Cu-Ag eutectic braze (810°C). The results are shown in Table 4-33. The "pull" in pounds is recorded continuously on a recorder attached to an Instron\* tensile tester. Thus the average plus the maximum and minimum "pulls" can be readily determined.

These results of Table 4-32 indicated that a "glassy layer" devitrification process due to furnace cycle and atmosphere variables may be responsible for the strength of the seal in the case of P-2 paint as P-1 is not affected by such changes. The results of Table 4-33 indicate different stress levels in the seal due to different brazing temperatures and cooling rates are responsible for variable seal strength.

---

\*Instron Engineering Corp., Canton, Mass.

TABLE 4-32

Tensile Test Results PSI on Body A Metal-Ceramic Seals\*  
 Brazed with Copper,  
 under Various Furnace Conditions

Paint	Metal Member	WL**	WR**	DR**
P-1	70/30,Cu/Ni	11,820	--	11,460
P-2	70/30,Cu/Ni	8,460	--	13,740
P-2	--	8,518	9,698	10,085
P-2	--	--	--	10,950
P-2	--	--	--	10,170

---

\*Average of five, all vacuum tight.

\*\*WL is wet tunnel furnace +60°F quick heat and cool.

WR is a wet retort furnace +60°F with a slow heat and cool.

DR is a dry retort furnace -80°F with a slow heat and cool.

---

TABLE 4-33

Peel Test Results (Pounds) on Body A  
Metal-Ceramic Seals\*

Paint	Braze	Plate	WR**	DR***
P-1	Copper	Copper	2	4
P-2	Copper	Copper	2	4
P-1	Cu-Ag	Nickel	18	--
P-2	Cu-Ag	Nickel	16	--

\*Average of 5

\*\*Wet retort furnace (+60°F dewpoint)

\*\*\*Dry retort furnace (-80°F dewpoint)

#### 4.4.12 Initial Metallizing Tests

Two series of metallizing experiments were run using the paints listed in Table 4-22 in order to "prove out" the correct manufacture of the paints, i.e., no cracks or blisters after drying and metallizing, and to see if the predictions made for the behavior of these paints would be verified in practice. Compositions of ceramics appear in Table 4-1.

In the first series of experiments, the main purpose was to obtain a qualitative relationship for the strength of bonds to be expected between the three principal refractory metals (Mo, W, Re) metallized onto three grades of alumina (94%, 97% and 99%  $\text{Al}_2\text{O}_3$ ). All the seals were vacuum-tight.

P-2 paint was sintered on Body A (94% alumina) and Body E (99% alumina) at  $1550^\circ\text{C}$  and  $1425^\circ\text{C}$ . P-4 metallizing paint (pure molybdenum) was also sintered on at  $1425^\circ\text{C}$ . The tensile test pieces were copper brazed in a retort furnace using wet hydrogen at  $1100^\circ\text{C}$ .

In addition, since Body C (97% alumina) was investigated extensively in Appendix A (Second Quarterly Report), P-2 was also metallized on it at  $1425^\circ\text{C}$ .

Two other special paints, P-11 ( $\text{WO}_3$ ) and P-12 (Re) were investigated in a preliminary fashion on Body A and Body C. These results are also given in Table 4-34.

The microstructure of P-2 metallizing on the 99% alumina ceramic body E, Fig. 4.58, shows the same open structure as P-2 on Body A, noted earlier in Fig. 4.49. The lower metallizing tensile strength on Body E as compared to Body A reflects the difference in their glass phase content at the interface, causing a variable "flypaper effect". No visible migration of glass phase into the metallizing is observed for P-2 on Body E.

The higher firing temperature of P-2 on Body A gives a higher strength because of glass flow out from this ceramic which increases the area of interfacial bonding. No such effect is noted for the 99% alumina body, indicating that the small amount of glass phase from the body and impurities in the metallizing paint makes a constant but minor contribution to total seal strength in this case (over the temperature range studied).

TABLE 4-34

Tensile Strength Results for Pure Refractory Metal  
and Metal-Oxide Paints on 94%, 97%, and 99% Alumina Ceramics  
Copper Braze - No Washer

Paint	Body	1425°C	1550°C
P-2	Body A	10,000	15,500 <sup>+</sup> (min.)
	Body E	6,000	6,000
	Body C	10,000*	---
P-4	Body A	6,500	---
	Body E	1,000	---
P-11	Body A	10,000	---
P-12	Body A	8,500	---
	Body C	9,300	---

Body A      94% Al<sub>2</sub>O<sub>3</sub>

Body C      97% Al<sub>2</sub>O<sub>3</sub>

Body E      99% Al<sub>2</sub>O<sub>3</sub>

\* Peel test value was 25 pounds with Cu-Ag braze, Ni plate,  
15 mil Kovar.

+Neck brakes.

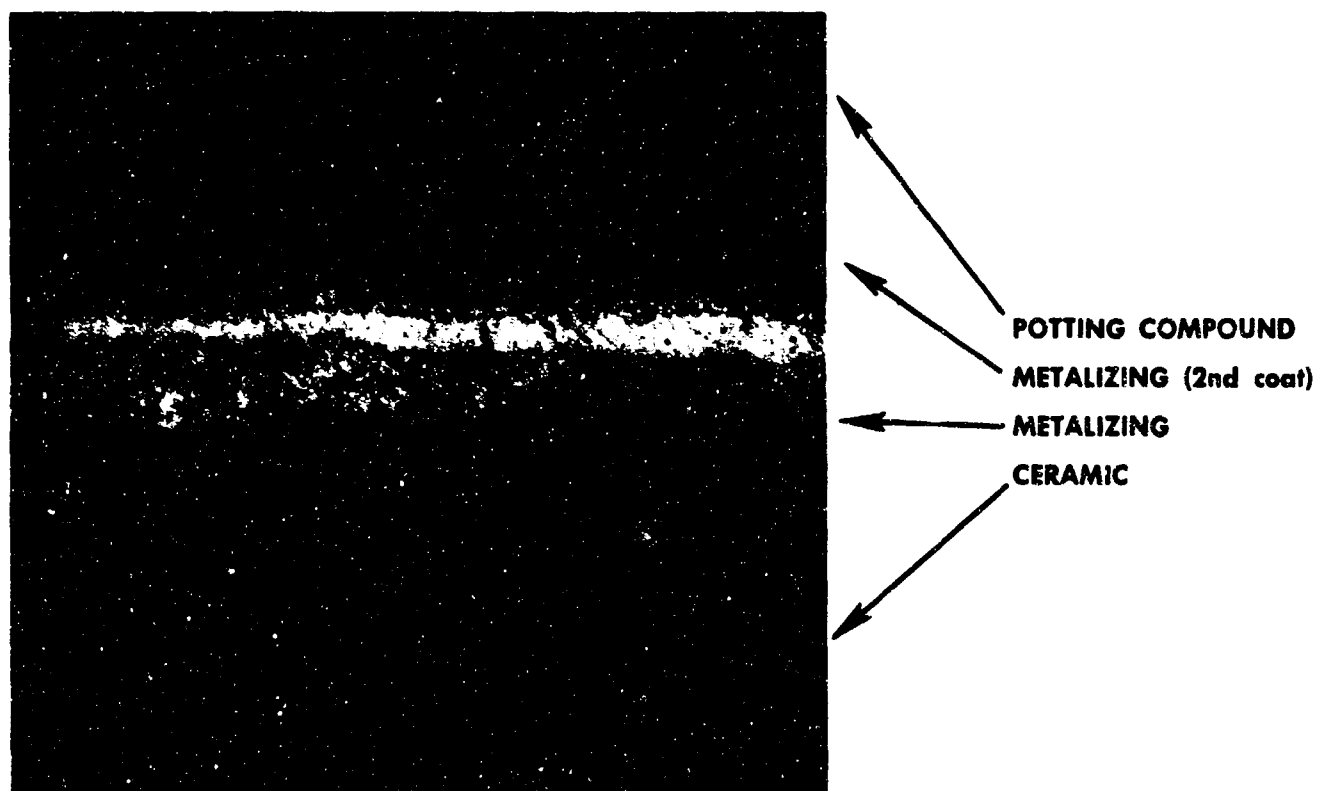


Figure 4.58: P-2 metallizing on Body E, 99% alumina. Metallized at 1425°C for ½ hour.

The lower strength of P-4 metallizing on Body A and Body E in comparison with P-2 metallizing is due to the substitution of the coarse grained molybdenum particles for the  $\text{MoO}_3$ . The possibility of chemical or mechanical reaction of the  $\text{MoO}_3$  with the alumina phase via the vapor or liquid phase is present.

Further, considering the data for P-2 and P-4, it is probable that the major adhesion mechanism on Body E with molybdenum oxide metallizing is due to the chemical and/or physical reaction between  $\text{Al}_2\text{O}_3$  which occurs some time in the firing cycle.

The low strengths obtained with P-2 and P-4 on Body E indicate that multi-component metallizing paints such as P-7 to P-10 are required to develop a high strength seal on +99% alumina ceramics.

The strength of the bond of P-2 metallizing on Body C, a 97.5% alumina ceramic, is accounted for by the fact that much greater flow out of the glass phase of the ceramic occurs than for Body A at the same metallizing temperature,  $1425^\circ\text{C}$ . This is due to the lower viscosity of the 1/1 over the 1/2 alkaline earth/silica flux composition of Body C over Body A. This factor more than compensates for the fact that there is only a third as much "glassy phase" present in Body C as in Body A. Also the thermal expansion of the glass phase is a closer match to molybdenum, Fig. 4.27.

The fact that  $\text{WO}_3$  and Re, as well as Mo and  $\text{MoO}_3$  provided good bonds to Body A in spite of (1) the low self sintering capability of these metal powders at  $1425^\circ\text{C}$  and (2) the small amount of glass phase flow out from the ceramic, indicates that adherence of isolated particles of these refractory metals to the glassy phase initially present on the surface of the ceramic ("the flypaper effect") is an important phenomena in ceramic metallizing adherence. The data are insufficient in quantity and variety to detail the effect of the variation in expansion coefficients of the refractory metals on the strength of the bond ( $W = 4.3 \times 10^{-6}$  in/in/ $^\circ\text{C}$ , Mo =  $5.5 \times 10^{-6}$  in/in, Re =  $6.5 \times 10^{-6}$  in/in/ $^\circ\text{C}$ ). Considering the type of layer formed in this case, the strength of the bond should not be affected to a major degree by the small differences in expansion coefficients noted above, since all are below the coefficient for alumina, i.e. the interfacial cermet layer is in compression, a favorable situation: the Rhenium metal paint is, however, nearer



the alumina expansion coefficient which means that the composite layer, the glass-metal layer, while still in compression will be a better match than the molybdenum glass layer; further the 1:1 glass of Body C does give an additional small increase in strength due to the better match as noted above.

The paints listed in Table 4-22 plus the two additional paints\* were painted onto Bodies A, 94%  $\text{Al}_2\text{O}_3$ , and H, 99.5%  $\text{Al}_2\text{O}_3$ . Two firing temperatures were employed, 1425°C and 1550°C. The usual atmosphere of 75% nitrogen, 25% hydrogen and a dewpoint of 100°F were used. The sintering time was 1/2 hour at temperature. The tensile test results of these paints on both bodies following a copper braze with a 20 mil 70-30 cupro-nickel sealing ring, are shown in Table 4-35.

It is not the intention to engage in a detailed evaluation of the results contained in Table 4-35, as the systems are too complex to permit very meaningful analysis. However, a brief discussion is in order. To reiterate, the main reason for running these tests was to obtain a preliminary idea of the behavior of these metallizing paints before committing them to the limited number of tensile test pieces of the special bodies that were available. Therefore, a limited sample size of only two test pieces was used in each test.

#### P-1 Metallizing Paint

The strength of this metallizing paint on the 94% ceramic is apparently little affected by temperature, indicating a wide sintering range for this metallizing as has been noted earlier. Taking these results in conjunction with the results for the 99.5% alumina, one can see that the manganese oxide and titanium dioxide react more with the alumina and "glassy" phase at higher temperatures and provide a superior bond for the 99.5% alumina at the higher temperature.

#### P-2 Metallizing Paint

The glassy phase from the 94% alumina body flows out into the molybdenum sponge at 1425°C and even more at

---

\*P-2M is a molybdenum oxide paint made in a high alumina ball mill using molybdenum balls. Analysis of this paint shows virtually no ball mill oxide contamination. To remove the last traces of contamination, a paint P-2MR was formulated using a rubber-lined ball mill and molybdenum balls.

TABLE 4-35

Tensile Test Data of the Special Paints on Body A  
(94% Alumina) and Body H (99.5% Alumina)  
Using a Copper Braze and 20 mil, 70-30  
Cupro-Nickel Metal Washer

Paint	Body A		Body H	
	1425°C	1550°C	1425°C	1550°C
P-1	15,900	15,525	9,150	12,775
P-2	15,575	17,250	3,180	2,120
P-2M	9,100	5,210	3,300	2,710
P-2MR	7,520	20,100	4,520	6,170
P-4	3,315	7,100	1,142*	938
P-5	957	13,700	1,540	1,939
P-6	17,500	11,720	975*	1,300
P-7	2,265	5,700	2,375	7,100
P-8	16,400	15,175	15,425	14,275
P-9	6,125	15,775	13,525	12,325
P-10	11,600	11,300	5,140*	8,160
P-11	11,450	16,100	4,260	10,500
P-12	1,700 <sup>+</sup>	--	1,965	2,830

<sup>+</sup>Cupro-Nickel braze attacked rhenium.

\*One leaker.

1550°C to give a high-strength bond. However, the use of the P-2M and P-2MR paint significantly lowers these tensile strength results at the 1425°C level, indicating that the impurities in P-2 are partially responsible for the high metallizing strength recorded. It is apparent from a comparison of the tensile strength data on the 99.5% alumina ceramic with that of the 94% alumina ceramic that the flow out of the glassy phase of the ceramic is the most important factor contributing to bonding strength.

### P-3 Metallizing Paint

No data have been obtained using this paint on alumina ceramics. Data obtained using BeO ceramics are reported later.

### Metallizing Paints P-4, P-5 and P-6\*

These three paints are considered together as they are all molybdenum metal paints. Consider the 94% ceramic first. The paints used all give a general increase in strength with metallizing temperature. This is expected because the molybdenum sinters better at higher temperatures and a glass phase flows out of the ceramic more readily at higher temperatures. Another interesting observation is that there is a general trend for the metallizing strength to increase as the particle size of the molybdenum decreases. This factor is complicated in the case of P-6 by minor impurities of nickel, iron, and chromium present in the molybdenum metal. These impurities are generally considered to aid sintering.

Surveying the situation with the 99.5% alumina, one sees very low metallizing strengths, indicating that flow-out of glass phase from the ceramic is not occurring. The slightly higher strengths recorded for the P-2 paints under these conditions are possibly due to the tendency of the molybdenum trioxide to volatilize and deposit a reduced layer of strongly adherent molybdenum on the surface of the alumina grains.

---

*P-4	Mo metal	-325 mesh Fansteel
P-5	Mo metal	-325 mesh 70% less than 10 microns, 5 micron average, G.E.
P-6	Mo metal	70% less than 5 microns, 1.65 micron avg., Sylvania.

#### P-7 Metallizing Paint

This metallizing paint is of interest to us because of the low dielectric loss characteristics displayed by it. The tensile strengths in all cases are rather low. This was expected, because it was observed during the manufacture of the glass that the glass shrank away from the molybdenum crucible, indicating that the glass had a very much higher thermal coefficient of expansion than the molybdenum itself. This would be deleterious in a metallizing paint oxide phase. It is, however, noted that the strength of the paints increases with temperature, due presumably, to an increase in alumina content in the paint, which in turn will reduce the thermal expansion of the glassy phase of the paint.

#### P-8 Metallizing Paint

This paint shows consistently high strengths on both ceramics at both temperatures. It was noted in the manufacture of the manganese silicate glass that it adhered very strongly to the walls of the molybdenum crucible on cooling. The crucible had to be destroyed in order to remove the glass.

#### Metallizing Paints P-9 and P-10

These paints are useful in the study of complex paints on the special bodies that we are considering because they enable the system being studied to remain a three-component metal oxide system. One leaker is reported in this system, but it may be due to a bad braze. The metallizing strengths are not exceptionally high on the present ceramics, but since the main objective of this project was to obtain insight into mechanisms rather than high bond strengths, this variation in strengths is to be welcomed rather than regretted.

#### Metallizing Paints P-11 and P-12

The relatively high strengths of the P-11 metallizing paint are unexpected, because tungsten might not be expected to sinter as well as molybdenum at these temperatures. This indicates that another factor, previously alluded to, is at work in this case. This factor, for want of a better name, we call the "flypaper effect". Obviously, tungsten is able to take better advantage of this effect than is molybdenum, because of the lower coefficient of expansion of tungsten in comparison to molybdenum. The fine

particle size of the decomposed tungsten oxide applies to advantage here, because small particles can cling to isolated patches of glass phase very readily.

P-12 shows the same characteristics as P-4 as might be expected from a metal paint. However, a high strength result was obtained when no cupro-nickel washer was used (Table 4-34). The lower strength obtained in Table 4-35 may be due to attack of the Rhenium by the nickel absorbed in the braze from the cupro-nickel brazing washer. Unfortunately, the results for the 1550°C temperature are not available. It will be expected that a significant increase in strength would occur in this case because of glass flow out and consolidation of the metal phase.

Following the above line of reasoning further, we can see that except where we have a paint which is consolidated by a glass phase flow out, we have a degradation of the seal in the second series of experiments due to either

- 1) attack of the metallizing by the nickel in solution  
or
- 2) stresses induced by the cupro-nickel washer.

The first factor is considered the most potent.

#### 4.4.13 Comments on Sealing Mechanisms

Evidence accumulated thus far shows several mechanisms of material movement that can lead to adherence, it being understood that the actual bond, whether chemical, mechanical or semi-conducting, cannot be affected until the metal and oxide phases are brought into near atomic contact. In practice several of these movements may occur in one system. These movements are -

- 1) "Glassy Phase" flow out from the ceramic
- 2) Metallizing melt phase wetting of the metal and ceramic
- 3) The "flypaper" sticking of the metal phase to the highly viscous phase on the surface of the ceramic. Photomicrographs of the surface of ground ceramics shows the presence of this glass phase.

- 4) Melting and/or vaporization of  $\text{MoO}_3$  or  $\text{WO}_3$  onto the surface of the ceramic and its subsequent reduction to the metal, leaving a large area transition oxide chemical bond at the interface.
- 5) Solid state reaction between the refractory metal and the ceramic giving again a point-to-point Mo-Mo-O-Al-O-Al chemical bond.

Some pertinent results of a parallel company sponsored program<sup>34</sup> may be mentioned at this point to supply further evidence of the existence of mechanism 4 and 5. Molybdenum was evaporated onto a ceramic surface and found to give vacuum tight seals of strengths approaching 20,000 psi. It is considered that the mobile molybdenum atoms are able to accommodate themselves intimately to the contours of the alumina surface which results in enough atomic interaction to form a strong bond, Fig. 4.59. It is probable that a transition Mo - Mo-O-Al-O layer exists at the interface.

Since mechanism 4 approximates the evaporation process, a vacuum tight seal may be expected to be obtained, whereas the solid-solid widely dispersed point contact of mechanism 5 could not be expected to give a useful bond.

The next section gives a more detailed study of these effects.

#### 4.5 Studies Using the Special Bodies

##### 4.5.1 Introduction of Seal Parameter Study

The series of alumina ceramics used covered a range of glass phase contents from about 20 volume percent to zero percent. The purpose of such a selection was to observe, among other things, the role which the glass phase plays in the sealing mechanism and to study the influence of such variables as the metallizing temperature.

Sapphire is the simplest ceramic that can be studied. On this program it was metallized with the single component paints, P-2M and P-4M as well as the more complex paints P-1 and P-7.

The corrosion of sapphire by silicate melts has been discussed in earlier reports and has been reported elsewhere in the literature.<sup>14,15,16</sup> This work shows that

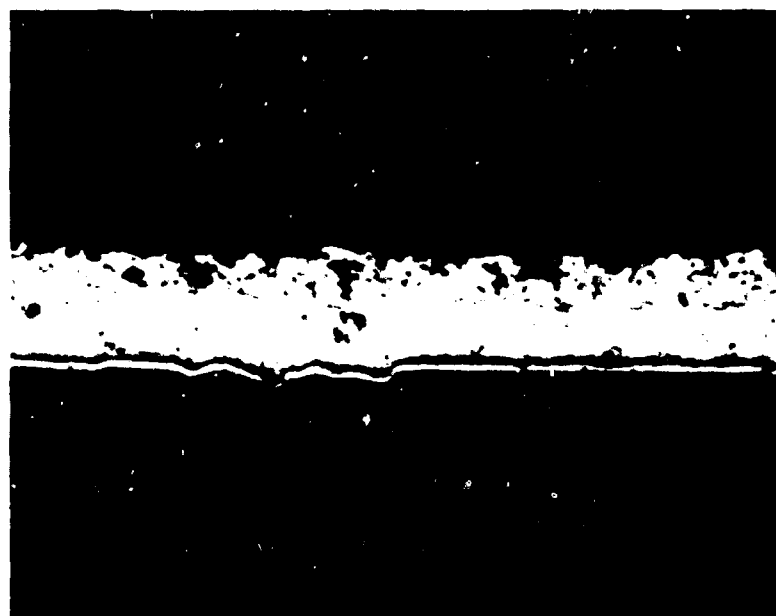


Figure 4.59: Top: Body H, 3 $\mu$  evaporated molybdenum metallizing, copper braze, P-1 metallizing, — Body A.  
Bottom: Body H, 1 $\mu$ . evaporated molybdenum metallizing copper braze 70/30 cupro-nickel metal member.

the solution of alumina is initially controlled by a chemical reaction at the interface which subsequently changes to a diffusion controlled reaction. Sapphire-melt couple work reported earlier in Section 4.2.3.2.6 of this report indicates that in narrow bi-facial zones such as the 2-10 micron "glassy" layer of metallizing the reaction remains chemically controlled indefinitely.

Contact angle studies of various melts on sapphire have been reported earlier in this report. It was shown that in both wet and dry hydrogen/nitrogen atmospheres that the wetting and adherence was good. The adherence of the silicate glasses to molybdenum substrates was also good; this result leads us to expect that a metallizing system composed of sapphire-silicate melt-molybdenum would give a good seal combination. Conversely, it has been shown earlier<sup>35</sup> that while the adherence of a MnO-TiO<sub>2</sub> melt on a sapphire plaque is good with a low contact angle, its adherence is poor on a molybdenum plaque; hence a combination sapphire-(MnO-TiO<sub>2</sub>)-molybdenum may not give a good seal combination.

Lucalox\* is the simplest polycrystalline ceramic that can be studied. It was obtained in three grain sizes to allow the effect of grain size in the absence of a glassy phase on the metallizing to be determined.

The remarks made above for sapphire will also hold for Lucalox\*.

The three bodies, 992, 942, and 941 will behave differently to sapphire as "glassy phase" flow out from the ceramic will occur. Thus the MnO-TiO<sub>2</sub> phase in P-1 metallizing will become a MnO-TiO-CaO-Al<sub>2</sub>O<sub>3</sub>-SiO<sub>2</sub> phase which can be expected to show good adherence (to sapphire and) to molybdenum and give a good seal combination.

Limits were set on the scope of this basic study in order to attain the other goals of the program, therefore, it was decided to devote the majority of the time to the study of a simple metallizing system, P-4M, while carrying out exploratory studies using the more complex paint systems listed in Table 4-22.

---

\*General Electric Co., Trade Name.



#### 4.5.2 Seal Parameter Studies

##### 4.5.2.1 Experimental Procedure and Results

##### 4.5.2.1.1 Sample Preparation

The first series of tests consisted of metallizing the five types of ceramics (941, 942, 992, Lucalox\* and sapphire) using P-4M paint at four different metallizing temperatures (1300°, 1425°, 1600°, and 1800°C) while keeping the metallizing paint composition, furnace atmosphere, and plate-braze-metal member assembly constant. The 941, 942, 992 and Lucalox\* bodies were differentiated further according to firing temperature and grain size, so that a total of 15 different bodies were studied. The variables under study with these bodies were the amount and composition (and resulting viscosity) of the glass phase and the alumina crystal size.

The tests used to evaluate the metallized specimens included (1) an electrical dc resistance test, (2) a scratch test following the sintering step to determine the quality of the metallizing, (3) leak check, tensile and peel tests to determine the mechanical properties of the seal, and (4) metallurgical examination of the seal to observe such processes as glass phase migration, sintering of the molybdenum metallizing, and braze-metallizing interaction. P-4M has a particle size extending from the 5 micron range down to the sub-micron range as shown in Fig. 4.43.

In order to avoid any contamination of the paint during processing, the mix was ground in a molybdenum lined ball mill using cylindrical molybdenum grinding media. The mill charge consisted of minus 325 mesh molybdenum metal, lacquer, and resin which were mixed in a 1:1 solid/liquid ratio by weight. This was ball milled for approximately 16 hours to get a #7 grind (6 to 12 micron maximum particle size range). Table 4-36 lists the results of spectrographic analyses of Fansteel\*\* molybdenum powder before milling and of P-4M paint after milling. The accuracy of the analyses is  $\pm$  a factor of 2, so it is apparent from the data that contamination by the ball mill was negligible within analytical limits.

---

\*General Electric Co., Trade Name.

\*\*Fansteel Metallurgical Corp., North Chicago, Illinois.

TABLE 4-36

## Spectrographic Analysis of P-4M Metallizing Paint

Element	Type 380 (Fansteel*) (Before Milling)	P-4M Paint (After Milling)
Mo	Principal constituent in both	
Si	0.1	0.15
Al	0.02	0.02
Ca	-	T
Mg	T	0.005
Mn	T	T
Fe	0.03	0.02
Co	T	0.001
Ni	0.01	0.006
Cu	0.003	0.005

Note: Values are  $\pm$  a factor of 2.

\*Fansteel Metallurgical Corp., North Chicago, Ill.

The silica trace in the molybdenum is regrettable, a purer molybdenum was not found until late in the program. The use of P-2M for experiments where an absence of silicon was critical circumvented possible mechanism confusion, however.

The metallizing paint was applied to the test specimens with a hand roller (striping tool). The paint thickness was monitored by weighing each piece before application, and after the paint was dried. The paint was dried under heat lamps at approximately 100°F.

The metallizing was sintered in a molybdenum-wound alumina tube furnace at the four temperatures mentioned above. The heating and cooling rates approximated a normal production furnace schedule and the soak time was one-half hour at peak temperature. The atmosphere was 75% nitrogen, 25% hydrogen, with a 100°F dewpoint.

#### 4.5.2.1.2 Scratch Test

In order to determine the relative hardness of the metallizing, the scratch test was performed. It consisted of scratching the sintered metallizing with a tungsten probe while observing the results under a 16X stereoscopic microscope. P-1 metallizing on Body A sintered at 1425°C was used as a standard. An arbitrary scale of 1 (soft) to 5 (hard) was employed. The standard was assigned a hardness of 5. The data are presented in Table 4-37.

Metallizing hardness increased with the sintering temperature. On some bodies, such as 941, hard metallizing was produced at lower temperatures than on other bodies. Metallizing sintered on Lucalox\* and sapphire at 1600°C was ranked as "soft" (2 and 1, respectively) to indicate poor adherence. The molybdenum particles were well sintered to each other, but the bond to Lucalox\* was weak, and to sapphire was almost non-existent. The metal layer was easily peeled off of the sapphire specimens. These results demonstrate the importance of atomic contact via the "glassy phase" of the ceramic in the development of the metallizing bond. Body 941 presumably contained a relatively large amount of melt with good mobility, while the Lucalox\* bodies contain no melt phase, (0.2% MgO, 99.8% Al<sub>2</sub>O<sub>3</sub>; first melt forms above 1900°C), and the sapphire, of course, is a single crystal.

\*General Electric Co., Trade Name.

TABLE 4-37

## Metallizing Scratch Hardness

Body Type	Ceramic Firing Temp. °C	Crystal Size, microns	Metallizing Temperature			
			1300°C	1425°C	1600°C	1800°C
941	1550	5.6	1	3	4	4
941	1600	8.4	1	3	4	4
941	1650	9.8	2	4	4	5
941	1700	10.4	3	5	5	5
942	1600	8.1	1	2	3	4
942	1650	10.3	1	2	3	4
942	1700	12.2	1	2	3	4
942	1750	22.1	1	2	4	5
992	1700	7.4	1	2	3	4
992	1750	25.0	1	2	3	5
992	1800	31.0	1	2	3	5
Lucalox*	unknown	5	n.d.	n.d.	2	3
Lucalox*	unknown	20	n.d.	n.d.	2	3
Lucalox*	unknown	40	n.d.	n.d.	2	4
Sapphire	single crystal		n.d.	n.d.	1 (flaked off)	1 (flaked off)

Scale: 1 (soft) to 5 (hard: P-1 on Body A @ 1425°C)

1. Soft, powdery, most particles removed without effort.
2. Soft. Some particles removed without effort.
3. Medium. Some particles removed with moderate effort.
4. Hard, metallic luster. Few particles removed.
5. Hard, metallic luster. No particles removed.

\*General Electric Co., Trade Name.

#### 4.5.2.1.3 Resistance Measurement

A very simple resistance measurement was made on each metallized body as an additional means of determining the degree of sintering or densification of the metallizing at each sintering temperature. The measurements were made on drum peel test samples on which the metallizing is applied to the large outer rim of the sample. A cut was made through the metallizing layer at one point, so the conductive path was around the entire circumference of the sample. Electrical contacts were made with copper probes on either side of the cut.

The measurements were made with a Wheatstone bridge and with a Simpson meter calibrated with 1.0 ohm and 0.1 ohm resistors. The accuracy of the measurements is limited by the quality of the contact made by the probes, so either instrument gave satisfactory results. All the reported data were obtained using the Simpson meter, but a portion was verified with the Wheatstone bridge to be sure of the accuracy of the results.

The resistance data are presented in Table 4-38. A brief examination of the table shows that the resistance decreases with higher metallizing sintering temperatures, as was expected. However, the data for metallizing sintered at 1300°C varies somewhat from one body to another. This variation may be linked to the action of the migrating melt phase of the ceramics. At this temperature, the melt may help pull the metal particles together, and thus be the predominant mechanism in consolidating the metallized layer. The variations at the low sintering temperature were probably related to the viscosity and amount of glass in each ceramic body. At the higher temperatures, the actual sintering of molybdenum particles becomes the predominant mechanism and proceeds at about the same rate on all bodies.

#### 4.5.2.1.4 Assembly Procedure

Tensile and peel test assemblies were made in essentially the same geometries as in previous work. The minor exceptions are the Lucalox\* and sapphire bodies which are in the form of small cylinders and flat discs respectively. These shapes were assembled for leak and tensile tests as illustrated in Fig. 4.60. The entire seal package consisted of ceramic or sapphire, P-4M metallizing, 0.0003 in. copper plate, 0.004 in. copper braze, and 0.020 in. 70/30 copper-nickel washer. They were brazed in wet hydrogen at 1100°C for 3 to 5 minutes.

---

\*General Electric Co., Trade Name.

TABLE 4-38

Metallizing Resistance, ohms

Body Type	Ceramic		Metallizing Temperature			
	Firing Temp. °C	Crystal Size, $\mu$	1300°C	1425°C	1600°C	1800°C
941	1550	5.6	1.8	0.5	0.4	0.5
941	1600	8.4	1.9	0.5	0.4	0.5
941	1650	9.8	1.8	0.7	0.4	0.4
941	1700	10.4	1.9	0.5	0.4	0.4
942	1600	8.1	6.0	0.8	0.5	0.6
942	1650	10.3	2.8	0.8	0.5	0.4
942	1700	12.2	2.0	1.0	0.4	0.4
942	1750	22.1	1.9	0.8	0.5	0.5
992	1700	7.4	1.9	0.9	0.5	0.5
992	1750	25.0	3.6	1.4	0.5	0.6
992	1800	31.0	4.4	0.4	0.4	0.4

Lucalox\*: Sample geometry was not suitable for resistance measurements.

\*General Electric Co. Trade Name.

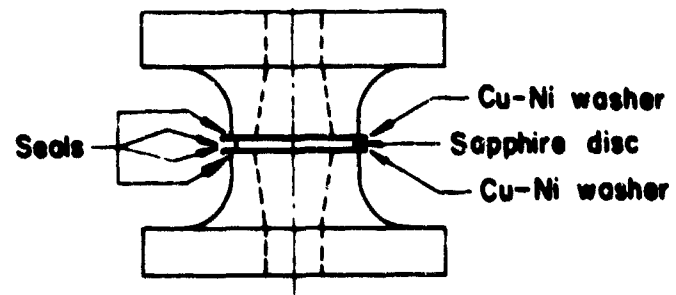
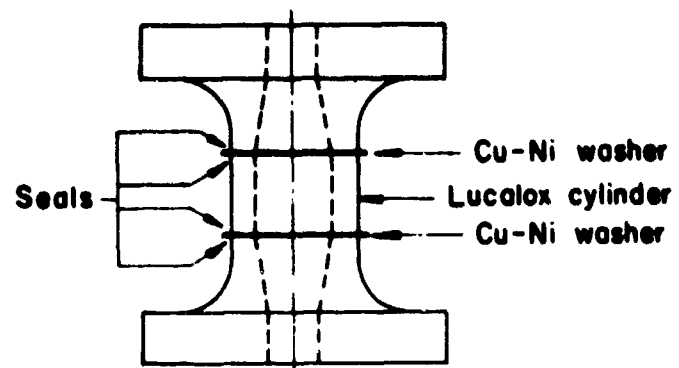


Figure 4.60. Lucalox\* cylinder (top) and sapphire disc (bottom) assembled for leak check and tensile testing.

A full series of peel test assemblies using Cu-Ag braze as well as copper braze was run for the purpose of comparing different seal stress conditions. All peel tests were made with an annealed Kovar 15 mil, nickel clad strip. Peel test samples to be Cu-Ag brazed were nickel plated. The plating was sintered for 10 minutes at 800°C in wet hydrogen. Cu-Ag brazes were made by heating to 810°C in wet hydrogen for less than five minutes. Peel strengths with Kovar and Cu-Ag braze have previously always been higher than with Kovar and copper braze. (Page 76, Third Quarterly Report and pp. 47-51, Fourth Quarterly Report.)

#### 4.5.2.1.5 Leak Check

All tensile test assemblies were given a leak check after brazing to see if a vacuum tight seal had been formed. This check was made by pulling a vacuum of  $10^{-5}$  Torr in the center hole of the assembly while directing a stream of helium over the seal area. A helium mass spectrometer, coupled to the vacuum system, triggered an alarm if helium penetrated the seal. This equipment could detect any leak greater than  $10^{-10}$  atmos.  $\text{cm}^3/\text{sec}$ .

Leak check results appear in Table 4-39. Data for the 94% alumina bodies (941 and 942) show that a vacuum tight seal was formed when the bodies were metallized at 1425°C or above. This results is closely associated with the degree of consolidation of the metallized layer which was indicated by the scratch and resistance test results. With the 99% alumina bodies (992), somewhat higher metallizing temperatures were required to effect a vacuum tight seal. Since the amount of glassy phase present in the bodies was the only major difference between the 94% and 99% alumina ceramics, the importance of the glass migration mechanism was again apparent.

#### 4.5.2.1.6 Tensile Test

Seal assemblies were tested for tensile strength on an Instron testing machine using a constant crosshead speed of one inch/min.\* The tensile test results obtained appear in Table 4-40. The general increase in tensile strength with increased metallizing temperature is obvious.

---

\*The effect of the crosshead speed on the results was examined by testing some assemblies at a speed of 0.1 in/min and was found to be insignificant.



TABLE 4-39

## Seal Leak Check

Body Type	Ceramic Firing Temp. °C	Crystal Size, $\mu$	Metallizing Temperature			
			1300°C	1425°C	1600°C	1800°C
941	1550	5.6	2 LKR	2 VT, 1 LKR**	2 VT	2 VT
941	1600	8.4	2 LKR	3 VT	2 VT	2 VT
941	1650	9.8	2 LKR	2 VT	2 VT	2 LKR
941	1700	10.4	2 LKR	2 VT	2 VT	1 VT, 1 LKR
942	1600	8.1	2 LKR	2 VT	2 VT	2 VT
942	1650	10.3	2 LKR	2 VT	1 VT, 1 LKR**	2 VT
942	1700	12.2	2 LKR	2 VT	2 VT	2 VT
942	1750	22.1	2 LKR	1 VT	2 VT	2 VT
992	1700	7.4	2 LKR	2 LKR	4 LKR*	2 VT
992	1750	25.0	1 VT, 1 LKR	2 VT	3 VT	1 VT, 1 LKR
992	1800	31.0	2 LKR	1 LKR*	2 VT	1 VT, 1 LKR
Lucalox <sup>†</sup> unknown		5	n.d.	n.d.	2 VT	1 VT, 1 LKR*
Lucalox <sup>†</sup> unknown		20	n.d.	n.d.	2 VT	2 LKR**
Lucalox <sup>†</sup> unknown		40	n.d.	n.d.	1 VT, 1 LKR	2 LKR**

## Note:

LKR - leaker

VT - vacuum tight

\* - porous ceramic

\*\* - bad braze

† General Electric Co., Trade Name.

TABLE 4-40

Seal Tensile Strength, psi

Body Type	Ceramic Firing Temp. °C	Crystal Size, "	Metallizing Temperature		
			1300°C	1425°C	1600°C
941	1550	5.6	2,225 SM**	6,960 SC**	11,185 SC**
941	1600	8.4	3,300 SM	9,625 SC	10,310 SC
941	1650	9.8	4,000 SM	9,685 SC	11,000 SC
941	1700	10.4	2,225 SM	9,610 SC	11,250 SC
942	1600	8.1	1,460 SM	4,075 SM	8,185 SC
942	1650	10.3	1,000 SM	4,460 SM	11,810 SC
942	1700	12.2	2,035 SM	6,385 SM	9,985 SC
942	1750	22.1	1,175 SM	4,250 SM	8,310 SC
992	1700	7.4	1,975 SM	1,385 SM	3,875 SM
992	1750	25.0	3,000 SM	3,375 SM	8,200 SM
992	1800	31.0	3,600 SM	4,700 SM	7,235 SM
Lucalox* unknown		5	n.d.	n.d.	5,525 SM
Lucalox* unknown		20	n.d.	n.d.	6,750 SM
Lucalox* unknown		40	n.d.	n.d.	6,237 SM
Lucalox* unknown		5	Evaporated metallizing (Ti, Co, Cu) : 11,500		
Sapphire single crystal			Evaporated metallizing (Ti, Mo, Cu) : 10,550		

\*\*Tensile failure location:

SM = In seal, metallizing parted from ceramic

SC = In seal, pulled ceramic with metallizing

\*General Electric Co., Trade Name.

The variation in strength between different ceramic bodies is also quite evident.

While general trends are reliable, a high confidence level in the actual value for any one point on the graphs would necessitate a much larger sample than two or three, because tensile and peel strength of seals is a statistical property.

#### 4.5.2.1.7 Peel Test

The Instron was also used for the drum peel test. The peel test sample was held in one fixture by a steel pin placed through the hole in the center of the ceramic. One end of the metal tab which had been brazed on the shoulder of the sample was clamped in the other fixture. As the fixtures were moved apart, the metal tab was stripped away from the ceramic, which was free to rotate about the pin. The force (in pounds) required to sustain the peeling action was recorded on a strip chart.

The results of peel tests appear in Table 4-41. The strength of some samples with weak bonds which were easily pulled by hand were reported as less than 0.5 pound. Specimens brazed with copper were compared with those with Cu-Ag brazes to determine the effect of the 290°C difference in brazing temperature. The mismatch in thermal expansion between Kovar and alumina increases considerably above 800°C and was expected to have an effect on the strength of the samples with copper brazes. The effect of this mismatch is most apparent on samples metallized at 1300°C, but some of the other results present a more confusing picture.

#### 4.5.2.1.8 Microstructure Examination

All the samples tested were cross-sectioned and examined. Typical microstructures are reported later in this section. (Figs. 4.70 through 4.73.)

#### 4.5.2.2 Analysis of Physical Property Data

The tables contain a great amount of useful data, but these data are difficult to analyze because they reflect the influence of numerous variables which come into play in the sealing process. These variables were discussed in great detail in the Second, Third and Fourth Quarterly Reports as the factors which directly determine the properties of ceramic-to-metal seals. The values of

Seal Peel Strength, lbs

\*Cu = Brazed with copper (1100°C)

<sup>†</sup>Cu-Ag = Brazed with copper-silver (810°C)

**Kovar metal members used on all assemblies.**

these factors are determined in turn by certain parameters which can be measured and controlled. The properties of the seal are thus determined by a three-link chain of physio-chemical processes. The first link in the chain consists of the independent variables or seal parameters. These are the physical or chemical factors that can be measured and controlled and include: the composition and microstructure of the ceramic body; the composition, microstructure and amount of metallizing; the metallizing sintering conditions including temperature, time and atmosphere; the amount, composition and sintering atmosphere, sintering time and sintering temperature of the plating; the braze material, amount, time, temperature and atmosphere during brazing; and the type, thickness and microstructure of the metal member. The second link consists of the dependent variables whose values cannot be directly measured or controlled during processing, so they must be manipulated indirectly through the independent variables. The dependent variables include; the amount, composition, viscosity, and interfacial energies of the ceramic melt phase; the ceramic crystallite size; the porosity, or degree of sintering of the metallizing; the interfacial energies, thickness, and porosity of the plating; the thickness, composition (alloy), and the interfacial energies of the braze-metal member; and the thermal expansion of all phases. The third link consists of the actual sealing mechanisms which are a combination of phenomena resulting from the interaction of the physio-chemical conditions of the second link. The sealing mechanisms include: the migration of the ceramic melt phase into the pores of the metallizing followed by super-cooling to form a continuous bridging glass phase adhering to the crystal phases of both ceramic and metallizing; adherence and limited alloying of the plating, braze, and metal member; slight yielding and elastic deformation of some layers to accommodate differences in their thermal expansion; and possibly, partial devitrification of the glass phase for stress-keying and crack-termination.

In this experimental program, the independent variables, (the first link) were directly controlled, measured, and varied, while the effectiveness of the sealing mechanisms (the third link) was measured by means of several physical tests. However, there was no direct control or measurement of the dependent variables (the second link) during processing. For this reason it is difficult to give simple explanations of the data. Seal data are presented in a manner which tends to associate them

with the independent variables (metallizing temperature, ceramic body types, etc.) although it is not proper to claim direct cause-and-effect relationships between the two, because the independent variables must act on and through the dependent variables in the second link in order to produce the seal. It is the purpose of supplementary experiments to show the relationships between the independent variables and dependent variables, then the relationships between the dependent variables and the sealing mechanisms will become more apparent. Therefore, it must be remembered that the associations discussed here are only indirect and are a result of the complex interactions of the numerous dependent variables.

The data on metallizing scratch hardness and metallizing resistance in Table 4-37 and Table 4-38 describe in a qualitative manner the effectiveness of a portion of the sealing mechanisms. These mechanisms include the sintering of the metallizing layer, migration of the ceramic melt phase into the metallizing, and adherence of the metallizing to the ceramic. The hardness data give an indication of melt migration and adhesion, while the resistance data indicate the degree of sintering and consolidation in the metallizing layer. Several trends are apparent in the tables. The degree of consolidation, melt migration and adherence generally increased at high metallizing temperatures and were greater on ceramics which had more melt phase or a more fluid melt phase. The ceramic body firing temperature is known to affect at least three of its properties: crystallite size, amount of melt phase and composition of melt phase. These factors influence such dependent variables as the melt viscosity, interfacial energies, and capillary forces, which in turn control the sealing mechanisms.

The major difference between 941 and 942 bodies was that metallizing on 941 was consolidated at lower temperatures than on 942. This difference is attributed to the difference in the viscosity of the melt phase of each body, 941 melts being less viscous than 942 melts as a result of the 1:1  $\text{SiO}_2/\text{CaO}$  ratio in the former which produces a more fluid melt. There was very little difference in the hardness of metallizing on 942 and 992 ceramics. The major difference between these ceramics was the amount of melt phase. The 942 bodies had about five times as much melt as 992. A comparison of these two groups of data seems to indicate that the viscosity of the melt phase and the ceramic crystallite size were more important factors than the amount of melt. The average crystallite size and

melt phase composition of bodies 942 (1750) and 992 (1750) were very similar, while the amount of melt in each was quite different, but the metallizing hardness on both bodies was nearly equal at all metallizing temperatures. This indicates that once a minimum amount of melt phase has migrated, there is no further benefit from additional melt. The results on Lucalox\* and sapphire were interesting because both represent materials which have no melt phase at metallizing temperature, but differ in that Lucalox\* is a polycrystalline material, (99.8%  $\text{Al}_2\text{O}_3$ ) while sapphire is a single crystal of  $\text{Al}_2\text{O}_3$ . There was moderate adherence to sapphire. The bonding may have resulted from a surface area effect or weak chemical bonding. The results on sapphire showed little or no evidence of chemical bonding. On the other hand, there was no real correlation between the crystal size of the Lucalox\* and the hardness of its metallizing to show the effect of surface area. Inter-crystalline spinel ( $\text{MgO} \cdot \text{Al}_2\text{O}_3$ ) in the Lucalox\* may have provided the adhesive link.

The data on seal vacuum quality, tensile strength, and peel strength in Tables 4-39, 4-40 and 4-41 respectively describe the combined effectiveness of all the sealing mechanisms. The tensile test data for the 941, 942 and 992 special alumina bodies are plotted against metallizing temperature in Figs. 4.61, 4.62 and 4.63. Peel strength data for the same ceramics (brazed with Cu and CuAg) also plotted against metallizing temperature appear in Figs. 4.64 through 4.69.

Plots of seal tensile strength on body 941 in Figure 4.61 rise rapidly from  $1300^\circ\text{C}$  to  $1425^\circ\text{C}$ , peak out at  $1600^\circ\text{C}$ , then drop or level out at  $1800^\circ\text{C}$ . The most prominent factor in these results was probably the fluidity of the melt phase in the respective ceramics at the various metallizing temperatures. The melt phase of the 941 bodies was consistently more fluid than either 942 or 992. Consequently, strong seals, which are produced in part by melt phase migration, were developed at lower temperatures on 941 than on 942 or 992 bodies (Figs. 4.52 and 4.63). In these latter two cases, the strength continued to increase as the metallizing temperature was increased to  $1800^\circ\text{C}$ . On all three bodies there was a greater spread of data at  $1800^\circ\text{C}$  than at lower temperatures. This may have resulted from the fact that the metallizing temperature was higher

---

\*General Electric Co. Trade Name.

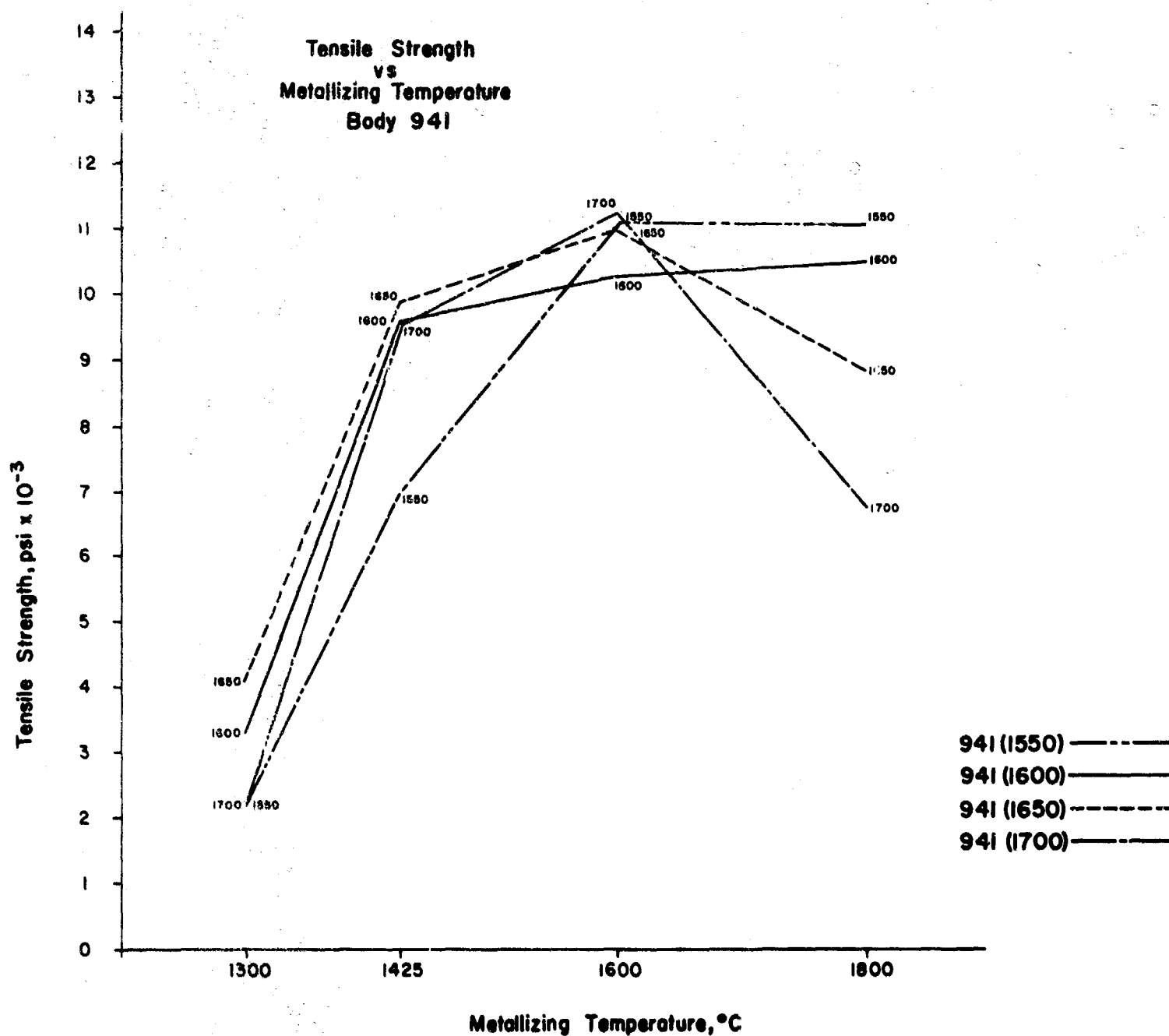


Figure 4.61: Plots of tensile strength of ceramic-to-metal seals on 941 alumina bodies originally fired at 1550°C, 1600°C, 1650°C, and 1700°C versus metallizing temperature.



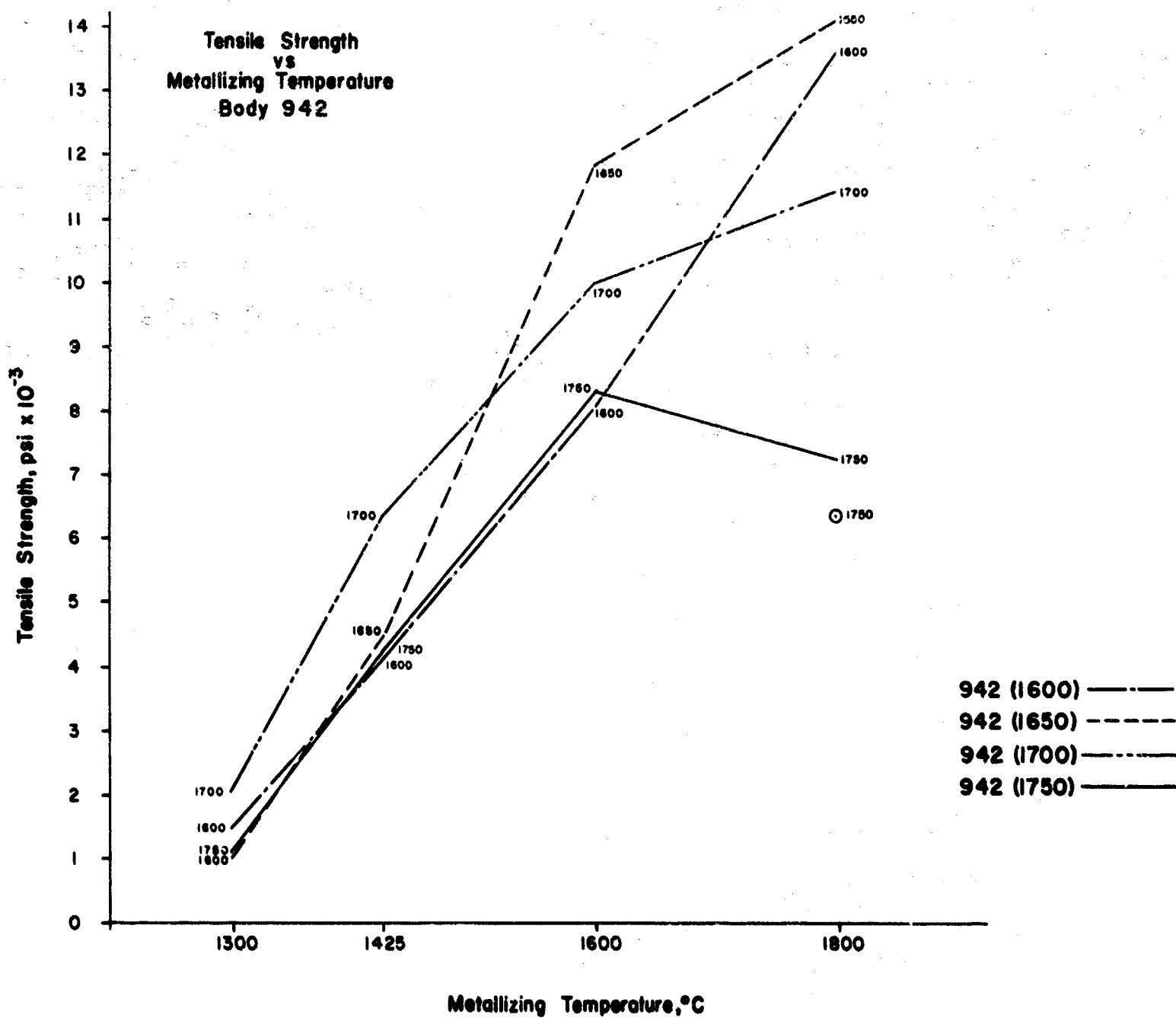


Figure 4.62: Plots of tensile strength of ceramic-to-metal seals on 942 alumina bodies originally fired at 1600°C, 1650°C, 1700°C, and 1750°C versus metallizing temperature.

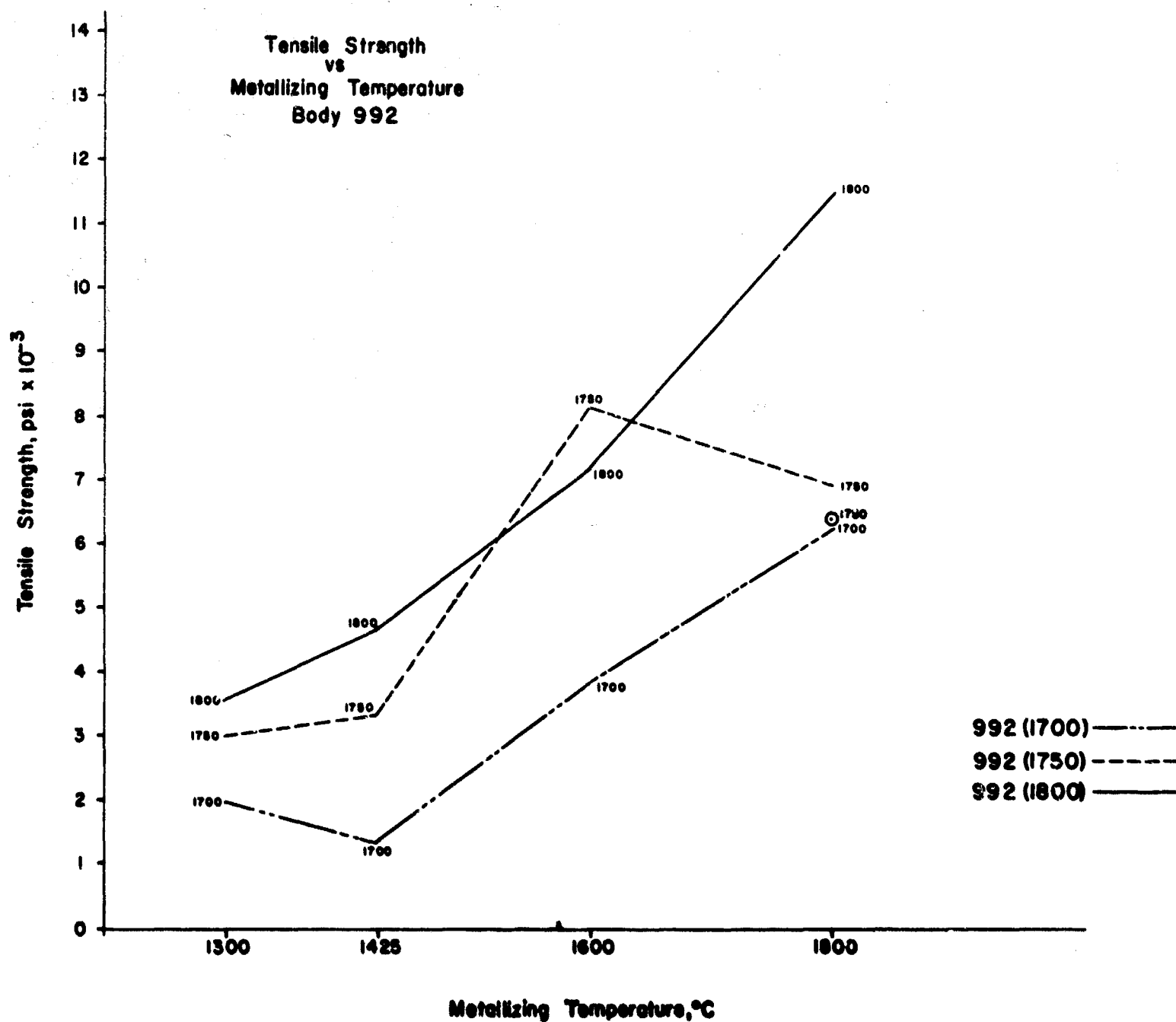


Figure 4.63: Plots of tensile strength of ceramic-to-metal seals on 992 alumina bodies originally fired at 1700°C, 1750°C, and 1800°C versus metallizing temperature.

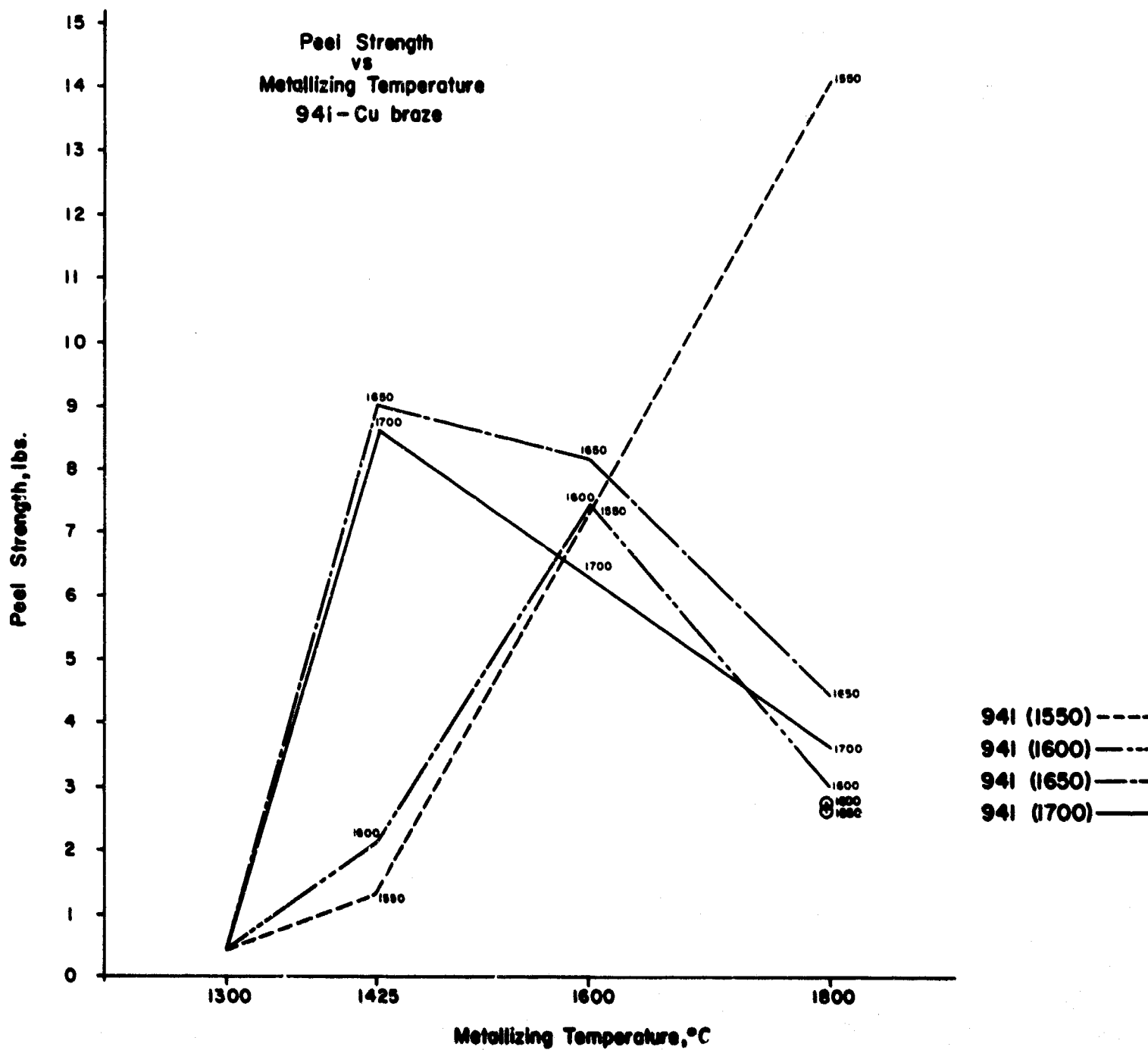


Figure 4.64: Plots of peel strength of ceramic-to-metal seals brazed with copper on 941 alumina bodies originally fired at 1550°C, 1600°C, 1650°C, and 1700°C versus metallizing temperature.

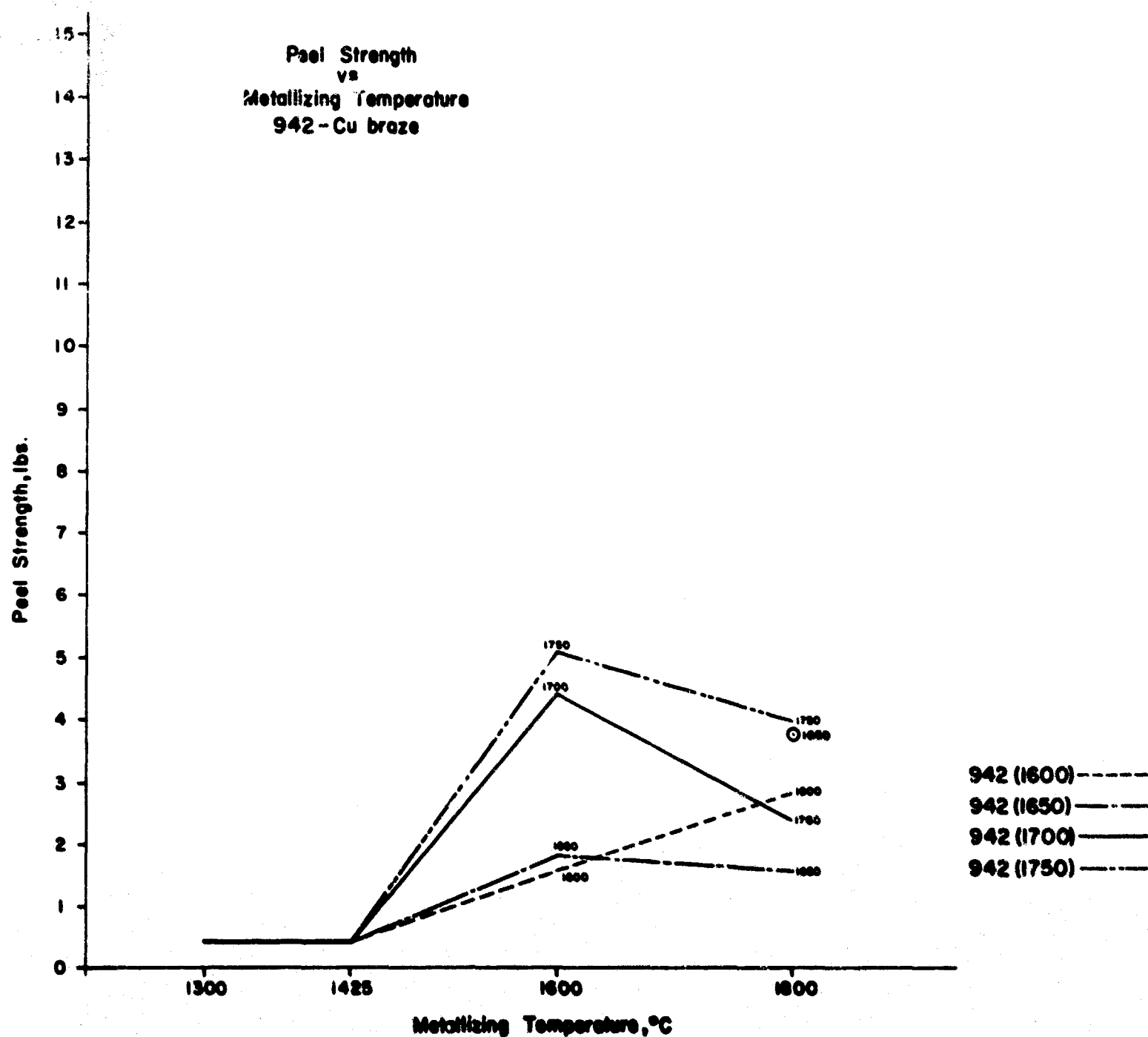


Figure 4.65: Plots of peel strength of ceramic-to-metal seals brazed with copper on 942 alumina bodies originally fired at 1600°C, 1650°C, 1700°C and 1750°C versus metallizing temperature.

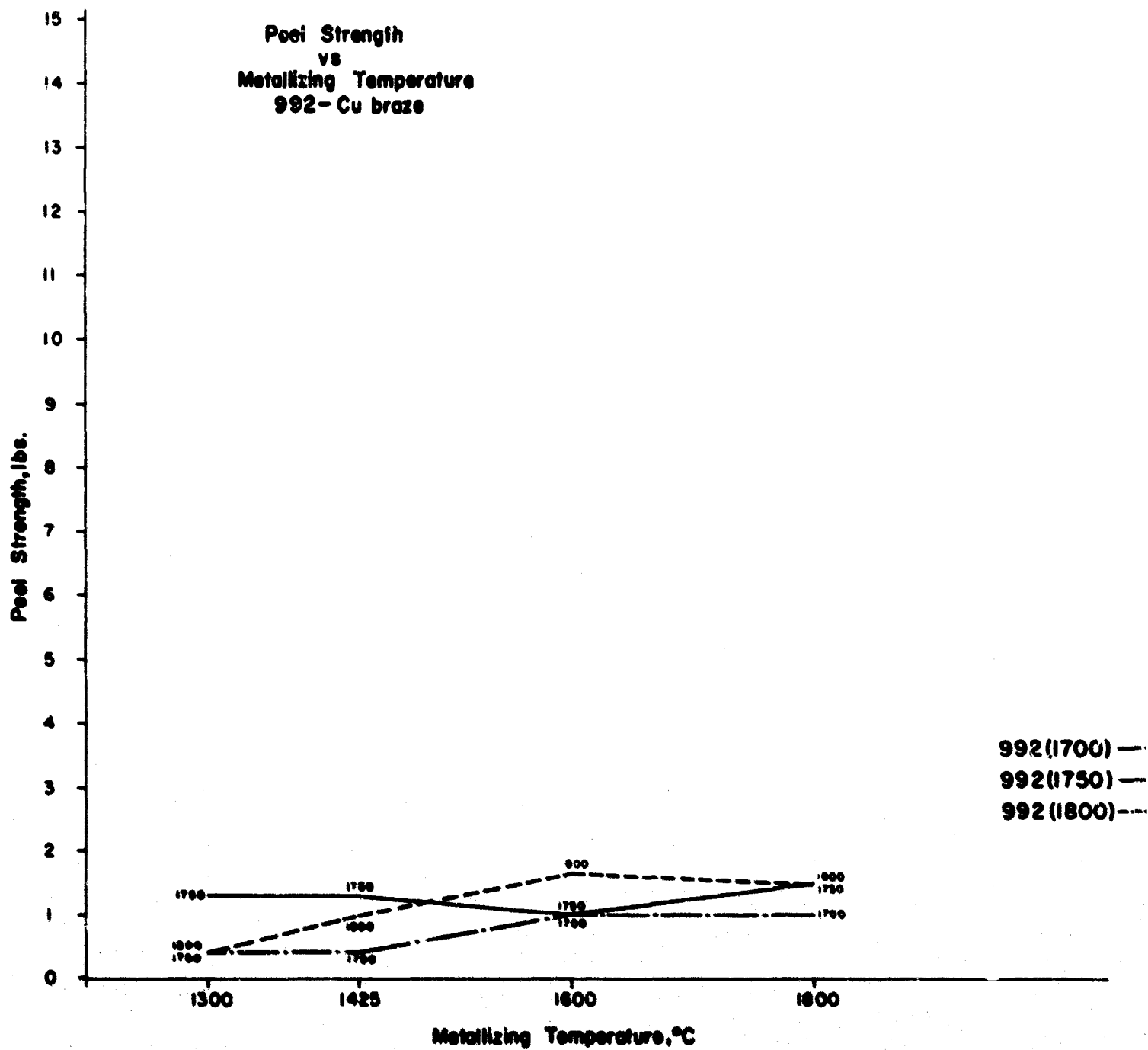


Figure 4.66: Plots of peel strength of ceramic-to-metal seals brazed with copper on 992 alumina bodies originally fired at 1700°C, 1750°C, and 1800°C versus metallizing temperature.

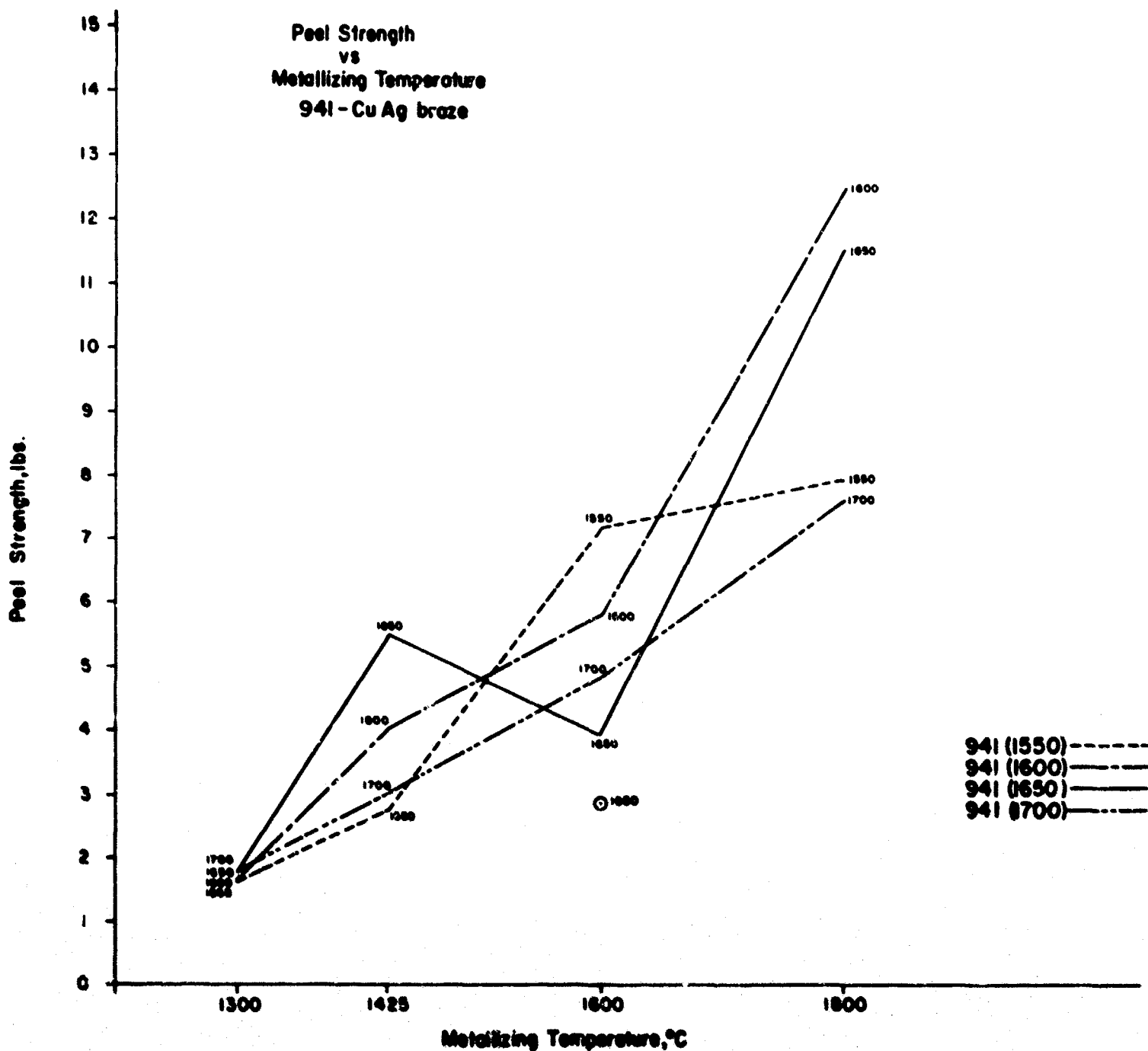


Figure 4.67: Plots of peel strength of ceramic-to-metal seals brazed with CuAg on 941 alumina bodies originally fired at 1550°C, 1600°C, 1650°C, and 1700°C versus metallizing temperature.

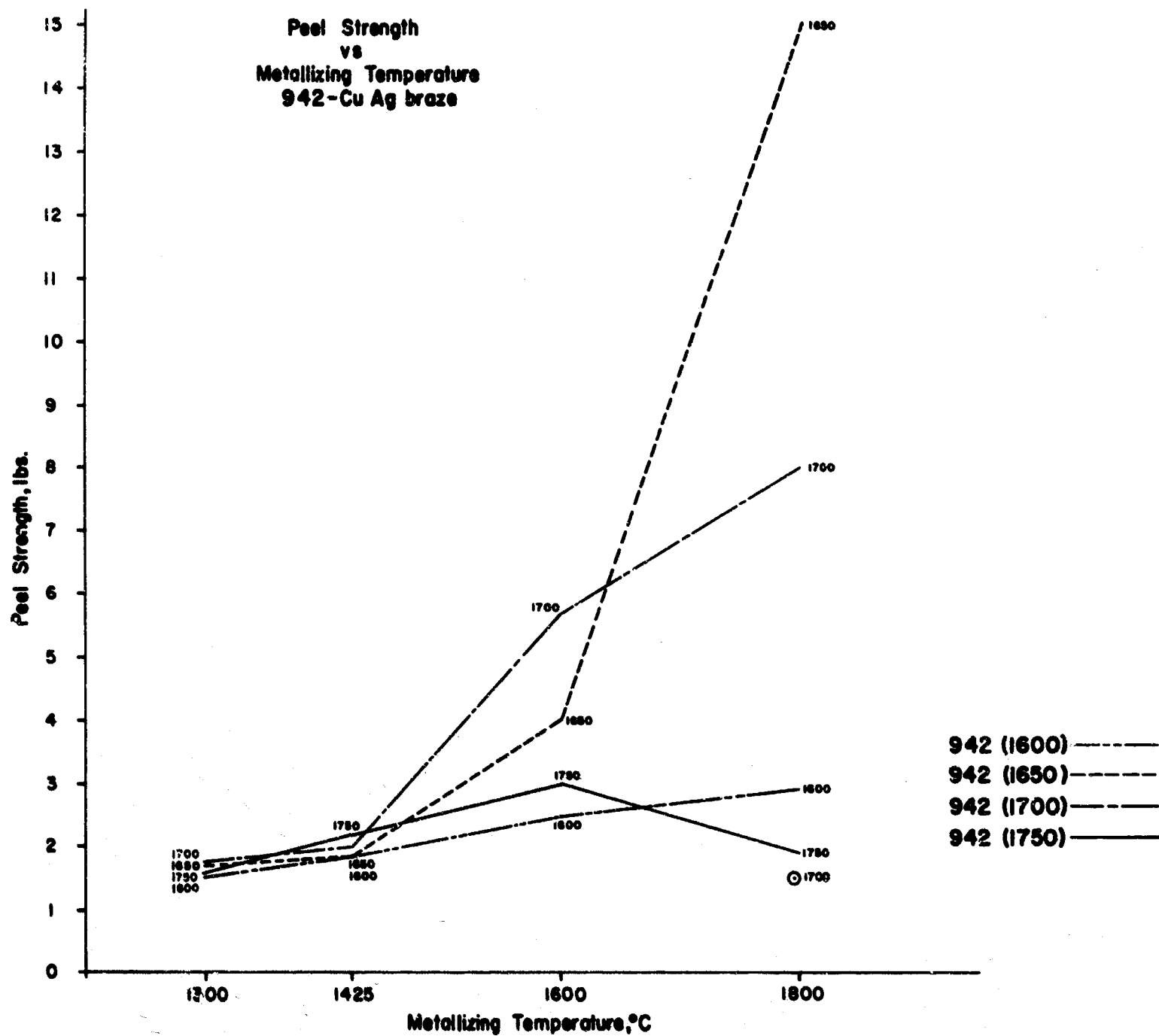


Figure 4.68: Plots of peel strength of ceramic-to-metal seals brazed with CuAg on 942 alumina bodies originally fired at 1600°C, 1650°C, 1700°C, and 1750°C versus metallizing temperature.

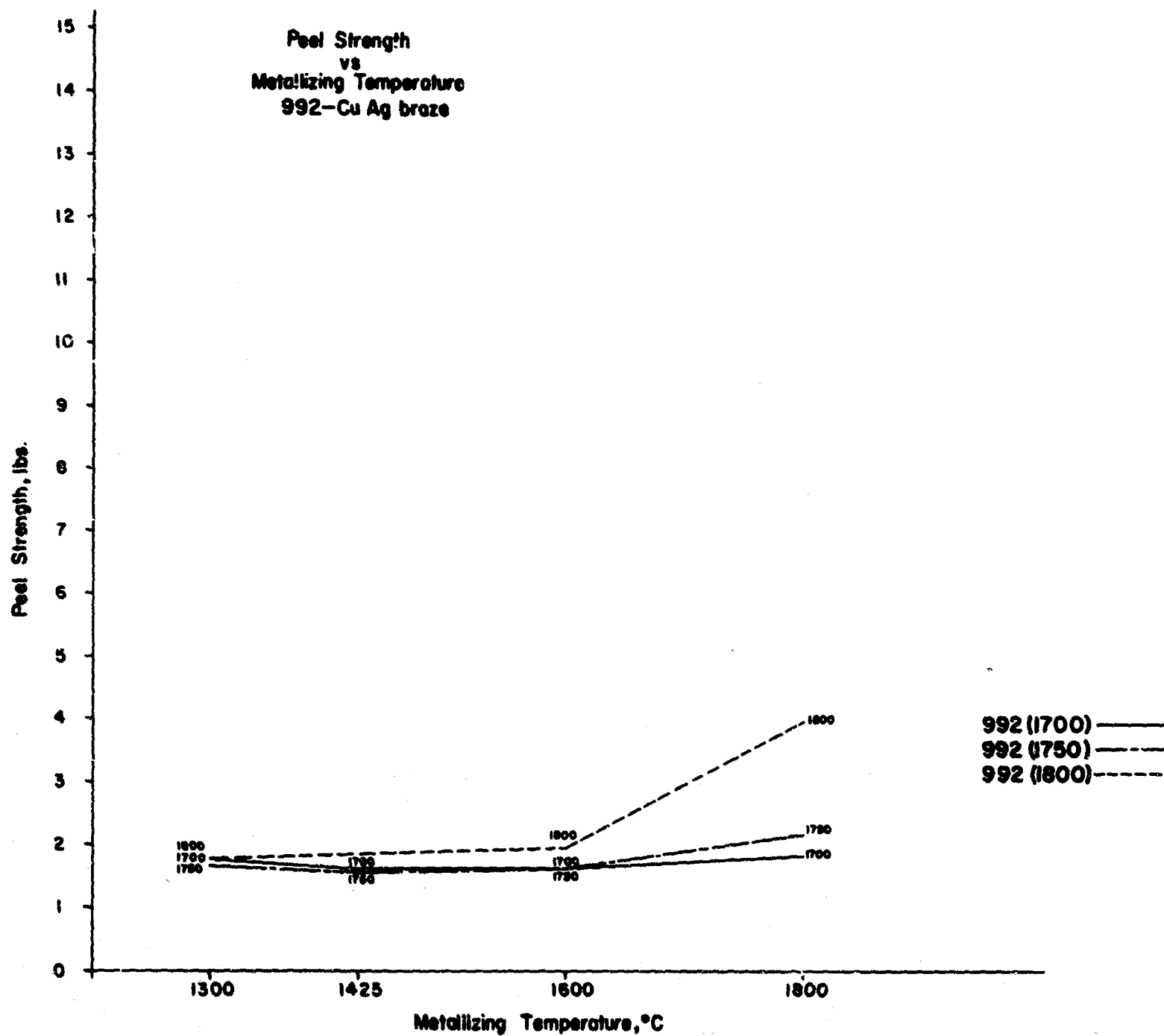


Figure 4.69: Plots of peel strength of ceramic-to-metal seals brazed with CuAg on 992 alumina bodies originally fired at 1700°C, 1750°C, 1800°C versus metallizing temperature.



than most of the body firing temperatures and caused major changes in the ceramic microstructure as the bodies attempted to reach equilibrium at the higher temperature. Some grain growth occurs, especially in 941 bodies, and more alumina is dissolved into the melt phase. During the subsequent copper braze cycle to 1100°C, some of that alumina can recrystallize and either strengthen or weaken the seal depending on the amount, grain size, and distribution of the crystal phase. The two 941 bodies whose seal tensile strength dropped the most at 1800°C (1650°C and 1700°C firing temperatures, Fig. 4.61) also produced some leaky seals at 1800°C (Table 4-39). This is further evidence of excessive devitrification of the glassy phase which probably occurred during the 1100°C braze cycle.

Peel strengths of copper braze seals on ceramics 941, 942 and 992 are plotted against metallizing temperatures in Figs. 4.64, 4.65 and 4.66 respectively. In Fig. 4.64 the plots of peel strength of bodies 941 (1650) and 941 (1700) peak at 1425°C, much lower than the other two plots. This could again be related to the amount and mobility of the melt phase of the bodies. The temperature, 1425°C, may be near a point of critical viscosity for the melt, which could make secondary factors such as ceramic crystal size and interfacial energies more prominent in affecting the mobility of the melt. The wide spread of peel strength values at the 1800°C metallizing temperature may again reflect the phenomenon of glass phase devitrification, which was discussed previously in connection with the tensile strength data.

Peel strength values for seals on bodies 942 and 992, Figs. 4.65 and 4.66, were generally much lower than on 941. The properties of the melt phase may also have been significant here. The 2:1 SiO<sub>2</sub>/CaO melts are more viscous than 1:1 SiO<sub>2</sub>/CaO melts and thus have less mobility and less tendency to devitrify. These factors may have caused the difference in strength. Consistently low values on 992 could be caused by insufficient melt to produce a good bond with the metallizing, although this did not appear to be the case in the tensile tests.

Peel strengths of 810°C copper-silver braze seals on ceramics 941, 942 and 992 are plotted against metallizing temperatures in Figs. 4.67, 4.68 and 4.69 respectively. These peel strengths are in the aggregate, higher and more closely related to the metallizing temperature than the copper brazed peel strength values. The major difference in sample preparation between the two

groups of samples was the brazing temperature: 1100°C for Cu braze versus 810°C for CuAg braze. This made a great deal of difference in the amount of stress introduced into the seal by differential thermal expansion of the alumina ceramic and the Kovar peel tab. The expansion of alumina and Kovar match fairly well to around 800°C, but they diverge rapidly above that temperature. As a result of this mismatch, considerable stress is produced in the copper brazed seals as they cool from the 1100°C braze temperature. This accounts partially for the generally irregular and lower peel strength of copper brazed peel assemblies. Another important dependent variable which is affected by the braze temperature is the viscosity of the glassy phase and its ability to devitrify. The 300°C difference in braze temperatures makes a great difference (orders of magnitude) in viscosity in the range which vitally affects crystallization.

There is less of a difference in the peel strength values for 941 and 942 bodies with CuAg brazes than there is for the same bodies with Cu brazes. This probably results from the lower seal stress conditions due to expansion mismatch and the diminished tendency for glassy phase devitrification. The greater tendency for the 941 body to devitrify separates it from 942 only when the temperature is high enough for that to occur. The CuAg braze temperature is not high enough to produce this effect. In fact, an annealing process takes place which tends to reduce the stress level in the glass. Alumino-silicate glasses are generally annealed in the 750°C-850°C region.

The data may alternately be plotted as a function of ceramic firing temperature at a given metallizing temperature or plotted on a three-variable, triangular diagram. Interesting conclusions may be reached from this approach. It appears that strength is not related to crystal size of the ceramic. However, in order to study this effect, a special study was made of this variable. This study is reported in a later section.

#### 4.5.2.3 Microstructure Analysis

Many of the tested seals were examined metallurgically to help explain the results. In each seal examined, the visual appearance of each component layer, ceramic, metallizing, plating, braze, and metal member, was examined in order to establish a relationship between its properties and the seal strength. The metallizing layer was found to vary the most in quality and to have the most dominant influence on seal characteristics of any of the seal components.

The relationship between each seal component and its effect on seal strength and vacuum tightness is discussed below.

#### 4.5.2.3.1 The Ceramic

Three general aspects of the ceramic portion of the seal structure were considered. They were (1) the structural changes which occurred in the ceramic during the metallizing sinter fire step, (2) the quality of the ceramic surface, and (3) the action of the glassy melt phase of the ceramic.

The most easily recognized change which occurred in the ceramics when they were exposed to metallizing temperatures was an increase in average crystallite size. Two extreme cases are shown in Figure 4.70. The top photomicrograph shows a seal to special alumina body 941 (1550) which was metallized at 1300°C and which has an average crystallite size of about 6 microns, changed little if any from what it was before it was metallized. The lower photomicrograph shows a seal to the same body, but the metallizing was sintered at 1800°C. The average crystallite size in the second sample is about 12 microns, a considerable increase from the initial size.

This sort of change was most pronounced in the 941 bodies because the melt phase of these bodies has a lower viscosity at elevated temperatures than either of the other aluminas and therefore permitted more diffusion of aluminum and oxygen ions through the melt to support crystal growth. Little or no growth occurs unless the ceramic is metallized at a temperature above the initial firing temperature, because the bodies had approached equilibrium at the firing temperature, and a higher temperature would be required to cause a measureable shift from those conditions.

The marked grain growth in 941 bodies also indicates that a similar change in the  $Al_2O_3$  content of the melt phase is taking place. This change must affect the melt viscosity and therefore its mobility. The viscosity would decrease with increasing temperature, but could either increase or decrease depending on whether the alumina content of the melt was initially below or above about 45 weight percent. Melt mobility appeared to be a primary factor determining the extent or ease of melt intrusion into the porous molybdenum metallizing layer. This was most evident in seals to 941 bodies which developed good strength at lower metallizing temperatures compared to the other bodies studied.

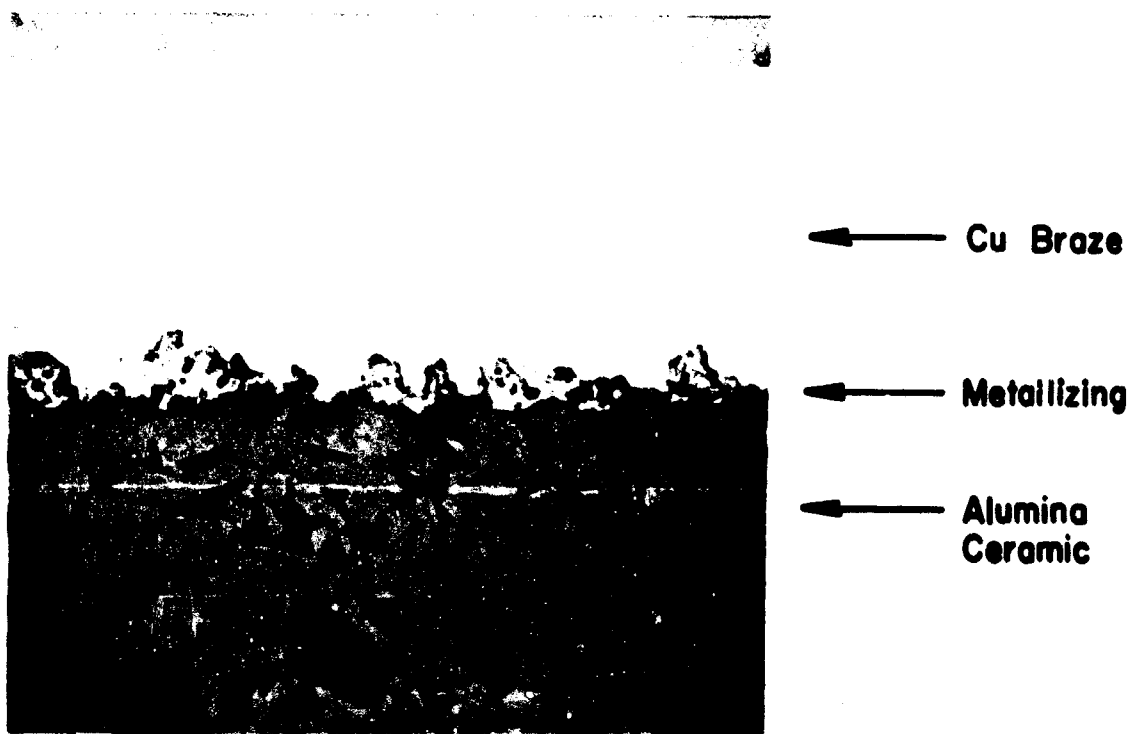


Figure 4.70: Photomicrographs of ceramic-to-metal seals on alumina body 941 (1550) metallized with P-4M at 1300°C (top) and 1800 C (bottom) showing the structural changes which occur when the ceramic is metallized at very high temperatures. (400X)

The average crystal size of 942 and 992 bodies changed very little when metallized at 1800°C. This implied that the composition of the melt phase was not greatly altered by the metallizing treatment either. However, there is evidence that the amount of melt did vary, increasing by dissolving some crystal phase at higher temperatures and then decreasing by again precipitating aluminum oxide.

Figure 4.71 (top) is a photomicrograph of a seal on alumina ceramic 942 (1650). The P-4M metallizing was sintered on at 1800°C. Evidence of growth caused by partial solution and recrystallization of alumina crystals appears at the interface between the molybdenum metallizing and the ceramic. The alumina crystal phase has grown to match the contours of the under-surface of the molybdenum mass. This resulted in an interlocking mechanical joint with very high tensile strength of 14,000 psi.

Figure 4.71 (bottom) shows a seal on alumina ceramic 992 (1800), also metallized at 1800°C. Here again the alumina and molybdenum have come into intimate contact forming a strong (11,500 psi), interlocking interface. The only noticeable difference between the interfaces on the 942 and 992 aluminas is the clarity of the dark line between the molybdenum and the alumina. This line may be the remaining portion of glassy phase. It is easily discernible in the seal on 942 (top), but is absent or unresolved in the 992 seal (bottom). In the seal in the bottom photo, where molybdenum and alumina appear to be in direct contact, it is possible that an  $\text{Al}_2\text{O}_3\text{-Mo}$  chemical bond has formed.

To further investigate the possibility of the formation of a chemical bond between alumina and molybdenum, seals were made with P-4M metallizing to Lucalox\* of three different nominal grain sizes, 5, 20 and 40 micron. The tests were performed with both polished and unpolished Lucalox\* surfaces to study the effect of surface finish on the interlocking grain phenomenon and its contribution to seal strength. Lucalox\* has no glassy phase as found in 941, 942 and 992 alumina ceramics, so the mechanism of bonding between the metallizing and ceramic must be a chemical bond, crystal-to-crystal interlocking, adhesion resulting from a reduction in surface energies, or some combination of the three.

None of the seals developed strength above 4000 psi, which indicated that whatever mechanism of bonding

---

\*General Electric Co. Trade Name.



Figure 4.71: Photomicrographs of ceramic-to-metal seals on alumina body 942 (1650) (top) and 992 (1800) (bottom) both metallized with P-4M at 1800°C. Interlocking grain structure may be seen at the interface between the molybdenum metallizing and the alumina surface. (400X)

TABLE 4-42

Tensile Strength of Seals to Polished and Unpolished  
Lucalox of Three Grain Sizes

Lucalox* Grain Size	Metallizing Temperature	Strength, psi	
		Unpolished	Polished
5 micron	1600°C	2038	n.d.
5	1800	2138	2200
20	1600	3725	3338
20	1800	2225	1950
40	1600	3388	3350
40	1800	3138	1563

was in effect was either weak by its nature or it was effective on only a fraction of the total interface. Results obtained with the 5 micron Lucalox\* were about the same value regardless of metallizing temperature or surface condition. Adhesion to 20 micron and 40 micron Lucalox\* bodies seemed to have a slight relationship to these two variables with the unpolished surface condition and 1600°C metallizing temperature having a slight tendency to produce better adhesion.

The lower metallizing temperature and relatively irregular surfaces were conditions which would be more likely to favor a mechanical type of bond or surface energy adhesion. If a true chemical type of bonding had predominated, then its strength should have increased with the higher metallizing temperature which would promote or accelerate the chemical reaction. However, this was not the case.

Further adhesion tests were made with P-4M sintered on polished sapphire discs at 1600°C and 1800°C. At both temperatures only minimal adhesion was achieved. The molybdenum particles sintered well to each other, forming a continuous metal sheet, but this sheet curled away from the sapphire surface and could be removed with little effort.

It was apparent that the stresses which develop in the layer of metallizing as a result of densification during sintering were great enough to affect the adhesion which developed between it and the ceramic. These stresses increase as higher sintering temperatures are used and would go unchecked on a smooth surface such as polished sapphire which presents a natural shear plane. On irregular surfaces with many crystallites jutting into the metallizing layer, the shearing tendency would be greatly diminished.

Because of this relationship between the stress in the metallizing layer and the surface condition of the ceramic, the results always indicated a mechanical type of adhesion.

The conditions which should have given isolated evidence of chemical bonding also contributed to the stress condition, thereby weakening or destroying any chemical bond which might have formed. Therefore the results of this particular experiment cannot be considered conclusive in confirming the mechanical adhesion theory or in repudiating the chemical bonding theory. In view of this conclusion, further experiments were programmed to investigate the chemical bonding mechanism. These are discussed later in section 4.5.3.

Most of the data still indicates that the glassy or melt phase of the ceramic is the predominant factor in the formation of strong and reliable seals. The flowing action of the melt at the metallizing temperature was relatively easy to detect in the model metallizing system used in this study. The P-4M metallizing paint was completely metallic, containing no additions which could form or contribute to a glassy melt. Therefore, any glassy material which was present in the metallizing after forming the seal could only come from the ceramic.

Two contrasting conditions are shown in Figure 4.72. Photomicrographs of body 942 (1700) with P-4M metallizing sintered at 1425°C and 1600°C show that the melt phase of the ceramic flowed into the molybdenum at 1600°C, but did not do so at 1425°C. The pore spaces of the metallizing sintered at 1425°C are filled with copper braze material. The pores of the 1600°C sintered metallizing are filled with glassy material which migrated from the ceramic. The glass thus forms a strong mechanical link between the ceramic and the porous sintered layer of metal particles. The tensile strength of the seal metallized at 1600°C was stronger by a factor of two. This difference



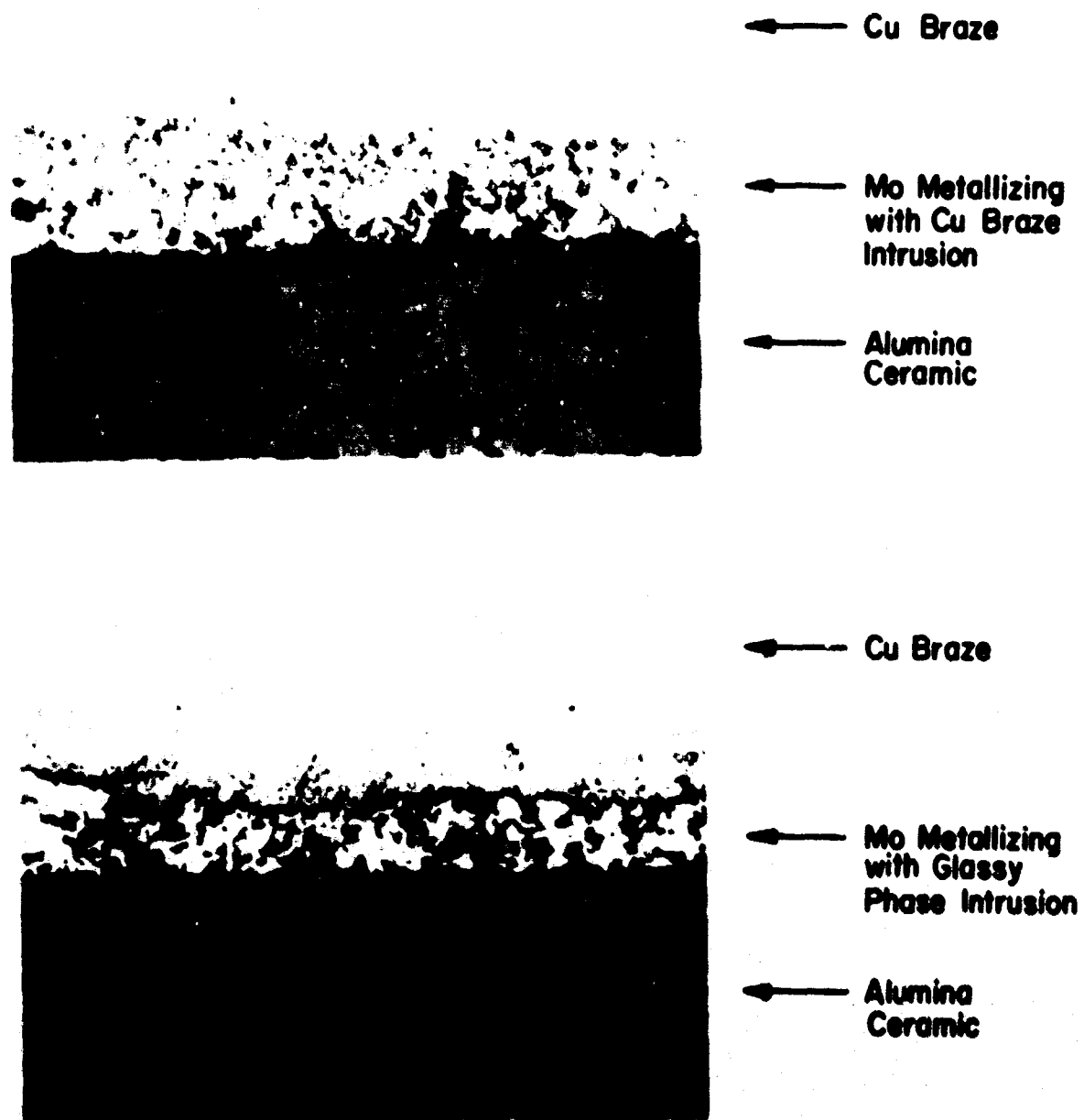


Figure 4.72: Photomicrographs of ceramic-to-metal seals on alumina body 942 (1700) made with P-4M metallizing sintered at 1425°C (top) and 1600°C (bottom). The glassy phase migrated into the metallizing when sintered at 1600°C, but not at 1425°C. (400X)

was attributed to the flow of the glassy phase material into the metallizing to connect the metal particles to the ceramic.

Similar comparisons have been made with numerous other seals to indicate the predominant influence of glassy melt phase migration on seal strength. This influence determined the shape of the curves in Figures 4.61, 4.62 and 4.63.

#### 4.5.2.3.2 The Metallizing

Several of the variables of the ceramic must also be considered metallizing variables because the two are so closely interrelated. Thus the melt phase may be considered as part of either, especially in common production metallizing paints which contain glass-forming oxide additions. Mechanical interactions produced by surface finish and interlocking growth of some crystal phases are also factors which may be associated with both the ceramic and the metallizing layers.

One process which occurs exclusively within the metallizing layer is the sintering or consolidation of that layer. In the model systems used in this study, the metallizing layer was consolidated by one or both of two processes. The first process was sintering of the fine molybdenum particles into a porous sponge. On ceramics which exuded no glassy phase, the metallizing remained as a porous layer whose density was primarily determined by the sintering temperature. The second process of consolidating the metallizing was the action of the melt phase of certain ceramics. A thin film of melt apparently formed on the surface of the ceramic, wet the adjacent molybdenum particles, and spread through the metal layer. As a consequence of this wetting action, the metal particles were drawn into and consolidated by the thin layer of melt.

Some amount of metal-to-metal sintering also occurred when particles came into direct contact under favorable conditions, but this process was retarded in the presence of the melt phase. This retardation resulted from the wetting action of the melt which tended to isolate the molybdenum particles.

The photomicrographs in Figure 4.73 illustrate the two situations. The top photo shows P-4M metallizing sintered together to form large separated grains. The molybdenum was mildly etched to bring out the fine crystal



← Cu Braze

← No Metallizing  
with Cu Braze  
Intrusion

← Lucalox\*  
Ceramic



← Cu Braze

← No Metallizing  
with Glassy  
Phase Intrusion

← Alumina  
Ceramic

Figure 4.73: Photomicrographs of ceramic-to-metal seals on Lucalox\* (top) and alumina ceramic 941 1600, (bottom) both metallized with P-4M at 1800°C. The molybdenum metallizing was etched for 4 sec. with a solution of potassium ferricyanide and sodium hydroxide. (800X)

structure of the grains which resulted from sintering together many smaller particles. The bottom photo shows P-4M metallizing sintered on alumina ceramic 941 (1600) at 1800°C. This ceramic has a fluid melt phase at 1800°C which flows readily and can be seen (dark gray) dispersed throughout the metallizing. The metallizing has sintered to some extent, but did not form grains as large as it did in the absence of glassy melt. Also, many smaller particles are isolated and floating about freely in the glassy layer. This sample also received a mild etch to bring out the molybdenum crystallite structure. The etchant was composed of 30 grams of potassium ferricyanide and 10 grams of sodium hydroxide dissolved in 100 ml of water.

The top photos in Figures 4.70 and 4.72 are examples of metallizing sintered to a lesser degree than is desirable. The molybdenum particles are well dispersed and of small size, indicating that little or no sintering has occurred. In both cases, the metallizing was saturated by copper in the subsequent braze operation due to its porous, spongy nature.

#### 4.5.2.3.3 The Plating

Nickel was electroplated on the metallized ceramics for CuAg (BT) brazes, while copper was plated for copper brazes. The purpose of the plating is to form a wetting layer to assure intimate contact between the braze and metallizing in order to form a strong and vacuum tight seal.

Deposition of metal ions from the plating bath requires two conditions. First, the metallizing must be conductive so that current may be carried through it from the contacts to the plating surface. Second, the surface must be such that electrons may be exchanged between the metallized surface and the copper or nickel cations in the bath. The fact that metallized ceramics were plated successfully was sufficient evidence to indicate that these two conditions existed, but they were not necessarily idealized.

The conductivity of the metallizing varied somewhat, Table 4-38, but was adequate for plating in all cases except when the metallizing actually flaked off.

The quality of the surface at which electron exchange occurred was quite variable. Some metallized ceramics which had little or no glassy phase in the metallizing had many tiny patches of ceramic exposed through the

metallizing. On others with generous amounts of glass present, the molybdenum particles at the surface were exposed in the manner of many tiny islands in a sea of glass. In both cases, the surfaces were plated with a uniform thickness of metal which generally followed the original surface contour.

Although electron exchange could not occur at every point on the surface because of the non-conductive ceramic and glass areas, there obviously were sufficient sites to provide the necessary electrons to build up the plated layer. It was not determined whether or not the irregular current density distribution caused local concentrations of plating at electron exchange sites, because the subsequent plating sinter-firing produced a more even distribution and thus destroyed any preferred distribution. The uniform thickness may have resulted from the sintering step, or the plating was initially deposited in that manner. Electrons could have been conducted laterally through the plating to overcome the effects of only spot sources of electrons.

Plating was employed to assure reliable brazes, but it did not appear to be the most critical step in forming strong vacuum tight seals. No seals were observed in which failure could be traced to the plating. Mechanical failures always occurred in the metallizing or the ceramic -- the brittle zones. However, the plating-braze layer is subjected to considerable stress and must adhere well to the metallizing and be able to yield to some extent in order to distribute more evenly the stress on the metallizing without failing itself.

#### 4.5.2.3.4 The Braze and Metal Member

Both CuAg (BT) and copper brazes were examined in this study. The most important braze variables as far as the seal is concerned are the melting temperature, braze hold time, mechanical properties, and dimensions.

The braze melting temperature determines the temperature from which stresses accumulate when the ceramic and metal member have different coefficients of thermal expansion. This is primarily a design problem and becomes more critical as dimensions increase.

A second factor arising from the brazing temperature is the effect this heat treatment has on other parts of the seal such as the glassy phase of the metallizing

and ceramic. Depending on the composition and phase relationships or stability of the glass, this heat treatment may anneal this material or allow it to devitrify to some degree. This is an important factor because it affects stress levels and distribution in the brittle seal zone where failure usually occurs. However, its direct study has been difficult because of the limited ability to control and measure all the variables contributing to this effect. Nevertheless, limited experiments were conducted to isolate this effect and they are discussed later.

The braze hold time or time above the liquidus temperature of the braze metal determines the extent of adhesion and alloying between the plating or metal member and the braze material. Hold time should be just long enough to allow the braze material to completely wet the surfaces to be joined and expel any entrapped gas. This is mainly a function of the mass and heat capacity of the assembly being brazed. More lengthy hold times caused various degrees of reaction with the plating, metallizing and metal member on the samples studied.

The mechanical properties of the braze metal such as tensile strength and hardness determine the response of the seal to the stresses which it encounters. The metal must be strong enough to resist failure of the seal in that area, yet it must yield under load to equalize the stress distribution over the seal area. Both brazes used in the study were satisfactory in this respect and were never indicated as a source of seal failure. (The "bad brazes" which were reported were all caused by jigging errors or overextended braze hold times, so were considered problems of execution, not design.)

It would be expected that in the case of the Kovar metal member employed in the peel test that the lower Cu Ag braze temperature would universally result in higher seal strengths as the stress due to the metal member would be lower. This was not found to be the case, however. The reason for this result must lie in the tendency of the glassy phase of the metallizing to devitrify at 1100°C. Sometimes this will increase the strength of the seal, sometimes it will decrease it, depending on the size and amount of crystals which are formed.

The effect of a variable stress induced by the metal member is shown in a later section.

#### 4.5.3 Supplementary Studies

##### 4.5.3.1 Bonding Mechanisms

The mechanisms of ceramic-to-metal seal adherence have been discussed in previous sections and the electrical results still to be reported shed further light on the nature of the bond which broadly is characterized as either chemical, semi-conducting or mechanical.

Experiments reported in this section concern themselves with the strength of a metallizing bond on sapphire formed as a consequence of:

- a) Evaporating molybdenum onto the sapphire surface
- b) Firing a  $\text{MoO}_3$  paint, P-2M, onto the sapphire.

##### 4.5.3.1.1 Evaporated Molybdenum\*

Several seals in the form of tab peel assemblies were made using sapphire bars one-tenth inch square and one inch long. Evaporated metallizing was applied to one of the polished 0.1" x 1.0" sides. The metallizing consisted of a flash of titanium, a 0.8 micron layer of molybdenum, and a flash of copper which was followed by a 0.5 mil copper plate. A 15 mil cupro-nickel tab was brazed on with either copper braze (1120°C for 3 minutes) or Cu-Ag (860°C for 2 min.).\*

The metal tab was removed by grasping one end of it and pulling in a direction perpendicular to the plane of the metal-sapphire interface. This was accomplished by holding the substrate in the lower jaws of an Instron testing machine, the metal tab in the upper jaws, and pulling apart at the rate of one inch per minute cross-head speed. The failure strength was recorded continuously as in the drum peel test described earlier.

The results are presented in Table 4-43 with some additional tab peel data using beryllia Body BA as the substrate and both evaporated and standard P-1 metallizing. The strength of most seals was low, but one evaporated seal on sapphire and all four standard metallized seals were

---

\*See also Table 4-40.

TABLE 4-43  
Tab Peel Results

Substrate	Metallizing	Braze	Pull Strength, lbs	
			Max.	Min.
Sapphire	Evap Mo	Cu	0.6	0.4
"	Evap Mo	Cu	0.9	0.6
"	Evap Mo	BT	0.6	0.4
"	Evap Mo	BT	6.5	4.5
BeO*	Evap Mo	Cu	1.25	1.0
"	Evap Mo	Cu	1.8	0.8
"	P-1	Cu	3.6	1.5
"	P-1	Cu	5.5	1.0
"	Evap Mo	BT	0.3	0
"	Evap Mo	BT	0	0
"	P-1	BT	2.8	1.8
"	P-1	BT	6.5	3.0

\*Body BA: 99.5% BeO



moderately strong. The results at least demonstrated that a strong evaporated seal can be made to sapphire, although not on a reliable basis as yet. Improving the reliability of this seal forming method is a worthy goal of a future study.\*

#### 4.5.3.1.2 P-2M Metallizing on Sapphire

P-2M metallizing paint was prepared from pure  $\text{MoO}_3$  and was ball milled in a molybdenum-lined ball mill with molybdenum grinding media. It was the same as P-4M except that P-2M used  $\text{MoO}_3$  while P-4M used powdered molybdenum metal.

P-2M paint was applied to sapphire discs of sufficient size (0.625 in. O. D.) to be brazed between the tensile testing faces of two CLM-15 ceramic test pieces. The paint was sintered at  $1600^\circ\text{C}$ , resulting in a soft, powdery layer which was not well sintered within itself, but which did adhere sufficiently to the sapphire so that it was very difficult to scrape all metal off the surface of a test piece.

The metallized sapphire discs were then copper plated and copper brazed between two CLM-15 test pieces as shown in Figure 4.60. Half the samples were assembled with 15 mil, 70/30 Cu/Ni washers and half without washers. Specimens without washers averaged around 1900 psi tensile strength; those with washers were near 2800 psi. About half the seals were vacuum tight. (P-1 metallizing normally gives strengths in the range of 5000-10,000 psi on sapphire.)

Post-test metallurgical examinations of polished seal cross-sections (see Figure 4.73a x 800) revealed that the copper from the plating and braze permeated the voids of the very porous metallizing and readily penetrated to the sapphire surface. Molybdenum particles were in intimate contact and apparently adhered well to the sapphire surface.

---

\*Future seals should employ thicker molybdenum metallizings in order to resist attack by the cupro-nickel braze phase; and for a Cu-Ag braze, also a 0.5 mil barrier nickel plate (see Figure 6.29 (top) ); in order to prevent penetration of the Cu-Ag braze along the copper grain boundaries and subsequent attack on the molybdenum. See 6th Quarterly Report, Figs. 4.14, 4.15, 4.11 and section 4.5.3, also this report, Figs. 6.33 and 6.74 (bottom). Brazing with Cu-Ag at  $800^\circ\text{C}$  rather than  $860^\circ\text{C}$  should also be tried.

This provided further evidence of a non-glassy phase bonding mechanism. It is possible that such bonding could occur by bringing the reduced metal powder into intimate contact with the clean sapphire surface, but a very likely contributor to this bonding mechanism is the additional molybdenum braze or "blush" which is deposited on the sapphire during the  $\text{MoO}_3$  reduction process. The adherence mechanism of the molybdenum braze is essentially the same as that of evaporated molybdenum metallizing.

#### 4.5.3.2 Crystal Size Factor

In order to isolate the effect of alumina grain size, the special ceramics 941 (1650) and 942 (1700) were re-fired for up to 50 hours at  $1600^\circ\text{C}$ ; i.e., for 2, 5, 10, 20 and 50 hours respectively. They were then metallized with P-4M paint at  $1600^\circ\text{C}$  and brazed with copper to Kovar tabs.

No significant correlation with crystal size could be determined using the small sample size of two. (See Section 4.5.2.1.6.)

#### 4.5.3.3 Glassy Phase Devitrification

Several anomalously high results in the strength tests conducted under Sections 4.5.2.1.6 and 4.5.2.1.7 were explained on the basis of metallizing glassy phase devitrification phenomena. Additional data was therefore obtained which helped to define the conditions under which the glassy phase of the ceramic-metallizing interface tend to precipitate the secondary crystalline phases, anorthite and gehlenite. An attempt was then made to relate this precipitation data to seal strength.

Two series of experiments were conducted. The first series consisted of an examination of the seals made earlier and reported in Figures 4.64 to 4.69. The second series was designed to eliminate some of the extraneous variables present in the first test series.

##### 4.5.3.3.1 First Series

Eleven drum peel samples of both 941 and 942 alumina ceramics representing several body firing temperatures, metallizing sintering temperatures, and two braze cycles were examined after peel testing to determine the presence of secondary phases. All metallic deposits were

removed from the surface by means of a 1:1 warm nitric acid etch until all chemical action ceased. The surface thus exposed was given an X-ray diffraction analysis.

The results of the analyses are presented in Table 4-44. The samples are divided into two groups, weak and strong, according to the results of the drum peel test. The second, third, and fourth columns indicate the thermal history of each sample, and the last column lists the types and relative amounts of secondary crystalline phases detected on the formerly metallized surface.

All the strong seals had little or no secondary crystalline phases present, while nearly all the weak seals had some amount of anorthite and/or gehlenite present in the glassy interface layer. The presence of secondary crystalline phases was generally related to the braze cycle to which the parts were exposed. This association also held for seal strength. Copper brazes generally resulted in weak seals and a partially devitrified glassy phase. The opposite was true of copper-silver braze.

The difference in devitrification tendencies can be attributed to the difference in braze temperatures, but to associate seal strength with the absence or presence of a secondary crystalline phase on the basis of these data would be premature. The data reported in Table 4-44 may be misleading because of the presence of other factors which also affect the seal strength. One such factor is the introduction of considerable thermal expansion mismatch between the Kovar peel tab and the ceramic when the assembly is brazed above the BT braze temperature. Thus the copper brazed seals have much more internal stress than the BT brazed seals, and this may account for their generally weaker condition. This variable is eliminated in the second series of experiments in which devitrification is produced in some samples by a heat treatment separate from the braze cycle. All samples were brazed with BT, so that the only major variable was the amount of secondary crystalline phase present.

#### 4.5.3.3.2 Second Series

Sets of 941 (1650) and 942 (1700) test pieces were metallized with P-4M metallizing sintered at 1600°C. One set (Group A) was kept as a standard and other sets were subjected to wet and dry hydrogen firings to 1100°C to simulate extended copper braze cycles. Kovar or cupronickel tabs were brazed on with BT, and peel tests were made.

TABLE 4-44

Secondary Phases Found in Ceramic-Metallizing Interface  
by X-Ray Diffraction Analysis

<u>STRONG SEALS</u>				
Body Type	Body Firing Temp.	Metallizing Temp.	Braze & Temp.	Type and Amount of Secondary Phases Present
941	1550	1800	Cu-1100°C	None detected
941	1550	1800	BT-810	N.D.
942	1650	1800	"	Gehlenite: VST
942	1650	1800	"	N.D.
<u>WEAK SEALS</u>				
942	1650	1800	Cu-1100	Anorthite: minor
942	1650	1600	"	An.:++,Gehl.:VST
942	1700	1800	"	N.D.
942	1750	1600	"	An.:Minor,Gehl.: minor
941	1550	1800	"	An.:VST,Gehl.:++
941	1600	1800	BT-810	N.D.
941	1600	1800	Cu-1100	Gehl.:VST

Amount present in Decreasing Order:

Most: ++  
 ↓  
 +  
 Minor  
 ↓  
 Least: V.S.T. = very slight trace

All remaining metallic molybdenum was then removed by a warm nitric acid leach, and the formerly metallized surface was subjected to X-ray diffraction analysis to identify crystalline phases other than alpha-alumina.

Peel test results on two such runs are presented in Table 4-45 and the X-ray data are presented in Table 4-46. Based on the general trends shown by the entire data, interpretive plots of peel strength versus amount of crystal precipitation, and both peel strength and crystal growth versus time are presented in Figures 4.74 - 4.81.

These X-ray diffraction crystallographic results may be compared with those presented in Table 4-12. The results of Table 4-12 show that the 1425°C fire is able to devitrify the anorthite phase completely (8.7%) in the 942 body, as it is heated to just 75°C below the liquidus temperature of this composition. The 1600°C fire\* is above the eutectic temperature, 1500°C (Figure 4.04), and rapid cooling results in only partial crystallization of the glass phase as shown by the zero hold time specimen. Subsequent reheating to 1100°C results in significant anorthite devitrification.

For the 941 body, Table 4-12 shows no gehlenite precipitation. The 1600°C fire\* and/or the presence of molybdenum surface nucleation sites has induced some gehlenite crystallization in the zero hold time sample.

In the case of the dry H<sub>2</sub> fire on the 941 ceramics, there is a general relationship between seal strength and glass phase devitrification up to the 20-minute time period as shown in Figures 4.74 and 4.75.

The 20 minute time corresponds to maximum devitrification of the glassy phase with the appearance of an anorthite phase, Figure 4.75. Beyond this time limit, it is apparent that ionic flow and/or diffusion of glass from the interior to the surface is taking place, which resorbs the gehlenite and anorthite crystallites in the metallizing layer. This in general results in a loss of seal strength.

It is noted that the strength results are, in general, higher with a cupro-nickel tab than with a Kovar tab. The cupro-nickel tab must induce less stress into the seal area.

\*in the present test series

TABLE 4-45

Peel Strength of Seals to Heat Treated Ceramics  
Kovar Unless Otherwise Indicated as Cupro-Nickel (cn)

I.D.	Treatment	941 (1650)		942 (1700)	
		Run #1	Run #2	Run #1	Run #2
A	Standard	1.33 (cn)	5.5	1.0 (cn)	5.7
B	1100°C, Dry H <sub>2</sub> , 1 min.	4.6 (cn)	2.4	4.5 (cn)	1.4
D	" 5 min.	5.2 (cn)	3.3	1.0 (cn)	3.1
E	" 20 min.	7.2 (cn)	4.6	3.1 (cn)	1.9
F	" 60 min.	6.3	2.5	1.0	6.4
G	" 180 min.	2.9	2.4	2.8	1.8
C	1100°C, Wet H <sub>2</sub> , 1 min.	7.0	5.1	1.5	5.5
H	" 5 min.	5.9	8.9	4.5	3.0
J	" 20 min.	5.9	7.5	4.2	4.3
K	" 60 min.	3.8	7.8	1.0	6.1
L	" 180 min.	3.6	9.8	1.7	4.2

TABLE 4-46

Secondary Phases Present in Ceramic-Metallizing Interface  
by X-Ray Diffraction Analysis

I.D.	Treatment	941 (1650)		942 (1700)	
		Crystal Precipitation Level Anorthite	Crystal Precipitation Level Gehlenite	Crystal Precipitation Level Anorthite	Crystal Precipitation Level Gehlenite
A	Standard	-	6	6	-
B	1100°C, Dry H <sub>2</sub> , 1 min.	-	5	7	-
D	" 5 min.	10	2	6	-
E	" 20 min.	10	1	2	-
F	" 60 min.	-	6	8	-
G	" 180 min.	-	4	4	-
C	1100°C, Wet H <sub>2</sub> , 1 min.	10	6	1	-
H	" 5 min.	-	-	7	-
J	" 20 min.	11	5	5	-
K	" 60 min.	10	3	7	-
L	" 180 min.	9	5	3	-

NOTE: Order of amounts present:

1 - Most  
↓  
11 - Least

All relative to each other.

Absolute Magnitude: 8%

Peel Strength, Pounds

7

6

5

4

3

2

1

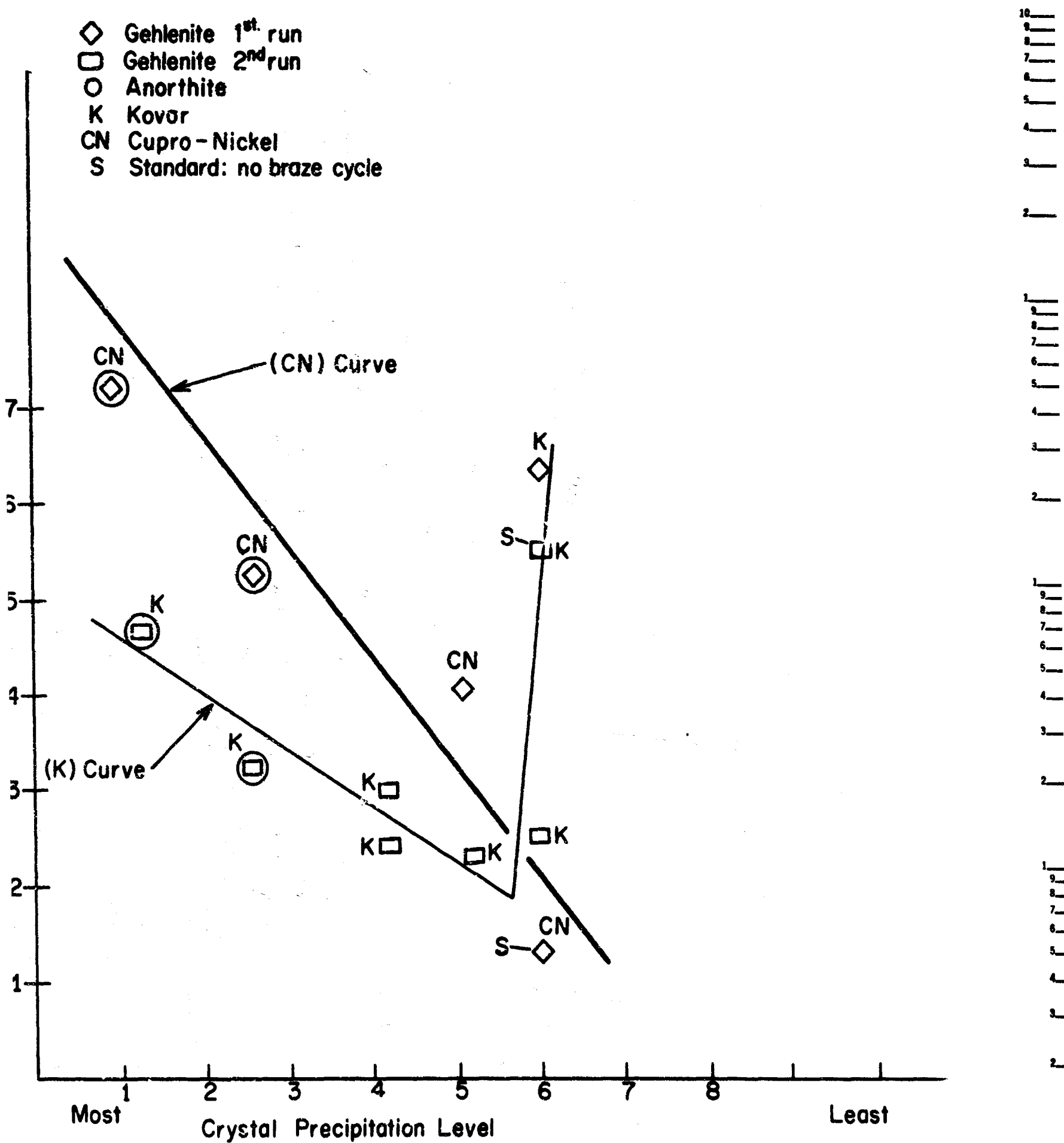


Figure 4.74: Peel strength versus secondary crystallite level in 941 ceramic after simulated braze cycles in dry hydrogen at 1100°C for various times. Kovar (K) or cupro-nickel (CN) peel tabs subsequently brazed at 800°C with Cu-Ag.



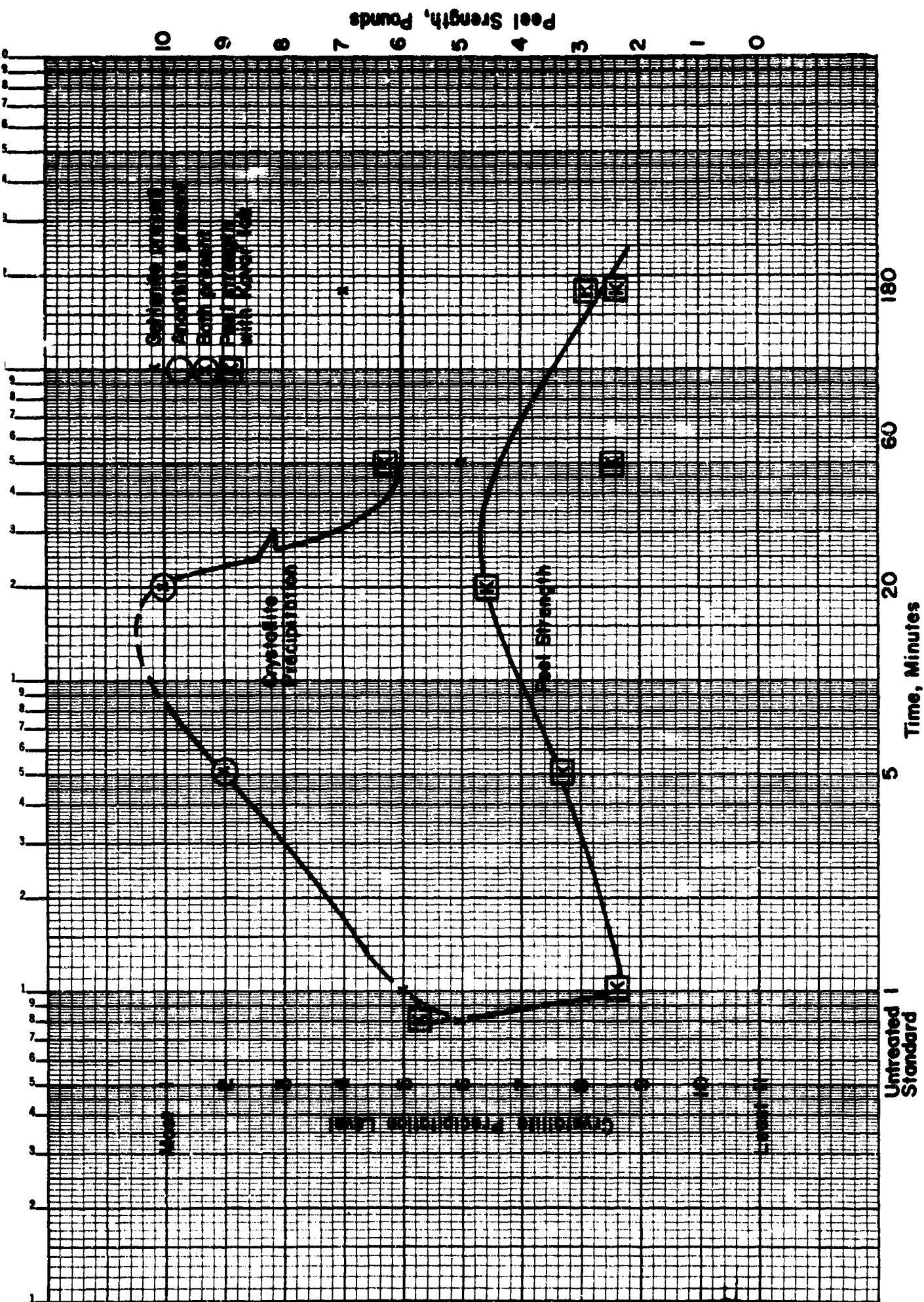


Figure 4.75: Secondary crystallite level and peel strength of 941 ceramic after simulated braze cycles in dry hydrogen at 1100°C for various times. Kovar peel tabs subsequently brazed at 800°C with Cu-Ag.

Peel Strength, Pounds



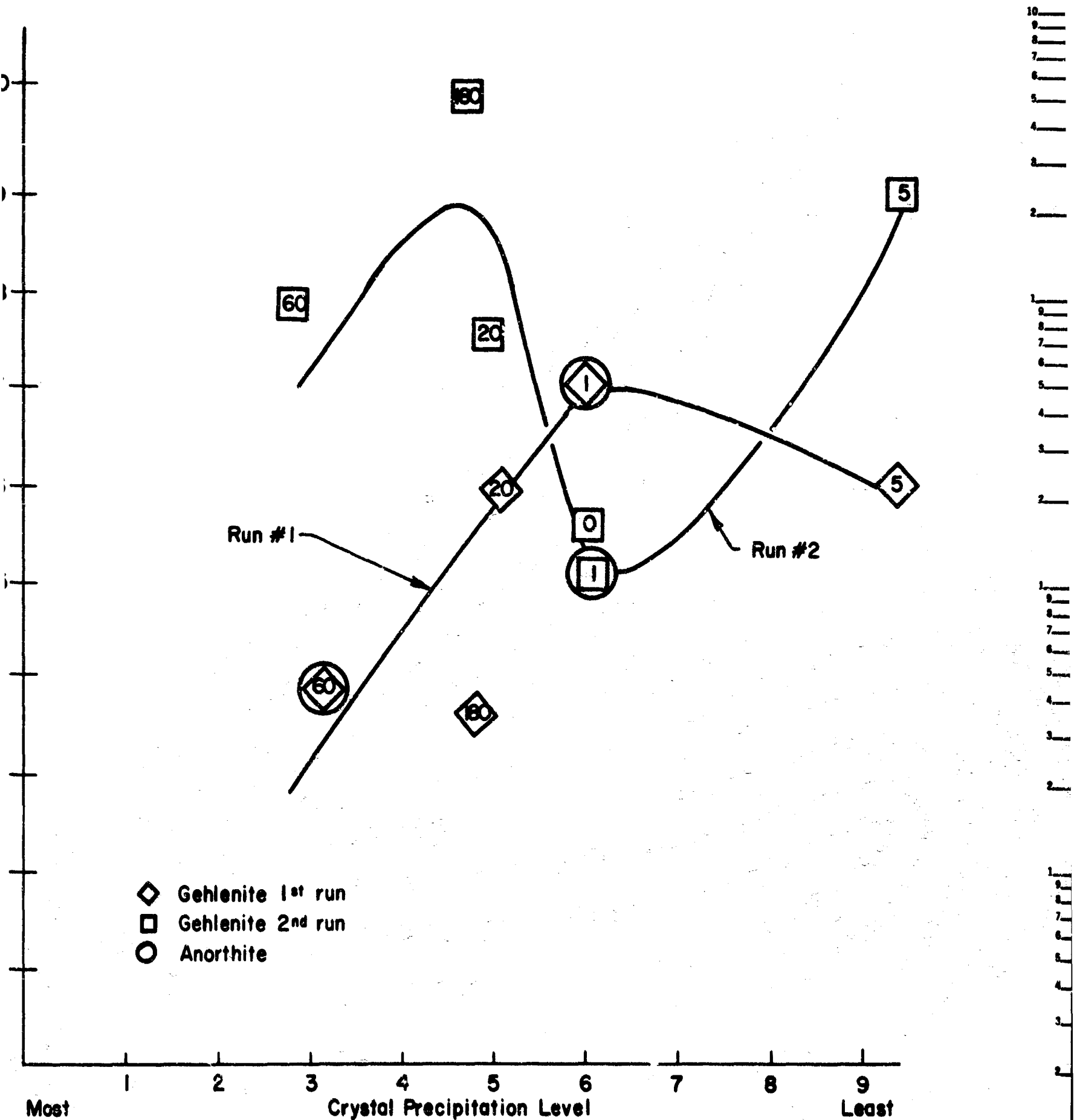


Figure 4.76: Peel strength versus secondary crystallite level in 941 ceramic after simulated braze cycles in wet hydrogen at 1100°C. Kovar peel tabs subsequently brazed at 800°C using Cu-Ag. Numbers indicate time of simulated braze cycle.

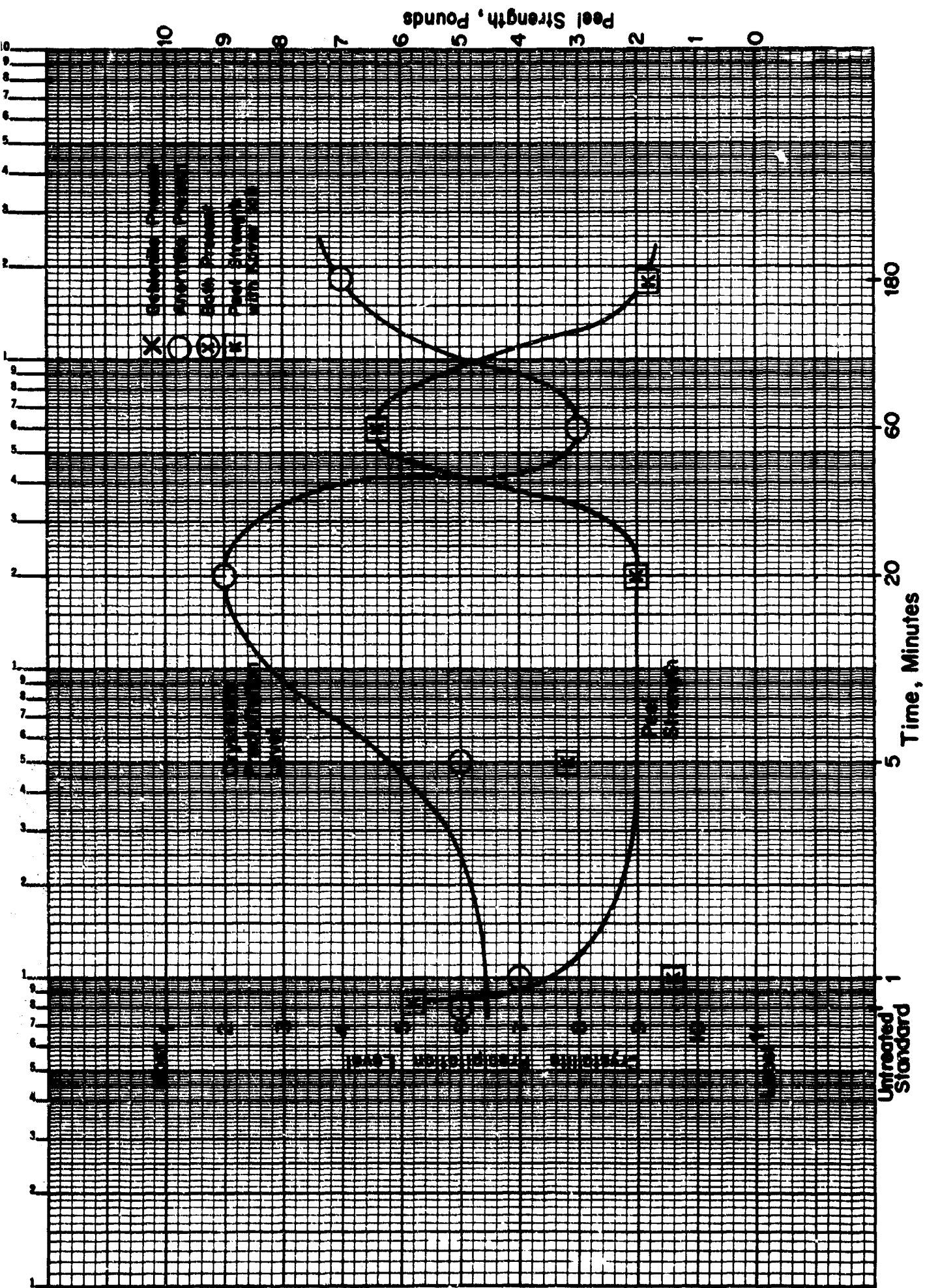


Figure 4.77: Secondary crystallite level and peel strength of 941 ceramic as a function of the length of time of simulated braze cycles at 1100°C in wet hydrogen. Kovar peel tabs subsequently brazed at 800°C with Cu-Ag.

Peel Strength, Pounds

1. 2. 3. 4. 5. 6. 7. 8. 9. 10

10  
9  
8  
7  
6  
5  
4  
3  
2  
1

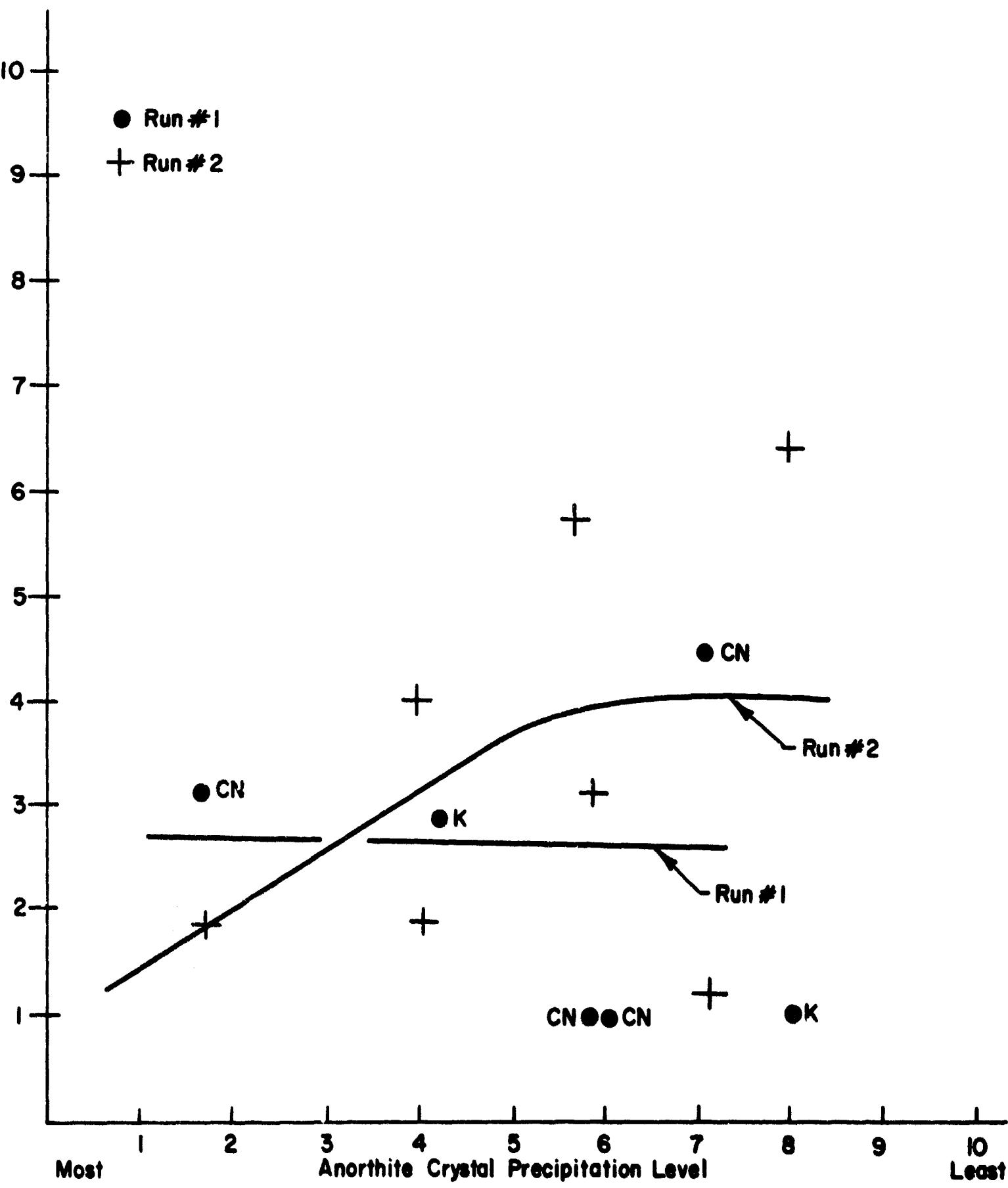


Figure 4.78: Peel strength versus secondary crystallite level in 942 ceramic after simulated braze cycles in dry hydrogen at 1100°C for various times. Kovar (K) on cupro-nickel (CN) peel tabs subsequently brazed at 800°C with Cu-Ag.

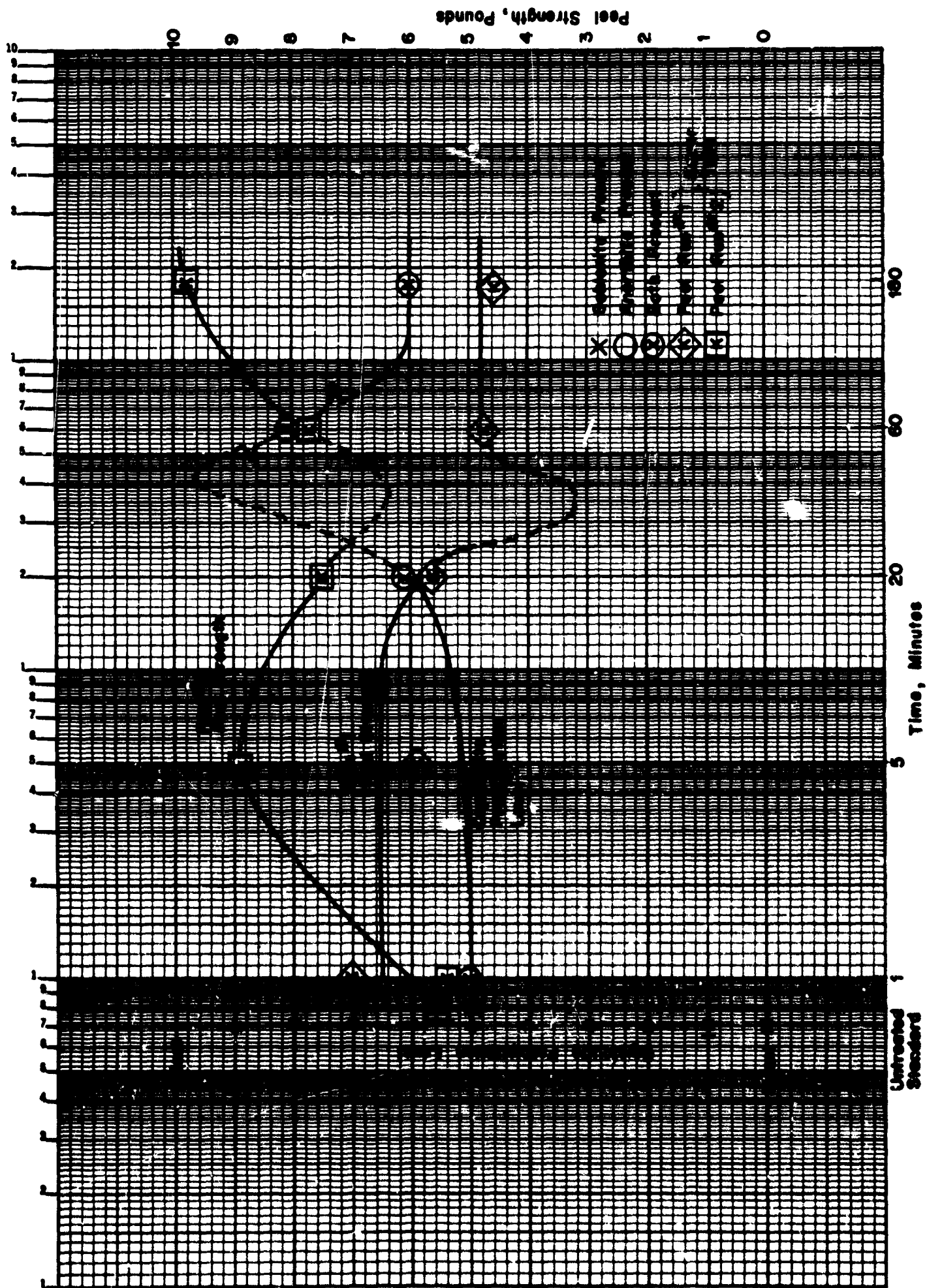


Figure 4.79: Secondary crystallite level and peel strength of 942 ceramic after simulated braze cycles in dry hydrogen at 1100°C for various times. Kovar peel tabs subsequently brazed at 800°C with Cu-Ag.

Peel Strength, Pounds

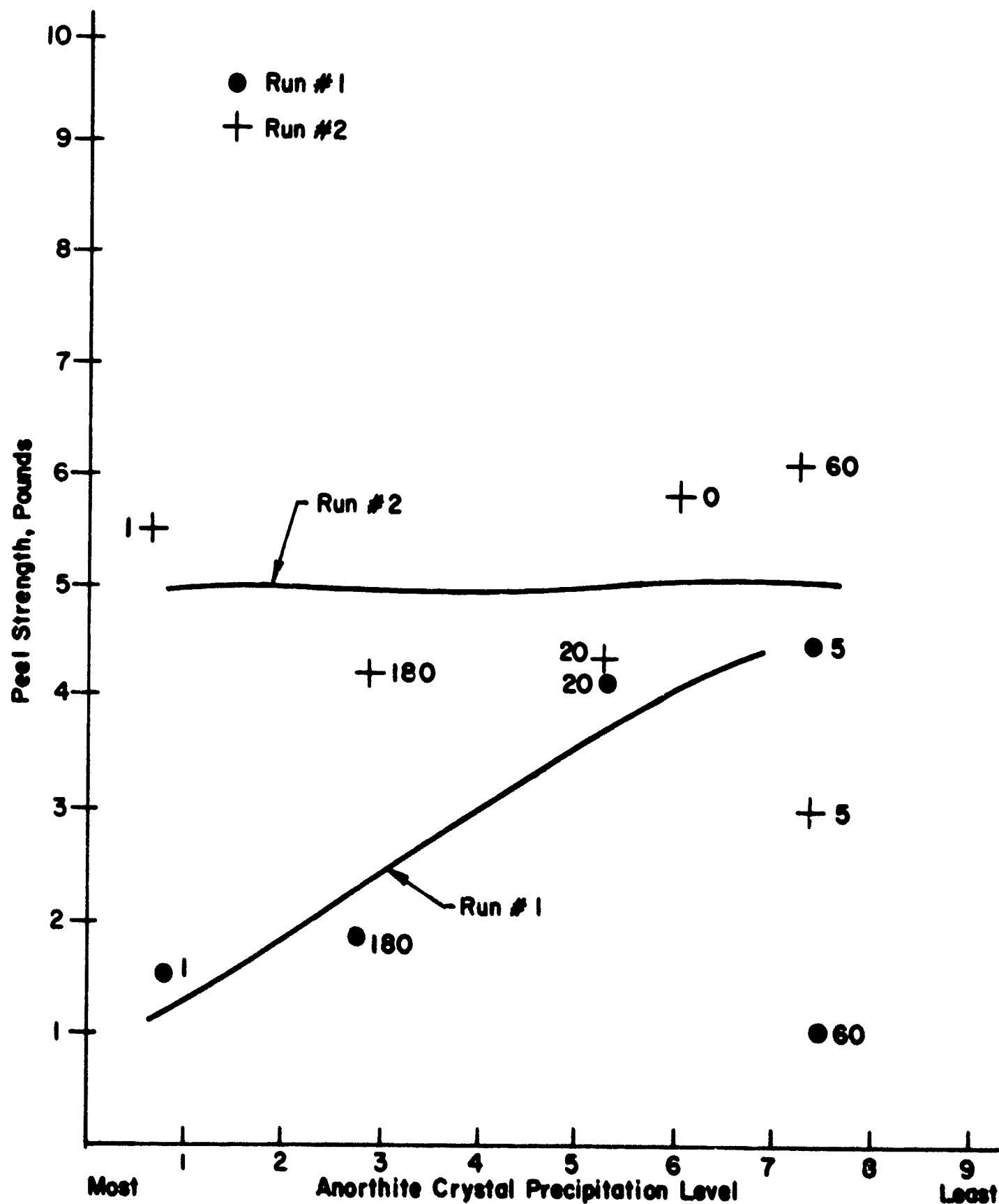


Figure 4.80: Peel strength versus secondary crystallite level in 942 ceramic after simulated braze cycles in wet hydrogen at 1100°C. Kovar peel tabs subsequently brazed at 800°C using Cu-Ag. Numbers indicate time of simulated braze cycle.

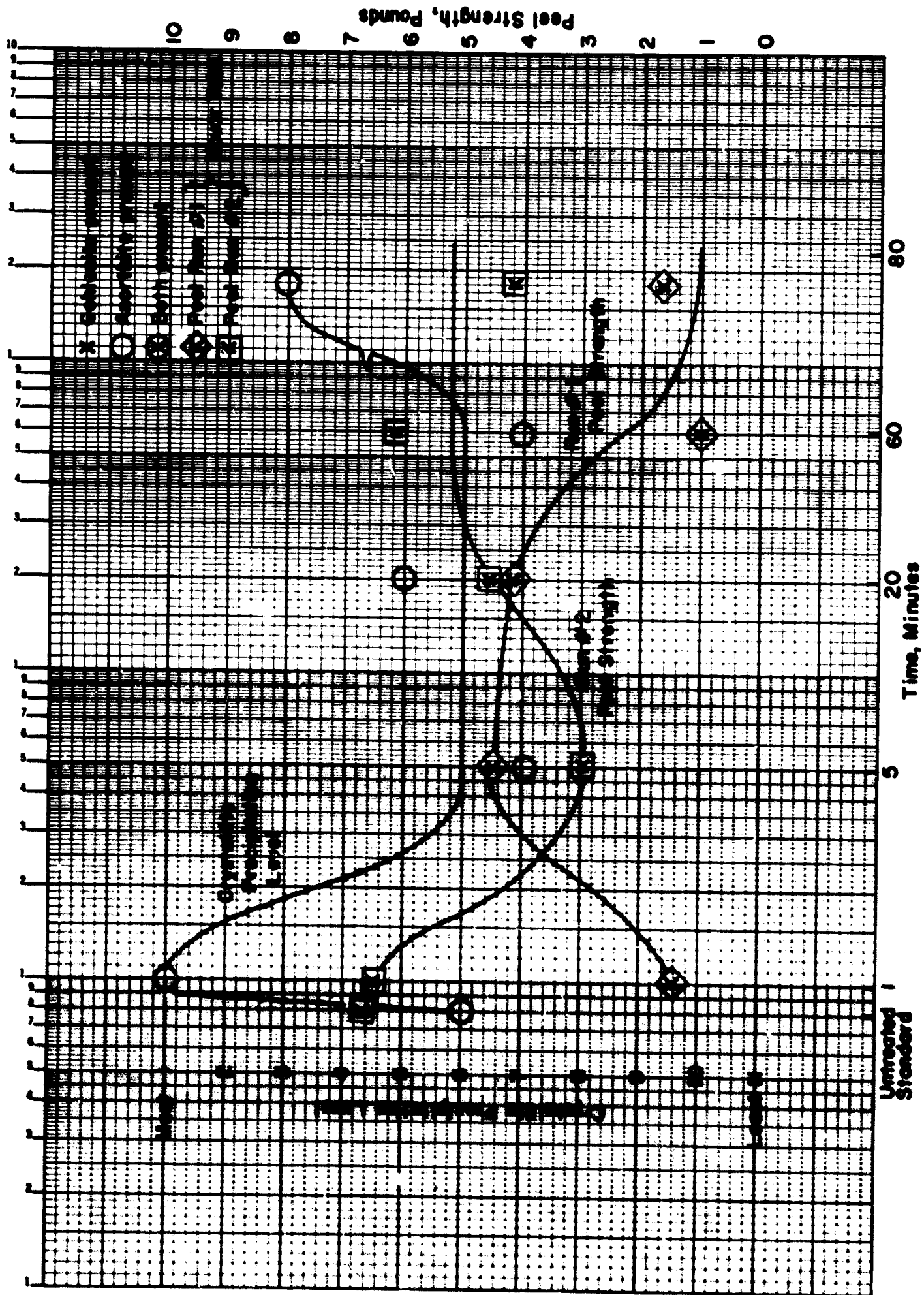


Figure 4.81: Secondary crystallite level and peel strength of 942 ceramic as a function of the length of time of simulated braze cycles at 1100°C in wet hydrogen. Kovar peel tabs subsequently brazed at 800°C with Cu-Ag.



The results of the wet hydrogen fire on the 941 metallizing show no direct relationship of peel strength with glassy phase devitrification, Figure 4.76.

General trends of both properties are noted with time, however, Figure 4.77, indicates that a third uncontrolled variable is present. This could be related to furnace conditions as the two runs show different peel strengths (glass diffusion and flow-out are very sensitive to furnace atmosphere). Figure 4.77 might be considered to show an inverse relationship of peel strength with crystal precipitation.

Again the interesting effect of increasing and decreasing gehlenite precipitation is noted, in this case, always associated with anorthite precipitation.

Inspection of the data on the 942 ceramics shows an inverse relationship of crystal precipitation amount with peel strength, the cupro-nickel metal member again not inducing as much stress into the seal and therefore showing no tendency to decrease in strength with increased crystal precipitation.

Again both in a wet or dry atmosphere crystal precipitation increases to a maximum as a function of time and then apparently decreases, Figures 4.78 through 4.81.

The main observations may be summarized:

- 1) There is a relationship of glassy phase devitrification with strength. In one case, seal strength increases with "devitrite" amount; in three cases, it tends to decrease. It might be hypothesized that in the first case, a highly siliceous glass phase remains, but not in the other three cases.
- 2) A qualitative relationship in (1) is obscured by:
  - (i) other variables
  - (ii) the small sample size employed, (strength data is essentially statistical)
  - (iii) the semi-quantitative nature of the X-ray data
  - (iv) the small amount of data obtained.



- 3) Glassy phase devitrification is a maximum between 5-30 minutes after start of the 1100°C soak. After the maximum is reached, the surface crystal species is resorbed. This resorption can be due to migration of ionic species from the interior of the specimen to the highly non-equilibrium surface grain boundary phase. (See Tables 4-10 and 4-12 and their accompanying discussion.) This diffused glass phase may again devitrify after a further long holding time (180 minutes).
- 4) A cupro-nickel metal member induces less stress into the seal area than a Kovar metal member.

#### 4.5.3.4 Effect of Metal Member

All tensile test specimens in the previous study employed 70-30 cupro-nickel metal member because of its known desirability, e.g., adequate strength and good ductility. However, a special comparison was made between 70-30 cupro-nickel and Kovar (Fe-Ni-Co) to demonstrate the difference between a "soft" and "hard" metal member. This comparison was made using special alumina body 992 metallized with P-4M, a combination known to give relatively weak seals which fail in the seal area rather than in the ceramic. (Copper braze was used.) This mode of failure was selected in order to make a clearer distinction between the effects of a "soft" and a "hard" metal member on the stress distribution in the seal area.

Tensile tests for seals with 70-30 cupro-nickel averaged 6180 psi versus 3885 psi with Kovar. Since all other sections of these seals were identical, the difference in strength was attributed to the additional ability of the cupro-nickel member to yield and relieve high local stress concentrations. The properties of the two metals which affect seal strength are compared in Table 4-47.

#### 4.5.3.5 Complex Metallizing Paints

A continuing seal parameter study must consider complex metallizing systems. However, this present work carries us to just the beginning of this subject.

In the electrical section the behavior of several metallizing paints on commercial ceramics, sapphire, 992 and Lucalox\* is noted, while a prior section has considered many

---

\*General Electric Co. Trade Name.

TABLE 4-47

## Mechanical Properties of Two Frequently Used Metal Members

Property	70-30 Cu-Ni	Kovar
Tensile strength, annealed	55,000 psi	75,000 psi
Yield Strength*		
0.5% offset	18,000 psi	54,700 psi
0.2% offset	14,500 psi	51,500 psi
Hardness, Rockwell B	40	82
Mean coefficient of thermal expansion to 1000°C	$16.3 \times 10^{-6}$	$13 \times 10^{-6}$

Note:

Although the nominal failure strength in neither type of seal exceeded the yield stress\* of its metal member, it is likely that in highly localized areas the stress was great enough to cause at least the softer metal to yield. This minute deformation allows the load to be transferred to a larger area. The total load then may be increased until the critical failure stress is exceeded at some point and followed immediately by failure of the sample.

\*Yield stress is an arbitrarily defined value whose magnitude is determined by the shape of the stress-strain curve. Some amount of plastic deformation may occur under stress much below the yield stress.

paints on bodies A, C, G and H.

It may be pointed out here the vastly different behavior of P-1 and P-7 metallizings on sapphire and 992 ceramic. It is noted that the sapphire surface is relatively not attacked by the P-7 metallizing, showing that the rate of chemical attack is low. The attack of the MnO-TiO<sub>x</sub> of the P-1 metallizing along preferential crystal directions of the sapphire is evident. (Figure 6.59.)

#### 4.6 Shear Test Study

The inadequacy of the tensile test has been previously pointed out.<sup>22</sup> It was therefore decided to initiate a study of shear test geometries as it was considered that shear is the predominant mode of stress under which failure of ceramic-to-metal seals occurs in actual tube practice. Encouraging results have been obtained in this initial exploratory study.

##### 4.6.1 Sample Geometry

The design chosen for shear testing seals utilized two ceramic cylinders, one of which fit inside the other. A short length (.050 to .100 in.) of the I.D. of the larger and the O.D. of the smaller cylinder were metallized and plated. The two parts were then mated and brazed together to form the assembly illustrated in Figure 4.82.

There are three advantages to this type of sample geometry. One is that the joint may be stressed in shear with a conventional compression tester requiring no unusual grippers or special equipment. Secondly, the specimen is such that the joint may be leak checked. This is not the case with the traditional overlapping plate geometry used for shear testing. A third feature is that all states of residual stress may be induced in the seal, which would aid in the design of O.D.-I.D. seals for such applications as pin seals and feed-thrus.

##### 4.6.2 Testing Methods

Two test loading techniques were investigated. In one, the specimen was placed with its big end down and a load was applied to the end of the small cylinder to cause the small cylinder to slip inside the larger one after failure of the joint. In another method, the specimen was inverted with the small cylinder in a hole and the end of the larger cylinder bearing on the rim of the hole. The load was

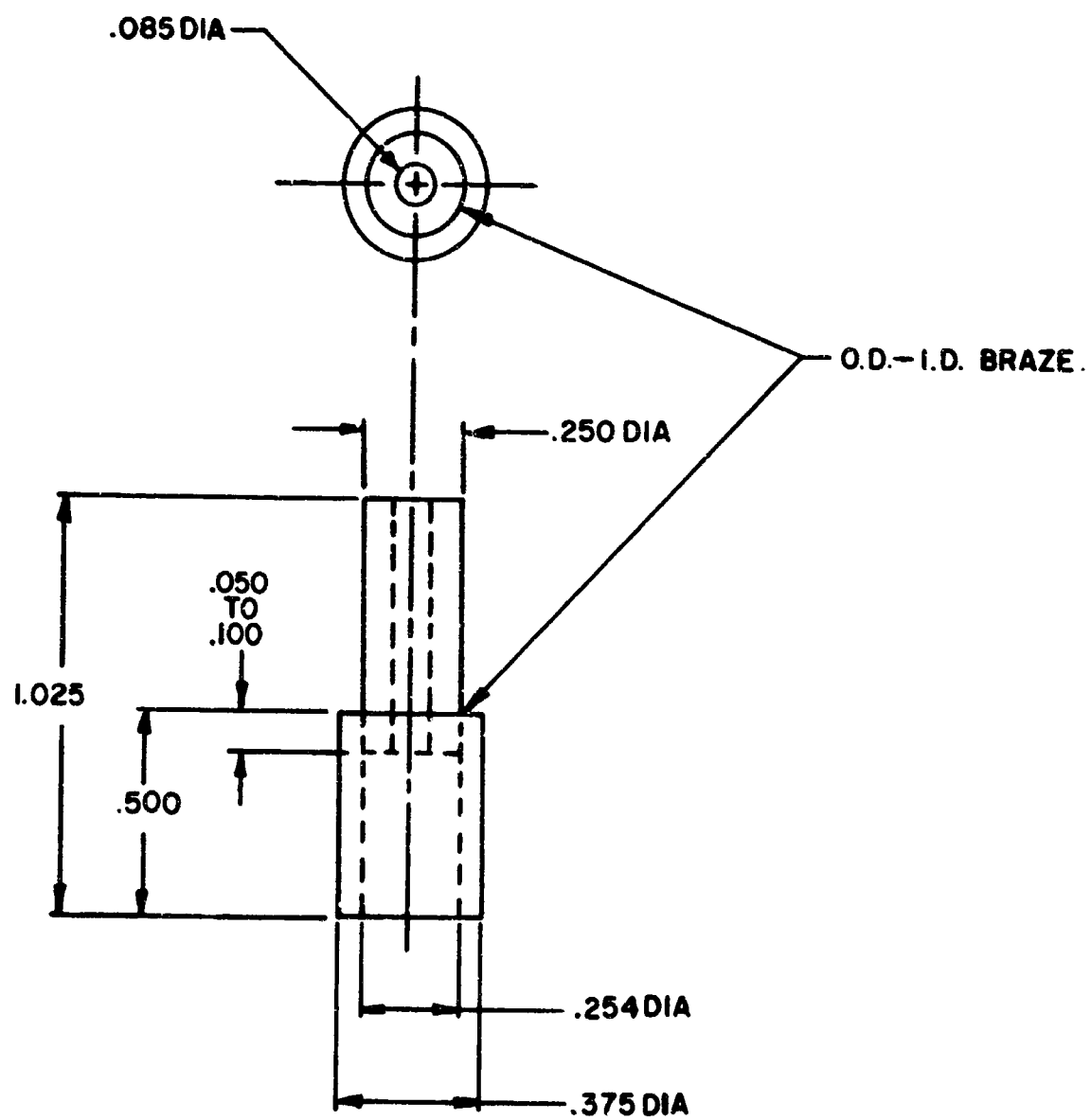


Figure 4.82: Shear test assembly consisting of two cylinders joined with an O.D.- I.D. braze.

applied through a rod to the end of the small cylinder inside the larger one which caused the smaller cylinder to be pushed out of the larger cylinder after failure of the joint. It was thought that the second method would avoid errors in results which might arise by wedging a braze fillet into the gap, because this method would push fillets out rather than wedge them in. However, the first method proved to be better because fillets were not a problem, and other difficulties arose in the inverted position which caused the outer ceramic cylinder to split open in nearly half the samples. Figure 4.83 shows a specimen in the preferred test position.

Materials used in the evaluation of this seal testing method included the typical braze metals, copper and BT (copper-silver eutectic), copper or nickel plating, P-1 metallizing, and cylinders of Body G ceramic, Kovar, or molybdenum. By selecting different combinations of materials for the inner and outer cylinder, the braze joint could be placed in any desired state of residual radial stress. A molybdenum outer cylinder brazed to a ceramic inner cylinder placed the joint in radial tension. A Kovar outer cylinder with a ceramic inner cylinder placed the joint in radial compression. The effect of residual seal stress on the ultimate seal shear strength could thus be studied by mixing materials and comparing results.

#### 4.6.3 Test Results and Discussion

The results of tests using several combinations of cylinder materials, plating, and braze are listed in Table 4-18. The table lists all materials used in each part of the seal structure, the residual radial stress which resulted from the combination, and the yield and failure stress of the joint. For the purpose of these tests, the yield stress was considered to be the stress at which plastic deformation began, or the first deviation from linearity of the stress-strain curve. This is not the conventional approach, in which it is defined as that stress at which some arbitrary amount of plastic deformation occurs (.2% or .5% offset), but it was suitably reproducible for the purposes of this work. With some specimens such as the ceramic-molybdenum combination (group 1) brittle failure occurred before plastic deformation, so no value for the yield stress could be obtained.

Yield occurred in all but a few specimens before failure, indicating deformation of the metallic portion of the seal occurred before brittle failure of the ceramic or metallizing. The yield stress varied considerably from one

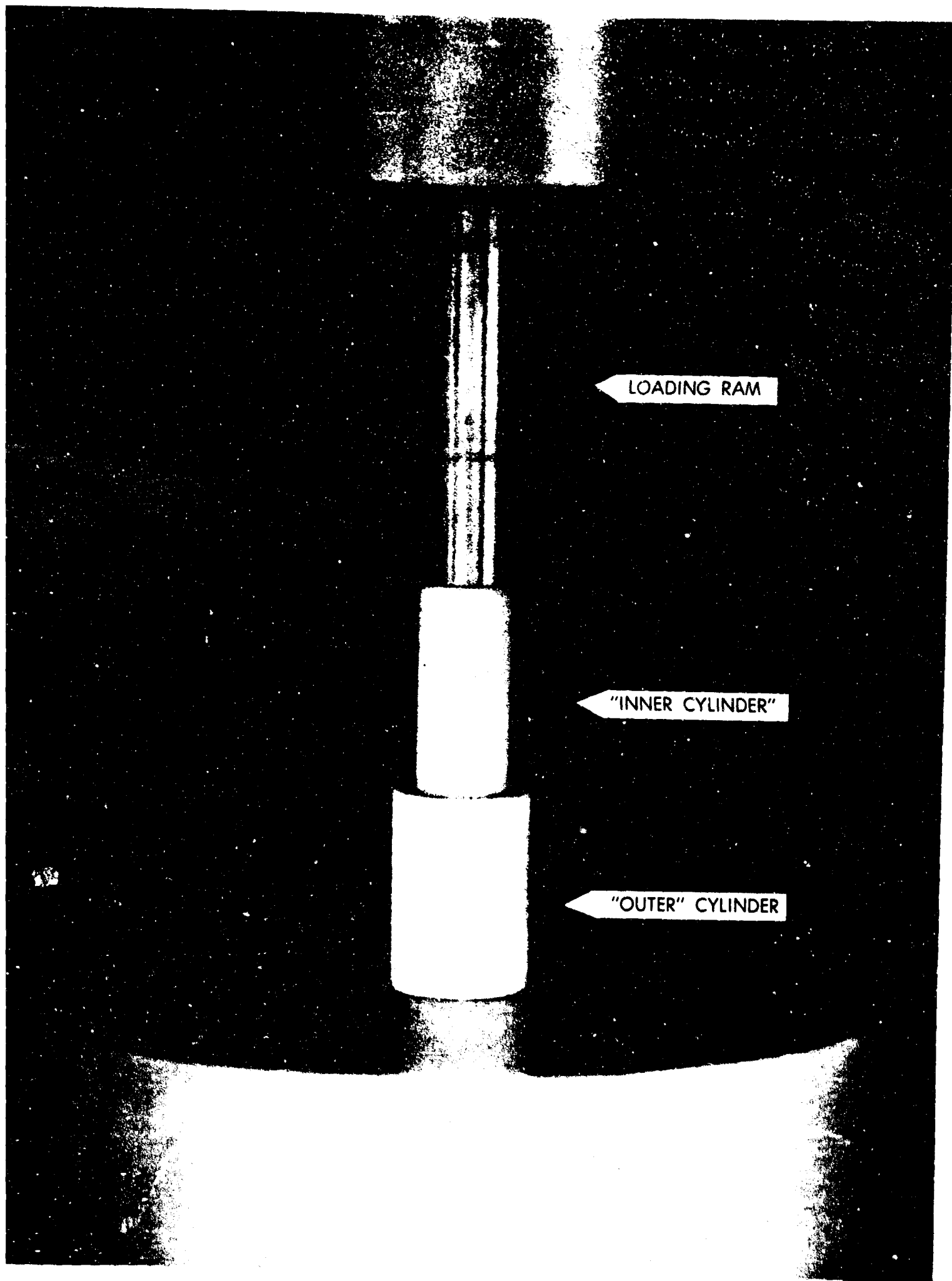


Figure 4.83: Concentric cylinder shear test specimen in loading position in Instron testing machine.

TABLE 4-48

Shear Test Results Obtained from Concentric Cylinder Specimen Geometry

Test Group <sup>+</sup>	Cylinder Inner	Material		Metallizing	Plating	Braze	Residual		Failure Stress, $T$ psi
		Outer					Stress in Joint	Yield Stress, psi	
1	Cer	Mo	P-1	Ni		BT	Ten.	N.D.	14,090
2	Kov	Cer	P-1	Ni		BT	Ten.	16,260	19,950
3	Cer	Kov	P-1	Ni		BT	Comp.	20,410	37,850
4	Cer	Cer	P-1	Ni		BT*	-	27,530	31,175
5	Cer	Cer	P-1	Ni		BT**	-	16,380	22,180
6	Cer	Cer	P-1	Cu		Cu	-	25,250	29,180
7	Cer	Cer	P-1	Cu		Cu	-	26,988	32,938

\*Braze length or cylinder overlap: 0.050 in.

\*\*Braze length or cylinder overlap: 0.075 in.

<sup>+</sup>Size of test group: 10 pieces.

group of samples to another, but was quite consistent within groups. This difference was expected to result from differences in the materials used to make the seal, but the dimensions of the braze gap seemed to have a much stronger effect. The residual stress induced in the joint definitely affected both the yield and the failure stress. In the case of group 1 samples, the joint may have been stressed in tension beyond its yield point, so that it failed in a brittle manner as soon as the shear stress was applied. No yield was observed in those samples before failure.

The shear failure stress of the test seals was most directly related to the state of residual stress in the joint, the dimensions of the braze gap, and the quality of the braze. The first four test groups best illustrate the effect of residual stress. The residual stress condition designed into each group was: (1) high degree of radial tension, (2) a moderate degree of radial tension, (3) a moderate degree of radial compression, and (4) practically no radial stress. The average failure stresses for these four conditions were 14,090 psi, 19,950 psi, 37,850 psi and 31,175 psi respectively. These results were qualitatively predicted from theory. The addition of a tensile stress component to the shear component contributes to the failure mechanism.

Test groups 4 and 5 illustrate the effect of braze gap dimensions and braze quality. The material compositions of the two were identical and braze conditions were the same, but the braze length (the amount the inner and outer cylinders were allowed to overlap) was 50 mils in group 4 and 75 mils in group 5. The longer brazes in group 5 were not the best quality because braze material did not flow sufficiently to completely fill the length of the gap. The difference in yield stress (4: 27,530 psi; 5: 16,380 psi) was more likely due to partial filling of the braze than any other cause. The braze area used to calculate the stress in group 5 was greater than the amount of area actually filled with braze, so the calculated stress was smaller than the true stress level in each particle of material.

A comparison of results in groups 4 and 6 shows some difference in yield and failure stress, but not as much as might be expected from the different brazes. The difference that did exist was probably related to the braze materials, but the similarity may be traced to the fact that the failure was a brittle failure which usually occurred in the metallizing-ceramic or metallizing-braze



interface. This was confirmed by visual examination of samples after testing.

Groups 6 and 7 illustrate the reproducibility of sample preparation and test technique. The two groups were assembled, brazed, and tested at different times, but the results from each were very similar.

The shear test method studied has considerable merit as a developmental or engineering test for seals because of the variety of data available from it. However, it may be less useful for basic seal mechanism studies because of the difficulty in avoiding residual stresses in the joint. (Even when identical materials are used for the inner and outer cylinders, the gap between them contracts with falling temperature.) Also, the ultimate state of stress from an atomistic viewpoint in either this shear test or a tensile test is that of tension, i.e. the atoms are pulled apart at failure. Even though the initial atomic movement in the shear test may be sliding motion (shear), the gradual necking in the joint caused by deformation leads to the introduction of a tensile component to the state of stress. The shear stress is then actually a vector with a shear (major) component and a tensile (minor) component. But since this is exactly the condition that exists at failure in an application such as a pin seal, it can be very useful as an engineering test.

1. S. S. Cole, H. W. Larisch, J. E. Inge, and K. H. Styhr, Jr., "Metal-to-Ceramic Seal Technology Study", Final Report, October, 1960, Sperry Gyroscope Company, Contract No. AF 30(602)2047, pg. 35.
2. "Tentative Method for Tension and Vacuum Testing Metallized Ceramic Seals", ASTM Designation: F19-61T, 1961 Book of ASTM Standards, Part 2, American Society for Testing and Materials, Philadelphia, Penn., 1961, pp. 1509-13.
3. E. F. Osborn and Arnulf Muan, Plate No. 1, "The System  $\text{CaO-Al}_2\text{O}_3\text{-SiO}_2$ ", in Phase Equilibrium Diagrams of Oxide Systems, The American Ceramic Society, Inc., Columbus, Ohio, 1960.
4. A. L. Gentile and W. R. Foster, "Calcium Hexaluminate and Its Stability Relations in the System  $\text{CaO-Al}_2\text{O}_3\text{-SiO}_2$ ", J. Am. Ceram. Soc., vol. 46 (2) 74-6 (1963).
5. E. T. Turkdogan and Patricia M. Bills, "A Critical Review of Viscosity of  $\text{CaO-MgO-Al}_2\text{O}_3\text{-SiO}_2$  Melts", Am. Ceram. Soc. Bull., vol. 39 (11) 682-7 (1960).
6. Paul Kozakevich, "Viscosity of Lime-Alumina-Silica Melts between 1600 and 2100°C", Metallurgical Society Conferences, vol. 7, Physical Chemistry of Process Metallurgy Part 1, Ed. George R. St. Pierre, Interscience Publishers, New York, N. Y., 1961, pp. 97-116.
7. J. S. Machin and Tin Boo Yee, "Viscosity Studies of System  $\text{CaO-MgO-Al}_2\text{O}_3\text{-SiO}_2$ : (II),  $\text{CaO-Al}_2\text{O}_3\text{-SiO}_2$ ", J. Am. Ceram. Soc., vol. 31 (7) 200-4 (1948).
8. L. R. Barrett and A. G. Thomas, "Surface Tension and Density Measurements on Molten Glasses in the  $\text{CaO-Al}_2\text{O}_3\text{-SiO}_2$  System", J. Soc. Glass Technol., vol. 43 179T-190T (1959).
9. T. B. King and P. J. Koros, "Diffusion in Liquid Silicates", Kinetics of High Temperature Processes, W. D. Kingery, Ed., Technology Press of Massachusetts Institute of Technology and John Wiley & Sons, Inc., New York, N. Y., 1959, pp. 80-85.
10. Helen Towers, Michel Paris, and John Chipman, "Diffusion of Calcium Ion in Liquid Slag", Am. Inst. Min. Met. Engr. Trans., vol. 197 1455-58 (1953).

11. Helen Towers and John Chapman, "Diffusion of Calcium and Silicon in a Lime-Alumina-Silica Slag", J. Metals, June, 1957, AIME Trans., vol. 209 (1957).
12. P. J. Koros and T. B. King, "The Self-Diffusion of Oxygen in a Lime-Silica-Alumina Slag", Based on a DSc. thesis by P. J. Koros, Mass. Inst. Tech., 1958.
13. John Henderson, Ling Yang, G. Derge, "Self-Diffusion of Aluminum in  $\text{CaO-SiO}_2\text{-Al}_2\text{O}_3$  Melts", Trans. of Metallurg. Soc. AIME, vol. 221 56-59<sup>3</sup> (1961).
14. L. Reed and L. R. Barrett, "The Slagging of Refractories I. The Controlling Mechanism in Refractories Corrosion", Trans. Brit. Ceram. Soc., vol. 54 (11) 671 (1955).
15. L. Reed and L. R. Barrett, "The Slagging of Refractories II. The Kinetics of Corrosion", Trans. Brit. Ceram. Soc., vol. 63 (10) 5-9-534 (1964).
16. Y. Oishi, A. R. Cooper, W. D. Kingery, "Dissolution in Ceramic Systems, III: Boundary Layer Concentration Gradients", J. Am. Ceram. Soc., vol. 48 (2) 88 (1965).
17. R. L. Coble, "Initial Sintering of Alumina and Hematite", J. Am. Ceram. Soc., vol. 41 (2) 55-62 (1958).
18. R. L. Coble, "Sintering Crystalline Solids. I. Intermediate and Final State Diffusion Models", J. Appl. Phys., vol. 32 (5) 787-792 (1961).
19. R. L. Coble, "Sintering Crystalline Solids. II. Experimental Test of Diffusion Models in Powder Compacts", J. Appl. Phys., vol. 32 (5) 793-799 (1961).
20. W. D. Kingery, Introduction to Ceramics, John Wiley & Sons, Inc., New York, N. Y., 1960, pg. 357.
21. W. D. Kingery, E. Niki, and M. D. Narasimhan, "Sintering of Oxide and Carbide-Metal Compositions in Presence of a Liquid Phase", J. Am. Ceram. Soc., vol. 44 (1) 29-35 (1961).
22. L. Reed, "Progress in Ceramic and Ceramic-to-Metal Seals", Presented at the 7th National Tube Techniques Conference, September 28-30, 1964, New York, N. Y.

23. C. A. Bruch, "Sintering Kinetics for the High Density Alumina Process", Am. Ceram. Soc. Bull., vol. 41 (12) 799-806 (1962).
24. George W. Morey, The Properties of Glass, Reinhold Publishing Corp., New York, N. Y., 1954.
25. Gerald B. Carrier, "Electron Microscopic Technique for Determining the Percent Crystallinity of Glass-Ceramic Materials", J. Am. Ceram. Soc., vol. 47 (8) 365-67 (1964).
26. Rustum Roy, "Note on the Role of Phase Equilibrium Considerations in Crystallization Studies of Glass", Read at Symposium on Nucleation and Crystallization Phenomena in Glasses and Melts, Presented by the American Ceramic Society in Toronto, Canada, April 25, 1961.
27. H. R. Wisely, "Investigation for the Development of Ceramic Bodies for Electron Tubes", Final Report, June, 1962, General Electric Company, Contract No. AF 19(604)-7410.
28. L. Reed, "Heat Treatment Studies on High Alumina Ceramics", Reprint from Sixth National Conference on Electron Tube Techniques", Pergamon Press, New York, N. Y., 1963.
29. Bennett S. Ellefson and Nelson W. Taylor, "Surface Properties of Fused Salts and Glasses: I. Sessile-Drop Method for Determining Surface Tension and Density of Viscous Liquids at High Temperatures", J. Am. Ceram. Soc., vol. 21 193-213 (1938).
30. L. Reed, R. McRae, C. Barnes, "Metallurgical Research and Development for Ceramic Electron Devices", Second Quarterly Report, January, 1963, Eitel-McCullough, Inc., Contract No. DA 36-039 SC-90903, Appendix I.
31. R. H. Berg, "Electronic Size Analysis of Sub-Sieve Particles by Flowing through a Small Liquid Resistor", Symposium on Particle Size Measurement, Special Technical Publication No. 234, American Society for Testing Materials, Philadelphia, Penn., 1958.
32. W. D. Kingery and M. Berg, "Study of the Initial Stages of Sintering Solids by Viscous Flow, Evaporation-Condensation, and Self-Diffusion", J. Appl. Phys., vol. 26 (10) 1205-12 (1955).
33. S. Cole, Jr. and H. Larisch, "Metal-to-Ceramic Seal Technology Study", First Technical Note, October, 1959, Sperry Gyroscope Company, Contract No. AF 30(602)2047, pg. 52.

34. Leonard Reed and R. C. McRae, "Evaporated Metallizing on Ceramics", Am. Ceram. Soc. Bull., vol. 44 (1) 12 (1965).
35. L. Reed, "Survey of the Factors Affecting Ceramic-to-Metal Sealing", Paper presented at the Fall Meeting of the Electronics Division of the American Ceramic Society, Philadelphia, Penn., September 16-18, 1964.
36. James R. Floyd, "Effect of Secondary Crystalline Phases on Dielectric Losses in High-Alumina Bodies, "J. Am., Cer. Soc. vol. 47 (11) 539-543 (1964).

Beryllia and quartz are important materials used as output windows in high power tubes. It was therefore necessary to investigate these materials on this program.

The investigation was confined to the investigation of commercial ceramics metallized with appropriate metallizing systems.

Beryllia ceramics are similar to alumina ceramics and come in 94% and 99.5% categories. Their microstructure is much like that of alumina ceramics as is shown in Fig. 5.01. Fused quartz is an entirely different material than beryllia or alumina, being glassy in nature rather than crystalline or a mixture of crystalline and glassy phases.

### 5.1 Beryllia Ceramics

Fig. 5.02 shows a 96% beryllia ceramic with P-1 metallizing sintered onto it. The bond strength in this system is about 8000 psi. This combination of materials represents the first commercial use of beryllia in an electron tube. (1957.) However, a significant increase in thermal conductivity can be made if a 99.5% beryllia ceramic is used in place of a lower beryllium oxide content ceramic. (Figure 2, showing this feature, is contained in the 2nd Quarterly Report.) Therefore, for this present study, we have considered 99.5% beryllium oxide ceramics exclusively. The chemical composition of the two bodies presently under consideration is given in Table 5-1.

The two 99.5% BeO bodies in the form of CLM-15 test pieces were metallized at 1425°C under the usual conditions of metallizing, using P-3 metallizing, and showed good tensile strength. Body BA had an average of 7200 psi (neck breaks) and Body EB had an average tensile strength of 13,300 psi. Body BA leaked, however, while Body BB was vacuum-tight. It was noted that Body BA showed extensive penetration of the melt-oxide phase metallizing into the beryllia ceramic. The depth of penetration was approximately three-sixteenths of an inch. Lower metallizing temperatures and different paints were next used on Body BA in order to improve the metallizing characteristics.

Polished sections of Body BB metallized with P-3 were prepared. Photomicrographs of metallizing sintered at 1325°C and 1425°C appear in Fig. 5.03. One notable feature

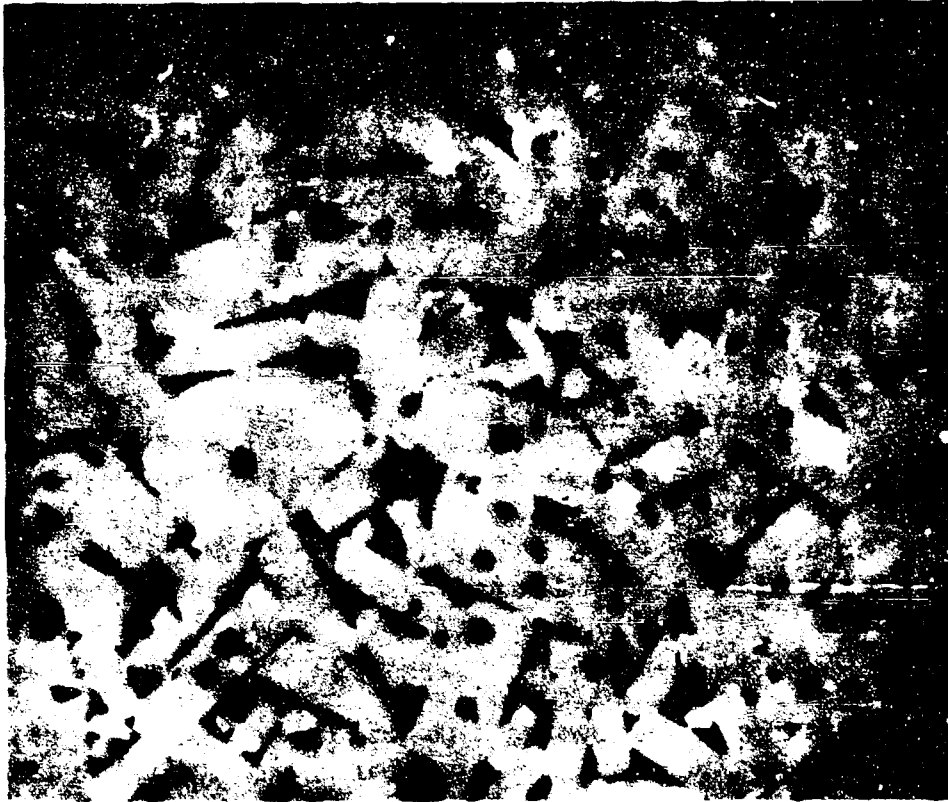


Figure 5.01: Microstructure of a 96% beryllia ceramic (400X) which shows similar characteristics to a 96% alumina ceramic.

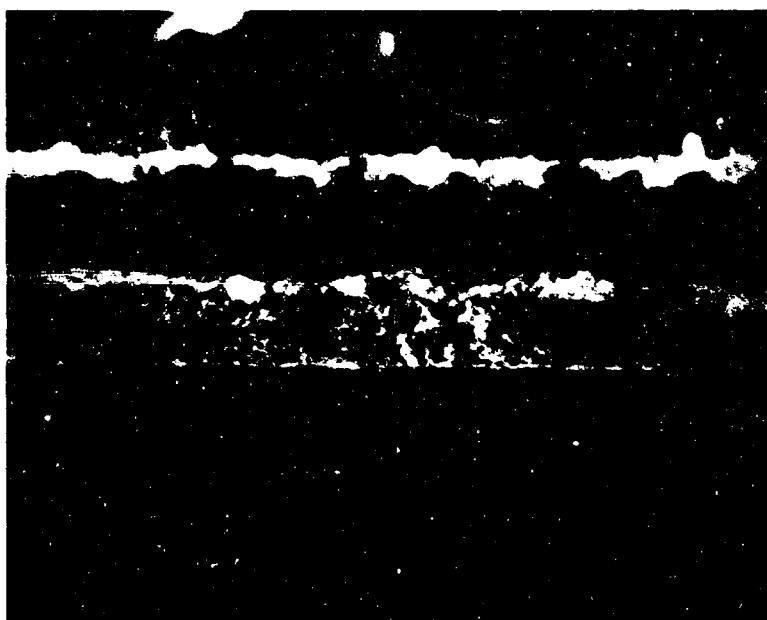


Figure 5.02: Microstructure cross-section of a ceramic metal seal of P-1 metallizing paint on a 96% beryllia ceramic (400X).



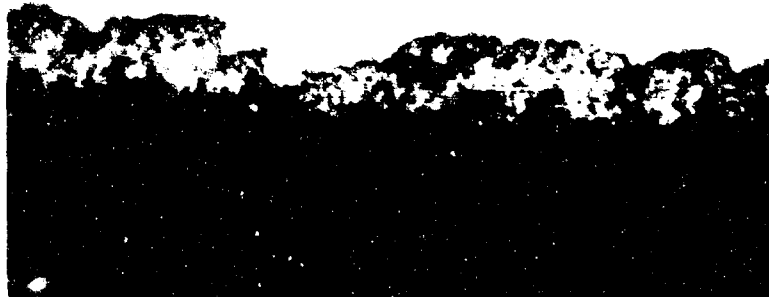


Figure 5.03: Photomicrographs of P-3 metallizing sintered at 1325°C (top) and 1425°C (bottom) on beryllia body BB. Cu-Au 60/40 braze, copper braze washer (400X).

TABLE 5-1

## Chemical Composition of Beryllia Ceramics

Oxide	Weight Per Cent Present	
	Body BA	Body BB
BeO	99.8	99.49
Al <sub>2</sub> O <sub>3</sub>	0.03	0.23
SiO <sub>2</sub>	0.01	0.16
MgO	0.20	0.07
CaO	0.10	0.01
Na <sub>2</sub> O	0.005	0.03
Fe <sub>2</sub> O <sub>3</sub>	0.01	0.01

of the metallizing in both photomicrographs is the presence of relatively large crystals in the glassy phase of the metallizing.

Microprobe analyses were made on seals made with P-3 metallizing on beryllia bodies BA and BB. This metallizing had been sintered at 1425°C. The data obtained with the microprobe are presented in Figs. 5.04 and 5.05. The bodies were analyzed for Mn, Si and Ti. The penetration of these elements into Body BA was extremely deep, being several thousand microns in each case. Penetration into Body BB was an order of magnitude less, ranging around 100 microns. The reason for this remarkable difference lies in the difference in microstructure and chemical composition of the two bodies. The prevalent secondary component in Body BA is MgO, while the most prevalent secondary components in Body BB are Al<sub>2</sub>O<sub>3</sub> and SiO<sub>2</sub> with some MgO. At the metallizing temperature, the secondary components in the beryllia combine with the non-metallic portion of the metallizing to form a modified melt phase. With very little

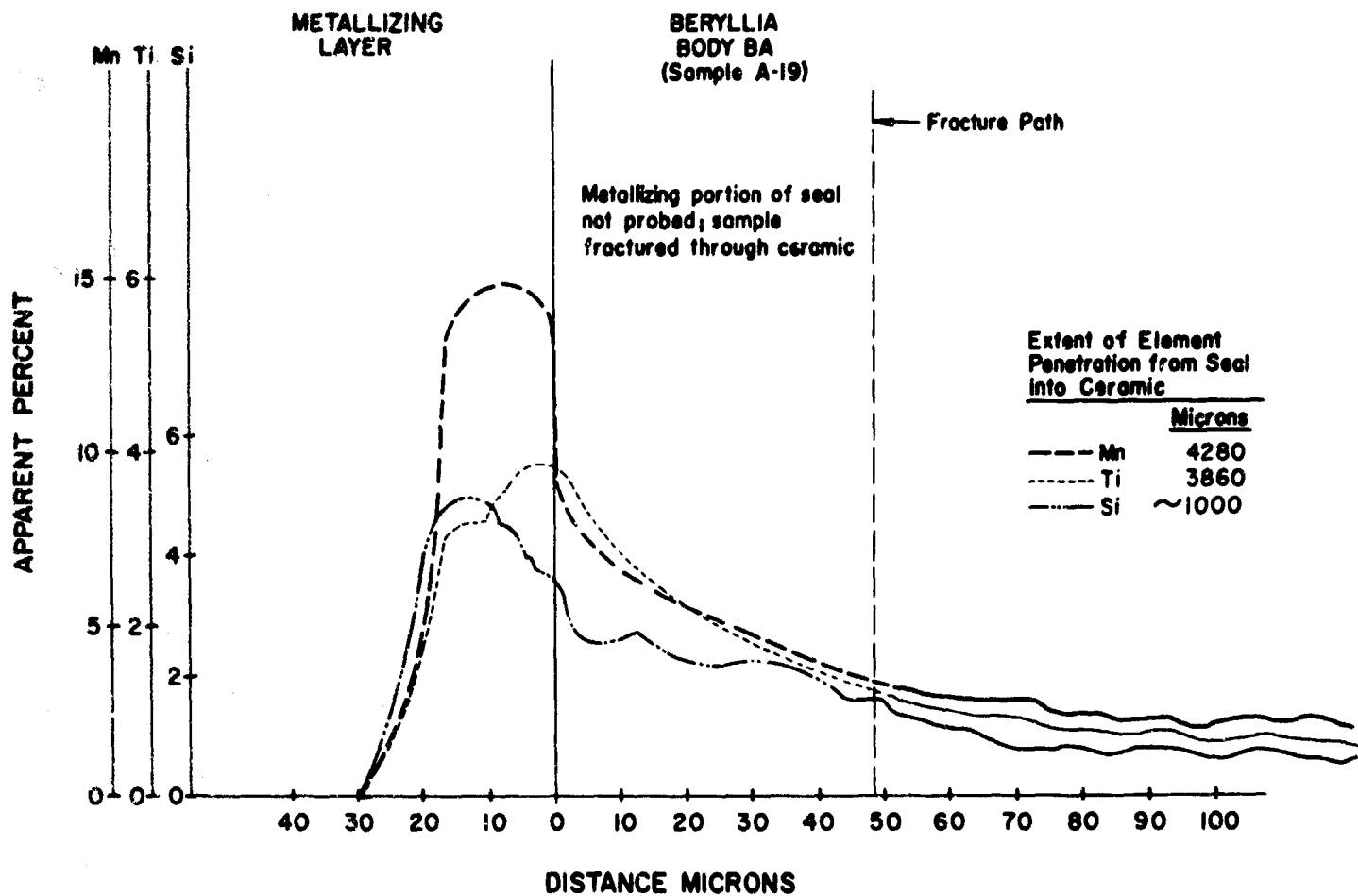


Figure 5.04: Electron microprobe trace of seal made with metallizing paint P-3 on beryllia body BA.

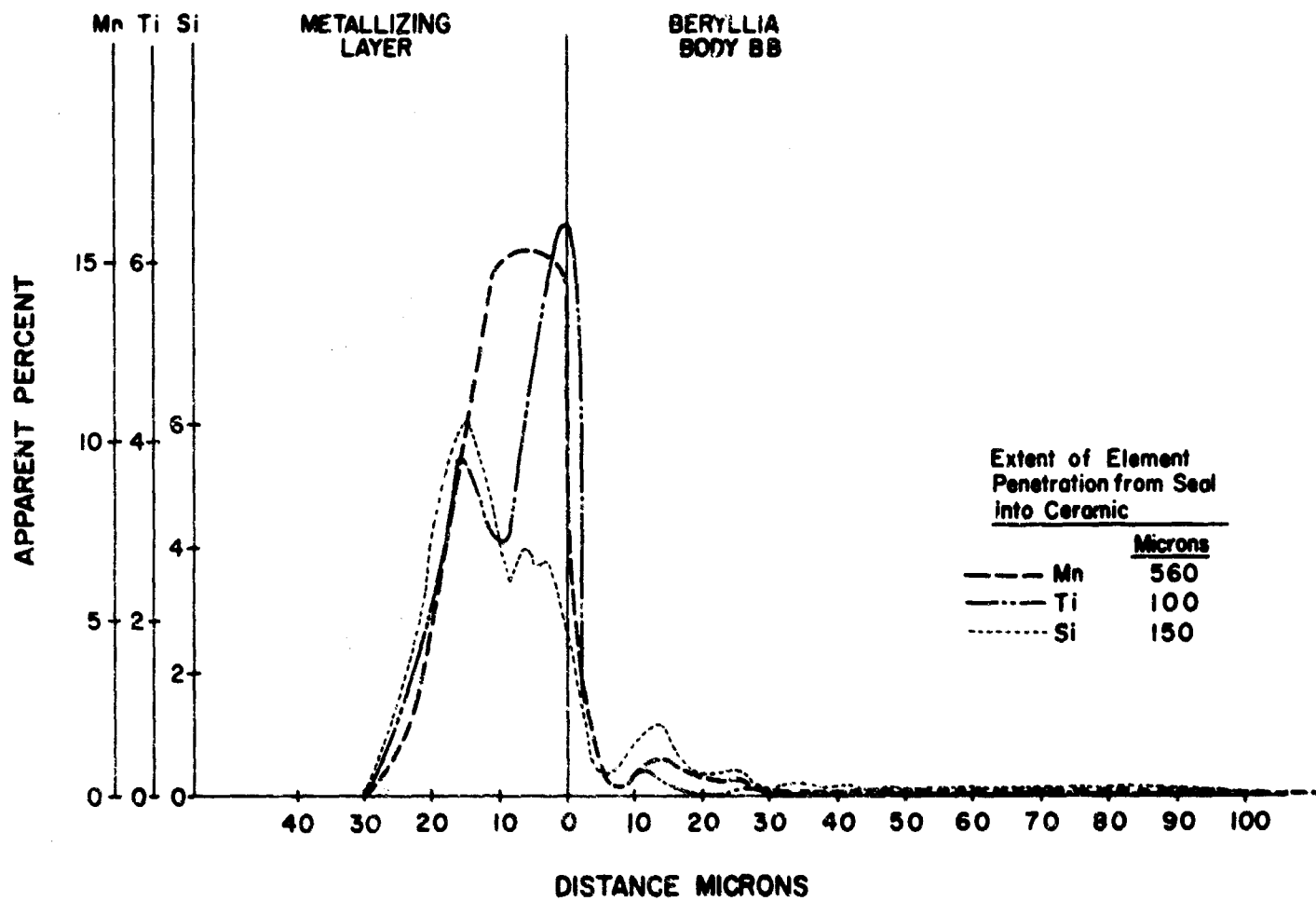


Figure 5.05: Electron microprobe trace of seal made with metallizing paint P-3 on beryllia body BB.

SiO<sub>2</sub> present in Body BA, the melt phase viscosity is much lower than the melt phase of Body BB, which contains much more than SiO<sub>2</sub>. This low viscosity results in high diffusion rates for the penetration of MnO and TiO<sub>2</sub> into Body BA.

P-3 metallizing paint was found to be susceptible to blistering of the molybdenum metallizing. This is due to evolution of oxygen from titanium compounds at some point in the metallizing firing schedule. The blistering may be avoided by using TiH<sub>2</sub> in place of TiO<sub>2</sub>, firing at a lower temperature, 1300°C - 1200°C, or by using paints which have no titania in them as has been done below by using P-8 and P-13.

Two metallizing paints, P-8\* and P-13\* were tested on beryllia bodies BA and BB (see Table 4-22) in order to develop a metallizing paint suitable for use with these beryllia bodies. Three metallizing temperatures were tried, 1200°, 1300° and 1400°C. Most of the work was done with Body BA, with Body BB just used in one test for purposes of comparison.

A scratch test identical to the one described in Task I was used to measure the hardness of the metallizing. Scratch test results are presented in Table 5-2. Paint P-13 produced consistently harder metallizing.

Tensile assemblies were made with 0.0005 in. copper plate, 0.004 in. 60/40 Cu-Au braze, and 0.020 in. copper washer. All BeO pieces were sealed to Body A alumina pieces and failed on the BeO side of the metal washer because the alumina had a higher tensile strength than the beryllia. All assemblies were vacuum tight. Tensile test results appear in Table 5-3. The best strengths were obtained with P-13 sintered at 1200°C. The strengths obtained with P-8 were comparable to P-13 except at the lowest sintering temperature.

All the assemblies pulled some ceramic or broke in the neck on the beryllia side when they failed in the tensile test. P-13 metallizing on an assembly of two pieces of Body A gave a strength of 11,887 psi. These two facts indicate that the weakest region of the assemblies which were tested was the beryllia ceramic rather than the seal

---

\*See Table 4-22 for composition.

TABLE 5-2

## Scratch Tests, Beryllia Metallizing

Body Type	Metallizing Temperature, °C	Hardness (1-5)*	
		P-8	P-13
BB	1300	3	4
BA	1200	2	4
BA	1200	2	4
BA	1300	2	3+
BA	1300	3	4
BA	1400	2+	3+
BA	1400	2	3

\*Same scale as used in Task 1.

TABLE 5-3  
Beryllia Tensile Test Results\*

Body Type	Metallizing Temperature, °C	Tensile Strength, psi	
		P-8	P-13
BB	1300	5,505	7,950
BA	1200	4,195	6,825
BA	1200	<u>5,100</u>	<u>7,050</u>
	Average	4,647	6,937
BA	1300	6,600	6,775
BA	1300	<u>6,875</u>	<u>6,675</u>
	Average	6,737	6,725
BA	1400	6,225	5,910
BA	1400	<u>5,000</u>	<u>6,625</u>
	Average	5,612	6,267

\*All assemblies were made with 0.0005 in. copper plate,  
0.004 in 60/40 Cu-Au braze, and 0.020 in. copper washer.  
All BeO pieces were sealed to Body A pieces, and failed on  
the BeO side. (P-13 on Body A pulled at 11,887 psi average.)  
All assemblies were vacuum tight.

area. The slight downward trend in strength with higher metallizing temperatures may be attributed to weakening of the beryllia ceramic as a result of the heat treatment and reaction with the metallizing. For this reason alone, the lower metallizing temperature is preferable.

The work summarized above outlined the development of successful metallizing systems for use with beryllia ceramics. The electron microprobe and microphotograph data provided a valuable insight into the corrective action required to produce a successful metallizing paint.

## 5.2 Fused Quartz-to-Metal Seals

An established process for sealing fused quartz to metal, which was described by Robert H. Dalton of Corning Glass Works, was tested<sup>1</sup>. The process employs sealing glass such as General Electric GSC1 or Corning CGW No. 7230 to join fused quartz or Vycor to thin (2 mils) platinum metal members.

Quartz tubing (0.178" O.D. x 0.087" I.D.) was used in the tests. GSC1 glass was ground minus 325 mesh, mixed with a lacquer vehicle, and applied to the ends of the quartz tubes to be joined. The glass was fused at 1250°C in air for 30 minutes and then cooled. Two glazed tubes were then butted together with a 2 mil platinum washer between them. A pressure of 2 psi was applied to the joint while the assembly was heated to 1350°C in air for 20 minutes. The pressure was maintained while the assembly was cooled. Several vacuum tight seals were made using this technique, but the strength of the joints was not determined because of the geometry of the samples. A one-inch quartz window was also processed and found to be vacuum tight.

In a second quartz sealing technique, molybdenum was evaporated onto a quartz disc. The disc was then sealed to a gold metal member by a pressure bonding technique<sup>2</sup>. A high strength vacuum tight seal resulted. The seal was sectioned and photomicrographed. The photo appears in Fig. 5.06. It shows two pieces of quartz diffusion bonded and sealed to a gold member in the center. A very thin layer (just under a micron) of molybdenum may be seen on the quartz members immediately adjacent to the interface.

Disc windows up to 4 inches in diameter were made by this process on an EIMAC sponsored program which ran parallel to this study.





- ← GOLD
- ← MOLYBDENUM
- ← QUARTZ

Figure 5.06: Photomicrograph of fused quartz-to-metal seal. The thickness of the deposited molybdenum layer is near the limit of resolution of the microscope. (400X)

1. Robert H. Dalton, "Sealing to Silica and Similar Glasses",  
Proceedings of the Eighth Symposium on the Art of  
Glassblowing, The American Scientific Glassblowers  
Society, Wilmington, Delaware, 1963.
2. O. Heil, U. S. Patent No. 3,115,957, December 31, 1963.

## 6.0 TASK III - ELECTRICAL STUDIES

### 6.1 General Introduction

#### 6.1.1 Sources of Electrical Loss

When considering a vacuum tight rf window structure, which must pass large amounts of power, one immediately becomes concerned with any losses introduced by the window. These losses are often of relatively low magnitude compared to the total power passed, but at high levels of power even a small loss produces unacceptable heating effects.

Windows generally have three recognizable sources of loss, each with distinct characteristics. The first of these occurs in the ceramic itself and is characterized by a certain dielectric constant and loss tangent. At the joint between waveguide and ceramic some metallurgical or mechanical bond must be made. The metal to which the ceramic is directly bonded forms the second region of interest. This is often a metallizing paint of relatively good conductivity whose surface (ceramic side) is irregular. The third region, distinct in itself, is the non-metallic "interface" region. This area extends from the metal boundary into the ceramic. The depth of penetration varies from a few microns to over 50 mils. It is formed by diffusion of the components of the metallizing paint into the glassy phase of the ceramic as shown in Figs. 4.50, 4.51, and 4.52. These components may react chemically with the glassy phase. The several loss mechanisms in a window may be summarized as follows:

#### i) Conduction currents:

In the ceramic there is a finite number of mobile charge carriers both positive and negative which in the presence of fields cause conduction currents to flow. One can define an effective conductivity of the ceramic which gives rise to  $I^2R$  loss.

In the metal boundary the number of free charge carriers is many orders of magnitude greater and hence a given applied field will cause a proportionately greater current to flow.

ii) Relaxation losses:

Losses may occur in a dielectric which are distinct from conduction effects. In certain materials, an applied electric field will cause polarization. This might be polarization of a bound electron with its nucleus, polarization of several positive and negative ions, etc. Each type of polarization has its own natural frequency. As frequency is varied, various polarization modes are excited. The characteristics of dielectrics are such that the displacement current flowing when a polarization mode is excited is not exactly  $90^\circ$  leading the applied field, but is some small angle less than  $90^\circ$ . This means the displacement current has a component in phase with this applied field giving rise to real losses (heat). Very simply, frictional heating takes place as the dipoles change orientation in the alternating field.

iii) Piezoelectric and magnetostrictive effects:

The ceramic material, particularly the interface region, if piezoelectric or magnetostrictive, will deform when an electric or magnetic field is applied. Frictional losses will occur, thereby creating heat.

iv) Semiconductor effect:

The interface region might form a semiconductor junction either between itself and the metallizing material or between areas of different properties in the interface. Losses then would be a function of current direction.

6.1.2 Electrical Properties as a Function of Microstructure and Chemistry

It is the purpose of this task to correlate the losses in the seal with studies of the microstructure programmed in Task I and additional studies carried out jointly with the electrical studies.

A microscopic examination of the metallizing shows that, as mentioned above, the metallizing is made up

of two basic components: (1) a metal portion, and (2) a non-metallic portion, as shown in Fig. 4.50. The microprobe data, Fig. 4.52, supports this conclusion.

The dc resistance of the metallic portion is essentially that of pure molybdenum (or other refractory metal); i.e.  $5.7 \times 10^{-6}$  ohm-cm. The resistivity of the non-metallic portion of P-1 metallizing can be determined by painting the non-metallic portion of P-1 metallizing only onto various ceramic bodies, including Body A and sintering under normal metallizing conditions. With a paint thickness of 0.5 mils, the resistivity is greater than  $1 \times 10^{11}$  ohms per square, indicating that the layer behaves as an insulator rather than as a semi-conductor at room temperature. Other compositions such as Mo-MnO-SiO<sub>2</sub>-TiO<sub>2</sub> (P-3) and Mo-TiO<sub>2</sub> have also been examined. The non-metallic portion of P-3 behaves as an insulator also, while the non-metallic portion of the latter behaves as a semi-conductor, and has resistivity in the range of  $1 \times 10^3$  to  $1 \times 10^6$  ohms per square depending on firing conditions and body type. Microscopic examination of the metallizing further reveals that the dc current through a metallizing layer will follow a tortuous path, thus accounting for the fact that the layer exhibits a resistance approximately 5 to 50 times greater than that shown by solid molybdenum.

The rf conduction characteristics of the layer must be different from that of a solid molybdenum layer since the electrical path width, in many cases, is less than the rf skin depth thickness for pure molybdenum (i.e. 1.15 microns at 10 Gc). Reference to Fig. 6.01 will clarify this point. This figure shows a schematic path through the metallizing, and indicates that, no matter how thick the metallizing is, some current must be carried in the overplate and braze for, at certain points in the continuous molybdenum conduction path, the total width of the path will always be less than 1.15 microns. The rf situation is thus as follows. When the metallizing is very thin, the current is carried almost exclusively within the overplate and braze region. As the metallizing becomes thicker, a portion of the current will be carried in the overplate and braze and a portion in the metallizing itself. This ratio will reach a fixed point beyond which further increase in metallizing thickness will result in no more current being carried in the metallizing.

The ratio may vary, indicating no current being carried in the metallizing, or all the current being carried

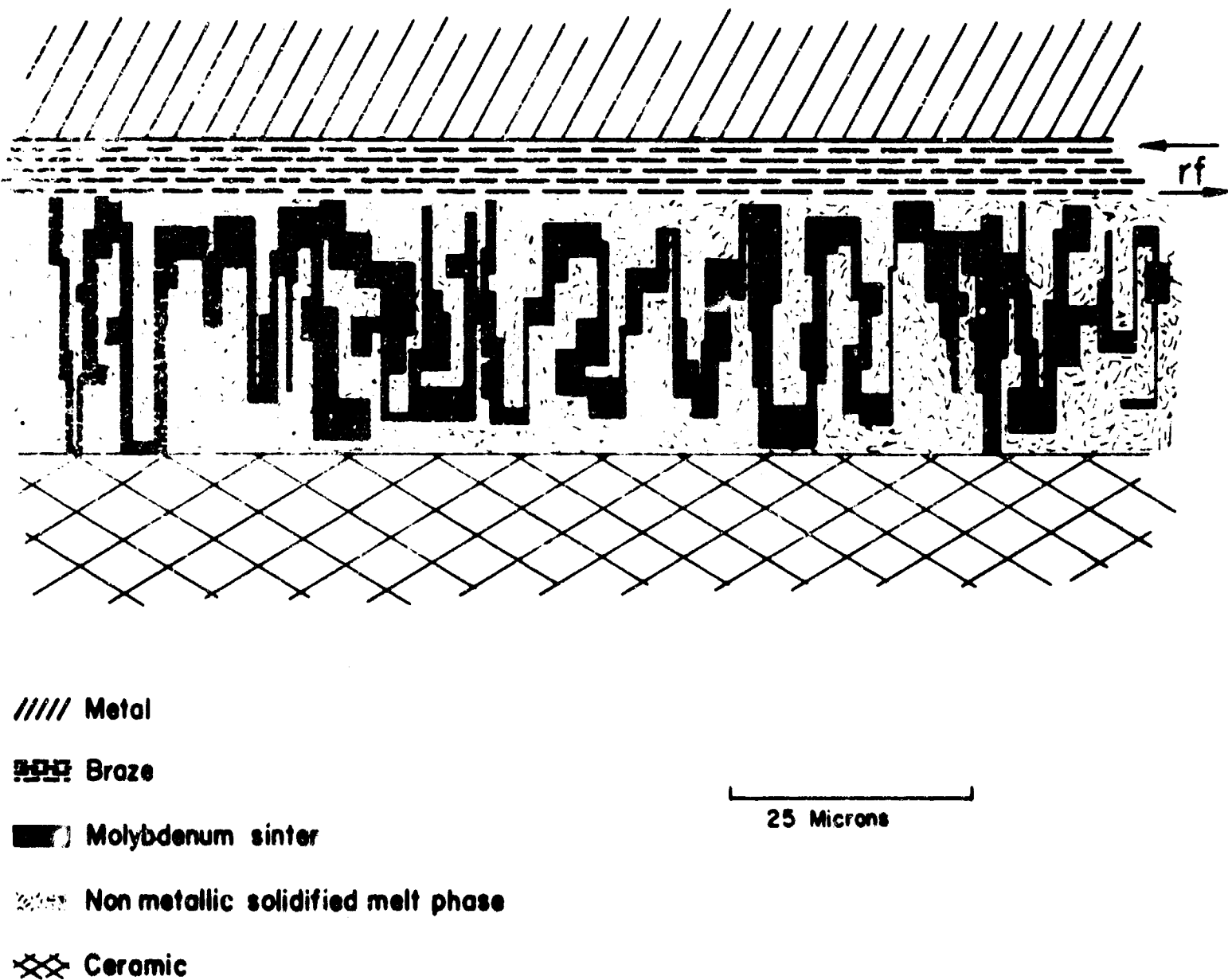


Figure 6.01: Schematic representation of Figure 4.50 illustrating the electrical path length and width through the metallizing.

in the metallizing in extreme cases, depending on the continuity of the molybdenum component as it is affected by the sintering time, temperature and other sintering parameters.

The rf dielectric losses in the seal area will be a function of the composition and amount of the interfacial glassy layer and the tendency of the non-metallic portion of the metallizing paint to interdiffuse with the grain boundary phase of the ceramic.

### 6.1.3 Program of Experimental Studies

The experimental electrical studies were programmed in three main areas:

- 1) dc resistivity measurements of the
  - (i) metallizing as a function of temperature
  - (ii) wetting layer as a function of processing variation
- 2) low power rf measurements
  - (i) conduction ( $I^2R$ ) studies
  - (ii) dielectric studies
- 3) high power rf studies

From the above discussion, it is obvious that much valuable information on the nature of current flow in the metallizing can be obtained from simple dc measurements. The temperature dependence of the resistivity can define the contribution of the metallic and non-metallic insulator or semi-conductor portion of the metallizing to the overall conduction process. The nickel or copper overplate may influence the metallizing as a consequence of high temperature diffusion alloying processes.

Low power rf experiments were then devised in order to isolate the two main sources of electrical loss so that the loss variation with paint composition and processing conditions could be systematically explored.

Lastly, it was desirable to determine the magnitude of the losses by a direct measurement technique; accordingly, high power rf studies were programmed and a total loss data obtained for a simulated window situation.

## 6.2 dc Electrical Measurements

### 6.2.1 Temperature Coefficient of dc Resistivity

#### 6.2.1.1 Relation to Total Seal Losses

Elaborate cooling systems have been designed to prevent high power microwave windows from overheating. Experiments with high average power demonstrate that a large heat conductivity of a window material is more important than a low loss factor. Beryllia ceramics prove, therefore, in general, better than high alumina ceramics. Most oxide ceramics, fortunately, have dielectric constants and loss tangents rising only slowly with increasing temperature, at least up to 600°C. This may not be the case at all for the losses in the seal area, however, because the dielectric in that region is actually highly contaminated. Microwave dissipation due to dielectric losses is, therefore, increased, and one can expect the loss tangent to rise fast with temperature. The other type of loss, due to conduction currents in the plane of the metallizing may be expected to depend on the temperature dependence of the metal component in the metallizing.

By far the simplest method of determining this characteristic is to measure the direct current conductivity of the metallizing on ceramics as a function of temperature. The dc conductivity is in direct relation to the microwave conduction losses as is shown by the following three equations describing wave propagation in waveguides:

$$P_{\text{lost}} = 2\alpha P_{\text{in}} l \quad (1)$$

where

$P_{\text{lost}}$  : power dissipated

$P_{\text{in}}$  : power incident

$\alpha$  : attenuation constant (see equation (2) ).

$l$  : length of waveguide section

$$\alpha = \frac{R}{\int b} \cdot \frac{1 + \frac{2b}{a} \left(\frac{\lambda}{2a}\right)^2}{\sqrt{1 - \left(\frac{\lambda}{2a}\right)^2}} \quad (2)$$



where

R : characteristic resistance (see equation (3) ).

$\xi = \sqrt{\frac{\mu}{\epsilon}}$  : intrinsic impedance

a : width of waveguide

b : height of waveguide

$\lambda$  : free space wavelength (m)

$$R = 10.88 \times 10^{-3} \sqrt{\left(10^7 \frac{1}{\sigma \lambda}\right)} \text{ ohms} \quad (3)$$

$\sigma$  : dc conductivity.

The microwave power dissipation due to conduction losses in the metallizing is, other factors being constant, inversely proportional to the square root of the dc conductivity:

$$P_{\text{lost}} = C \times \frac{1}{\sqrt{\sigma}} \quad C = \text{constant} \quad (4)$$

Equations (2) and (3) refer to the propagating dominant mode in a rectangular waveguide only, but the general statement in (4) is applicable also to resonance structures such as microwave windows, supporting propagating and standing waves.

Results of the dc measurements of the thermal coefficient of resistivity in the metallizing will indicate the trend with temperature of the microwave conduction losses in ceramic-to-metal seals.

#### 6.2.1.2 Experimental Set-Up

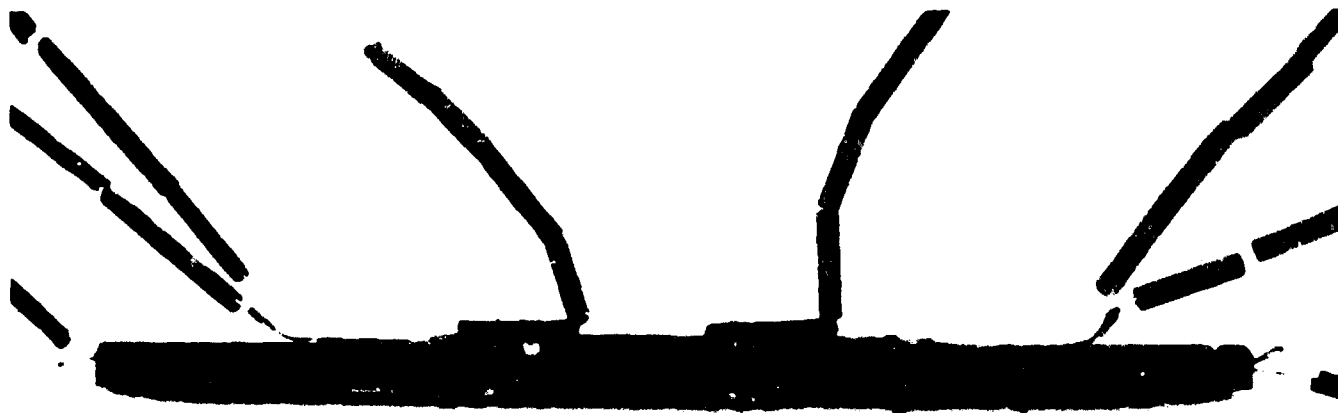
The experimental work consisted in the investigation of the thermal coefficient of dc resistivity for various kinds of metallizing<sup>†</sup> on two kinds of alumina ceramics.\*

Figure 6.02 is a photograph of a test sample. A metallized ceramic strip is provided with two heavy copper contacts brazed to the ends. Two wires for the measuring current and the detection of the voltage drop are attached.

---

\*Bodies A and E as per Table 4-1.

<sup>†</sup>Metallizings as per Table 4-22.




  
ONE INCH



Figure 6.02: Measurement of thermal coefficient of resistivity in metallizing on ceramic. Test sample strapped to ceramic heater.

The sample is mounted on another ceramic, which has a heater filament inserted. The temperature is directly measured on the metallizing surface with two chromel-alumel thermocouples, one in the center of the sample, the other close to the end, in order to check in all experiments the evenness of the temperature distribution. The test sample is surrounded with a heat shield (not shown in the photo), which helps to establish an even temperature distribution by reducing radiative losses connected with heat flows and temperature gradients. Measurements were made up to 800°C in a demountable vacuum system with a pressure lower than  $5 \times 10^{-5}$  Torr. Data were taken during the complete heating and cooling cycle. Only samples with completely reversible changes were evaluated.

The electric circuitry is straightforward as shown in Fig. 6.03. Resistivity is measured from the voltage drop across the sample produced by an accurately measured current.

#### 6.2.1.3 Results

The thermal coefficient of resistivity is defined as the change of resistance of a test sample relative to the resistance at zero degrees centigrade per degree centigrade.

This quantity is generally a function of temperature. Listing only one or two values for specified temperature ranges means that original measuring curves have been evaluated with linear approximations. Fig. 6.04 gives as an example the original measuring curve of sample No. 10 (metallizing P-3 on Body A). Resistance data upon heating and cooling are marked as dots and circles, respectively. At 400°C, there seems to be a slight "kink" in the curve. Averaging, therefore, extends over the temperature ranges 0-400°C and 400-800°C. In other cases such "kinks" occur as low as 300°C.

Representing results as the resistance of test samples as a function of temperature as in Fig. 6.04 does not allow an easy comparison between samples of different kinds. It is, therefore, desirable to normalize the values of resistance at 0°C (extrapolated from the value at 25°C) and plot the ratio of the resistance at temperature versus the resistance (normalized) at 0°C as a function of temperature. Fig. 6.05 gives an example which compares the resistances of samples No. 3 (annealed, 0.001" thick strip of molybdenum), No. 4 (metallizing paint P-1 on Body A) and

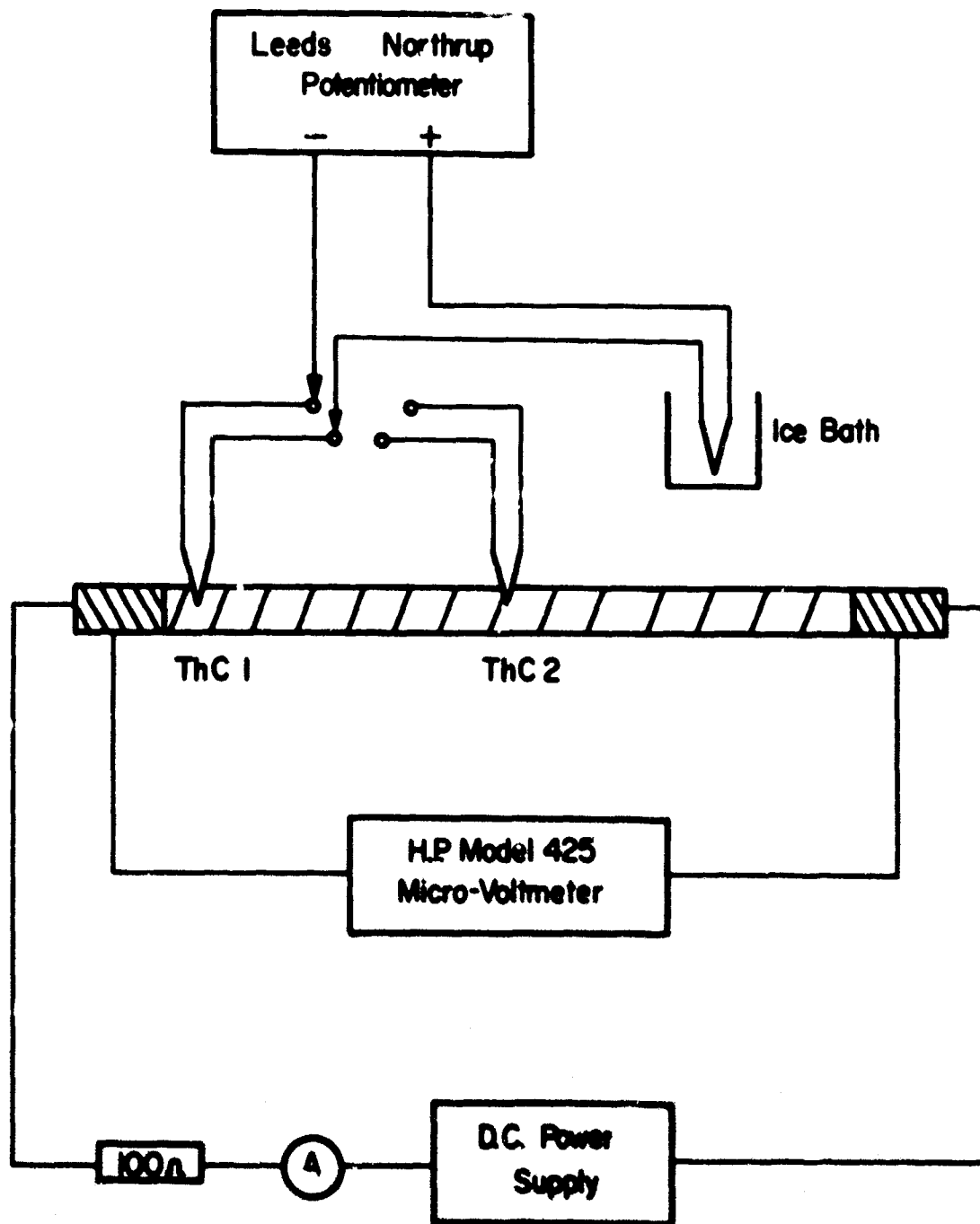


Figure 6.03: Circuitry for measurement of thermal coefficient of resistivity.

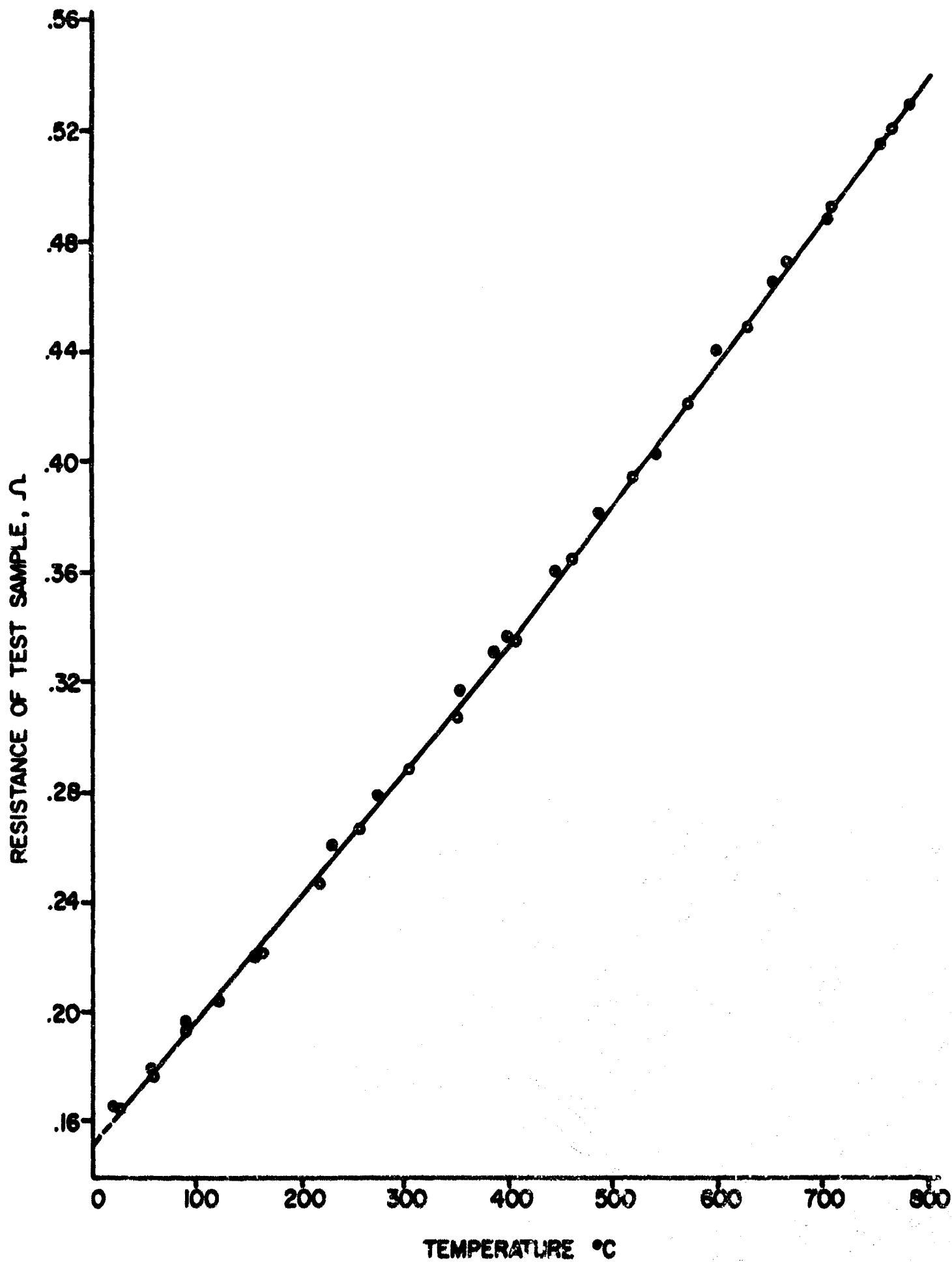


Figure 6.04: Resistance versus temperature of test sample No. 10 (metallizing P-3 on Body A).

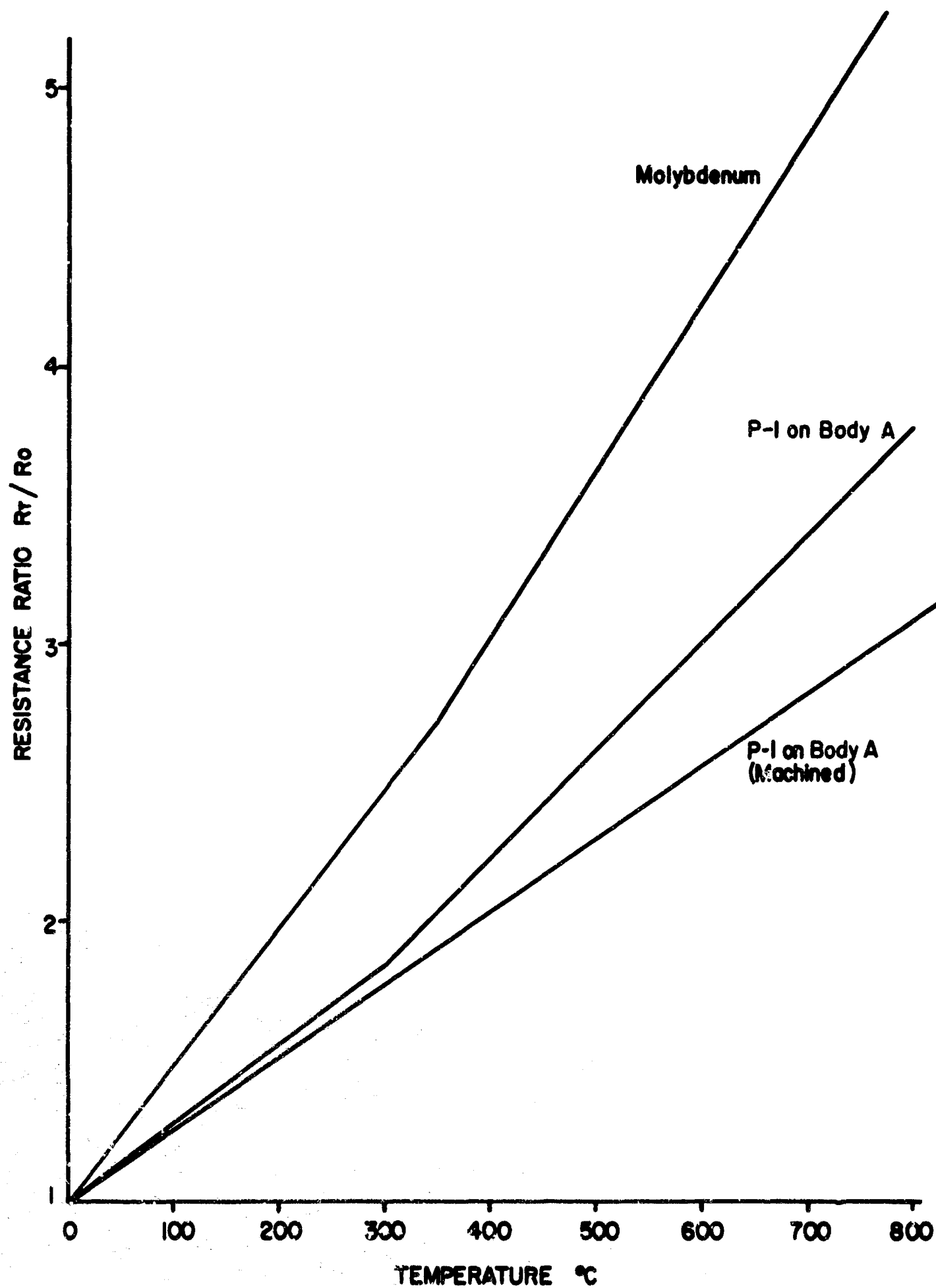


Figure 6.05: Measured resistance ratio  $R_T/R_0$  of three samples as a function of temperature.

No. 5 (metallizing paint P-1 on Body A machined down). In this way, the unimportant absolute resistance values are eliminated, and the slope of the curve can be easily related to the thermal coefficient of electrical resistivity,  $\alpha$ , according to

$$\frac{R_T}{R_0} = \alpha T + 1 \quad (5)$$

Table 6-2 provides back-up information, namely the lengths, widths, and thicknesses of the metallizing layers and the resistances measured at room temperature. Resistivities and resistances per square shown in Table 6-1 were calculated from these data.

Figs. 6.06 through 6.11 contain the measuring data in graphical form for each comparison of samples. Figs. 6.12, 6.13 and 6.14 show the cross-section of significant metallizing layers mentioned in the text. Numbers on the curves key to the sample description and the thermal coefficient of dc resistivity in Tables 6-1 and 6-2.

#### 6.2.1.4 Discussion of Results

In a metallizing layer, molybdenum particles are partly sintered and suspended in the glassy phase. Some compositions, especially the ones with titanium dioxide, suggest that they may behave like semiconductors. The contribution of the metal portion to electrical conduction is much larger than the effect of the suspected semiconductor portion of the metallizing. Measuring results shown in Fig. 6.05, however, clearly demonstrate how the presence of a glassy phase with a negative thermal coefficient of electrical resistivity reduces the measured coefficient of pure molybdenum (top curve). The metallizing layer adjacent to the ceramic has a higher glass content. Reducing the metallizing thickness by machining off surface layers therefore increases the average glass content. Correspondingly, a still lower thermal coefficient is obtained, as shown in the lowest curve in Fig. 6.05.

With this introduction a complete evaluation of all measuring results is reported below, together with microscopic investigations of the significant test samples.

TABLE 6-1

## Measured Thermal Coefficients of dc Resistivity

Sample No.	Metal. Paint	Ceramic	Remarks	Resistivity at 25°C (ohm cm)	Surface Resistance (ohms per square)	Thermal Coefficient of Resistivity 10 <sup>-3</sup> /°C
1	-	-	0.002" moly strip, unannealed	-	-	4.9 (20-450°C) 5.7 (450-875°C)
2	-	-	0.001" moly strip, unannealed	7.1 x 10 <sup>-6</sup>	2.8 x 10 <sup>-3</sup>	4.5 (20-350°C) 5.2 (350-825°C)
3	-	-	0.001" moly strip, annealed (1 hour 950 C, vacuum)	7.3 x 10 <sup>-6</sup>	2.9 x 10 <sup>-3</sup>	5.0 (25-350°C) 6.0 (350-775°C)
4(P) 257	P-1 <sup>+</sup>	Body A	fired at 1425 C, 1/2 hr. wet hydrogen-nitrogen	44 x 10 <sup>-6</sup>	1.1 x 10 <sup>-2</sup>	2.9 (20-300°C) 3.8 (300-825°C)
5(P)	P-1	A	thickness reduced by machining	47 x 10 <sup>-6</sup>	5.8 x 10 <sup>-2</sup>	2.6 (20-825°C) -
6(P)	P-1	A	No. 4 partly leached with nitric acid	123 x 10 <sup>-6</sup>	9.3 x 10 <sup>-2</sup>	3.3 (20-825°C) -
7(P)	P-1	Body E	-	63 x 10 <sup>-6</sup>	3.5 x 10 <sup>-2</sup>	3.0 (20-300°C) 3.3 (300-825°C)
8(P)	P-1	E	thickness reduced by machining	46 x 10 <sup>-6</sup>	4.0 x 10 <sup>-2</sup>	2.6 (20-350°C) 3.0 (350-750°C)
9(P)	P-1	E	thickness further reduced by machining	27 x 10 <sup>-6</sup>	5.9 x 10 <sup>-2</sup>	2.5 (20-300°C) 3.0 (300-750°C)
10(P)	P-3 <sup>x</sup>	A	-	31 x 10 <sup>-6</sup>	1.4 x 10 <sup>-2</sup>	3.1 (20-400°C) 3.4 (400-800°C)



Sample No.	Metal. Paint	Ceramic	Remarks	Resistivity at 25°C (ohm cm)	Surface Resistance (ohms per square)	Thermal Coefficient of Resistivity 10 <sup>-3</sup> /°C
11 (P)	P-3	A	thickness reduced by machining	34 x 10 <sup>-6</sup>	3.8 x 10 <sup>-2</sup>	2.8 (20-400°C) 3.0 (400-825°C)
12	P-3	E	-	33 x 10 <sup>-6</sup>	3.3 x 10 <sup>-2</sup>	3.2 (20-835°C)
13 (P)	P-4 <sup>xx</sup>	A	-	226 x 10 <sup>-6</sup>	6.4 x 10 <sup>-2</sup>	3.5 (25-750°C)
14	P-4M <sup>xx</sup>	E	-	263 x 10 <sup>-6</sup>	1.7 x 10 <sup>-2</sup>	3.5 (25-350°C) 3.9 (350-750°C)
15	Ti-11 <sup>xxx</sup>	A	-	37 x 10 <sup>-6</sup>	4.1 x 10 <sup>-2</sup>	2.6 (25-350°C) 2.7 (350-775°C)
16	Ti-11	A	thickness reduced by machining	41 x 10 <sup>-6</sup>	6.2 x 10 <sup>-2</sup>	2.3 (25-275°C) 2.8 (275-750°C)
17	Ti-11	A	No. 15 leached with nitric acid	49 x 10 <sup>-6</sup>	6.9 x 10 <sup>-2</sup>	2.5 (25-300°C) 2.7 (300-750°C)
18	P-1	A	fired at 1600°C, 1/2 hr. wet hydrogen-nitrogen	45 x 10 <sup>-6</sup>	4.1 x 10 <sup>-2</sup>	3.4 (25-250°C) 3.9 (250-750°C)
19	Ti-11	A	No. 17 heavily leached with nitric acid	1550 x 10 <sup>-6</sup>	3.0	-1.2 x 10 <sup>-3</sup> (25-175°C), -0.8 x 10 <sup>-3</sup> (175-425°C)
20	Ti-11 (glass only)	E	fired at 1600°C, 1/2 hr. wet hydrogen-nitrogen	unstable (10 <sup>-4</sup> )	-	negative
21	P-3 (glass only)	E	fired at 1600°C, 1/2 hr. wet hydrogen-nitrogen	unstable (10 <sup>-6</sup> )	-	negative
22	P-1 (modified)	E	1/6 Mo content of regular P-1	39 x 10 <sup>-6</sup>	6.5 x 10 <sup>-2</sup>	3.3 (0-300°C) 3.5 (300-750°C)

Sample No.	Metal. Paint	Ceramic	Remarks	Resistivity at 25°C (ohm cm)	Surface Resistance (ohms per square)	Thermal Coefficient of Resistivity 10-3/°C
23	-	E	bare ceramic	$1 \times 10^{14}$	-	negative
24 (P)	P-1	E	slightly electro-polished	$350 \times 10^{-6}$	$16 \times 10^{-2}$	3.2 (25-750°C)
25 (P)	P-1	E	heavily electro-polished	$6100 \times 10^{-6}$	3.6	3.1 (25-500°C) 2.7 (500-750°C)
26 (P)	Mo (evap)	E	-	$27 \times 10^{-6}$	$2.9 \times 10^{-2}$	4.1 (25-450°C) 4.7 (450-750°C)
27 (P)	Mo (evap)	E	fired at 1425°C, 1/2 hr. wet hydrogen-nitrogen	$13.7 \times 10^{-6}$	$2.2 \times 10^{-2}$	3.9 (25-400°C) 4.4 (400-750°C)
28	Ti-11	E	oxidized in air at 535°C fired in vac at 850°C 1/2 hr.	N/A	N/A	3.2 (0-425°C) 2.4 (425-725°C)
29	Ti-11	E	oxidized in air at 535°C, fired in vac at 850°C 1/2 hr.	N/A	N/A	1.1 (0-200°C) 0.33 (200-440°C) -0.37 (440-700°C)

(P) denotes that a photomicrograph of a metallurgical cross-section is shown in this report.  
+MoO<sub>3</sub> - 75.9%, MnO<sub>2</sub> - 19.9%, TiO<sub>2</sub> - 4.2%.

xMoO<sub>3</sub> - 71.5%, MnO<sub>2</sub> - 19.8%, TiO<sub>2</sub> - 4.2%, SiO<sub>2</sub> - 4.5%, fired at 1425°C, 1/2 hr. wet hydrogen-nitrogen.

xxMo - 100%, ground in Mo lined mill with Mo balls, fired at 1600°C, 1/2 hr. wet hydrogen-nitrogen.

xxxMoO<sub>3</sub> - 95%, TiO<sub>2</sub> - 5%, fired at 1425°C, 1/2 hr., wet hydrogen-nitrogen.

NOTE: Normal sintering temperature, 1425°C, unless otherwise noted.

TABLE 6-2

Metallizing Dimensions and Resistances of Samples in Table 6-1

Sample No.*	Length (cm)	Width (cm)	Thickness of Metall. ( $10^{-3}$ cm)	Resistance at 25°C (ohm)	Remarks
1	8.1	-	5.0	0.06	irregular geometry of strip
2	7.6	0.18	2.5	0.12	
3	7.1	0.20	2.5	0.10	
4	7.0	0.63	4.1	0.12	
5	7.2	0.63	0.8	0.66	
6	5.7	0.63	1.3	0.84	
7	7.1	0.51	1.8	0.49	
8	5.2	0.51	1.1	0.41	
9	5.3	0.51	0.46	0.62	
10	6.9	0.63	2.3	0.15	
11	6.8	0.63	0.9	0.41	
12	7.6	0.51	1.0	0.50	
13	7.1	0.63	3.5	0.76	
14	7.1	0.63	1.5	1.96	
15	7.7	0.63	0.9	0.50	
16	7.5	0.63	0.7	0.74	
17	7.6	0.63	0.7	0.83	
18	7.4	0.63	1.1	0.48	
19	6.6	0.63	0.51	31.50	
20	7.1	0.63	-	$16.3 \times 10^3$	irreversible changes of resistivity
21	6.9	0.63	-	$2 \times 10^6$ (435°C)	" " "
22	6.8	0.63	0.6	0.7	
23			bare ceramic		
24	7.5	0.63	2.2	1.9	(0.4 ohms originally)
25	7.5	0.63	1.7	43.0	" "
26	4.3	0.63	0.94	0.19	
27	5.25	0.63	0.63	0.18	
28	4.1	0.63	1.1	0.67	(0.1 ohms originally)
29	4.1	0.63	irreg.	40.00	(0.2 ohms originally)

\*For identification see Table 6-1.

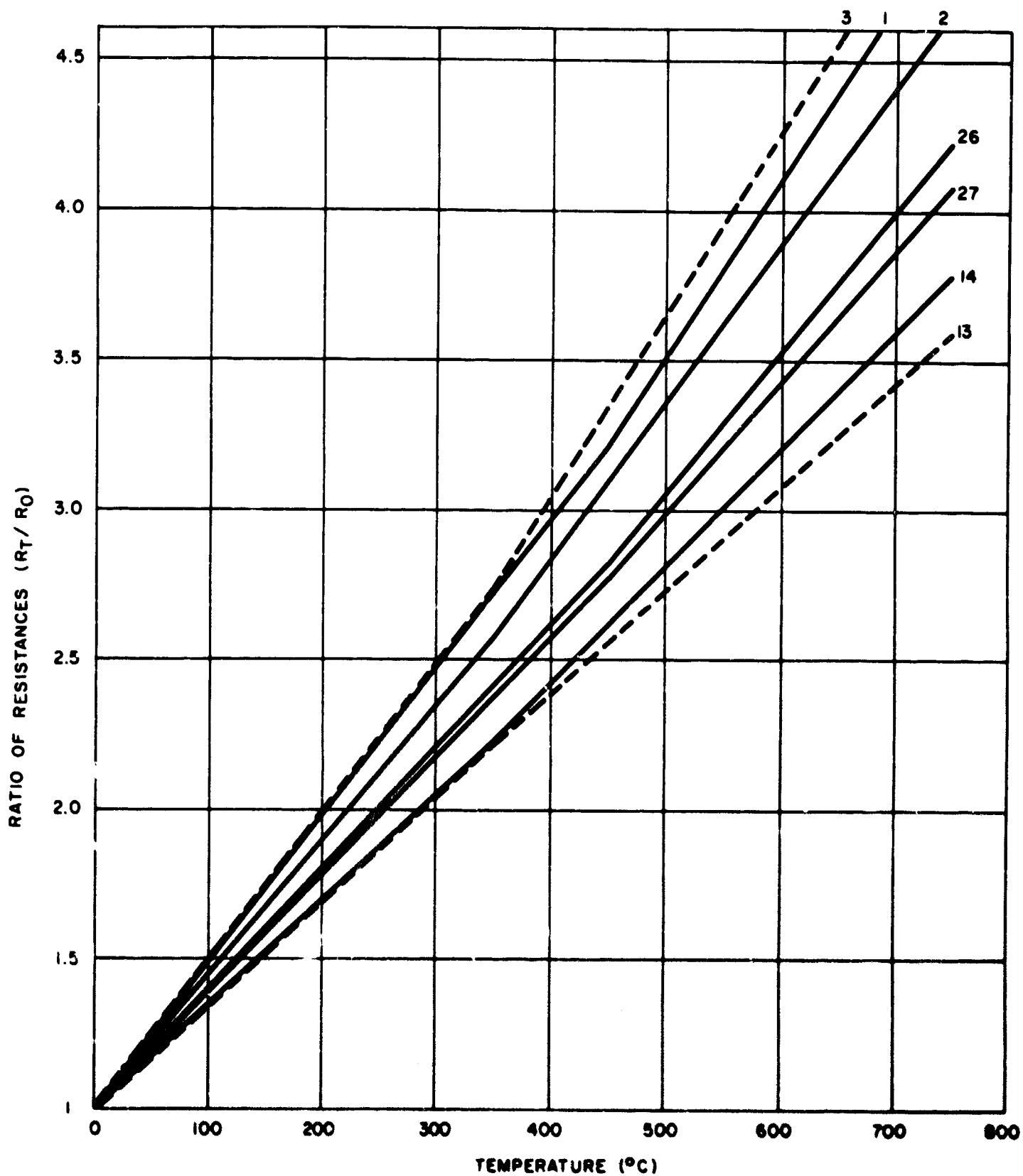


Figure 6.06: Measured resistance ratio vs temperature of test samples. (1) molybdenum strip, 0.002" thick, unannealed. (2) molybdenum strip, 0.001" thick, unannealed. (3) molybdenum strip, 0.001" thick, annealed. (13) P4-M on Body A. (14) P4-M on Body E ceramic. (26) molybdenum, evaporated on Body E ceramic. (27) molybdenum evaporated on Body E ceramic, fired at 1425°C for ½ hour in wet hydrogen-nitrogen atmosphere.

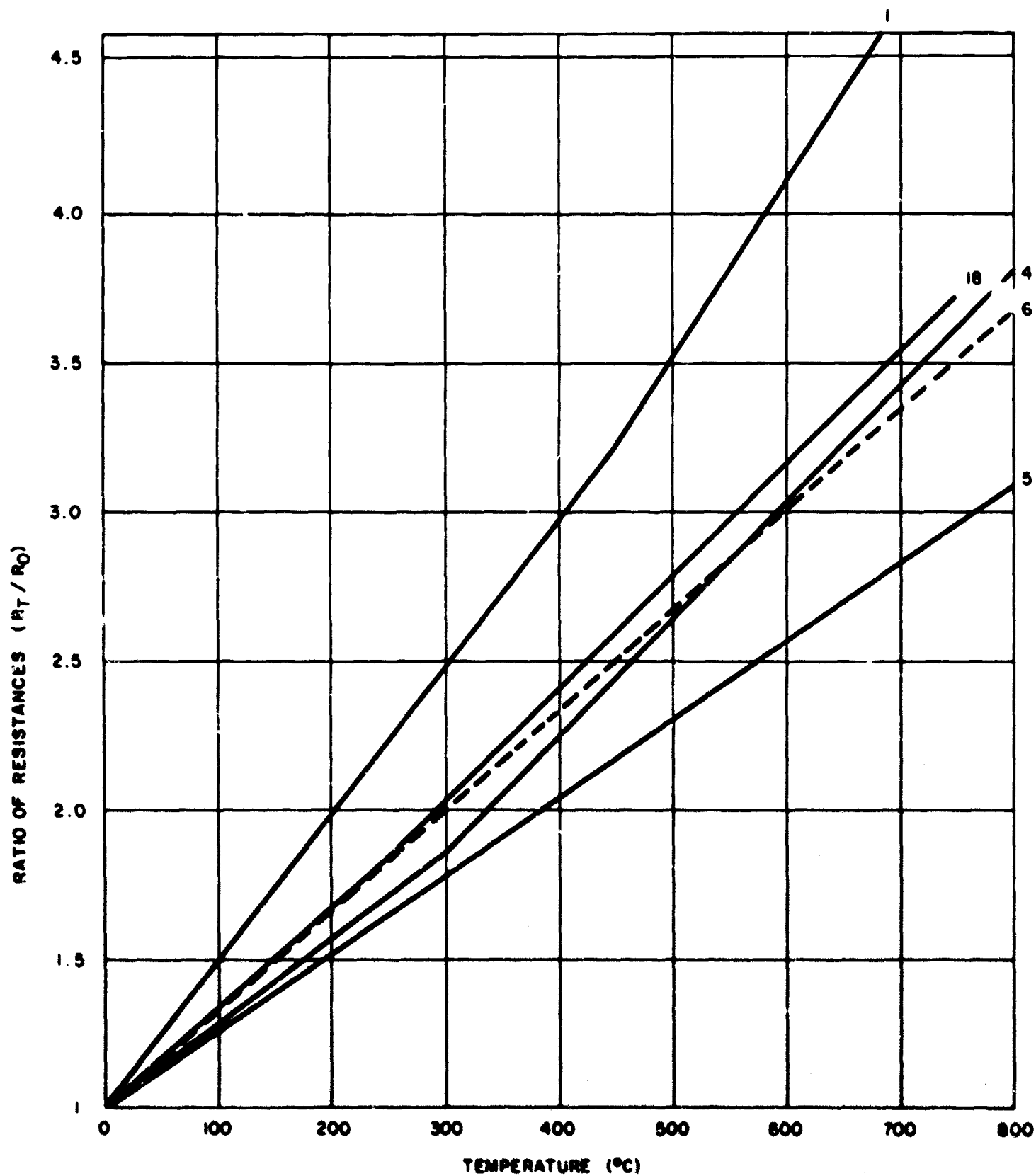


Figure 6.07: Measured resistance ratios vs temperature of test samples. (1) molybdenum strip, 0.002", unannealed. (4) P-1 on Body A ceramic. (5) P-1 on Body A ceramic, thickness reduced by machining. (6) P-1 on Body A ceramic, partly leached with nitric acid. (18) P-1 on Body A ceramic, fired at 1600°C.

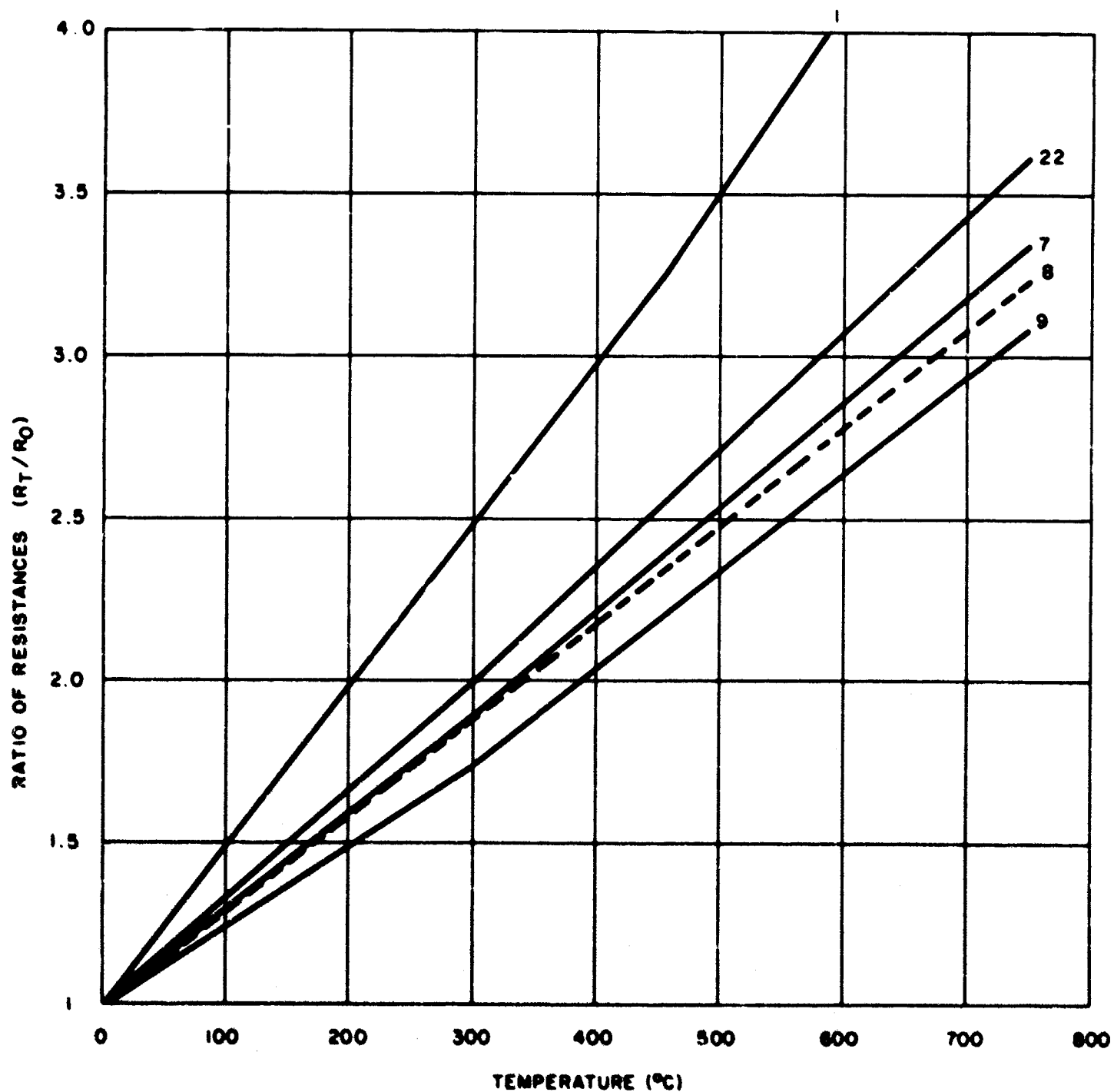


Figure 6.08: Measured resistance ratios vs temperature of test samples. (1) molybdenum strip, 0.002", unannealed. (7) paint P-1 on Body E ceramic. (8) paint P-1 on Body E, thickness slightly reduced by machining. (9) paint P-1 on Body E thickness further reduced. (22) P-1 (modified with 1/6 molybdenum content of regular P-1 paint) on Body E ceramic.

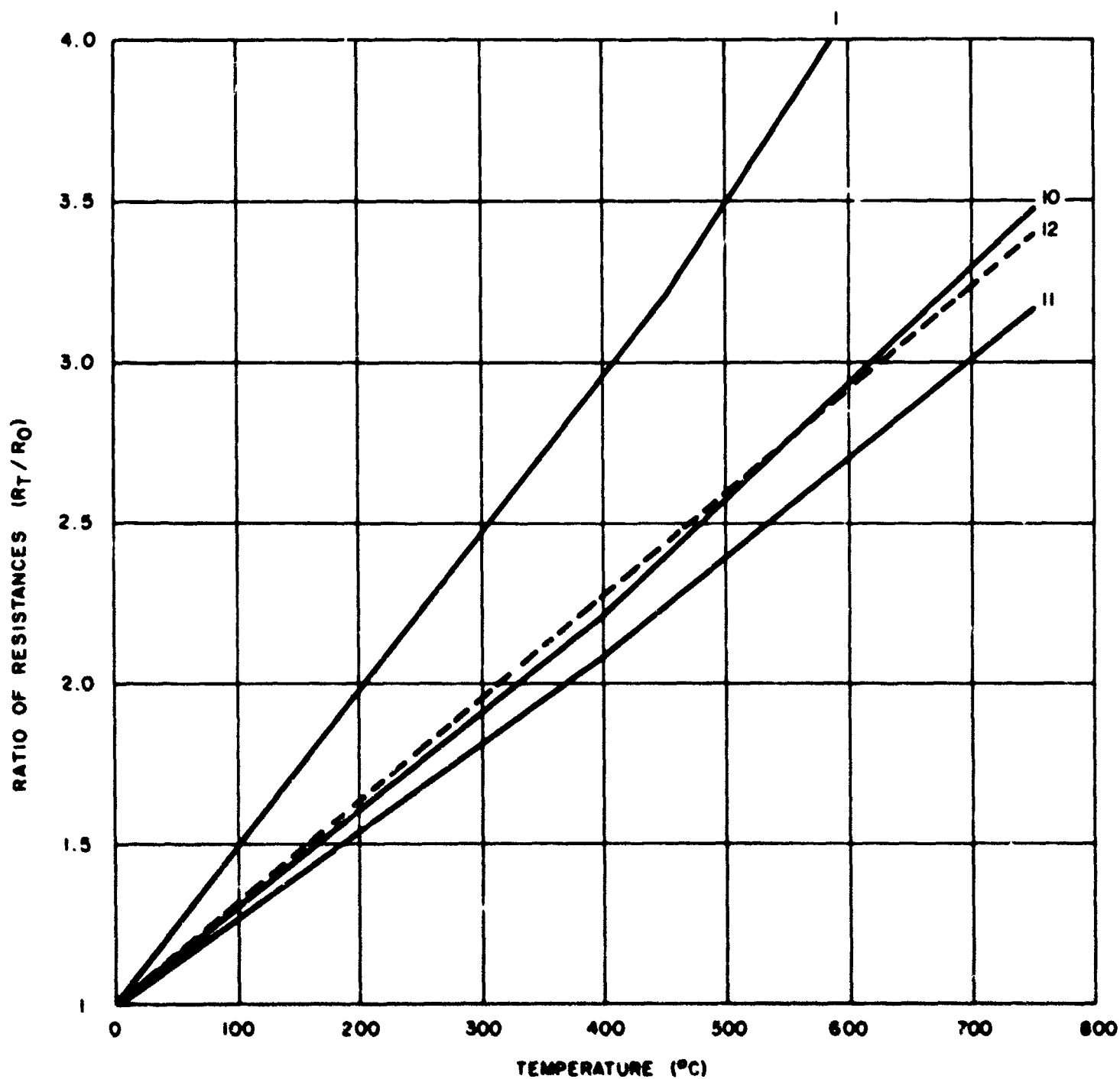


Figure 6.09: Measured resistance ratios vs temperature of test samples. (1) molybdenum strip, 0.002", thick, unannealed. (10) paint P-3 on Body A ceramic. (11) paint P-3 on Body A ceramic, thickness reduced by machining. (12) paint P-3 on Body E ceramic.

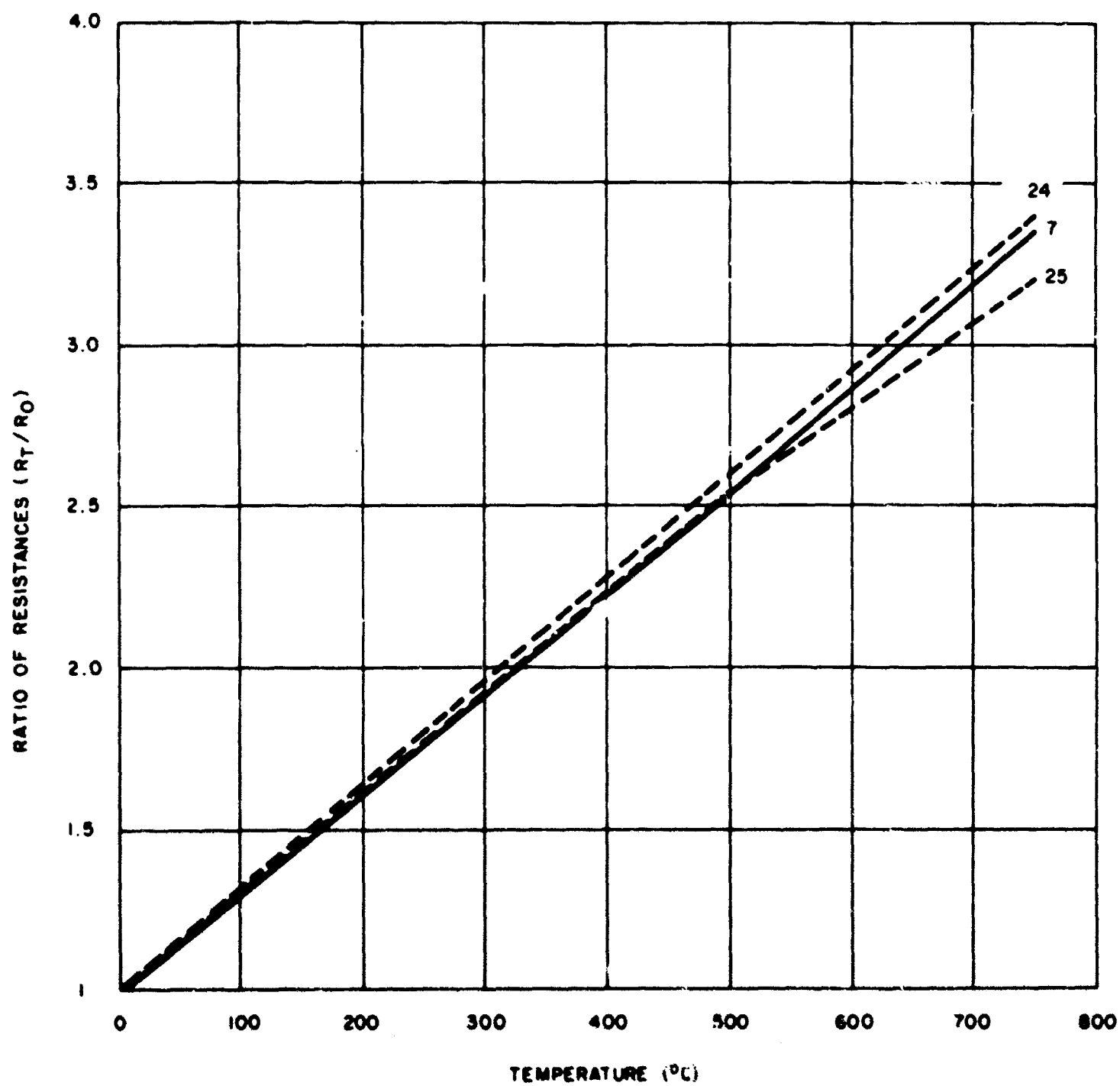


Figure 6.10: Measured resistance ratio vs temperature of test samples. (7) paint P-1 on ceramic Body E. (24) paint P-1 on ceramic, slightly electropolished. (25) paint P-1 on ceramic Body E, heavily electropolished.



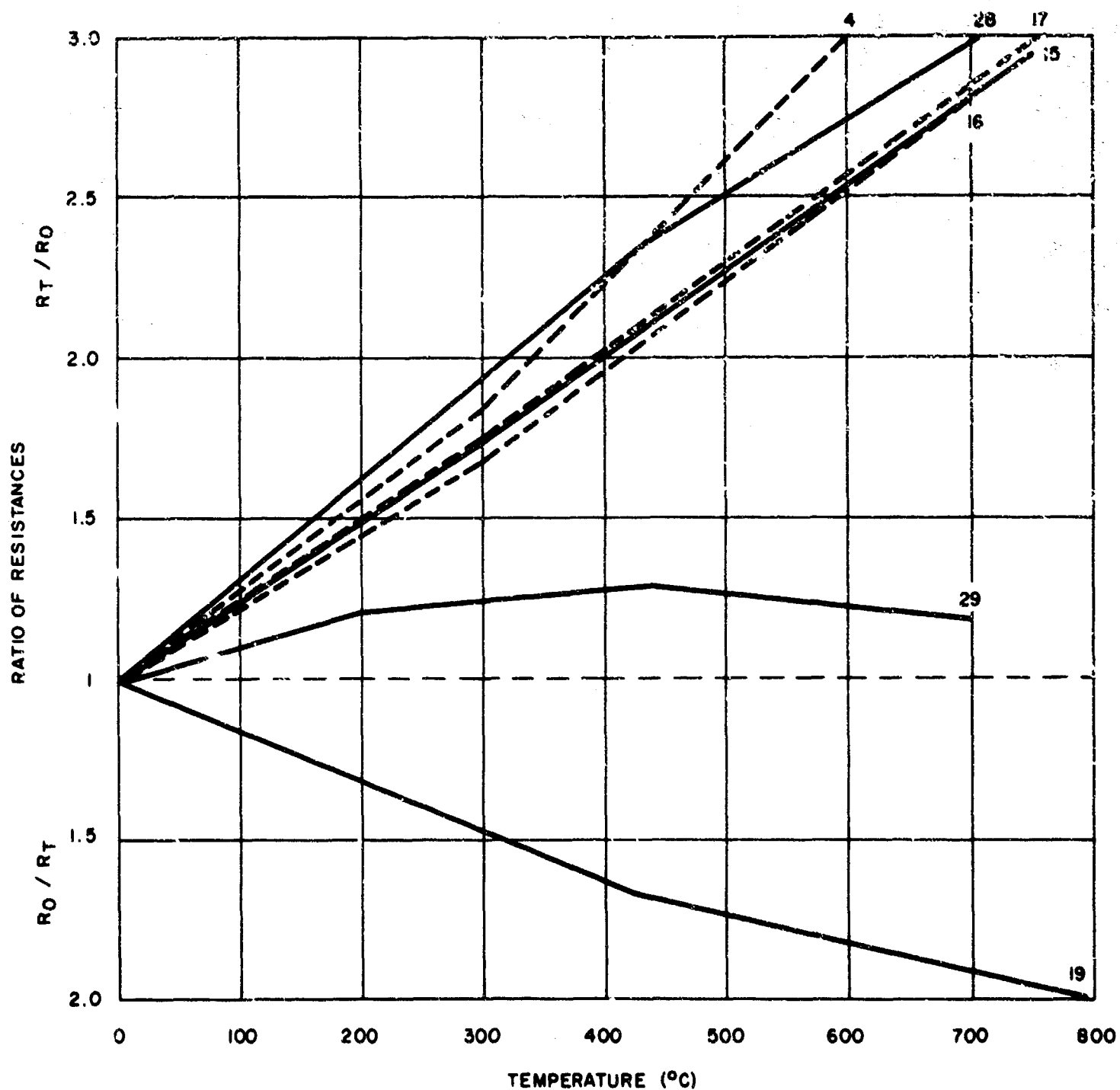
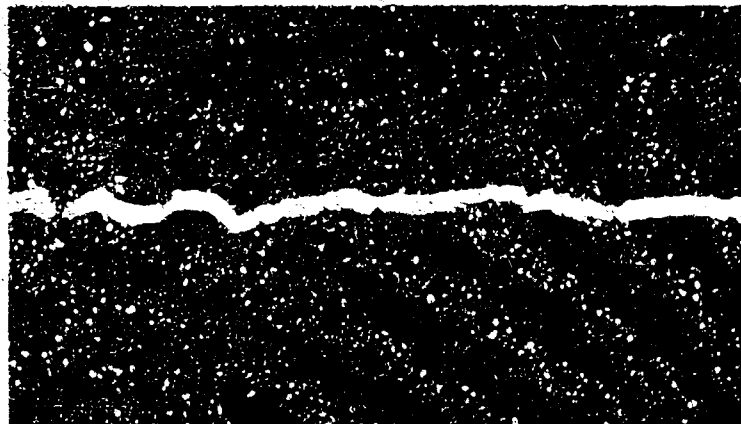
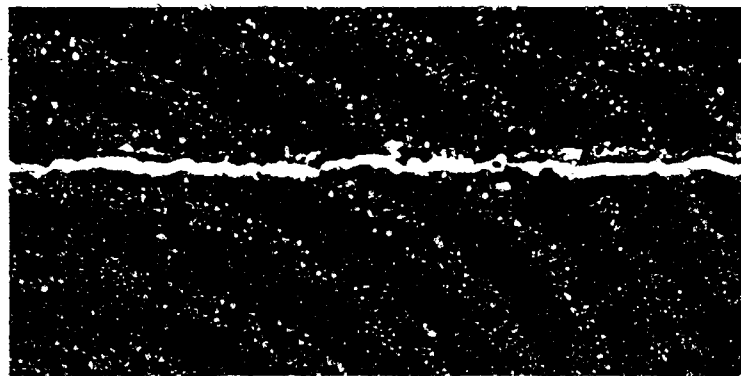


Figure 6.11: Measured resistance ratios vs temperature of test samples. (4) paint P-1 on ceramic Body A. (15) paint Ti-11 on ceramic. (16) paint Ti-11 on ceramic Body A, slightly machined. (17) paint Ti-11 on ceramic Body A, leached with nitric acid. (19) paint Ti-11 on ceramic Body A, heavily leached with nitric acid. (28) paint Ti-11 on ceramic Body E, oxidized in air. (29) paint Ti-11 on ceramic Body E, heavily oxidized in air.



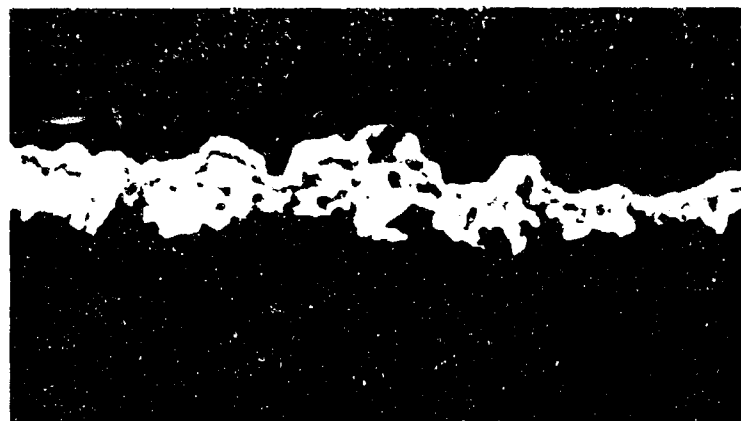
a) # 26

← Evaporated molybdenum  
on  
← Body E



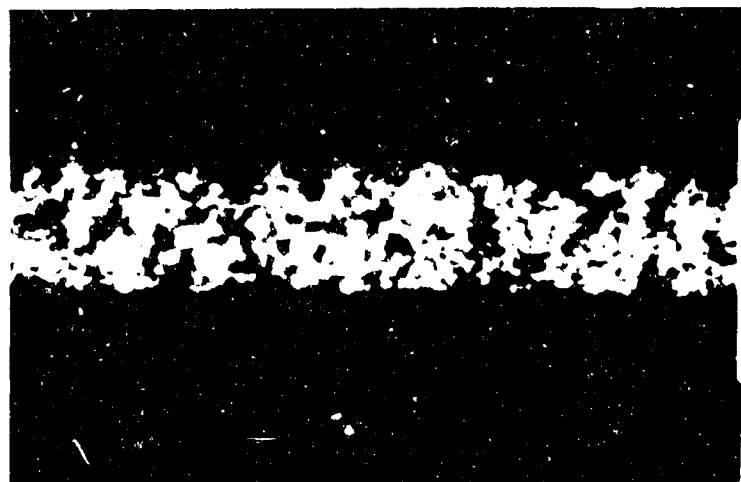
b) # 27

← Molybdenum evaporated on  
← Body E, fired at 1425°C,  
1/2 hr. in wet H<sub>2</sub>/N<sub>2</sub>



c) # 13

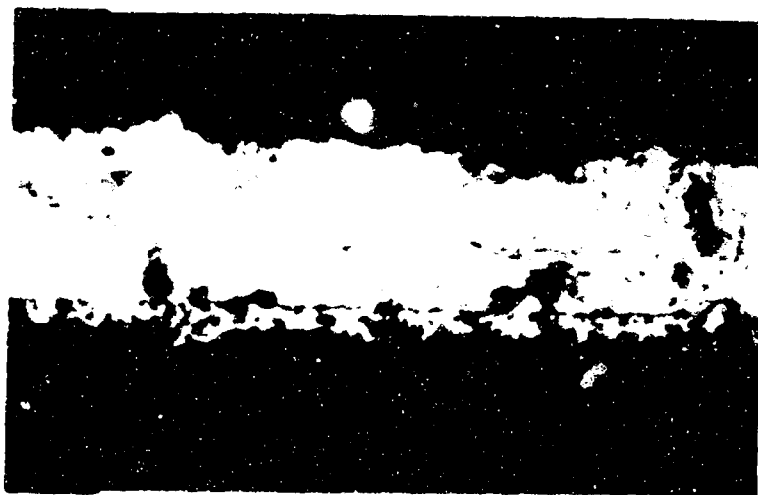
← P-4M  
on  
← Body A



d) # 4

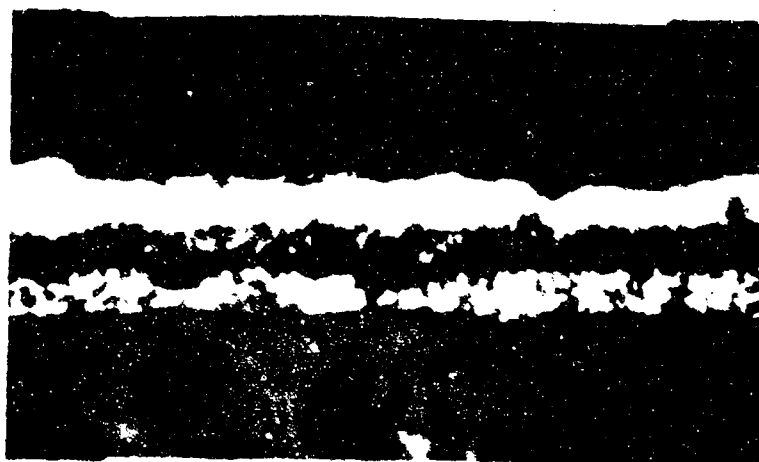
← P-1  
on  
← Body A

Figure 6.12: Photomicrographs (400X) of test samples. Metallizings in (a), (b), (c) have been overplated after the measurements.



a) # 5

← P-I (Machined)  
on  
← Body A



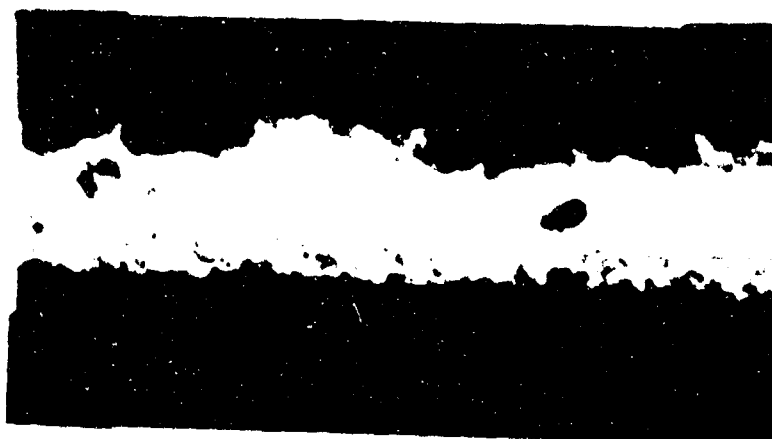
b) # 6

← P-I, partly leached (dark)  
on  
← Body A



c) # 7

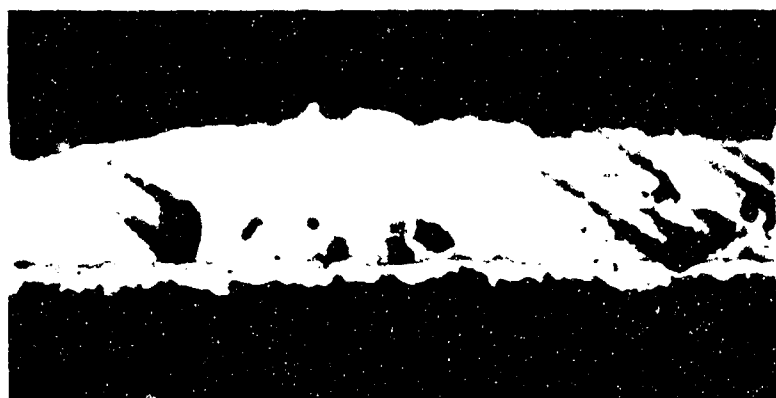
← P-I  
on  
← Body E



d) # 8

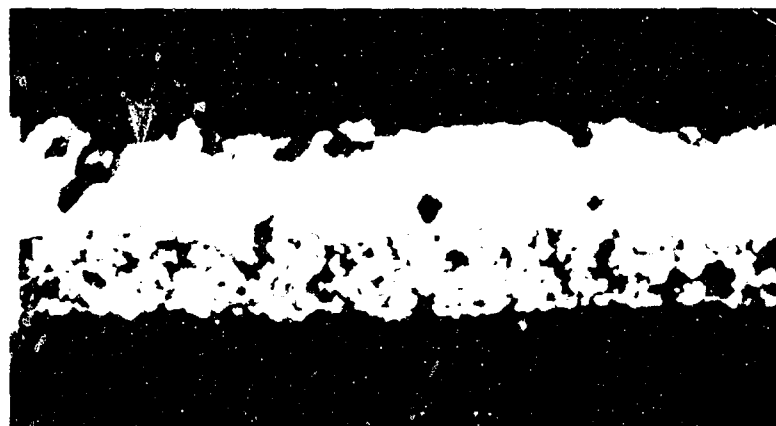
← P-I (Machined)  
on  
← Body E

Figure 6.13: Photomicrographs (400X) of test samples. Metallizings have been overplated after the measurements.



a) # 9

← P-1 (Machined)  
on  
← Body E



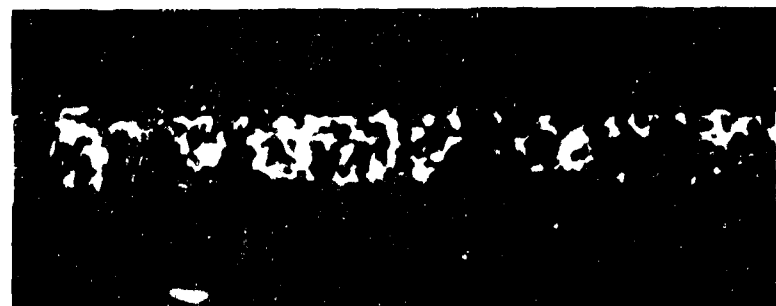
b) # 10

← P-3  
on  
← Body A



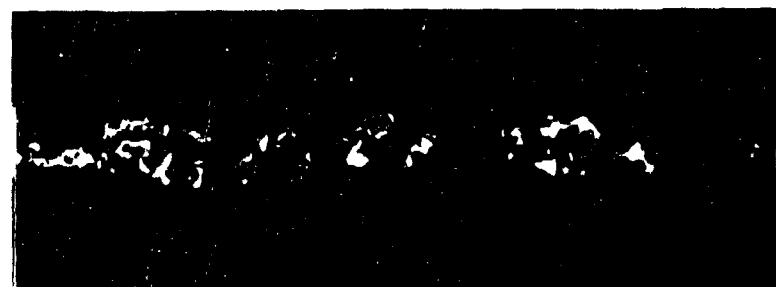
c) # 11

← P-3 (Machined)  
on  
← Body A



d) # 24

← P-1 (Electropolished)  
on  
← Body E



e) # 25

← P-1 (Heavily electropolished)  
on  
← Body E

Figure 6.14: Photomicrographs (400X) of test samples. Metallizings in (a), (b), (c) have been overplated after the measurements.

Finer methods of investigation such as X-ray diffraction or electron diffraction would have to be applied in order to explain the lower thermal coefficient of the coating either as an interaction with the ceramic substrate or in terms of the structure of the evaporated layer.

Curves 13 and 14 were obtained with P4-M metallizing paint on Body A and E ceramics fired on at 1600°C. This coating has a still lower coefficient than the evaporated metallizing although this paint consists of pure molybdenum powder and does not introduce any extraneous melt phase. Firing this paint at 1600°C rather than the normal sintering temperature of 1425°C used for the bulk of the samples, increases the interaction with the ceramic in order to provide the glass bonding phase. Measured resistivities are about 10 to 20 times as high as in the evaporated molybdenum layer. Metallurgical cross-sections indicate very irregular layers with paint agglomerations (Fig. 6.12c). There is only a very slight difference in the thermal coefficient at higher temperatures for the two different substrates with curve 13 being the lower one as expected. Ceramic A provides more glass for penetration into the metallizing, and the thermal coefficient of electrical resistivity is reduced or the metallizing behaves in a "less metallic" manner.

In Figure 6.07: Curve 1, obtained with molybdenum foil, is repeated for reference. Curve 18, for P-1 on A ceramic fired at 1600°C, is very close to curves 13 and 14 (see Fig. 6.06), and its metallurgical cross-section has the same characteristic appearance, it is irregular in thickness and has a number of agglomerations and gaps. The addition of melt phases in paint P-1 compared with P4-M does not affect the thermal coefficient of resistivity. Fired at the standard temperature of 1425°C, paint P-1 shows a lower thermal coefficient (curve 4). Reduced metal and melt phase are well interspersed (Fig. 6.12d). There are many more interruptions of the metal structure in the paint, and the melt phase thus contributes more to the electrical conduction. In spite of this, paint P-1 shows a lower resistivity than the higher fired pure metallic paint P4-M both after a 1425°C or 1600°C firing. Many contact points between small molybdenum aggregates seem to be more effective than the fewer contacts between large agglomerations in the paint sintered without the help of penetrating glass. Previous investigations showed an accumulation of the melt phase between the metallizing and the ceramic, suggesting a larger contribution of the melt phase to electrical conduction in this layer.

In sample No. 5, the surface layer of the fired P-1 metallizing is machined off (Fig. 6.13a). While the resistivity (ohm-cm) of the coating is practically not affected, the resistance per square is increased by a factor of five compared with sample No. 4 due to the reduction of the thickness. Curve 5 indicates a lower thermal coefficient of electrical resistivity and confirms that the metallizing nearer to the ceramic behaves "less metallic". It was thought that leaching of the metallizing paint with nitric acid (curve 6, dashed) would remove part of the molybdenum and would also increase the relative contribution of the melt phase. However, the acid probably affects the melt phase also. Sample No. 6 shows practically the same thermal coefficient as sample No. 4, although the resistance per square is increased by a factor of 2.5. About half of the original metallizing layer is changed by the leaching as can be seen in the metallurgical cross-section of Sample No. 6 in Fig. 6.13b.

In Figure 6.08: Curves 7, 8 and 9 obtained for metallizing P-1 on Body E ceramic, slightly machined P-1 metallizing, and the same metallizing further reduced in thickness, respectively, demonstrate also the more glassy behavior of layers in the metallizing closer to the ceramic. Changes in the thermal coefficient are smaller than between curves 4 and 5 in Fig. 6.07 because Body E ceramic (99% alumina) in samples 7, 8 and 9 provides very little melt phase as compared to Body A (94% alumina). Figures 6.13c and d, and 6.14a show the degree of machining in the metallurgical cross-sections of samples 7, 8 and 9. Determinations of the metallizing thickness are not accurate enough to place much emphasis on the calculated resistivities. The values are, however, in the same range as for P-1 on Body A ceramics. Curve 7 (P-1 on Body E) is lower than curve 4 in Fig. 6.07 (P-1 on Body A). This is surprising at first, because one would expect the additional glass in the case of the Body A substrate to cause a smaller thermal coefficient. On the other hand, it may be the melt penetrating into the metallizing which causes a higher degree of sintering of the reduced molybdenum oxide by pulling the particles together so that a more metallic conduction results.

The above argument is confirmed by curve 22. It is still higher than for paint P-1 on Body E (curve 7), although it refers to a modified paint P-1, in which the molybdenum oxide content has been reduced to one-sixth of the standard amount. It is, therefore, not so much the composition of the paint, but the degree of sintering, which determines if it behaves more or less metallic. A more

metallic conduction is characterized by a higher thermal coefficient of electrical resistivity.

In Figure 6.09: Paint P-3, contains silica in addition to the manganese oxide and titania in paint P-1. The thermal coefficients of paint P-3 on Body A and Body E are practically the same (curve 10 and curve 12) demonstrating that the silica addition corrects the deficiency shown above by P-1 paint on Body E ceramic. Figs. 6.14b and c show the original and machined metallizing P-3 on Body A. Machining increased the resistance per square by a factor of 2.5, proportional to the degrees of thickness. The thermal coefficient is also reduced when the coating is machined (compare curves 10 and 11). The resistivity of the metallizing is slightly lower than that of paint P-1.

In Figure 6.10: Another way of removing elementary molybdenum from the metallizing was tried in addition to leaching with nitric acid. Molybdenum was depleted under conditions used for electropolishing (1 part  $\text{H}_2\text{SO}_4$ , 4 parts  $\text{H}_3\text{PO}_4$ , 4 parts  $\text{H}_2\text{O}$ ,  $25^\circ\text{C}$ , 1.2 amps/cm<sup>2</sup>) in order to take off molybdenum exposed on the surface in a rather regular fashion. Surprisingly, both samples 24 and 25 treated this way had thermal coefficients practically equal to the original paint (curve 7), although the actual measured resistances have been increased appreciably in the procedure (from 0.4 ohms to 1.9 ohms and 40 ohms, respectively, or from  $63 \times 10^{-6}$  ohm-cm to  $350 \times 10^{-6}$  ohm-cm and  $6,100 \times 10^{-6}$  ohm-cm respectively). The metallurgical cross-sections in Figs. 6.14d and e show the large alterations in the paints. Electropolishing removed a large amount of the molybdenum, especially in sample 25. However, it affected the metallizing paint throughout the whole thickness, leaving molybdenum (white areas) more dispersed than in the original paint.

In Figure 6.11: The three almost identical curves 15, 16 and 17 refer to paint Ti-11 on ceramic Body A. A slight machining, which increased the resistance from  $4.1 \times 10^{-2}$  ohms per square to  $6.2 \times 10^{-2}$  ohms per square (sample 16), as well as leaching with nitric acid (sample 17) which caused the same increase in the surface resistance, did not affect the thermal coefficient of resistivity. However, this paint, Ti-11, on Body A is "less metallic" compared with paint P-1 (sample 4), although the latter has relatively more glass-forming components. This may be interpreted as due to the highly semiconductive nature of the  $\text{TiO}_x$ -containing non-metallic phases. As in other cases,

sintering of the molybdenum was enhanced by the glass, which pulled metallic particles together so that many metallic contacts were established. A much more severe leaching of Ti-11 with nitric acid, which increased the surface resistance from  $4.1 \times 10^{-2}$  ohms per square to 3 ohms per square produced a coating with negative coefficients of electrical resistivity (curve 19). This behavior must be interpreted with reservations. Heavy leaching does not attack the metallized surface evenly, it is apt to produce gaps in the conductive path. A metallurgical cross-section shows an unproportionately large amount of molybdenum left, which is in contradiction to the relatively high resistance of the sample. The value of resistivity listed is only an average and not too meaningful in this particular case, because the total resistance is practically determined by a small area, as is the semiconductive behavior.

Yet another method of removing molybdenum from fired metallizing, for increasing the relative melt content is to oxidize the samples in air at 540°C and subsequently drive off the formed  $\text{MoO}_3$  at 850°C in vacuum. Samples No. 28 and 29 were treated this way to different degrees, raising the original resistances by factors of 7 and 200, respectively (see Table 6-2). It required the more severe treatment to achieve a thermal coefficient of resistivity shown in Fig. 6.11, curve 29, which is very low and positive, almost zero, and low and negative, in various temperature ranges.

#### 6.2.1.5 Molybdenum and Melt Phase in Metallizing as Parallel Conductors

All metallizing formulations, including the pure molybdenum paint P-4M and the evaporated molybdenum, had a lower thermal coefficient of electrical resistivity than the measured molybdenum foils strapped on the ceramic heater. Resistivities of all these coatings were low which indicated that the main conduction mechanism was metallic. But there must be still another contribution which reduced the thermal coefficient. An equivalent circuit representing the situation, therefore, consists of a conductor of molybdenum with the resistance  $R_m$  shunted with the melt phase, a semiconductor with the relatively high resistance  $R_g$ . The total measured resistance at temperature T is then:

$$R = R_m R_g / (R_m + R_g) \quad (6)$$



In Fig. 6.06: Samples No. 1, 2, 3 consist of molybdenum foils strapped on a ceramic heater. They show the highest thermal coefficients of dc resistivity measured in all experiments. Nos. 1 and 2 differ slightly, probably due to different degrees of cold working in the production of the foils. Annealing (No. 3), however, causes only a small increase in the thermal coefficient. Its values ( $5 \times 10^{-3}/^{\circ}\text{C}$  and  $6 \times 10^{-3}/^{\circ}\text{C}$ , respectively) are in agreement with some published data for bulk molybdenum, which cover fairly wide ranges of values. Examples from the literature are  $3.3 \times 10^{-3}/^{\circ}\text{C}$  ( $25^{\circ}\text{C}$ ) and  $4.8 \times 10^{-3}/^{\circ}\text{C}$  ( $1000^{\circ}\text{C}$ ) in the Handbook of Chemistry and Physics, 44th Edition 1961;  $4.4 \times 10^{-3}/^{\circ}\text{C}$  ( $727^{\circ}\text{C}$ ) in W. H. Kohl, Materials and Techniques for Electron Tubes, 1960. Kinks in the curves with a steeper slope in the higher temperature range indicate an increase of the averaged coefficient with temperature. Curves 26 and 27 were obtained for evaporated molybdenum coatings on Body E ceramics at a substrate temperature of about  $900^{\circ}\text{C}$ .

Sample No. 27 was given an additional firing cycle of 1/2 hour at  $1425^{\circ}\text{C}$  in wet hydrogen-nitrogen atmosphere. Both thermal coefficients are lower than for molybdenum foil, but there is no appreciable difference between them. Metallurgical cross-sections in Fig. 6.12a and b indicate no visible interaction with the ceramic, even at the high firing temperature. Resistivities and resistances per square of the evaporated coatings are in the intermediate range between solid molybdenum and molybdenum metallizing paint. Firing of the evaporated molybdenum layer reduces the resistivity by a factor of two, thus indicating that the electrical properties are atomic and microstructure structure dependent, e.g. oxygen dissolved interstitially in the molybdenum lattice causes a change in resistivity.\*

The large decrease in resistivity is probably due to three factors:

1. Oxygen dissolved in the lattice.
2.  $\text{MoO}_x$  in the grain boundaries.
3. Interaction of Mo with the  $\text{Al}_2\text{O}_3$  and grain boundary phases.

---

\*A study of oxygen solubility and diffusion is presently underway in the laboratory. Oxygen solubility is being determined in terms of dc electrical resistivity.  
NASA Contract No. NAS3-7626.

In accordance with equation (5) above, the definitions of the thermal coefficients of electrical resistivity of the total metallizing, the molybdenum and the melt phase contained in it ( $\alpha$ ,  $\alpha_m$ ,  $\alpha_g$ , respectively) read as follows:

$$R/R_0 = \alpha T + 1 \quad (7)$$

$$R_m/R_{m0} = \alpha_m T + 1 \quad (8)$$

$$R_g/R_{g0} = \alpha_g T + 1 \quad (9)$$

The coefficients  $\alpha$  and  $\alpha_m$  have been measured directly, while the coefficient  $\alpha_g$  for the melt phase is to be determined.

Writing equation (6) for the temperatures  $T$  and  $T = 0^\circ\text{C}$  one obtains for the total resistance ratio:

$$R/R_0 = \frac{(R_m/R_{m0}) \cdot (R_g/R_{g0}) \cdot (1 + R_{g0}/R_{m0})}{R_m/R_{m0} + R_{g0}/R_{m0} \cdot R_g/R_{g0}} \quad (10)$$

or expressed in terms of the thermal coefficients and the temperature  $T$ :

$$\alpha T + 1 = \frac{(\alpha_m T + 1) \cdot (\alpha_g T + 1) \cdot (1 + R_{g0}/R_{m0})}{(\alpha_m T + 1) + R_{g0}/R_{m0} \cdot (\alpha_g T + 1)} \quad (11)$$

this equation is to be solved for  $\alpha_g$ , the thermal coefficient of electrical resistivity of the melt phase in the metallizing. There is no way of knowing the resistance ratio  $R_{g0}/R_{m0}$  of the melt phase and the molybdenum at  $0^\circ\text{C}$ . Therefore, values are assumed for this ratio covering a wide range, and values for  $\alpha_g$  are calculated with the help of equation (11) setting the temperature  $T = 400^\circ\text{C}$ .

Table 6-3 below shows the computed thermal coefficients of electrical resistivity of the melt phase in metallizing for several assumed resistance ratios at  $0^\circ\text{C}$ . Naturally, the thermal coefficient for the glass in the metallizing comes out to be negative. It is surprisingly little dependent on the resistance ratio at zero degrees centigrade.

Curve 19 in Fig. 6.11 indicates a negative thermal coefficient of  $-1.2 \times 10^{-3}$  in the temperature range of  $0^\circ\text{C}$  to  $175^\circ\text{C}$  for the heavily leached Ti-11 metallizing and confirms the above concept. It falls into the range shown feasible in Table 6-3 on the following page.

TABLE 6-3

Computed Thermal Coefficients of Electrical Resistivity

Resistance Ratio $R_{go}/R_{mo}$	Thermal coefficient of electrical resistivity of the melt phase, $\alpha_g$
10	- $1.03 \times 10^{-3}/^{\circ}\text{C}$
20	- 1.65
50	- 2.13
100	- 2.28
200	- 2.40
500	- 2.46

## 6.2.2 Effect of Wetting Layer (Overplate) on the Resistivity of the Metallizing

### 6.2.2.1 Influence of rf Conduction Losses

When the metallizing layer is thin, some of the rf current will be carried in the overplate and braze regions; the composition of the overplate is therefore important. Also sintering of the overplate will cause a diffusion alloying of the nickel (or copper, or iron) overplate into the metallizing with a consequent increase in resistivity.

Accordingly, these effects were studied in simple experiments with prolonged and repeated sinter firing of nickel and copper plate on a large number of metallized ceramic rings.

### 6.2.2.2 Experimental

Standard ceramic rings (2.356 in. O.D., 1.990 in. I.D., 0.075 in. thick) of Body A were metallized on one side with P-1 metallizing paint and fired at 1425°C. A radial cut produced resistors with a length of 17.5 cm and a width of 0.51 cm ( $17.5 \div 0.51 = 34.4$  squares\*). DC resistances were measured with a bridge and copper probes. Contact resistances amounted to 0.008 ohms and had to be considered only on copper plated samples with resistances as low as 0.123 ohms.

Four groups of four samples each were tested. Table 6-4 below lists data of one representative sample of each group. Thicknesses of the metallizing and thick plating layers were determined from metallurgical cross-sections of the samples. Irregularities were large and, therefore, these numbers are only for reference, as are the calculated resistivities. All values were obtained before the sinter firing of the overplates.

Resistances of the rings were measured after metallizing them. These were then nickel or copper plated and remeasured. After each sinter firing step, resistances were again measured. There were four sinter firings at

---

\*Dimensionless ratio of length to width of resistor which is used in the definition of surface resistivity (ohms/square).

TABLE 6-4

Thicknesses of Metallizing and Plating on Representative Test Samples.  
Measured Resistances, Surface Resistances and  
Deducted Resistances

Sample of Group No. :	1	2	3	4
Thicknesses of metallizing (mils)	0.3	0.3	0.6	0.5
Resistance (ohm)	1.95	1.67	0.99	0.99
Resistivity of metallizing (ohm cm)	$42 \times 10^{-6}$	$37 \times 10^{-6}$	$43 \times 10^{-6}$	$36 \times 10^{-6}$
Surface resistance of metallizing (ohms per square)	$5.6 \times 10^{-2}$	$5 \times 10^{-2}$	$2.9 \times 10^{-2}$	$2.8 \times 10^{-2}$
Plating	nickel	nickel	nickel	copper
Thickness of plating (mils)	0.07	0.2	0.07	0.3
Total resistance (ohms)	1.52	0.43	0.76	0.15
Combined resistivity (ohm cm)	$41.5 \times 10^{-6}$	$16 \times 10^{-6}$	$38 \times 10^{-6}$	$8.9 \times 10^{-6}$
Combined surface resistance (ohms per square)	$4.2 \times 10^{-2}$	$1.3 \times 10^{-2}$	$2.2 \times 10^{-2}$	$0.4 \times 10^{-2}$

900°C for 1/2 hour each, two firings at 900°C for 1 hour followed by three firings at 1000°C for 1 hour each, all in a wet hydrogen atmosphere.

The experiments were designed to study reaction mechanisms. It is rather unusual for metallized and nickel plated ceramics in electron tube structures or in micro-electronic applications to go through extended high temperature treatment.

#### 6.2.2.3 Results

Figs. 6.15 through 6.18 show resistances of test samples measured after each processing step starting with the metallizing and the overplating. The relative resistances which are plotted are referred to the initial resistances of the metallized ceramic rings. See the above Table 6-4 for absolute values.

All curves in Figs. 6.15, 6.16 and 6.17 for nickel plated samples show a more or less pronounced minimum. The lowest minimum in Fig. 6.15 was, of course, obtained with the relatively thickest nickel plating. The resistance went down slightly after the first sintering step as a result of the consolidation of the plated layer. The next firing caused a sharp increase of the resistance which indicated strong interaction between the nickel plating and metallizing. Note that further firings at 900°C lasted for one hour. After the fifth step at 900 C, the curves level off, indicating that equilibrium had almost been reached. A higher firing temperature of 1000°C in the following firings lead again to an increase of resistance and to a final leveling off of the measured resistance. The maximum increase of measured resistances was to 195% referred to the resistances of the metallized ceramic. It occurred on the sample with the thickest nickel plating which also had the lowest minimum. The conclusion to be drawn from this fact is that the reaction was limited by the amount of nickel available.

Fig. 6.16 confirms the latter statement. As can be seen from the relatively lower minima, a much thicker nickel plating was applied. Again, resistances climbed after the second firing steps. The curves again level off after the series of 900°C firing steps and after the three subsequent 1000°C firings. Referred to the metallizing resistances, the increases are not as high as in the previous group of samples, but actually the alloying of nickel and molybdenum, which leads to a high resistivity coating is

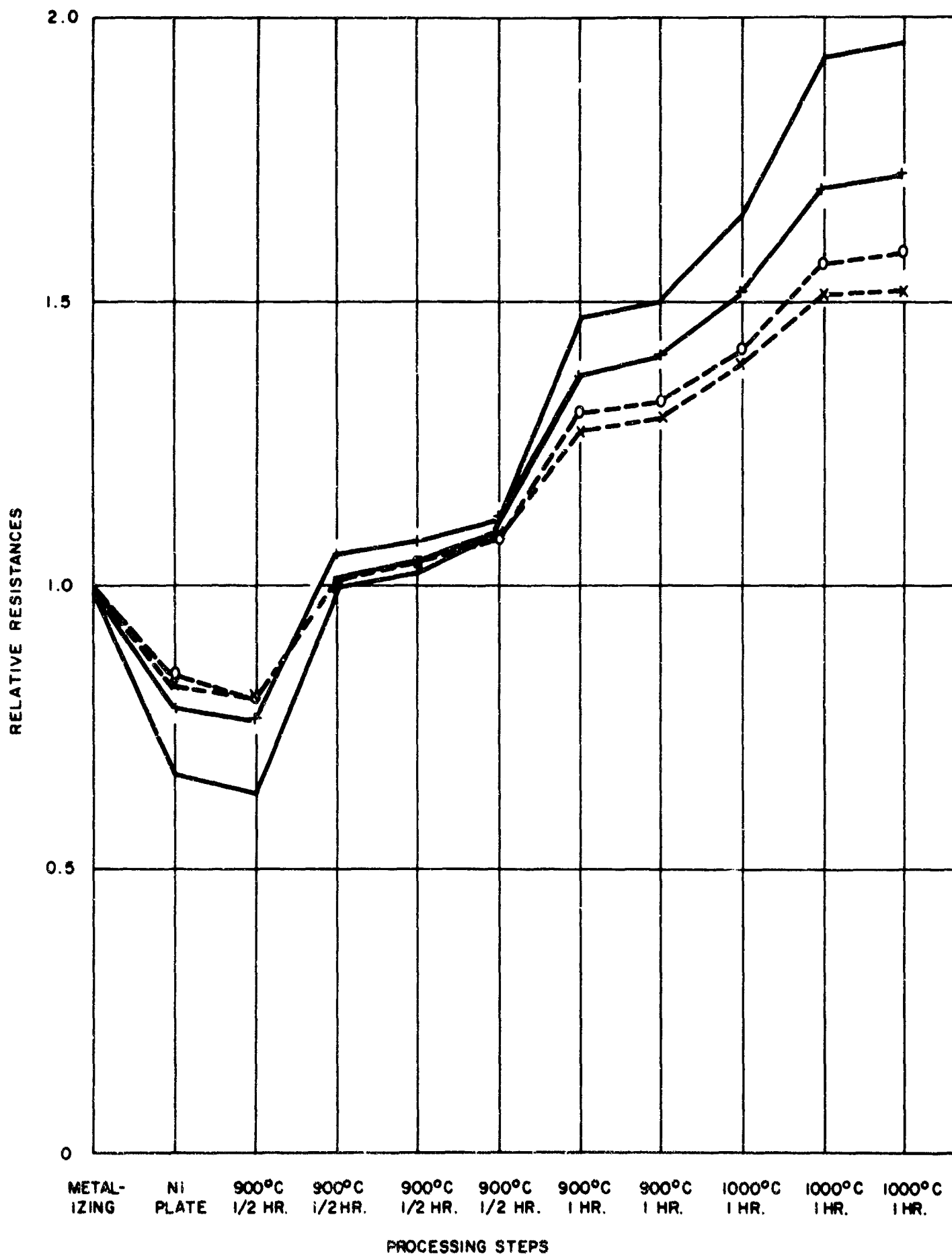


Figure 6.15: Interaction of Ni wetting layer with P-1 metallizing on Body A ceramic. Relative resistance as a function of processing steps. Data obtained from four samples of group I, Table 6-4.

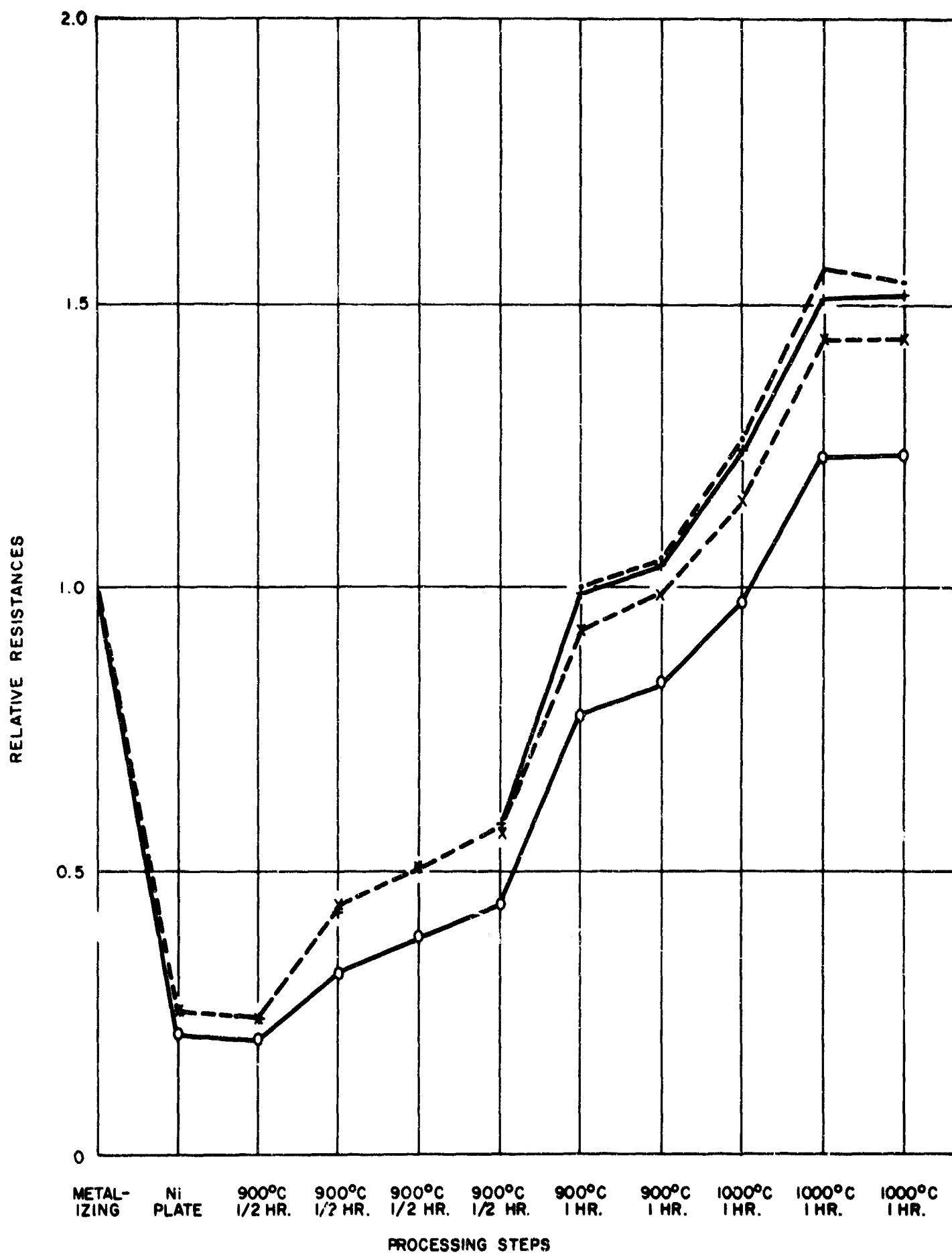


Figure 6.16: Interaction of Ni wetting layer with P-1 metallizing on Body A. Relative resistance as a function of processing steps. Data obtained from four samples of Group 2, Table 6-4.



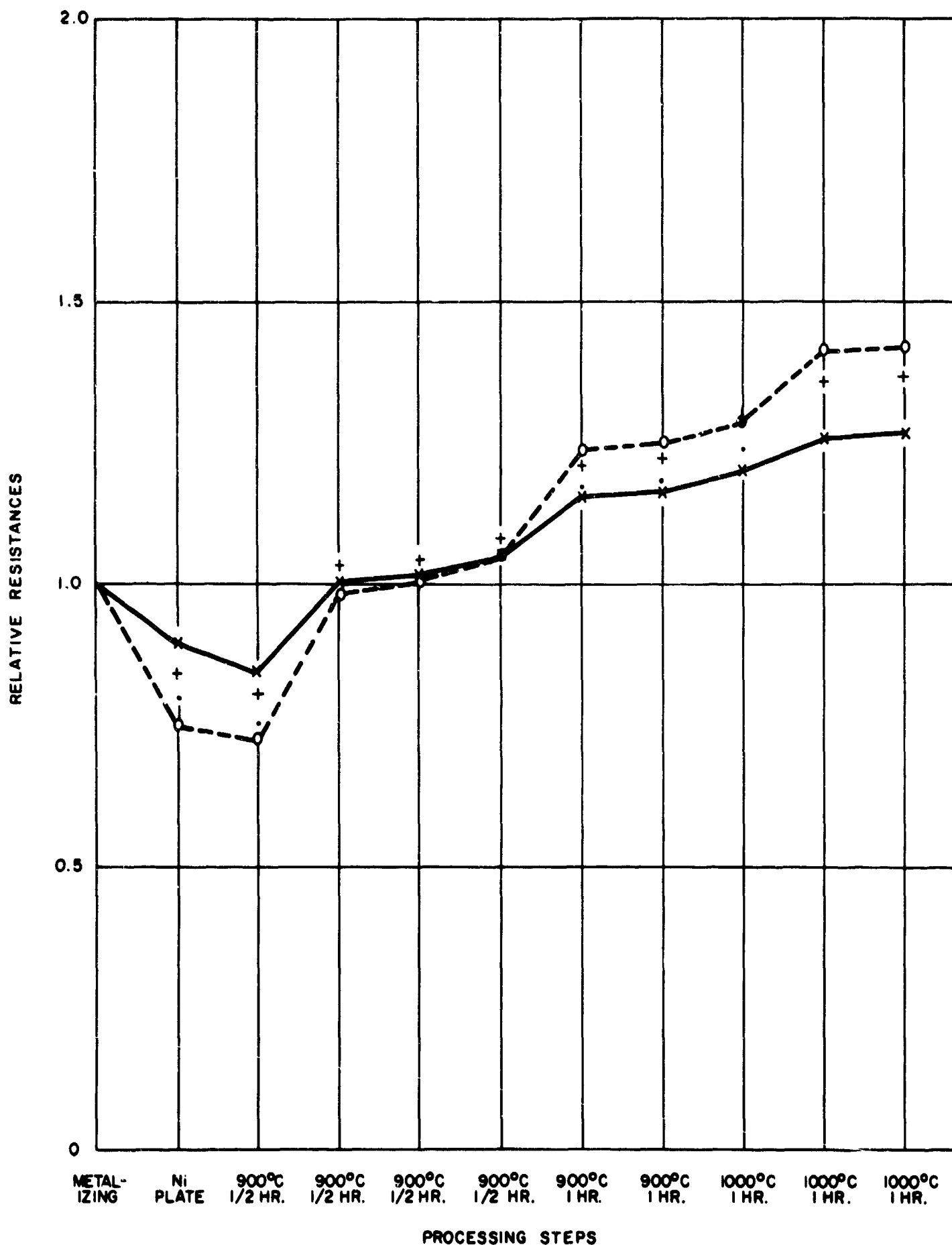


Figure 6.17: Interaction of Ni wetting layer with P-1 metallizing on Body A. Relative resistance as a function of processing steps. Data obtained from four samples of Group 3, Table 6-4.

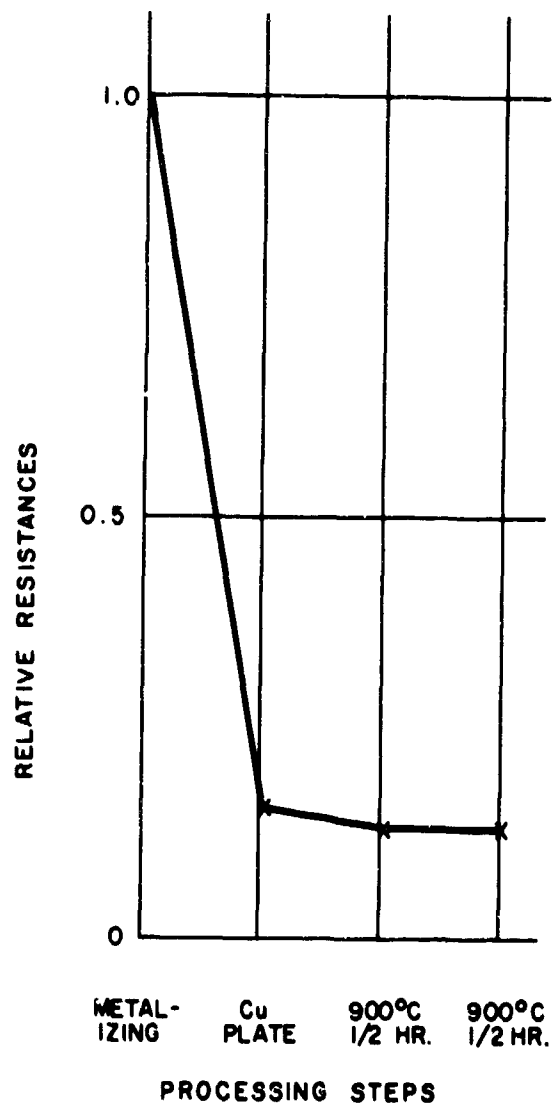


Figure 6.18: Interaction of Cu wetting layer with P-1 metallizing on Body A ceramic. Relative resistance as a function of processing steps.

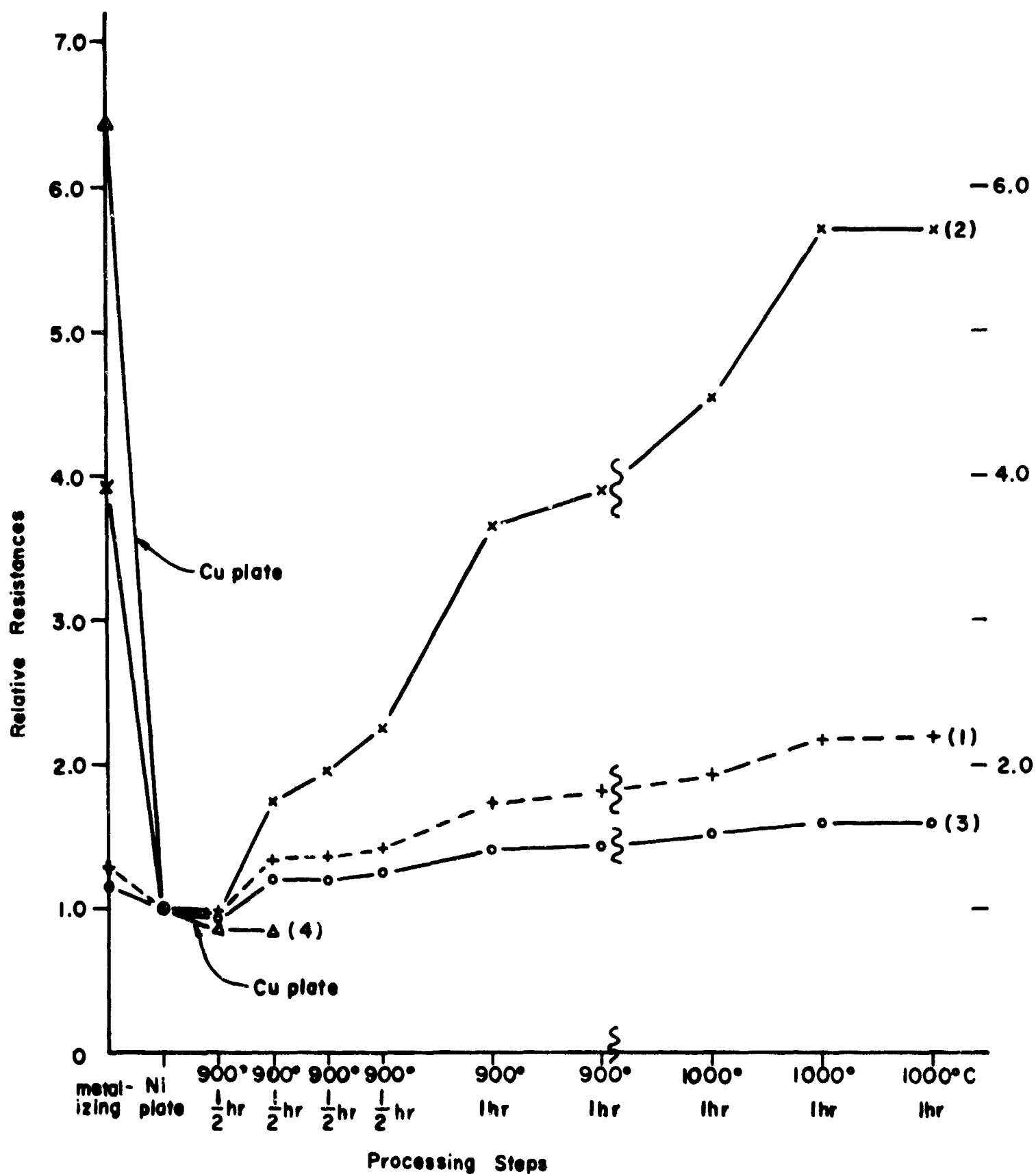


Figure 6.19: Relative resistance of metallized and over-plated Body A substrates as a function of sinterfiring. (1) 0.3 mil metallizing, 0.07 mil Ni-plate; (2) 0.3 mil metallizing, 0.02 mil Ni-plate; (3) 0.6 mil metallizing, 0.07 mil Ni-plate; (4) 0.5 mil metallizing, 0.3 mil Cu-plate.

more obvious if one considers the increase from the minimum. It amounts to a factor of 7.6, as compared with the corresponding increase by a factor of 3.1 in the previous group of samples with thin nickel plating. Again the larger amount of nickel available provided for the more pronounced interaction leading to the high resistance.

Results with the next group of samples, relatively thick metallizing, and thin nickel plating, again proved the same point. Increases of resistances were relatively low, the thickest nickel plating causing the largest increase.

Finally, metallized ceramic rings were overplated with copper and sinter fired. See Fig. 6.18 for the resulting resistances. As expected, the resistances were initially decreasing and constant after the second sinter firing. There was no evidence from the resistance data of an interaction between copper and molybdenum. From the data of Table 6-4, column 4, the resistivity of copper in ohm cm was calculated and found to be  $4 \times 10^{-6} \Omega \text{ cm}$ , which is twice the reported value for that of bulk OFHC copper.

Data in Figs. 6.15 through 6.18 are summarized in Fig. 6.19 for one representative sample out of each group. The scale on the abscissa has been adjusted to distinguish between the half-hour and the one-hour firing steps. The break in the curves indicates the switch over to 1000°C sintering. Relative resistances are now referred to the overplated samples. This way, increases of resistances show up more clearly; especially curve (2) stands out.

### 6.3 rf CONDUCTION LOSS MEASUREMENTS

#### 6.3.1 Introduction

The rf losses in ceramic-metal seals, since they will be due to currents in a confined area near the metal wall, can be described by an equivalent surface resistivity. By placing a sample of metallized ceramic inside a resonant cavity, one can measure the effective surface resistivity of the interface in several ways. One method is to measure the change of a property associated with the cavity such as Q, input impedance or power necessary to excite the cavity to a given level. The cavity can then be calibrated against a material of known resistivity. A more sensitive method of measuring these properties is the bridge technique wherein one can measure the deviation of some property of the cavity

containing the test ceramic from that of a standard cavity. The same quantities can be measured by either technique.

An example of each method is found in the literature. The first method was used by Dehn and Close<sup>1</sup> in which they measured the Q of a test cavity containing the material to be tested. The cavity used was a right circular cylinder operated in the TE<sub>111</sub> mode. The ceramic samples were brazed to the interior surface of the removable end plates of the cavity. The samples were placed near a region of high magnetic field so as to insure maximum currents across the ceramic-metal interface and hence maximum loss. A second requirement on the sample placement was that it be in a region of low electric field.

By noting the frequency of the half-power points on the response curve of the cavity, the Q may be readily calculated from 
$$\frac{\Delta f_{3db}}{f_0} = \frac{1}{Q}$$

where  $\Delta f_{3db}$  is the difference in frequency between the half power points and  $f_0$  is the resonant frequency of the cavity. A curve of cavity Q versus end plate resistivity was calculated and compared with Q measurements with end walls of known resistivity (materials such as Pb, Sn, Brass). By the use of this curve a measured Q of an unknown sample can be readily converted to an equivalent surface resistivity.

The bridge method was used by Ernst and Purl<sup>2</sup>. Two right circular cylindrical cavities were used in the TM<sub>020</sub> mode. The fields are such that a ring shaped sample with one flat side (the interface) placed against the end of the cavity can be located in a region of high magnetic field and low electric field. The sample is placed in one cavity (the test cavity). A lossy material is introduced into the second cavity and is adjusted by a micrometer screw so that the loss inserted is some function of micrometer reading. The two cavities are connected to the two equal arms of a Magic Tee. When power is fed to the third arm, the difference in the input admittance of the two cavities relative to each other is related to the amount of power present at the fourth arm of the Magic Tee. When the admittances are equal, no power appears in the fourth arm. The power out of arm four is proportional to the square of the difference of cavity admittances. As in the work of Dehn and Close<sup>1</sup>, the system is calibrated by utilizing samples of known resistivity and plotting their values versus the loss-inserting-micrometer reading. When an unknown sample is tested, its effective interface resistivity is read from the calibration curve.

### 6.3.2 Selected Measurement Technique

In this present research, for the evaluation of losses in ceramic-to-metal seals due to conduction currents, an admittance bridge was used similar to that of Ernst and Purl<sup>2</sup>. By placing a sample of metallized ceramic in a resonator in a region of high magnetic field and low electric field, maximum conduction currents will flow along the seal area while minimum displacement currents will be present in the ceramic; hence conduction losses will predominate. The effect of these losses will be to lower the resonator  $Q$ . Looking into a resonator from the input waveguide, the incident wave sees infinite admittance except at the resonant frequency. Near resonance the input admittance to the resonator drops until at resonance it reaches some low value. The resonant input admittance of the resonator is a function of the resonator  $Q$ , so that a change in resonator  $Q$  can be measured by noting the change in resonator input admittance.

As noted previously, the admittance bridge method used in this work compares the relative admittance of a sample resonator with a standard resonator by utilizing a Magic Tee. The Magic Tee has the property that if power is fed into arm three, the power flowing in the fourth arm is proportional to the square of the difference of the admittances presented to its two equal arms. Hence two resonators, identical in all respects, connected to a Magic Tee's equal arms, at all frequencies will cause zero power to flow in arm four if power is applied to arm three. Now, if a small loss is introduced into one of the resonators, at the resonant frequency, the input admittances will no longer be equal. Power will flow in the fourth arm which is proportional to the square of the difference in input admittance of the two resonators. If an equal loss is inserted in the second resonator, the bridge will be brought back to a balance condition and hence no power will flow through the fourth arm. By calibrating the loss introduced into the second resonator, the relative lossiness of the first resonator can be determined.

### 6.3.3 Sample Preparation

Three series of seal samples were prepared during the program.

The initial test sample consisted of a plated metallized ceramic ring brazed to a 10 mil cupro-nickel disc which in turn was tinned to a copper sample holder. All the

exposed metal surfaces were silver plated in order to minimize rf losses (except in the seal area). Because the 10 mil disc warped, it was replaced by a 20 mil disc which utilized a back-up wafer seal as shown in Fig. 6.20.

General details of the seal construction follow. Specific seal construction is discussed later.

#### 6.3.3.1 The Ceramic

The samples were fabricated from Lucalox\* or Body A in the form of a flat ring 1.207" O.D. x 0.703" I.D. x 0.100" high.

#### 6.3.3.2 The Metallizing

The metallizing paint compositions P-1 and P-2 were used. The latter paint was sintered at 1550°C as well as 1425°C. A spray application gave the most uniform coating thickness\*\* and was utilized. Copper, nickel, titanium and molybdenum were also evaporated onto ceramics to give metallizing films in the range 1-10 microns. Non-metallic coatings of MnO-TiO<sub>2</sub> were also fired onto substrates.

The amount of coating on actual parts could be determined by weighing and by measuring with a micrometer after spraying. In addition, test pieces sprayed at the same time were cross-sectioned after sinter firing and examined metallurgically to measure sintered coating thickness and to detect any thinning at the edges.

The thickness of the metallizing was in general determined from the calibration curve, Fig. 4.48. This calibration curve was drawn from data obtained by plotting the unfired sprayed weight of P-1 paint applied to 1" discs of Body A versus the cross-sectioned and microscopically measured thickness of the same discs after sinter firing.

#### 6.3.3.3 The Plating

Copper, iron and nickel plating of the metallizing were evaluated with selected brazing alloys. The copper was

---

\*General Electric Co. trade name.

\*\*Film metallizing would also be satisfactory if the film thickness could be controlled.

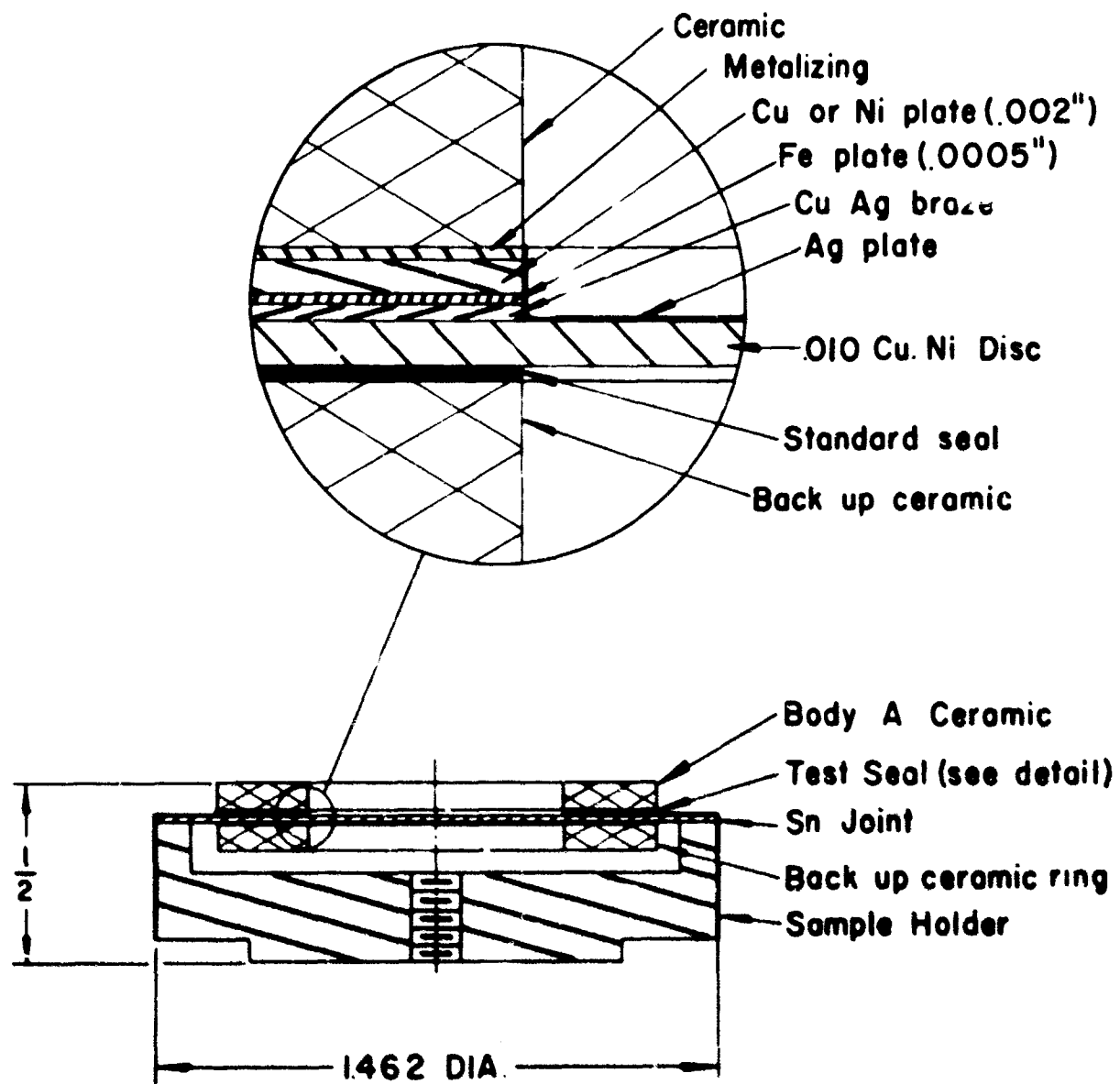


Figure 6.20: RF conductivity test assembly. Showing layered structure of an iron barrier layer seal and showing back up ceramic used to reduce seal stresses.



plated to  $12\mu$  minimum thickness and the nickel to  $25\mu$ . The nickel was plated and sintered in two "build up" stages. The plated parts were sintered at  $800^{\circ}\text{C}$  or  $900^{\circ}\text{C}$  for 1/2 hr. in hydrogen.

The iron layer was plated on top of either the copper or nickel layer to a minimum thickness of  $12\mu$  and sintered. It was brazed unsintered in the second series of tests in order to minimize interdiffusion of the plated layers. In a third series it was sintered at  $800^{\circ}\text{C}$  and a nickel (unsintered) overplate then plated on top. A visual inspection for blistered plating was made after sintering.

#### 6.3.3.4 The Brazed Assembly

In the first series of tests nickel and copper plated samples were brazed to 70/30 cupro-nickel discs with copper braze.

Nickel or copper plated and subsequently iron-plated samples were brazed with Ag-Cu braze in series two. An additional nickel plate was inserted in series three.

Representative production type seals were made such as nickel plated metallizing, Ag-Cu brazed to nickel plated Kovar; and copper plated metallizing Au-Cu brazed to copper. Special evaporated metallizing seals were also brazed.

A direct transition, copper-to-ceramic, seal was fabricated. This represented an optimized low loss situation. The ceramic was first electroless copper plated\* or vapor plated just enough to give a conductive surface, then electroplated to over  $40\mu$ . The strength of the copper-ceramic bond was quite weak (20 psi) so the plated ceramics in this instance were simply tinned to the sample holder for the seal rf conductivity test.

The brazed subassemblies of the type described were tinned to a solid copper test piece base which is part of the rf test cavity. Before placing in the cavity, the assemblies were cleaned and silver plated. The silver was plated to about  $20\mu$  thickness which is well in excess of the

---

\*Enthone process using "Enplate Cu-400" with Sn activator.

skin depth at test conditions. The silver covered the tinned joints and covered any material which may have blushed out during brazing. A cross-section of a typical assembly was shown in Fig. 6.20.

#### 6.3.3.5 The Standard Assembly

The standard assembly consisted of a clean ceramic, Body A, glued with a minimum amount of low loss polystyrene cement to a gold-plated copper cup holder.

Several standard assemblies were constructed for the purpose of placing them in the test resonator and the standard resonator to obtain an initial balance on the cavities. They were also used in the standard resonator in the loss measurements to balance out the bulk ceramic effects in the two cavities.

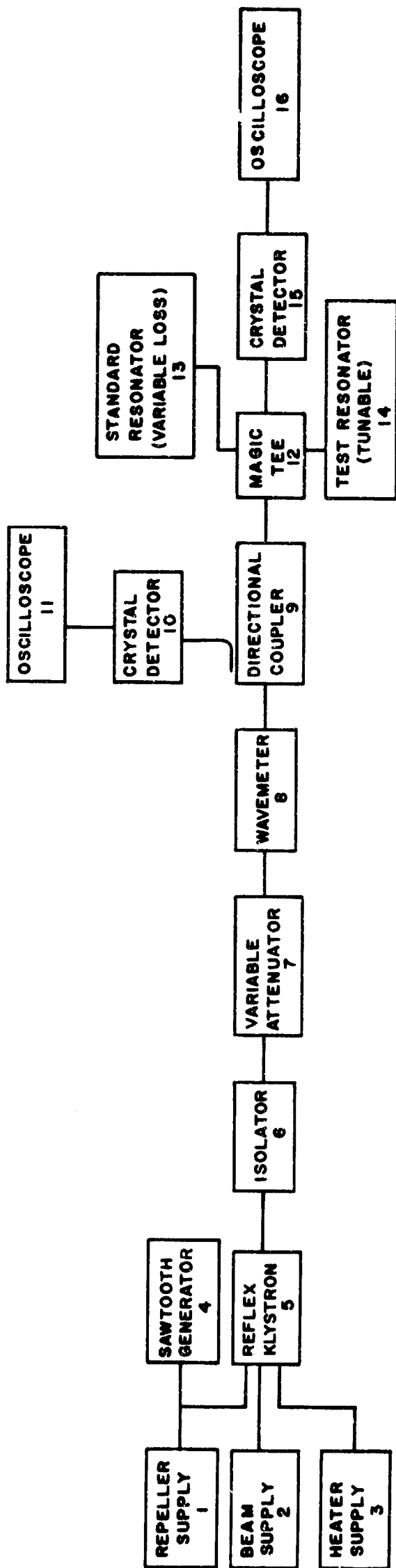
#### 6.3.4 Equipment and Experimental Procedures

##### 6.3.4.1 Assembly of Apparatus

The block diagram of the test setup used in the first six quarters is shown in Fig. 6.21. The general layout of the equipment is shown in Figs. 6.22 and 6.23. For the third and last series of tests a simplification was introduced in the test setup by using a Hewlett-Packard 716A power supply for the reflex klystron. This replaced the repeller supply, beam supply, heater supply, and sawtooth generator shown in the block diagram of Fig. 6.21.

A cross-sectional drawing of the tunable resonator which contains the ceramic-metal sample to be tested is shown in Fig. 6.24. The entire assembly is constructed of OFHC copper stock. The inner surfaces were fine machined, polished and then chemically polished to produce as smooth a surface as possible. The base and top ring were plated with silver on their common surfaces and hydrogen brazed together. Visual inspection of the interior of the joint showed good contact and very little blushing of the silver. Simultaneous to this operation, a short section of waveguide was silver brazed to the slot milled in the side of the resonator.

The connection between the resonator body and the removable top utilizes an rf choke to minimize losses due to poor electrical contacts and to reduce variations in readings due to changes in electrical contact. When machining the top, it was found impossible to turn a good



- |                                |                                     |
|--------------------------------|-------------------------------------|
| 1. FLUKE MODEL 301C            | 9. HEWLETT-PACKARD MODEL X752C      |
| 2. HEWLETT-PACKARD MODEL 712B  | 10. HEWLETT-PACKARD MODEL 420B      |
| 3. EIMAC                       | 11. TEKTRONIX MODEL 5130            |
| 4. TEKTRONIX MODEL 1S2         | 12. DEMORNAY BONARDI XBAND "DBG-655 |
| 5. EIMAC A.075                 | 13. EIMAC                           |
| 6. UNILINE MODEL 88-96         | 14. EIMAC                           |
| 7. HEWLETT-PACKARD MODEL X375A | 15. HEWLETT-PACKARD MODEL X421A     |
| 8. FXR MODEL X402A             | 16. TEKTRONIX MODEL 503             |

Figure 6.21: Block diagram of admittance bridge equipment for measuring  $I^2R$  conduction losses in metallizing.



Figure 6.22: Close-up of admittance bridge showing Magic-T and matched resonators. Ceramic samples in foreground.

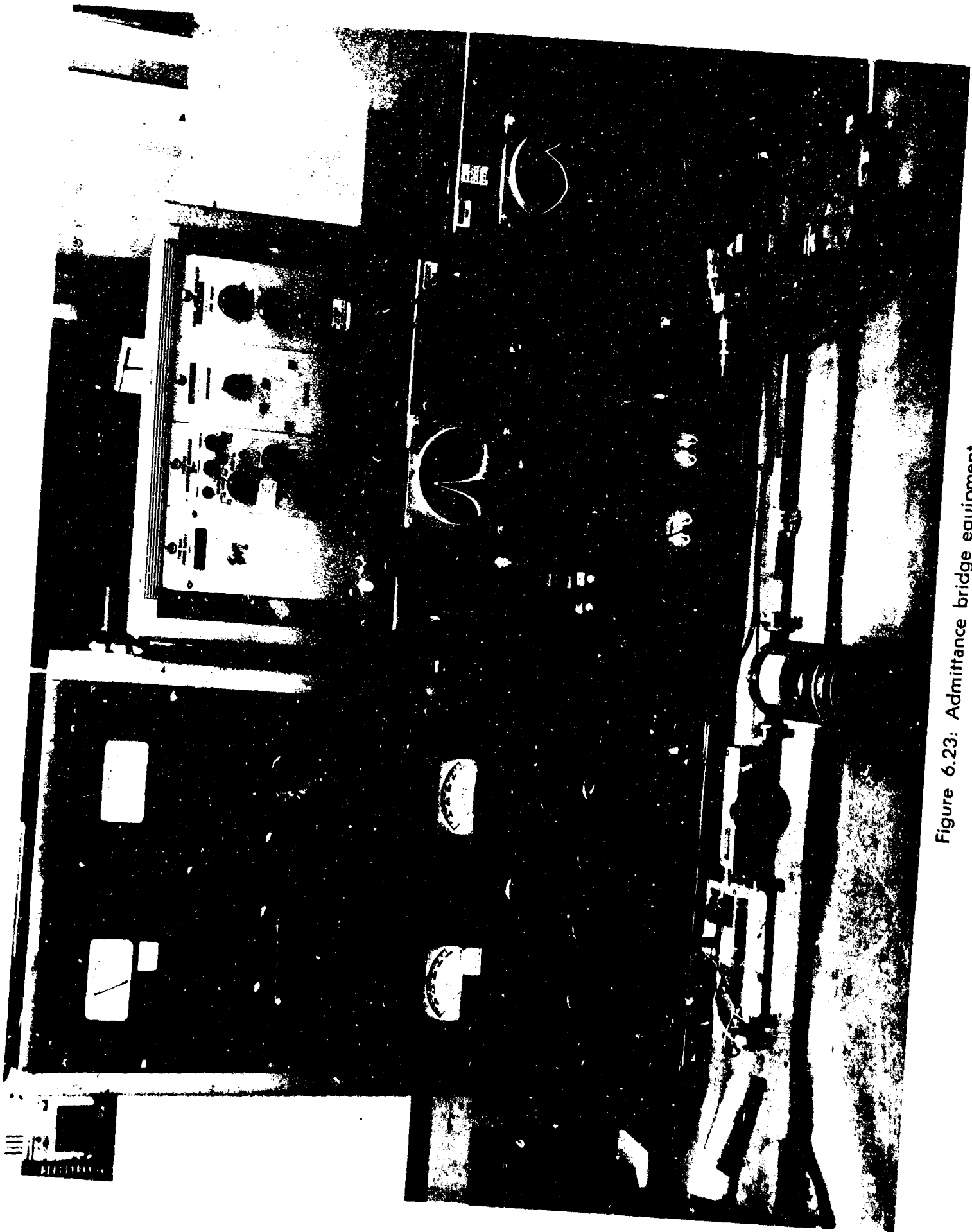
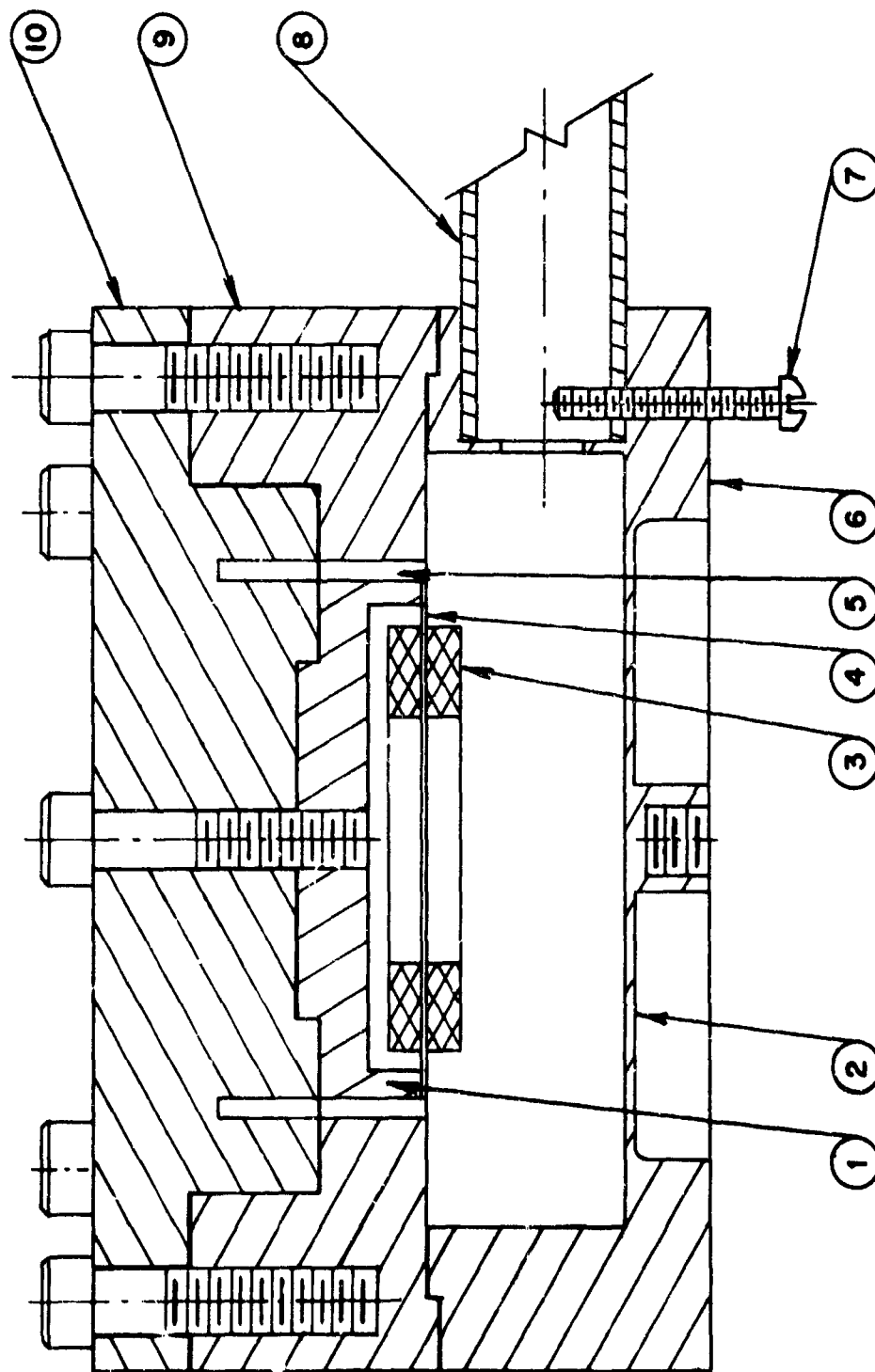


Figure 6.23: Admittance bridge equipment.

## ADMITTANCE BRIDGE TEST RESONATOR



- 10. TOP
- 9. TOP RING
- 8. WAVEGUIDE
- 7. COUPLING SCREW
- 6. BASE
- 5. CHOKER
- 4. TEST PIECE DISC
- 3. CERAMIC TEST PIECE
- 2. TUNING DIAPHRAGM
- 1. REMOVABLE TEST PIECE BASE

Figure 6.24: Admittance bridge test resonator.

choke slot in the top, so the center of the top was made in the form of a plug, the thickness of which was equal to the slot depth. It was silver brazed in place and note was taken of a small fillet formed in the bottom of the groove.

A number of the test piece bases (shown as number one in Fig. 6.24) were constructed so that several ceramic-metal samples could be tested within a short time.

A brazed ceramic-metal assembly was tinned to the test piece base (as discussed previously) and the assembly was placed in the cavity. The need for a separate test piece base for each specimen is not necessary as the discs from one batch of samples may be un-tinned and new ones tinned in place.

The standard resonator was constructed nearly identically to the test resonator. The tuning diaphragm was omitted and a 0.125-inch hole drilled in the side 90° from the coupling hole. A micrometer screw was bracketed in front of the hole so that the penetration into the resonator of a lossy rod could be measured accurately. This rod provided the loss in the standard resonator with which to balance the seal loss in the test resonator.

The interior of the tunable resonator and the standard resonator were gold plated.

Well into the program, when the third test series samples were mounted in the tunable test resonator, it was found that they protruded 0.015-inch on the average, deeper into the test cavity than earlier samples had. Consequently, it was found that the resonance frequencies were on average 120 Mc lower than the resonance frequency of the variable loss standard cavity (9200 Mc). The admittance bridge measurement, however, requires identical coupling and identical resonance frequencies of the test and standard cavities in order to balance the conduction losses of the test samples with the artificially introduced losses in the standard cavity. The corresponding change of resonant frequency had to be compensated for by retuning the standard resonator.

The retuning required an excessive deflection of the 20 mil thick cavity bottom. Consequently, the copper wall of the cavity, already work hardened from previous tuning cycles, tore after a few measurements. It was then replaced by a copper disc which, unfortunately, withstood only a few tuning attempts before it broke also.

A new cavity bottom was then made. The retuned cavity caused a change in the reference point for the lossy rod penetrating into the standard resonator. In order to tie later measurements as closely as possible to the previous ones, the conduction loss in the ceramic-metal seals was always compared against the old "#4 gold standard", a clean ceramic glued with a minimum of low loss cement to a gold plated cup holder. Remeasuring the samples #83 and #87 (from the first series of tests) showed that the new loss indication was, on the average, lower by 22 units.

#### 6.3.4.2 Determination of the Cavity Q

The Q of the resonator was determined by measuring the VSWR of the line terminated by the resonator. The Eimac 1075 reflex klystron used in the bridge measurements was also used here. It was necessary to square wave modulate the tube as the VSWR indicator is only sensitive to a square wave modulated signal. The modulation was achieved by superimposing a square wave on the dc repeller voltage. It was possible to drive the tube out of oscillation during half the cycle and into oscillation during the other half of the square wave cycle, hence square wave amplitude modulating the tube. Since the frequency of oscillation of the klystron is a function of the repeller voltage, it is imperative that the tops of the square waves be flat. A slope of a few millivolts in the flat portion will modulate the frequency enough to throw doubts on the validity of any measurements taken. By carefully choosing the klystron operating parameters, a frequency deviation of less than two hundred kilocycles at 9.5 Gc was obtained. This was deemed sufficient for rough measurements of Q. With the resonator in place, a plot was made of standing-wave ratio as a function of frequency. From this plot the unloaded Q may be determined as outlined by Ginzton<sup>3</sup>. The unloaded Q of the test resonator (with chemically polished inner surfaces) was measured as 13,700.

It was noticed early in the program that the copper interiors of the cavities became tarnished several days after chemical cleaning. In the interest of long term stability, the resonators were given a thin coating of gold plate. This would stabilize the Q of the resonators although lowering it slightly. Upon measurement, the internal Q of the test resonator was found to have dropped to 11,200. The Q of the gold plated standard resonator was also measured and was found to be 12,700 with the effect of the adjustable loss entirely removed. Although the Q's were lowered appreciably, the resonators were left as they were as results of



measurements on ceramic samples determined that the change in Q was not significant.

#### 6.3.4.3 Operation of rf Admittance Bridge

In order to obtain a complete null condition as the frequency is swept across the resonant frequency of the system, the characteristics of each equal arm of the Magic Tee must be identical. The lengths of the waveguide sections connecting the Magic Tee to the resonators must be equal as must the coupling to the resonators. The resonant frequency and internal Q of the resonators must also be equal. Even if the admittances presented to the equal arms of the Tee are equal, the power flowing from the fourth arm may not be zero<sup>4</sup> unless the Tee has been matched at the frequency of interest.

The above conditions were met as follows: The Magic Tee was ordered from the manufacturer to be matched at 9.5 Gc. The test resonator was tuned so that the resonant frequencies of the two cavities coincided, and the Q of the standard resonator was adjustable so that the Q's were equal. The coupling of both resonators was adjustable, so that both couplings were made equal. The lengths of the waveguide sections varied by less than 0.035 inch. This had some effect on the completeness of the null because difficulty was encountered in obtaining a complete null in the actual setup. However, the accuracy of the measurements was not significantly affected as will be seen later.

The accuracy of the measurements increases as the bridge becomes more unbalanced, since the rate of change of power out of the fourth arm with respect to the difference in input admittances is proportional to the difference in input admittances.

The output of the Magic Tee was detected and applied to the vertical input of an oscilloscope. As the bridge became more unbalanced, the oscilloscope vertical deflection increased. Hence, either a dc blocking voltage had to be applied, or the vertical amplifier of the oscilloscope had to be switched to a less sensitive range. The first possibility would have added another source of error and another adjustment to make. The latter suggestion decreased bridge sensitivity by decreasing change in oscilloscope deflection with change in resonator loss. In practice then, a compromise had to be reached. The reference unbalance point was adjusted such that a change in loss micrometer setting of one Division resulted in the greatest

change in oscilloscope deflection, 0.4 cm deflection out of 8.0 cm in this case. In the measurements, then, loss was inserted in the standard resonator until a prescribed unbalance was reached. The driving power was set to a fixed reference level at all times.

As originally designed, the loss in the standard resonator was effected by a one-eighth inch diameter rod of carbon, inserted in a hole in the side of the resonator. The depth of penetration was controlled and measured by a micrometer screw. It was determined that the carbon was not lossy enough and that it also detuned the resonator. The carbon rod was replaced by a lucite tube in which a small roll of lossy paper had been inserted. The loss increased, but the loss probe insertion necessary was still greater than was desirable. The hole was increased in size to 0.200 inch and a correspondingly larger lucite tube prepared. The probe insertion necessary to produce adequate loss was reduced to about 0.100 inch. The lossy paper was sealed in with plastic cement to prevent changes due to humidity.

The resonators were originally designed to resonate at 9.500 Gc. As constructed, they resonated at a few megacycles above that figure. The detuning effect of the ceramic test pieces was sizable, bringing the resonant frequency near 9.200 Gc. The samples had to be prepared from ceramics of uniform dimensions and were mounted uniformly from piece to piece as the tunable resonator had a range of only 15 megacycles. The bridge was assembled and power applied. The test resonator was adjusted to an undercoupled state with a bare ceramic in place.

The standard resonator also had a bare ceramic in place. The standard resonator coupling was adjusted as follows: The tuning of the test resonator was adjusted along with the loss and the coupling of the standard resonator until a null was observed on the oscilloscope. At this point the coupling of the two resonators was assumed to be equal.

#### 6.3.4.4 Measurement Procedure

The prepared sample was inserted in the test resonator. An identical ceramic ring was inserted in the standard resonator. The test resonator was tuned to resonance as indicated by a minimum oscilloscope deflection. The power from the klystron was measured by viewing the output of a directional coupler on an oscilloscope (see

Fig. 6.21) and adjusted to give a pre-determined deflection. The klystron was adjusted so that the mode peak occurred at the resonant frequency of the resonators. The micrometer screw was then adjusted to give a predetermined output from the output arm of the Tee. After each adjustment of the micrometer, the tuning was checked to bring both resonators to the same frequency. After this iterative series of adjustments was made, the incident power was again checked. The micrometer reading was then recorded and another sample inserted.

### 6.3.5 Equipment Checkout

#### 6.3.5.1 Reproducibility as a Function of Time

Upon completion of the bridge apparatus, during the second quarter, sample holders without ceramics were constructed of several materials, the object being to check the sensitivity of the apparatus. Two gold plated holders were made as well as a chrome plated one and one with a disc of 70/30 copper-nickel alloy soldered to the surface of the copper holder. With a gold holder in the standard resonator and a gold holder in the test resonator, the bridge was brought to balance (i.e. to the calibrated off-balance condition). The other two samples were compared with the gold one. The chrome plated sample was found to require an additional insertion of the loss slug of 0.0225 inches. (Henceforth the insertion will be given in divisions, where one division equals 0.001 inch. So the above would be 22.5 divisions.) The copper-nickel alloy sample required 31.8 divisions. By making measurements several times over a space of an afternoon, it was found that the measurements were repeatable to less than one division accuracy.

Later, at the start of the series II tests in the fourth quarter, a somewhat similar program was carried out. This is reported next.

Six "standards" with a range of resistivities between 1.4 and 81 ohm centimeters were made in which the "seal" area consisted of the material noted in Table 6-5. The balance of the assembly was silver plated and the ceramic member glued over the seal area with three small spots of low loss polystyrene\* cement. These standards were measured

---

\*Low loss polystyrene Q - Dope (General Electric Co.).

TABLE 6-5

Conduction Loss Data at 9.15 Gc on Body A Test Pieces

Glued to Noted Sample Holder

SAMPLE HOLDER			20 mil Tinned Disc	Micrometer Reading	Loss
Surface	Bulk	Electro- plate			
Cu	Cu	-	-	646	-4 <sup>++</sup>
Ag	Cu	yes	-	-	-19.2
Au	Cu	yes	-	625.5	0
Cr	Cu	yes	-	583.3	43.5
CuNi	Cu	-	70/30 Cu-Ni	527.3	99.5
Kovar	Cu	-	Kovar	466.1	160.1
Invar	Cu	-	Invar	396.8	230.0

<sup>++</sup>Obtained during the seventh quarter.

in the same manner as brazed assemblies, being compared to the gold reference assembly. The silver standard had a lower resistivity and lower loss than the gold reference, so the  $\Delta$  Ag is of the opposite sign from all the other measurements given in Table 6-5.

Using published resistivity values for the standards, a plot of resistivity versus micrometer reading is given in Fig. 6.25. Three actual seals subsequently reported are also plotted on Fig. 6.25. From these figures the sensitivity of the test procedure is seen to be quite adequate for the present work. It may be noted that the derived resistivity of the seals,  $20-40 \times 10^{-6}$  ohm-cm, is in the same range as the dc measurements reported in Table 6-1, showing excellent correlation of the dc and rf resistivity measurements.

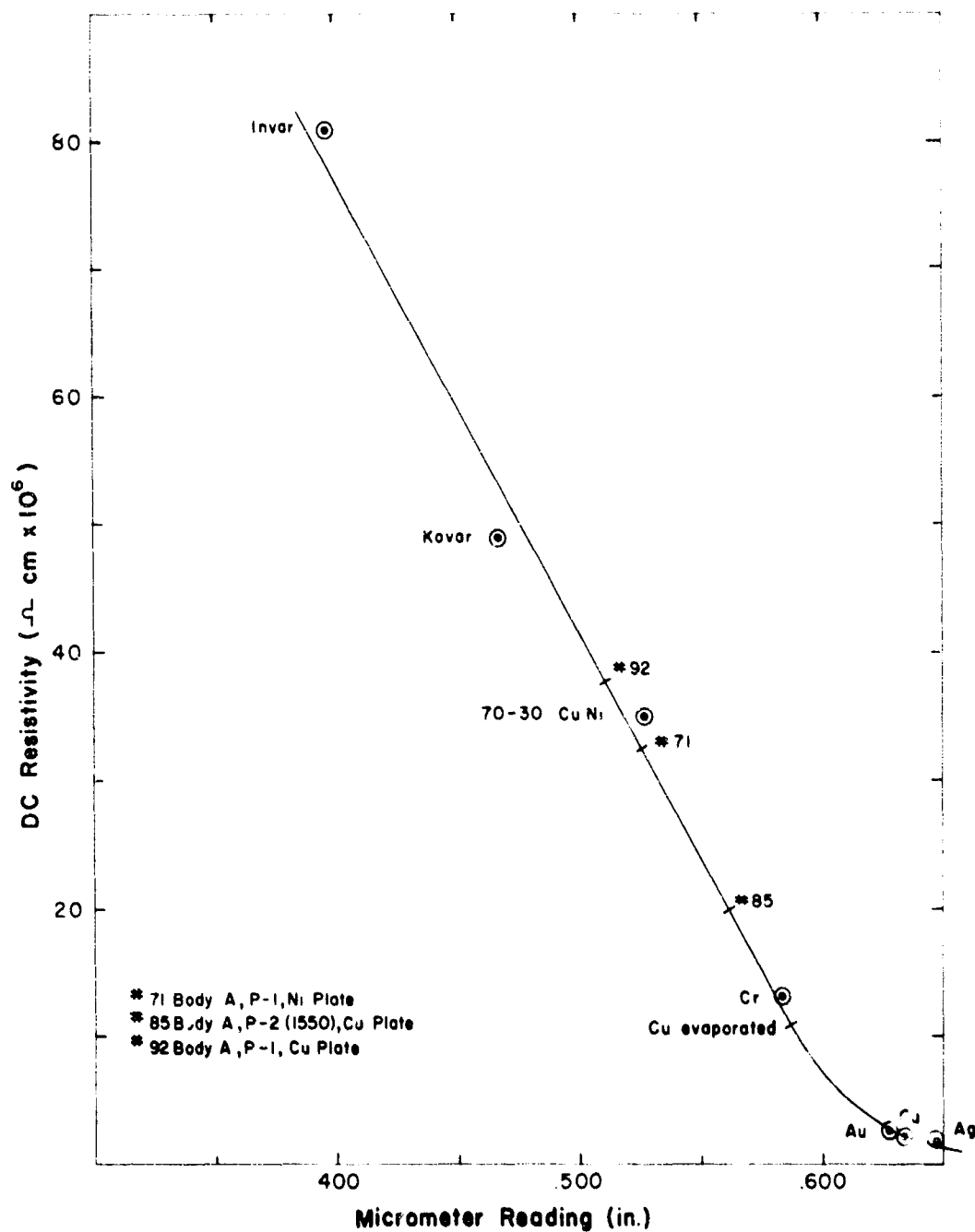


Figure 6.25: Plot of micrometer reading versus published resistivity of the six calibration assemblies (See text). Selected data from actual seals included for reference.

#### 6.3.5.2 Standard Test Piece

The standard, to which all test samples consistently were compared, is a raw ceramic of the composition used in the test piece. Two such standards were prepared. The two gold-plated sample holders were used, as the gold is insensitive to oxidation effects. Samples of Body A were glued in place on the sample holder by very small amounts of polystyrene cement. Centering was good but not absolute. The two standards were designated numbers 0 and 00. If the two standards are identical, then one could expect that a standard made from any of the bare sample ceramics should have identical loss properties as numbers 0 and 00. In effect then, a check on the two standards should indicate if the bare standard ceramic is cancelling out the bulk ceramic losses present before metallizing. As it turned out, the plastic cement used to bond the ceramic to the holder was the dominating factor in any differences seen between samples 0 and 00.

#### 6.3.5.3 Alignment of Ceramics

An investigation was made to determine the importance of the test piece being concentric with the center-line of the resonator. A test piece which has been eccentrically mounted will exhibit varying degrees of loss depending on its orientation with respect to the coupling hole. Tests were run to determine whether the range of loss encountered is a good indication of sample eccentricity. The results of this test show that eccentricity can be estimated from loss data for deviations greater than 0.013 inches off center (Fig. 6.26). The loss varies approximately 3 divisions at this point. For smaller eccentricities, apparently non-uniformities in the seal or ceramic overshadow the effects of centering.

#### 6.3.5.4 Sensitivity of Micrometer Reading with Cavity Q

The micrometer insertion loss to give various cavity Q's with the standard ceramic in place was determined. These results are given in Fig. 6.27.

From this data the cavity Q associated with the various samples listed in Section 6.3.5.1 can be found, as also can the Q for various ceramic-to-metal seal test assemblies mentioned in Section 6.3.5.1 (and reported later in Table 6-11).

It can be seen that the Q of the standard cavity of 11,000 is significantly reduced to 4,000 by the emplacement of even the low loss silver standard with its attached ceramic.

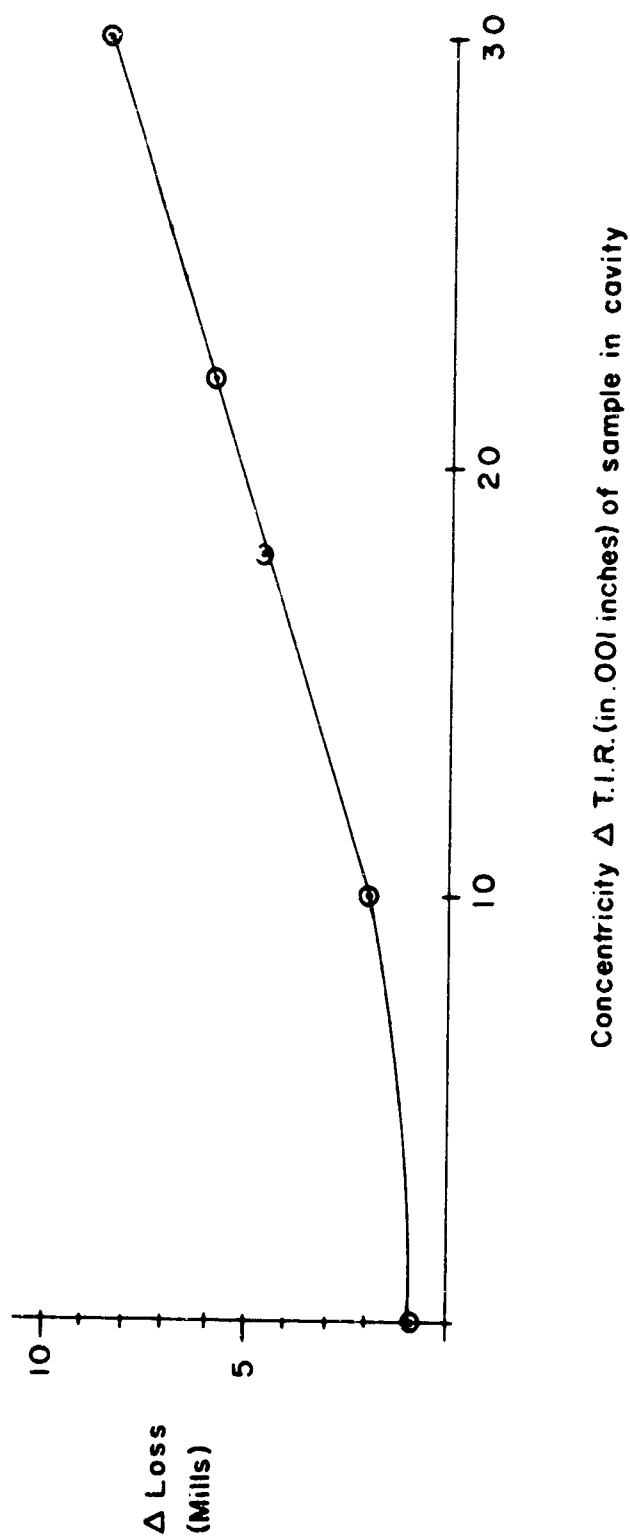


Figure 6.26: Plot of relationship between concentricity of ceramic-metal seal in test cavity,  $\Delta$ TIR, and change in measured cavity loss (in mils of insertion of lossy material into standard cavity) as sample holder is rotated.

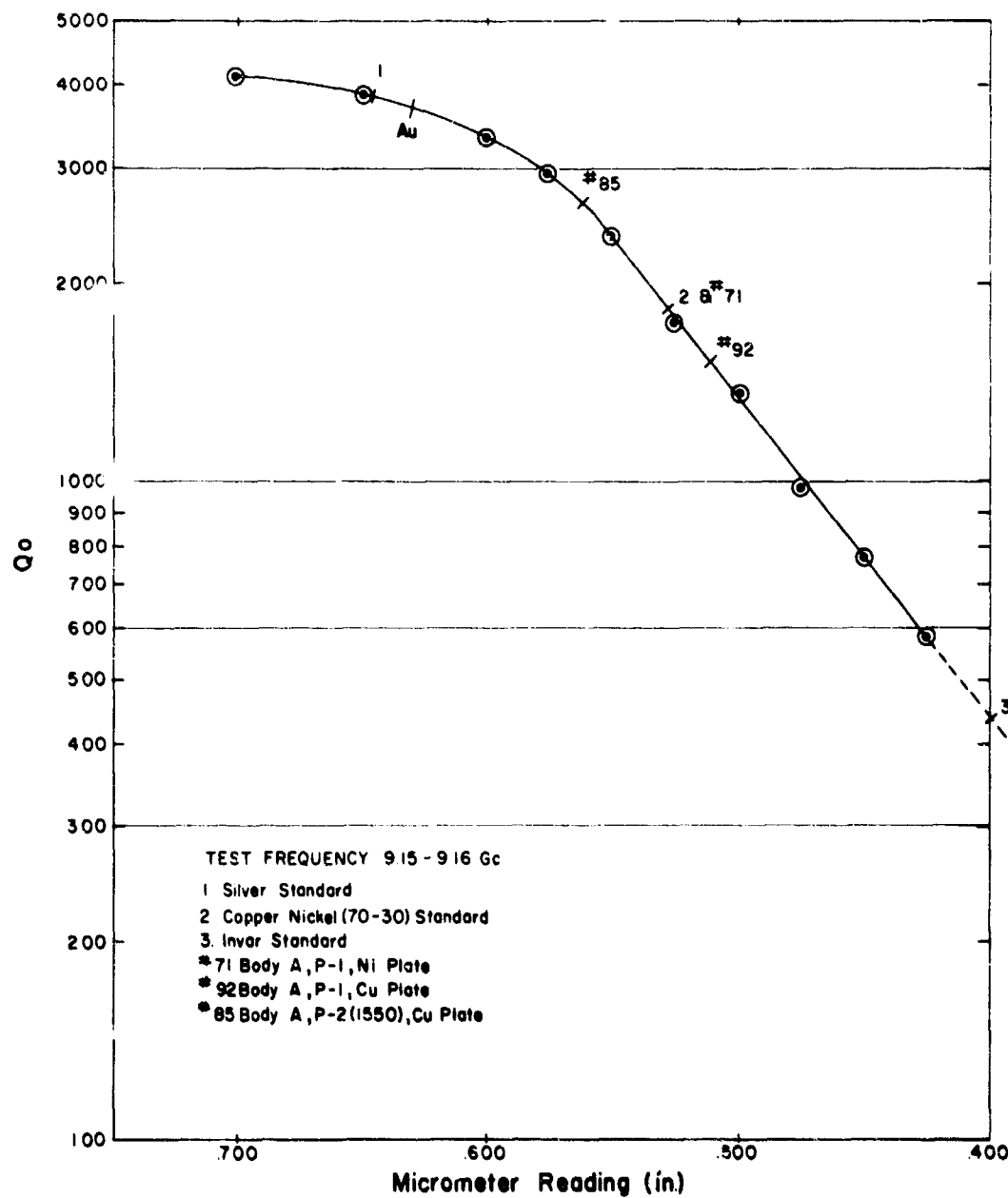


Figure 6.27:  $Q_o$  of standard cavity used in conduction loss measurements plotted as a function of micrometer reading. Selected data giving the various  $Q$ 's of the test cavity with various assemblies including the standard are included for reference.



#### 6.3.6 Results

The loss measurements were conducted in three separate series during the second and third quarters, the fourth quarter and the sixth quarter respectively, the results are therefore reported in this sequence.

##### 6.3.6.1 First Series

The initial series of seals consisted of Body A, P-1 or P-2 metallizing of various thicknesses - sintered nickel or copper plate - copper braze to cupro-nickel metal member. As a reference check, electroless copper plate on Body A with a tin activated surface was tin soldered to a copper holder - it showed a loss of 48.2 units, sample #60.

The collected data on the tested seals are given in Table 6-6. The reference specimens were checked at the beginning and end of the measurement run which was made in a single 10-hour period. A shift of 3.7 divisions was noted, which is well within experimental error.

##### 6.3.6.2 Second Series

In order to reduce the  $I^2R$  losses exhibited by the seals in the first series, a second test series was programmed. The results are given in Table 6-7. An unsintered iron barrier layer was used to isolate the copper or nickel plate from the braze. In this case Cu-Ag braze (M.P. 780°C) was used. The thickness of the metallizing and plate was such that the rf currents were carried only in these layers.

An evaporated copper seal tinned to a copper sample holder was also evaluated. A loss of 50 units was obtained. These results are also given in Table 6-7.

The micrometer setting required for balance is indicated in Table 6-7. If more than one reading was taken, the readings were averaged.

The gold plated reference standard designated Au in Table 6-5 was measured at the beginning and end of the test run which was completed in one working day. A drift from 636.8 to 616.5 (micrometer setting) was noted. As Fig. 6.27 shows, this is on the high Q end of the Q versus micrometer reading curve. The slope of the curve in this region is only about one-third that of the lower portion, where most of the actual seals were measured. The draft corresponded, therefore, in terms of precision to 6.7

TABLE 6-6

Series 1, Conduction Loss Data at 9.15 Gc on Body A

Test Pieces Sealed to Cupro-Nickel (70-30)

with Copper Braze

Sample No.	Metallizing Paint	Thickness* in x 10 <sup>3</sup>	Plate <sup>+</sup>	Loss**
48	P-1	.14	Cu	69.6
44	"	.18	Cu	77.1
47	"	.26	Cu	79.3
3	"	.98	Cu	92.1
1	"	.98	Cu	90.7
6	"	1.10	Cu	99.1
5	"	1.20	Cu	99.9
4	"	1.42	Cu	93.5
19	"	3.17	Cu	98.0
22	"	3.29	Cu	93.6
37	"	.17	Ni	120.2
17	"	1.02	Ni	103.8
14	"	1.03	Ni	99.9
39	"	1.96	Ni	93.8
42	"	2.24	Ni	88.6
52	P-2	.17	Cu	81.2
51	"	.19	Cu	97.6
54	"	.20	Cu	148.5
53	"	.23	Cu	184.6
55	"	.32	Cu	134.6
12	"	.61	Cu	83.9
35	"	1.07	Cu	108.3
27	"	1.12	Cu	136.6
32	"	1.14	Cu	148.0
58	"	.18	Ni	122.7
56	"	.20	Ni	134.6
57	"	.26	Ni	136.8
8	"	.86	Ni	146.6
31	"	.88	Ni	136.3
29	"	.91	Ni	132.3
30	"	.93	Ni	141.4
33	"	1.03	Ni	130.8
60	-	-	Cu	48.2

\*From calibration Curve #5 (see 3rd Quarterly Report).

\*\*In .001 inches of lossy material required to balance Impedance Bridge Test Circuit.

+Sintered at 800°C.

TABLE 6-7

Series 2, Conduction Loss Data at 9.15 Gc on Body A

Test Pieces with Ag-Cu Braze Sealed to Cupro-Nickel (70/30)

Sample No.	Metallizing Paint	Thickness in $\times 10^3$	Plate <sup>+</sup>	Plate Sinter Temp. (X100)	Loss
64	P-1	.12	Ni	8	111.9
65	"	.20	"	8	103.1
63	"	.22	"	8	102.5
66	"	.25	"	8	109.2
71	"	.76	"	9	100.0
81	"	1.04	"	8	79.7
78	"	1.25	"	8	71.5
67	"	.21	Cu	9	101.3
91	"	.22	"	9	85.7
92	"	.83	"	9	114.1
93	"	1.46	"	8	116.3
69	"	1.93	"	9	120.4
96	P-2	.36	Cu	9	127.7
98	"	.78	"	9	122.3
84	P-2 (1550)*	.52	"	8	83.8
85	"	.86	"	8	64.7
88	"	1.35	"	8	67.6
83	P-2 (1550)*	.56	Ni	8	72.4
86	"	.94	"	8	68.8
87	"	1.56	"	8	65.8
103	Cu (evap)	-	Cu	-	50.4
104	Cu (evap)	-	"	-	45.6

<sup>+</sup>0.002 mils thick  
then iron plate

\*Sintered at 1550°C then 1425°C.

divisions in the region of the measured seals. Cause for the drift was not resolved. The column designated "loss" is the difference in micrometer readings between the test sample being measured and the average of the readings on the Au standard. This average 626.8 compares favorably with the 625.5 average determined in a similar fashion with the same gold reference during Series I (Section 6.3.5.1). The data for the two runs is therefore comparable with no further adjustment. The variables being tested are, in nearly all cases, separated by considerably more than the 6.7 divisions of possible error.

#### 6.3.6.3 Third Series

The test samples were arranged in four main groups:

1. Barrier layer seals
2. Typical ceramic-to-metal seals
3. Low-loss evaporated seals
4. Non-metallic "seals".

Additional barrier layer seals were programmed because the unsintered iron plated-copper plated samples were penetrated by the Cu-Ag braze in the second test series. (The iron plate was not sintered in order to reduce inter-diffusion of Cu and Fe.) The iron plate was sintered on at 800°C and an unsintered nickel plate completed the barrier layer. Cu-Ag braze to a 70/30 Cu-Ni metal member was used. Lucalox\* was also used as a ceramic in addition to Body A in order to introduce a variable which would influence the sintering of the metallizing layer.

Detailed processing of the seals is as follows:

P-1 metallizing of various thickness, t, fired at 1425°C for 30 minutes in wet H<sub>2</sub> and N<sub>2</sub>, 1:3  
Cu or Ni overplate, 1 mil, sintered at 900°C for 30 minutes in wet H<sub>2</sub>  
Fe plate, 1 mil, sintered at 800°C for 30 minutes in wet H<sub>2</sub>  
Ni plate, 0.5 mil, no sinter  
Cu-Ag braze, 4 mil, flag indication + 30 seconds hold in wet H<sub>2</sub>  
70/30 Cu-Ni, 20 mil thick.

---

\*General Electric Co. trade name.

In order to obtain loss data on "production type" seals,

1. Body A - P-1 metallizing - copper plate -  
Cu-Au braze - Kovar
2. Body A - P-1 metallizing - nickel plate -  
Cu-Ag braze - 70/30 cupro-nickel

were programmed.

Several low loss seals also were programmed. These essentially consisted of evaporated copper, nickel or molybdenum onto Body A or Lucalox\*.

In order to further study loss mechanisms the loss induced by the non-metallic portions of the metallizings was also evaluated.

The results of these four series of tests are given in Tables 6-8, 6-9, 6-10 and 6-11. Asterisks on some sample numbers in the tables indicate that photomicrographs (400X) of these samples are presented in this report and that the microstructures shown are discussed later.

The relative loss figures presented in these tables cannot be directly compared to the data presented in Tables 6-5 and 6-6 for, as previously mentioned in section 6.3.4.1, the cavity was reworked for the third series of tests. New Body A samples and Lucalox\* test pieces protruded further into the cavity than the initial samples.

---

\*General Electric Co. Trade Name.

TABLE 6-8

## Series 3, Barrier Layer Seals

Sample No.	Ceramic	Thickness in $\times 10^3$	Plate	Loss**
200*	Body A	.1	Cu	53
201*	↓	.3	↓	66
202*		.5		88
203		.7		84
204		1.2	↓	77
205*		2.6		87
206		.1	Ni <sup>+</sup>	109
207*		.2	↓	103
208		.3		32
209		1.3	↓	2
210		1.6		-
211*	Lucalox <sup>++</sup>	.1	Cu	21
212	↓	.3	↓	51
213		.5		62
214		.9		70
215		1.6	↓	50
216		1.6		57
217		.1	Ni <sup>+</sup>	62
218		.2	↓	46
219		.3		62
220		.8	↓	72
221	↓	1.2		76
222		2.0	↓	114

\*Two layers of 0.5 mil thickness each, both sintered.

\*Cross-sections of these samples are shown in photomicrographs.

\*\*Add 22 units to convert to "old units" (Series 1 and 2).

<sup>++</sup>General Electric Co. Trade Name.

TABLE 6-9

## Series 3, Loss in Standard Ceramic-to-Metal Seals

Sample No.	Loss**	Description
<u>Body A</u>		
223	75	P-1 metallizing, fired at 1425°C for 30 minutes in wet H <sub>2</sub> and N <sub>2</sub> , 1:3, of various thicknesses, t, in mils
224*	103	Cu-overplate, 0.5 mil, sintered at 900°C for 30 minutes wet H <sub>2</sub>
		Cu-Au braze, 4 mil, flag indication + 30 seconds hold in wet H <sub>2</sub>
		Kovar, 10 mil thick, Ni plated (0.4 mil), sintered at 900°C for 30 minutes in wet H <sub>2</sub>
<u>Body A</u>		
225*	83	P-1 metallizing, 0.5 mil fired at 1425°C for 30 minutes in wet H <sub>2</sub> and N <sub>2</sub> , 1:3
		Ni overplate, 0.5 mil, sintered at 900°C for 30 minutes in wet H <sub>2</sub>
		Cu-Ag braze, 4 mil, flag indication + 30 seconds hold in wet H <sub>2</sub>
		70/30 Cu-Ni, 20 mil thick.

\*\*Add 22 units to convert to "old" units (Series 1 and 2).

TABLE 6-10

## Series 3, Evaporation Metallized Seals

Sample No.	Loss**	Description
226*	91	Body A, polished with diamond paste $6\mu$ , $3\mu$ , $1\mu$ , $0.25\mu$
227	84	Ti (evaporated film) $0.1\mu$ thick, $1080^{\circ}\text{C}$ , $2 \times 10^{-5}$ Torr Mo (evaporated film) $4\mu$ thick, however $3\mu$ according to Fig. 4.08), $1080^{\circ}\text{C}$ , $2 \times 10^{-5}$ Torr Cu (evaporated film) $4\mu$ thick, about $600^{\circ}\text{C}$ , $2 \times 10^{-5}$ Torr Cu plate, 1 mil, $800^{\circ}\text{C}$ sinter for 10 minutes in wet $\text{H}_2$ Fe plate, 0.5 mil, $800^{\circ}\text{C}$ sinter for 10 minutes in dry $\text{H}_2$ Ni plate, 1 mil, $800^{\circ}\text{C}$ sinter for 10 minutes in wet $\text{H}_2$ Cu-Ag braze, 4 mil, flag indication + 30 seconds hold in wet $\text{H}_2$ 70/30 Cu-Ni, 20 mil thick
230	121	Lucalox, polished with $6\mu$ , $3\mu$ , $1\mu$ , $0.25\mu$ diamond paste
231	-	Ni (evaporated film), $0.05\mu$ thick, $1080^{\circ}\text{C}$ , $2 \times 10^{-5}$ Torr Mo (evaporated film), $0.5\mu$ thick (nominal), $1080^{\circ}\text{C}$ , $2 \times 10^{-5}$ mm Hg Cu (evaporated film), $4\mu$ thick, about $600^{\circ}\text{C}$ , $2 \times 10^{-5}$ Torr Cu plate, 1 mil, sintered in vacuum for 10 minutes Fe plate, 0.5 mil, sintered in vacuum for 10 minutes Ni plate, 1 mil, sintered in vacuum for 10 minutes Cu-Ag braze, 4 mil, flag indication + 30 seconds hold in wet $\text{H}_2$ 70/30 Cu-Ni, 20 mil thick
229	116	Body A, unpolished Ni (evaporated film), $5\mu$ thick Ni plate, 2 mil, no sinter Cu-Ag braze, 4 mil, flag indication + 30 seconds hold in wet $\text{H}_2$ 70/30 Cu-Ni, 20 mil thick



Sample No.	Loss**	Description
228*	56	Body A, polished with 6 $\mu$ , 3 $\mu$ , 1 $\mu$ , 0.25 $\mu$ diamond paste Cu (evaporated film) 5 $\mu$ thick, about 600°C, 2 x 10 <sup>-5</sup> mm Hg Ni plate, 2 mil, no sinter Cu-Ag braze, 4 mil, flag indication + 30 seconds hold in wet H <sub>2</sub> 70/30 Cu-Ni, 20 mil thick
232	65 <sup>++</sup> 55 <sup>+++</sup>	Body A, unpolished MnO-TiO <sub>2</sub> fired at 1425°C for 30 minutes in wet H <sub>2</sub> and N <sub>2</sub> , 1:3, then 810°C braze cycle in wet H <sub>2</sub>
233*	65 <sup>+++</sup> 50 <sup>++</sup>	Cu (evaporated film), 4 $\mu$ thick, about 600°C, 2 x 10 <sup>-5</sup> Torr Cu plate, 2 mil, no sinter
235 234	102 <sup>++</sup> -	Body A, unpolished MnO-TiO <sub>2</sub> fired at 1425°C for 30 minutes in wet H <sub>2</sub> and N <sub>2</sub> , 1:3, then 1100°C braze cycle with flag indication + 5 minutes hold in wet H <sub>2</sub> Cu (evaporated film), 4 $\mu$ thick, about 600°C, 2 x 10 <sup>-5</sup> mm Hg Cu plate, 2 mil, no sinter

<sup>++</sup>Glued to sample holder (copper, silver plated) with polystyrene Q-Dope (General Electric)  
<sup>+++</sup>Tinned to sample holder-Copper, plate penetrated but evaporated film intact.

\*\*Add 22 units to convert to "old" units (Series 1 and 2).

TABLE 6-11

## Non-Metallic "Seals"

---

Sample No.	Relative Loss	Description
		Body A, unpolished
		P-1 metallizing, metallic portion leached out with 50% nitric acid for 30 minutes at 150°F glued to copper (silver plated) sample holder with polystyrene Q-Dope*
236	21	(Paint thickness 0.1 mil)
237	27	(Paint thickness 1.1 mil)

---

\*General Electric Co.

---

### 6.3.7 Discussion of Results

#### 6.3.7.1 Introduction

The three series of experiments carried out during the program fall into seven systematic groupings as outlined below. The discussion is therefore largely conducted in terms of these groupings.

Owing to the geometry of the test cavity, the rf current will be carried in the metal layers next to the ceramic ring, (if the ring behaves as a perfect insulator). In this study, these layers are:

1. A copper sample holder to which is glued\* a bare ceramic (Table 6-5).
2. An electroplated layer of
  - a. Silver
  - b. Gold (standard)
  - c. Chromiumon the copper sample holder to which a bare ceramic is glued (Table 6-5).
3. Same as for 2a but with a 'lossy' non-metallic layer sintered onto the ceramic surface (#236, #237).
4. A copper evaporated and electroplated (#103, #104) or electroless plated (#60) metallizing on the ceramic which is tinned to a copper sample holder.
5. A copper evaporated and electro-plated layer on a 'lossy' ceramic surface which is glued or tinned to an electro-silver-plated copper sample holder (#232, #233, #235).
6. A copper, or nickel, or titanium-molybdenum evaporation plated layer on a ceramic with additional plated "barrier" layers which is Cu-Ag brazed to a 70/30 cupro-nickel disc which in turn is tinned to a copper sample holder (#226-#231).
7. A refractory metallizing sintered layer on a ceramic with various electroplated layers on it, which is then brazed to a metal disc which in turn is tinned to a copper sample holder. This group

---

\*Low loss polystyrene Q-Dope (General Electric).

constitutes the balance of the samples. The various subdivisions are:

- 7.A P-2 metallizing, copper or nickel plate, copper braze
- 7.B P-2 metallizing, copper or nickel plate, iron plate Cu-Ag braze
- 7.C P-1 metallizing, copper or nickel plate, copper braze
- 7.D P-1 metallizing, copper or nickel plate, iron plate, Cu-Ag braze
- 7.E P-1 metallizing, copper or nickel plate, iron plate, nickel plate, Cu-Ag braze
- 7.F P-1 metallizing, nickel plate, Cu-Ag braze.

(all these samples use 70/30 cupro-nickel braze discs, all types are metallized on Ceramic A while those in 7.E are also metallized on Lucalox\*, 7.E.1)

- 7.G P-1 metallizing; copper plate, Cu-Au braze, nickel plated Kovar or Cu-Ag braze 70/30 cupro-nickel.

It is proposed to discuss the results in terms of the above groupings rather than by time sequence as was used in the results section, since a better understanding of the  $I^2R$  loss process may thus be obtained.

#### 6.3.7.2 Skin Depth

The rf currents are carried in the surface layers or "skin" of a metallic conductor. The "so called" skin depth is the depth at which the rf current has fallen to a value of  $1/e$  of the current at the surface, or 36.8%. For the purposes of this study it may be assumed that in a homogeneous layer all the rf current is carried in a surface layer which is four skin depths thick. Reservations concerning a heterogeneous layer volume are discussed below.

The skin depth at 9.15 Gc of various pure metals and metal alloys is plotted in Fig. 6.28 as a function of their dc resistivity.

The skin depth of the evaporated or electroless copper plated layer, #60, #103, #104 can be obtained by

---

\*General Electric Co. Trade Name.

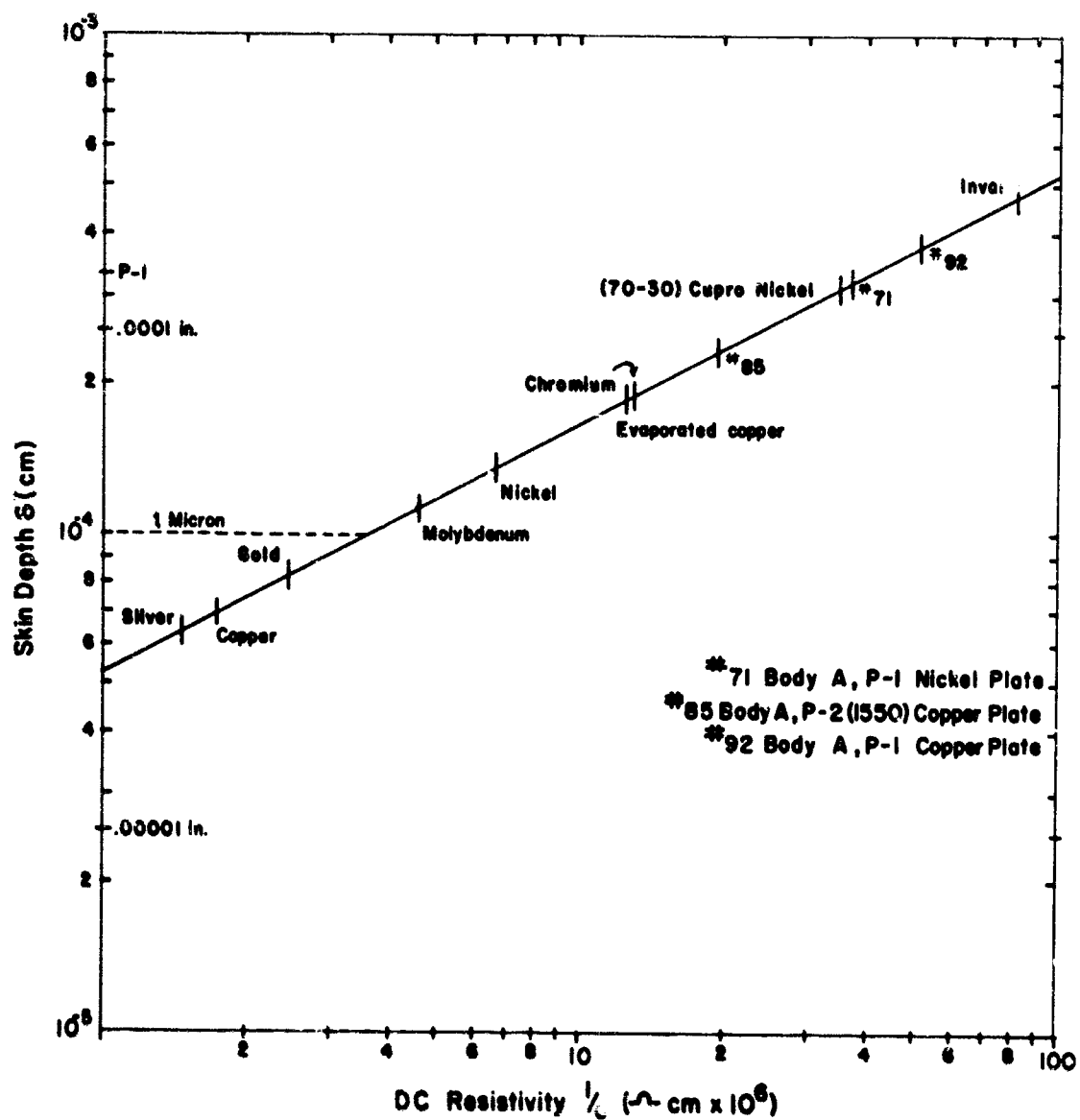


Figure 6.28: Skin depth at 9.15 Gc versus electrical resistivity.

taking its rf relative loss figure (or rather the cavity insertion rod micrometer reading), obtaining its equivalent dc resistivity from Fig. 6.26, and using this dc resistivity to obtain the skin depth from Fig. 6.28. The equivalent dc resistivity obtained in that case, of  $12 \times 10^{-6}$  ohm-cm, is higher than the dc resistivity of bulk OFHC copper  $1.7 \times 10^{-6}$  ohm-cm, or the value of  $4 \times 10^{-6}$  a/cm obtained for a plated layer on top of a metallizing layer, (Table 6-4, column 4) as determined by the techniques discussed earlier in section 6.2.2. This is partially because the copper-ceramic interface forms a tortuous path along which the majority of the rf surface currents flow, and partially because the interface can also contain a varying amount of semi-conducting oxides to form the heterogeneous interfacial layer. A skin depth of 1.9 microns is obtained from the  $12 \times 10^{-6}$  ohm-cm resistivity which means that the rf current is carried in the 7.6 microns of copper adjacent to the ceramic surface (0.3 mils).

By the heterogeneous nature of the volume in the interfacial region of the metallizings considered in this section, we mean that the region through which the current will flow is composed of volumes of gradually and/or abruptly varying resistivity in addition to layers which may be mechanically separate. It cannot be expected therefore that the simple concept of "skin depth" developed for homogeneous materials will quantitatively apply in this instance. An analysis of the heterogeneous effect has not been attempted in this study and the simple "skin depth" concept is used. It is possible that some of the data which cannot be completely explained would yield to this analysis, however, in turn this would require more experimentation in order to refine the data.

#### 6.3.7.3 Group I A Copper Sample Holder to which is Glued a Bare Ceramic (Table 6-5)

When compared to the "gold standard", a ceramic glued to a copper test piece base gives, as expected, a negative loss (Table 6-5) because the dc and rf resistivity of copper is less than that of gold. Any effect of the glue joint at the ceramic-metal interface and the "lossiness" of the ceramic has been compensated for by the initial balancing of the cavities (6.3.3.5, 6.3.4.3, 6.3.5.3).

6.3.7.4      Group II  
An Electroplated Layer of   a) Silver,  
b) Gold (standard)   (c) Chromium on the Copper  
Sample Holder to which a Bare Ceramic is  
Glued (Table 6-5)

As silver is less lossy than gold, as expected, it shows a negative reading. Chromium is more resistive than gold and shows a positive micrometer reading. Since the chromium is silver plated except under the ceramic, whereas the gold standard is not, the increased lossiness under the ceramic is somewhat offset by the decreased lossiness in the silver plated region. As the current flow is maximum under the ceramic and the resistivity of gold and silver is relatively comparable, this effect will be of a second order.

Since all the tested assemblies in this report were silver plated, the above situation holds true throughout the study.

In retrospect, it would appear that gold plating throughout would have been advisable (if cost considerations could be neglected).

6.3.7.5      Group III  
An Electroplated Layer of Silver on the Copper  
Sample Holder to which the Ceramic is Glued.  
The Ceramic had a "lossy" non-metallic layer  
sintered onto its surface.   (Table 6-11)

The nitric acid treatment has effectively leached out the molybdenum from the metallizing as the loss is the same despite the large differences in metallizing thickness. The resulting loss, 46 "old" units, is therefore the contribution of losses due to effects other than conduction and may be assumed to consist of dielectric losses in the heterogeneous  $\text{MnO-TiO}_2\text{-SiO}_2\text{-CaO-MgO-Al}_2\text{O}_3$  non-conducting or semi-conducting component of the metallizing (see also sections 6.3.7.6 and 6.3.7.7) as the effect of the polystyrene glue is cancelled out.

6.3.7.6      Group IV  
A Copper Evaporated and Electroplated (#103, #104)  
or Electroless Plated (#60) Metallizing on the  
Ceramic which is tinned to a copper sample  
holder. (Tables 6-6, 6-7)

This group of evaporated or electroless copper plated ceramics has already been discussed in section 6.3.7.2. The seals were made as examples of simulated crunch seals and were expected to display the lowest loss of any seals that could be made. This expectation was realized but the loss of 48 units was 52 units higher than initially expected (see section 6.3.7.3) due to effects such as those discussed in section 6.3.7.2.

6.3.7.7      Group V  
A Copper Evaporated and Electroplated Layer on  
a 'Lossy' Ceramic Surface which is Glued  
or Tinned to an Electro-Silver-Plated  
Copper Sample Holder (#232, #233, #235)  
Table 6-10)

This group was synthesized to further study the effects of the dielectric layer. Pure  $\text{MnO-TiO}_2$  powders were painted and sintered onto the ceramic. The increased amount of  $\text{MnO-TiO}_2$  has perhaps increased the dielectric loss\*, but more likely the increased loss is due to:

- (i) A combination of factors similar to those discussed in sections 6.3.7.5 and 6.3.7.6 giving a loss of 75 "old" units for the tinned samples.
- (ii) In the case of the glued samples a loss of 87 old units occurs, due to the inferior conductivity of physically discrete layers as opposed to metallurgically bonded layers via a tinning process; i.e., there is a high junction resistance.

The very high loss of sample #235, 124 old units, cannot conclusively be explained. It may be due to a very inferior electrical junction occurring between the copper

\*Also, phenomena such as piezoelectric or semi-conduction may be enhanced in this sample.



plate and silver plated base or it may be due to phase changes which occurred in the non-metallic volume, such as anorthite and  $\text{MnO} \cdot \text{TiO}_x$  formation, after the  $1100^\circ\text{C}$  wet hydrogen firing.

6.3.7.8      Group VI  
A Copper, or Nickel, or Titanium-molybdenum  
Evaporation Plated Layer on a Ceramic with  
Additional Plated "Barrier" Layers which is  
Cu-Ag Brazed to a 70/30 Cupro-Nickel Disc which  
in turn is Tinned to a Copper Sample Holder  
(#226-#231) (Table 6-10)

These evaporated metallizings with various overplates were prepared to obtain loss measurements on the "simplest" practical metallizing systems which could be devised.

The copper sample 228# shows a loss of 78 units because part of the current is carried in the copper, part in the nickel (6.3.7.2) and part in the interfacial cupro-nickel diffused zone due to the heat treatment experienced during the Cu-Ag braze operation. Table 6-12 gives the resistivity range in this system. In retrospect, it is obvious that a thick copper plate should have been employed prior to nickel plating the sample.

The loss of the nickel evaporated and electro-plated layer at 138 ohm units is as expected, see Table 6-12, and furnishes a valuable end point for the data plotted in succeeding sections.

TABLE 6-12

Room Temperature Resistivity of Selected Copper,  
Nickel and Molybdenum Alloys

Composition (wt %)	Resistivity (ohm cm)	Reference
99.99 Cu	$1.69 \times 10^{-6}$	b
99.9 Cu 0.1 Ni	$2.0 \times 10^{-6}$	a
99.0 Cu 1.0 Ni	$3.0 \times 10^{-6}$	a
98.0 Cu 2.0 Ni	$4.4 \times 10^{-6}$	a
96.9 Cu 3.1 Ni	$5.3 \times 10^{-6}$	a
95.7 Cu 4.3 Ni	$6.9 \times 10^{-6}$	a
94.7 Cu 5.3 Ni	$8.1 \times 10^{-6}$	a
80.0 Cu 20.0 Ni	$24.6 \times 10^{-6}$	c
70.0 Cu 30.0 Ni	$34.0 \times 10^{-6}$	c
55.0 Cu 45.0 Ni	$49.0 \times 10^{-6}$	d
40.0 Cu 60.0 Ni	$47.0 \times 10^{-6}$	a
30.0 Cu 70.0 Ni	$43.0 \times 10^{-6}$	a
20.0 Cu 80.0 Ni	$29.0 \times 10^{-6}$	a
99.99 Ni	$7.8 \times 10^{-6}$	b
62 Ni, 30 Mo, 5 Fe	$135.0 \times 10^{-6}$	d
99.95 Mo	$5.2 \times 10^{-6}$	d

- a) Goldsmith, A., Waterman, T. E., and Hirschhorn, H. J., Handbook of Thermophysical Properties of Solid Materials, Armour Research Foundation, Macmillan, New York, 1961.
- b) Bureau of Standards, from Handbook of Chemistry and Physics, Chemical Rubber Publishing Company, Ed.-in-Chief Hodgman, C. D., 1951.
- c) Wilkins, R. A., and Bunn, E. S., Copper and Copper Base Alloys, McGraw-Hill, New York, 1943.
- d) Metals Handbook, A. S. M., Editor, Lyman, T., 1948.

The molybdenum evaporated plated layer is a high strength vacuum tight layer and it was felt that this would give a low loss layer. (The dc conductivity work had not been carried out at this time.) In actual fact, the layer was quite lossy. This was due to several facts.

- (i) The dc conductivity of a pure molybdenum evaporated layer is half way between that of pure molybdenum sheet and a regular metallizing such as P-1, as shown in Table 6-1.
- (ii) The formation of a Ti-Mo alloy due to high temperature interdiffusion processes with much higher resistivity.
- (iii) Factors such as those outlined for copper in 6.3.7.2 come into play, i.e., the formation of  $TiO_x$ , and oxygen dissolved in the metal.

The fact that the loss on Body A utilizing Mo-Ti layers is in between the copper and nickel situations, at 109 old units, is in agreement with their relative resistivities, but in view of the complexities listed above is somewhat fortuitous.

The higher loss of the sample evaporated on Lucalox\* is explained on the basis of the much thinner layer of molybdenum which resulted in the formation of a high loss Ti-Mo-Cu intermetallic alloy layer. The fact that Lucalox\* is the substrate is not considered significant.

Fig. 6.29 shows metallurgical cross-sections of the Cu and Mo-Ti samples. The various evaporated, electroplated and brazed layers can easily be seen.

---

\*General Electric Co. Trade Name.

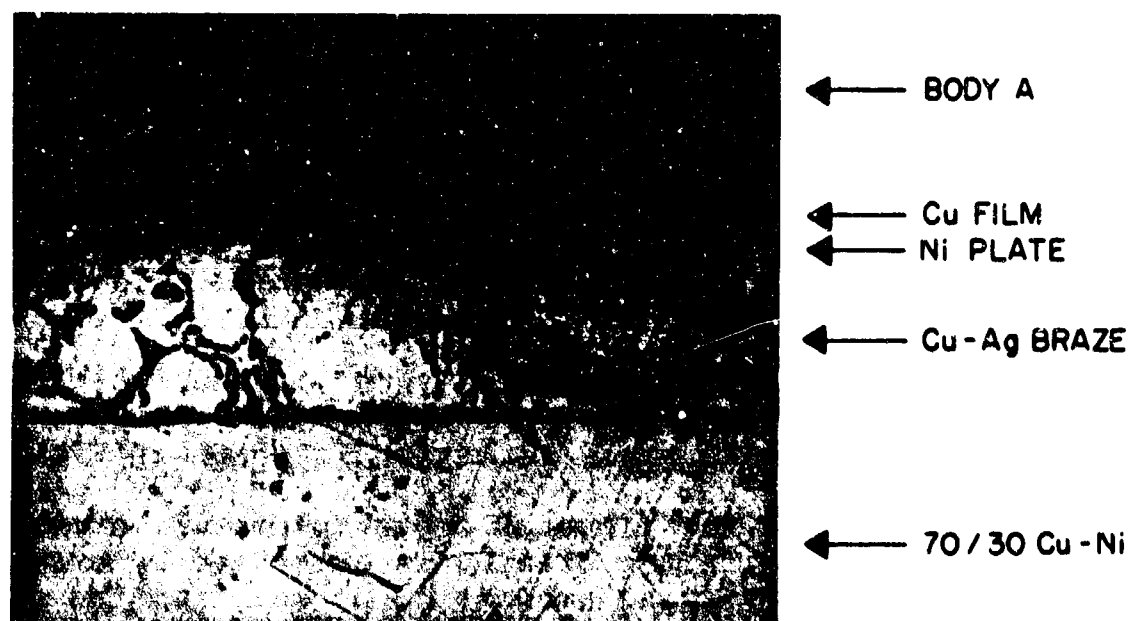
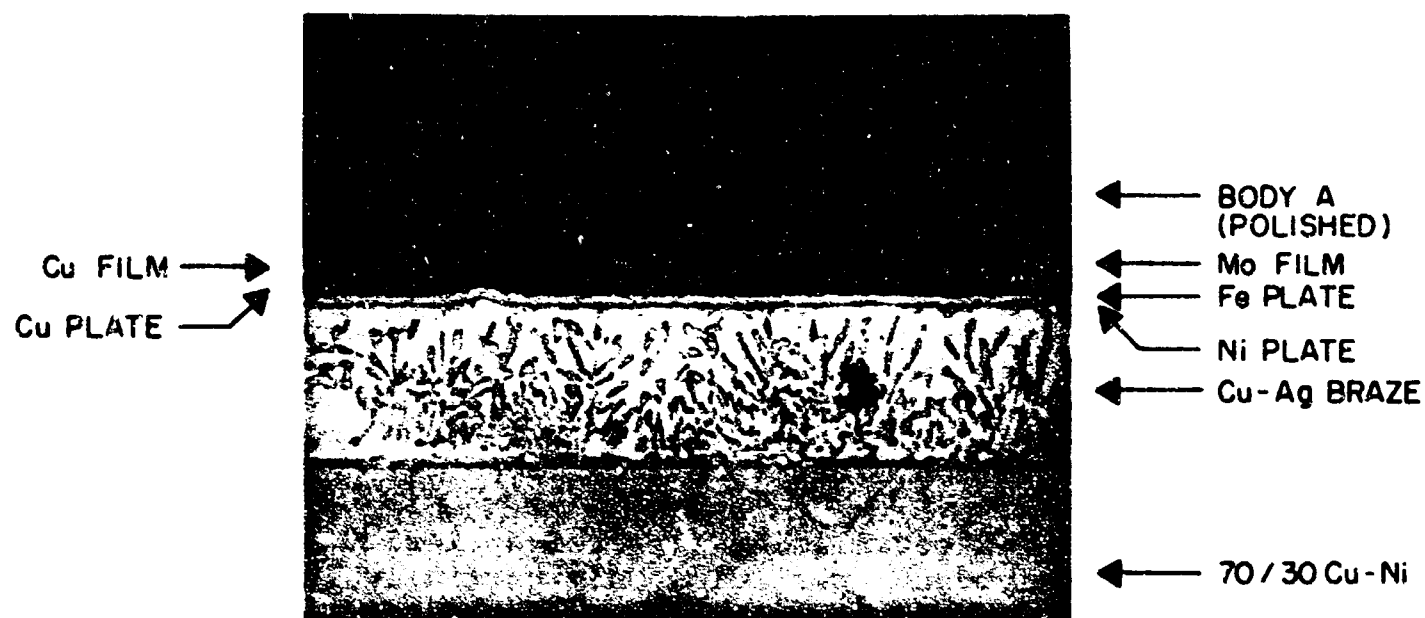


Figure 6.29: Photomicrographs (400X) of sample #266, a seal with active metals evaporated on a polished ceramic (top), and sample #228 with copper evaporated on a polished ceramic (bottom).

#### 6.3.7.9

##### Group VII

A Refractory Metallizing Sintered Layer  
on a Ceramic with Various Electroplated Layers  
on it, which is then brazed to a Metal Disc  
which in turn is tinned to a Copper Sample Holder.  
This group constitutes the balance of the samples.

The examination of these ceramic-to-metal seal samples constitutes the large bulk of the work.

Both P-1 and P-2 metallizings (Table 4-23 have previously been described in detail. Figs. 4.49 and 4.50 show their microstructure. Their microstructure has been further analyzed with X-ray diffraction, electron microscope and electron microprobe techniques.

P-2 metallizing sintered at 1425°C is a porous sponge of molybdenum particles only partially infiltrated by the glassy grain boundary phase of the ceramic. After sintering at 1550°C (P-2-1550) it becomes densely sintered and well infiltrated by the glassy grain boundary phase. The contrasting microstructures of these two conditions is shown in Fig. 6.30. The former metallizing is extensively penetrated by copper plate.

P-1 metallizing sintered at 1425°C is a molybdenum sintered sponge infiltrated by a reacted semi-conducting heterogenous mass of  $\text{MnO-TiO}_x\text{-CaO-MgO-SiO}_2\text{-Al}_2\text{O}_3$ . The low  $I^2R$  losses that occur in this phase(s) have been discussed directly above (6.3.7.6, 6.3.7.7). The effect of the layer on the lowering of the dc coefficient of resistivity has also been discussed in section 6.2.

#### 6.3.7.9.1

##### Sub Groups 7.A and 7.B

##### P-2 Metallizing-Copper Plate

The P-2 (1425°C) metallizing which is copper plated gives data which is random as a function of metallizing thickness. This situation is shown in Fig. 6.31.

The liquated copper plate which permeates the metallizing, after brazing is augmented by a copper braze containing varying amounts of nickel from the cupro-nickel metal member. This infiltrated metallizing (sub-group 7.A) gives a high loss Mo-Ni-Cu intermetallic complex on solidification. The conduction loss would be expected to be and is very sensitive to brazing time and brazing temperature variations.

Fig



Figure 6.30: Photomicrographs of P-2 metallizing fired at 1425°C (top) and 1550°C (bottom). Subsequently copper plated, Fe barrier layer, Cu-Ag braze (400X).

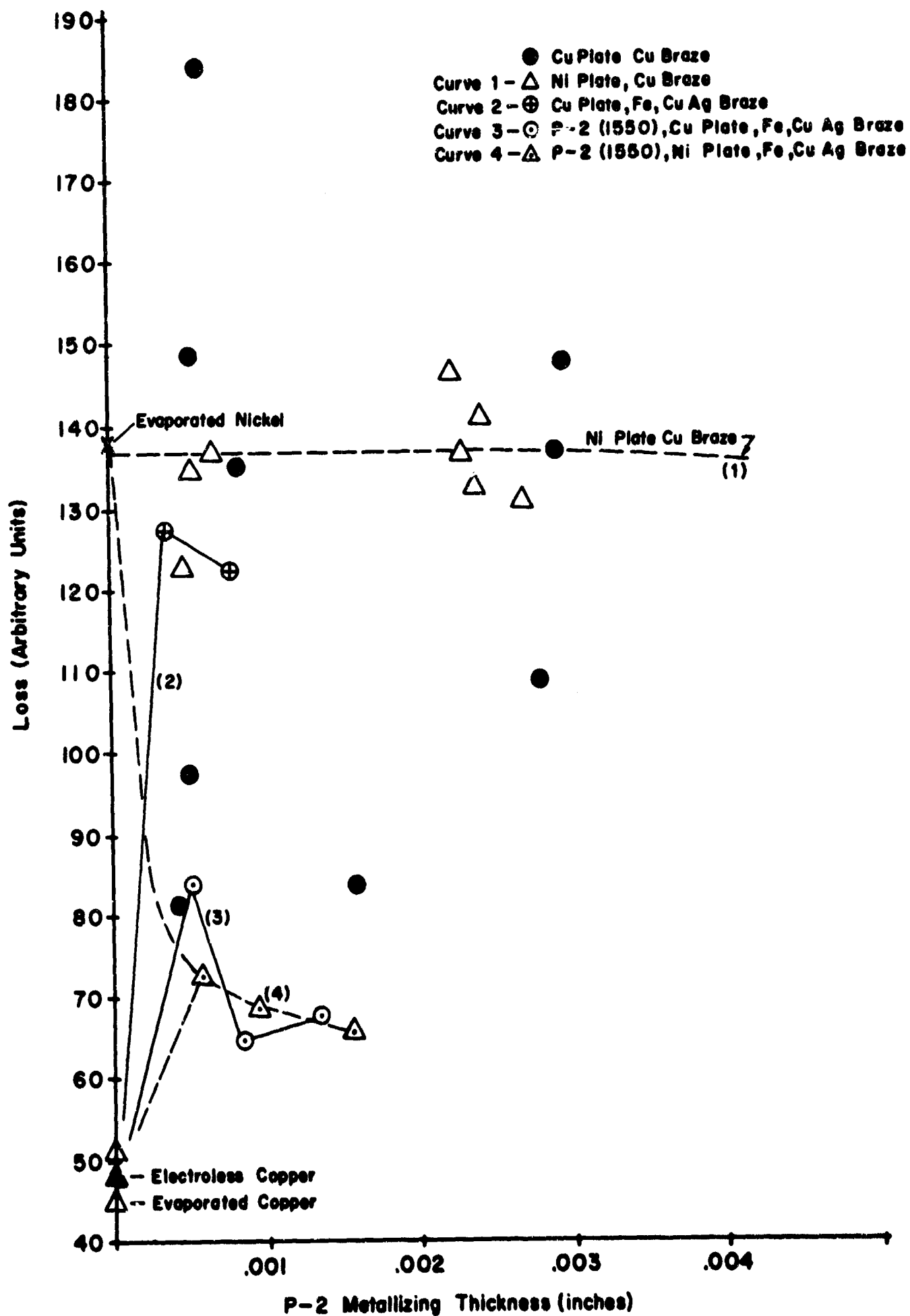


Figure 6.31: Conductive loss data for P-2 metallizing on Body A. Metallizing sintered at 1425°C unless otherwise noted.

An attempt to reduce this variation (due to liquation of the copper plating layer) and to give a low loss layer was made by brazing with Cu-Ag at 810°C (versus 1100°C for copper braze). An unsintered iron barrier layer was inserted to prevent the attack of the Cu-Ag braze on the underlying molybdenum metallizing which was infiltrated by the copper plate. The small amount of data obtained (Fig. 6.31, curve 2) indicates that a low loss situation was not attained. This must be due to the fact that several percent of copper can go into solid solution in the molybdenum phase, thus raising its resistivity.

Sintering of the P-2 metallizing to 1550°C and otherwise identical subsequent processing to that of the previous paragraph does give a very low loss situation. A seal with 66 loss units is the lowest loss displayed by any conventional seal on this program (Fig. 6.31, curve 3). The initial peak in the loss curve at the 0.4 mil metallizing thickness is again due to a portion of the current being carried in the heterogenous Mo-Cu interfacial boundary region. At greater thicknesses, the current is carried exclusively in the pure unpenetrated molybdenum metallizing which must therefore be lower loss.

#### P-2 Metallizing-Nickel Plate

The P-2 metallizing, nickel plate situation is somewhat similar to the initial situation discussed above, Fig. 6.31, curve 1. The 1425°C metallizing allows the nickel plate to permeate the metallizing and at the copper brazing temperature of 100°C and a solid state Ni-Mo reaction will ensue. This reaction results in a high loss interfacial film of Mo-Ni intermetallics forming throughout the metallizing (Table 6-12). Again, this situation is corrected by the 1550°C sintering (Fig. 6.31, curve 4). Also, as the metallizing layer gets thicker, the loss again decreases, i.e. the current is more and more carried in the metallizing layer instead of the higher loss Mo-Ni and nickel interfacial layers.



6.3.7.9.2    Sub Group 7.C  
P-1 Metallizing, Copper or Nickel Overplate,  
Copper Brazed

The loss values utilized in these seals are shown in Fig. 6.32 on curves 1 and 2.

As expected, the losses, utilizing a copper overplate and braze, progressively increase as more current is carried in the metallizing layer, while they decrease in the case of a nickel overplate and copper braze. An equal loss is experienced in both cases when the current is carried exclusively in the metallizing layer.

While this simple explanation is fortuitously convincing for this isolated segment of the data, a more thorough treatment is required to fully explain the data as may be seen from succeeding discussions.

6.3.7.9.3    Sub Group 7.D  
P-1 Metallizing, Copper or Nickel Overplate,  
and Iron Plate, Cu-Ag Braze

While the brazing with copper is feasible with a cupro-nickel member, it is desirable to braze with Cu-Ag (or gold bearing brazes) when brazing to copper. Accordingly, an iron plated layer was inserted between the copper plate and the Cu-Ag braze to prevent attack of the copper by the Cu-Ag. A loss situation less than that obtained in Fig. 6.32, curve 1, was expected, as no nickel-molybdenum interaction (due to solution of Ni from the cupro-nickel, see microprobe data Fig. 6.34) could occur.

A much higher loss was, in fact, experienced (Fig. 6.32, curve 3). Although once again the loss levels are indicating that the current is carried exclusively in the thicker metallizing layers, this higher loss may partially be explained by penetration of the Cu-Ag braze through the Fe barrier layer as shown in Fig. 6.33 (top). The dc resistivity change alone could not be responsible, however. (See later Table 6-12.) Ideally, the barrier layer separates the various layers of the seal as shown in Fig. 6.34, but as shown above, breakdown of the seal layers does occur with penetration of the Cu-Ag up to, but not into, the metallizing layer (Fig. 6.35). This fact was established by carrying out further microprobe studies on seal No. 93, Fig. 6.36, which are shown in Fig. 6.37.

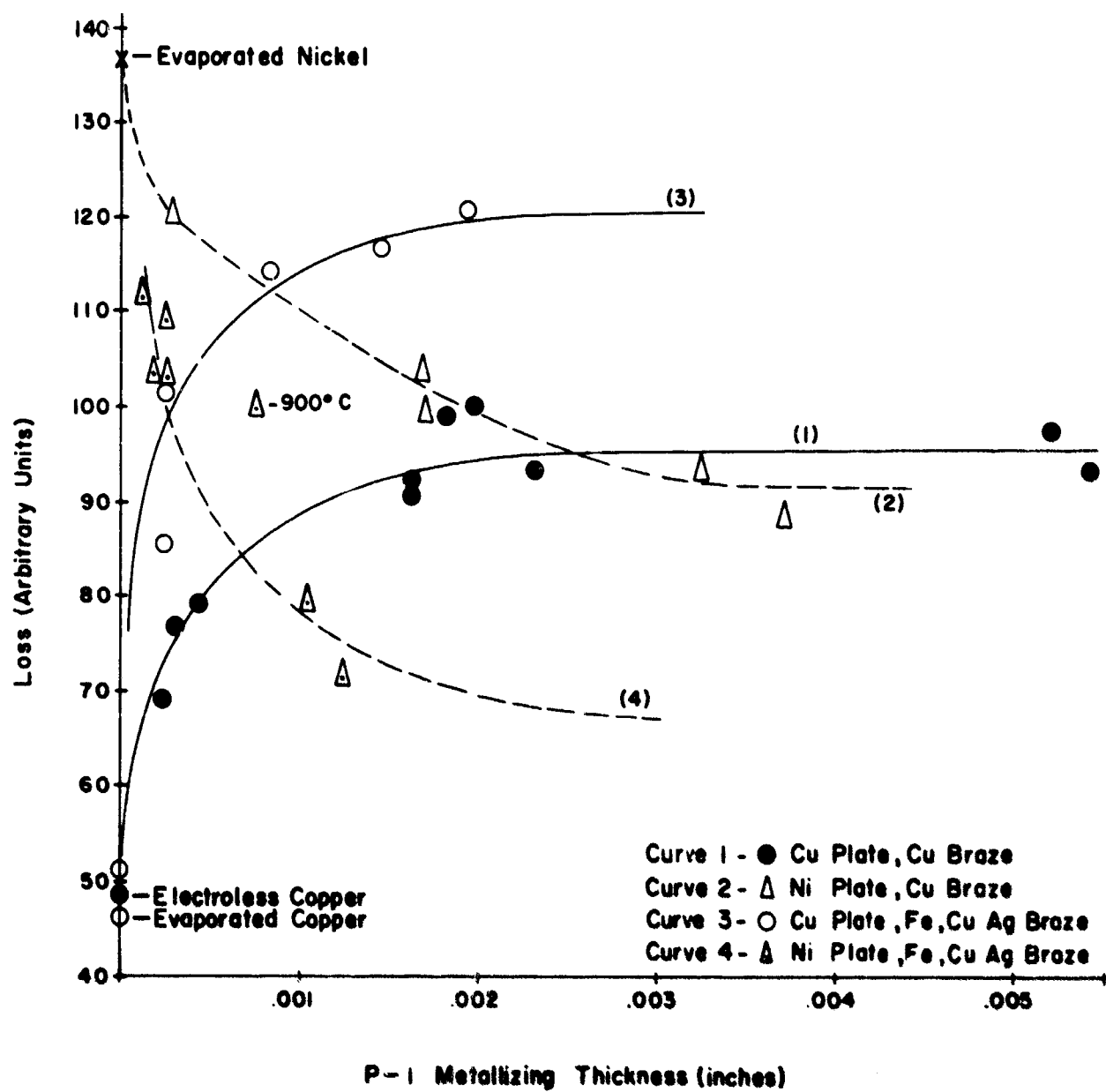


Figure 6.32: Conductive loss data for P-1 on Body A. Metallizing sintered at 1425°C.

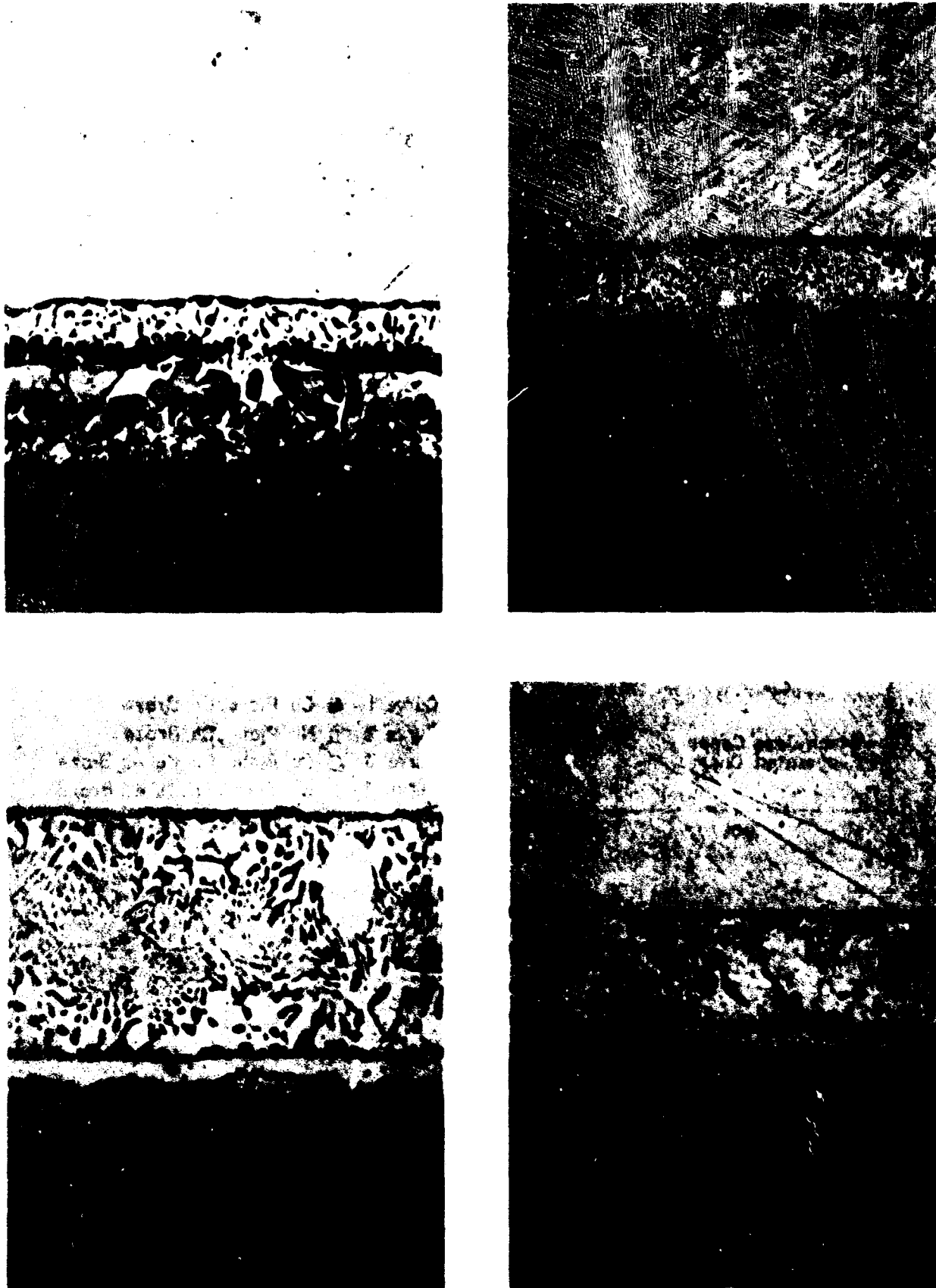


Figure 6.33: Photomicrographs of Cu-Ag braze penetration through Fe barrier layer into Cu (top) and Ni (bottom) metallizing overplate (400X).

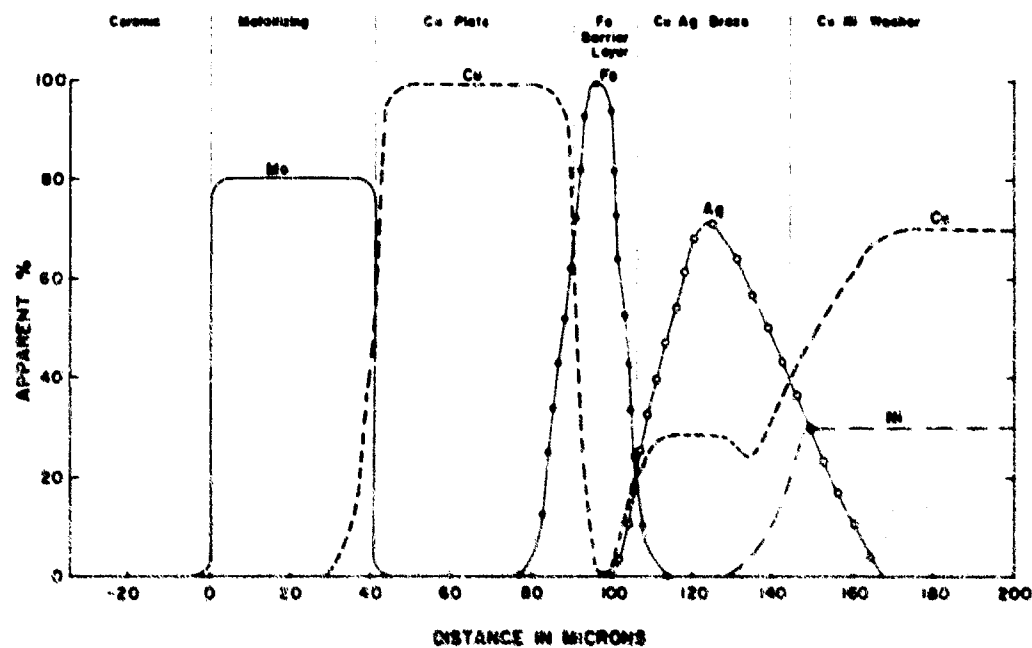


Figure 6.34: Microprobe analysis of iron barrier layer seal. Data was averaged.

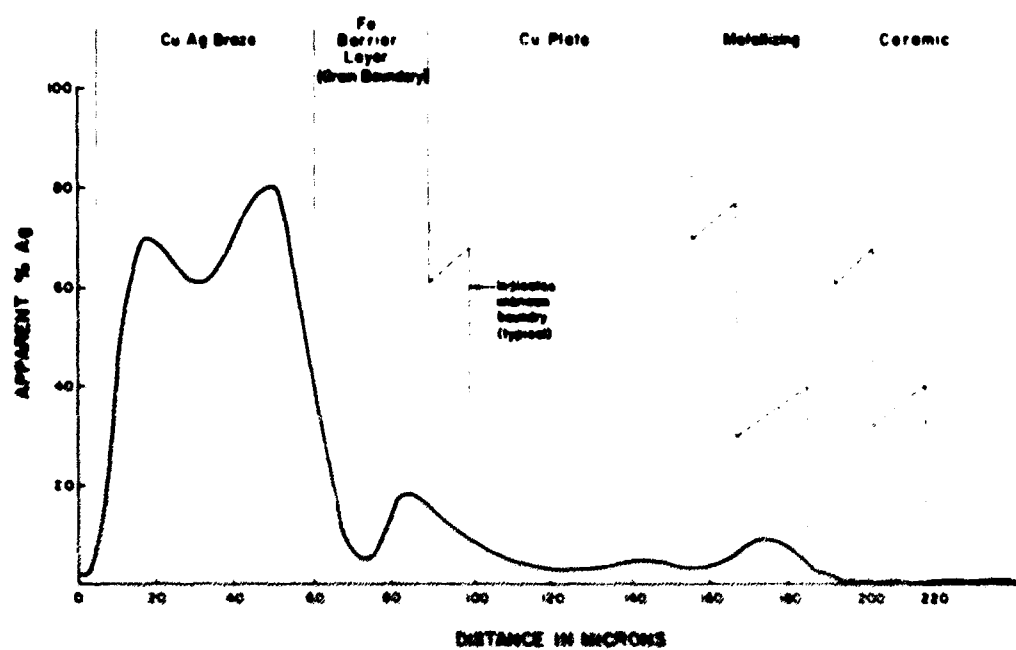


Figure 6.35: Microprobe analysis of iron barrier layer seal described in text showing silver scan across seal in the region of a grain boundary discontinuity in the iron barrier layer.

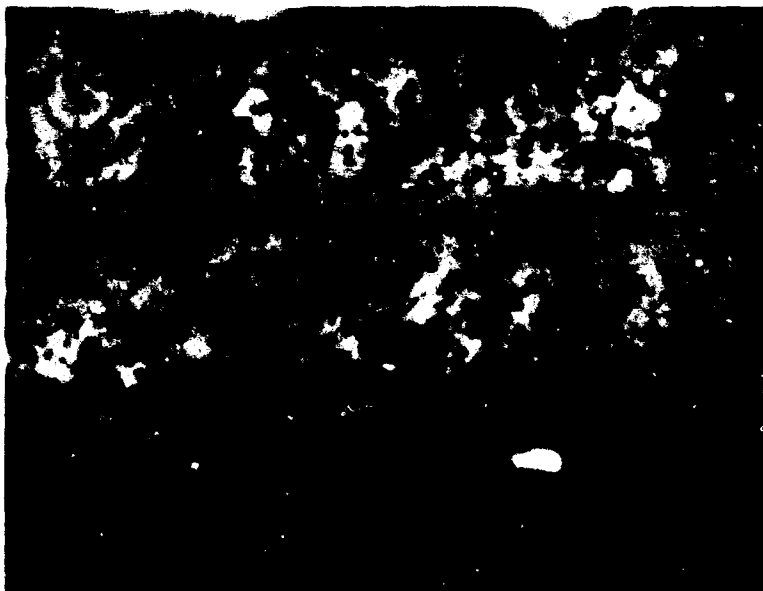


Figure 6.36: Photomicrograph of conduction loss sample #93 (P-1, Body A, Cu plate, Fe barrier layer, Cu-Ag braze). (850X).

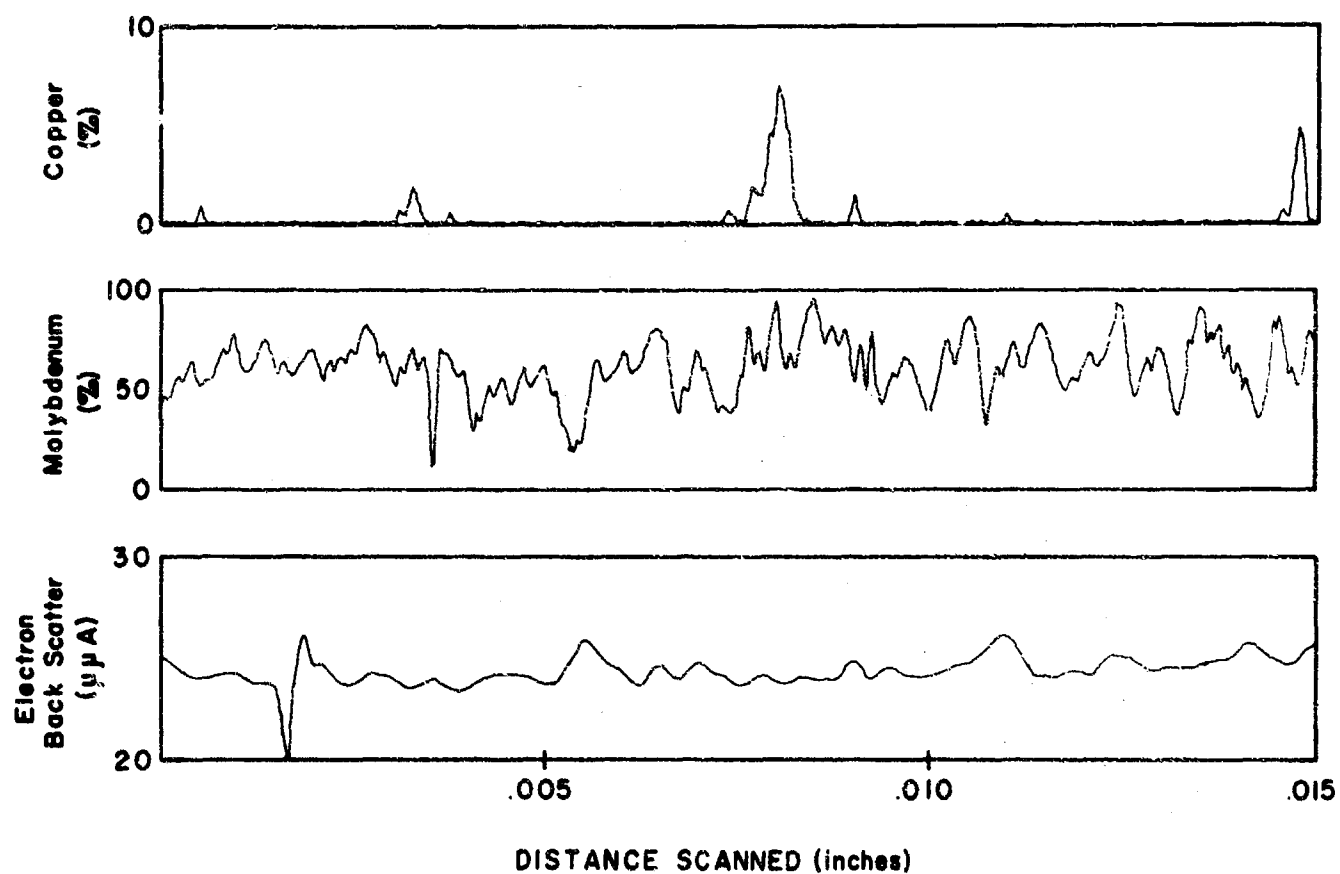


Figure 6.37: Microprobe analysis of Mo and Cu in conduction loss sample #93 (P-1 Body A, Cu plate Fe barrier layer, Cu-Ag braze). Ag and Ni were below limit of detectability. Scans were parallel to metallizing — ceramic interface 0.0005 in. into metallizing.

One must conclude that although the current is carried in the metallizing region either (1) the overplate and other layers must provide a variable impedance which is electrically reflected into the metallizing layer, or more probably (2) the metallizing is altered in some so far undetectable fashion by the subsequent processing treatments such as solid solution of the copper in the molybdenum phase.

The opposite loss situation is true for the nickel plate - iron barrier layer series curve 4 in Fig. 6.32. The nickel plate - molybdenum metallizing interaction zone sees a maximum of 800°C (Cu-Ag braze temperature) as opposed to the 1100°C copper braze temperature of curve 2. Consequently much less high loss Mo-Ni intermetallic is formed in the metallizing layer and at the interface and lower losses result. An intermediate loss situation was obtained in the case of one nickel plated sample sintered at 900°C. The concept of the influence of seal layers other than the metallizing directly carrying the rf currents must be invoked for the two cases under consideration (nickel and copper overplate) in order to explain the different points at which the losses appear to level off. (Fig. 6.32, curves 2 and 4.)

6.3.7.9.4    Sub Group 7.E, 7.F  
P-1 Metallizing, Copper or Nickel Plate,  
with or without Iron Plate, Nickel Plate,  
Cu-Ag Braze

These data\* utilizing seal construction shown in Fig. 6.38 (top) are plotted in Fig. 6.39 together with data from the previous sub group 7.D.

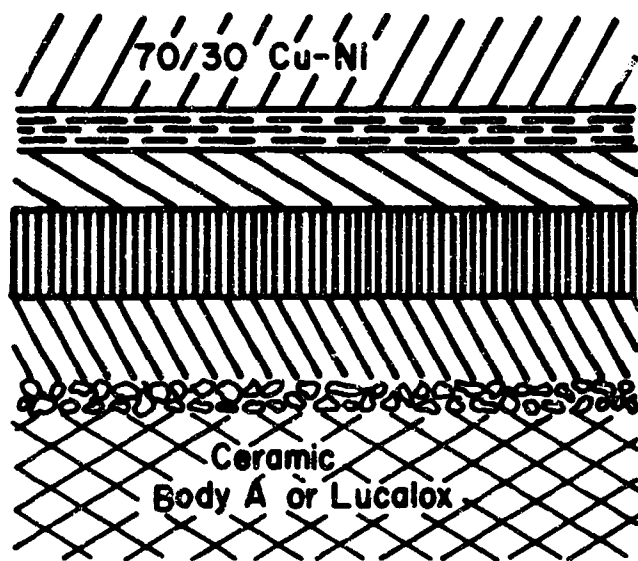
The use of a Fe-Ni barrier layer was an attempt to minimize the penetration of the Cu-Ag braze through to the base plating layer of copper or nickel as is ideally shown in Fig. 6.38. However, this barrier layer also was not 100% effective as is shown by Figs. 6.40 and 6.41.

Despite the random penetration of the copper layer by the Cu-Ag braze, the results are consistent among themselves and with the previous data, Fig. 6.39, curve 1. Photo-micrographs of three seals showing metallizing of different thicknesses with correspondingly increased losses

---

\*Omitting that using a Lucalox (General Electric Co. Trade Name) base, which is reported later in 6.3.7.9.6.





Cu-Ag braze  
 0.5 mil Ni plate  
 1.0 mil Fe plate  
 1.0 mil Cu or Ni plate  
 P-1 metallizing (variable thickness)

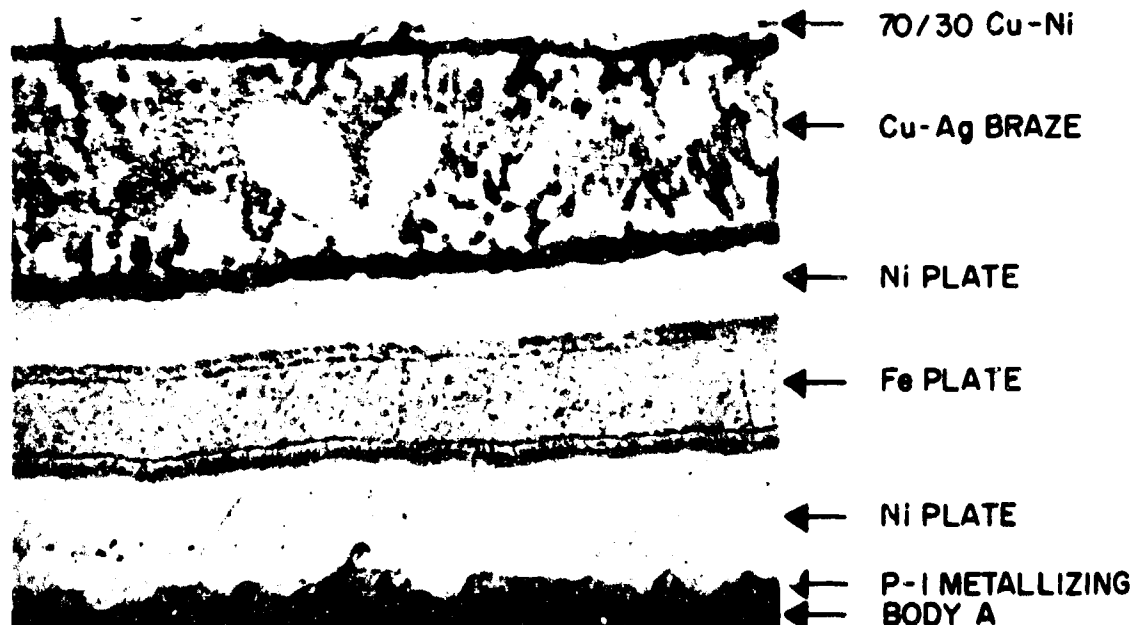


Figure 6.38: Schematic cross-section of ceramic-to-metal seal with iron-nickel barrier layer (top); photomicrograph (400X) of sample #207 (bottom).

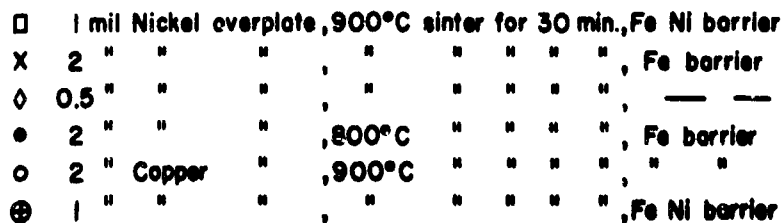


Figure 6.39: Plot of I<sup>2</sup>R losses at 9.15 G c versus metallizing thickness for P-1 on Body A with overplate of copper or nickel. All specimens were prepared with a barrier layer and a CuAg eutectic braze and 70/30CuNi metal member (see text).

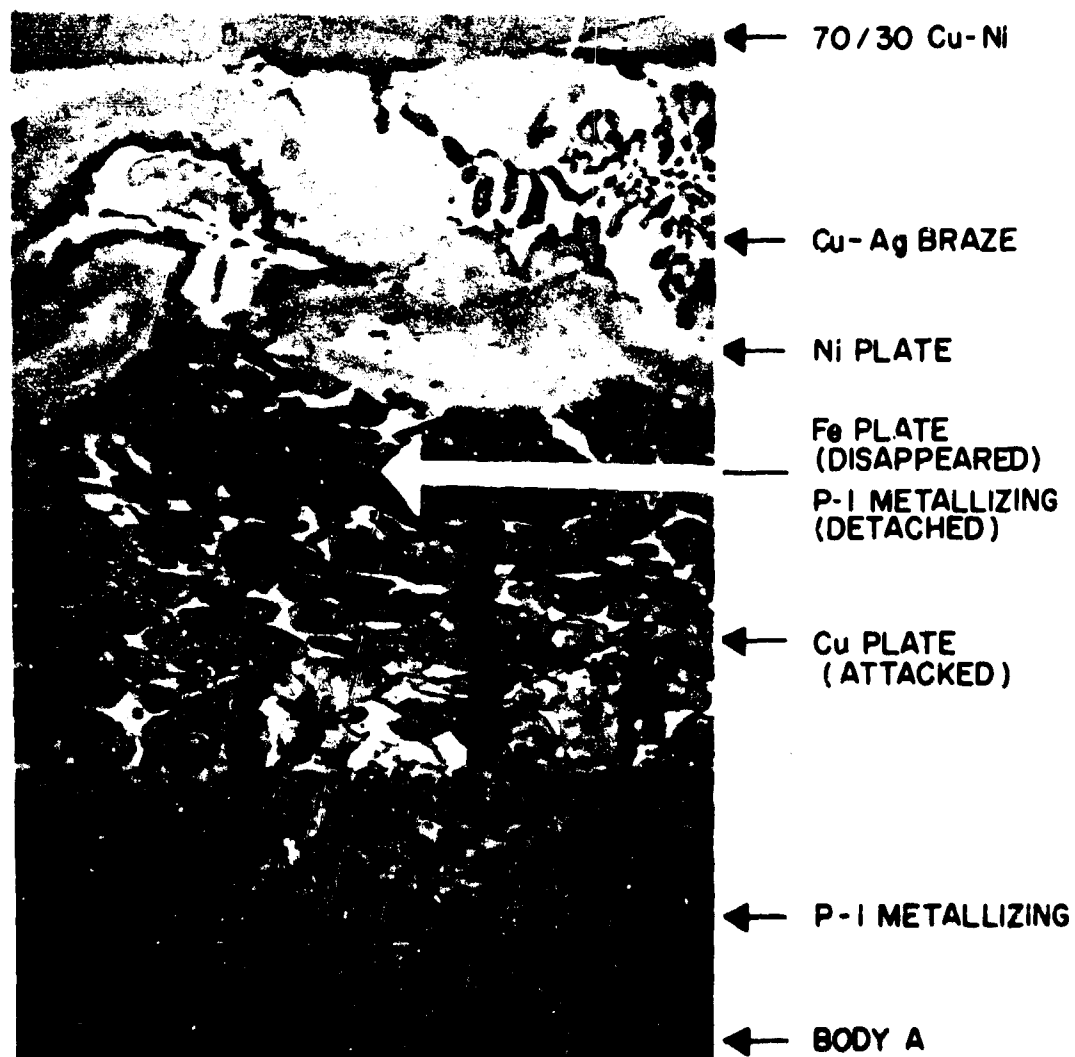


Figure 6.40: Photomicrograph (400X) of sectioned sample #205, showing failure of barrier layer and detachment of portion of metallizing. See Table 6-8 for data.

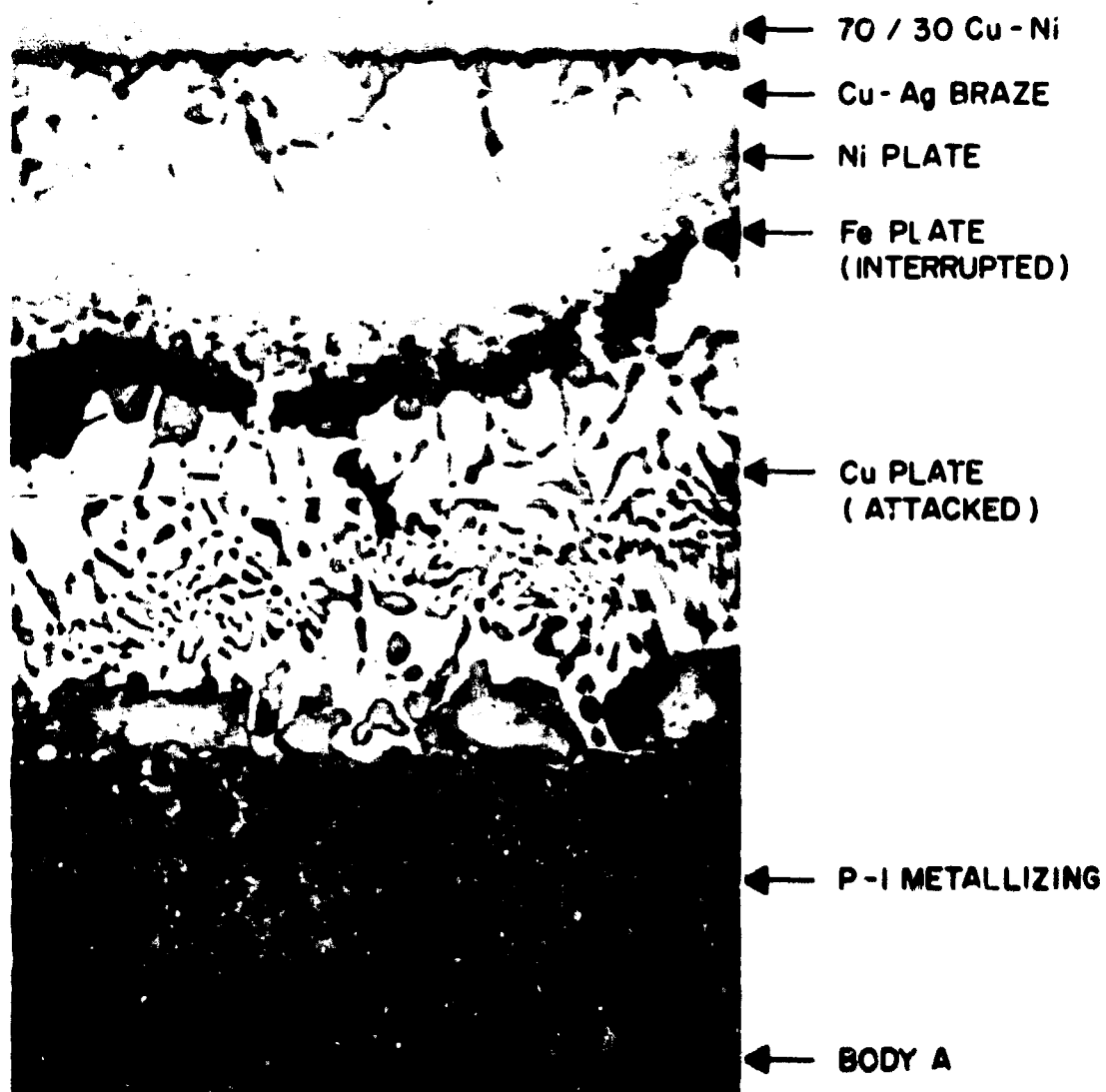


Figure 6.41: Photomicrographs (400X) of sectioned sample #205 showing disruption of iron barrier layer (dark) and partial dissolution of copper overplate. See Table 6-8 for data.

are shown in Fig. 6.42. The bottom seal shows extensive Cu-Ag penetration of the copper layer. The physical heterogeneity of the seals is obvious from these cross-sections. A contributory factor to the consistency of the data, despite the variable penetration of the Cu-Ag braze, is due to two factors:

1. The dc resistance of Cu-Ag is similar to copper, Table 6-13.
2. At metallizing thicknesses greater than 1 mil the rf currents are carried almost completely in the metallizing layer.

When utilizing a nickel overplate on the metallizing, in no case (either in 7.D, 7.E or 7.F) was the nickel plate penetrated by the Cu-Ag through to the metallizing. The use of the iron or iron-nickel barrier layer shown in Fig. 6.38 is therefore superfluous as is shown in Fig. 6.43 (bottom). This being so, the three seals denoted by  $\diamond$ , X and  $\square$  on Curve 2 all have an intact, 900°C sintered, nickel plate next to the metallizing; and therefore show an intelligible trend. The losses are between those in which the nickel plate is sintered on at 800°C and those sintered at 1100°C. The somewhat higher losses for the  $\square$  points are due to an additional sintering of the nickel plate in the course of sintering on the iron portion of the iron nickel barrier layer as would be expected (see Fig. 6.19).

#### 6.3.7.9.5 Sub-Group 7.G

P-1 Metallizing, Copper Plate, Cu-Ag or Cu-Au Braze, 70/30 Cupro-Nickel or Nickel-Plated Kovar Respectively (Table 6-9)

Together with Sub-Group 7.F, these represent conventional seals. Cross-sections of these seals are shown in Fig. 6.43. Table 6-13 shows the resistance of the Cu-Au braze to be high in comparison to copper or Cu-Ag. Consequently, the losses as shown in Table 6-9 are higher for a 0.5 mil metallizing thickness, but not drastically so.

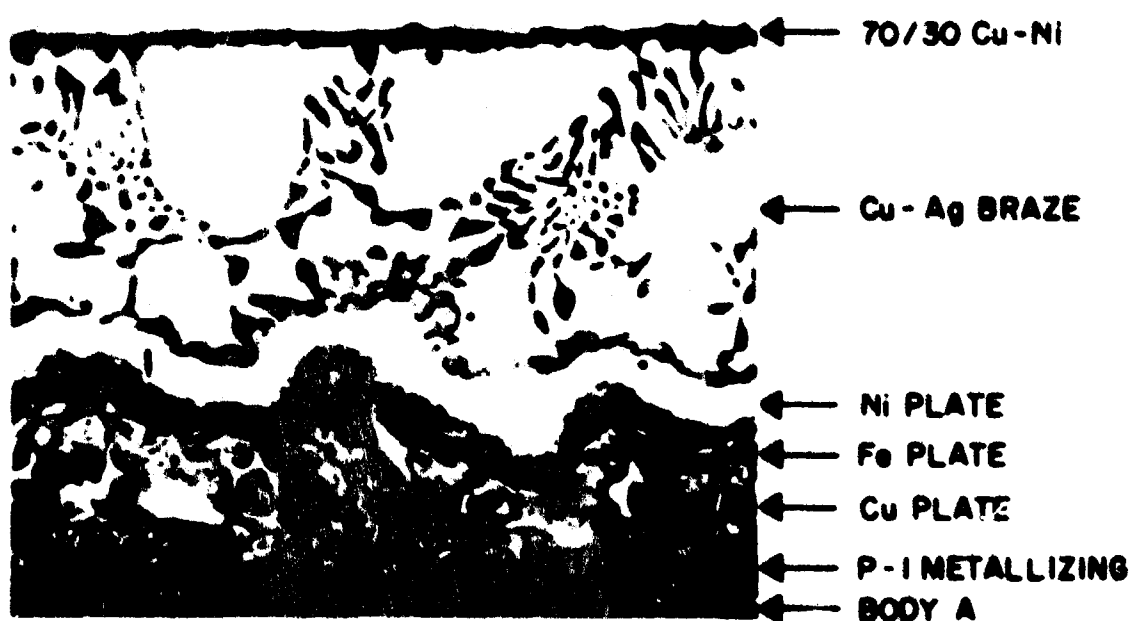
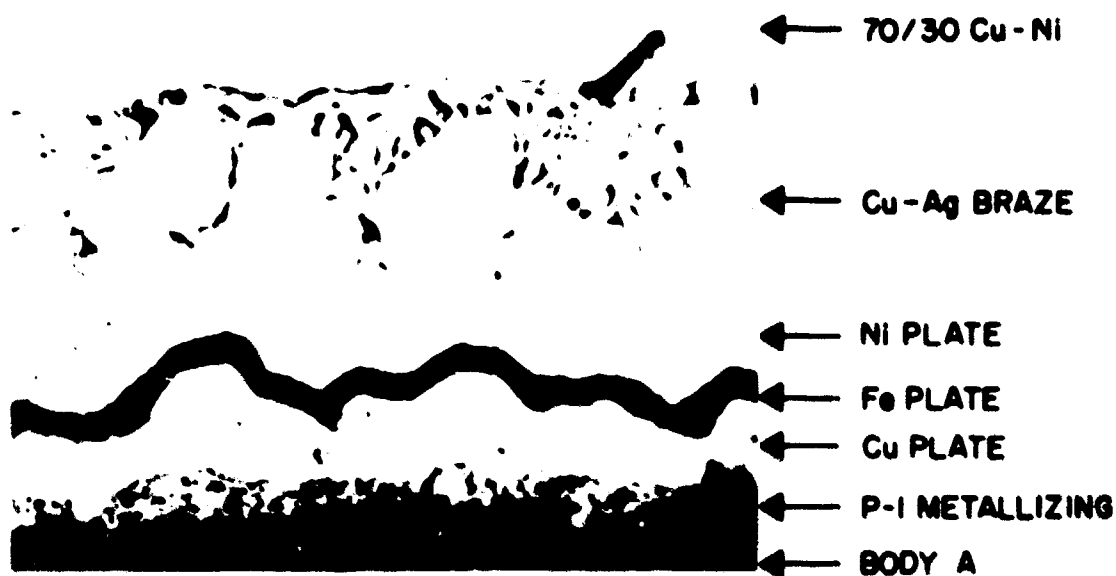
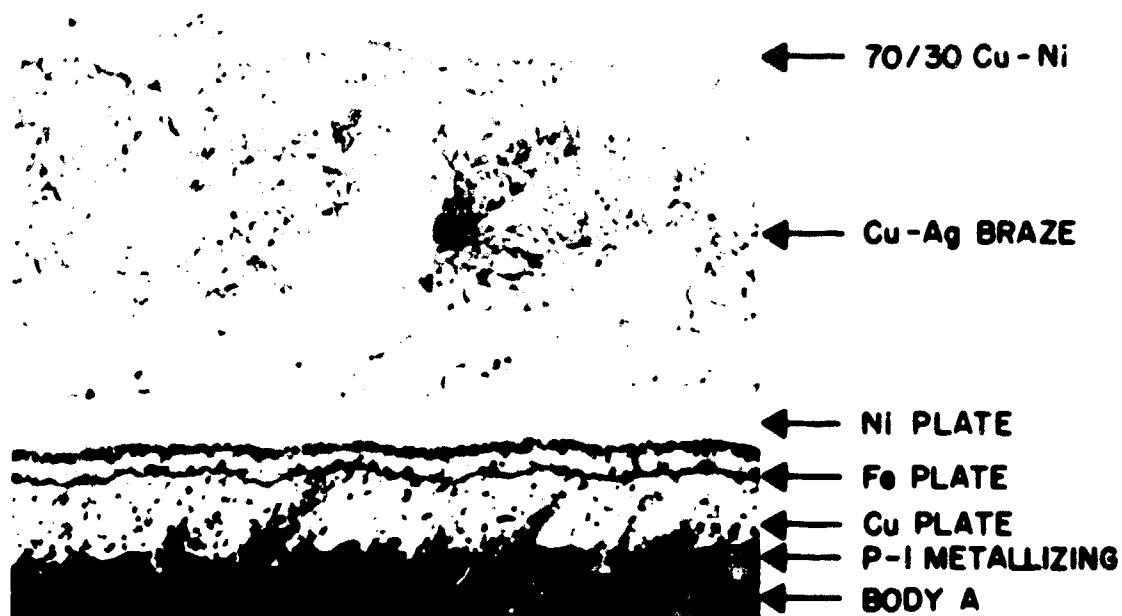


Figure 6.42: Photomicrographs (400X) of samples #200 (top) with 53 units of relative loss, #201 (center) with 66 units of relative loss, #202 (bottom) with 38 units of relative loss. See Table 6-8 for data.

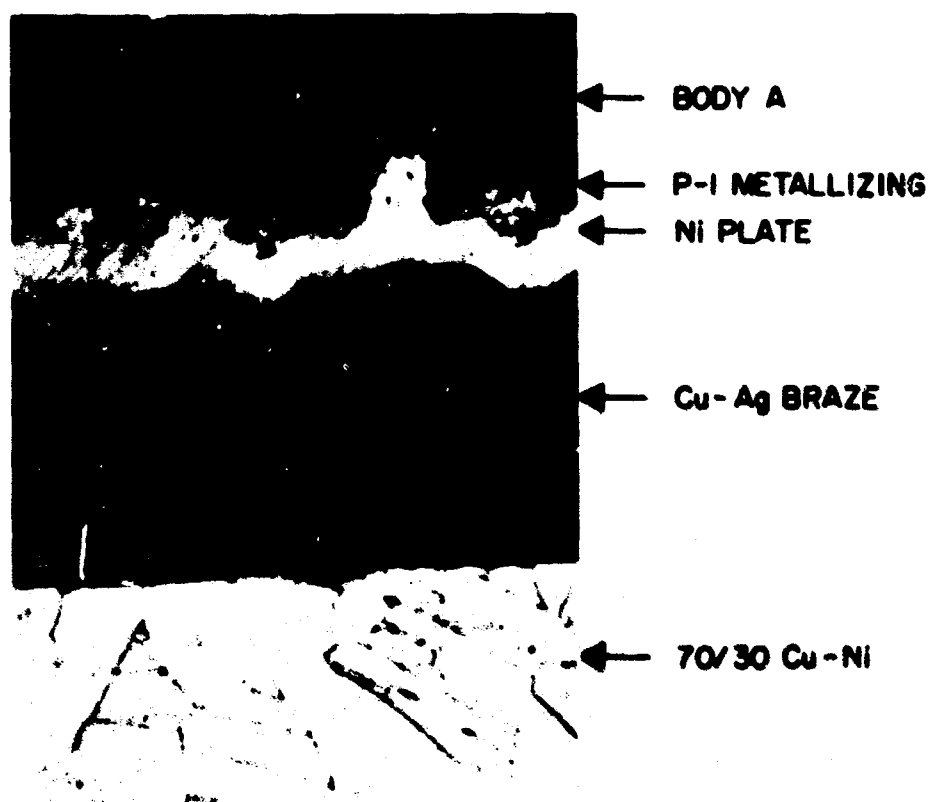
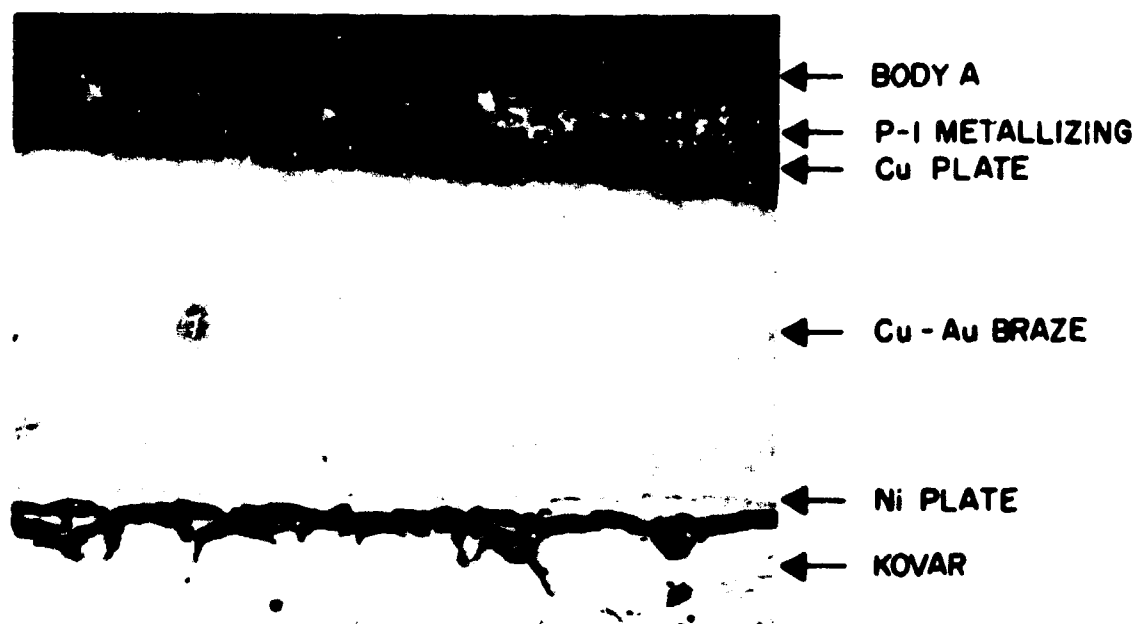


Figure 6.43: Photomicrographs (400X) of sample #224 (top) and sample #225 (bottom).

TABLE 6-13

## Room Temperature Resistivity of Selected

## Braze Materials

Material	Composition (wt %)	Measured Resistivity* (microhm cm)	Published Data <sup>5</sup> (microhm cm)
OFHC Copper	99.9 + Cu	1.775	1.69
35-65 <sup>+</sup>	65 Cu, 35 Au	8.65	
50-50 <sup>+</sup>	50 Cu, 50 Au	11.22	
80-20 <sup>+</sup>	20 Cu, 80 Au	13.59	
24K gold	99.9 + Au	2.365	2.44
NIORO <sup>+</sup>	82 Au, 18 Ni	16.35	
NICORO <sup>+</sup>	62 Cu, 35 Au, 3 Ni	12.95	
CUSIL <sup>+</sup>	72 Ag, 28 Cu	2.175	

\*Determined from measurements on 20-foot lengths of 0.010 inch wire.

<sup>+</sup>From WESGO, Belmont, California.



6.3.7.9.6 Sub-Group 7.E.1  
P-1 Metallizing on Lucalox\*, Copper or Nickel  
Plate, Cu-Ag Braze (Table 6-8)

The data obtained using Lucalox\* as a base given in Table 6-8 is plotted in Fig. 6.44.

As explained previously, due to the difference in the loss measuring equipment working point, this data is not directly translatable to that employing Body A.

In this case, the loss characteristics are reversed for the nickel and copper overplate situations. The metallizing is not vacuum tight on Lucalox\* and tends to have micro-fissures and pores. This means that the metallizing is penetrated by the plate.

In the case of the copper plate, the losses generally follow the usual pattern, being almost identical to those displayed by curve 1 in Fig. 6.32, although the dotted line indicates that a more complex electrical interaction may occur.

In the nickel plate case, it appears that the formation of the lossy Ni-Mo intermetallic is dependent on the amount of molybdenum available to react with the nickel plate. As the metallizing volume increases, so the losses increase in an exponential fashion.

The losses would be expected to assume the more characteristic pattern of Fig. 6.39 if the metallizing were replaced by a metallizing such as P-3 which forms a vacuum tight seal on Lucalox\*.

---

\*General Electric Co. Trade Name.

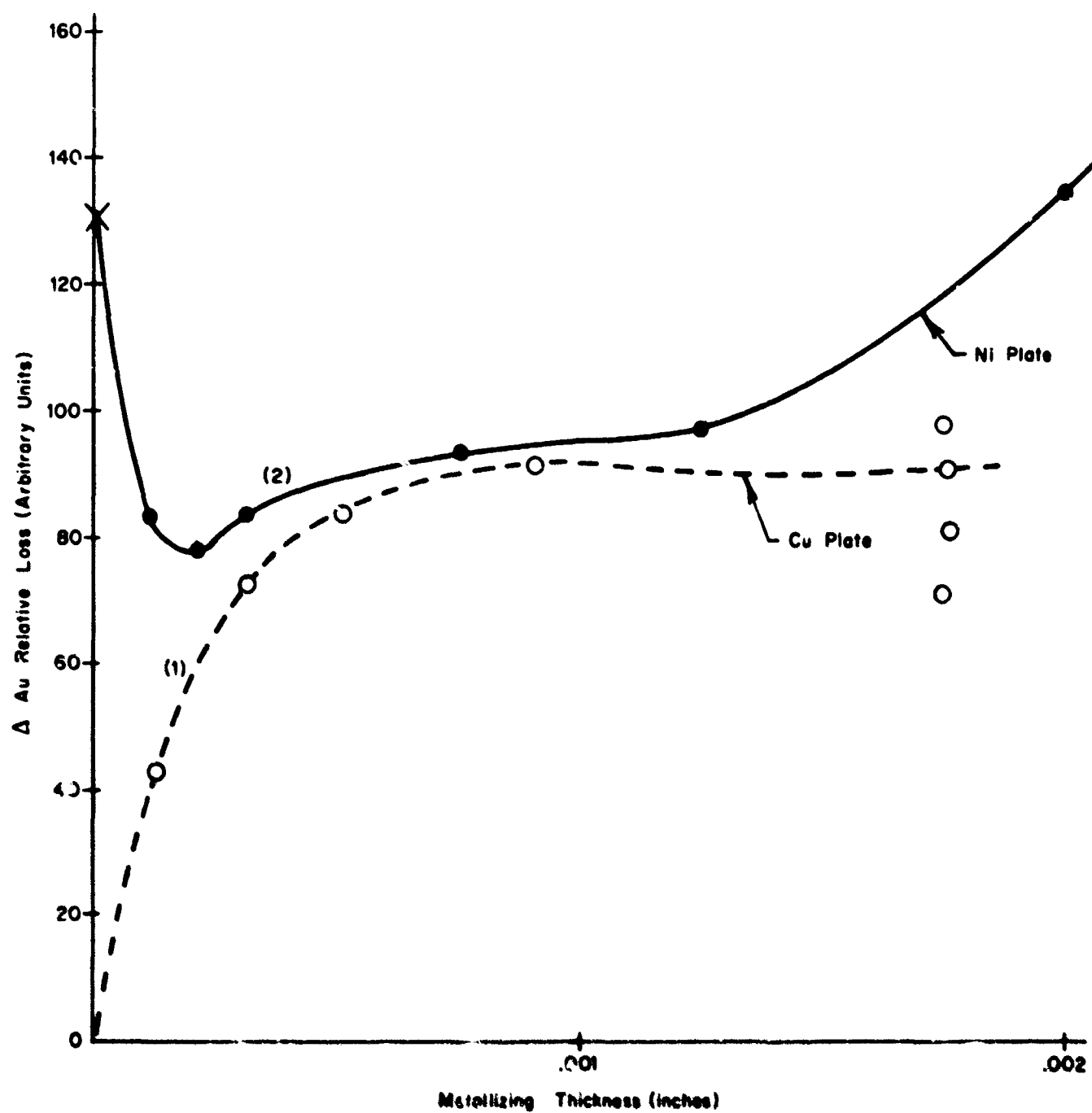


Figure 6.44:  $I^2R$  (conduction) losses versus metallizing thickness for P-1 on Lucalox<sup>®</sup> with overplate of copper or nickel. The specimens were prepared with a barrier layer and a CuAg eutectic braze (see text).

## 6.4 DIELECTRIC LOSSES

### 6.4.1 Introduction

The property of the ceramic-to-metal seal to be measured is the loss arising from phenomena other than conduction currents (due to the presence of mobile charge carriers) in the interface region. If a ceramic-to-metal seal is placed in a region of high normal electric field and little or no magnetic field, the tangential conduction current flowing should be at a minimum, while the loss component of the displacement current, herein called dielectric loss, should be high. Unfortunately, conduction currents due to the presence of electric fields in material of finite bulk resistivity can also be expected. The success of an experiment in separating the two loss mechanisms hinges on the relative magnitude of the above effects.

By inserting the sample between the posts of a re-entrant type  $TM_{010}$  resonator, the above requirements should be met. The bulk of the electric field is between the re-entrant posts of the cavity, while the magnetic field is a maximum at the outer radius of the resonator and decreases to zero at the axial center. If a solid cylindrical test sample is placed between the posts, the electric field will be perpendicular to the interface at the interface if the resonator is symmetric about a plane defined by the interface. A measurement of resonator  $Q$  will indicate the relative loss of various samples.

The method of measuring the internal  $Q$  of the resonator follows Ginzton<sup>3</sup>. The measurement involves taking readings of the input standing wave ratio of the resonator as a function of frequency near the resonance point. By a knowledge of the coupling coefficient, the standing wave ratio at the 3db power points can be calculated and from this the  $Q$  can easily be found.

The first cavity, and its 0.200" diameter by 4.0" long test pieces, investigated proved to be unsatisfactory. No results were obtained with this geometry. Briefly, the problem was dilution of introduced metallized seal loss effects by a large volume of unaffected ceramic.

The reader is referred to the second and third quarterly reports for further details.

Excerpts from the second and third quarterly reports and a diagrammatic sketch of the first cavity constructed, Fig. 6.45, are given here, however:

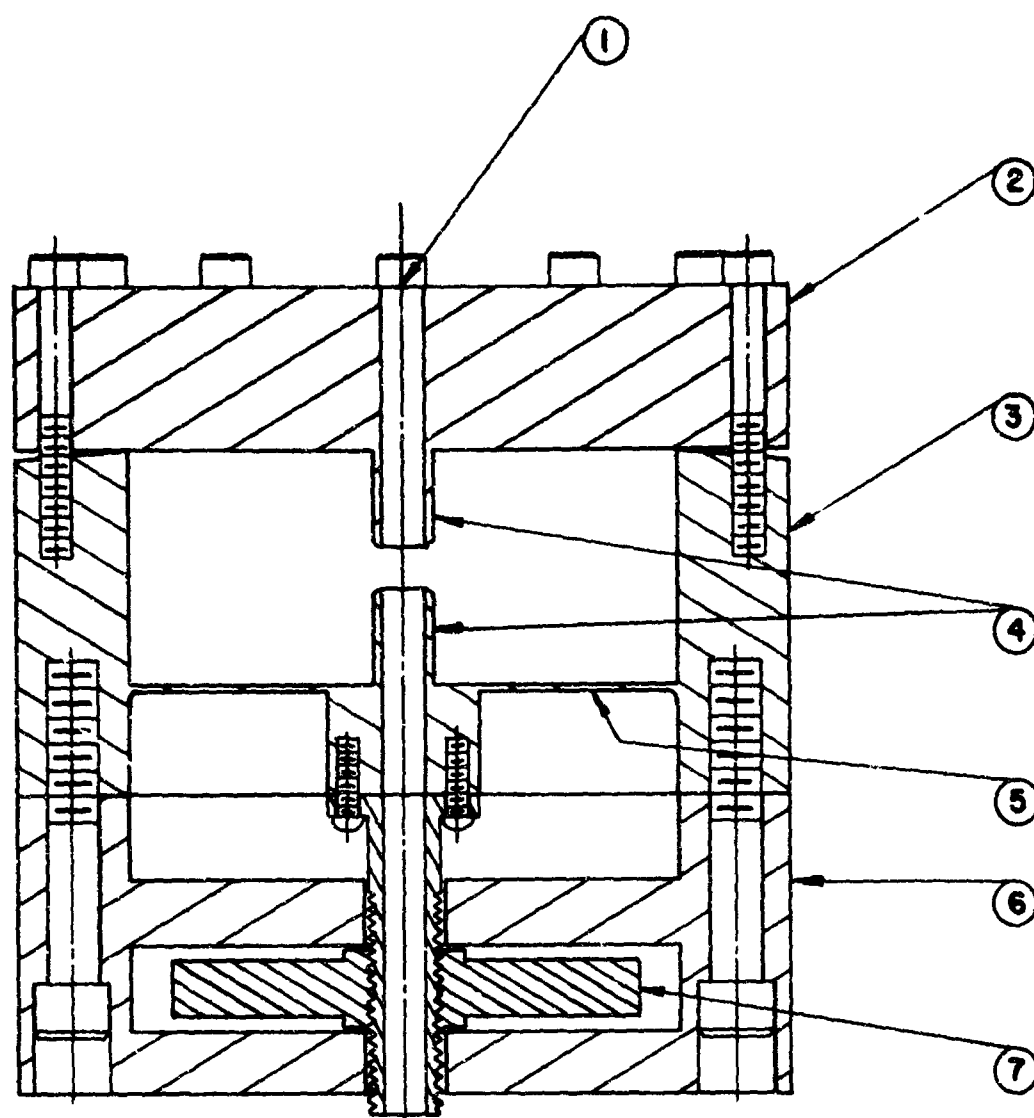
"Test specimens for the dielectric loss determination consist of .200" x 4.0" ceramic rods. The rods are cut in the middle, ground flat, metallized and plated on each end, and brazed back together, thus introducing the dielectric losses of two ceramic-metal seals simultaneously into the test resonator. The first ceramic test specimens consist of Body A metallized with P-1, copper plated, and copper brazed."

"The internal Q of the resonator was measured as nearly 14,000 with no ceramic in the gap (2424 mc). Insertion of a bare 94% alumina ceramic rod (0.200" diameter x 4" long) lowered the Q to around 1300 at 1997 mc. Subsequent measurements on two pieces metallized and brazed together on the ends indicated that the additional loss introduced by the seal was on the same order of magnitude as the bulk loss of the ceramic. Variations due to experimental error masked any change due to introduction of the seal."

Clearly, to see an effect it was necessary to reduce the ratio of pure ceramic to contaminated ceramic (that which had been penetrated by metallizing). A new cavity was designed which would accommodate disc shaped samples of 0.200 inch diameter. The posts on this resonator were made solid instead of hollow since with narrow gap spacings (compared with gap diameter) the fields in the hollow post cavity would be non-uniform across the gap, as well as having transverse components. The disadvantage of a solid post configuration is that the cavity must be disassembled to remove and replace the ceramic test piece.

In retrospect, in view of similar results with 94% alumina ceramics experienced with the second cavity which was designed (and which was used for all the dielectric loss experimental data obtained on this program), it is possible that the initial cavity made would have proved adequate for the needs of the program.

The second cavity, the modified test specimen and the experimental procedure proved satisfactory and are discussed below.



- 1. HOLE FOR INSERTION OF TEST PIECE
- 2. RESONATOR TOP
- 3. RESONATOR BASE
- 4. RE-ENTRANT POSTS
- 5. TUNING DIAPHRAGM
- 6. TUNING JIG
- 7. TUNING NUT

Figure 6.45: Resonator for dielectric loss measurements.

Three series of results were obtained. They may be categorized as follows:

- (i) Initial "prove-in" results
- (ii) Systematic experiments designed to establish certain hypothesis as facts.
- (iii) Experiments carried out to refine the data of (ii), to establish the relative contribution of conduction losses and to test "low loss" seals.

#### 6.4.2. Sample Preparation and Experimental Set-up

##### 6.4.2.1 The Cavity

The second cavity designed and built is shown in Fig. 6.46. The top post was designed to be removable so that the ceramic specimen could be placed in the cavity easily. The top post was made hollow and saw cuts made along the axis near the point of contact with the inner surface of the cavity top. A tapered screw is threaded into the top post so that when it is screwed in, it forces the walls of the top post outward tightening the joint between post and top. The coupling loop can be rotated to allow adjustment of the coupling.

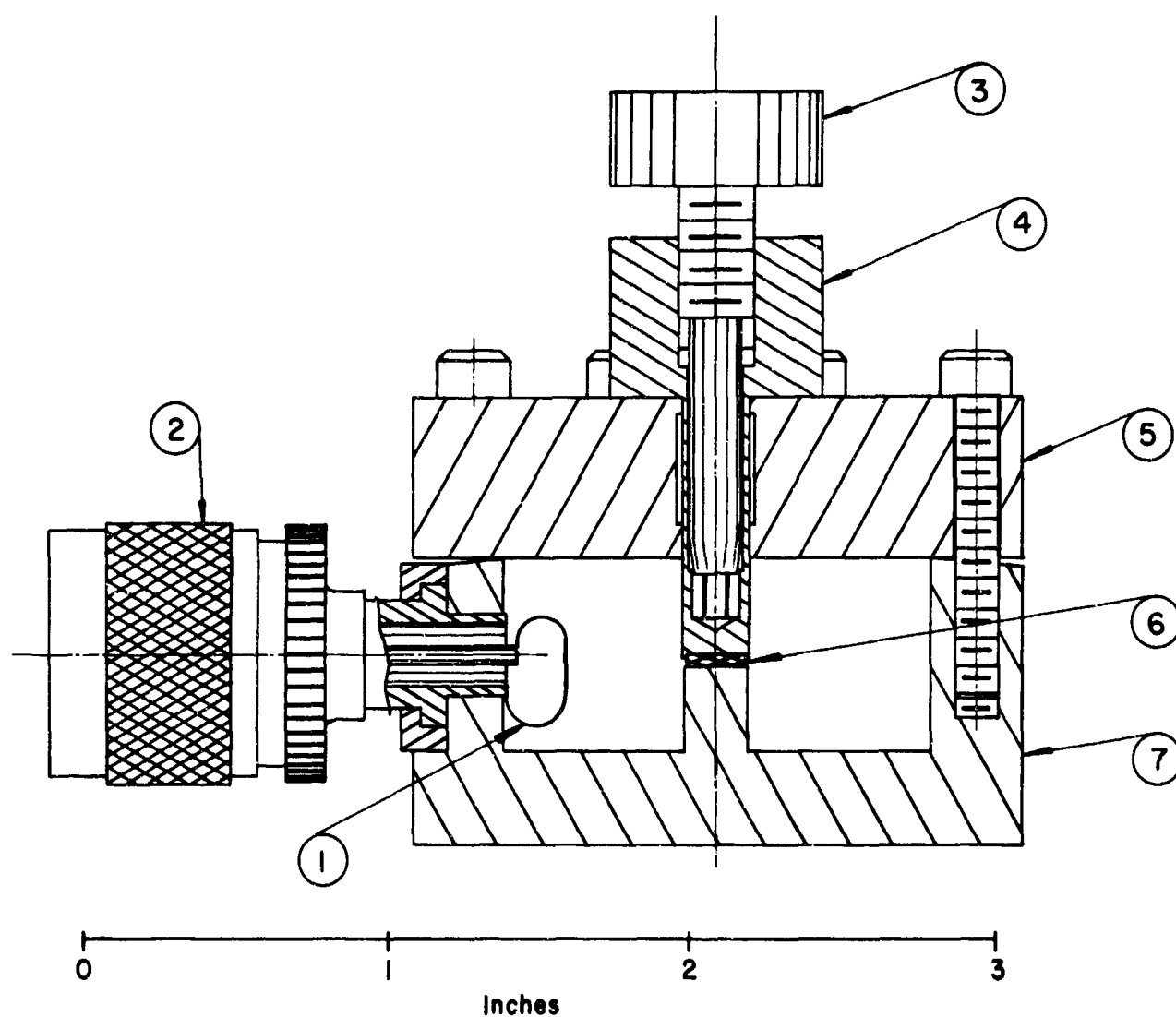
The cavity was designed for samples 0.060 inch thick. It is possible, however, to test pieces down to about 0.010 inch thick, with corresponding lowering of resonant frequency.

##### 6.4.2.2 Sample Preparation

The geometry of the dielectric loss test piece is a 0.200 inch diameter disc. The thickness of the sample must be between 0.050 and 0.070 inch to keep the resonant frequency of the cavity within the desired limits. Most measurements were with discs 0.060 inch thick. A few were made with two stacked 0.030 inch thick discs. Raw ceramics of 0.050/0.060 and 0.070 inch were used for calibration purposes.

The dielectric test samples were metallized only. The plating and braze were omitted since they do not contribute significantly to this type of loss.

The ceramics used were Body A (94%  $\text{Al}_2\text{O}_3$ ) and Body H (99.5%  $\text{Al}_2\text{O}_3$ ). The metallizing consisted of P-1,



- |                             |                        |
|-----------------------------|------------------------|
| 1. Coupling loop            | 5. Top                 |
| 2. Type N coaxial connector | 6. Ceramic test sample |
| 3. Top post expansion screw | 7. Resonator base      |
| 4. Expanding top post       |                        |

Figure 6.46: Redesigned dielectric loss cavity.

P-2, and P-3 (g) a  $\text{MnO}_2$ ,  $\text{TiO}_2$ ,  $\text{SiO}_2$  glass. The recorded thickness of the coatings of Series (1) is from calibration curve #5, Figure 13, 3rd Quarterly Report, and should be used as a comparison reference only. They may be modified by the data presented in Fig. 4.48. The thickness of the coatings in Series (3) is from direct metallurgical cross-section examination.

Further sample preparation detail is more appropriately reported within the individual experimental series sections.

#### 6.4.2.3 Equipment Set-up and Measurement Accuracy

A block diagram of the system is drawn in Fig. 6.47. Since the measurements are to be made at 2.2 to 2.3 Gc, it is more convenient to use coaxial lines instead of waveguide. Coupling to the resonator is by means of a small loop, placed in a region of high magnetic field. By rotating the loop, the coupling may be varied. A portion of the power from the Hewlett-Packard Model 616B generator is sampled and fed to a Hewlett-Packard transfer oscillator and the frequency measured by a Hewlett-Packard electronic counter. The signal passes through a coaxial slotted line and thence to the resonator - the standing wave ratio is read on a Hewlett-Packard standing wave indicator. Phase data may also be read from the slotted line.

The Hewlett-Packard Model 616B generator after three hours warm up was adequately stable as a signal source. Although its tuning rate is high, it was more convenient to operate than the klystron oscillator which was used initially.

A new signal generator became available during the sixth quarter prior to the third series of experiments. The experimental set-up was thus simplified. (Fig. 6.48.)

The Hewlett-Packard 8614A Signal Generator has two outputs, an uncalibrated, unmodulated one to provide the signal for the frequency measurement with an electronic counter and the main output furnishing the signal square wave modulated for indication on the VSWR meter.

A 30db directional coupler was inserted to measure the signal reflected at the cavity and find the resonance frequency easily and tune in precisely.



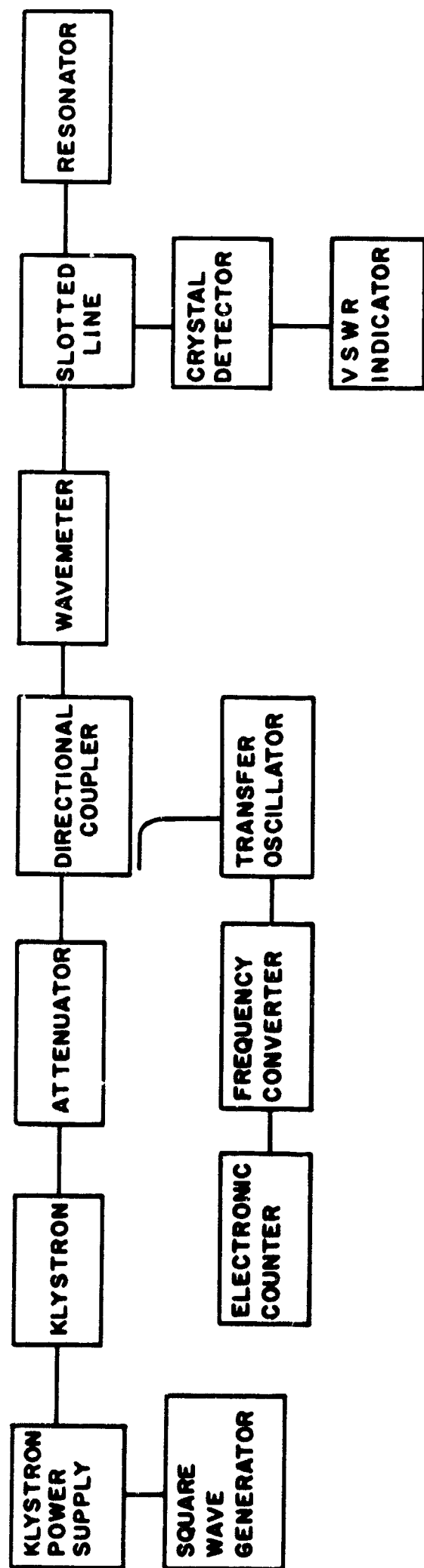


Figure 6.47: Block diagram of "Q" measurement for dielectric loss data at ceramic-metal seal interface.

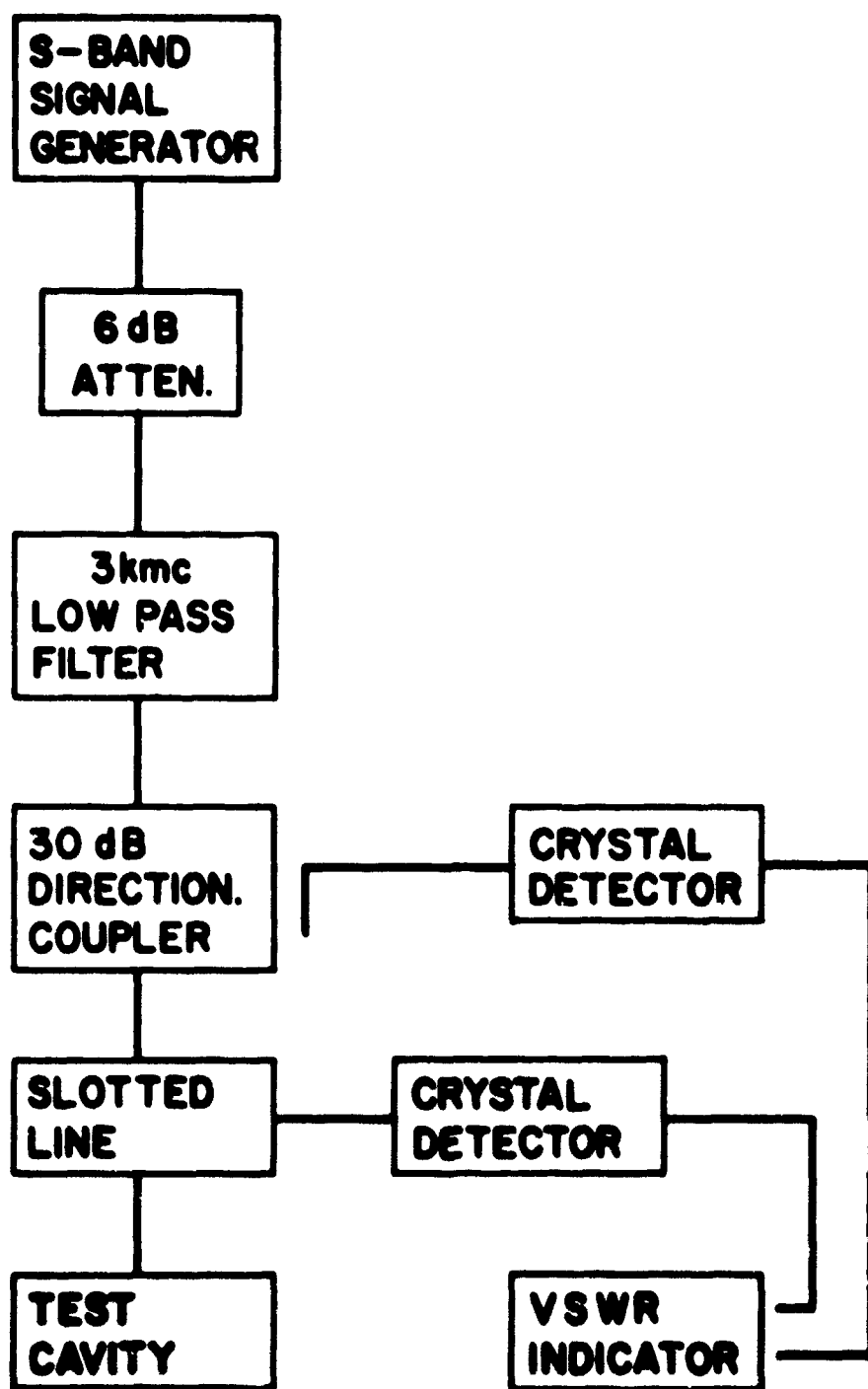


Figure 6.48: Block diagram of "Q" measurement for dielectric loss data at ceramic-to-metal seal interface.

The scatter of data on the same sample in the same test series (see Series 3, Table 6-18) was attributed to two facts. The unmodulated output of the signal generator showed some frequency modulation connected with the square wave modulation of the measuring signal. On account of this, the frequency measurement with the electronic counter was somewhat erratic in some cases as could be detected from the appearance of the resonance curves. The detrimental effect of frequency modulation in further work could be avoided by withdrawing a more attenuated signal from the source. The second cause for scatter in the loss data and for variations of the cavity resonance frequency with the sample reinserted was assumed to be the mounting of the sample between the two posts of the re-entrant cavity. The removable, inserted post carrying the pill-shaped sample had a shoulder to prevent the test sample from gliding to the side. But there was about 0.010 inch of play; that was the amount of disalignment by which the sample could be off center. Unfortunately, the location of the sample between the posts was very critical.

The results are given in terms of the quality,  $\frac{f_0}{\Delta f}$  (at 3 db down points) of the test cavity. A large value indicates low losses of the inserted test samples and vice versa.

With the low loss ceramics tested, the measured loss differences resulting from test disc thickness variations between 0.059 and 0.061 inch were not significant compared with the metallizing introduced losses. The data therefore assumes a constant sample thickness of 0.060 inch. In almost every case, two identical samples were measured and the Q averaged. Reductions in Q of less than 10% for the averaged samples are of questionable significance as disclosed by retesting of the same sample over a period of time (days), and by testing identically treated samples.

A more rigorous "control" system was instituted in the second series of test runs. All samples, raw and metallized, were given simultaneous cleaning and firing procedures, including the 1425°C metallizing sinter fire. It was noted that the results obtained in the second series of tests showed higher cavity Q's and greater reduction in Q on metallizing than the first test series. The Q shift was greater than the 10% considered significant. Day-to-day correlation by retesting of identical samples during the second test period still indicated 10% as significant, however.

It was concluded that the second series results are more accurate.

A typical plot of data for the first test series and a Q calculation is shown in Fig. 6.49.

#### 6.4.3 Experimental Procedure and Results

##### 6.4.3.1 Series 1

Specimens of Body A and Body H with P-1 and P-2 metallizing were tested. In addition, specimens of Body H were painted with the non-metallic phase of P-3 consisting of  $MnO_2$ ,  $TiO_2$  and  $SiO_2$  (P-3g). The dielectric loss test specimens were not plated or brazed after metallizing since the loss mechanisms being evaluated in this test are not concerned with the metallic portions of the seal. Data from the tests on these specimens are given in Tables 6-14 and 6-15. Most tests were on 0.060 inch thick discs. Raw ceramics of 0.050, 0.060, and 0.070 inch were also tested and four tests made on stacks of two 0.030 inch specimens.

The data taken on different days was not always consistent. The cause for this has not been resolved but is possibly due to wide humidity variations. To compensate for this the data has been adjusted to numbers relative to the raw ceramics indicated as Standards #1 and #2 which were run with each group of tests. Adjustments of 10 to 20% were required, though in most cases this is still less than the differences noted between the test variables. Sample #26 gave anomalous readings, but see section 6.4.4.4.1.

Unless noted, the specimens were sintered at  $1425^{\circ}C$  for 1/2 hour. Certain specimens, noted, were rerun through the same procedure to further diffuse the non-metallic phase of the metallizing into the ceramic substrate. The number of additional sintering runs is indicated.

##### 6.4.3.2 Series 2

The previous tests showed that with the 94%  $Al_2O_3$  ceramics the additional losses in the test piece resulting from metallizing are scarcely detectable. The samples prepared in this series therefore utilized the lower loss Body H (99.5%  $Al_2O_3$ ), single crystal sapphire (Linde), and the special #992 ( $1750^{\circ}C$ ) body prepared expressly for this program.



TABLE 6-14

Series 1, Dielectric Loss Data on Body A (94% Al<sub>2</sub>O<sub>3</sub>)

As Received and When Painted

with Noted Metallizing

Sample No.	Ceramic Thickness (in. 001 in.)	Metallizing & Thickness* (mil)	Adjusted Measured Cavity Q	Remarks
19	50.0	bare	1533	Standard #1
23	61.3	bare	1389	
27	70.5	bare	1268	
22	71.5	bare	1311	
13	61.2	.84 of P-1	1385	{ 2 surfaces painted; 2 1/2 hours at 1425°C
15	61.0	.90 of P-1	1401	
16	61.1	.90 of P-1	1381	
11	61.1	.92 of P-1	1312	
10	61.0	.98 of P-1	1408	
14	61.1	1.22 of P-1	1326	
9-10	30.9 - 30.9	1.04 - 1.02	1243	
X-X	30.? - 30.?	? - ?	1098	
12	60.9	1.46 "	1128	
24	61.1	.84 of P-2	1052	
30	60.9	.95 of P-2	1177	Anamolous data
28	61.3	.98 of P-2	1280	
26	61.6	1.00 of P-2	(758)	
27	61.0	1.02 of P-2	1240	
29	61.2	1.14 of P-2	1270	

\*From Calibration Curve #5, 3rd Quarterly Report, Figure 13.

TABLE 6-15

Series 1, Dielectric Loss Data on Body H (99.5% Al<sub>2</sub>O<sub>3</sub>)

As Received and when Coated

with Noted Metallizing

Sample No.	Ceramic Thickness (in. 001 in.)	Metallizing & Thickness* (mil)	Adjusted Measured Cavity Q	Remarks
48	50.5	bare	2210	
49	50.6	bare	1912	
37	59.8	bare	2196	Standard #2
38	59.9	bare	2100	
37-38	31.0-30.4	bare	2063	2 pieces
51	70.9	bare	1726	
34	61.6	.42 of P-1	1100	
33	61.1	.52 of P-1	1115	
33-34	30.7-31.6	.52 - .54	868	2 surfaces painted
40	59.9	1.10 of P-2	1732	
39	60.6	1.16 of P-2	2094	
44	61.3	.08 of P-3(g)	1560-863	2nd set of numbers
43	61.0	.16 of P-3(g)	1570-1082	after additional
35	60.6	.18 of P-3(g)	1398-998	1 1/2 hrs. at
36	60.7	.62 of P-3(g)	1135-	1425°C

\*From Calibration Curve #5, 3rd Quarterly Report, Figure 13.

The test pieces were metallized with P-1, P-2 and P-7. The unfired weight of the applied metallizing was recorded in each case. Sintering was at 1425°C for 1/2 hour with the exceptions noted below.

The P-1 and P-7 metallizing paints on the #992 (1750) body were given additional firings up to 8 hours total time at 1425°C. Raw ceramic control samples were run with each lot and firing sequence.

Table 6-16 lists the data collected with Body H and sapphire samples. Table 6-17 lists the data collected with the 992 (1750) samples.

The measured cavity Q's tended to be higher during these measurements than those taken during the previous series. Lower atmospheric humidity during this test period may account for the shift. Since the  $\Delta Q$  of bare versus metallized ceramic is used for interpretation in most cases, the variation of Q is not a reason for concern.

A non-metallized Body H disc was used as a standard to check day-to-day shift in Q. The presented data were taken on two days only and the shift was from  $Q_0 = 2430$  to  $Q_0 = 2498$ , or 2.75%, which is well below the  $\Delta Q$  of 10%, which is considered as significant.

Two samples of each variable were measured. Correlation between samples was usually satisfactory. The amount of blush up the sides of the 0.200" diameter by 0.060" thick disc is relatively uncontrollable and is the most probable cause for those discrepancies of up to 25%  $\Delta Q$  which did occur.



TABLE 6-16

Series 2, Dielectric Loss Data at 2 Gc on Body H (99.5 Al<sub>2</sub>O<sub>3</sub>)  
 and Sapphire with Noted Metallizing,  
 Sintered 1/2 Hour at 1425°C, No Plating.  
 Ceramic Discs Nominally 0.060 In. Thick

Sample No.	Ceramic	Metallizing	Wt. of Metallizing* (mg.)	Measured Q
1	Body H	P-1	2.8	802**
2	"	"	3.5	872
3	"	P-2	6.7	1795
4	"	"	6.3	2045
5	"	P-7	5.6	1695
6	"	"	5.4	1520
7	"	none	-	2430
8	"	"	-	2310
45	Sapphire	P-1	3.2	2130
46	(Linde)	"	3.4	2010
47	"	P-2	6.9	2265
48	"	"	4.0	2115
49	"	P-7	5.2	2104
50	"	"	5.0	2240
51	"	none	-	2975
52	"	"	-	2980

\*Actual weight on 0.200" diameter disc.

\*\*Average of 797 and 810.

TABLE 6-17

Dielectric Loss Data at 2 Gc on Body 992 (1750)

with Noted Metallizing.

Sintering Time at 1425°C Noted. No Plating.

Ceramic Discs Nominally 0.060" Thick

Sample No.	Metallizing	Wt. of Metallizing* (mg)	Sintering Time	Measured Q
17	none	-	1/2 hr.	2560
18	"	-	1/2	2675
25	"	-	1	2590
43	"	-	8	2085
44	"	-	8	2585
11	P-1	3.4	1/2	1747
12	"	2.0	1/2	1339**
21	"	3.7	1	1470
22	"	1.9	1	1261
27	"	2.9	2	767
28	"	3.9	2	732
40	"	2.6	8	633
13	P-2	5.1	1/2	2118
14	"	6.2	1/2	1831
15	P-7	12.6	1/2	1970
16	"	10.0	1/2	1612***
23	"	7.7	1	1962
24	"	10.1	1	1982
41	"	4.8	3	2137
42	"	6.4	3	1660****

\*Actual wt. on 0.200 diameter disc.

\*\*Average of 1320 and 1358.

\*\*\*Average of 1558 and 1670.

\*\*\*\*Average of 1667 and 1653.

#### 6.4.3.3 Series 3

Table 6-18 shows the results obtained on the samples tested in this series. These were measured over a four-day period with a number of repetitions in order to check the reproducibility of the data.

#### 6.4.4 Discussion

The losses measured in this test as discussed previously, section 6.4.1, are created largely by displacement currents. The losses in the entire ceramic, both in the portion affected by the metallizing and the unaffected portion, combine to lower the Q of the test cavity.

Whereas the results were presented in three series the discussion is given a different but more systematic treatment. First the ceramic alone is considered, both raw and modified by the non-metallic phase of a metallizing paint. Then the losses induced purely by a pure metallic layer on the ceramic are considered. An attempt is made to segregate the metallic portion of a conventional metallizing from the metallized ceramic by leaching with nitric acid. The remaining altered ceramic is then subjected to various treatments and the Q of the ceramic measured. This is followed by a consideration of the above phenomena in several metallizing paints and body compositions.

##### 6.4.4.1 Ceramic Losses

Figs. 6.50 and 6.51 show the dielectric loss factor of various bodies used in this study versus frequency and alumina content respectively. The relative lowering of the cavity Q with different disc thicknesses of Body A 94% alumina and Body H 99.5% alumina are shown in Fig. 6.52.

The increase in loss as a function of cavity Q using manufacturers loss data for Body A, Body H and Linde sapphire is determined in Fig. 6.53. From this plot, the loss of other ceramic bodies either raw or metallized can be determined. For instance the dielectric loss of 992-1750 is determined as  $6 \times 10^{-4}$  at 2 Gc. The loss of altered ceramics shown on this graph is discussed later.

The three points given for Body H represent the spread in the experimental values of Q obtained in the three series of experiments. This spread has been discussed previously. The results follow the expected trends and so will not be discussed further.

TABLE 6-18

Series 3, Dielectric Loss Data at 2 Gc on Body H Test Samples  
with Noted Metallizing and Subsequent Treatment

Sample	Paint and Thickness (mil)	Remarks	Measured Q
76	P-1 0.8	Leached	1050, 980, 1020, 1040
76S	P-1 0.6	Leached & sanded once with SiC	700
77	P-1 0.5	No treatment	1350, 1200
78	P-1 1.9	Leached	1010, 1100, 1510, 960
78S <sub>1</sub>	P-1 1.9	Leached & sanded once with Al <sub>2</sub> O <sub>3</sub>	1200
78S <sub>2</sub>	P-1 1.9	Leached & sanded twice with Al <sub>2</sub> O <sub>3</sub>	1150
79A	P-1 1.9	Leached	860, 940, 920
79AS	P-1 1.9	Leached & sanded once with Al <sub>2</sub> O <sub>3</sub>	1370
80A	P-1 1.5	No treatment	1180, 1170
81A	P-1 1.6	No treatment	1150
82A	P-1 1.7	Leached	970
83	P-2 0.5	No treatment	1800
84	P-2 0.5	No treatment	1940
87	Cu evaporated, 1 mil Cu plate	No treatment	2390
88	Cu evaporated, 1 mil Cu plate	No treatment	2170
90	P-2M 1.4	No treatment	2030
92	Standard, blank ceramic	Leached	2460, 2530, 2500
93	Standard, blank ceramic	No treatment	2570, 2560, 2200, 2090, 1870
94	Standard, blank ceramic	No treatment	2330
95	Ti (500 Å) - Mo-Cu evaporated, Cu plate		2100, 1660, 2800
96	Ti (500 Å) - Mo evaporated Cu plate	(Oxidized)	1290

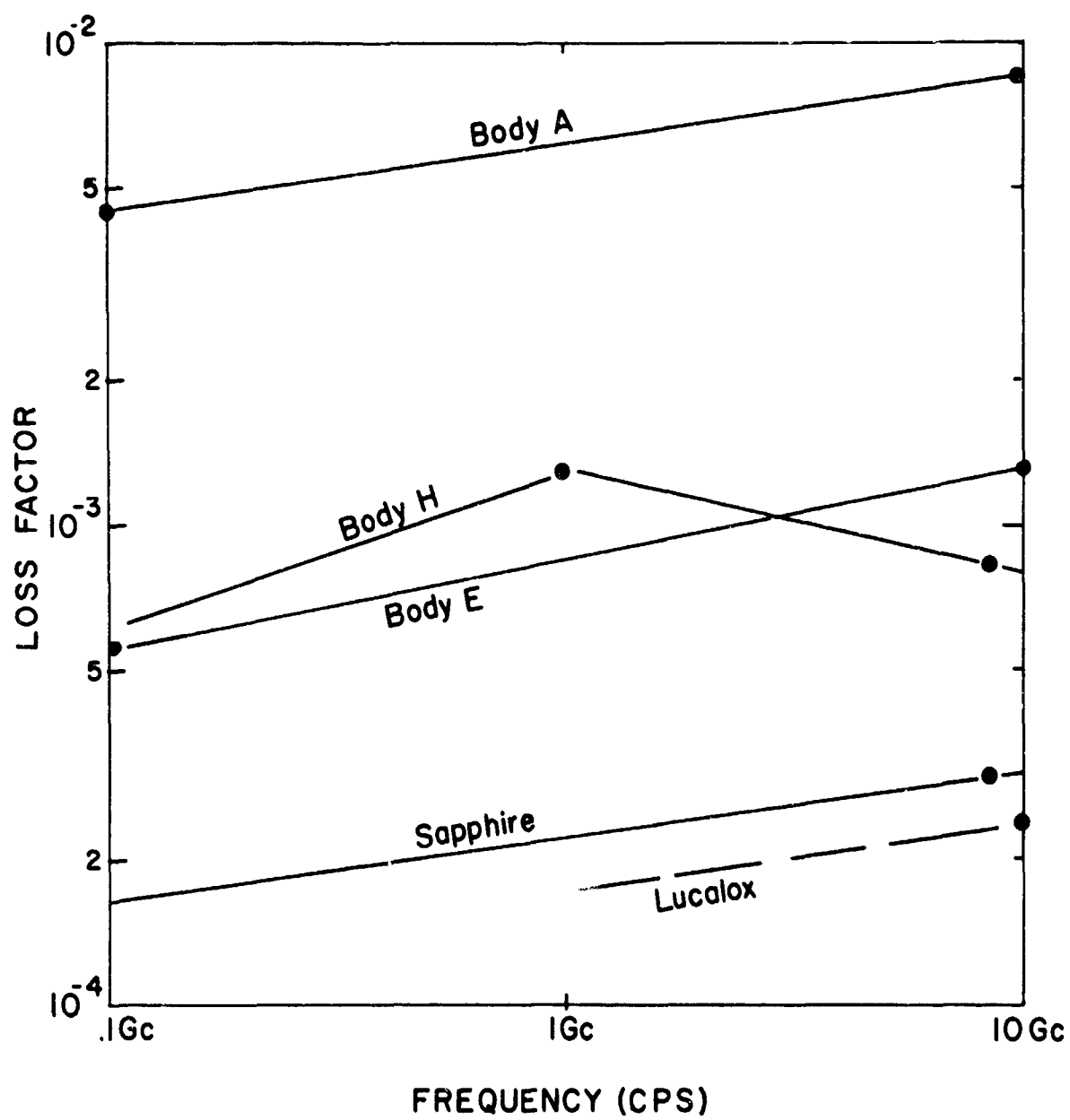


Figure 6.50: Dielectric loss factor for selected ceramic bodies versus frequency. Values are from manufacturers' data sheets.

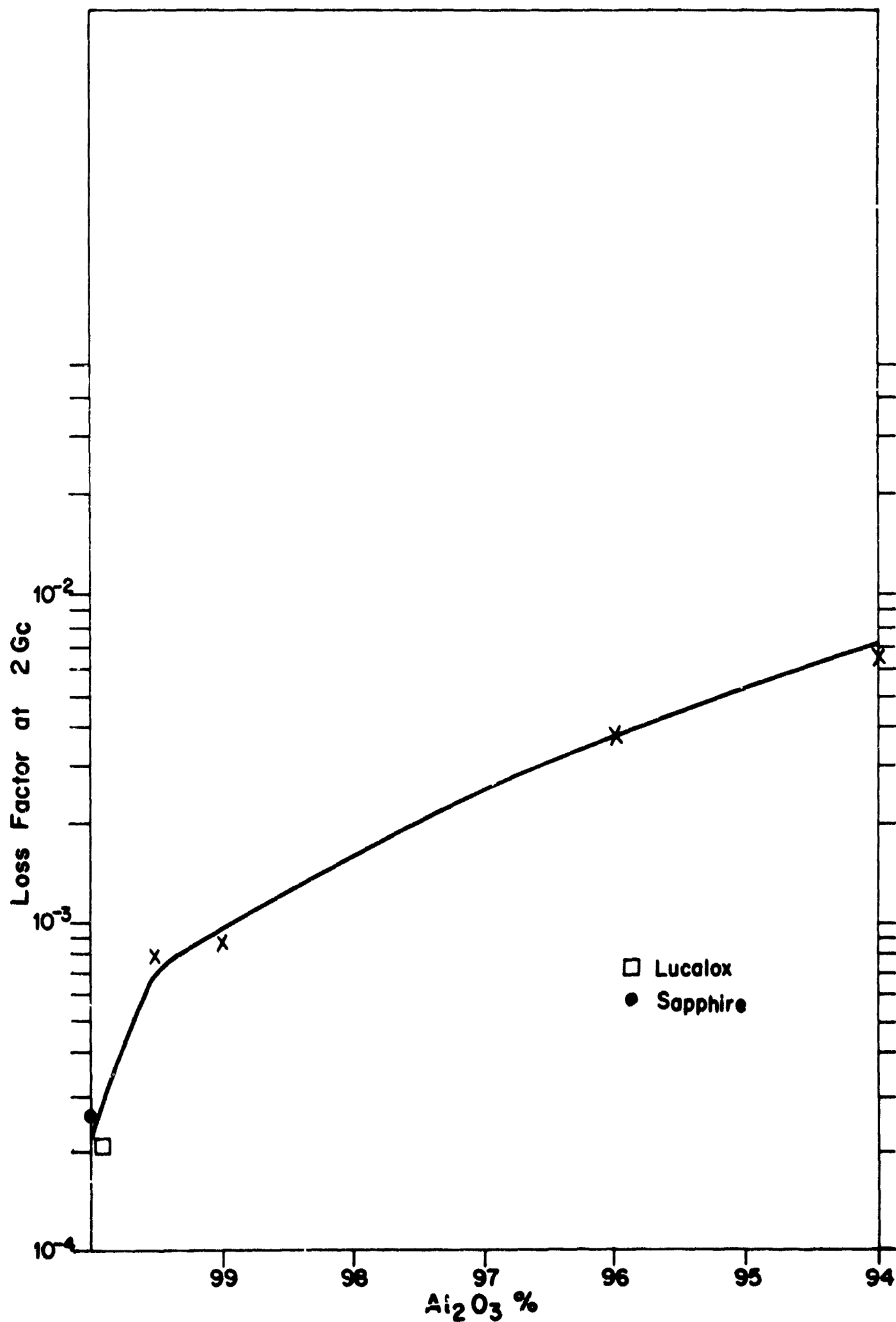


Figure 6.51: Dielectric loss for alumina bodies versus frequency.

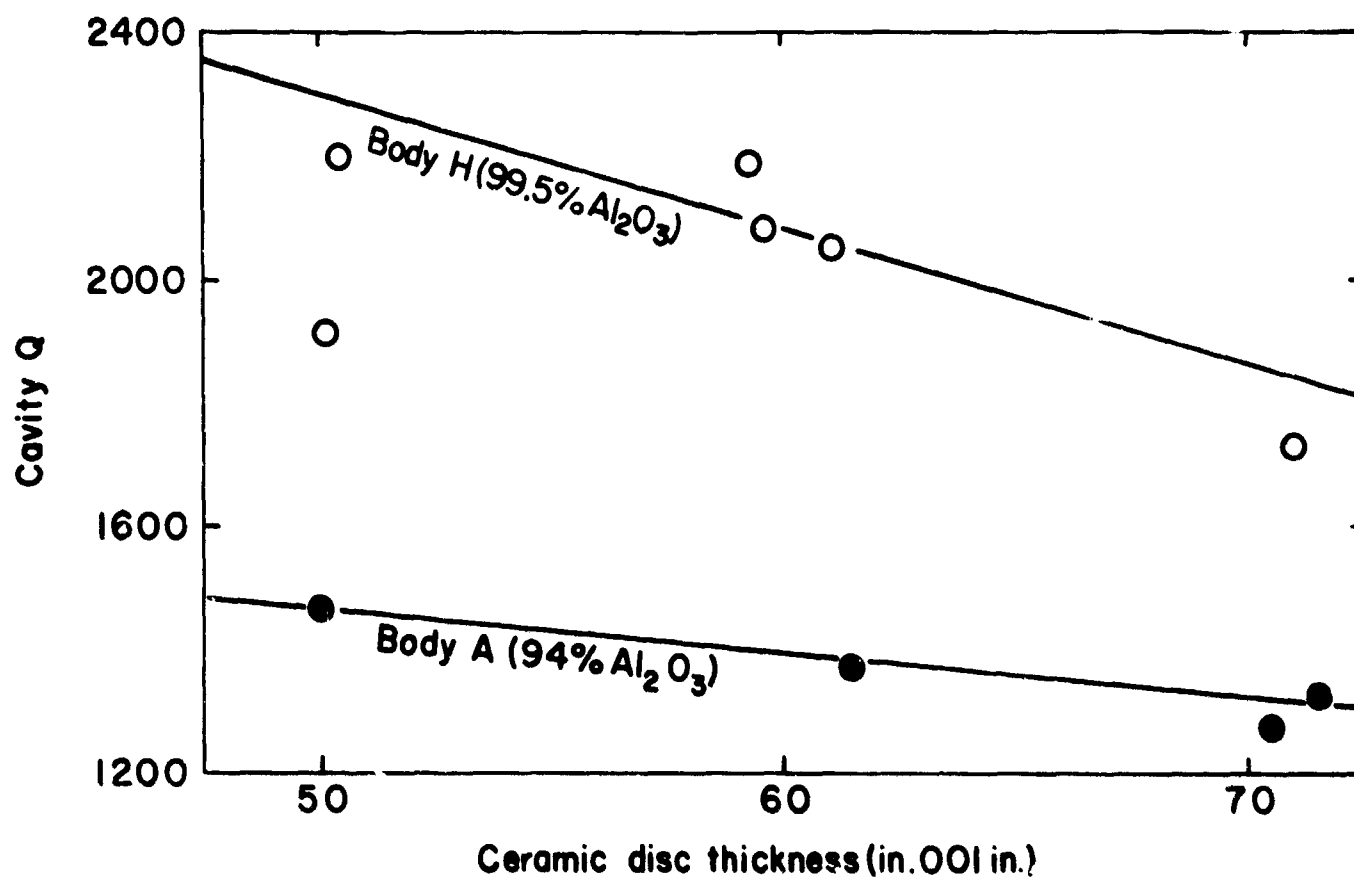


Figure 6.52: The dielectric test cavity Q as a function of ceramic disc thickness.

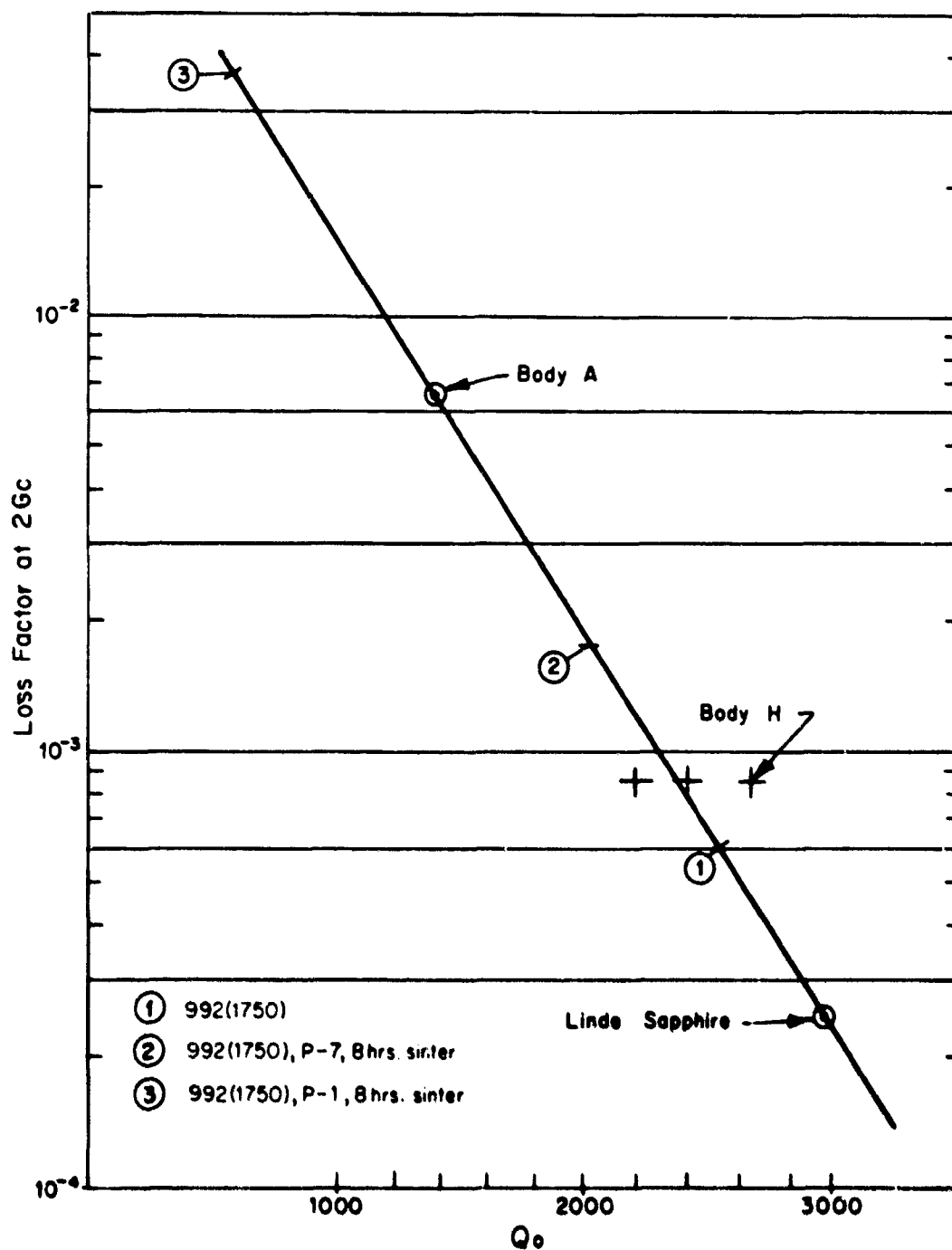


Figure 6.53: Loss factor at 2 Gc versus dielectric loss test cavity  $Q_0$  plotted from manufacturers loss figures and test data on Body A, Body H and Linde Sapphire. The line is drawn through the values obtained during the second test series. The  $Q_0$  intercepts of three selected data points are indicated for reference only (see text).



#### 6.4.4.2 Altered Ceramic Losses

It was important early in the program to establish the relative magnitude of dielectric loss introduced by a non-metallic portion of a commercial paint in order to determine if the experiment was a sufficiently sensitive tool to perform the task at hand. Accordingly, P-3(g),  $\text{MnO-TiO}_2\text{-SiO}_2$ , was painted on a raw ceramic disc. The results are given in Table 6-19. It can be seen that a significant drop in cavity Q occurred both as a function of amount of P-3g reacted and with the time of reaction. The first result is self evident. The second result is ascribed to the P-3(g) melt partially remaining on the surface of the ceramic during the first 1/2 hour fire period, and continuing to diffuse into the grain boundaries of the ceramic and to react with the alumina phase of the ceramic. Thus the amount of melt phase increases as a function of time and produces additional loss.

The relative consistency of the Q value after two hours at 1425°C indicates that the reaction initially is diffusion limited but is subsequently amount, limited.

It should be mentioned that a reduction in cavity Q would also occur if a glassy phase approximating the composition of the grain boundary phase of the ceramic,  $\text{MgO-CaO-SiO}_2\text{-Al}_2\text{O}_3$ , were painted on. This is apparent from Figs. 6.51 and 6.53. It is therefore of interest to determine what additional drop in Q or loss factor is due to a "lossy" glass phase, such as  $\text{MnO-TiO}_2\text{-SiO}_2$  being introduced into the ceramic.

One milligram of P-3g applied to the 99.5% ceramic disc (120 milligrams) is approximately 1% of the weight of the body but the composite unreacted or partially reacted (1/2 hour at temperature) body will behave more like a 99% alumina body. After extensive reaction (2 hours) it will then behave more nearly like a 98.5% alumina body as additional alumina will have entered the melt grain boundary phase. This would also be true of the latter paint ( $\text{MgO-CaO-SiO}_2\text{-Al}_2\text{O}_3$ ) if the  $\text{Al}_2\text{O}_3$  were omitted.

The three cases under consideration are outlined in Table 6-19.

TABLE 6-19

Dielectric Loss Increase in Body H (99.5%  $\text{Al}_2\text{O}_3$ )  
Resulting from Application of P-3(g),  $\text{SiO}_2$ ,  $\text{TiO}_2$ ,  $\text{MnO}_2$  Glass, to One Surface\*

	Total Alumina Content	Crystalline Alumina Content**	Equivalent Ceramic Body***	Measured Q	Type I**		Type II***	
					Dielectric Loss Factor	Dielectric Loss Factor	Dielectric Loss Factor	Dielectric Loss Factor
<u>Case #1</u> Raw 99.5% $\text{Al}_2\text{O}_3$ disc (29.4 mg)	99.5%	99%	99.5%	2150-2400	$8.5 \times 10^{-4}$			
<u>Case #2</u> Disc with 1 mg of glass on surface	98.5%	98.5%	99%	1416	$9 \times 10^{-4}$		$5 \times 10^{-3}$	
<u>Case #3</u> Disc with glass totally diffused in	98.5%	97.0%	98.5%	981	$1.5 \times 10^{-3}$		$1.5 \times 10^{-2}$	

\*Case 2 and 3 are approximated by 1/2 and 2 hours of sintering respectively.  
Q is not a linear function of loss.

\*\*Assuming 1 part of  $\text{Al}_2\text{O}_3$  in solution with each part of glassy phase in the ceramic body (this is a minimum with the system under consideration). In Case #2 the glass is still on the surface only.

\*\*\*See text.

The loss factor of the equivalent ceramic body with added  $\text{CaO-MgO-SiO}_2\text{-Al}_2\text{O}_3$  phase is given in Type I. This is obtained directly from Fig. 6.51. The corresponding losses induced by the  $\text{MnO-TiO}_2\text{-SiO}_2$  phase is given as Type II. This is obtained by taking the measured Q's of the discs and determining the loss factor from Fig. 6.53.

It can be seen that the loss factor of the body is significantly increased over that of an equivalent  $\text{MgO-CaO-SiO}_2\text{-Al}_2\text{O}_3$  body of similar alumina content. The loss factor is equivalent to that of a 94% and 90% body for the reaction times of 1/2 hour and 2 hours respectively.

#### 6.4.4.3 Pure Metallic Layer on Ceramic

Table 6-18 gives the losses induced using evaporated copper metallizing (Fig. 6.54) or Ti-Mo-Cu evaporated metallizing on the ceramic. Although the losses tend to increase over that of the raw ceramic, the increase is not considered significant. The contribution of any  $\text{Cu}_2\text{O}$  or  $\text{TiO}_x$  formed to increase the dielectric loss is negligible because of the small volume involved. This may not be so for the conduction loss case previously considered. When the copper plate is oxidized, #96, the contribution of the  $\text{CuO}$  formed is then significant:

These latter results, #95, #96 also indicate that  $I^2R$  losses are negligible in the present situation.

#### 6.4.4.4 Conventional Metallizings on Body A and Body H

Having obtained a "feel" for the physical chemistry of the loss process, it is desirable to consider the effects of metallizing a 94% and 99.5% body with conventional metallizing paints. A typical series of results (Series I) is presented in Figs. 6.55 and 6.56. The following sections consider all three series.

##### 6.4.4.4.1 Pure Metallizing Paint P-2

Continuing the sequence of discussing systems of increasing complexity let us consider a pure molybdenum paint, P-2. As P-2 was ground in an alumina ball mill it picked up 1% of  $\text{CaO-MgO-SiO}_2\text{-Al}_2\text{O}_3$ . The same paint, P-2M, was also prepared in a molybdenum mill ground with molybdenum balls.

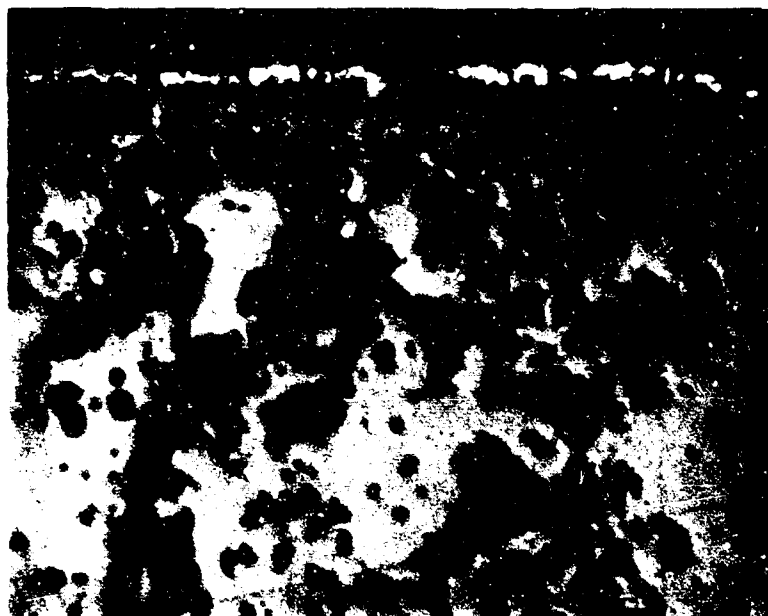


Figure 6.54: Photomicrograph of Body H test sample (400X) #95 (500 Å Ti, 5,000 Å Mo evaporated, Cu plated to 0.17 mil)

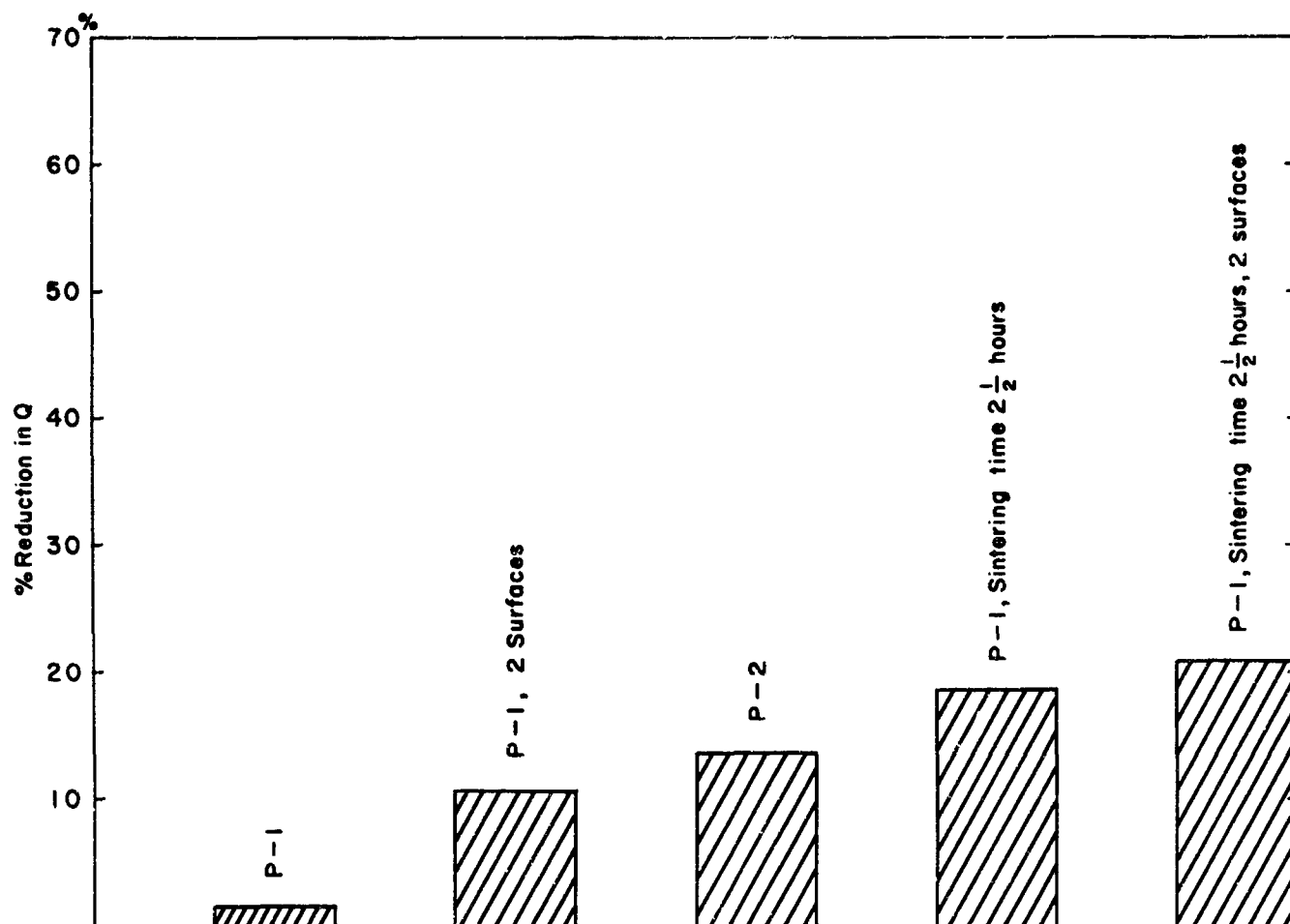


Figure 6.55: Reduction in cavity Q resulting from noted metallizing paint only on 0.060" thick Body A ceramic discs. Test frequency 2 Gc. Sintering time 1/2 hour at 1425°C unless noted. Single surface metallized unless noted.

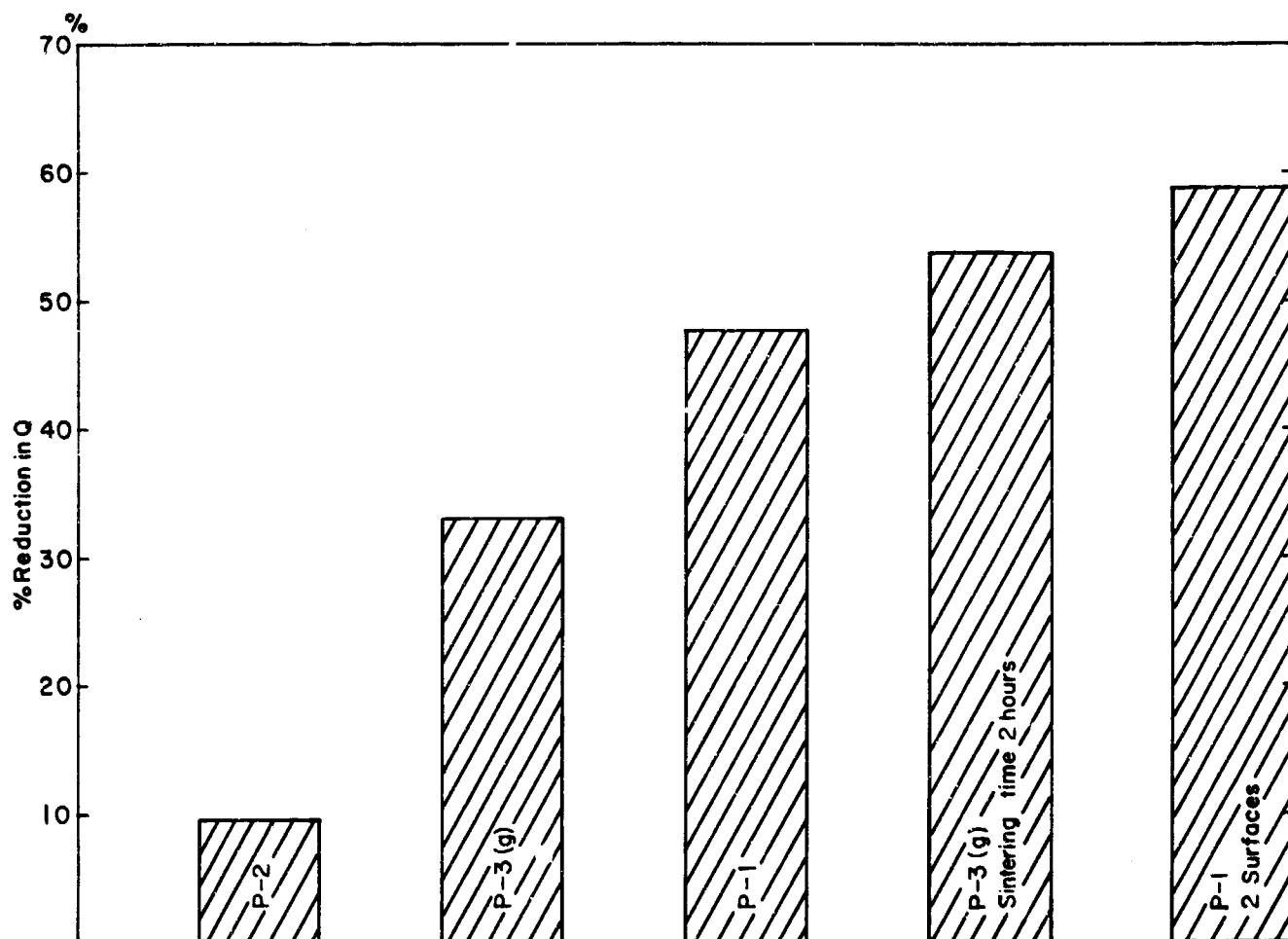


Figure 6.56: Reduction in cavity Q resulting from noted metallizing paint only on 0.060" thick Body H ceramics 99.5%  $\text{Al}_2\text{O}_3$ . Test frequency 2 Gc. Sintering time  $\frac{1}{2}$  hour at 1425°C unless noted. Single surface metallized unless noted.

The two paint batches showed no significant variation in Q. (Table 6-18, #83, #84, #90.) For our purposes, therefore, P-2 may be considered as a pure molybdenum metallizing paint. Any loss introduced into a system using this paint must therefore be due to some change induced into the system by processing, as it has been shown above that a molybdenum layer evaporated onto the surface does not induce additional loss. The specimens considered in all three series #39, #40; #1, #2; #83, #84, #90 gave lower Q values by  $15 \pm 5\%$  than the Body H raw ceramic indicating that some change in the chemistry of the system was occurring.

The change noted with the 99.5% alumina was also noted with the P-2 metallizing paint sintered onto Body A, the 94% alumina body. Again giving 12% lower Q values than the raw ceramic, the absolute Q values naturally being very much lower.

The dc conductivity measurements described earlier had also shown a lowering of the temperature coefficient of resistance for P-4M metallizing (similar to P-2) as compared to evaporated metallizings. It is apparent therefore that the glass or glass-metal interface has induced in it a semi-conducting and/or lossy material. X-ray diffraction analysis of the glassy phase of the P-2 metallizing on Body A showed anorthite formation. This condition has been shown to introduce a high dielectric loss<sup>5</sup> into a ceramic over a ceramic containing only the undevitrified glassy phase.

The same situation must hold for Body H also. The amount of anorthite present is too small to be detected by X-ray diffraction, however.

The anomalous low Q data noted in Table 6-14 can be explained on the basis of more extensive anorthite formation.

#### 6.4.4.4.2 Complex Metallizing Paint P-1

Considerable loss would be expected to be introduced into a ceramic body by the MnO and TiO<sub>x</sub> components of the metallizing paint. The dc coefficient of resistivity results, section 6.2, showed that the reacted layer behaved as a semiconductor, consequently considerable dielectric loss would be expected to occur in this layer. Because of the difference in the amount of glass phase present, Body H will

have a grain boundary phase much richer in MnO and  $\text{TiO}_x$  than will Body A. This, coupled with the fact that the initial Q of the cavity with Body H is much higher, will result in a much higher attenuation for the P-1 Body H system.

A lowering in cavity Q of  $53 \pm 5\%$  is noted in the three series (Tables 6-15, 6-17 and 6-18) for Body H. The experiment was not sufficiently sensitive to detect significant differences in loss as a function of the amount of paint originally sintered on.

A silica rich  $\text{SiO}_2 - (\text{MnO}_2 - \text{TiO}_2) - \text{CaO} - \text{MgO} - \text{Al}_2\text{O}_3$  system, P-3g on Body H, is less lossy than P-1 on Body H (Tables 6-15, 6-19) despite the five-fold concentration of the non-metallic phase. This result demonstrates the modifying effect of a silicate addition on the loss by removing the lossy MnO,  $\text{TiO}_x$  phase present in the (P-1) - Body H system. The MnO,  $\text{Al}_2\text{O}_3$  phase is retained however. The loss of the resulting glass phase will be heavily dependent on the oxidation state of the titanium ion in this phase. Within the limits of normal metallizing cycles this is determined primarily by the time and temperature allowed for diffusion and only secondly by the amount initially present, as has been shown above. The amount of surface painted (i.e. painting both sides of a disc) will affect the loss, however, because the volume of diffused material will alter.

The system P-1 on Body A displayed no significant loss. In order to demonstrate that an increase in loss was occurring it was necessary to paint both surfaces with P-1 metallizing and/or increase the sintering time for 2-1/2 hours in order to diffuse the MnO and  $\text{TiO}_2$  further into the ceramic. (The microprobe data in Table 4-51 indicated that the bulk of the MnO and  $\text{TiO}_2$  only diffuses 15 mils into the ceramic in a 1/2 hour sintering at  $1425^\circ\text{C}$ .)

These latter results might have been predicted from the results reported earlier in this section. The dilution of the MnO,  $\text{TiO}_2$  components of P-1 by 14% of grain boundary silicate phase is a more extreme case than that noted previously.

This dilution effect coupled with a very low Q for the raw ceramic Body A indicates that dielectric loss reduction in metallizing systems utilizing 94% alumina ceramics is not feasible as the losses introduced by the metallizing components are of the same order as those originally present in the ceramic.



#### 6.4.4.4.3 Leached P-1 Metallizing on Body H

The dielectric losses of the raw ceramic and the separate constituents of the metallizing have been investigated. It remained to be shown that the conduction losses in an actual sintered and reacted molybdenum layer or any "induced" effect on the non-metallic "glassy phase" was not significant under the electrical conditions prevailing for the "dielectric" experiment. This was accomplished by leaching out the molybdenum with 50% nitric acid. In some cases this was followed by sanding the layer with silicon carbide or alumina. Typical microstructures that resulted are shown in Figs. 6.57 and 6.58.

The results (Table 6-18) confirmed expectations. Losses were not reduced by the leaching process. Dielectric losses were progressively reduced by a continuing  $\text{Al}_2\text{O}_3$  sanding process, because the lossy dielectric was also progressively removed. It was noted that sanding with silicon carbide did increase losses. This is because of the "lossy" SiC particles which embedded themselves in the ceramic surface.

#### 6.4.5 Comparison of Various Metallizings on +99% Alumina Bodies

Having established the loss mechanisms in metallized ceramics, the studies were extended to additional low loss ceramics and employing the metallizings P-1 and P-2 noted above and also a low loss metallizing, P-7.

Body H is a 99.5% alumina having a 1:1  $\text{SiO}_2$ /alkaline earth ratio whereas 992 (1750) is a 2:1 99% alumina ceramic. Linde sapphire, of course, is 99.99% alumina with no crystal grain boundaries.

P-7 is low loss because of the  $\text{BaO-SiO}_2$  non-metallic component which reacts with the alumina phase to form a low loss glass.

In Fig. 6.59 photomicrographs of P-1 and P-7 metallizing sintered for 1/2 hour at  $1425^\circ\text{C}$  to Linde sapphire are shown. (The P-2 sample could not be polished because of numerous pull-outs in the metallizing.)

The reaction is obviously chemically controlled as denoted by the selective attack on the alumina crystal phase and can be seen to have progressed much faster with the  $\text{MnO-TiO}_x$  melt than with the  $\text{BaO-SiO}_2$  melt.

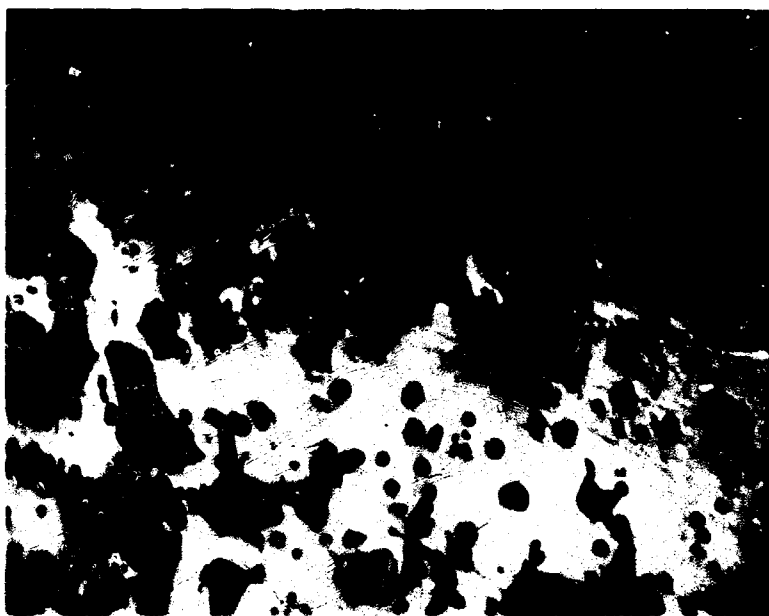


Figure 6.57: Photomicrographs of Body H test samples (400X). Top: #81A (1.6 mil of P-1 metallizing). Bottom: #82A (1.7 mil of P-1 metallizing, leached).

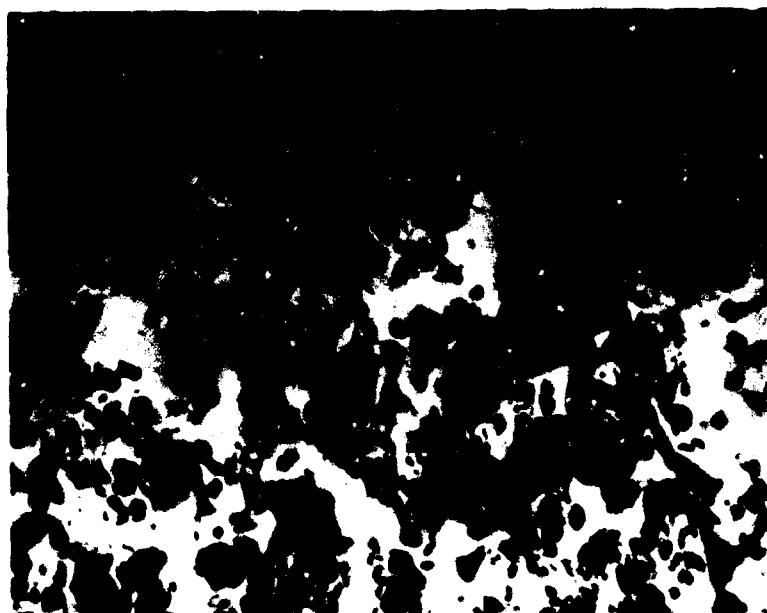


Figure 6.58: Photomicrograph of Body H test sample (400X) #78 S2 (0.5 mil of P-1 metallizing, leached and sanded off).

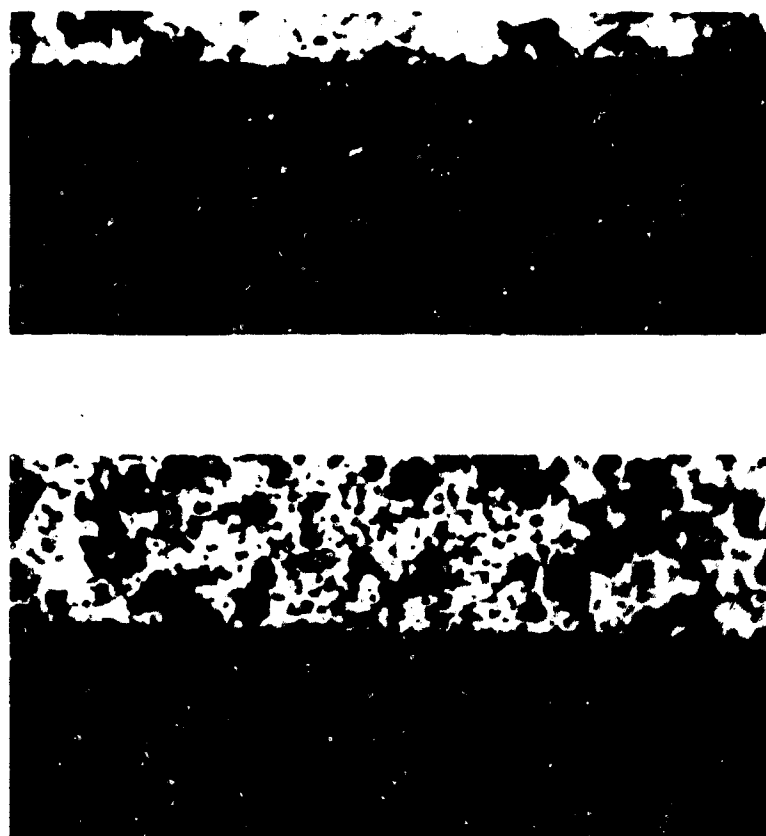


Figure 6.59: Photomicrographs of P-1 (top) and P-7 (bottom) on Linde sapphire. Dielectric loss samples sintered one-half hour at 1425°C (400X).

In the case of reaction of these paints with the 992 (1750) ceramic, increased grain boundary diffusion of the metallizing melt phase occurs as a function of time as shown in Fig. 6.60. Also increased chemical reaction occurs at the surface as a function of time as denoted by more pronounced etching (selective solution) of the alumina crystal phase and increase in the amount of the interfacial melt phase, Fig. 6.61.

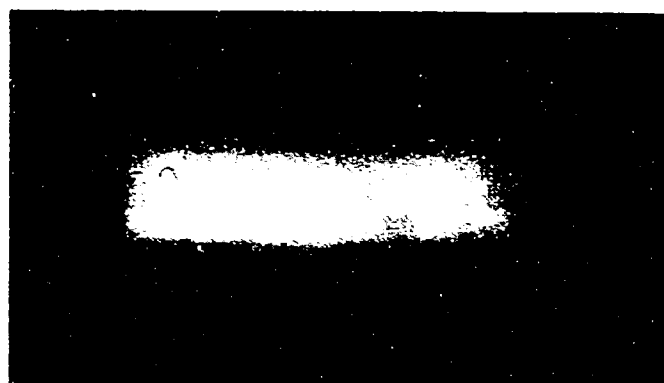
It may be noted that the extent of diffusion is a function of the composition of the grain boundary phase of the ceramic. In the case of sapphire the diffusion is zero. The grain boundary phase of Body H is much less viscous than 992 ceramic so that despite the fact that there is twice as much grain boundary phase in the 992 ceramic the diffusing distance of the melt ions of the metallizing paint can be expected to be much greater in Body H. (See section 5.0.)

The loss results for sapphire, Body H and 992 ceramic given in Tables 6-16 and 6-17 have been plotted in Fig. 6.62. For sapphire the "lossy" phase is confined to a narrow interfacial region, so the drop in Q is relatively small and constant.

The reduction in cavity Q with P-2 paint must be due in the case of sapphire to aluminum molybdate formation and to the 1% of  $\text{MgO-CaO-SiO}_2\text{-Al}_2\text{O}_3$  introduced during processing. Additional "glassy phase" has migrated into the metallizing in the case of 992 (1750) and Body H. Anorthite has been cited previously as the loss producing phase in the above instance.<sup>5</sup> Solution of molybdenum in the glassy phase may also result in a loss producing phase.

As expected, the losses introduced by the use of the P-7 paint is less than the P-1 paint in all three instances. The increase in loss with either P-1 or P-7 paint is directly related to the extent of metallizing melt phase migration into the grain boundaries of Body H or 992 (1750) ceramics.

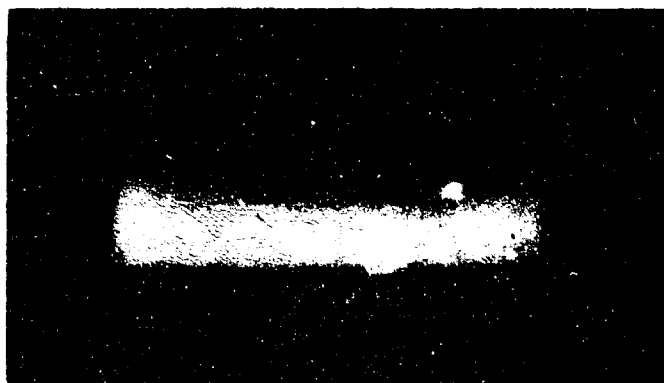
Further loss data pointing up the influence of melt phase migration on diffusion is shown in Fig. 6.63. It had previously been noted that with P-3g the loss increased in Body H with 2 hours diffusion over 1/2 hour diffusion. This situation was also found to hold true for the data reported in Tables 6-15 and 6-17 and plotted in Fig. 6.63. It thus appears that, although further diffusion is taking place after 2 hours (Figs. 6.60 and 6.61) an



½ HR.

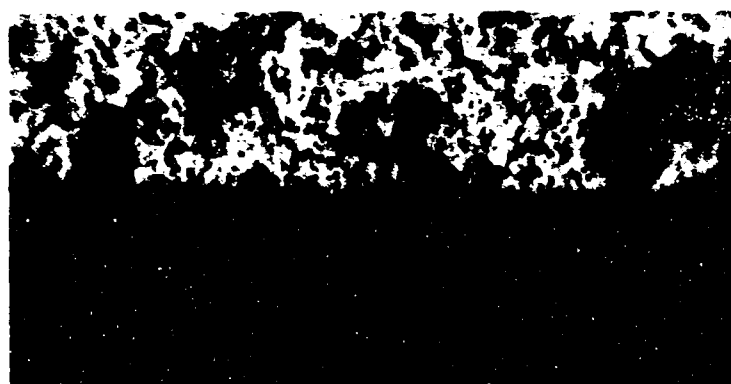


2 HR.

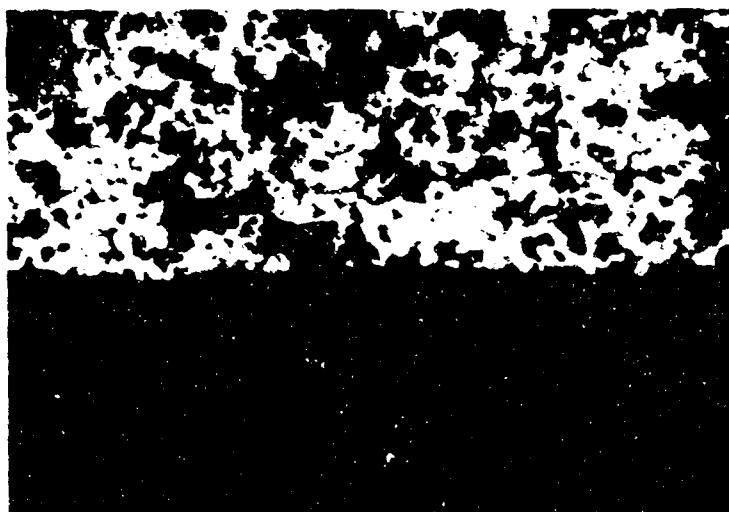


8 HR.

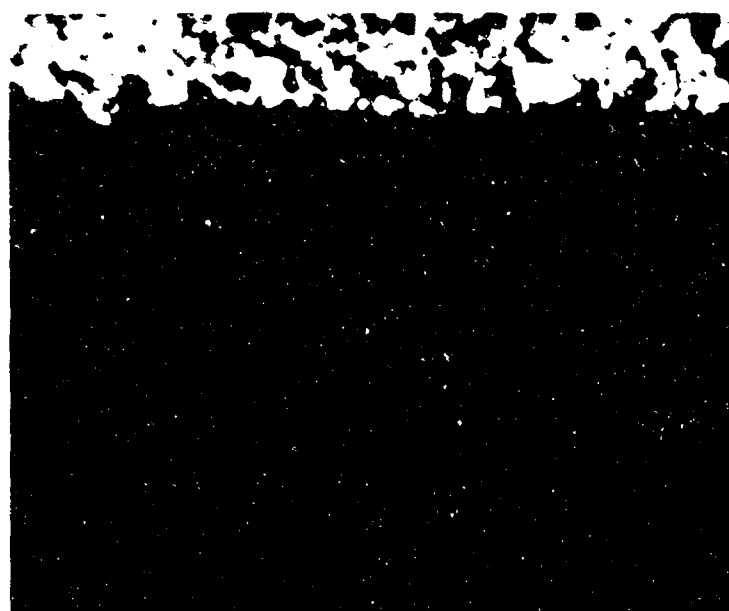
Figure 6.60: Photographs of sectioned dielectric loss specimens (0.200 in. wide by 0.060 in. thick) showing P-1 metallizing diffusion into Body 992 (1750) at 1425°C with increasing time (10X).



1/2 HR.



2 HR.



8 HR.

Figure 6.61: Photomicrographs of P-7 metallizing reaction with Body 992 (1750) at 1425°C for increasing times (400X).

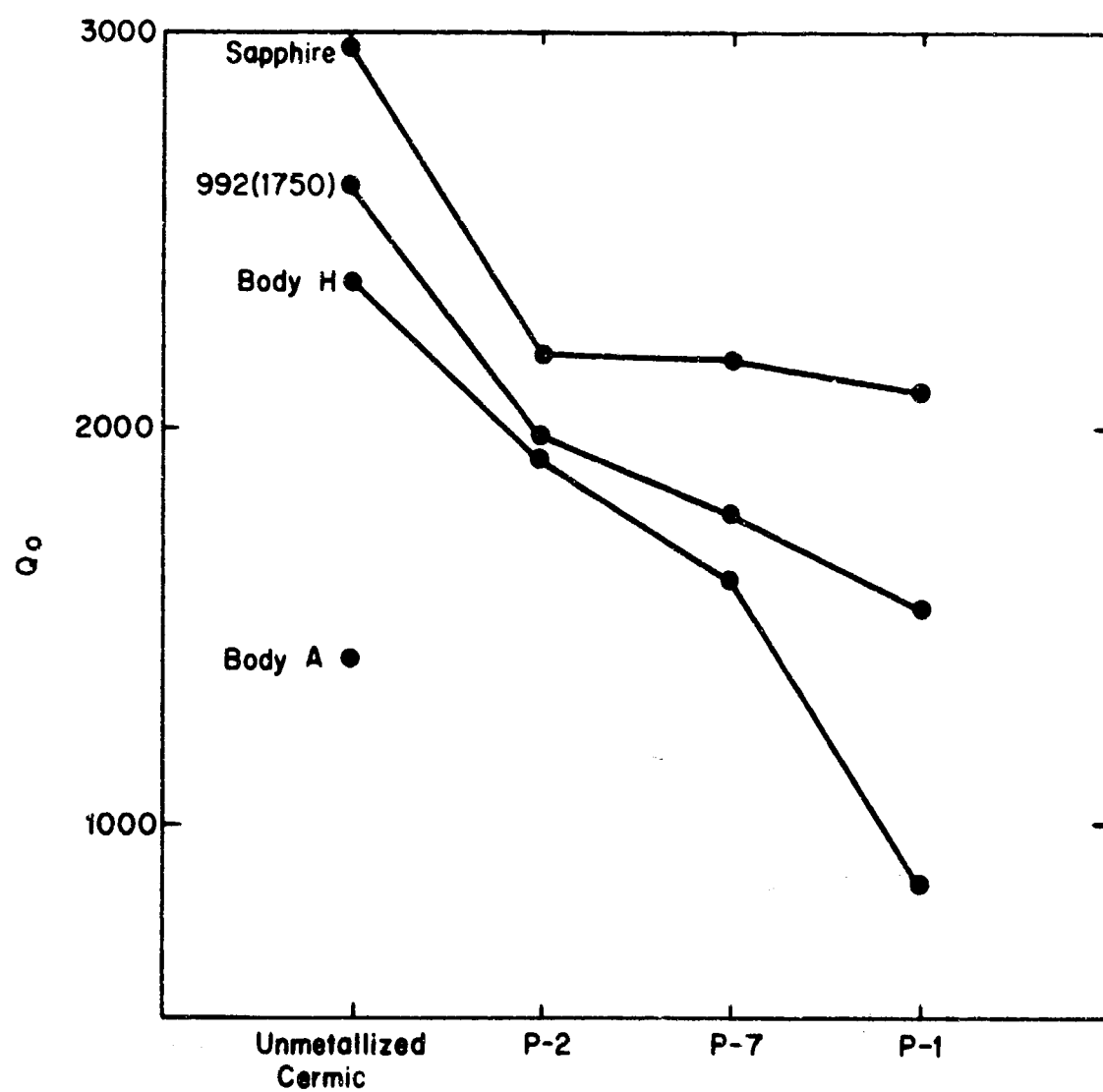


Figure 6.62: Dielectric loss test cavity  $Q_0$  with various ceramic samples in gap. The unmetallized and metallized samples were fired at  $1425^{\circ}\text{C}$  for  $\frac{1}{2}$  hour.



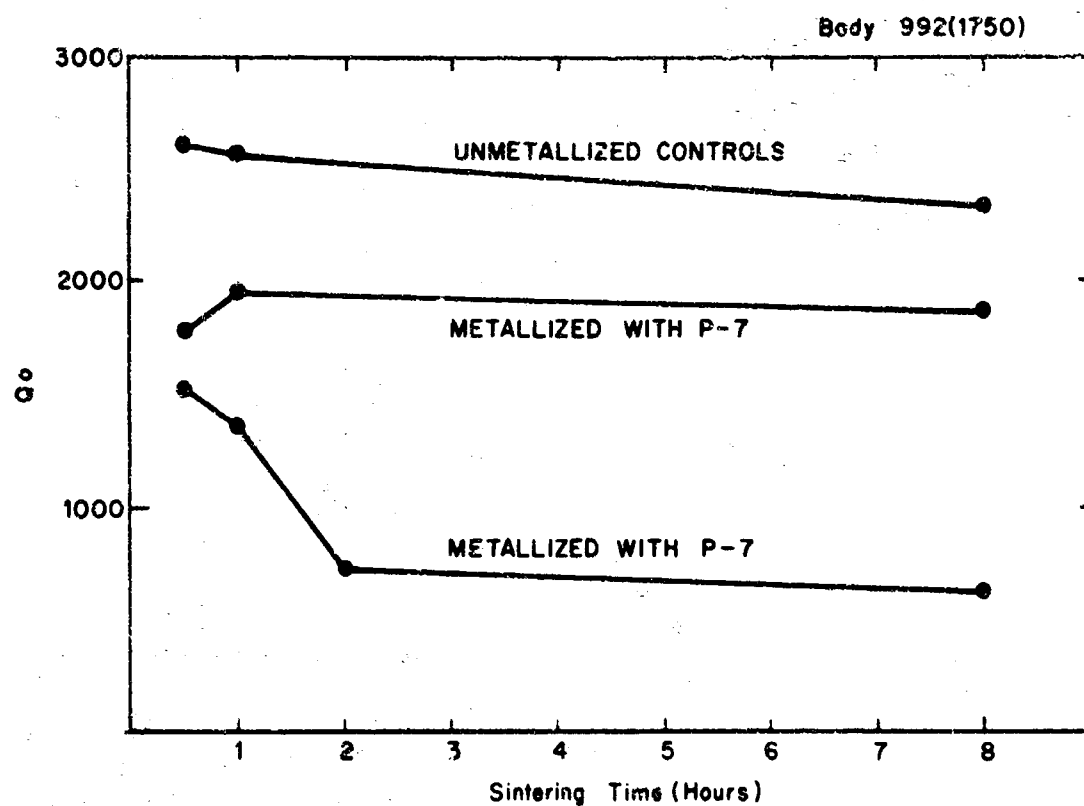


Figure 6.63: Dielectric loss test cavity  $Q_o$  versus 1425°C firing time. Ceramic was Body 992 (1750) in all cases.

equilibrium loss situation is reached after 2 hours, indicating that the reaction is amount limited.

The losses are determined from Fig. 6.53. It can be seen that the P-1 loss is an order of magnitude more than P-7 metallizing.

## 6.5 HIGH POWER MEASUREMENTS

### 6.5.1 Introduction

Recapitulating, the objective of Task III is to investigate the effects of the loss-producing variables of a ceramic-to-metal seal on the electric losses in radio-frequency fields and to arrive at the design of low-loss seals.

In low power rf measurements, losses due to degradation of the dielectric qualities in the ceramic next to the seal region were distinguished from losses due to conduction currents parallel to the seal in the metallizing and overplate. The results did not indicate the relative importance of the two types of losses or the relative contribution of the seal losses to the total dissipation in a waveguide window.

The first set of calorimetric measurements of ceramic-to-metal seal losses of representative configurations using a 10 KW, 8 Gc rf source were performed in the 9th quarter of the contract in order to provide absolute loss data. Those measurements gave us our first indication of the magnitude of the total losses occurring in a ceramic-to-metal seal and demonstrated our ability to compare seal losses with the rf losses in an empty copper waveguide.

The remaining problem was to measure the absolute amount of dissipation due to dielectric losses and conduction losses separately in typical seals and to attempt to minimize such losses. Accordingly, these two modes of seal loss were separated and measured independently in a second set of measurements carried out during the 11th and 12th quarters of the contract.

The equipment and its operation discussed in this report deals mainly with the "set-up" used for the second series of experiments. This "set-up" is a modification of that used in the first series of experiments. The first "set-up" has been adequately described in the 8th and 9th Quarterly Reports.

The copper test cells used in the first set of calorimetric measurements each had three cooling channels. The center channel cooled the test seal, while the outer two channels served to isolate the test cell from the rest of the waveguide and to give an empty waveguide power dissipation value. A detailed drawing of this test cell appeared in Fig. 4.01 of the 9th Quarterly Report. Seals tested in this group were all made using P-1 metallizing paint and 95.5% alumina substrates (Body I) .025" thick. The metallizing thickness ranged from about 0.1 mil to 1.7 mil and either nickel or copper plating was used. All brazes were made with copper-silver eutectic (BT). The waveguide walls to which the four thin dielectric plates (constituting a windowette) were brazed were .014 inch thick. The original waveguide wall had been reduced to this dimension by machining away part of the outside of the waveguide to provide the water cooling channels. The water channels were completed with Lucite cover plates.

In the second set of measurements, the waveguide test cells were extended to have five cooling channels each in order to accommodate a larger number of test seals in each test cell. Fig. 6.64 is a photograph of a completed unit; its cross-section is shown in Fig. 6.65. Compared with previous units, only one other minor change was introduced; the remaining wall thickness of the waveguide in the channels was increased to .024" from the previous .014". Using the two outer channels for cooling purposes and insulation against heat influx from the flanges, the three inner sections were available for the placement of test seals. All were connected in series and the rf energy dissipation in each "windowette" was measured simultaneously in the set-up described below in Section 6.5.5.1.

The ceramic used in most of the 2nd series of seals was a 99.5% alumina, Body H, in the form of 0.050" thick substrates. Two cells with .050" thick 99.8% BeO ceramic, Body BA, and one with the previously used .025" thick Body I substrates were also tested. The change in ceramic was programmed in order that dielectric losses might be noted. The first set of measurements showed that the loss of the 96% alumina dielectric swamped the losses introduced by the metallizing of the body. Metallizing formulae, braze types and methods of applying each were chosen in order to verify or disprove various hypotheses on the nature of seal electrical losses as well as to develop low loss seals. These choices are listed in Table 6-20.

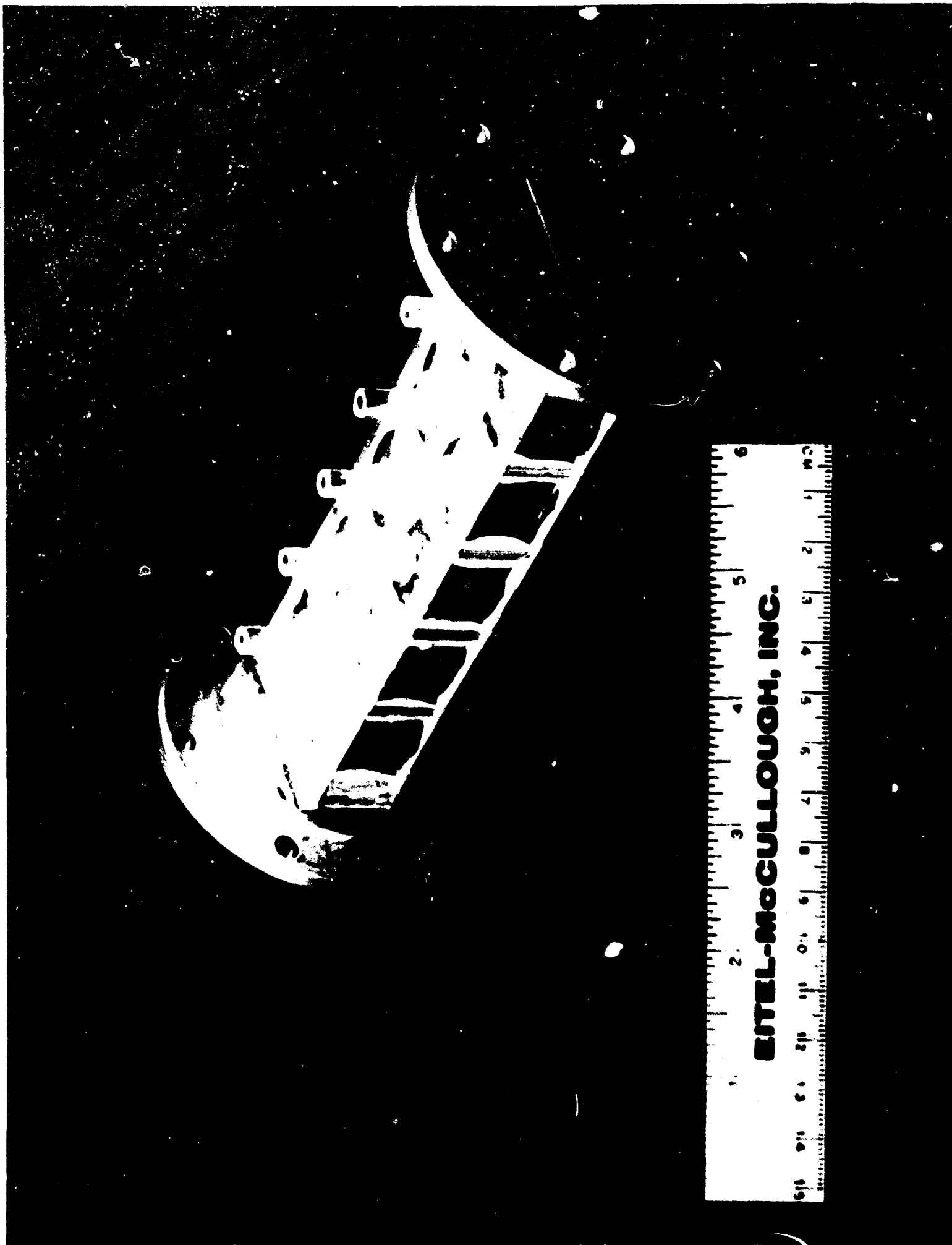


Figure 6.64: Five-channel waveguide test cell used in second series of high power calorimetric loss measurements.



TABLE 6-20

## Physical Characteristics of Test Cells

Cell Number	Channel Number	Frame Geometry	Ceramic Thickness	Metallizing Thickness	Plating Thickness	Braze	Reason for Selection
First Test Series							
1	One Channel Test Cells	Full-4 walls	Body I 0.025 in.	P-1 0.1 mil	Nickel 1.25-1.9 mil	Cu-Ag	Used to establish the relationship between rf losses and metallizing thickness with either copper or nickel plate.  See Fig. 6.73.
2	-	Full-4 walls	"	P-1 0.1 mil	Copper 0.9 mil	"	
3	-	Full-4 walls	"	P-1 0.2 mil	Nickel 0.8-1.0 mil	"	
4	-	Full-4 walls	"	P-1 0.3 mil	Copper 1 mil	"	
5	-	Full-4 walls	"	P-1 1.7 mil	Nickel 0.6 mil	"	
6	-	Full-4 walls	"	P-1 1.7 mil	Copper 0.7 mil	"	
Second Test Series							
1	Three Channel Test Cells	Full-4 walls	Body I 0.025 in.	P-1 1.0 mil	Nickel 0.5 mil 850°C, 15 min done twice	Cu-Ag	Provide additional data points to add to first series of tests. Provide link between first and second test series. Provide empty waveguide loss value.
2	-	Empty	-	-	-	-	
3	-	Full-4 walls	Body I 0.025 in.	P-1 1.0 mil	Copper 1.0 mil	Cu-Ag	

Cell Number	Channel Number	Frame Geometry	Ceramic Thickness	Metallizing & Thickness	Plating & Thickness	Braze	Reason for Selection
2	1	Full-4 walls	Body H 0.050 in.	P-1 2 mils	Copper 1 mil	Cu-Ag	Thick standard production metallizing: moderate to high loss expected.
	2	Side walls only	Body H 0.050 in.	P-1 2 mils	Copper 1 mil	Cu-Ag	Window frame geometry to separate conduction losses from dielectric losses.
	3	Broad walls only	Body H 0.050 in.	P-1 2 mils	Copper 1 mil	Cu-Ag	
3	1	Full-4 walls	Body H 0.050 in.	P-1 polished 0.7 mils	Copper 1 mil	Cu-Ag	Attempt to obtain thin metallizing by polishing down a normal coating.
	2	Empty	-	-	-	-	Provide empty waveguide loss value.
	3	Broad walls only	Body H 0.050 in.	P-1 polished 0.7 mils	Copper 1 mil	Cu-Ag	
4	1	Full-4 walls	Body H 0.050 in.	P-7 1 mil	Copper 1 mil	Cu-Ag	"Low dielectric loss" metallizing paint.
	2	Side walls only	Body H 0.050 in.	P-7 1 mil	Copper 1 mil	Cu-Ag	Window frame geometry to separate conduction losses from dielectric losses.
	3	Broad walls only	Body H 0.050 in.	P-7 1 mil	Copper 1 mil	Cu-Ag	
5	1	Full-4 walls	Body H 0.050 in.	P-3 1 mil	Copper 1 mil	Cu-Ag	Standard production metallizing.
	2	Side walls only	Body H 0.050 in.	P-3 1 mil	Copper 1 mil	Cu-Ag	Window frame geometry to separate conduction losses from dielectric losses.
	3	Broad walls only	Body H 0.050 in.	P-3 1 mil	Copper 1 mil	Cu-Ag	
6	1	Full-4 walls	Body H 0.050 in.	Evaporated Ti 0.1 $\mu$ Mo 0.25 $\mu$ Cu 0.5 $\mu$	Copper 5 mil	Cu-Ag	Proposed low loss metallizing/seal system.
	2	Side walls only	Body H 0.050 in.	"	Copper 5 mil	Cu-Ag	Window frame geometry to separate conduction losses from dielectric losses.
	3	Broad walls only	Body H 0.050 in.	"	Copper 5 mil	Cu-Ag	



Cell Number	Channel Number	Frame Geometry	Ceramic Thickness	Metallizing Plating & Thickness	Braze	Reason for Selection
7	1	Full-4 walls	Body H 0.050 in.	P-3 polished Copper 3 mils	Cu-Ag	Thick standard production metallizing polished to reduce loss.
	2	Empty	-	-	-	
	3	Full-4 walls	Body H 0.050 in.	P-3 polished Copper 2 mils	Cu-Ag	Provide empty waveguide loss value.
8	1	Full-4 walls	Beryllia Body BA 0.050 in.	P-1 0.5 mil	Copper 1 mil	Standard production metallizing on high thermal conductivity beryllia.
	2	Side walls only	"	P-1 0.5 mil	Copper 1 mil	Separate conduction losses from dielectric losses.
	3	Broad walls only	"	P-1 0.5 mil	Copper 1 mil	
9	1	Full-4 walls	Beryllia Body BA 0.050 in.	P-3 1 mil	Copper 1 mil	Standard production metallizing on high thermal conductivity beryllia.
	2	Side walls only	"	P-3 1 mil	Copper 1 mil	
	3	Broad walls only	"	P-3 1 mil	Copper 1 mil	Separate conduction losses from dielectric losses.
10	1	Full-4 walls	Body H 0.050 in.	P-1 0.8 mil	Nickel: 0.5 mil 850°C 15 min. Done twice.	Similar to channel 1, cell 1 of 2nd series but with thicker Body H window frames. Compare Body I to Body H ceramics.
	2	Empty	-	-	-	
	3	Full-4 walls	Body H 0.050 in.	P-1 0.8 mil	Copper 1 mil	Provide empty waveguide loss value. Compare Nicoro braze to Cu-A <sub>j</sub> braze.

Test cell #1 contained the .025" thick Body I ceramics to provide a check on the previous set of measurements. Test cells #2 through #7 and #10 contained Body H substrates, and test cells #8 and #9 contained the Body BA substrates. A study of Table 6-20 shows that some cells were intended to compare different metallizing preparations or brazes. Other cells used the same type of seal throughout, but included three geometric configurations: (1) seals on all four walls of the waveguide, (2) seals on the side walls only, and (3) seals on the broad walls only. Total seal losses measured in (1) could then be broken down into conduction losses measured in (2) and combined conduction and dielectric losses measured in (3). A position in each of several test cells was also left empty so that energy dissipated per unit length of the empty copper waveguide could be measured.

#### 6.5.3 Cold Testing

Test seals used in the first set of measurements were cold tested for the VSWR (voltage standing wave ratio) and matching frequency, as a function of the frame width, i.e. the dimension of the ceramic which runs parallel to the axis of the waveguide. These tests indicated the dimensions of the frames to be used in the 1st series of calorimetric tests. A VSWR of just a fraction greater than unity was obtained.

These values were also of use in determining the best frame width to be used in the second set of tests. This procedure was described in Section 4.3 of the 8th and in Section 4.2 of the 10th Quarterly Reports. Frame widths selected on the basis of these tests were .830" for Body I, .680 for Body H, and .710 for Body BA.

The notable difference in frame width between Body I and Body H was necessitated by the difference in their thickness, .025" and .050" respectively and their dielectric constants. The waveguide wavelength of 1.749" (at 8 kmc) was reduced to 1.360" in the section containing the .050" thick dielectric frame.

The VSWR of each test cell in the second group was measured between 7.5 and 8.5 kmc to detect spurious reflections and resonances set up by interaction between the seals and thus assure safe operating conditions for the klystron and to select the best operating frequency near 8 kmc.

The test cell VSWR was first measured on each cell individually, then on groups of three or four cells assembled as they would be later in high power loss measurements. The results of all VSWR measurements made on the five-channel test cells are presented in Table 6-21. The resonance frequencies in the second column were the frequencies at which the test cells exhibited the minimum voltage standing wave ratios as shown in the third column. These numbers, like those for the VSWR at 7.9 kmc in the fourth column, were always the upper limits, because the VSWR may be influenced by reflecting obstacles in the microwave circuitry other than the dielectric frame. Other reflections may occur at the termination of the waveguide and at waveguide flanges. It was on the basis of the VSWR measurement results that the klystron operating frequency of 7.9 kmc was selected for the second set of high power tests.

#### 6.5.4 Calorimetric Instrumentation

##### 6.5.4.1 Principles of Calorimetric Measurements

Calorimetric indication of microwave dissipation in dielectric-to-metal seals is the direct way of measuring losses absolutely. It also closely simulates the practical solution to the problem of cooling high power microwave windows. Instrumentation is simpler than is that employed for the low power microwave measurement of seal losses using cavity techniques. The price paid for this, however, is the requirement of relatively high microwave power for the experiment. Using propagating waves in waveguides and expecting a dissipation in the test structure on the order of 0.1 percent, a microwave source delivering 10 KW must be used.

##### 6.5.4.2 Preparation of Calorimetric Measurements

Microwave energy dissipation in the dielectric-to-metal seals was determined by measuring the temperature rise of the cooling water upon passing through each of the cooling channels of the test cell. The instrumentation was designed to measure reliably a minimum of one watt; refer to Figure 6.22 for the set-up used in the second set of measurements. Two differential thermopiles\* Model 189A and one Model 389A were used to indicate temperature differences in the three central channels of the test cell. The thermopile output voltages were routed through a selector switch

---

\*From Sierra Electronic Corporation

TABLE 6-21

## Test Cell VSWR Measurement Results

Cell No.	Resonance Frequency	Minimum VSWR	VSWR at 7.9 Kmc
1	7.57 Kmc	1.00	1.14
2	8.10	1.00	1.08
3	8.22	1.03	1.035
4	7.54	1.00	1.11
5	7.60	1.04	1.14
6	8.32	1.00	1.13
7	7.65	1.04	1.08
8	7.67	1.00	1.06
9	8.01	1.00	1.01
10	7.57	1.04	1.07
1-2-4	7.89	1.035	1.04
3-5-7-10	7.92	1.00	1.03
9-6-8	7.87	1.05	1.06

and indicated on a Hewlett-Packard Model 425A dc Micro-Volt-Ammeter.

The heart of the calorimetric measuring and cooling system was the constant temperature water container. This reservoir contained a thermostatically controlled electric heater, a small mixer, a water cooling coil, and a pump to circulate the water through the entire test system. A mixer-buffer container was placed in the water line between the reservoir and the test cell to prevent surges of water of a slightly higher or lower temperature than desired. The water was then routed through one outer cooling channel of the test cell, through the cold arm of the first thermopile, through the first test seal cooling channel, through a short length of lucite tubing containing a four-watt electric heater, and through the hot arm of the first thermopile. This sequence was repeated through the next two test channels, then the water was returned through the other outer cooling channel to the reservoir. The small heaters in the water stream could be turned on or off to permit the operator to make a calibration check on the thermopiles during operation without otherwise disturbing the set-up. Water returning to the reservoir flowed into a 100 ml graduate to provide a means to measure the flow rate. The period required to fill the graduate was timed with a stop watch. A switching box was used to energize each heater separately as well as to direct the output of each thermopile to the microvolt-ammeter.

All three thermopiles were calibrated in terms of output voltage per degree C of temperature difference of the water flowing through the two branches. The thermopiles were calibrated before their use in the high power measurements using the temperatures and flow rates actually employed in the tests. There was some minor difference between the two calibrations, but the preliminary calibration permitted some calculations during testing. Both calibrations were made using the set-up shown in the diagram, Fig. 6.67, and the photograph, Fig. 6.68, which consists of two constant temperature water circulation systems.

Water in one system was run through the hot side of the thermopiles while water in the other was run through the cold side. The final calibration was made using 32.8°C as the cooler temperature and varying the temperature of the warmer water stream from 32.7°C to 33.7°C. Using data thus obtained, the following thermopile outputs were

# 

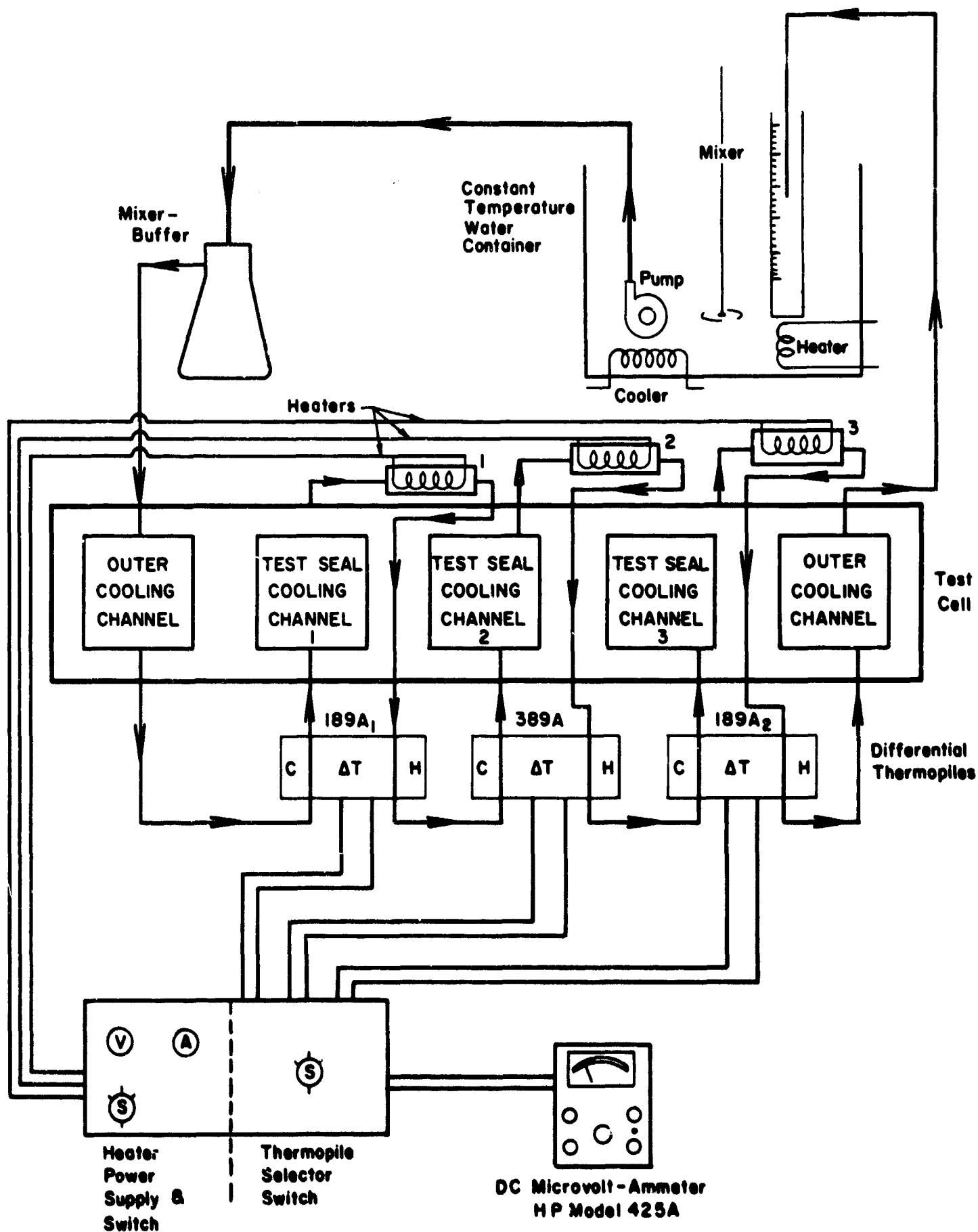


Figure 6.66: Schematic diagram of test set-up for second series of high power calorimetric loss measurements shown also in Figures 6.70, 6.71, and 6.72.

# THERMOPILE CALIBRATION

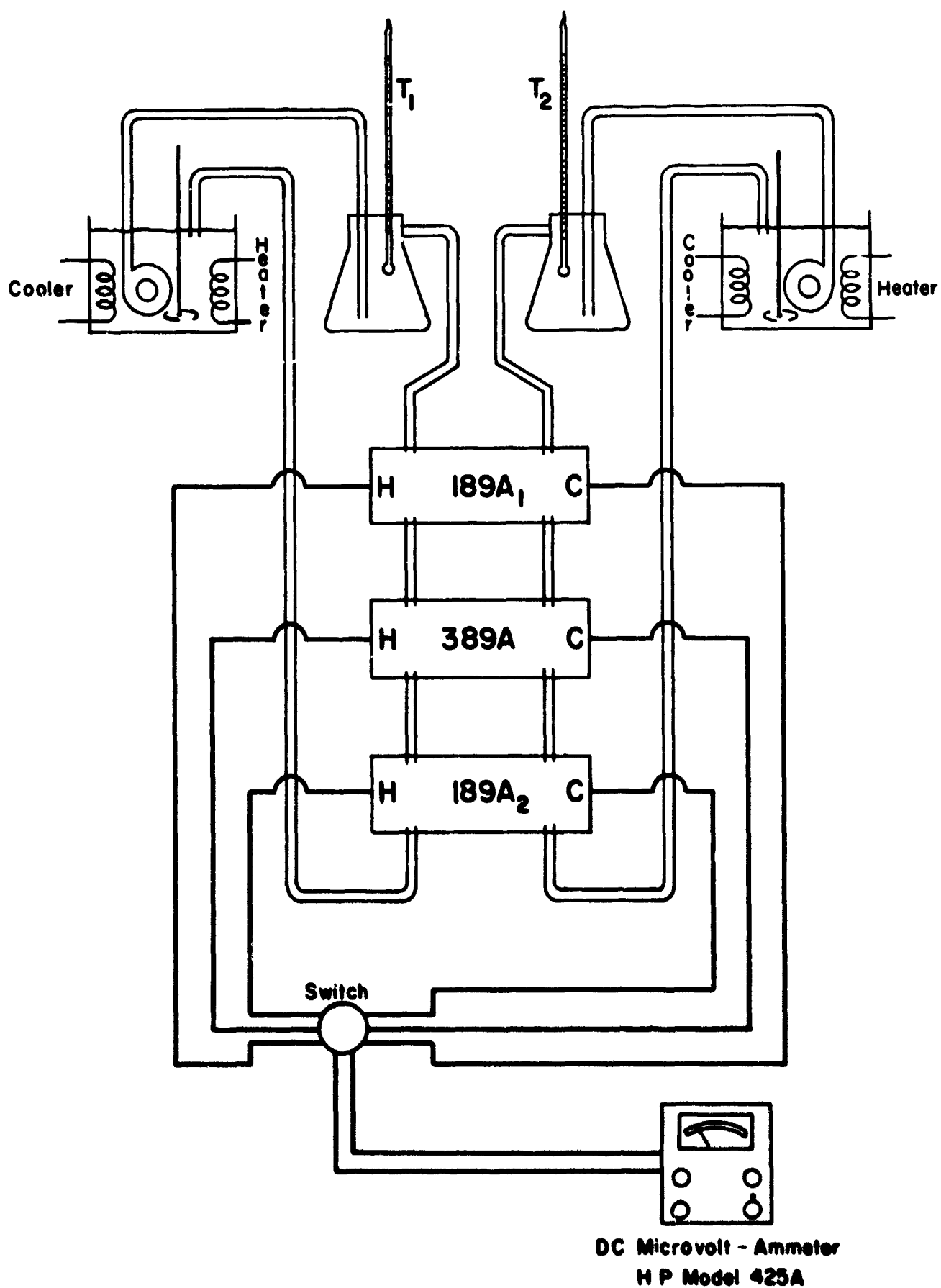


Figure 6.67: Schematic diagram of set-up used to calibrate thermopiles for the second series of high power calorimetric loss measurements.

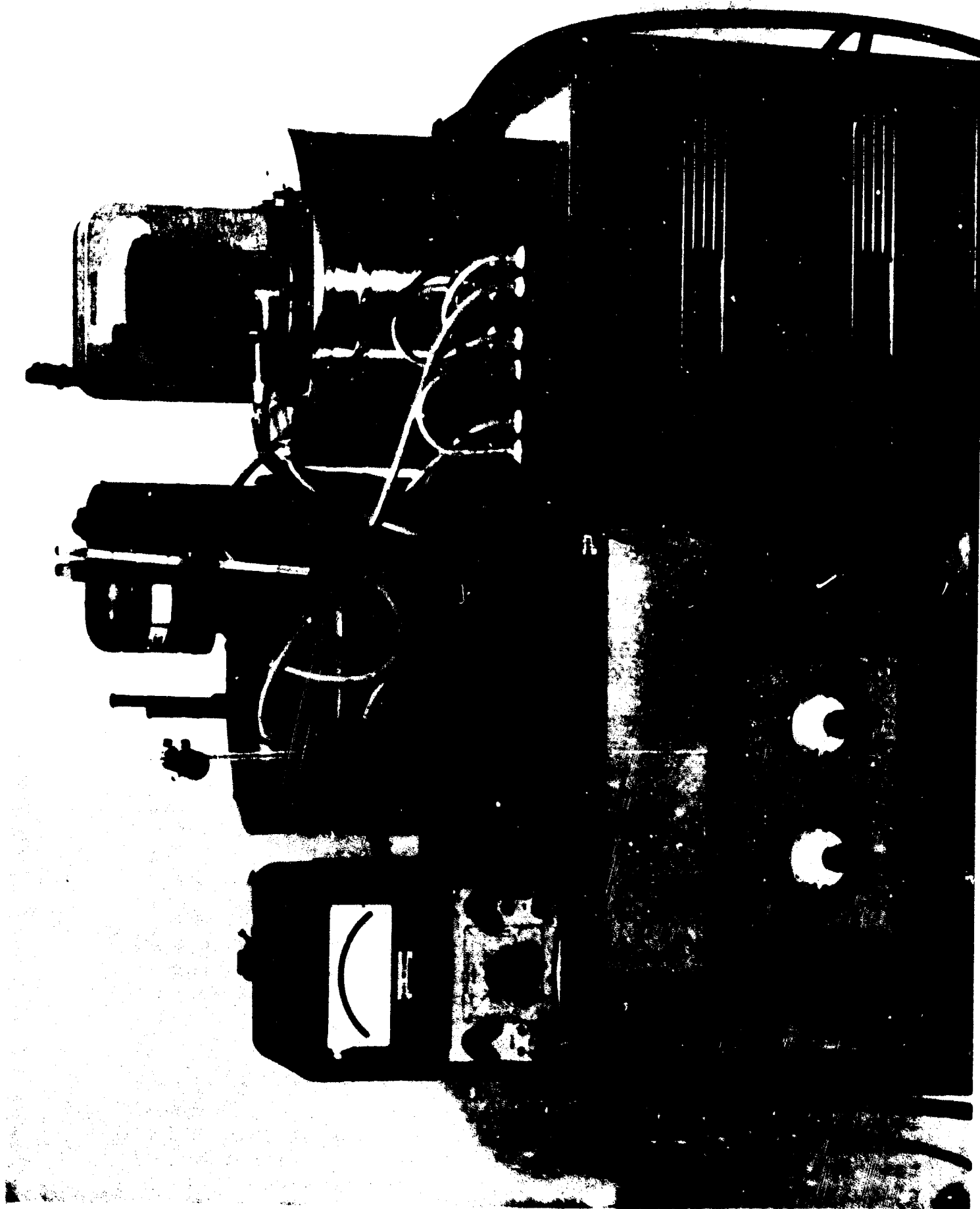


Figure 6.68: Photograph of thermopile calibration equipment diagrammed in Figure 6.67.



calculated:

Model 189A, Differential Thermopile (used in Channel one): 1.03 mv/degrees C

Model 389A Differential Thermopile (used in Channel two): 3.16 mv/degrees C

Model 189A, Differential Thermopile (used in Channel three): 1.02 mv/degrees C.

With water as the coolant, the power,  $P$  (in watts), dissipated in each channel of the test cell is related to the flow rate,  $F$  (in ml/sec), and the output voltage,  $V$  (in millivolts), of the differential thermopiles through the following equations:

$$\text{Channel 1: } P = 4.062 \times V \times F \text{ (Model 189A}_1\text{)} \quad (12)$$

$$\text{Channel 2: } P = 1.325 \times V \times F \text{ (Model 389A)} \quad (13)$$

$$\text{Channel 3: } P = 4.110 \times V \times F \text{ (Model 189A}_2\text{)} \quad (14)$$

#### 6.5.5 Calorimetric Measurements

##### 6.5.5.1 Experimental Set-up for High Power Microwave Measurements

Experiments with high power microwaves were performed in one of Eitel-McCullough's test stations for high power klystrons. The block diagram in Fig. 6.69 shows the arrangement. The 10 milliwatt CW signal from a Hewlett-Packard 693B Sweep Oscillator set at a frequency of 7.9 kmc was amplified in a Hewlett-Packard 493A Microwave Amplifier with an output of 20 to 300 milliwatts. The final amplifier was an Eimac X3050 tube, a tunable 5-cavity klystron amplifier with a C.W. output of 20 kw.

Power was transmitted through all the test cells (three or four) connected in series and was absorbed and measured calorimetrically in a water load. Dissipation in each cell was neglected against the total transmitted power. The closed loop calorimetric measuring system described in the previous section (including Fig. 6.66) was connected to the cell under test. Working at a power level of 10 kw required cooling of the other parts of the transmitting line, the tube-to-waveguide transitions and the test cells not being measured, in order to protect the circuitry from overheating. This was accomplished by an

## HIGH POWER TEST SET-UP

## MICROWAVE CIRCUIT

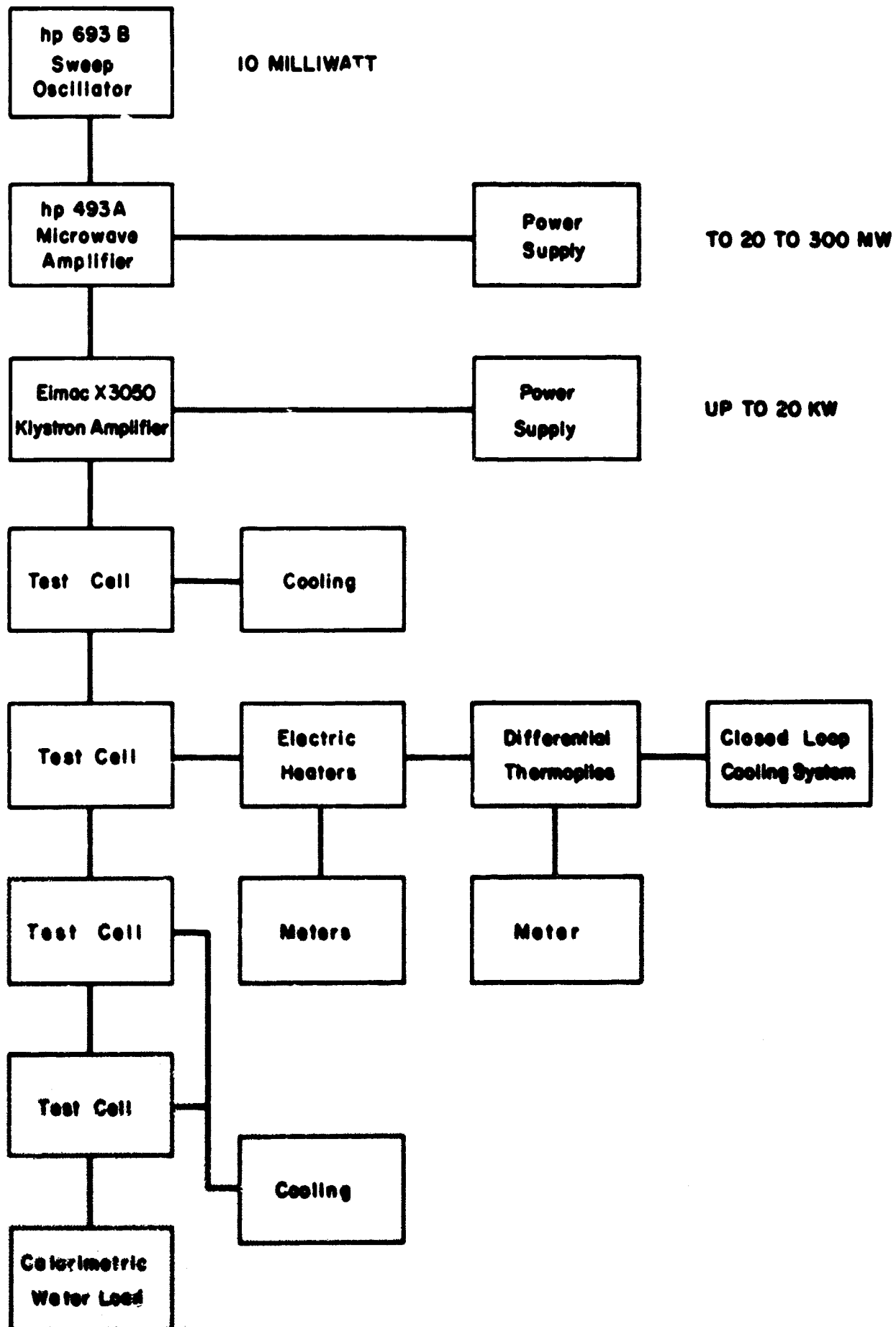


Figure 6.69: Block diagram of microwave circuitry used in second series of high power calorimetric loss measurements.

independent secondary cooling circuit routed through all transitions and all five channels of each waveguide cell not under test.

Detailed views of the test arrangement appear in Figs. 6.70, 6.71 and 6.72. Fig. 6.70 is an overall view of the test site with the klystron amplifier in the center-rear, four test cells with attached cooling water tubes extending to the right from the klystron, and the three differential thermopiles suspended above the test cells. The stand in the foreground holds the constant temperature water container, which is immediately to the right of the technician's head. The technician's hand is on the dc micro volt-ammeter used to measure thermopile output. On its right is the panel containing the heater and thermopile selector switches and the heater ammeter and voltmeter. In front of the switch panel is the stop watch used for timing the water flow.

Fig. 6.71 is a close-up of the four waveguide test cells in Fig. 6.72. The black object in the lower extreme left corner is the mixer-buffer container from which water flows to the cell under test. The klystron is at left-center. The three differential thermopiles in the upper-center are suspended in an inverted position from their support bracket. The two hoses draped over the thermopiles are part of the secondary cooling system and can be seen joining hose manifolds on two cells not under test. All the hoses directly below the thermopiles are part of the closed loop cooling system for the cell under test. It should be noted that only two of the three heaters indicated in Fig. 6.66 are present in the photograph. (Lucite tubes with square lucite end plates.) Heater #1 had been removed for repair and was not replaced until after the photograph was taken. Wires from the thermopiles and heaters connect to the switch box just out of view at the bottom of the photograph.

Fig. 6.72 is another close-up of the set-up showing the Hewlett-Packard signal generators in the left background. The HP 693B Sweep Oscillator is on the bottom of the stack, and the HP 493A Microwave Amplifier is above it. The smaller instrument at extreme top left is a voltmeter. The klystron may again be seen at right behind the row of test cells. The mixer-buffer container is the black flask in the left foreground. A thermometer calibrated in  $0.01^{\circ}\text{C}$  increments is inserted through the top of the container to measure input water temperature. Part of the main water container is at the extreme left.

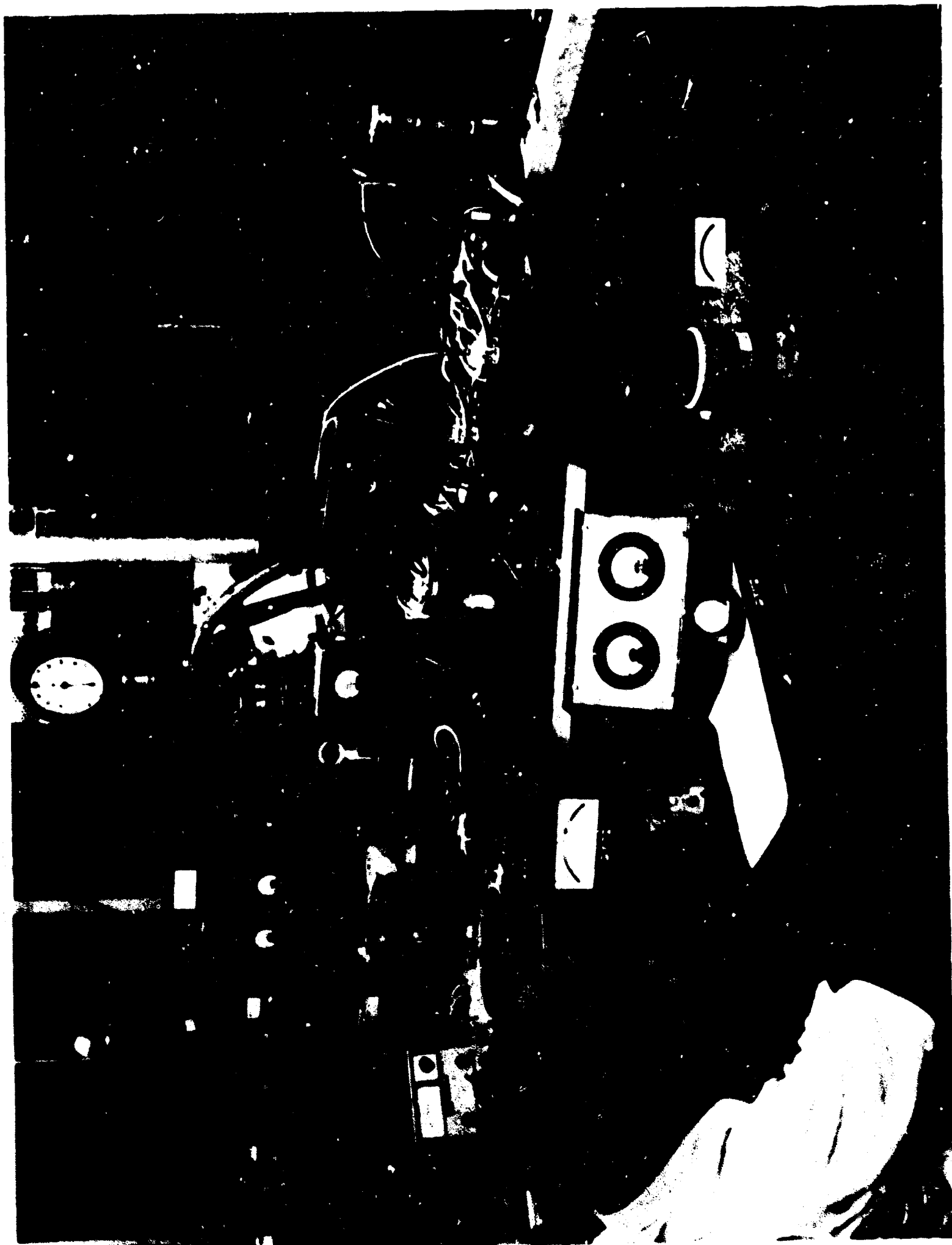


Figure 6.70: Test set-up for second series of high power calorimetric loss measurements at 8 kmc.



Figure 6.71: Close-up of test cells and thermopiles in test set-up for second series of high power calorimetric loss measurements.

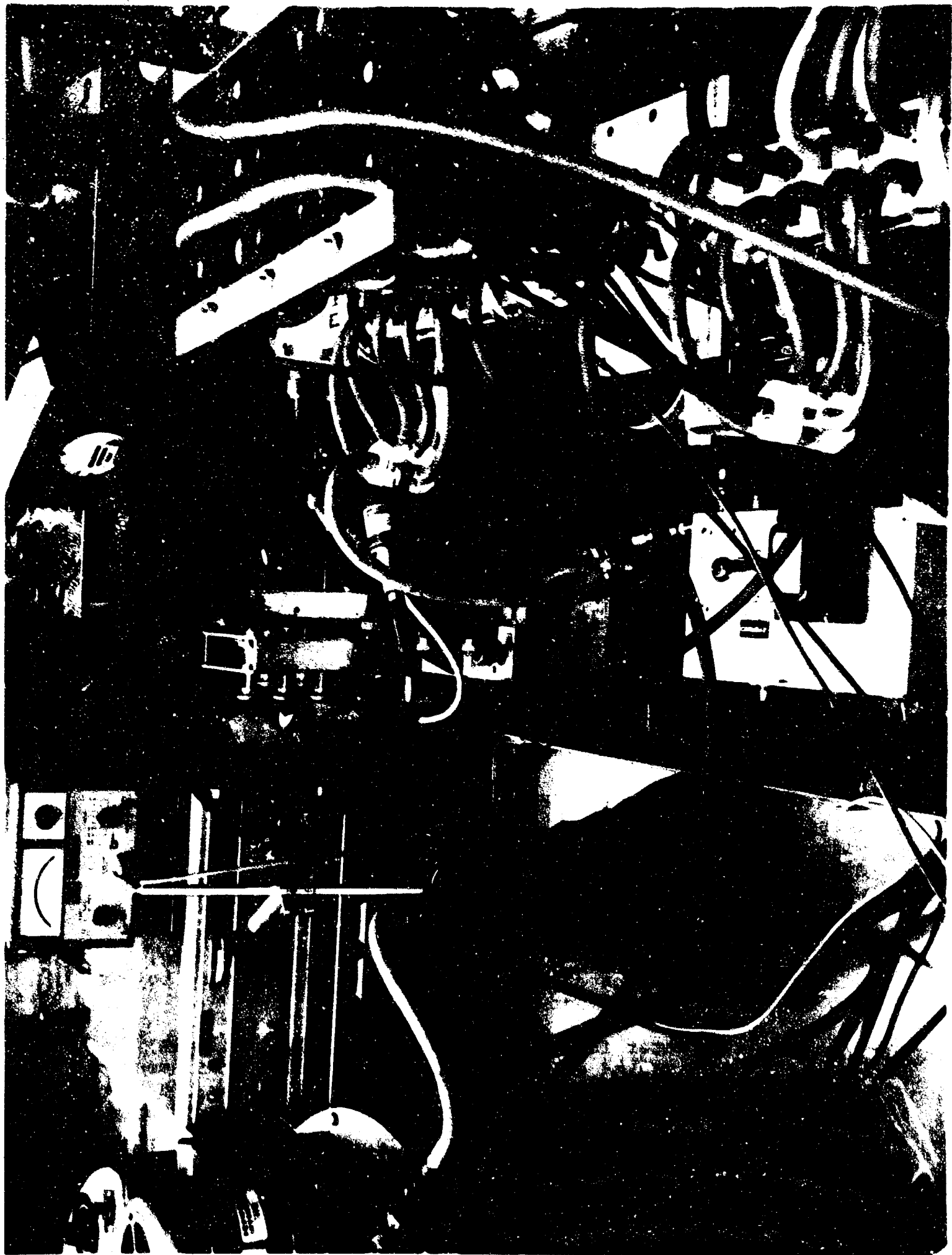


Figure 6.72: Close-up of test set-up for second series of high power calorimetric loss measurements showing signal generator (8 kmc), amplifier, and klystron at rear.

By following the water flow in the diagram, Fig. 6.66, along with comparison to and careful study of Fig. 6.71, a good understanding of the calorimetric measuring system may be gained.

#### 6.5.5.2 Experimental Procedure

Essentially the same procedure was followed in both groups of calorimetric seal loss measurements. The first group of measurements was discussed generally on pages 11 through 13 of the 9th Quarterly Report. Procedures used in the second group are discussed here in more detail.

Each group of waveguide test cells was assembled in the same order and orientation in which it had been previously cold tested for the VSWR. All water and electrical connections were made as shown in Figs. 6.69 and 6.71. Water from the closed loop system and the secondary cooling system was circulated, all leaks and bubbles were eliminated and a systematic check of all measuring instruments was made.

Experiments prior to measurements made on the first group of test cells showed that the second order effects of changes in the closed-loop flow temperature on the measurements could not be tolerated. Constancy of temperature to better than  $0.1^{\circ}\text{C}$  was required. Therefore, an operating temperature  $5^{\circ}\text{C}$  above room temperature was selected, which was maintained with the thermostatically controlled heater in the closed-loop system. Additional heat input from the microwave dissipation was small compared with heat losses to the environment and to another water cooler in the main container. Thus, the heat to be measured did not disturb the temperature equilibrium. Heat losses from the waveguide, the connecting rubber hoses and the differential thermopiles were indicated by negative readings of the dc micro volt-ammeter. Later readings with the microwaves transmitted were always referred to the negative reading, also called the adjusted zero level, which was checked before and after each experiment.

A water flow rate of 10 cc/sec (0.15 gal/min) was used. It assured effective cooling and fast attainment of equilibrium temperature and still provided measurable temperature differences between the input and output of the cooling channels on the order of  $0.5^{\circ}\text{C}$ .

Several readings were taken at each measuring point to establish the zero reference condition with no microwave power transmitted. Each heater was then energized

in turn and the readings were taken with approximately four watts of power supplied as indicated by the ammeter and voltmeter for the heater power supply. This procedure provided data for checking the calibration of the thermopiles.

The klystron was then put in operation and microwave power was transmitted through the waveguide test cells. The transmitted power was measured with immersion thermometers and a flowmeter in a calorimetric waterload. Representative values were: a temperature difference of 9.9°C at a water flow of 3.9 gal/min. at a power transmission of 10.2 kw.

The klystron power was calculated as follows:

$$P_{\text{tube}} = 264 (T_2 - T_1) (F_w) \quad (15)$$

where:  $P_{\text{tube}}$  = tube output power, kilowatts

$T_2 - T_1$  = temperature difference of outlet and inlet water, °C

$F_w$  = water flow rate, gallons per minute

264 = constant including unit conversion factors.

Klystron output power during each measurement in the second group of measurements is listed in Column 1, Table 6-22. The klystron was operated at 10 kw for all test cells and at 5 kw for repeated measurements on four test cells.

In determining the power transmitted through the test cells, the progressive drop in power along the test cell line due to absorption in each cell was neglected against the total power transmitted. The total power absorbed by the assembled test cells, associated flanges and transitions was estimated (2/3 was measured directly) at less than 300 watts. The validity of this approximation was confirmed by placing several cells at different positions in the test cell line. No differences in power absorption were detected.

Several sets of readings were taken at all measuring points with each heater on at the usual four watts and again for each test channel with heaters off. Microwave power was again turned off and another set of readings was taken to recheck the zero power reference values. On



some test cells the entire procedure was repeated at half the usual power level (5 kw) in order to provide a scaling factor check on the calorimetric measuring system.

Power dissipation in the test cells was calculated using the water flow rate in the cooling channels (Column 2, Table 6-22), the output voltage developed by each differential thermopile (Column 3, Table 6-22) and equations 12, 13 and 14 on page 404. This gave directly the amount of power dissipated in the seal cooled by each cooling channel. The water temperature in the mixer-buffer container (see Fig. 6.66) was monitored to keep it within the temperature range for which the thermopiles had been calibrated.

The result of the preceding calculation, the power loss per channel, was then refined in order to discriminate between the power dissipated in the immediate seal area from dissipation in the bare waveguide walls on either side of the seal. This empty waveguide associated with each channel extended to the center line of the ribs separating the channel from adjacent channels, as shown in Fig. 6.65. Since the bare walls were also cooled by the water in the channel, their contribution had to be considered. A similar calculation was used to separate losses occurring on the empty walls where the partial seal configurations were used. Calculations of this type were made possible by measuring losses in a section of empty waveguide. From this result, and knowing the total length of waveguide cooled by each channel, (Column 6, Table 6-22) the power loss per unit length of empty waveguide was calculated. At least one such empty channel was present in each of the three groups of test cells in the second set of measurements in order to provide empty waveguide power loss data for each group independently. Power dissipated exclusively in the seal was then related to the power level of the klystron at the time of testing and reported as a percent of klystron output power (Column 5, Table 6-22). Percent klystron power loss per unit length of seal was also calculated (Column 7, Table 6-22).

Another number called "enhancement of dissipation" was developed in order to enable comparison of one seal to another without the confusion of different amounts of loss in the empty waveguide caused by changes in standing wave conditions from one test group to the next. This number put all the results on the same basis. Power loss per

centimeter in the seal (Column 7, Table 6-22) was divided by power loss per centimeter in an empty waveguide (also Column 7, Table 6-22) run in the same test group. Seal loss was thus reported as a multiple of the empty waveguide loss, or the factor by which the seal enhanced or increased power dissipation in the waveguide (Column 8, Table 6-22).

In the several test cells which were designed for measuring dissipation in the side walls or broad walls exclusively for one particular seal composition, the ratio of loss in side walls to broad walls was of primary interest (Column 9, Table 6-22). The theoretical ratio of conduction loss in the side walls to the broad walls of the waveguide was determined by calculation to be 0.26:1. When the ratio determined experimentally was less than 0.26:1, the additional loss in the broad walls was attributed to dielectric loss which can occur only in the broad walls. If the ratio was greater than 0.26:1, (which would indicate a negative amount of dielectric loss) it was an indication of an error in the data or an inconsistency in the seal structure which upset the ratio of side wall to broad wall conduction losses.

In order to provide a check on the accuracy of the calorimetric measuring system during each run, a measured amount of electrical power (approximately four watts) was supplied in turn to each of the three heaters in the calorimetric measuring system (see Fig. 6.66). The water flow and thermopile output voltage were recorded and the measured power was calculated from these data. The measured power was then compared to the power supplied to the heater to obtain a check on the accuracy of the measuring system and an estimate of the amount of heat lost from the water as it flowed through tubes from the cooling channel or heater to the differential thermopiles.

These values were not presented in the table because there were so many of them; at least three for every cooling channel. However, they were always very near and less than the four watts of electrical power supplied to the heaters and indicated that the calorimetric measuring system was operating satisfactorily.

As a further check on the system, several of the test cells were retested by placing them in a different position in the test cell sequence. Any differences due to electrical effects would thus be detected. The measurements indicated that the measured seal loss was independent of test cell position.

TABLE 6-

			HIGH POWER rf LOSS MEASUREMENTS			
Cell No.	Position	Seal Description See Table 6-20	Test Group	Window Frame	Tube Output Power	Waveguide Water Flow
				Con-fig.	$P_t, kw$	$F_{wg}, cc/sec$
1	1	Body I, P-1, Ni, BT	3	Full*	10.6	10.2
	2	Empty	3	Empty*	10.9	10.2
	3	Body I, P-1, Cu, BT	3	Full	10.7	10.2
1	1	Body I, P-1, Ni, BT	3	Full	5.0	10.2
	2	Empty	3	Empty	5.0	10.2
	3	Body I, P-1, Cu, BT	3	Full	5.0	10.2
1	1	Body I, P-1, Ni, BT	1	Full	10.55	10.0
	2	Empty	1	Empty	10.55	10.0
	3	Body I, P-1, Cu, BT	1	Full	10.55	10.0
2	1	Body H, P-1, Cu, BT	1	Full	10.34	8.40
	2	Body H, P-1, Cu, BT	1	S.W.*	10.34	8.40
	3	Body H, P-1, Cu, BT	1	B.W.*	10.34	8.40
2	1	Body H, P-1, Cu, BT	1	Full	10.01	8.2
	2	Body H, P-1, Cu, BT	1	S.W.	10.01	8.2
	3	Body H, P-1, Cu, BT	1	B.W.	10.45	8.2
3	1	Body H, P-1 (Pol.), Cu, BT	2	Full	10.80	10.5
	2	Empty	2	Empty	10.80	10.5
	3	Body H, P-1 (Pol.), Cu, BT	2	B.W.	10.80	10.5
4	1	Body H, P-7, Cu, BT	1	Full	10.55	10.76
	2	Body H, P-7, Cu, BT	1	S.W.	10.55	10.76
	3	Body H, P-7, Cu, BT	1	B.W.	10.55	10.76

Column Number: (1) (2)

TABLE 6-22

## HIGH POWER rf LOSS MEASUREMENT RESULTS

Band	Tube Output Power $P_t$ , kw	Waveguide Water Flow $F_{wg}$ , cc/sec	Voltage Differential V, mV	Power Loss in Cell $P_l$ , watts	Loss as % of Tube Output $\% P_t$	Cell Length Consid'rd. L, cm	% Power Lost per cm $\% P_t/\text{cm}$	Enhancement of Dis. Seal/w guide
11*	10.6	10.2	0.41	17.0-1.31=15.69	0.1480	2.11	.0702	3.13
pty*	10.9	10.2	0.48	6.49	0.0596	2.66	.0224	1.00
11	10.7	10.2	0.436	18.3-1.32=16.98	0.1588	2.11	.0752	3.36
11	5.0	10.2	0.180	7.46-.6=6.86	0.1372	2.11	.0650	2.97
pty	5.0	10.2	0.215	2.91	0.0583	2.66	.0219	1.00
11	5.0	10.2	0.205	8.59-.6=7.99	0.1600	2.11	.0757	3.46
11	10.55	10.0	0.418	16.96-1.38=15.58	0.1477	2.11	.0700	2.94
pty	10.55	10.0	0.505	6.69	0.0634	2.66	.0238	1.00
11	10.55	10.0	0.445	18.30-1.38=16.92	0.1603	2.11	.0760	3.19
11	10.34	8.40	0.46	15.7-2.29=13.41	0.1296	1.73	.0749	3.15
11*	10.34	8.40	0.73	8.12-5.67=2.45	0.0737	1.73(.332)	.0413	1.70
11*	10.34	8.40	0.47	16.2-3.17=13.03	0.1260	1.73(.736)	.0990	4.1
11	10.01	8.2	0.525	17.5-2.12=15.38	0.1537	1.73	.0888	3.7
11	10.01	8.2	0.79	8.58-5.56=3.02	0.0302	1.73(.332)	.0526	2.2
11	10.45	8.2	0.488	16.4-3.21=13.19	0.1261	1.73(.736)	.0992	4.1
11	10.80	10.5	0.70	29.8-2.84=26.96	0.2495	1.73	.1442	5.1
pty	10.80	10.5	0.582	8.1	0.0750	2.66	.0282	1.0
11	10.80	10.5	0.285	12.3-4.18=8.12	0.0752	1.73(.736)	.0592	2.1
11	10.55	10.76	0.53	23.2-2.34=20.86	0.1976	1.73	.1142	4.8
11	10.55	10.76	0.767	10.9-5.79=5.11	0.0484	1.73(.332)	.0843	3.5
11	10.55	10.76	0.46	20.3-3.24=17.06	0.1617	1.73(.736)	.1271	5.3
	(1)	(2)	(3)	(4)	(5)	(6)	(7)	(8)

B

# EMENT RESULTS

ge r- l V	Power Loss in Cell $P_1$ , watts	Loss as % of Tube Output % $P_t$	Cell Length Consid'rd. L, cm	% Power Lost per cm % $P_t$ /cm	Enhancemt. of Dissip. Seal/wave- guide	Loss Ratio: <u>Side Walls</u> Broad Walls
	17.0-1.31=15.69	0.1480	2.11	.0702	3.13	N.A.
	6.49	0.0596	2.66	.0224	1.00	<u>.0046</u> .0178
	18.3-1.32=16.98	0.1588	2.11	.0752	3.36	N.A.
	7.46-.6=6.86	0.1372	2.11	.0650	2.97	N.A.
	2.91	0.0583	2.66	.0219	1.00	<u>.0045</u> .0174
	8.59-.6=7.99	0.1600	2.11	.0757	3.46	N.A.
	16.96-1.38=15.58	0.1477	2.11	.0700	2.94	N.A.
	6.69	0.0634	2.66	.0238	1.00	<u>.0049</u> .0189
	18.30-1.38=16.92	0.1603	2.11	.0760	3.19	N.A.
	15.7-2.29=13.41	0.1296	1.73	.0749	3.15	<u>2.45</u> 9.42+3.61
	8.12-5.67=2.45	0.0237	1.73 (.332)	.0413	1.73	
	16.2-3.17=13.03	0.1260	1.73 (.736)	.0990	4.16	0.188
	17.5-2.12=15.38	0.1537	1.73	.0888	3.74	<u>3.02</u> 11.62+1.57
	8.58-5.56=3.02	0.0302	1.73 (.332)	.0526	2.21	
	16.4-3.21=13.19	0.1261	1.73 (.736)	.0992	4.16	0.229
	29.8-2.84=26.96	0.2495	1.73	.1442	5.11	N.A.
	8.1	0.0750	2.66	.0282	1.00	<u>.0058</u> .0224
	12.3-4.18=8.12	0.0752	1.73 (.736)	.0592	2.10	N.A.
	23.2-2.34=20.86	0.1976	1.73	.1142	4.80	
	10.9-5.79=5.11	0.0484	1.73 (.332)	.0843	3.54	
	20.3-3.24=17.06	0.1617	1.73 (.736)	.1271	5.34	0.3

(4)

(5)

(6)

(7)

(8)

(9)

TABLE 6-

			HIGH POWER rf LOSS MEASUREMENTS			
Cell No.	Position	Seal Description See Table 6-20	Test Group	Window Frame Con-fig.	Tube Output Power $P_t$ , kw	Waveguide Water Flow $F_{wg}$ , cc/sec
1	1	Body I, P-1, Ni, BT	3	Full*	10.6	10.2
	2	Empty	3	Empty*	10.9	10.2
	3	Body I, P-1, Cu, BT	3	Full	10.7	10.2
1	1	Body I, P-1, Ni, BT	3	Full	5.0	10.2
	2	Empty	3	Empty	5.0	10.2
	3	Body I, P-1, Cu, BT	3	Full	5.0	10.2
1	1	Body I, P-1, Ni, BT	1	Full	10.55	10.0
	2	Empty	1	Empty	10.55	10.0
	3	Body I, P-1, Cu, BT	1	Full	10.55	10.0
2	1	Body H, P-1, Cu, BT	1	Full	10.34	8.40
	2	Body H, P-1, Cu, BT	1	S.W.*	10.34	8.40
	3	Body H, P-1, Cu, BT	1	B.W.*	10.34	8.40
2	1	Body H, P-1, Cu, BT	1	Full	10.01	8.2
	2	Body H, P-1, Cu, BT	1	S.W.	10.01	8.2
	3	Body H, P-1, Cu, BT	1	B.W.	10.45	8.2
3	1	Body H, P-1 (Pol.), Cu, BT	2	Full	10.80	10.5
	2	Empty	2	Empty	10.80	10.5
	3	Body H, P-1 (Pol.), Cu, BT	2	B.W.	10.80	10.5
4	1	Body H, P-7, Cu, BT	1	Full	10.55	10.76
	2	Body H, P-7, Cu, BT	1	S.W.	10.55	10.76
	3	Body H, P-7, Cu, BT	1	B.W.	10.55	10.76

Column Number:

(1)

(2)

TABLE 6-22

## HIGH POWER rf LOSS MEASUREMENT RESULTS

Flow	Tube	Waveguide	Voltage	Power Loss in	Loss as % Cell	% Cell	% Power	Enhance
Rate	Output	Flow	Differ-	Cell	of Tube	Length	Lost per	of Dis
g.	$P_t$ , kw	$F_{wg}$ , cc/sec	ential	$P_1$ , watts	Output	Consid'rd.	cm	Seal/g
			V, mV		% $P_t$	L, cm	% $P_t$ /cm	guid
1*	10.6	10.2	0.41	17.0-1.31=15.69	0.1480	2.11	.0702	3.13
ty*	10.9	10.2	0.48	6.49	0.0596	2.66	.0224	1.00
1	10.7	10.2	0.436	18.3-1.32=16.98	0.1588	2.11	.0752	3.36
1	5.0	10.2	0.180	7.46-.6=6.86	0.1372	2.11	.0650	2.9
ty	5.0	10.2	0.215	2.91	0.0583	2.66	.0219	1.0
1	5.0	10.2	0.205	8.59-.6=7.99	0.1600	2.11	.0757	3.4
1	10.55	10.0	0.418	16.96-1.38=15.58	0.1477	2.11	.0700	2.9
ty	10.55	10.0	0.505	6.69	0.0634	2.66	.0238	1.0
1	10.55	10.0	0.445	18.30-1.38=16.92	0.1603	2.11	.0760	3.1
1	10.34	8.40	0.46	15.7-2.29=13.41	0.1296	1.73	.0749	3.1
.*	10.34	8.40	0.73	8.12-5.67=2.45	0.0237	1.73 (.332)	.0413	1.7
.*	10.34	8.40	0.47	16.2-3.17=13.03	0.1260	1.73 (.736)	.0990	4.1
1	10.01	8.2	0.525	17.5-2.12=15.38	0.1537	1.73	.0888	3.7
.	10.01	8.2	0.79	8.58-5.56=3.02	0.0302	1.73 (.332)	.0526	2.2
.	10.45	8.2	0.488	16.4-3.21=13.19	0.1261	1.73 (.736)	.0992	4.1
1	10.80	10.5	0.70	29.8-2.84=26.96	0.2495	1.73	.1442	5.1
ty	10.80	10.5	0.582	8.1	0.0750	2.66	.0282	1.0
.	10.80	10.5	0.285	12.3-4.18=8.12	0.0752	1.73 (.736)	.0592	2.1
1	10.55	10.76	0.53	23.2-2.34=20.86	0.1976	1.73	.1142	4.8
.	10.55	10.76	0.767	10.9-5.79=5.11	0.0484	1.73 (.332)	.0843	3.5
.	10.55	10.76	0.46	20.3-3.24=17.06	0.1617	1.73 (.736)	.1271	5.3
	(1)	(2)	(3)	(4)	(5)	(6)	(7)	(8)

B

# EMENT RESULTS

Age	Power Loss in Cell $P_1$ , watts	Loss as % of Tube Output $\% P_t$	% Cell Length Consid'rd. $L$ , cm	% Power Lost per cm $\% P_t/\text{cm}$	Enhancement of Dissip. Seal/wave-guide	Loss Ratio: <u>Side Walls</u> Broad Walls
	17.0-1.31=15.69	0.1480	2.11	.0702	3.13	N.A.
	6.49	0.0596	2.66	.0224	1.00	<u>.0046</u> .0178
5	18.3-1.32=16.98	0.1588	2.11	.0752	3.36	N.A.
0	7.46-.6=6.86	0.1372	2.11	.0650	2.97	N.A.
5	2.91	0.0583	2.66	.0219	1.00	<u>.0045</u> .0174
5	8.59-.6=7.99	0.1600	2.11	.0757	3.46	N.A.
3	16.96-1.38=15.58	0.1477	2.11	.0700	2.94	N.A.
5	6.69	0.0634	2.66	.0238	1.00	<u>.0049</u> .0189
5	18.30-1.38=16.92	0.1603	2.11	.0760	3.19	N.A.
	15.7-2.29=13.41	0.1296	1.73	.0749	3.15	<u>2.45</u> 9.42+3.61
	8.12-5.67=2.45	0.0237	1.73 (.332)	.0413	1.73	
	16.2-3.17=13.03	0.1260	1.73 (.736)	.0990	4.16	0.188
5	17.5-2.12=15.38	0.1537	1.73	.0888	3.74	<u>3.02</u> 11.62+1.57
	8.58-5.56=3.02	0.0302	1.73 (.332)	.0526	2.21	
3	16.4-3.21=13.19	0.1261	1.73 (.736)	.0992	4.16	0.229
	29.8-2.84=26.96	0.2495	1.73	.1442	5.11	N.A.
2	8.1	0.0750	2.66	.0282	1.00	<u>.0058</u> .0224
5	12.3-4.18=8.12	0.0752	1.73 (.736)	.0592	2.10	N.A.
	23.2-2.34=20.86	0.1976	1.73	.1142	4.80	
7	10.9-5.79=5.11	0.0484	1.73 (.332)	.0843	3.54	
	20.3-3.24=17.06	0.1617	1.73 (.736)	.1271	5.34	0.3
	(4)	(5)	(6)	(7)	(8)	(9)



TABLE 6-22

Cell No.	Position	Seal Description See Table 6-20	Test Group	Window Frame Con-fig.	Tube Output Power $P_t$ /kw	Waveguide Water Flow $F_{wg}$ , cc/sec	Voltage Differ- ential V, mV
5	1	Body H,P-3 (20EU), Cu,BT	2	Full	10.8	10.4	0.345
	2	Body H,P-3 (20EU), Cu,BT	2	S.W.	10.8	10.4	0.525
	3	"	2	B.W.	10.8	10.4	0.325
6	1	Body H,Evap,Ti,Mo,Cu,BT	3	Full	10.1	10.1	0.665
	2	"	3	S.W.	10.1	10.1	0.83
	3	"	3	B.W.	10.2	10.1	0.385
6	1	"	3	Full	5.24	10.1	0.317
	2	"	3	S.W.	5.24	10.1	0.42
	3	"	3	B.W.	5.24	10.1	0.21
7	1	Body H,P-3 (Pol.), Cu,BT	2	Full	9.7	10.3	0.295
	2	"	2	Empty	9.7	10.3	0.425
	3	"	2	Full	9.7	10.3	0.380
8	1	Body BA,P-1,Cu,BT	3	Full	10.2	10.2	0.32
	2	"	3	S.W.	10.2	10.2	0.55
	3	"	3	B.W.	10.2	10.2	0.322
8	1	"	3	Full	5.25	10.2	0.157
	2	"	3	S.W.	5.35	10.2	0.275
	3	"	3	B.W.	5.35	10.2	0.167
9	1	Body BA,P-3,Cu,BT	3	Full	10.2	10.0	0.95
	2	"	3	S.W.	10.2	10.0	0.857
	3	"	3	B.W.	10.2	10.0	0.46

Column Number: (1) (2) (3)

TABLE 6-22 (Continued)

Test Group	Window Frame Con-fig.	Tube Output Power $P_t$ /kw	Waveguide Water Flow $F_{wg}$ , cc/sec	Voltage Differential V, mV	Power Loss in Cell $P_l$ , watts	Loss as % of Tube Output % $P_t$	Cell Length Consid'rd L, cm
2	Full	10.8	10.4	0.345	14.6-2.26=12.34	0.1143	1.73
2	S.W.	10.8	10.4	0.525	7.23-5.50=1.73	0.0160	1.73(.332)
2	B.W.	10.8	10.4	0.325	13.9-3.13=10.77	0.0957	1.73(.736)
3	Full	10.1	10.1	0.665	27.3-2.1=25.2	0.2495	1.73
3	S.W.	10.1	10.1	0.83	11.1-5.20=5.9	0.0584	1.73(.332)
3	B.W.	10.2	10.1	0.385	16.0-2.93=13.07	0.1281	1.73(.736)
3	Full	5.24	10.1	0.317	13.0-1.09=11.91	0.2275	1.73
3	S.W.	5.24	10.1	0.42	5.62-2.70=2.92	0.0557	1.73(.332)
3	B.W.	5.24	10.1	0.21	8.72-1.51=7.21	0.1375	1.73(.36)
2	Full	9.7	10.3	0.295	12.3-2.03=10.27	0.1059	1.73
2	Empty	9.7	10.3	0.425	5.8	0.0598	2.66
2	Full	9.7	10.3	0.380	16.1-2.03=14.07	0.1450	1.73
3	Full	10.2	10.2	0.32	13.3-1.97=11.33	0.1111	1.80
3	S.W.	10.2	10.2	0.55	7.44-5.23=2.21	0.0217	1.80(.332)
3	B.W.	10.2	10.2	0.322	13.5-2.82=10.68	0.1048	1.80(.736)
3	Full	5.25	10.2	0.157	6.5-1.01=5.49	0.1047	1.80
3	S.W.	5.35	10.2	0.275	3.7-2.74=0.96	0.0180	1.80(.332)
3	B.W.	5.35	10.2	0.167	7.0-1.47=5.53	0.1034	1.80(.736)
3	Full	10.2	10.0	0.95	38.6-1.97=36.63	0.3590	1.80
3	S.W.	10.2	10.0	0.857	11.35-5.23=6.12	0.0600	1.80(.332)
3	B.W.	10.2	10.0	0.46	18.9-2.82=16.08	0.1577	1.80(.736)

Column Number: (1) (2) (3) (4) (5) (6)

**B**

Continued)

Power Loss in Cell $P_l$ , watts	Loss as % of Tube Output % $P_t$	Cell Length Consid'rd L, cm	% Power Lost per cm % $P_t$ /cm	Enhancemt. of Dissip. Seal/wave- guide	Loss Ratio: <u>Side Walls</u> Broad Walls
14.6-2.26=12.34	0.1143	1.73	.0661	2.94	<u>1.73</u> 6.65+4.12
7.23-5.50=1.73	0.0160	1.73 (.332)	.0279	1.24	0.161
13.9-3.13=10.77	0.0957	1.73 (.736)	.0783	3.48	
27.3-2.1=25.2	0.2495	1.73	.1440	6.43	
11.1-5.20=5.9	0.0584	1.73 (.332)	.1018	4.54	0.45
16.0-2.93=13.07	0.1281	1.73 (.736)	.1007	4.50	
13.0-1.09=11.91	0.2275	1.73	.1314	5.87	
5.62-2.70=2.92	0.0557	1.73 (.332)	.0971	4.34	0.405
3.72-1.51=7.21	0.1375	1.73 (.36)	.1081	4.82	
12.3-2.03=10.27	0.1059	1.73	.0611	2.72	
5.8	0.0598	2.66	.0225	1.00	<u>.0046</u> .0179
16.1-2.03=14.07	0.1450	1.73	.0837	3.72	N.A.
13.3-1.97=11.33	0.1111	1.80	.0617	2.76	<u>2.21</u> 8.50+2.18
7.44-5.23=2.21	0.0217	1.80 (.332)	.0362	1.62	
13.5-2.82=10.68	0.1048	1.80 (.736)	.0789	3.52	0.207
5.5-1.01=5.49	0.1047	1.80	.0581	2.60	<u>0.96</u> 3.70+1.83
3.7-2.74=0.96	0.0180	1.80 (.332)	.0300	1.34	0.174
7.0-1.47=5.53	0.1034	1.80 (.736)	.0780	3.48	
38.6-1.97=36.63	0.3590	1.80	.1995	8.91	
11.35-5.23=6.12	0.0600	1.80 (.332)	.1002	4.48	0.38
18.9-2.82=16.08	0.1577	1.80 (.736)	.1189	5.31	
(4)	(5)	(6)	(7)	(8)	(9)

\*\*

\*\*

\*\*

C

### 6.5.5.3 Results and Discussion

Data obtained in the first set of measurements on the three-channel test cells were used to calculate the amount of power dissipated in each seal section. These results were then plotted (Fig. 6.73) to illustrate the relationship between power loss in seals and metallizing thickness for both nickel and copper plating. What was clear from the data in Fig. 6.73 was that the magnitude of power dissipated in the seal was determined primarily by the resistivity of the conductive material in the current-carrying zone immediately adjacent to the window dielectric. This is as expected, as dielectric seal losses in a 95.5% alumina ceramic cannot be distinguished from bulk seal losses.

#### 6.5.5.3.1 Characteristics of Ceramic-to-Metal Seals Tested in First Test Series

Table 6-20 lists the characteristics of the six seals tested in the first series. Waveguide window seals were simulated with a frame of Body I (96%  $\text{Al}_2\text{O}_3$ ) ceramic plates of 0.025" thickness and 0.830" width brazed into a rectangular J-band waveguide. The thickness of P-1 metallizing (75% Mo, 21% MnO, 4%  $\text{TiO}_2$ ) was varied between 0.0001" and 0.0017". One half of the samples carry copper overplate on the metallizing; the other half is nickel overplated. The latter variation will allow a comparison of results of these absolute measurements with previous relative measurements of conduction losses involving nickel overplated and copper overplated metallizing in test samples.

The data on metallizing and plating thicknesses were confirmed by sectioning samples. Fig. 6.74 shows photomicrographs (400X) of sections of the seals in test cell No. 3 (top) and No. 6 (bottom). In the upper picture the thin metallizing is not easily distinguishable from the nickel plate and is very irregular. The value of the thickness given in the table, therefore, is an average. The nickel overplate is intact. As an interesting feature, copper can be seen to have precipitated on the interface of the nickel overplate and copper-silver braze. Radio-frequency losses are, of course, not affected by that. The lower photomicrograph in Fig. 6.74 shows the seal in test cell No. 6 with thick metallizing. The copper overplate has been partially dissolved by the copper-silver braze. Approximately 50 percent of the metallizing surface is covered by copper, and the rest by a copper-silver alloy.

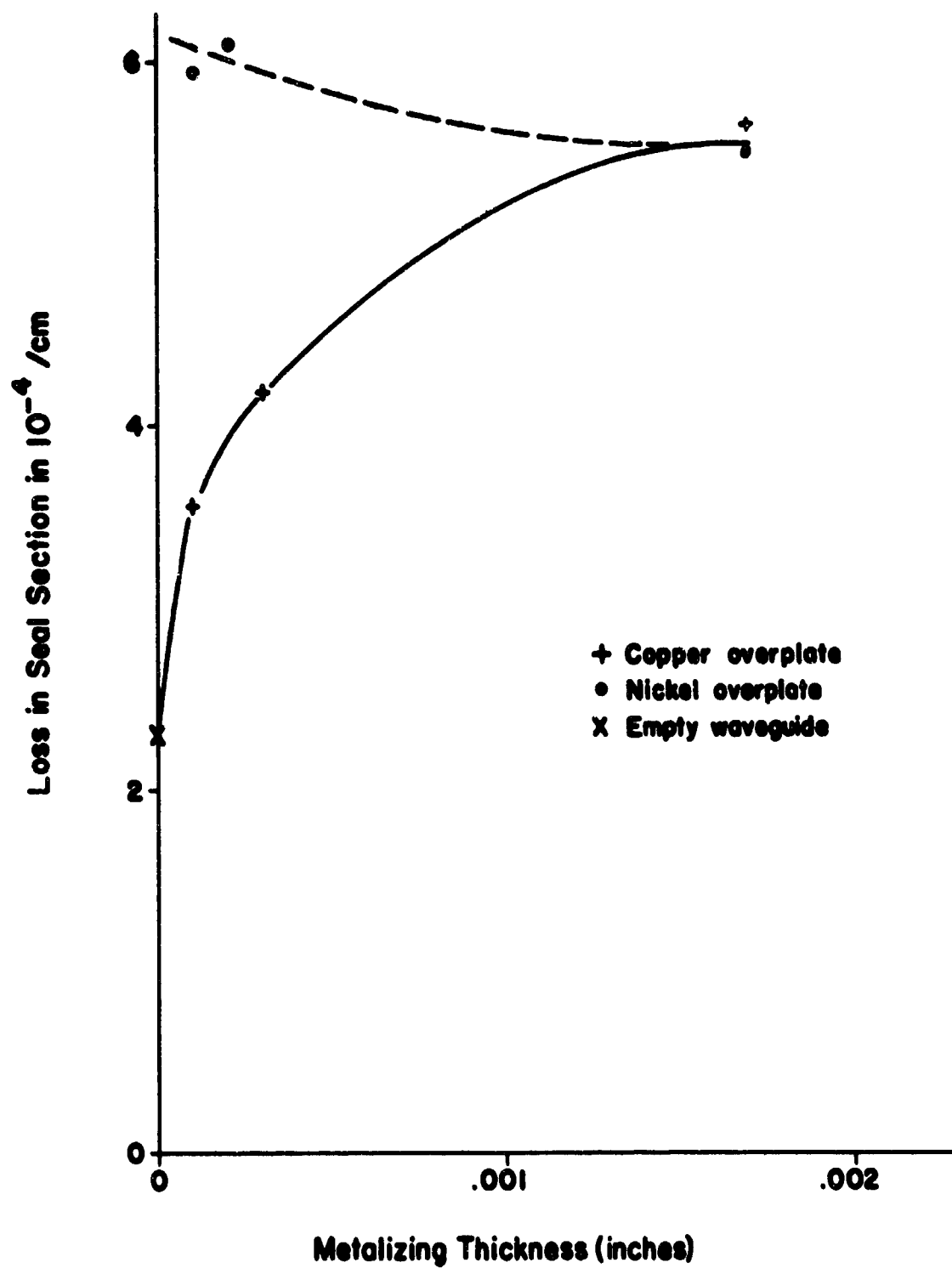


Figure 6.73: Power loss in dielectric-to-metal seal section of waveguide test cell vs metallizing thickness as a fraction of transmitted power.

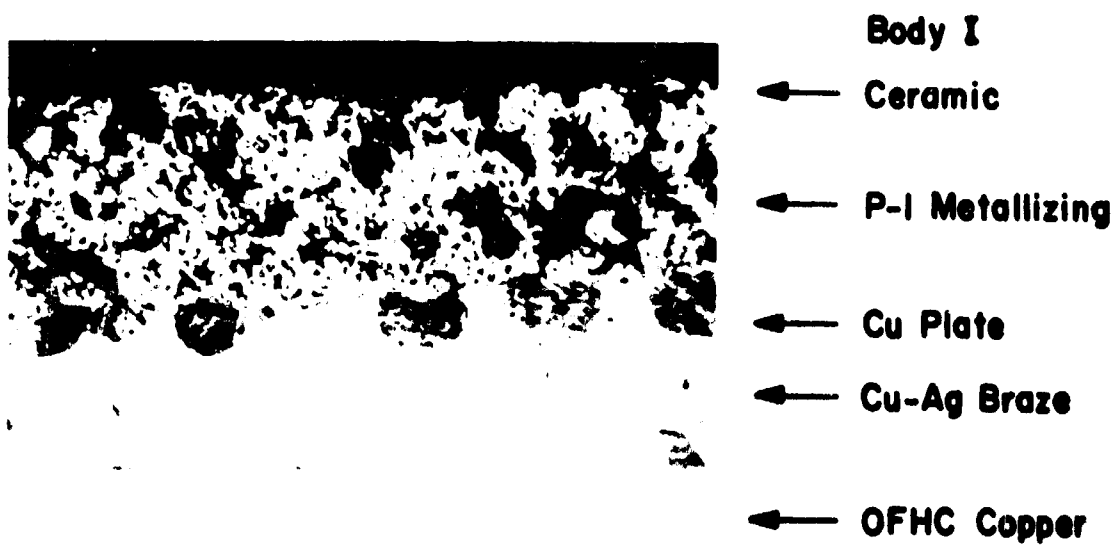
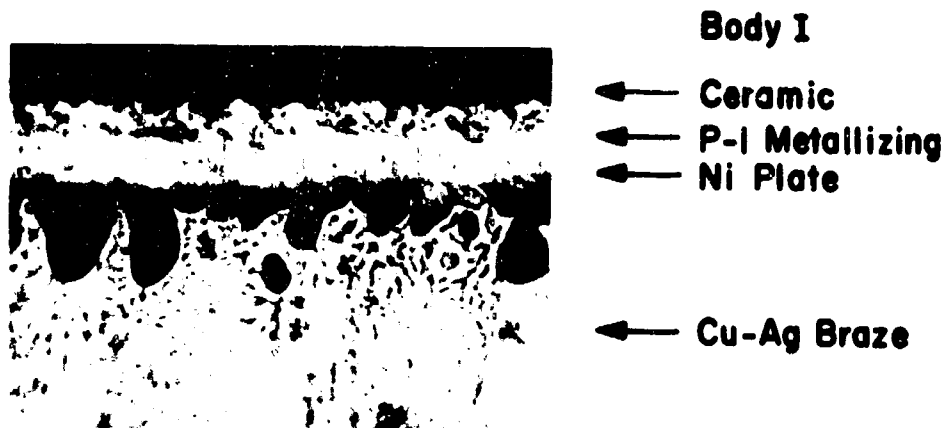


Figure 6.74: Sectioned seals in test cells No. 3 and No. 6.

As pointed out with many photos of sections in previous reports, the degree of interaction between various components of the dielectric-to-metal seals depends very critically on details of the sealing procedures, especially the hold times in the brazing step.

Both sections were scanned with an electron beam microprobe for the elements Cu, Ag, Ni, Mo, Mn (Fig. 6.75). Referring again to the top picture in Fig. 6.74 the seal in test cell no. 3, some of the visible features were clearly confirmed. These are the attack of the copper wall by the braze material, and the precipitation of copper from the braze on the nickel overplate. The irregularity of the metallizing shows as an overlapping of the molybdenum and nickel trace in Fig. 6.74 (top). The width of the molybdenum trace indicates a metallizing thickness of 0.4 mils. Manganese from the metallizing diffused into the ceramic and was detected 150 microns (6 mils) inside the ceramic accumulated in the grain boundaries or glassy phase regions of the alumina. The seal in test cell No. 6, Fig. 6.74 bottom picture, is characterized by the thick metallizing, which shows as a 2 mil wide peak on the Mo-scan in Fig. 6.75 (bottom). Again, manganese is shown to penetrate into the ceramic.

#### 6.5.5.3.2 Test Results

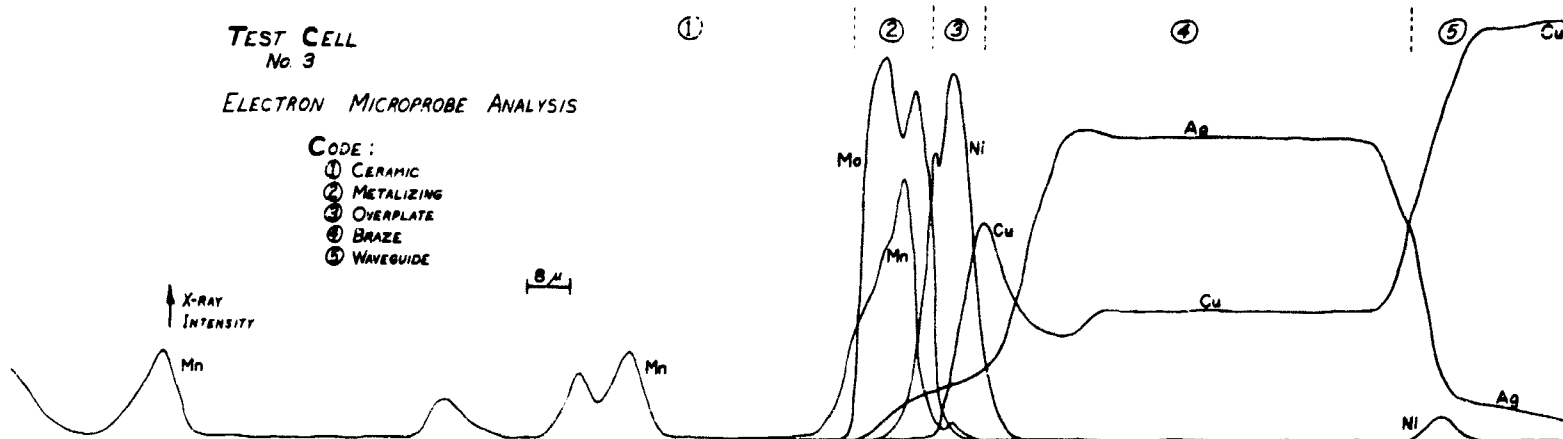
Test data obtained were the dissipation in all three cooling channels, and dissipation in the central channel. The difference between the two values is attributable to rf losses in the empty waveguide sections between the seal and the flanges on either side. Dissipation was related to the power transmitted and to the length of waveguide. Fig. 6.73 shows the measured ratio of power loss and transmitted power per travelled length of waveguide containing the seal plotted against the metallizing thickness. Copper overplating results in losses increasing with metallizing thickness to a constant value. The samples with nickel overplating came down from higher losses to this constant value with the thickness of metallizing increasing. Point (x) for zero metallizing thickness indicates losses measured in the empty portions of the waveguide test cells. Compared with this value, dissipation in the sealed portion is larger by a factor of about 2.5 for a metallizing thickness of about 0.001". The trend of losses with metallizing thickness is very similar to curves obtained for relative conduction losses measured previously and shown in Fig. 4.03 of the 7th Quarterly Report. Conduction losses are, therefore, predominant in the total seal dissipation.

TEST CELL  
No. 3

ELECTRON MICROPROBE ANALYSIS

CODE:

- ① CERAMIC
- ② METALIZING
- ③ OVERPLATE
- ④ BRAZE
- ⑤ WAVEGUIDE



TEST CELL  
No. 6

ELECTRON MICROPROBE ANALYSIS

CODE:

- ① CERAMIC
- ② METALIZING
- ③ OVERPLATE
- ④ BRAZE
- ⑤ WAVEGUIDE

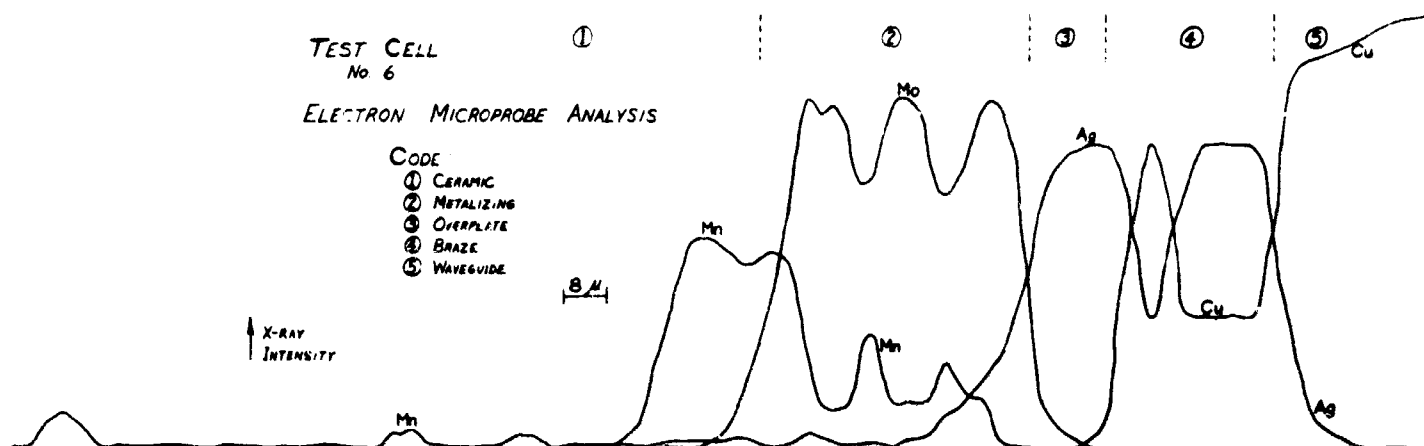


Figure 6.75: Electron microprobe analyses of seals in test cell No. 3 (top) and No. 6 (bottom).



#### 6.5.5.3.3 Discussion of Results

The purpose of this section is to relate the measured dissipation in the seal of a dielectric frame to the power losses in the seal of a rectangular slab window with a thickness of half a wave length. From the trend of the seal losses with metallizing thickness and from the pattern of the essentially undisturbed dominant mode, we may assume that dissipation in the seal is due to conduction losses caused by the wall currents flowing in the seal area. The results with the dielectric frame are now to be applied to the losses in the seal of a solid slab window.

In general, when an empty waveguide is filled completely with an ideal (loss-free) dielectric, wall conduction currents and the corresponding losses are increased due to changes in the electric and magnetic field distribution. Attenuation in J-band waveguide is increased from 1.5 db/100 feet to 3.3 db/100 feet when the empty waveguide is filled with a loss-free dielectric of a dielectric constant of 9.3. In terms of power, this is an increase of losses by a factor of 2.3. A resonant window being only half a wave length thick will cause a smaller increase of wall losses compared with a long dielectric-filled section because it maintains a different field distribution. The transverse electric field is reduced only towards the center area of the window. It is, therefore, reasonable to assume that the increase of wall losses will amount to a factor less than 2.3, estimated here to be 1.5.

A representative value of measured loss in the seal section is  $5.7 \times 10^{-4}/\text{cm}$  (see Fig. 6.73) of the power transmitted. A rectangular resonant window being 0.73 cm thick for transmission of 8 kmc, causes a power loss of  $4 \times 10^{-4}$ . This number is to be multiplied by the above factor of 1.5 to give  $6 \times 10^{-4}$ , which represents the dissipation in the dielectric-to-metal seal of a solid window.

Numbers available in the literature for total window dissipation average at  $3 \times 10^{-3}$  of the power transmitted. Compared with this number, our results indicate that the dissipation in the seal of a rectangular slab microwave window can be expected to be about 20 percent of the total heating.

The percentage of seal losses is larger for windows of very low-loss materials and for windows scaled down in size for use at frequencies above X-band.

The magnitude of loss in the seals is closely related to the thickness of metallizing used on the ceramic because this thickness comprised most of the zone in which the skin current flowed.

When thick metallizing was used, the conductive zone consisted entirely of molybdenum metallizing and whatever plating was used was outside the zone and did not affect losses. When very thin metallizing was used, the zone consisted primarily of the plating, nickel or copper, and the braze, thus the losses resulting from currents flowing in this zone were determined by the resistivity of the plating-braze layer. In the case of nickel, the losses were higher because the resistivity of nickel and the molybdenum-nickel intermetallic compounds ( $\text{MoNi}_4$ ,  $\text{MoNi}_3$ ,  $\text{MoNi}$ ) which were formed were higher than the metallizing alone. In the case of the copper plated seals, the losses were low (approaching the loss in an empty waveguide) because most of the skin currents were carried in the low resistivity copper or copper-silver braze layer, and no alloying involving molybdenum and copper or copper-silver took place.

The high power loss results presented in the curves of Fig. 6.73 were remarkably similar to the data obtained using the low power  $I^2R$  techniques described in section 6.3. Such strong agreement in results obtained from two very different measuring techniques was evidence that the results were most dependable.

Data obtained in the second set of measurements on the five-channel test cells were used as in the first set, but the cells were designed to indicate the relative magnitude of dielectric and conductive losses as well as to compare several seal compositions according to their relative lossiness as summarized in Table 6-20. The results of the second group of measurements appear in detail in Table 6-22.

Test cell #1 was constructed so as to provide a tie with the loss versus metallizing thickness data which was obtained in the first set of measurements which is presented in Fig. 6.73. A detailed description of this seal is in Table 6-22. This test cell was to provide additional data in the one mil metallizing portion of the

curve in Fig. 6.73 by comparing nickel plating to copper plating in full window frames with all other variables such as one mil metallizing thickness and Cu-Ag braze the same.

The results from runs under three different combinations of power level and cell orientation (see Table 6-22) all indicated the seal with copper plating had the higher loss and the loss in both types of seals was higher than the results from the previous set of tests. It was expected that the nickel plated seal would have the higher loss (see Fig. 4.06 9th Quarterly Report) but, as it did not, metallurgical examinations of the copper plated and the nickel plated seals were made in order to seek an explanation of the results.

Photomicrographs of polished cross-sections of both seals appear in Fig. 6.76. The seal with nickel plating appears in the upper photo. The metallizing is about 1.2 mils thick, but the nickel plated layer has been attacked by the Cu-Ag braze and only a thin layer remains. Nearly all of the skin currents would flow in the metallizing, so the  $I^2R$  losses would originate there. The seal with copper plating is shown in the lower photo. The metallizing is the same thickness as is the other seal. The copper plating is in better condition than the nickel plate, but there are many braze gaps. In this seal, the  $I^2R$  losses would occur in the metallizing layer as in the nickel plated seal. Because of the metallizing thickness involved, the difference in loss between the two seals was certainly caused by a factor other than the type of plating. The higher loss in the copper plated seal could be an effect of the braze gaps or might be attributed to a higher resistivity of the metallizing which could not be determined by a metallurgical examination. However, the copper plated metallizing did not polish well because it was very brittle or punky. This condition could also give the metallizing greater electrical resistivity and thereby increase the losses in this region.

The reason for both loss values being higher than comparable seals in the previous series of measurements remained unexplained. It may have resulted from a high VSWR in the second series of tests as compared to the first, but this at first did not seem to be the case because loss per centimeter measured in empty waveguide channels was practically identical to that in the earlier measurements for all runs. However, the empty waveguide loss values for the first group of measurements were obtained from outer cooling channels whose temperature could have been affected by losses originating in the flanges at each end of the test cells. This would

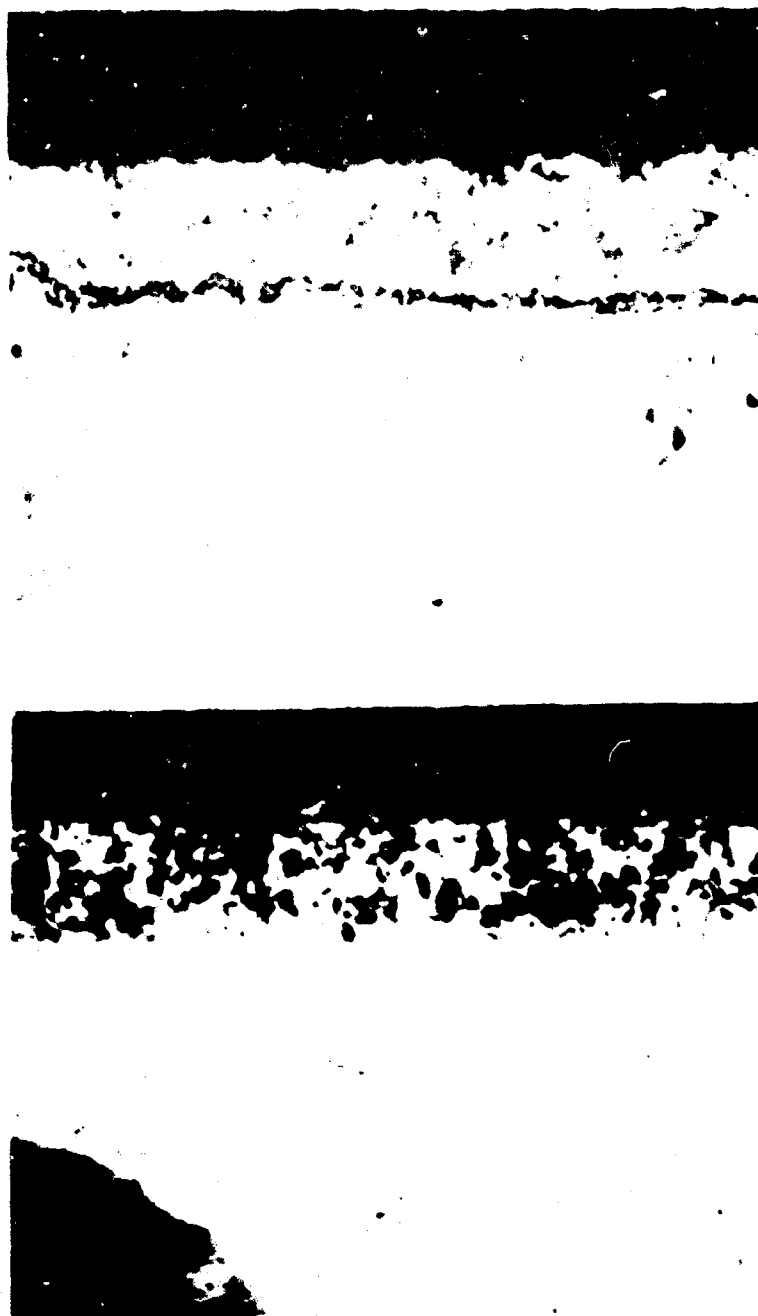


Figure 6.76: Top — Body 1 ceramic with P-1 metallizing, thin nickel plating and Cu-Ag braze.  
 Bottom — Body 1 ceramic with P-1 metallizing, copper plating, and Cu-Ag braze showing  
 part of a braze gap.

result in empty waveguide loss readings which were in error on the high side. They would then appear equal in magnitude to empty waveguide losses, measured in thermally isolated central channels, in the five-channel test cells used in the second test series. The latter might, in fact, be higher than in the three-channel test cells because of a higher local VSWR in the five-channel cells.

The results from cells 2, 5, 7 and 8 (see Tables 6-20 and 6-22) were credible and consistent with each other and with theory. The most useful information obtained was in regard to the relative amounts of dielectric and conduction losses. The ratio of conduction loss in the side walls to total loss in the broad walls (0.19:1 average of five) was always less than the 0.26:1 side wall to broad wall ratio of conduction loss only, which was obtained by calculation.

This was sufficiently removed from the ratio of the side wall to broad wall areas (0.45:1) to indicate that the results were determined by factors other than simple seal area ratios. The difference between the calculated conduction loss ratio of 0.26:1 and the measured loss ratios which averaged 0.19:1 was attributed to the dielectric loss in the broad walls.

The amount of dielectric loss in the broad walls was calculated from the results by assuming it to be the quantity necessary to shift the side wall to broad wall loss ratio from 0.26:1 to the measured ratios which averaged 0.19:1. For example, in the first run on cell #2, 2.45 watts and 13.03 watts dissipation (from Column 4, Table 6-22) were measured in the side walls and broad walls respectively to give a ratio of  $2.45/13.03 = 0.188$ . If the broad wall loss was only 9.42 watts, the ratio would have been 0.26:1. Therefore 9.42 watts were attributed to conduction loss in the broad walls and the additional 3.61 watts were attributed to dielectric loss. The loss ratio was broken down as follows:

$$\frac{\text{Side Wall Loss}}{\text{Broad Wall Loss}} = \frac{\text{Conduction Loss}}{\text{Conduction+Dielectric Loss}} = \frac{2.45}{9.42+3.61} = 0.188$$

The magnitude of dielectric loss measured in these test cells was about equal to the amount of conduction loss in the side walls, an average of about 1/4 of the total loss in the broad walls, or 1/5 of the total loss for the entire seal. Therefore, conduction loss was the pre-dominant contributor to the total seal losses, so efforts

to reduce seal losses should concentrate on minimizing those conditions which contribute to conduction losses.

This approach may consist of minimizing the quantity of high resistance material such as molybdenum and maximizing the low resistance material such as copper. This concept was tested in cell number 6 using evaporated molybdenum metallizing (see Table 6-20). The results from this test cell were unsatisfactory because of separation of the evaporated copper from the evaporated metallizing which left numerous voids in the seals. Diversion of skin currents by these voids caused abnormally high losses in the seals which could not be considered a true picture of the quality of this type of seal.

Further analysis of the dc conduction and rf conduction data presented in this final report indicates that the premise that a molybdenum evaporated seal will be low loss is in error. The results obtained are thus not unexpected on this count also.

The results from cells 3, 4, 6, 9 and 10 were inconclusive and were apparently affected by some anomaly or unaccounted for variables. Losses in the seals in these test cells were unusually high and, in most, the side wall to broad wall loss ratio was too high to enable calculation of dielectric losses. The data has been exhaustively re-checked. No sources of error can be detected. It is regrettable that a third series of experiments cannot be programmed to resolve these discrepancies.

The overall high power rf loss data presented shows —

- 1) that the seal losses were of the order of 0.1% of the total rf power transmitted per cm of seal length (in direction of waveguide axis).
- 2) the results confirm those presented for the prior electrical measurements. The lowest loss seal investigated is thin metallizing which is copper plated and Cu-Ag brazed (see Fig. 6.73).
- 3) the dielectric losses for the metallized 99.5% alumina (Body H) is approximately one fourth of that due to conduction.
- 4) Dielectric losses introduced due to metallizing paint reactions in 94% alumina bodies can be neglected.

While further analysis of the data may be made as in other sections, in the interest of brevity, it is left to the interested reader to consider Table 6-22 in more depth than has been attempted in this summary.

1. R. A. Dehn and J. N. Close, "Surface Resistivity of Metals and Dielectric-Metal Joints", Proceedings of the Fourth National Conference on Tube Techniques, New York University Press, 1959.
2. E. W. Ernst and O. T. Purl, "Electrical Losses in Ceramic-to-Metal Seals", University of Illinois Technical Report.
3. Edward L. Ginzton, Microwave Measurements, McGraw-Hill Book Company, Inc., 1957.
4. Carol G. Montgomery, Technique of Microwave Measurements, McGraw-Hill Book Company, Inc., 1947.
5. James R. Floyd, "Effect of Secondary Crystalline Phases on Dielectric Losses in High-Alumina Bodies", J. Am. Ceram. Soc., vol. 47 (11) 539-43 (1964).



## 7.0 SUMMARY

### 7.1 Introduction

The main purpose of this study was to better understand the electrical properties of ceramic-to-metal seals and, if necessary, improve them. An interpretative analysis of the knowledge concerning ceramic-to-metal seals was presented in the first four quarterly reports. This analysis coupled with "probing" key experiments was conducted as a prelude to intensive experimental work.

The experimental work can be broken down into two areas -

- (1) electrical studies concerning the seal region, (Task III) and
- (2) supporting studies to outline the main parameters involved in ceramic-to-metal sealing (Tasks I and II).

The purpose of Tasks I and II was to act as a firm interpretive support to Task III. Although at first these studies were distinct, by the end of the program they had constructively intermeshed.

In order to present a logical picture of ceramic-to-metal seal technology, the basic principles\* involved are first reviewed, this is followed by a discussion of the experimental aspects of the main "supporting studies" and concluded with a review of the experimental electrical studies.

### 7.2 Basic Seal Considerations

Fig. 4.36 shows a schematic micro-structure of a 94% alumina ceramic, Body A (Table 4-1). Two distinct phases can be seen, the alumina ( $\text{Al}_2\text{O}_3$ ) crystal phase and the glassy phase surrounding the crystals.

Fig. 4.37 shows the phases in more detail and Fig. 4.38 shows that the "glassy" phase can undergo modification by subsequent heat treatment, e.g., at  $1100^\circ\text{C}$ . This modification involves the precipitation of crystals of anorthite ( $\text{CaO} \cdot 2\text{SiO}_2 \cdot \text{Al}_2\text{O}_3$ ) from the glassy phase. This

---

\*A condensed version of the first four quarterly reports.

phenomena is termed "devitrification". The glassy phase amount, composition and devitrification tendency are all important in determining the manufacture of a reliable ceramic-to-metal seal.

Fig. 7.01 shows a schematic of the metallizing systems commonly used for electron tubes. The first system (A) shows a metallizing paint (see Table 4-22) composed of molybdenum, silica and manganese, P-8, sintered onto a sapphire substrate. On heating this paint to metallizing temperature ( $1400^{\circ}\text{C}$ ) in a wet hydrogen-nitrogen atmosphere, the  $\text{MnO-SiO}_2$  combines with the alumina of the substrate and generates a molten mass which draws the particles of molybdenum together to create a sintered metal sponge. On cooling, the melt solidifies and forms a chemical and/or semi-conductive bond both with the molybdenum sintered sponge and with the alumina substrate which is vacuum tight. The metallized ceramic is now ready for plating with a wetting layer and a subsequent braze to a metal member to complete the ceramic-to-metal seal.

Fig. 7.01 (B) shows the result of the same type of process on a 99% alumina body and Fig. 7.01 (C) similarly shows the same on a 94% alumina. In the case of the latter system, it is possible to use just pure molybdenum powder, such as P-4M, suspended in a lacquer as the metallizing paint. At the metallizing temperature of  $1400^{\circ}\text{C}$ , the molybdenum particles will sinter together on the ceramic surface and concurrently the glassy phase of the ceramic will become fluid enough to flow out from the ceramic and infiltrate the pores of the molybdenum sponge. On cooling, the glassy phase will remain strongly adherent to the sintered sponge and to the alumina ceramic and will form a vacuum tight bond. As before, this system can then be brazed to the metal member to complete a vacuum tight seal.

Fig. 4.50 shows a cross-section of a 94% alumina ceramic seal. On close inspection of the glassy phase interface of this seal, one can observe crystal species which have devitrified during the initial cooling or subsequent brazing processes. Such physical changes are shown to affect the performance of the ceramic-to-metal seal, (section 4.5.3.3).

In order to investigate the physical chemistry and crystallography of the ceramic-to-metal seals further, electron microprobe trace analyses of the metallizing have been conducted. This technique has been supplemented with

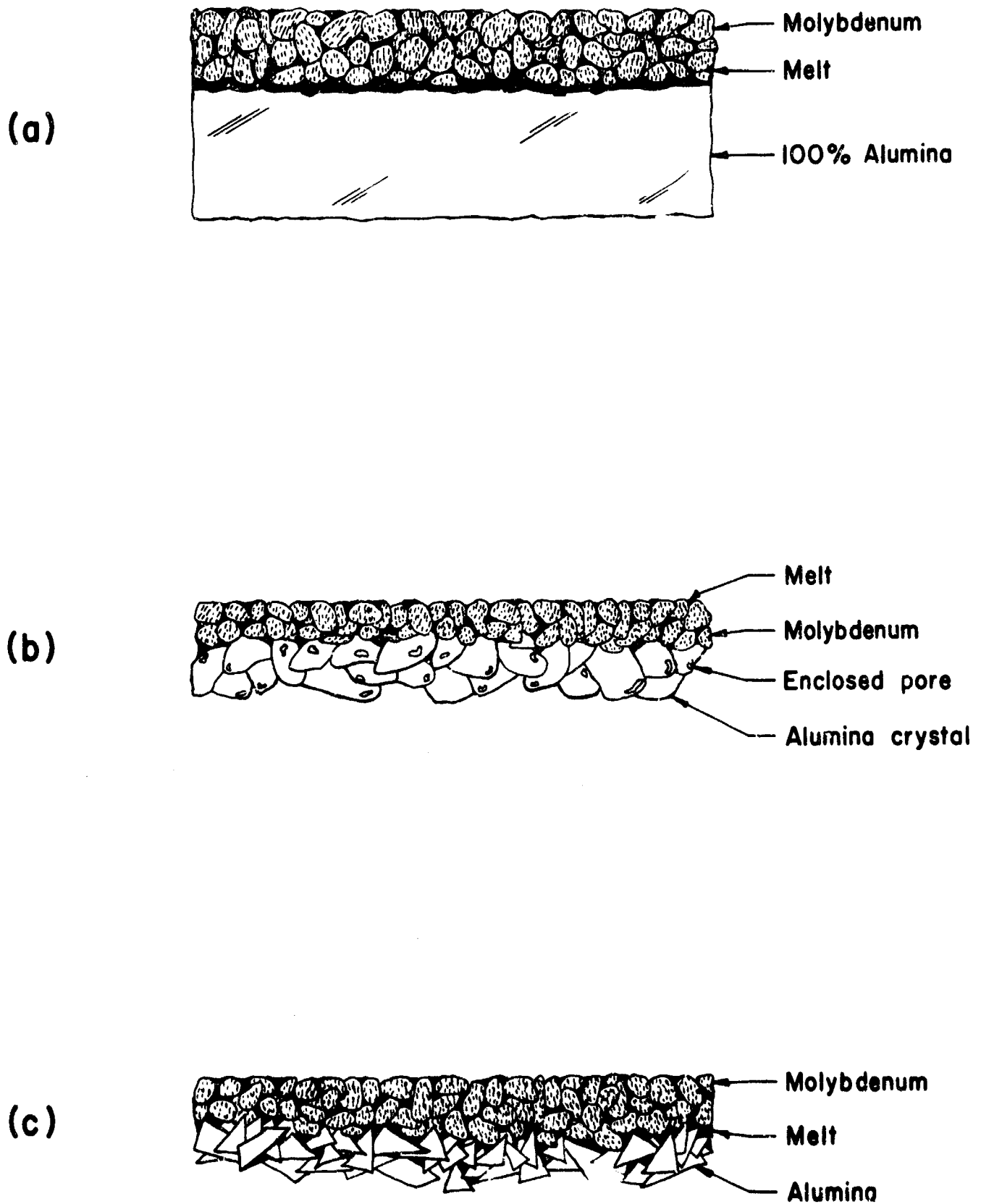


Figure 7.01: Schematic representation of a metallized layer on (a) single crystal sapphire (b) a 99.5% alumina body (c) a 94% alumina body.

spectrographic analysis, X-ray diffraction analysis and with electron microscope scans of interesting areas. Typical examples of the results of these techniques are given in Figs. 4.52, 4.53, 4.56 and Table 4-27.

The mechanical performance of ceramic-to-metal seals has been determined using the direct tensile test vehicles shown in Figs. 4.01, 4.02 and the "micro-tensile" peel test vehicles shown in Fig. 7.02. Figs. 4.83 and 4.84 show a shear test arrangement that was developed, as an analysis of the stresses at the seal interface indicating that a shear test was also of interest in evaluating seals.

Fig. 7.03 schematically shows that in the shear stress situation, each layer of the seal has to support the full loading imposed upon it while in the tensile test situation, due to its lower modulus of elasticity, the weak glassy layer tends to be supported by the adjacent stronger metallic and ceramic layers.

A cross-section of a torn seal from the drum peel shear test is shown in Fig. 7.04.

### 7.3 Supporting Studies

The number of component oxides involved in ceramic systems are rather small but still sufficiently large to be confusing. It was therefore decided in the main experimental phase of this program to investigate a model ceramic system: the calcium oxide, aluminum oxide, silica system ( $\text{CaO-SiO}_2\text{-Al}_2\text{O}_3$ ). With this in mind, three bodies were formulated from the following components:

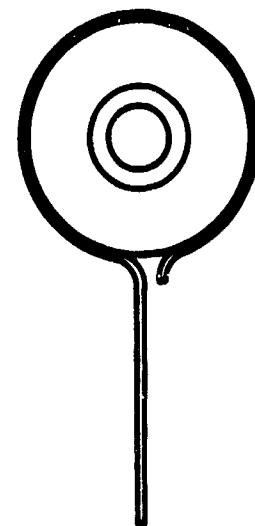
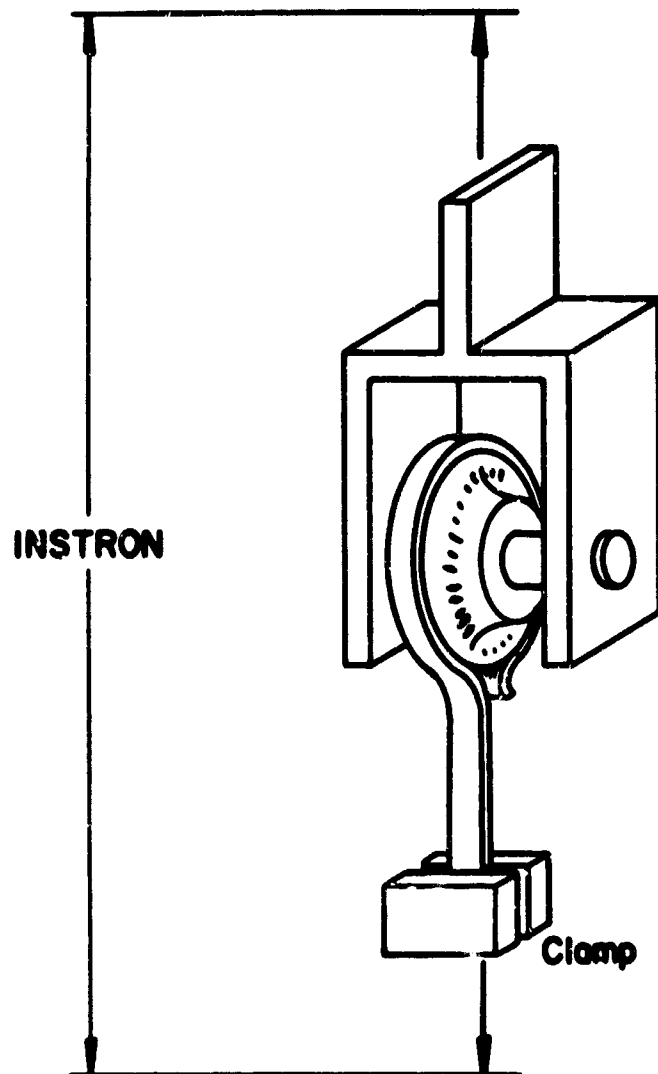
$\text{SiO}_2\text{:CaO} / 1\text{:}1$  - balance 94%  $\text{Al}_2\text{O}_3$  - Body 941

$\text{SiO}_2\text{:CaO} / 2\text{:}1$  - balance 94%  $\text{Al}_2\text{O}_3$  - Body 942

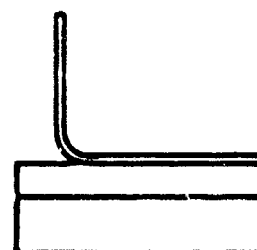
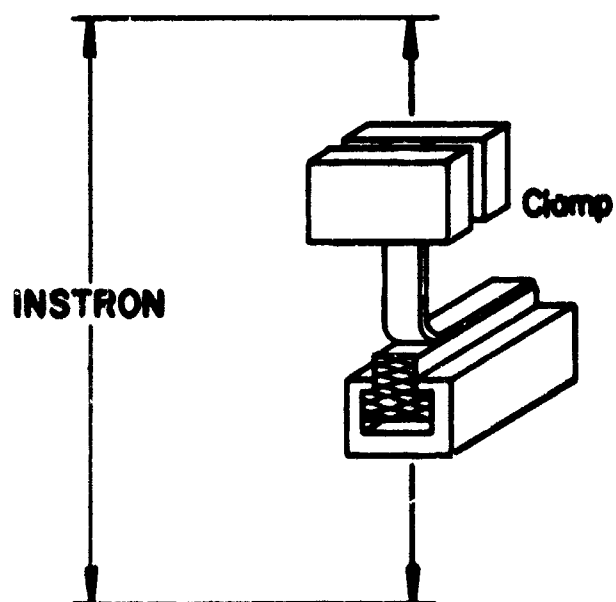
$\text{SiO}_2\text{:CaO} / 2\text{:}1$  - balance 99%  $\text{Al}_2\text{O}_3$  - Body 992

at five different maturing temperatures. In addition, G. E. Lucalox (99.75% alumina, 0.25% MgO) and sapphire (100%  $\text{Al}_2\text{O}_3$ ) were investigated, (Table 4-1). The grain size of the special alumina ceramics was obtained as a function of the firing temperature of the ceramic, Fig. 4.08.

The  $\text{CaO-SiO}_2\text{-Al}_2\text{O}_3$  phase diagram was intensively studied and two binary phase diagrams at the joins 1:1  $\text{SiO}_2\text{/CaO-Al}_2\text{O}_3$  and 2  $\text{SiO}_2\text{/CaO-Al}_2\text{O}_3$  were constructed, Figs. 4.03 and 4.04. From the knowledge of the diffusion-corrosion phenomena of alumina by calcia-alumina-silica



**Drum Peel  
Test Piece  
(ASTM CLM-15)**



**Tab Peel  
Test Piece**

**Figure 7.02: Diagrammatic representation of drum peel and tab peel test fixturing.**

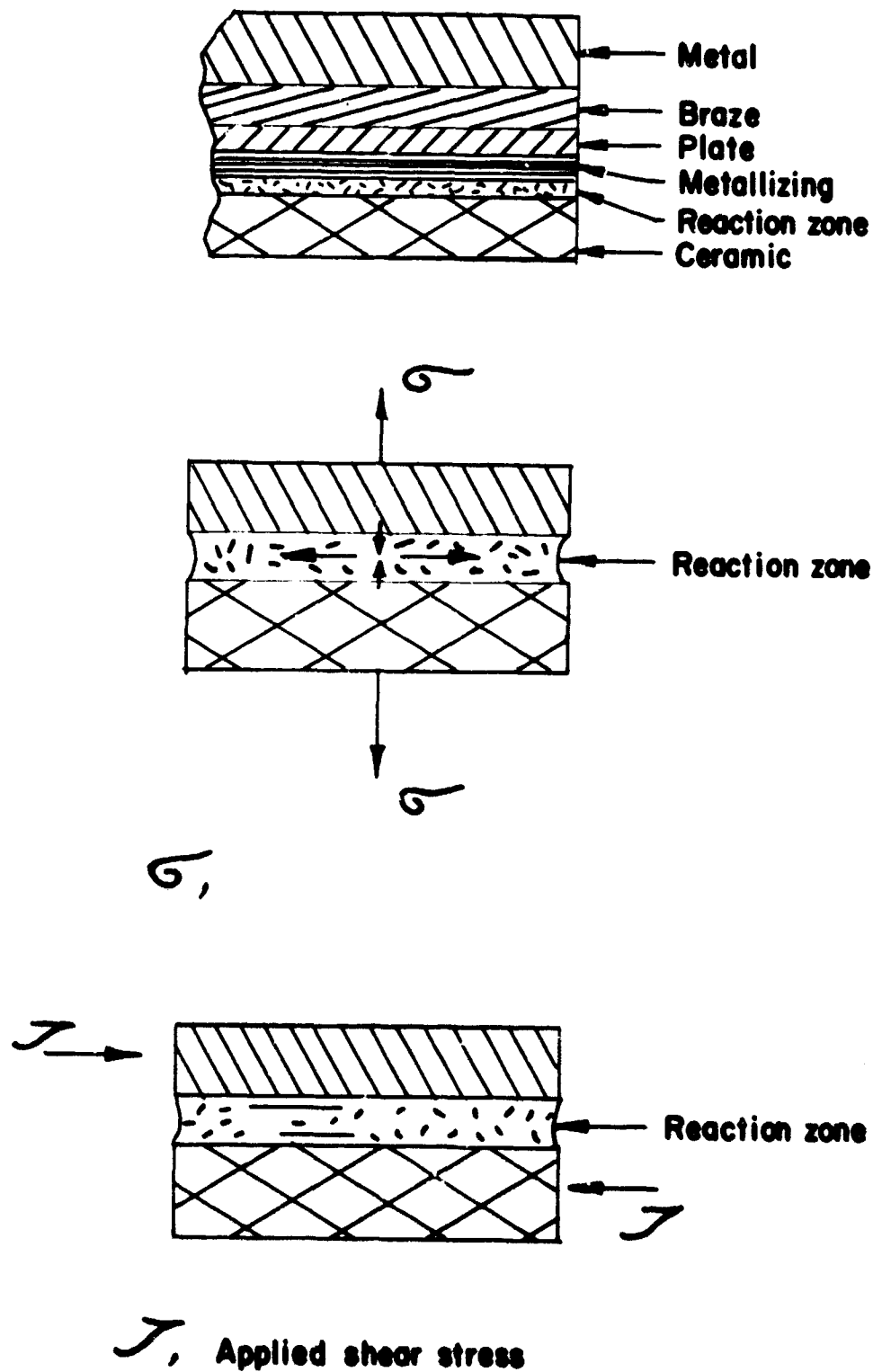


Figure 7.03: (a) Schematic diagram of seal showing laminar construction (idealized).

(b) Application of tensile stress to laminate results in effective opposing of compressive stresses in the lower-modulus, nonmetallic phases, which partially offsets the tensile stress. The lower the modulus for a given material strength (of the reaction zone material) the greater the seal strength.

(c) Application of shear stress is equally felt by all layers of laminate and weakest layer determines the seal strength.



Figure 7.04. Ceramic-to-metal seal, using Body E, showing parting in the weakest layer of the seal. Silver-copper braze alloy has penetrated the unplated Kovar giving the weakest zone.

melts, the rate controlling solution mechanism in micro-thicknesses of melts in ceramics and metallizing layers was found to be due to chemical control, Section 4.2.3.2.6. Micro-structure (grain growth) considerations supplemented by X-ray diffraction data on the interior and exterior crystalline condition of the ceramic bodies after various processing conditions, Figs. 4.10, 4.11, 4.12 indicated that "near" equilibrium condition is obtained in the special bodies. Confirmation of this finding was attempted by estimating the amount of glassy phase present as presented by electron microscope scans of the micro-structure of the ceramics. Attempts were also made to obtain precise chemical analysis of the glassy phase of the ceramic by electron microprobe and conventional chemical analysis techniques. From such studies, together with sag bar studies, Table 4-1, and prior viscosity work on molten glasses reported in the literature, Figs. 4.24 and 4.25, the viscosity or fluidity of the glassy phase was found. This information is of prime usefulness in developing a quantitative picture of the mechanisms underlying the metallizing process.

The integrated information obtained above also enables one to interpret MoR strength data versus firing temperature of the ceramic and the deformation behavior of the ceramic under load during metallizing.

Many metallizing paints were formulated to test our specific mechanical and electrical hypothesis, with regard to seal behavior; the paints were listed in Table 4-22. The particle size distribution of the molybdenum metal paint single phase system, P-4M, as analyzed by the Coulter electronic counter technique, is shown in Fig. 4.43. This technique has for the first time allowed one to obtain accurate particle size distribution for a metallizing composition and is a valuable process control tool.

The paint analyzed above is shown in Fig. 4.72, after being metallized to a 942 body at two temperature levels. At the lower metallizing temperature (1425°C), as predicted from the viscosity data garnered above, no flow out of the glassy phase occurred, while at the higher temperature (1600°C) complete glassy phase flow-out did occur. As shown in Figs. 4.62, 4.65, 4.68, this corresponded with a dramatic increase in seal strength and also with metallized surface hardness, Table 4-36. Similar results were obtained with the 941 and 992 ceramic bodies.



Experimental studies were carried out on the properties of the glassy phase of the special ceramic bodies in order to obtain additional insight into the metallizing process. Such work included devitrification studies, sessile drop surface tension measurements, thermal expansion measurements, metal evaporation-deposition substrate studies, sintering studies and chemical solution kinetics concerning the solution of molybdenum in the glassy phase. The results of these techniques confirmed the general picture that was developed concerning ceramic-to-metal seals. For instance, it was found that the contact angle between the metal member and the glass sessile drop increased from  $15^\circ$  to  $60^\circ$  as the furnace atmosphere went from the wet hydrogen-nitrogen mixture (+  $100^\circ\text{F}$  dew point) to a dry mixture of  $-100^\circ\text{F}$  dew point. This correlates with the well known fact that it is easier to metallize in a wet atmosphere than in a dry atmosphere. It was established that chemical and/or semi-conducting bond mechanisms were responsible for the actual joining of the refractory metal to the oxide substrate. For this bonding to occur, either the metal phase had to be deposited on the oxide substrate by vapor phase processes or the oxide phases had to move by viscous flow processes (e.g. glassy phase migration) in order that the initial atom-to-atom contact could be made.

The work on alumina ceramics was extended to beryllium oxide, Table 5-1, and fused quartz. Consideration was also given to boron nitride (BN). Fig. 5.03 shows a cross-section of a BeO ceramic-to-metal seal. As an example of the utility of the microprobe technique, one should examine the results of traces conducted across two BeO ceramics that are shown in Fig. 5.04 and 5.05. The marked difference in penetration of MnO and  $\text{TiO}_x$  from the metallizing paint (Mo-MnO- $\text{TiO}_2$ ) can be completely explained in terms of composition and consequent viscosity of the glassy phase initially present in the ceramic. Fig. 5.06 shows a cross-section of quartz to metal seal which employs the technique of evaporated metallizing and pressure sealing, using evaporated Ti followed by molybdenum and gold as the metallizing members, which is pressure sealed to a gold metal member at  $800^\circ\text{C}$ .

#### 7.4

#### Electrical Studies

The electrical studies were programmed concurrently with the mechanical studies. These studies fall into three main areas -

- (1) dc resistivity measurements of metallizing as a function of temperature
- (2) low power rf measurements which may be subdivided into conduction ( $I^2R$ ) studies and dielectric studies
- (3) high power rf studies.

The metallic conduction path through the metallizing layer is rather tortuous as is shown schematically in Fig. 6.01. Consequently the resistance of the metallizing layer is 10 to 100 times greater than that of a pure molybdenum layer. Such data was used as an index of the progress of the sintering of the molybdenum layer, Table 4-37. It was found that a marked drop in resistance occurs as the molybdenum metal particles are sintered and drawn together by emergent glassy phase from the ceramic.

A determination of the coefficient of electrical resistivity enables one to obtain an insight into the relative contributions of metallic conduction and non-metallic semi-conduction behavior to the overall conduction process occurring in the ceramic-to-metal seal; typical data is presented in Fig. 6.06. As the amount of non-metallic phase in the metallizing layer is increased, so the coefficient of electrical resistivity becomes less positive. Fig. 6.11 shows that when the metallic portion of the metallizing is partially or completely removed, the temperature coefficient of the remaining layer becomes negative, thus displaying its semi-conducting nature.

It may be noted from Fig. 6.06 that even in the absence of semi-conduction inducing oxides such as MnO and TiO<sub>2</sub> in the glassy layer, the layer still displays a small measure of semi-conducting behavior. This can be due to solution of molybdenum as molybdenum metal and molybdenum ions through the bulk of the glassy phase as well as to boundary effects at the glass-metal interface.

An analysis of the results of the dc electrical studies leads to the development of the theory that a chemical and/or semi-conducting bond exists at the interface between

the metallic and the glassy layers of the metallizing. While in the case of a glassy insulator phase such as  $\text{CaO-SiO}_2\text{-Al}_2\text{O}_3$ , chemical bonding may predominate, in the case of the addition of the variable valence ions Mn and Ti as  $\text{MnO}$  and  $\text{TiO}_2$  to the metallizing phase, it is to be expected that a semi-conducting bonding mechanism will become important.

The plated "wetting" layer which is often placed on top of the metallizing can influence its electrical properties as is shown in Fig. 6.19. Whereas a copper layer does not increase the electrical resistivity of the layer as a function of processing time at high temperatures ( $800^\circ\text{C}$  -  $1000^\circ\text{C}$ ), nickel, by its continued diffusion into and reaction with the metallizing layer to form Mo-Ti inter-metallic compounds, raises the resistance and consequent rf losses in the seal region.

Fig. 6.24 shows a 10 Gc test cavity used to determine  $I^2R$  losses. The ceramic-to-metal seal is placed in the region of high current density to maximize conduction losses; using a balance bridge method, the lossiness of the cavity is compared against a standard cavity in which the loss can be continuously changed by means of a variable-length, lossy insert rod joined to a micrometer head. Typical results are shown in Fig. 6.32. In the case of the copper wetting layer, used in conjunction with the P-1, Mo-MnO- $\text{TiO}_2$ , metallizing on Body A, a 94% alumina ceramic, one can see that as the thickness of the metallizing increases, the losses increase, for more and more current is carried in the metallizing. With the use of the nickel plate wetting layer, the losses decrease as the metallizing thickness increases. This result is to be completely expected in view of the dc results described above and shown in Fig. 6.19.

The low power dielectric loss measurements were carried out in the test cavity shown in Fig. 6.46. A 60 mil thick metallized ceramic disc was placed between the pillars of the re-entrant cavity in the region of high electrical field intensity in order to maximize the dielectric losses due to the semi-conducting and insulating components of the metallizing layer. The reduction in the quality of the cavity as determined from VSWR measurements was taken as the indicator for dielectric loss. Typical quality (Q) values on various metallizing on ceramics as a function of various ceramics are shown in Fig. 6.62. Further information presented in Fig. 6.63 concerns the increase of dielectric loss as a function of sintering time and by inference, sintering temperature.

Dielectric losses may be minimized by eliminating oxides such as  $MnO$  and  $TiO_2$  from the metallizing paint and substituting low loss glasses such as barium-aluminum-silicate in the metallizing layer on +99% alumina ceramics. In the case of the 94% alumina ceramics, pure molybdenum could be used and the dielectric losses were again minimized as the glassy phase occurring in such ceramics is low loss, although it was found that a 94% alumina displayed the same order of loss regardless of the metallizing.

Having obtained an understanding of the factors influencing losses in seals, attention was turned to measuring losses in ceramic-to-metal seals for the high power situation. A 10 kw klystron operating at 8 Gc was used to pass power into a number of waveguide cells containing "windowettes" of the ceramic-to-metal seals under investigation. The diagrammatic set-up of one such cell showing the frame-like construction of the windowettes and the water coolant channels is shown in Fig. 6.65. By using a minimum of ceramic, one is able to measure the electrical losses arising purely from the effects of introducing the ceramic-to-metal seals into the waveguide. Fig. 6.70 shows the general view of the equipment including the calorimetric set-up, the waveguide assembly, the klystron power source and the associated electrical equipment used. The temperature rise recorded was of the order of  $1^{\circ}C$  and was measured using differential thermopiles. Fig. 6.73 presents typical results obtained with this set-up and Table 6-66 gives a detailed tabulation of all the measurements made. The losses occurring in ceramic-to-metal seals are of the order of 0.1% of the power transmitted. It should be noted that the results on 96% alumina bodies correlate remarkably well with the low power conduction loss measurements shown in Fig. 6.32, indicating that dielectric losses were relatively low (as noted previously).

- 1) It has been shown from the average of ten measurements that the ceramic-to-metal seal region accounts for approximately 25% of the total window loss in the microwave output window and is absolutely of the order of 0.1% at 10 Gc. At higher frequencies, this proportion can be expected to increase as the relative amounts of metallizing and ceramic window volume increases. In addition to usage on high power klystrons, the low loss metallizing development in this study can profitably be used on planar triodes and reflex klystrons.
- 2) The dielectric loss for the metallized 99.5% alumina ceramic is approximately one fourth of that due to conduction.
- 3) Dielectric losses introduced due to metallizing paint reactions in 94% alumina can be neglected.
- 4) Low "dielectric" loss metallizing may be produced by using pure molybdenum metallizing on glass containing ceramics; evaporated molybdenum or BaO-SiO<sub>2</sub>-Mo metallizing on glass-free alumina bodies.
- 5) Low "conduction" loss metallizing is achieved by using extremely thin "painted on" metallizing. Thin evaporated metallizing was not low loss. For amenable geometries, a copper to ceramic "crunch" seal is the best.
- 6) A semi-quantitative picture of metallizing behavior which identifies the main parameters, both physical and electrical, which contribute toward making acceptable ceramic-to-metal seals has been developed and is concisely reviewed in the summary, Section 7.0. It was established that chemical and/or semi-conducting bond mechanisms were responsible for the actual joining of the refractory metal to the oxide substrate. For this bonding to occur, either the metal phase had to be deposited on the oxide substrate by vapor phase processes or the oxide phases had to be moved by viscous flow processes (e.g., glassy phase migration) in order that the initial atom-to-atom contact could be made.

- 7) The work on the physical and electrical properties fused together in such a fashion that they complement each other and show that electrical techniques can constitute the most powerful means of investigating the sealing mechanisms associated with ceramic-to-metal seals.
- 8) The study has been mainly concerned with alumina ceramics but it was proven possible to build on the concepts developed, to produce high quality beryllia and quartz seals. It is confidently expected that an expansion of the technology gained can be made to include ceramics such as boron nitride which offers considerable promise as a superior window material. Boron nitride may very well be considered a 4th generation window material in succession to glass, alumina and beryllia sequentially.
- 9) In spite of the optimistic conclusion statements made above, a wide gulf still exists between the knowledge generated to date and the ability to predict the occurrence of highly reliable seals in tubes from first principles. This is because although the principles underlying good ceramic-to-metal seals are known, the multitude of paints and ceramics used in the industry permit an infinite number of physio-chemical reactions to proceed. These reactions, needless to say, have not all been investigated. It is extremely difficult to predict from first principles when a glassy phase will or will not devitrify after reaction with a complex metallizing paint. It is therefore of some importance to develop standard metallizing processes and standard ceramic bodies for use in the industry with well known reproducible characteristics.
- 10) Allied technical areas have benefited, such as heater technology; for instance, one is now able to gain an insight into the mysteries causing heater failure when the polarity of the heater-cathode leads are reversed, to develop printed heaters, ceramic substrates for cathode use and to further understand the 'measles' effect on ceramic surfaces.
- 11) Other technological areas have also benefited, such as those of printed circuit technology, semi-conductor packaging, high temperature ceramic-to-metal seals and a general understanding of ceramic body microstructure and physical chemistry.

## 9.0

## RECOMMENDATIONS

- 1) A detailed picture of ceramic-to-metal sealing processes may be obtained by surveying the eleven quarterly reports and this final report. However, the interpretive analysis presented in earlier reports should be modified by subsequent experimental findings. It is therefore suggested that a monograph on the subject be prepared to update the analysis. The data presented could be augmented by several chapters on the metallurgy of the metal member of the ceramic-to-metal, a subject largely ignored in the present program. A chapter on stress analyses could also be included; as could a chapter on the application of the knowledge gained to semiconductor packaging technique and to printed circuit technology. A special report is in preparation on the latter subject.
- 2) Following the thoughts presented in the ninth point in the conclusions, section 10.0, it is obviously important to further develop the test procedures for seals initiated on this program and to refine stress analysis techniques for predicting seal failure; areas of effort which need serious consideration.
- 3) Boron nitride sealing techniques should be developed; see point 8.

## **10.0**

### **ACKNOWLEDGEMENTS**

The efforts of the following persons, whose contributions enabled the successful completion of the program, are gratefully acknowledged.

J. Mann, D. Boilard, and W. Stolte for their assistance in making VSWR measurements on the waveguide test cells for the high power calorimetric loss measurements and for their help in setting-up and operating the test station and klystron where these measurements were made.

J. Thomson, G. Phillips, and R. Hofheins for the preparation of samples for photomicrographs, electron photomicrographs, electron probe microanalysis, and X-ray diffraction analysis, as well as preparation of test specimens and assemblies for the seal parameters study and the low and high power electrical measurements.

H. Mein and F. Burris for the preparation of evaporated coatings of titanium, molybdenum, and copper on ceramics and fused quartz and for work on other test sample for the seal parameter study.

M. Kosinski for performing the spectrographic analyses.

D. Harding, D. Enochs, B. Vogel, B. Meek and M. Wheatley for preparation of curves and illustrations.

E. Sena and L. Martin for preparation of photographs.



## 11.0 SUBCONTRACTS

The electron probe microanalyses were subcontracted from the first through the ninth quarter to the Center for Materials Research, Stanford University, and were carried out by Mr. G. Martin under the administrative direction of Professor R. Huggins. From the tenth quarter to the end of the program, electron probe microanalyses were performed at Materials Analysis Company, Palo Alto, by Mr. R. Wolf.

X-ray diffraction analyses and electron microscopy were subcontracted to Sloan Research Industries, Inc., Santa Barbara, and were performed by Dr. R. Sloan and Mr. W. Gardner.

The special bodies 992, 942 and 941 were fabricated by Western Gold and Platinum, Belmont, California.

12.0 IDENTIFICATION OF KEY TECHNICAL PERSONNEL

The participants in the Eitel-McCullough program contributed the following time during the period: 1 April through 30 June, 1965.

	<u>Hours</u>
L. Reed	184
W. Wade	486
R. Pape	82
J. Thomson	284
G. Phillips	332
H. Meyn	308

Robin B. Pape  
Research Scientist  
Device Research Laboratory

Mr. Pape received his BA degree in Physics from Hofstra University in 1962. He was employed from 1955 to 1960 in the Electronic Tube Division of Sperry Gyroscope Company where he was assigned to materials evaluation and techniques investigation for the Tube Techniques Section of the Tube Research Department. In 1960, he joined Thomas Electronics as Project Engineer for Microwave Tube Component Development and Production. Upon receiving his degree in 1962, he joined the Magnetron Development Section at Amperex Electronic Corporation.

In 1963, Mr. Pape joined Eitel-McCullough as a Development Engineer with the voltage tunable magnetron group of the Microwave Tube Division.

In 1965, Mr. Pape joined the Device Research Laboratory, Research Division, as a Research Scientist. His present responsibilities are in the area of special device development.

13.0

APPENDIX I

FACTORS INFLUENTIAL IN BONDING CERAMICS TO METALS

(L. Reed)

Summary of Meeting held May 18, 1965, at  
Eitel-McCullough, San Carlos, California.

Those in Attendance were:

S. Leefe, USAECOM, Fort Monmouth, N. J.

O. Heil, Heil Scientific Laboratory

J. White, Sperry, Gainesville, Florida

S. Colgate, Florida University Consultant, Sperry

L. Reed, Eitel-McCullough

Ceramics generally are multi-component systems. For example, in the case of alumina consisting of the crystal phase,  $Al_2O_3$  and a grain boundary glassy phase, formed from silica, calcia, magnesia and other compounds. The latter forms a lower temperature melting phase than the ceramic as a whole.

It is possible for a metal to be placed on such a surface and for bonding to occur to the metal member and the ceramic via a flow of glass from the ceramic onto the metal substrate. A common way of achieving intimate bonding is to substitute metal powder for solid metal sheet in order to provide for a more intimate contact of the metal with the ceramic. When such a powder is placed on the ceramic and is heated to a temperature sufficient to make the glass phase of the ceramic mobile (generally over  $1200^{\circ}C$ ) then the glass will flow out under the action of capillary forces to coat the grains of the sintered molybdenum sponge.

At lower temperatures, i.e.  $1100^{\circ}C$ , the viscosity of the glass may be such that it is unable to flow appreciably

and it may only plastically deform in the vicinity of the metal particles to partially coat them, by what may be termed a "fly paper" effect.

Non-metallic additions are often added to metallizing mixes to lower the viscosity and increase the plasticity of the "melt" layer. Both in high temperature and low temperature, metallizing systems reaction of multi component metallizing mixes with the ceramic will occur. In the former system subsequent diffusion of ions such as  $Mn^{2+}$  will take place up to several 100 microns into the alumina grain boundaries. In the latter system, the diffusion will be localized to a range of several microns and will not be detected necessarily by the electron microprobe techniques.

In both cases, the phenomena so far described is only a part of the complete bonding mechanism. We have thus far provided a means for bringing the metal particles into intimate contact with the non-metallic particles of the system. The ultimate mechanism of bonding the non-metallic phase to the metallic phase requires further elaboration. This bonding may be described in terms of electrical forces. The bond can be a chemical bond (ionic bond) or may be a semi-conducting bond, especially when non-stoichiometric compounds such as  $MnO$ ,  $TiO_2$ , etc. are added to the metallizing mix. Both types of bonds will involve the exchange of electrons.

It is possible that both chemical bonding and semi-conducting bonding might be present at the same point in the system, or different points in the same system, respectively, if the system is not at equilibrium.

In summary, therefore, we should say that the necessary conditions for bonding are that there be intimate contact between the non-metallic and the metallic phase of the system and that a chemical or semi-conducting bond be present to promote satisfactory adherence. Calculations made by Prof. Colgate indicate that the lower limit of the bonding forces are several thousand psi at the metal-melt interface. However, it is felt that these bonding forces are in general an order of magnitude or greater than the forces which actually cause seal failure. It is felt that the mechanism leading to the destruction of conventional type of seals is one of crack initiation at the surface of the solidified melt phase, followed by crack propagation through the solidified melt layer. It is further felt that the bond can be strengthened if crack terminators are placed in the path of the crack to prevent further propagation. Such a crack terminator could be a crystal species such as galaxite,  $\text{MnO} \cdot \text{Al}_2\text{O}_3$ .


The second class of metallizing system is that which is formed by evaporation, ion sputtering or chemical vapor deposition of molybdenum or other metal onto the ceramic

surface. Once again, it is mandatory that intimate contact be established between the metal layer and the alumina substrate. In this case, intimate contact is established because the molybdenum is deposited atom by atom and will seek the lowest energy site on the alumina substrate. In order to achieve uniform deposition over the entire surface, it is important to move the source or the substrate so that shadowing does not occur over any region to be deposited. (This of course is not necessary in the case of chemical vapor deposition.) It is not necessary for the refractory metal being deposited to have the same structure as the underlying substrate for this epitaxial deposition to occur. It is most probable that a gradual transition of properties from the ceramic to the metal will occur, which may or may not incorporate some oxygen in the transition layer depending upon the degree of vacuum employed. We feel it is premature at this point to further discuss the bonding mechanism, but again it could be some type of chemical or semi-conducting bond.

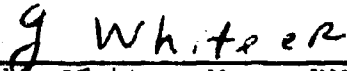
We feel that the meeting between Sperry, Heil Laboratories and Eimac, chaired by Stanley Leefe (USAEL) resulted in a most fruitful discussion and that the areas covered showed that almost complete agreement existed on the subjects discussed. Furthermore, we feel that the

three projects\* display just the correct amount of overlap to give USAEL and the scientific community a basic picture of ceramic-to-metal sealing, upon which to build a firm foundation for further understanding of this complex process.

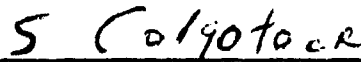
We appreciate the opportunity that has been afforded us by our coming together, and sincerely hope we will be able to repeat this in the future as the occasion warrants.



Len Reed, Mgr., Device Research Lab.  
Eitel-McCullough, Inc.



John White, Mgr. PMDL (Sperry)



Sam Colgate (Florida Univ. Consultant  
Sperry)



Oscar Heil (Heil Laboratories)

---

\*Currently funded at Heil Laboratories, Sperry, Gainesville  
and Eimac, San Carlos.



## 14.0 APPENDIX II

### DETAILED TABLE OF CONTENTS

<u>SECTION</u>	<u>PAGE NO.</u>
1.0 PURPOSE	1
1.1 Purpose of Contract	1
1.2 Objective of Program	1
1.3 Tasks	1
2.0 ABSTRACT	3
3.0 PUBLICATIONS, LECTURES, REPORTS AND CONFERENCES	5
4.0 TASK I, SEAL PARAMETER STUDY	8
4.1 General Ceramic Considerations	10
4.2 Special Ceramics	15
4.2.1 Introduction	15
4.2.2 Microstructure Consider- ations	19
4.2.3 The Glassy Phase	34
4.2.3.1 Molecular Structure	34
4.2.3.2 Composition and Amount	40
4.2.3.2.1 Equilibrium Phase Diagram Studies	43
4.2.3.2.2 Optical and Electron Microscope Studies	44
4.2.3.2.3 Mineralogical Analysis	52
4.2.3.2.4 Electron Microprobe Analysis	60
4.2.3.2.5 Chemical Analysis	61
4.2.3.2.6 Reaction Rate Studies	62
4.2.3.3 Properties of the Glassy Phase	72
4.2.3.3.1 Viscosity	72
4.2.3.3.2 Ionic Diffusion	78
4.2.3.3.3 Thermal Expansion	80
4.2.3.3.4 Contact Angle Studies	85
4.3 Commercial Bodies- Microstructure Considerations	101
4.4 Exploratory Metallizing Studies	107
4.4.1 Introduction	107
4.4.2 The Paint	114
4.4.3 Firing Conditions	114
4.4.4 Sintering of the Metalli- zing	114

<u>SECTION</u>		<u>PAGE NO.</u>
4.4.5	Solution of Molybdenum	120
4.4.6	Adherence	122
4.4.7	Chemical Reduction	123
4.4.8	Glassy Phase Inter- diffusion	129
4.4.9	Composition of the Glassy Phase	138
4.4.10	Seal Strength versus Metallizing Temperature	145
4.4.11	Seal Strength as a Function of Brazing Conditions	147
4.4.12	Initial Metallizing Tests	150
4.4.13	Comments on Sealing Mechanisms	158
4.5	Studies Using the Special Bodies	159
4.5.1	Introduction of Seal Parameter Study	159
4.5.2	Seal Parameter Studies	162
4.5.2.1	Experimental Procedure and Results	162
4.5.2.1.1	Sample Preparation	162
4.5.2.1.2	Scratch Test	164
4.5.2.1.3	Resistance Measurement	166
4.5.2.1.4	Assembly Procedure	166
4.5.2.1.5	Leak Check	169
4.5.2.1.6	Tensile Test	169
4.5.2.1.7	Peel Test	172
4.5.2.1.8	Microstructure Examination	172
4.5.2.2	Analysis of Physical Property Data	172
4.5.2.3	Microstructure Analysis	187
4.5.2.3.1	The Ceramic	188
4.5.2.3.2	The Metallizing	195
4.5.2.3.3	The Plating	197
4.5.2.3.4	The Braze and Metal Member	198
4.5.3	Supplementary Studies	200
4.5.3.1	Bonding Mechanisms	200
4.5.3.1.1	Evaporated Molybdenum	200
4.5.3.1.2	P-2M Metallizing on Sapphire	202
4.5.3.2	Crystal Size Factor	203
4.5.3.3	Glassy Phase De- vitrification	203

<u>SECTION</u>		<u>PAGE NO.</u>
	4.5.3.3.1 First Series	203
	4.5.3.3.2 Second Series	204
	4.5.3.4 Effect of Metal Member	218
	4.5.3.5 Complex Metallizing Paints	218
4.6	Shear Test Study	220
	4.6.1 Sample Geometry	220
	4.6.2 Testing Methods	220
	4.6.3 Test Results and Discussion	222
4.7	References - Task I	227
5.0	TASK II, BERYLLIA AND QUARTZ STUDY	231
5.1	Beryllia Ceramics	231
5.2	Fused Quartz-to-Metal Seals	241
5.3	References - Task II	243
6.0	TASK III - ELECTRICAL STUDIES	244
6.1	General Introduction	244
	6.1.1 Sources of Electrical Loss	244
	6.1.2 Electrical Properties as a Function of Micro-structure and Chemistry	245
	6.1.3 Program of Experimental Studies	248
6.2	d.c. Electrical Measurements	249
	6.2.1 Temperature Coefficient of d.c. Resistivity of Metallizing	249
	6.2.1.1 Relation to Total Seal Losses	249
	6.2.1.2 Experimental Set-up	250
	6.2.1.3 Results	252
	6.2.1.4 Discussion of Results	256
	6.2.1.5 Molybdenum and Melt Phase in Metallizings as Parallel Conductors	273

SECTIONPAGE NO.

6.2.2	Effect of Wetting Layer (Overplate) on the Resistivity of the Metallizing	277
6.2.2.1	Influence of rf Conduc- tion Losses	277
6.2.2.2	Experimental	277
6.2.2.3	Results	279
6.3	rf CONDUCTION LOSS MEASUREMENTS	285
6.3.1	Introduction	285
6.3.2	Selected Measurement Technique	287
6.3.3	Sample Preparation	287
6.3.3.1	The Ceramic	288
6.3.3.2	The Metallizing	288
6.3.3.3	The Plating	288
6.3.3.4	The Brazed Assembly	290
6.3.3.5	The Standard Assembly	291
6.3.4	Equipment and Experi- mental Procedures	291
6.3.4.1	Assembly of Apparatus	291
6.3.4.2	Determination of the Cavity Q	297
6.3.4.3	Operation of rf Admittance Bridge	298
6.3.4.4	Measurement Procedure	299
6.3.5	Equipment Checkout	300
6.3.5.1	Reproducibility as a Function of Time	300
6.3.5.2	Standard Test Piece	303
6.3.5.3	Alignment of Ceramics	303
6.3.5.4	Sensitivity of Micro- meter Reading with Cavity Q	303
6.3.6	Results	306
6.3.6.1	First Series	306
6.3.6.2	Second Series	306
6.3.6.3	Third Series	309
6.3.7	Discussion of Results	316
6.3.7.1	Introduction	316
6.3.7.2	Skin Depth	317
6.3.7.3	Group I	319
6.3.7.4	Group II	320
6.3.7.5	Group III	320
6.3.7.6	Group IV	321

SECTIONPAGE NO.

6.3.7.7	Group V	321
6.3.7.8	Group VI	322
6.3.7.9	Group VII	328
6.3.7.9.1	Sub-Groups 7.A and 7.B	328
6.3.7.9.2	Sub-Group 7.C	332
6.3.7.9.3	Sub-Group 7.D	332
6.3.7.9.4	Sub-Groups 7.E and 7.F	339
6.3.7.9.5	Sub-Group 7.G	344
6.3.7.9.6	Sub-Group 7.G.1	348
6.4	Dielectric Losses	350
6.4.1	Introduction	350
6.4.2	Sample Preparation and Experimental Set-up	353
6.4.2.1	The Cavity	353
6.4.2.2	Sample Preparation	353
6.4.2.3	Measurement Set-up	355
6.4.3	Experimental Procedure and Results	359
6.4.3.1	Series 1	359
6.4.3.2	Series 2	359
6.4.3.3	Series 3	366
6.4.4	Discussion	366
6.4.4.1	Ceramic Losses	366
6.4.4.2	Altered Ceramic Losses	372
6.4.4.3	Pure Metallic Layer on Ceramic	374
6.4.4.4	Conventional Metallizings on Body A and Body H	374
6.4.4.4.1	Pure Metallizing Paint P-2	374
6.4.4.4.2	Complex Metallizing Paint P-1	378
6.4.4.4.3	Leached P-1 Metallizing on Body H	380
6.4.5	Comparison of Various Metallizings on +99% Alumina Bodies	380
6.5	High Power Measurements	390
6.5.1	Introduction	390
6.5.2	Calorimetric Test Cell	391
6.5.3	Cold Testing	397
6.5.4	Calorimetric Instrumentation	398
6.5.4.1	Principles of Calorimetric Measurements	398
6.5.4.2	Preparation of Calori- metric Measurements	398

<u>SECTION</u>		<u>PAGE NO.</u>
6.5.5	Calorimetric Measurements	404
6.5.5.1	Experimental Set-up for High Power Microwave Measurements	404
6.5.5.2	Experimental Procedure	410
6.5.5.3	Results and Discussion	417
6.5.5.3.1	Characteristics of Ceramic-to-Metal Seals Tested in First Test Series	417
6.5.5.3.2	Test Results, Second Series	420
6.5.5.3.3	Discussion of Results	422
6.6	References - Task III	429
7.0	SUMMARY	430
7.1	Introduction	430
7.2	Basic Seal Considerations	430
7.3	Supporting Studies	433
7.4	Electrical Studies	439
8.0	CONCLUSIONS	442
9.0	RECOMMENDATIONS	444
10.0	ACKNOWLEDGEMENTS	445
11.0	SUBCONTRACTS	446
12.0	IDENTIFICATION OF KEY TECHNICAL PERSONNEL	447
13.0	APPENDIX I - Factors Influential in Bonding Ceramics to Metals	449
14.0	APPENDIX II - Detailed Table of Contents	454

UNCLASSIFIED

Security Classification

DOCUMENT CONTROL DATA - R&D		
(Security classification of title, body of abstract and indexing annotation must be entered when the overall report is classified)		
1. ORIGINATING ACTIVITY (Corporate author) EIMAC, A Division of Varian Associates San Carlos, California		2a. REPORT SECURITY CLASSIFICATION <b>UNCLASSIFIED</b> 2b GROUP N/A
3. REPORT TITLE  METALLURGICAL RESEARCH & DEVELOPMENT FOR CERAMIC ELECTRON DEVICES		
4. DESCRIPTIVE NOTES (Type of report and inclusive dates) Final Report - 1 Jul 62 - 30 Jun 65		
5. AUTHOR(S) (Last name, first name, initial)  Reed L.; Wade W.; Vogel S.; McRae R.; Barnes C.		
6. REPORT DATE January 1966	7a. TOTAL NO. OF PAGES 539	7b. NO. OF REFS
8a. CONTRACT OR GRANT NO. DA 36-039 SC-90903 b. PROJECT NO. OST-7900-21-223-15 c. d.	9a. ORIGINATOR'S REPORT NUMBER(S)  TR-66-1 9b. OTHER REPORT NO(S) (Any other numbers that may be assigned this report)	
10. AVAILABILITY/LIMITATION NOTICES  Distribution of this document is unlimited.		
11. SUPPLEMENTARY NOTES Sponsored by Advanced Research Projects Agency	12. SPONSORING MILITARY ACTIVITY U. S. Army Electronics Command Fort Monmouth, New Jersey AMSEL-KL-TQ 07713	
13. ABSTRACT  See attached sheet		

DD FORM 1473  
1 JAN 64

UNCLASSIFIED

Security Classification

13.     ABSTRACT

Fifteen special 94% and 99% alumina ceramics in the system  $\text{SiO}_2\text{-CaO-Al}_2\text{O}_3$  with a  $\text{SiO}_2/\text{CaO}$  ratio of 1:1 and 2:1 were fabricated and their behavior characterized. A combination of phase diagram interpolations, density and strength determinations, optical and electron microscope planimetric and crystal growth studies, X-ray diffraction and electron microprobe studies, and chemical analysis of their glassy phases, established that equilibrium was very nearly reached at their maturing temperature. Cooling tended to freeze in the high temperature state although crystal phases such as anorthite, gehlenite and calcium hexaluminate were partially precipitated in some cases.

It was tentatively established that the rate determining mechanism of alumina solution both during the initial processing of the ceramic and during its subsequent reaction during metallizing with refractory metal paints containing oxide additions, was the chemical reaction rate.

The composition of the bulk and surface grain boundary phases of the ceramic was used to determine the viscosity of its melt phase. This, in turn, was used to predict the occurrence of highly electrical conductive, high strength, vacuum tight, ceramic-to-metal seals when metallized with a pure metal paint. Devitrification, thermal expansion, sintering, surface energy, dissolution, diffusion, crystal size, microscope, X-ray diffraction, electron microprobe and spectrographic studies were also used to predict the occurrence of high and low strength vacuum tight ceramic-to-metal seals on the twelve complex metallizing paint systems investigated.

Lucalox\*, sapphire, beryllia and fused quartz vacuum tight seals were made and their sealing mechanisms were examined as were those of several commercial alumina ceramics.

It was established that chemical and/or semi-conducting bond mechanisms were responsible for the actual sealing process of refractory metal to the oxide substrate.

---

\*General Electric Company trade name for a 99.75% alumina body.



For this bonding to occur either the metal phase had to be deposited on the oxide substrate by vapor phase processes or the oxide phases had to move by viscous flow processes (e.g., glassy phase migration) in order that the initial atom to atom contact could be made.

The electrical studies included dc resistance measurements, low power rf conduction and dielectric loss studies, and high power loss studies. It was shown that the metallizing layer is made up of metallic, semi-conductive and insulating layers. Conduction losses are minimized by using thin metallizing and a copper braze. Dielectric losses are only important for +99% aluminas and they account for a quarter of the total metallizing losses. The total metallizing losses are about 25% of the total window losses which, in turn, are about 0.3% of the transmitted power at 10 Gc.

In addition to usage on high power klystrons, the low loss metallizing development in this study can profitably be used on planar triodes and reflex klystrons.

UNCLASSIFIED

Security Classification

14. KEY WORDS	LINK A		LINK B		LINK C	
	ROLE	WT	ROLE	WT	ROLE	WT
Seals Ceramic-Metal Electron Tubes rf Seal Losses Windows, Microwave Microprobe Metallizing Paints						

## INSTRUCTIONS

1. **ORIGINATING ACTIVITY:** Enter the name and address of the contractor, subcontractor, grantee, Department of Defense activity or other organization (*corporate author*) issuing the report.

2a. **REPORT SECURITY CLASSIFICATION:** Enter the overall security classification of the report. Indicate whether "Restricted Data" is included. Marking is to be in accordance with appropriate security regulations.

2b. **GROUP:** Automatic downgrading is specified in DoD Directive 5200.10 and Armed Forces Industrial Manual. Enter the group number. Also, when applicable, show that optional markings have been used for Group 3 and Group 4 as authorized.

3. **REPORT TITLE:** Enter the complete report title in all capital letters. Titles in all cases should be unclassified. If a meaningful title cannot be selected without classification, show title classification in all capitals in parenthesis immediately following the title.

4. **DESCRIPTIVE NOTES:** If appropriate, enter the type of report, e.g., interim, progress, summary, annual, or final. Give the inclusive dates when a specific reporting period is covered.

5. **AUTHOR(S):** Enter the name(s) of author(s) as shown on or in the report. Enter last name, first name, middle initial. If military, show rank and branch of service. The name of the principal author is an absolute minimum requirement.

6. **REPORT DATE:** Enter the date of the report as day, month, year, or month, year. If more than one date appears on the report, use date of publication.

7a. **TOTAL NUMBER OF PAGES:** The total page count should follow normal pagination procedures, i.e., enter the number of pages containing information.

7b. **NUMBER OF REFERENCES:** Enter the total number of references cited in the report.

8a. **CONTRACT OR GRANT NUMBER:** If appropriate, enter the applicable number of the contract or grant under which the report was written.

8b, 8c, & 8d. **PROJECT NUMBER:** Enter the appropriate military department identification, such as project number, subproject number, system numbers, task number, etc.

9a. **ORIGINATOR'S REPORT NUMBER(S):** Enter the official report number by which the document will be identified and controlled by the originating activity. This number must be unique to this report.

9b. **OTHER REPORT NUMBER(S):** If the report has been assigned any other report numbers (*either by the originator or by the sponsor*), also enter this number(s).

10. **AVAILABILITY/LIMITATION NOTICES:** Enter any limitations on further dissemination of the report, other than those imposed by security classification, using standard statements such as:

- (1) "Qualified requesters may obtain copies of this report from DDC."
- (2) "Foreign announcement and dissemination of this report by DDC is not authorized."
- (3) "U. S. Government agencies may obtain copies of this report directly from DDC. Other qualified DDC users shall request through \_\_\_\_\_."
- (4) "U. S. military agencies may obtain copies of this report directly from DDC. Other qualified users shall request through \_\_\_\_\_."
- (5) "All distribution of this report is controlled. Qualified DDC users shall request through \_\_\_\_\_."

If the report has been furnished to the Office of Technical Services, Department of Commerce, for sale to the public, indicate this fact and enter the price, if known.

11. **SUPPLEMENTARY NOTES:** Use for additional explanatory notes.

12. **SPONSORING MILITARY ACTIVITY:** Enter the name of the departmental project office or laboratory sponsoring (*paying for*) the research and development. Include address.

13. **ABSTRACT:** Enter an abstract giving a brief and factual summary of the document indicative of the report, even though it may also appear elsewhere in the body of the technical report. If additional space is required, a continuation sheet shall be attached.

It is highly desirable that the abstract of classified reports be unclassified. Each paragraph of the abstract shall end with an indication of the military security classification of the information in the paragraph, represented as (TS), (S), (C), or (U).

There is no limitation on the length of the abstract. However, the suggested length is from 150 to 225 words.

14. **KEY WORDS:** Key words are technically meaningful terms or short phrases that characterize a report and may be used as index entries for cataloging the report. Key words must be selected so that no security classification is required. Identifiers, such as equipment model designation, trade name, military project code name, geographic location, may be used as key words but will be followed by an indication of technical context. The assignment of links, rules, and weights is optional.

UNCLASSIFIED

Security Classification